Modelling continental rift dynamics

Habilitationsschrift

zur Erlangung des akademischen Grades
Doctor rerum naturalium habilitatus (Dr. rer. nat. habil.)
in der Wissenschaftsdisziplin Geophysik

eingereicht an der
Mathematisch-Naturwissenschaftlichen Fakultät
der Universität Potsdam

von

Sascha Brune

geboren am 1. Februar 1980
in Waren (Müritz)

Potsdam, September 2018

Published online at the
Institutional Repository of the University of Potsdam:
https://doi.org/10.25932/publishup-43236
https://nbn-resolving.org/urn:nbn:de:kobv:517-opus4-432364

This thesis is dedicated to my parents.

Content

Summary 7

Chapter I - Introduction 9

1. Rifts and Rifted Margins 10
2. Previous Approaches in Rift Modelling 14
3. Rift processes, forces, strength 19
4. Rift dynamics: Previews insights and open questions 21

Chapter II - 2D Models 35

Rift migration explains continental margin asymmetry and crustal hyper-extension 36

Rifted Margin Architecture and Crustal Rheology: Reviewing Iberia-Newfoundland, Central South Atlantic, and South China Sea 45

Climate changes control offshore crustal structure at South China Sea continental margin 70

Abrupt plate accelerations shape rifted continental margins 77

Chapter III - 3D Models 93

Controls of inherited lithospheric heterogeneity on rift linkage: Numerical and analogue models of interaction between the Kenyan and Ethiopian rifts across the Turkana depression 94

Modelling suggests that oblique extension facilitates rifting and continental break-up 114

Oblique rifting of the Equatorial Atlantic: Why there is no Saharan Atlantic Ocean 130

Evolution of stress and fault patterns in oblique rift systems: 3D numerical lithospheric-scale experiments from rift to breakup 134

Chapter IV - Global Analyses 158

Oblique rifting: the rule, not the exception. 159

Potential links between continental rifting, CO_2 degassing and climate change through time 185

Summary

Continental rift systems open up unique possibilities to study the geodynamic system of our planet: geodynamic localization processes are imprinted in the morphology of the rift by governing the time-dependent activity of faults, the topographic evolution of the rift or by controlling whether a rift is symmetric or asymmetric. Since lithospheric necking localizes strain towards the rift centre, deformation structures of previous rift phases are often well preserved and passive margins, the end product of continental rifting, retain key information about the tectonic history from rift inception to continental rupture.

Current understanding of continental rift evolution is based on combining observations from active rifts with data collected at rifted margins. Connecting these isolated data sets is often accomplished in a conceptual way and leaves room for subjective interpretation. Geodynamic forward models, however, have the potential to link individual data sets in a quantitative manner, using additional constraints from rock mechanics and rheology, which allows to transcend previous conceptual models of rift evolution. By quantifying geodynamic processes within continental rifts, numerical modelling allows key insight to tectonic processes that operate also in other plate boundary settings, such as mid ocean ridges, collisional mountain chains or subduction zones.

In this thesis, I combine numerical, plate-tectonic, analytical, and analogue modelling approaches, whereas numerical thermomechanical modelling constitutes the primary tool. This method advanced rapidly during the last two decades owing to dedicated software development and the availability of massively parallel computer facilities. Nevertheless, only recently the geodynamical modelling community was able to capture 3D lithospheric-scale rift dynamics from onset of extension to final continental rupture.

The first chapter of this thesis provides a broad introduction to continental rifting, a summary of the applied rift modelling methods and a short overview of previews studies. The following chapters, which constitute the main part of this thesis feature studies on plate boundary dynamics in two and three dimension followed by global scale analyses (Fig. 1).

Chapter II focuses on 2D geodynamic modelling of rifted margin formation. It highlights the formation of wide areas of hyperextended crustal slivers via rift migration as a key process that affected many rifted margins worldwide. This chapter also contains a study of rift velocity evolution, showing that rift strength loss and extension velocity are linked through a dynamic feed-back.

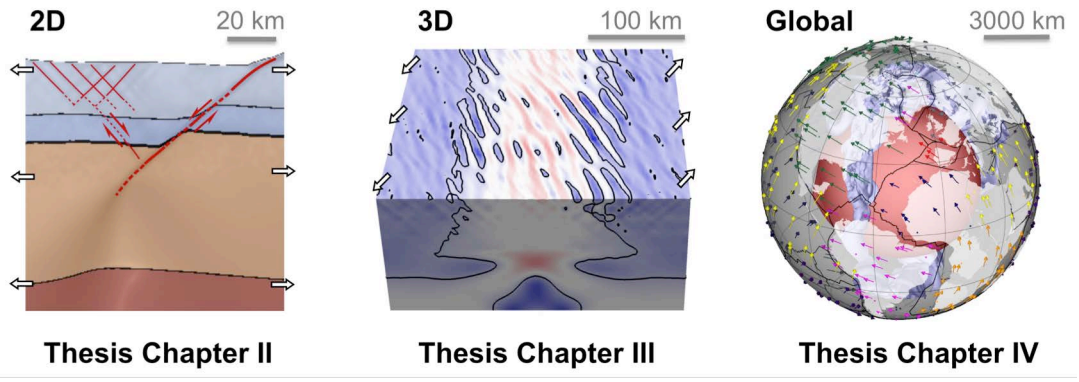

Fig. 1: Structure of the thesis
Apart from the introductory chapter, this thesis is divided in three parts focussing on 2D and 3D rift dynamics as well as on global scale.

This process results in abrupt accelerations of the involved plates during rifting illustrating for the first time that rift dynamics plays a role in changing global-scale plate motions. Since rift velocity affects key processes like faulting, melting and lower crustal flow, this study also implies that the slow-fast velocity evolution should be imprinted in rifted margin structures.

Chapter III relies on 3D Cartesian rift models in order to investigate various aspects of rift obliquity. Oblique rifting occurs if the extension direction is not orthogonal to the rift trend. Using 3D lithospheric-scale models from rift initialisation to breakup I could isolate a characteristic evolution of dominant fault orientations. Further work in Chapter III addresses the impact of rift obliquity on the strength of the rift system. We illustrate that oblique rifting is mechanically preferred over orthogonal rifting, because the brittle yielding requires a lower tectonic force. This mechanism elucidates rift competition during South Atlantic rifting, where the more oblique Equatorial Atlantic Rift proceeded to breakup while the simultaneously active but less oblique West African rift system became a failed rift. Finally this Chapter also investigates the impact of a previous rift phase on current tectonic activity in the linkage area of the Kenyan with Ethiopian rift. We show that the along strike changes in rift style are not caused by changes in crustal rheology. Instead the rift linkage pattern in this area can be explained when accounting for the thinned crust and lithosphere of a Mesozoic rift event.

Chapter IV investigates rifting from the global perspective. A first study extends the oblique rift topic of the previous chapter to global scale by investigating the frequency of oblique rifting during the last 230 million years. We find that approximately 70% of all ocean-forming rift segments involved an oblique component of extension where obliquities exceed 20°. This highlights the relevance of 3D approaches in modelling, surveying, and interpretation of many rifted margins. In a final study, we propose a link between continental rift activity, diffuse CO_2 degassing and Mesozoic/Cenozoic climate changes. We used recent CO_2 flux measurements in continental rifts to estimate worldwide rift-related CO_2 release, which we based on the global extent of rifts through time. The first-order correlation to paleo-atmospheric CO_2 proxy data suggests that rifts constitute a major element of the global carbon cycle.

Chapter I - Introduction

1. Rifts and Rifted Margins

The Earth below our feet is constantly shaped by geodynamic processes that deform the crust and mantle of our planet. These processes are responsible for fragmenting Earth's surface into tectonic plates by focusing most of the surface deformation to plate boundaries like rifts, but also mid ocean ridges, or subduction zones. Deciphering geodynamic processes is highly challenging because they often transcend a large range of spatial scales (Fig. 1): plate tectonics is driven by convection cells with a size of ~3000 km, but at Earth's surface, the majority of strain is focused in relatively narrow plate boundaries such as rift zones of ~100 km width, which are further separated in individual horsts and grabens with a width of ~1 to 20 km.

In continental rift systems, Earth's crust is dissected by brittle faults, ductile shear zones, and magmatic activity that may finally lead to continental rupture and the formation of a new ocean basin. The East African Rift system features snapshots of several characteristic phases for the evolution of continental rifts (Fig. 2, Corti, 2009; Ebinger and Scholz, 2011; Ring, 2014). The Okavango rift for instance represents a very early rift stage where initial normal faults link up along-strike in successively forming immature border faults (Kinabo et al., 2008). Further north, the Kenya rift features an intermediate rift stage where movement on impressive border faults has lead to rift flank uplift and the formation of a pronounced axial rift valley. Continental extension in the Afar region, however, illustrates the later stages of continental rifting (Bastow and Keir, 2011) with extensive magma-assisted rifting over an unusually hot mantle (Armitage et al., 2015). Once continental rupture is achieved, the newly formed margins of the continents are no longer part of the global plate boundary network. The tectonic activity decreases, which is why these areas are often termed passive margins. Since the breakup of Pangea, more than 100,000 km of passive continental margins have been formed, which makes them the most common tectonic features on Earth, two times longer than subduction zones and mid-oceanic spreading centres (Bradley, 2008). Many of those margins are covered with thick sedimentary packages that not only host georesources, but also provide a valuable record of syn-rift tectonic activity and of post-rift vertical motion. However, not all rifts proceed to breakup and many so-called failed or aborted rifts can be found within the continents, for instance the Mid-continental rift in North America (Merino et al., 2013), the North Sea in Europe (Bell et al., 2014) or the West and Central African rifts (Guiraud and Maurin, 1992).

The breakup of Pangea, Earth's latest supercontinent, commenced in early Mesozoic times around 250 million years ago and is by far the best-documented supercontinent fragmentation. This long-lasting event has been reconstructed plate tectonically by linking global marine geophysical observations with regional data sets providing a detailed kinematic history of plate motion (e.g. Müller et al., 2016). Pangea breakup started in Triassic times at around 240 million years ago (Ma) with the Central Atlantic rift

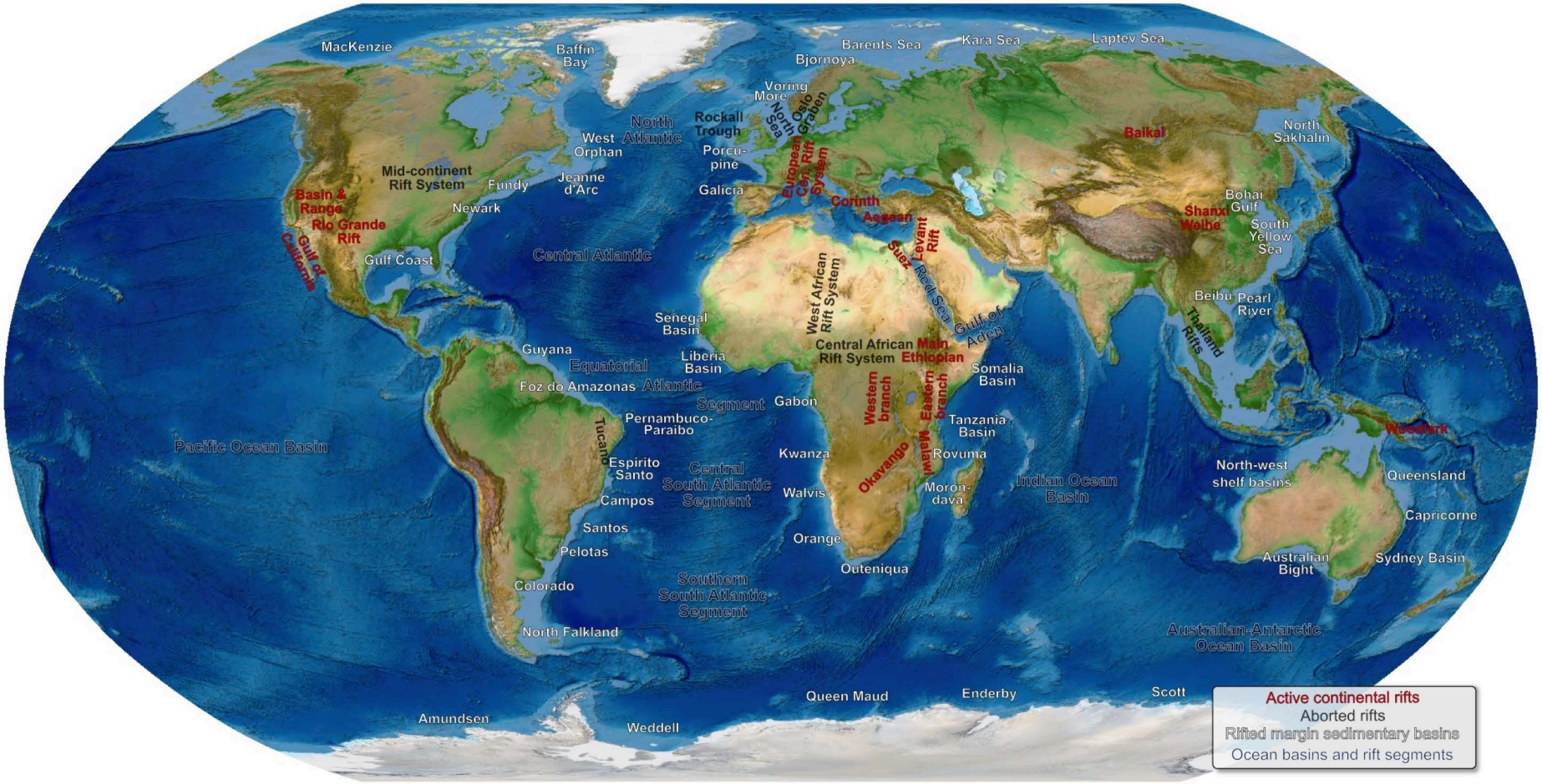

Fig. 2: Continental rifts and rifted margins overview.
The world map depicts major presently active rifts, rifted margin basins along with aborted rift systems. The names of the rift basins are based on Meyer et al. [2007]. The background map is a modified topographic image of Etopo1 [Amante and Eakins, 2009].

splitting Gondwana in the south from Laurasia in the north (Fig. 3). During the Jurassic, Gondwana separated into West Gondwana (South America, Africa, Arabia) and East Gondwana (Antarctica, Australia, India, Madagascar) along the East African continental margin. The most extensive global rift episode of the Phanerozoic however occurred in the early Cretaceous between 140 and 110 million years ago, with simultaneous extension within all post-Pangea landmasses. During this time, rifting occurred between India and Antarctica, Australia and Antarctica, Africa and South America, as well as North America and Eurasia. Continental rifting between North America, Greenland and Eurasia involved a protracted extension history, with final breakup along the sheared margins of Spitsbergen and Greenland occurring only in Miocene times (Jakobsson et al., 2007). At present continental breakup occurs in the Red Sea (Augustin et al., 2014) and the Woodlark rift (Taylor et al., 1995; Eilon et al., 2015), while active rifting is taking place for instance in the East African rift (Ebinger and Scholz, 2011), the Rio Grande rift (Ricketts et al., 2016), or in the Gulf of Corinth (Bell et al., 2011).

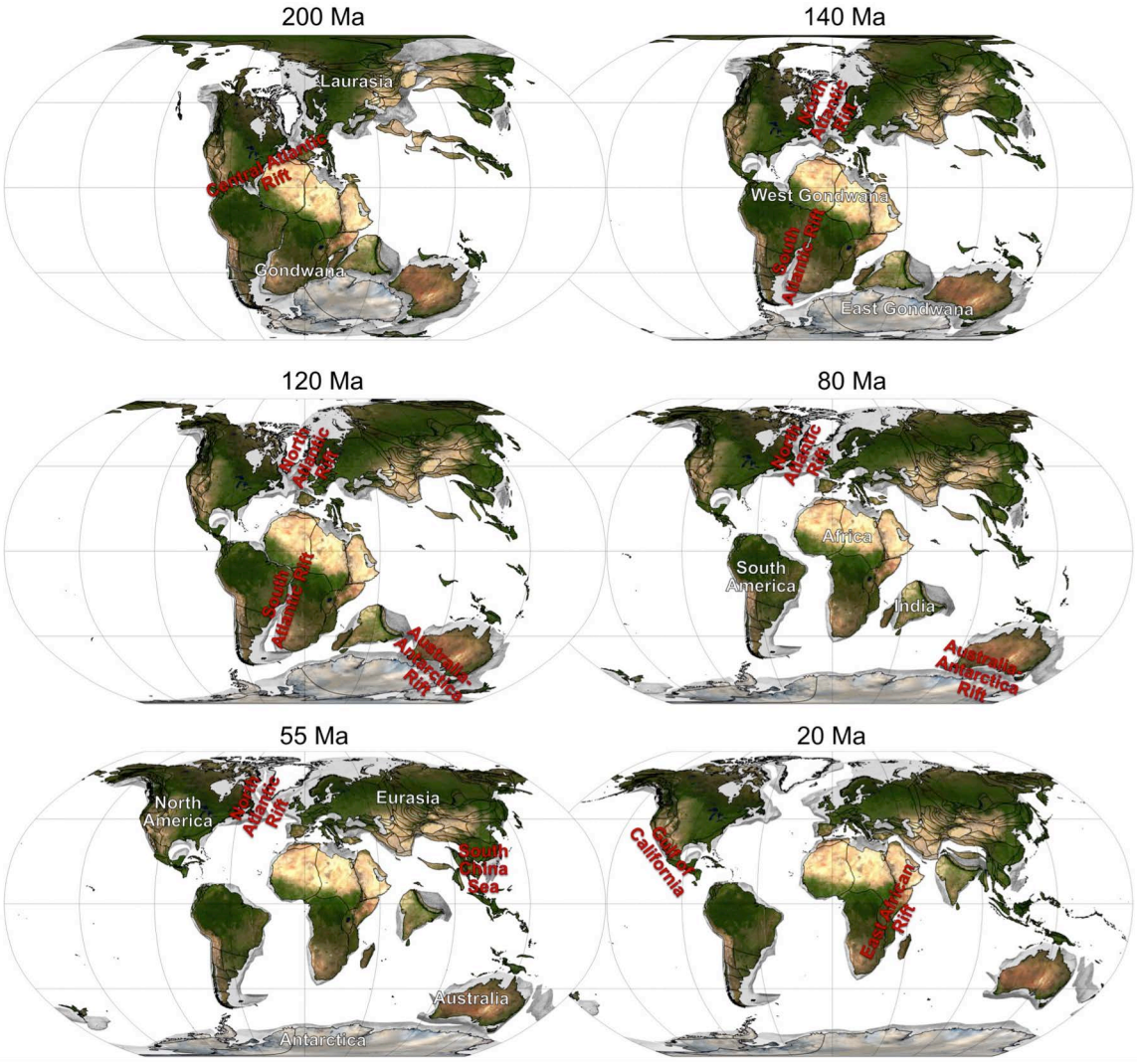

Fig. 3: Plate motion and major rift episodes since 200 Ma.
Major active rift systems are annotated in red, continental landmasses in white. Black contour lines depict present-day coastlines and intra-continental tectonic boundaries. For reference only, continents show present-day vegetation and ice cover. All polygons and rotations are from Müller et al. (2016) reconstructed using GPlates.

Different classifications of continental rifts (Şengör and Natal'in, 2001; Ziegler and Cloetingh, 2004) have been based on (1) the tectonic setting, (2) the width of a rift, and (3) the degree of involved magmatism. In the following I summarize these three classifications and their key characteristics.

The first classification according to the tectonic setting involves four rift types: (1) intra-continental rifts, (2) back-arc rifts, (3) syn-orogenic rifts, and (4) post-orogenic rifts. *Intra-continental rifting* often takes place along old suture zones within continents and may induce breakup of the continent forming a new oceanic basin. The Pangea-dissecting rifts mentioned above and the present-day East African rift system belong to this type of rift. *Back-arc rifting* takes place in continental lithosphere adjacent to subduction zones and reflects the time-dependent history of subduction where rift kinematics are governed by mantle wedge dynamics, mantle flow, and slab properties (Sdrolias and Müller, 2006; Sternai et al., 2014). Back-arc extension may result in short phases of extension that are often overprinted by later compression such as in the Andes (Maloney et al., 2013). In other cases however, back-arc rifting my actually lead to crustal break-up and the formation of marginal ocean basins like in the case of the Mediterranean (Faccenna et al., 2001; Magni et al., 2014), the Sea of Japan (Van Horne et al., 2017), or the South China Sea (Cullen et al., 2010). But these smaller oceanic back-arc basins tend to be not as long-lived as major ocean basins and are often closed again following changes in the tectonic configuration of the subduction zone. *Syn-orogenic rifting* is induced by changes in the lithospheric stress field due to mountain building, such as the Upper Rhine Graben that is thought to be caused by the Alpine collision (Schumacher, 2002) and the Baikal rift where a pre-existing shear zone has been reactivated by the India-Eurasia collision (Logatchev and Zorin, 1992; Petit and Déverchère, 2006). *Post-orogenic rifting* occurs when hot and over-thickened crust of young orogenic belts collapses gravitationally. This process takes place for instance in the Himalayan–Tibetan orogen (Yin, 2010; Pang et al., 2018), and the North American Basin and Range province (Hamilton, 1987; Tirel et al., 2008). The latter became a type example where large amounts of extension localized in a wide array of normal faults (Wernicke, 1985).

The second type of classification refers to the width of a continental rift, which constitutes an important but easily accessible observable. In *wide rifts* like those of the Basin and Range or the Aegean Sea, a broad array of normal faults creates alternating horst and graben morphology. Slip along individual faults does not lead to Moho uplift, but is instead compensated by lower crustal flow, eventually leading to the formation of continental core complexes (Whitney et al., 2013; Brun and Sokoutis, 2018). *Narrow rifting* with a width less than 100 km, takes place if crust and mantle are coupled, which produces few large faults cutting through the entire crust. This style of rifting is representative for large parts of the East African rift (Ebinger et al., 1999), the Baikal rift (van der Beek, 1997), the Rhine Graben (Brun and Wenzel, 1991; Michon and Merle, 2000), and the Rio Grande rift (Ricketts et al., 2016). Since passive margins are formed during rift evolution one might expect that wide rifts generate wide margins while narrow rifts produce narrow margins. Indeed

this arguments seems to be correct for wide margin pairs like the South China Sea (e.g. Franke et al., 2014). However there are many examples that do not fit this scheme because they feature conjugates margins where one is wide and the other narrow such as the Iberia-Newfoundland rift (Ranero and Pérez-Gussinyé, 2010; Sutra and Manatschal, 2012), the central South Atlantic (Blaich et al., 2009; Unternehr et al., 2010), the North Atlantic (Lundin and Doré, 2011), Australia-Antarctica rift (Direen et al., 2012; Espurt et al., 2012), as well as Eastern Australia and the Lord Howe Rise (Lister et al., 1991). This observed margin asymmetry suggests a more complex evolution of margin formation that appears to occur quite frequently.

A third and common way of classifying rifts distinguishes between non-volcanic rifts (e.g. Baikal or the western branch of the East African rift system) and volcanic rifts (e.g. Afar or Kenya), which are often used as analogue cases for the early rift evolution of magma-poor and magma-rich rifted margins. A clear-cut value for the amount of volcanism to differentiate between volcanic and non-volcanic rifts does not exist. But it is clear that even the non-volcanic Baikal rift exhibits some degree of melting at depth, which is capable of compensating crustal thinning (Thybo and Nielsen, 2009). Despite this caveat, there are a few key differences between the magma-rich and magma-poor types that are especially visible in the post-breakup configuration at rifted margins. *Magma-rich rifted margins* feature anomalously thick (>10 km) oceanic crust and significant amounts of volcanic flows (Mutter et al., 1982; Eldholm et al., 2000). They are often associated with mantle plumes and the emplacement of large igneous provinces (Coffin and Eldholm, 1994; Menzies et al., 2002). Well-studied examples of magma-rich margins comprise the North Atlantic conjugates (Mjelde et al., 2008; Brown and Lesher, 2014; Koptev et al., 2017), the west Indian margin (Minshull et al., 2008; Armitage et al., 2012; Nemčok and Rybár, 2017), and the southern South Atlantic (Blaich et al., 2009; Becker et al., 2014). *Magma-poor rifted margins* obviously exhibit minor intrusions during crustal thinning. The following margins have been proposed to belong to this category: the Iberia-Newfoundland conjugates (Hopper et al., 2004; Reston, 2007), the central South Atlantic segment (Contrucci et al., 2004; Aslanian et al., 2009), the South China Sea (Franke, 2013; Zhou and Yao, 2009), and the eastern Gulf of Aden (Leroy et al., 2012). In addition to the low amount of magma these margins also feature wide areas of highly stretched (so-called hyper-extended) continental crust with a thickness of less than 10 km, where crust and mantle deformation appears to be tightly coupled (Ranero and Pérez-Gussinyé, 2010; Mohn et al., 2014). This classification becomes even more complex when considering temporal evolution: an initial rift stage may feature magma-poor characteristics, while a later rift phase may involve large amounts of volcanism.

2. Previous Approaches in Rift Modelling

Unravelling the dynamics of plate boundary deformation is intrinsically complex. On one hand this is due to the cross-scale nature of plate boundaries deformation that includes strain localization on grain-size level, the evolution of brittle faults and ductile shear zones, the deformation of crust

and lithosphere as well as the connection to large-scale mantle convection. On the other hand, many different processes affect plate boundary dynamics including for instance solid-state creep, fracturing, melting, hydrothermal convection, isostasy and dynamic topography, as well as erosion and sedimentation. Geodynamic modelling necessarily involves simplification of the natural complexity, while the employed assumptions need to correspond to the individual research question and the involved spatial and temporal scales. With respect to rift dynamics, four different kinds of modelling approaches have been very successful in isolating relevant processes and key parameters: (1) analogue, (2) analytical, (3) numerical, and (4) plate tectonic modelling. In the following, I briefly summarize each of these modelling approaches with respect to rift dynamics. In Chapters II-IV of this thesis, I will employ all of these approaches, but with numerical modelling being the primary tool.

2.1. Analogue modelling

In analogue experiments, ductile or brittle deformation is reproduced using materials like silicon putty or sand, respectively. In nature, geodynamic processes operate on spatial scales of tens to hundreds of kilometres and on temporal scales of thousands to millions of years. In analogue experiments these processes are scaled to the laboratory environment, i.e. spatial scales of ~0.01 to 1 m with a duration of minutes to days (Hubbert, 1937). This necessitates the use of materials with dynamically similar behaviour so that the relative impact of individual processes is analogous to the natural case.

One type of analogue rift model focuses on the evolution of fault patterns by using of setup with a single brittle layer reminiscent of the brittle upper crust (e.g. Withjack and Jamison, 1986; Tron and Brun, 1991; Mart and Dauteuil, 2000; Corti et al., 2003; Sokoutis et al., 2007). While this setup is relatively easy to build and reproduce, it has the disadvantage of not accounting for isostasy, which limits the experiment to the early rift stages. This problem is overcome in lithospheric-scale models that include a layer representing the asthenosphere. Including isostatic compensation in the model asthenosphere opens the possibility to investigate rift evolution from inception to intermediate rift stages (Corti, 2008; Autin et al., 2010; Nestola et al., 2013; Molnar et al., 2017).

2.2. Analytical modelling

First powerful analytical approaches to model the evolution of rifts and sedimentary basins date back to the late 70s and early 80s addressing the thermal evolution of an extensional basin. Analytical modelling is the most transparent method since all assumptions and derivations can be captured through mathematical formulation. Another advantage of analytical solution is that they can be evaluated quasi-instantaneously on computers, which makes them an efficient ingredient in more complex numerical models. Unfortunately, this speed comes at a high price, since only very simple problems can be resolved through purely analytical methods.

One of the first analytical rift models computes the subsidence and heat flow during pure-shear continental extension (McKenzie, 1978) with dramatic impact on the academic community. Shortly thereafter, Royden and Keen (1980) provided an analytical formulation for depth-dependent extension, which appears to better capture the subsidence evolution at some rifted margins. These two models, however assumed that the lithosphere thins instantaneously and a time-dependent element was incorporated into the uniform thinning model (Jarvis and McKenzie, 1980). A more detailed formulation of the time-dependent extension however has been brought forward that models continental rifting as a series of discrete stretching events, each separated by a period of cooling (Karner et al., 1997).

2.3. Numerical modelling

Almost in parallel with the analytical methods, numerical approaches for rift tectonics were developed (e.g. Beaumont et al., 1982; England and McKenzie, 1982; Houseman and England, 1986). Transcending the tight constraints of analytical methods, these new numerical models allowed for more complex geometries, non-linear rheologies, radiogenic and shear heating within a self-consistent dynamic framework.

Recently, this branch of rift modelling has seen extensive development of new codes and their application to various rift settings and processes (e.g. Lavier and Manatschal, 2006; Pérez-Gussinyé et al., 2006; Buiter et al., 2008; Schmeling, 2010; Petersen et al., 2010; Wallner and Schmeling, 2010; Huismans and Beaumont, 2011; Beaumont and Ings, 2012; Liao and Gerya, 2014; Davis and Lavier, 2017; Naliboff et al., 2017; Korchinski et al., 2018; Armitage et al., 2018). All of these studies, however, represent rifting as a 2D process. While this assumption is correct for some cylindrical rift segments, one needs to carefully assess whether the conclusions of these 2D models still hold in three dimensions.

When accounting for 3D deformation, however, the computational effort rises dramatically, which often puts severe limits on the spatial model resolution. One approach to deal with that problem, is to focus on 3D crustal deformation only, which neglects crust-mantle coupling and deep isostatic compensation and thus limits the approach to wide rift systems or to the very first rift stage (Katzman et al., 1995; Allken et al., 2011). However, 3D lithospheric-scale setups including complex non-linear rheologies became feasible recently, due to intensive numerical model development and advances in parallelising geodynamic modelling software (van Wijk, 2005; Petrunin and Sobolev, 2008; Le Pourhiet et al., 2012; Burov and Gerya, 2014; Liao and Gerya, 2015; Koptev et al., 2015; Ammann et al., 2017; Duclaux et al., 2017; Mondy et al., 2017; Le Pourhiet et al., 2018). Selected results of previous key 2D and 3D models will be discussed along with the topic of this thesis in the following sections.

Numerical geodynamic code [SLIM3D]

In this thesis I use the software SLIM3D (Semi-Lagragian Implicit Model for 3 Dimensions), our in-house code developed by Popov and Sobolev (2008). SLIM3D allows studying the time-dependent evolution of lithospheric-scale tectonic systems in two and three dimensions. It combines thermal processes within the lithosphere (heat conduction, radiogenic heat generation, shear heating) and the three fundamental processes of rock deformation (brittle failure, elastic straining, viscous flow) in a joint thermo-mechanical solution.

SLIM3D uses the Arbitrary Lagrangian-Eulerian Method (ALE) to solve the thermo-mechanically coupled conservation equations of momentum, energy, and mass. The code features a free surface at the top boundary, kinematic or constant force boundary conditions at the sides, while at the bottom boundary isostatic equilibrium is realized by means of the Winkler foundation, where in- and outflow of material is accounted for (e.g. Gerya, 2010). Remeshing is conducted in order to track the motion of the free surface and to avoid large grid distortion. During remeshing, we use the particle-in-cell method in order to resolve advection of the material phases and history variables, like accumulated strain.

Since SLIM3D involves an elasto-visco-plastic rheology formulation, it can reproduce a wide range of lithospheric deformation processes like faulting, flexure and lower crustal flow. The viscous strain rate component simultaneously accounts for two creep mechanisms: diffusion and dislocation creep. Brittle deformation is incorporated using the Mohr-Coulomb failure model. Moreover, SLIM3D includes full compressibility, linear elasticity, and shear heating, viscous and frictional strain softening, and power-law related strain rate softening. Importantly, all simulations are strictly based on experimental rheological data for major rock types.

2.4. Plate tectonic modelling

Tectonic reconstructions of past plate motion incorporate a wealth of geotectonic data collected during marine magnetic surveys, geochronological measurements from dredged or drilled rocks, from satellite missions and geological field studies (e.g. Torsvik et al., 2009; Moulin et al., 2010; Müller et al., 2016, 2018; Nirrengarten et al., 2018). Together, these data sets can be used to investigate the kinematic history of Earth's tectonic plates within the last several hundred million years and ultimately to elucidate the underlying processes that drive plate tectonics.

The classic approach to deduce the relative motions between two divergent plates is through the oceanic domains, since oceanic magnetic anomalies and gravity data are key observables that can be used to precisely date and reconstruct the sea floor spreading history (Wessel and Müller, 2015). During the continental rift stage, i.e. prior to the establishment of a mid-ocean ridge, the powerful field data from the ocean floor are missing, which obscures the kinematic history of past rift systems.

Restoring the pre-rift continental configuration of two plates requires an estimate of the amount of syn-rift thinning, which can be based on present-day crustal thickness (Kneller et al., 2012; Williams et al., 2011). The time of rift inception can be deduced from different lines of evidence, for instance the age of the oldest syn-rift sediment layers or rift-associated volcanism. In order to quantify the magnitude and the direction of the rift velocity one needs to carefully consider a diverse range of geological indicators such as dates of exhumed and volcanic rocks, seismic tectono-stratigraphy, and also from geotectonic markers within plate boundary sections outside of the rift zone (Heine et al., 2013; Sutra et al., 2013). Regional syn-rift plate kinematic models became available recently for the opening of the North, South, and Central Atlantic (Barnett-Moore et al., 2016; Kneller et al., 2012; Heine et al., 2013, respectively), for Australia-Antarctica rifting (Williams et al., 2011), the South China Sea opening (Zahirovic et al., 2014) and for the Gulf of California (McQuarrie and Wernicke, 2005).

An asset of these syn-rift tectonic models is that the associated rift velocities and directions provide testable predictions for geophysical observations such as crustal scale fault heaves, seismic stratigraphy, or well-derived subsidence rates (Ranero and Pérez-Gussinyé, 2010; Cowie et al., 2015). Moreover, these tectonic models open the very promising way of integrating observational data sets with numerical simulations of lithosphere extension. Chapter II and III of this thesis contains several articles that follow precisely this approach in order to reveal new aspects of the interaction between rift tectonics and plate motions.

Plate reconstruction software [GPlates / pyGPlates]

For the plate tectonic reconstruction component of this thesis I employed GPlates (https://www.gplates.org), which is an open-source tool for building and visualizing the plate-kinematic history of our planet (Müller et al., 2018). GPlates uses topological plate models in order to represent Earth's tectonic plates along with their boundaries and other major features such as fracture zones, hot-spot tracks, and large igneous provinces. It has been jointly developed by the University of Sydney, the California Institute of Technology and the Geological Survey of Norway. During the last years, it became the global standard for analysing Earth's evolution in a plate tectonic context.

In its original form, GPlates is a graphical user interface (GUI) that allows easy-access to tectonic reconstructions. Until recently however, no quantitative script-based tool existed to facilitate the in-depth analysis of geotectonic reconstructions. This problem has been remedied by establishing the GPlates Python library 'pyGPlates', which can be downloaded freely at http://www.gplates.org/download.html. pyGPlates enables access to GPlates functionality through the Python programming language allowing to evaluate plate tectonic reconstructions in a programmatic and flexible way.

3. Rift processes, forces, strength

Structures and dynamics of continental rifts are affected by a combination of local and far-field forces. These forces interact with the tectono-rheological rift configuration, which produces the characteristic normal fault patterns, horst and graben structures as well as transfer zones visible in Earth's rifts and rifted margins (Ebinger and Scholz, 2011; Buck, 2015). In this section I briefly summarize the local and far-field processes that play a role during rifting and the associated forces.

3.1. Local and far-field forces

Originally, rifts have been classified in active or passive types, where active rifts are a result of thermal upwelling of the sublithospheric mantle whereas passive rifts are thought to be generated by far field tectonic forces (Şengör and Burke, 1978). However, it could be shown that this classification was not as clear-cut as originally thought (Ziegler and Cloetingh, 2004), and it was even suggested that there is a temporal transition from passive to active rifting within a single rift system (Huismans et al., 2001; Mondy et al., 2017). This is why active and passive rift types are now considered to be end-members of a continuous rift spectrum that is a result of several important rift processes.

Major processes and the orientation of their associated forces are shown in Fig. 4. Far-field forces are transmitted elastically through the plate interior and may by due to the classical driving forces of plate tectonics: slab pull, slab suction, ridge push and basal drag (Forsyth and Uyeda, 1975; Conrad and Lithgow-Bertelloni, 2006). The flow of sublithospheric mantle influences rifting via two processes: (1) Upward flow causes dynamic topography, which increases the gravitational potential energy, and ultimately adds up to the tensional body force (Bott and Kusznir, 1979; Lithgow-Bertelloni and Silver, 1998). (2) Divergent mantle flow beneath the rift couples to the base of the lithosphere on both rift sides and thus produces shear stresses, which further enhance rifting. Lithospheric thinning generates a pressure gradient at depth, which is referred to as 'rift suction' and that is compensated by the inflow of asthenospheric mantle beneath the rift. The thermal buoyancy of these upwelling hot mantle rocks are the source of another local force within the rift (Huismans et al., 2001) that may eventually have regional-scale relevance in the presence a mantle plume, such as under East Africa (Bagley and Nyblade, 2013).

Isostasy exerts obvious control on local topography, where stretched and faulted crust has been thinned, which generates the characteristic valley depressions within a rift. Simultaneously, material is redistributed by surface processes generating positive or negative vertical loads in depocenters and erosional areas, respectively (Burov and Poliakov, 2001). Lithospheric cooling has a pronounced impact for small rift velocities (van Wijk and Cloetingh, 2002) as well as during the post-rift phase (Petersen et al., 2015) by causing a negative thermal buoyancy that pushes the lithosphere down. Ultimately, this vertical load might be released by delamination (Göğüş, 2015).

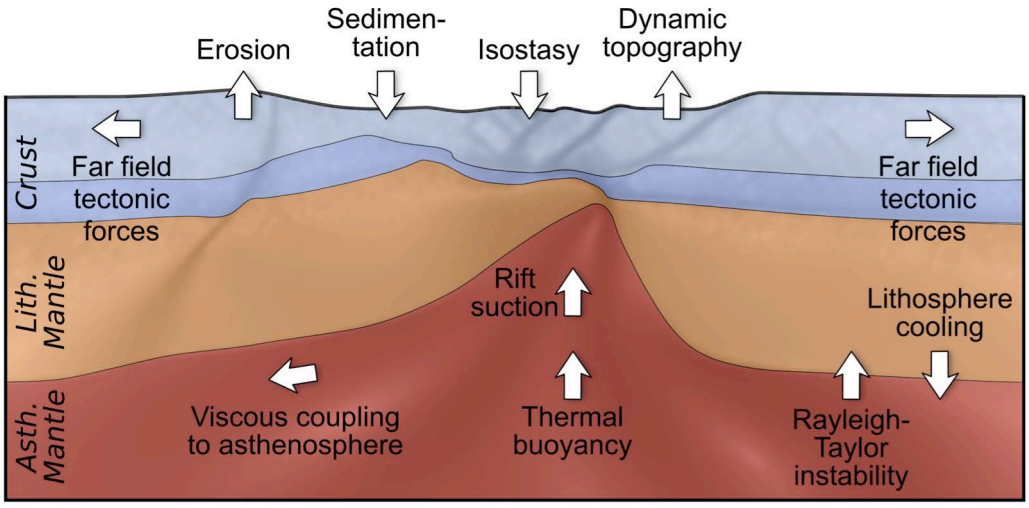

Fig. 4: Key processes and forces affecting rift dynamics.
White arrows show the orientation of the acting force. Asthenospheric and lithospheric mantle is shown in red and orange, while crust is depicted in blue. Modified from Brune (2018).

3.2. Rift strength vs. driving force

The strength of the intact continental lithosphere can be estimated by means of simplified yield strength profiles (Stüwe, 2007). When comparing the integrated strength of the lithosphere to the available plate tectonic forces, such as slab pull and basal drag, it seems that the latter are too small to deform standard continental lithosphere (e.g. Buck, 2004). This so-called 'tectonic force paradox' is especially striking when considering that some plates rift apart without being exposed to strong slab pull, such as in the East African rift system, which is surrounded on most sides by mid-ocean ridges. This argument suggests that rift initiation is governed by a combination of inherited weakness and dynamic softening mechanisms, which is further corroborated by the fact that suture zones inherited from the unification of tectonic plates are preferentially reactivated once the continent is thrown into extension. The emplacement of hot and buoyant mantle plumes under active continental rifts is another cause of reduced lithospheric strength which could provide the trigger for final continental rupture (Buiter and Torsvik, 2014). However, in many cases continental extension commenced before the arrival of a mantle plume, which rules out plumes as causative drivers of continental rifts. Another weakening process is the generation and migration of partial melts, which may efficiently heat the lithosphere if magma intrusion rates are high (Bialas et al., 2010; Daniels et al., 2014). If on the other hand intrusion rates are low, the frozen mafic dikes would strengthen the lithosphere causing the rift to be deflected or even inhibited.

The processes discussed above weaken the rift. Another way to avoid the tectonic force paradox is to locally increase the extensional force, which could be achieved by means of stress focussing: the local stress acting on the rift can be significantly larger if the source of tensional stress is much larger than the resisting portion of the plate boundary network. This is the case when break-up propagates along strike within a single rift zone, which occurred during the south-to-north propagating break-up in the South Atlantic (Moulin et

al., 2010; Torsvik et al., 2009). In this argument, changes in rift kinematics are usually considered to be a result of large-scale changes in plate motions. In Chapter II however, I will show that contrary to previous wisdom, the rift-internal strength evolution may indeed provide feed-back to large-scale plate movements.

4. Rift dynamics: Previews insights and open questions

Diverse surveys and campaigns have shown that rifts and rifted margins feature a large structural variety supposedly resulting from the interaction of tectonics, partial melting, inherited lithospheric architecture, and sediment supply. The relative impact of these factors and the structural details differ between individual rift systems, which hinders our understanding of rift evolution in general. One key approach of addressing the complexity of rift dynamics is to focus on simple setups in order to isolate key processes even though they are only relevant for specific end-member cases or during certain rift phases. Nevertheless, this approach has been very successful and enabled the research community to isolate some of the main mechanisms of continental rift evolution. In this section, I review some of these previous findings, describe some open questions and summarize solutions that I address in Chapter II-IV of this thesis.

4.1. Rifting in two dimensions

The pre-rift lithospheric setup affects rift dynamics in terms of tectonic inheritance, the thermo-rheological configuration, and the availability of melts. It was shown that the primary geometry of a rift, i.e. the width of a rift system and its symmetry are controlled by the degree of coupling between upper crust and mantle (Buck, 1991; Huismans and Beaumont, 2003). Decoupling of crust and mantle produces wide rifts like the Basin and Range province, the Aegean or the South China Sea (Fig. 5), where faulting is restricted to the uppermost crust and where lower crustal flow balances fault activity and impedes crustal thinning and the formation of a localising necking instability (Huismans and Beaumont, 2011). This degree of decoupling necessitates a pronounced low-viscosity crustal layer, which can be generated by elevated crustal temperatures, a very weak crustal flow law, or an over-thickened crust for instance in orogenic plateaus. But if crust and mantle are tightly coupled, few large faults will emerge that cut straight through the crust and form a narrow rift. In this case one distinguishes between symmetric and asymmetric rifts (Huismans and Beaumont, 2003; Buiter et al., 2008), whereas mode selection is controlled by the rheological setup, the extension rate and the involved weakening processes. Brittle-dominated settings under slow extension tend to generate predominantly asymmetric rift basins with a single large border fault like the Baikal rift (van der Beek, 1997). Symmetric narrow rifts or moderately asymmetric cases like the Upper Rhine Graben (Michon and Merle, 2000) emerge when dominated by viscous processes and under fast extension (Buiter et al., 2008).

Until recently, even state-of-the-art numerical models on lithospheric-scale (van Wijk and Cloetingh, 2002; Behn et al., 2002; Huismans and Beaumont, 2003) were not able to capture the transition from rifting to break-up with sufficiently high resolution to resolve the thin crustal layer observed in many continental margins (Lundin and Doré, 2011; Peron-Pinvidic et al., 2013). The existence of this wide areas of so-called hyperextended crust and its apparently asymmetric distribution between conjugate margin pairs was an open question so far (Fig. 6, Unternehr et al., 2010). I address this question within Chapter II in Brune et al. (2014; 2017) by proposing the mechanism of steady-state rift migration. During this process, the crust on one side of the rift is weakened by hot upwelling mantle, whereas the other side is not affected and remains colder and stronger. New faults form only on the warm, weak rift side, while those of the strong side eventually become inactive. This leads to a sideways motion of the rift system, which is equivalent to conveying crustal material from the one side of the rift to the other. These transferred crustal blocks are strongly extended by the rift and finally constitute the enigmatic thin crustal slivers of the hyperextended margin. The establishment of this process requires a reassessment of seismic data and the tectonic evolution of specific margins (Fig. 6) and holds strong implications for the peak heat and subsidence evolution at rifted continental margins.

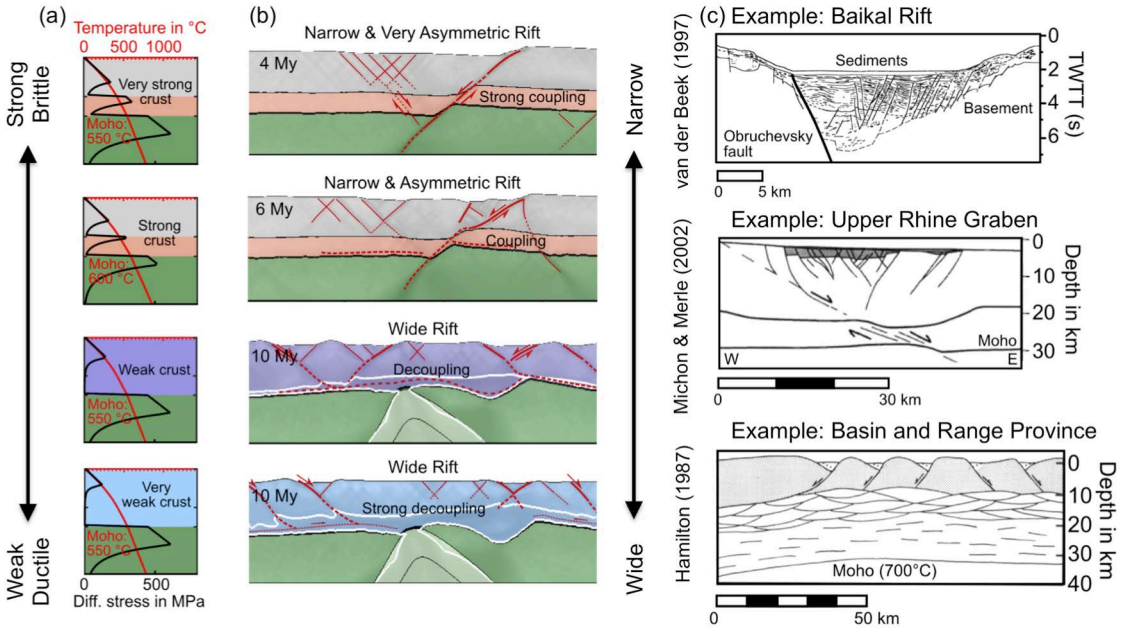

Fig. 5: Rift width and asymmetry.
The four numerical models illustrate the impact of crustal strength on the localization of rift structures within a simplified, laterally homogenous lithosphere. ***(a)*** *Yield strength profiles representative for the typical degree of inner-crustal strength contrast. All models feature the same thermal configuration except for M2, which has a higher Moho temperature. M1 and M2 feature the same rheological layering, while M3 and M4 are models with a homogeneous crust of comparably weak rheology. All flow laws are based on rheological experiments; for more details on the model setup, see Brune et al. (2017)* ***(b)*** *The width and symmetry of the rift are controlled by the degree of coupling between the brittle upper crust and the mantle. Strong crust generates narrow rifts and weak crust results in wide rifts. The tendency to form asymmetric rifts is more pronounced if highly non-linear brittle deformation prevails.* ***(c)*** *Representative examples of a very asymmetric narrow rift (Baikal), a moderately asymmetric narrow rift (Upper Rhine Graben), and a wide rift (Basin and Range).*

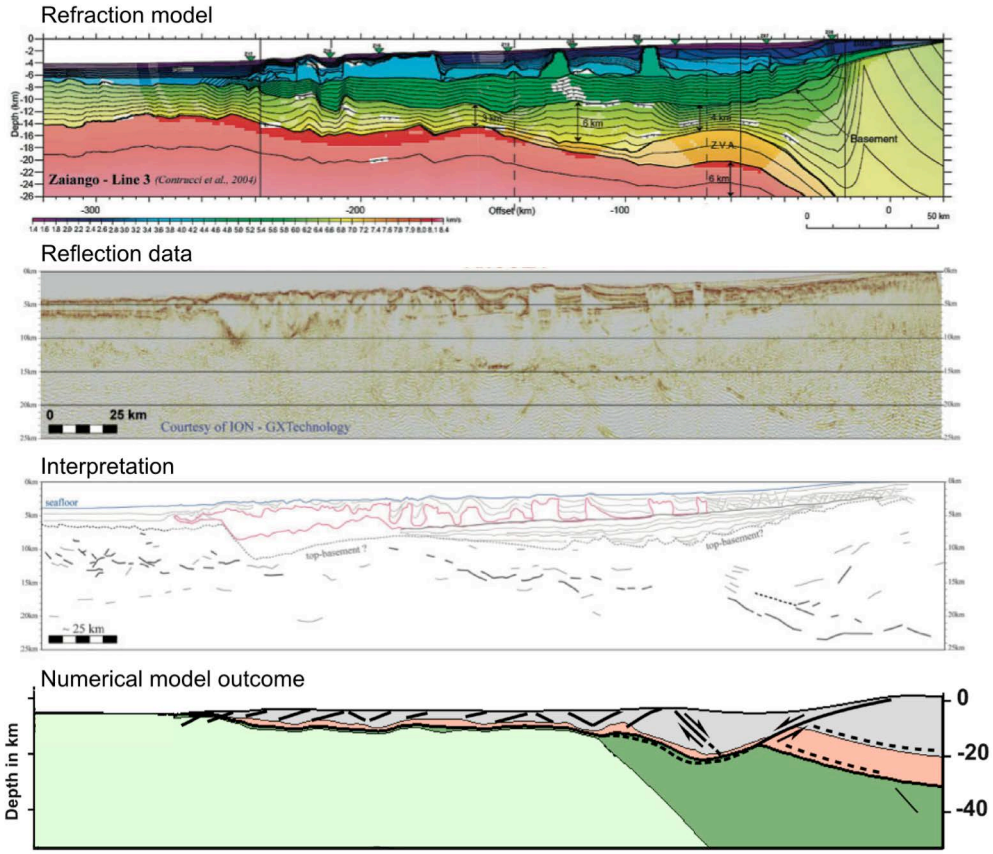

Fig. 6: Imaging and interpreting rifted margins.
Reproducing passive margin structures with numerical forward models opens the possibility to infer time-dependent processes and variables such as characteristic fault history, subsidence, and surface heat flow. This is exemplified here for the Central South Atlantic segment with seismic refraction and reflection data collected offshore Congo and Angola (Contrucci et al., 2004, Unternehr et al., 2010, and Brune et al. 2017).

Isostatic subsidence during rifting creates accommodation space for deep sedimentary basins. If continental rupture is accomplished, these rifted margin basins cool steadily and sink continuously to great ocean depths. Basins of the South China Sea, however appear to defy this rule (Sun et al., 2008). Instead of slowing down, subsidence even accelerated, postdating break-up by several million years. In a study that is included in Chapter II of this thesis (Clift et al., 2015), we investigated the interplay of sedimentation and lower crustal flow of wide rifted margins. Lower crustal flow is a vital ingredient in understanding Asian orogen dynamics (Clark and Royden, 2000) and low-viscosity crust has been proposed to explain the low topographic gradients of the South China Sea (Clift et al., 2002). In our study, we combined geophysical observations and well data with numerical forward modelling to show that the exceptionally weak continental crust of the South China Sea began to flow under a time-dependent sedimentary load. The time-dependency of the sedimentation rate appears to be related to a change of South Asia's climate about 23 million years ago, which lead to intensification of the monsoon and thus to enhanced erosion in the high Asian mountain chains (Sun and Wang, 2005; Clift et al., 2014).

The modelling community agrees that rift velocity exerts key control on the structural evolution of a continental rift through several distinct mechanisms: (1) Rift velocity governs the relative importance of conductive versus advective heat transport (van Wijk and Cloetingh, 2002; Svartman Dias et al., 2015; Tetreault and Buiter, 2017). (2) It affects the local strain rate and thereby the non-linear viscosity, the depth of the brittle-ductile transition and the amount of shear heating (Huismans and Beaumont, 2003; Burov, 2007; Duretz et al., 2015). (3) Finally, rift velocity correlates with the rate of asthenospheric upwelling and associated decompression melting (Pérez-Gussinyé et al., 2006; Schmeling, 2010; Davis and Lavier, 2017). In numerical models of rifted margin formation, the extension velocity is often assumed to be constant (Pérez-Gussinyé et al., 2006; Brune et al., 2014; Koptev et al., 2017). This can be justified through the argument that the relative plate velocity defining the local extension rate results from large-scale plate tectonics and that the associated driving forces are independent of the rift process. However, we questioned this argument in Brune et al. (2016), which is part of Chapter II, by analysing recent plate tectonics reconstructions. We showed that the rift velocity of major rift post-Pangea rift systems did not remain constant; in contrast, it featured a distinct two-phase velocity evolution where the rift initially stretches very slowly, but then accelerates very quickly before the onset of fast rupture. Using numerical and analytical modelling techniques, we found that rift strength exerts major control on the relative motion between involved plates. Our analyses revealed that the abrupt rift acceleration prior to breakup is caused be the non-linear strength loss during lithospheric necking. This illustrates that rift processes have strong impact on large-scale plate motions during times of continental fragmentation.

4.2. Rifting in three dimensions

From the modelling perspective it is very convenient to assume a cylindrical rift with no along-strike changes because this allows for higher resolution in 2D models while simultaneously reducing the overall complexity of the system. This may be desirable for certain research questions, but it is also obvious that natural rifts are 3D features that show along-strike variability, for instance related to segmentation, inherited structures, and oblique extension.

Segmentation has been documented in active rifts (e.g. Keranen et al., 2004; Keir et al., 2015) and at passive margins alike (Fournier et al., 2004; Franke et al., 2007). It is thought to commence with the formation of segmented en-échelon border faults as inferred from the East African Rift (Ebinger and Scholz, 2011; Corti et al., 2018) and may finally evolve into segmented mid-ocean ridges separated by transform faults (Ammann et al., 2017). Strong segmentation involving rift geometry and crustal asymmetry are also documented for the highly oblique Gulf of California. In this case, the formation of rift segments was caused by oblique extension and along-strike changes in sedimentation rate, magmatism, and mantle properties (Lizarralde et al., 2007; Bialas and Buck, 2009; Wang et al., 2009).

Continental rifts often occur in former suture zones, which makes them an integral component of the Wilson cycle (Wilson, 1966; Buiter and Torsvik,

2014). For instance, ~65% of the South Atlantic Rift reactivated rock fabrics that formed as part of the pan-African mobile belt (de Wit et al., 2008), while large parts of the East African Rift system reactivated tectonic elements of the Proterozoic Mozambique Belt (Daly et al., 1989). It is not entirely clear, which process guides the rift along the former suture. In some places of the East African rift Neogene fault activity seems to follow Proterozoic foliations (Hetzel and Strecker, 1994), but in other places foliations appear to play a less important role (Hodge et al., 2018). But it is also the existence of failed rifts that exerts key control on present-day rift structures in East Africa. The Central African shear zone for instance cut east-west through the African continent in Cretaceous times thinning the crust in East Africa by up to 25%. These regions of thinned crust are visible as prominent low-lands of the Turkana depression and affect the linkage dynamics of the Ethiopian and the Kenyan rift arms (Ebinger et al., 2000).

The tectonic linkage of two rift segments has been modelled previously by imposing two weak elongate seeds in a laterally homogeneous crust or lithosphere (Allken et al., 2012; Zwaan et al., 2017; Le Pourhiet et al., 2017). The resulting structures can be classified as (1) distributed pure shear mode, (2) an overlapping mode that in some cases involves the formation of a microplate, and (3) a connecting mode generating transform faults. Building on these insights, we studied how the existence of an inherited band of thinned crust affects the linkage of two rift segments (Brune, Corti, et al., 2017). The 3D model design is based on observations from the Turkana depression accounting for crust and lithosphere that has been thinned during the Cretaceous failed rift event. By using both analogue and numerical experiments, we show that the inherited structures are responsible for the dramatic change in rift style from narrow rifting north and south of the Turkana depression to wide, distributed extension in the interior of the Turkana area. The failed inherited rift structures also cause a westward bend of the Kenyan rift and an eastward bend of the Ethiopian rift within the Turkana depression.

Another major process requiring 3D modelling approaches is oblique rifting that occurs when the rift velocity is not perpendicular to the rift trend. Oblique rifting has been extensively studied using geological and geophysical techniques in the Main Ethiopian rift (Corti, 2008), and the Gulf of California (Atwater and Stock, 1998; Fletcher et al., 2007), but also in rifted margins such as the Gulf of Aden (Leroy et al., 2012) and the Equatorial Atlantic (Heine et al., 2013). Additional insights on oblique extensional tectonics come from observation at obliquely spreading mid-ocean ridges, for instance the Reykjanes and Mohns Ridge (Dauteuil and Brun, 1993) as well as the South West Indian Ridge (Dick et al., 2003). In Chapter III, I describe the results of a rather surprising modelling study of oblique rifting (Brune et al., 2012). We used simple analytical and more realistic 3D numerical models in order to compute the tectonic force that is required to maintain a given rift velocity. The main result was that less force is needed to rift under oblique extension than through orthogonal rifting. The underlying reason is that brittle yielding necessitates less tectonic force when the orientation of divergence is oblique to the rift. We compared orthogonal extension and strike-slip end-members and found that the required force is almost 2 times less for strike-slip

deformation. We therefore concluded that relative plate motions involving a significant component of rift obliquity are mechanically preferred.

This insight can be related to the Cretaceous plate tectonic evolution of the Equatorial South Atlantic region (Heine and Brune, 2014, included in Chapter III). During opening of the South Atlantic, the Equatorial Atlantic rift segment competed with the simultaneously active West-African rift zone. We elucidate the dynamics of this region by linking plate tectonic reconstructions and 3D geodynamic modelling and showed that after 20-30 million years of coexisting rift arms, the West-African rift failed while the Equatorial Atlantic rift finalized continental breakup. A key difference between both arms was that the Equatorial Atlantic rift deformed at higher obliquity, which effectively helped in localising strain whereas the less oblique West African rift became inactive.

The structural evolution during oblique rifting has been the topic of many previous analogue models (Schreurs and Colletta, 1998; Autin et al., 2010; Philippon et al., 2015; Zwaan et al., 2016). The majority of earlier studies focussed on crustal scale extension and unanimously agree that the initial fault directions strike with an azimuth that bisects the extension-orthogonal direction and the rift trend (e.g. Withjack and Jamison, 1986; Tron and Brun, 1991; Clifton et al., 2000). This result can be further backed up by analytical modelling of an elasto-plastic material (Withjack and Jamison, 1986). Modelling of larger amounts of bulk extension necessitates lithospheric-scale models because the necking process plays an important role. These kind of analogue experiments agree with the initially intermediate fault orientation of earlier studies, but feature also rift-parallel and extension-orthogonal fault populations during later rift stages (Agostini et al., 2009; Autin et al., 2010). A drawback of most analogue models is that it is difficult to include thermal processes, which hampers the study of later rifts phases and breakup. Numerical models can help to address this issue, which is why I conducted 3D lithospheric-scale models of varying rift obliquity (Brune, 2014), a study that is part of Chapter III. The models show a characteristic evolution of surface fault patterns starting with coalescence of initially distributed faults with intermediate fault directions into en-échelon shear zones. These shear zones exhibit a broad distribution of fault directions while rift-parallel orientations emerge successively. Pre-breakup localization abruptly terminates the en-échelon stage and intermediate as well as extension-orthogonal fault azimuths take over. This result falsifies the approach to use fault-perpendicular directions as proxies for paleo-plate movements, since changes in fault direction may arise intrinsically during rift evolution, and may not be related to plate motion changes.

4.3. Rifting as a global scale process

The kinematic evolution of continental rifts always includes a global geodynamic component. Rift dynamics are closely linked to kinematics of other plate boundaries, simply due to conservation of Earth's surface area. In this aspect, an increase of rift velocity during the South Atlantic opening (Heine et al., 2013; Brune et al., 2016) might explain the simultaneous closure of back-arc basins in the proto-Andean region (Maloney et al., 2013). On the other hand, subducting slabs and the subsequent generation of mantle

convection cells adds divergent mantle flow underneath a potential zone of extension. Therefore the slab penetration depth could control the distance between trench and rift, not only for back-arc basins but also for intra-continental rift systems (Zilio et al., 2017). Other processes that link rift tectonics and global geodynamics are potential thermal insulation under super-continents (Coltice et al., 2007; Heron and Lowman, 2014), the involvement of plumes during active or passive rifting (Şengör and Burke, 1978; Ebinger and Sleep, 1998; Burov and Gerya, 2014; Wolstencroft and Davies, 2017), but also global geochemical cycles, for instance of carbon (Lee et al., 2016; Foley and Fischer, 2017).

Building on previous articles that addressed oblique rift architecture and the required forces for oblique extension, I investigate the global-scale distribution of rift obliquity in Chapter IV of this thesis (Brune et al., 2018). To this aim, I analyse global plate tectonic reconstructions for the rift obliquity and its temporal evolution at any small-scale rift segment contained in the reconstruction of the last 230 million years. A statistical analysis of this data set reveals that roughly 70% of all rifts evolved with an oblique rift component, i.e. where rift obliquities are larger than 20°. This result shows that oblique rifting rather appears to be the rule on Earth than the exception. In some cases, we also find a correlation between rift velocity and rift obliquity that might be explained with the mechanism that oblique rifting is mechanically preferred (Brune et al., 2012): the Australian plate, for instance, initially separated from Antarctica with a sub-orthogonal rift direction and at slow rate. But at ~100 Ma, the relative plate velocity became oblique while simultaneously the rift velocity increased (Ball et al., 2013; Whittaker et al., 2013). A similar process has been discussed for rifting in the Gulf of California (Bennett and Oskin, 2014).

For several decades, rifts have been suspected to affect the global carbon cycle (Kerrick, 2001), but only recent measurements allow quantitative estimates of rift-related CO_2 degassing rates. These measurements of diffuse (i.e. non-volcanic) CO_2 release have been taken in a variety of rift systems: the narrow Rio Grande rift (Smith, 2016), the wide Basin and Range rift (Jolie et al., 2016), the collision-related Eger rift (Weinlich et al., 1999), the East African Rift system's magma-poor western branch (Barry et al., 2013) and its magma-rich eastern branch (Muirhead et al., 2016). Analysis of carbon and helium isotopes of the collected gas samples revealed a mantle fingerprint, which provides strong evidence that rifts have to be considered a vital element of the deep carbon cycle. In the last manuscript of this thesis (Brune, Williams, et al., 2017), we analysed the extent of the global rift system through time and compared it to paleo-atmospheric CO_2 proxy data. We showed that the time-dependent rift length evolution exhibits a first-order correlation to atmospheric CO_2 content. We therefore suggested that rift-related CO_2 degassing constitutes a key component of Earth's deep carbon cycle.

References

Agostini, A., Corti, G., Zeoli, A., and Mulugeta, G., 2009, Evolution, pattern, and partitioning of deformation during oblique continental rifting: Inferences from lithospheric-scale centrifuge models: Geochemistry Geophysics Geosystems, v. 10, p. Q11015, doi: 10.1029/2009GC002676.

Allken, V., Huismans, R.S., and Thieulot, C., 2012, Factors controlling the mode of rift interaction in brittle-ductile coupled systems: A 3D numerical study: Geochemistry Geophysics Geosystems, v. 13, p. Q05010, doi: 10.1029/2012GC004077.

Allken, V., Huismans, R.S., and Thieulot, C., 2011, Three-dimensional numerical modeling of upper crustal extensional systems: Journal of Geophysical Research, v. 116, p. B10409, doi: 201110.1029/2011JB008319.

Ammann, N., Liao, J., Gerya, T., and Ball, P., 2017, Oblique continental rifting and long transform fault formation based on 3D thermomechanical numerical modeling: Tectonophysics, doi: 10.1016/j.tecto.2017.08.015.

Armitage, J.J., Collier, J.S., and Minshull, T.A., 2012, The importance of rift history for volcanic margin formation: Nature, v. 465, p. 913–917, doi: 10.1038/nature09063.

Armitage, J.J., Ferguson, D.J., Goes, S., Hammond, J.O.S., Calais, E., Rychert, C.A., and Harmon, N., 2015, Upper mantle temperature and the onset of extension and break-up in Afar, Africa: Earth and Planetary Science Letters, v. 418, p. 78–90, doi: 10.1016/j.epsl.2015.02.039.

Armitage, J.J., Petersen, K.D., and Pérez-Gussinyé, M., 2018, The Role of Crustal Strength in Controlling Magmatism and Melt Chemistry During Rifting and Breakup: Geochemistry, Geophysics, Geosystems, v. 0, doi: 10.1002/2017GC007326.

Aslanian, D., Moulin, M., Olivet, J.-L., Unternehr, P., Matias, L., Bache, F., Rabineau, M., Nouzé, H., Klingelheofer, F., Contrucci, I., and Labails, C., 2009, Brazilian and African passive margins of the Central Segment of the South Atlantic Ocean: Kinematic constraints: Tectonophysics, v. 468, p. 98–112, doi: 10.1016/j.tecto.2008.12.016.

Atwater, T., and Stock, J., 1998, Pacific-North America Plate Tectonics of the Neogene Southwestern United States: An Update: International Geology Review, v. 40, p. 375–402, doi: 10.1080/00206819809465216.

Augustin, N., Devey, C.W., van der Zwan, F.M., Feldens, P., Tominaga, M., Bantan, R.A., and Kwasnitschka, T., 2014, The rifting to spreading transition in the Red Sea: Earth and Planetary Science Letters, v. 395, p. 217–230, doi: 10.1016/j.epsl.2014.03.047.

Autin, J., Bellahsen, N., Husson, L., Beslier, M.-O., Leroy, S., and d'Acremont, E., 2010, Analog models of oblique rifting in a cold lithosphere: Tectonics, v. 29, p. TC6016, doi: 10.1029/2010TC002671.

Bagley, B., and Nyblade, A.A., 2013, Seismic anisotropy in eastern Africa, mantle flow, and the African superplume: Geophysical Research Letters, v. 40, p. 1500–1505, doi: 10.1002/grl.50315.

Ball, P., Eagles, G., Ebinger, C., McClay, K., and Totterdell, J., 2013, The spatial and temporal evolution of strain during the separation of Australia and Antarctica: Geochemistry, Geophysics, Geosystems, v. 14, p. 2771–2799, doi: 10.1002/ggge.20160.

Barnett-Moore, N., Müller, D.R., Williams, S., Skogseid, J., and Seton, M., 2016, A reconstruction of the North Atlantic since the earliest Jurassic: Basin Research, p. 1–26, doi: 10.1111/bre.12214.

Barry, P.H., Hilton, D.R., Fischer, T.P., de Moor, J.M., Mangasini, F., and Ramirez, C., 2013, Helium and carbon isotope systematics of cold "mazuku" CO2 vents and hydrothermal gases and fluids from Rungwe Volcanic Province, southern Tanzania: Chemical Geology, v. 339, p. 141–156, doi: 10.1016/j.chemgeo.2012.07.003.

Bastow, I.D., and Keir, D., 2011, The protracted development of the continent-ocean transition in Afar: Nature Geoscience, v. 4, p. 248–250, doi: 10.1038/ngeo1095.

Beaumont, C., and Ings, S.J., 2012, Effect of depleted continental lithosphere counterflow and inherited crustal weakness on rifting of the continental lithosphere: General results: Journal of Geophysical Research: Solid Earth, v. 117, p. B08407, doi: 10.1029/2012JB009203.

Beaumont, C., Keen, C.E., and Boutilier, R., 1982, On the evolution of rifted continental margins: comparison of models and observations for the Nova Scotian margin: Geophysical Journal International, v. 70, p. 667–715, doi: 10.1111/j.1365-246X.1982.tb05979.x.

Becker, K., Franke, D., Trumbull, R., Schnabel, M., Heyde, I., Schreckenberger, B., Koopmann, H., Bauer, K., Jokat, W., and Krawczyk, C.M., 2014, Asymmetry of high-velocity lower crust on the South Atlantic rifted margins and implications for the interplay of magmatism and tectonics in continental breakup: Solid Earth, v. 5, p. 1011–1026, doi: 10.5194/se-5-1011-2014.

van der Beek, P., 1997, Flank uplift and topography at the central Baikal Rift (SE Siberia): A test of kinematic models for continental extension: Tectonics, v. 16, p. 122–136, doi: 10.1029/96TC02686.

Behn, M.D., Lin, J., and Zuber, M.T., 2002, A continuum mechanics model for normal faulting using a strain-rate softening rheology: implications for thermal and rheological controls on continental and oceanic rifting: Earth and Planetary Science Letters, v. 202, p. 725–740, doi: 10.1016/S0012-821X(02)00792-6.

Bell, R.E., Jackson, C.A.-L., Whipp, P.S., and Clements, B., 2014, Strain migration during multiphase extension: Observations from the northern North Sea: Tectonics, v. 33, p. 2014TC003551, doi: 10.1002/2014TC003551.

Bell, R.E., McNeill, L.C., Henstock, T.J., and Bull, J.M., 2011, Comparing extension on multiple time and depth scales in the Corinth Rift, Central Greece: Geophysical Journal International, v. 186, p. 463–470, doi: 10.1111/j.1365-246X.2011.05077.x.

Bennett, S.E.K., and Oskin, M.E., 2014, Oblique rifting ruptures continents: Example from the Gulf of California shear zone: Geology, v. 42, p. 215–218, doi: 10.1130/G34904.1.

Bialas, R.W., and Buck, W.R., 2009, How sediment promotes narrow rifting: Application to the Gulf of California: Tectonics, v. 28, p. TC4014, doi: 200910.1029/2008TC002394.

Bialas, R.W., Buck, W.R., and Qin, R., 2010, How much magma is required to rift a continent? Earth and Planetary Science Letters, v. 292, p. 68–78, doi: doi: DOI: 10.1016/j.epsl.2010.01.021.

Blaich, O.A., Faleide, J.I., Tsikalas, F., Franke, D., and Leon, E., 2009, Crustal-scale architecture and segmentation of the Argentine margin and its conjugate off South Africa: Geophysical Journal International, v. 178, p. 85–105, doi: 10.1111/j.1365-246X.2009.04171.x.

Bott, M.H.P., and Kusznir, N.J., 1979, Stress distributions associated with compensated plateau uplift structures with application to the continental splitting mechanism: Geophysical Journal International, v. 56, p. 451–459, doi: 10.1111/j.1365-246X.1979.tb00177.x.

Bradley, D.C., 2008, Passive margins through earth history: Earth-Science Reviews, v. 91, p. 1–26, doi: 10.1016/j.earscirev.2008.08.001.

Brown, E.L., and Lesher, C.E., 2014, North Atlantic magmatism controlled by temperature, mantle composition and buoyancy: Nature Geoscience, v. 7, p. 820–824, doi: 10.1038/ngeo2264.

Brun, J.-P., and Sokoutis, D., 2018, Core Complex Segmentation in North Aegean, A Dynamic View: Tectonics, v. 37, p. 1797–1830, doi: 10.1029/2017TC004939.

Brun, J.P., and Wenzel, F., 1991, Crustal-scale structure of the southern Rhinegraben from ECORS-DEKORP seismic reflection data: Geology, v. 19, p. 758–762, doi: 10.1130/0091-7613(1991)019<0758:CSSOTS>2.3.CO;2.

Brune, S., 2014, Evolution of stress and fault patterns in oblique rift systems: 3-D numerical lithospheric-scale experiments from rift to breakup: Geochemistry, Geophysics, Geosystems, v. 15, p. 3392–3415, doi: 10.1002/2014GC005446.

Brune, S., Corti, G., and Ranalli, G., 2017, Controls of inherited lithospheric heterogeneity on rift linkage: Numerical and analog models of interaction between the Kenyan and Ethiopian rifts across the Turkana depression: Tectonics, v. 36, p. 2017TC004739, doi: 10.1002/2017TC004739.

Brune, S., Heine, C., Clift, P.D., and Pérez-Gussinyé, M., 2017, Rifted margin architecture and crustal rheology: Reviewing Iberia-Newfoundland, Central South Atlantic, and South China Sea: Marine and Petroleum Geology, v. 79, p. 257–281, doi: 10.1016/j.marpetgeo.2016.10.018.

Brune, S., Heine, C., Perez-Gussinye, M., and Sobolev, S.V., 2014, Rift migration explains continental margin asymmetry and crustal hyper-extension: Nature Communications, v. 5, doi: 10.1038/ncomms5014.

Brune, S., Popov, A.A., and Sobolev, S.V., 2012, Modeling suggests that oblique extension facilitates rifting and continental break-up: Journal of Geophysical Research, v. 117, p. B08402, doi: 10.1029/2011JB008860.

Brune, S., Williams, S.E., Butterworth, N.P., and Müller, R.D., 2016, Abrupt plate accelerations shape rifted continental margins: Nature, v. advance online publication, p. 1–4, doi: 10.1038/nature18319.

Brune, S., Williams, S.E., and Müller, R.D., 2017, Potential links between continental rifting, CO 2 degassing and climate change through time: Nature Geoscience, v. 10, p. 941–946, doi: 10.1038/s41561-017-0003-6.

Brune, S., Willliams, S.E., and Müller, R.D., 2018, Oblique rifting: the rule, not the exception.: Solid Earth Discussions, p. 1–26, doi: https://doi.org/10.5194/se-2018-63.

Buck, W.R., 2004, Consequences of asthenospheric variability on continental rifting, *in* Rheology and Deformation of the Lithosphere at Continental Margins, Columbia University Press New York, v. 62, p. 1–30.

Buck, W.R., 1991, Modes of Continental Lithospheric Extension: Journal of Geophysical Research-Solid Earth, v. 96, p. 20161–20178, doi: 10.1029/91JB01485.

Buck, W.R., 2015, The Dynamics of Continental Breakup and Extension, *in* Treatise on Geophysics, 2nd Edition, Vol 6 - Crust and Lithosphere Dynamics, Oxford, Elsevier.

Buiter, S.J.H., Huismans, R.S., and Beaumont, C., 2008, Dissipation analysis as a guide to mode selection during crustal extension and implications for the styles of sedimentary basins: Journal of Geophysical Research-Solid Earth, v. 113, p. B06406, doi: doi:10.1029/2007JB005272.

Buiter, S.J.H., and Torsvik, T.H., 2014, A review of Wilson Cycle plate margins: A role for mantle plumes in continental break-up along sutures? Gondwana Research, v. 26, p. 627–653, doi: 10.1016/j.gr.2014.02.007.

Burov, E.B., 2007, Plate Rheology and Mechanics, *in* Treatise on Geophysics Vol 6 - Crust and Lithosphere Dynamics, p. 99–151.

Burov, E., and Gerya, T., 2014, Asymmetric three-dimensional topography over mantle plumes: Nature, v. 513, p. 85–89, doi: 10.1038/nature13703.

Burov, E., and Poliakov, A., 2001, Erosion and rheology controls on synrift and postrift evolution: Verifying old and new ideas using a fully coupled numerical model: Journal of Geophysical Research-Solid Earth, v. 106, p. 16461–16481, doi: 10.1029/2001JB000433.

Clark, M.K., and Royden, L.H., 2000, Topographic ooze: Building the eastern margin of Tibet by lower crustal flow: Geology, v. 28, p. 703–706, doi: 10.1130/0091-7613(2000)28<703:TOBTEM>2.0.CO;2.

Clift, P.D., Brune, S., and Quinteros, J., 2015, Climate changes control offshore crustal structure at South China Sea continental margin: Earth and Planetary Science Letters, v. 420, p. 66–72, doi: 10.1016/j.epsl.2015.03.032.

Clift, P., Lin, J., and Barckhausen, U., 2002, Evidence of low flexural rigidity and low viscosity lower continental crust during continental break-up in the South China Sea: Marine and Petroleum Geology, v. 19, p. 951–970, doi: 10.1016/S0264-8172(02)00108-3.

Clift, P.D., Wan, S., and Blusztajn, J., 2014, Reconstructing chemical weathering, physical erosion and monsoon intensity since 25 Ma in the northern South China Sea: A review of competing proxies: Earth-Science Reviews, v. 130, p. 86–102, doi: 10.1016/j.earscirev.2014.01.002.

Clifton, A.E., Schlische, R.W., Withjack, M.O., and Ackermann, R.V., 2000, Influence of rift obliquity on fault-population systematics: results of experimental clay models: Journal of Structural Geology, v. 22, p. 1491–1509, doi: 10.1016/S0191-8141(00)00043-2.

Coffin, M.F., and Eldholm, O., 1994, Large igneous provinces: Crustal structure, dimensions, and external consequences: Reviews of Geophysics, v. 32, p. 1–36.

Coltice, N., Phillips, B.R., Bertrand, H., Ricard, Y., and Rey, P., 2007, Global warming of the mantle at the origin of flood basalts over supercontinents: Geology, v. 35, p. 391–394, doi: 10.1130/G23240A.1.

Conrad, C.P., and Lithgow-Bertelloni, C., 2006, Influence of continental roots and asthenosphere on plate-mantle coupling: Geophysical Research Letters, v. 33, p. 4 PP., doi: 200610.1029/2005GL025621.

Contrucci, I., Matias, L., Moulin, M., Geli, L., Klingelhofer, F., Nouze, H., Aslanian, D., Olivet, J.L., Rehault, J.P., and Sibuet, J.C., 2004, Deep structure of the West African continental margin (Congo, Zaire, Angola), between 5 degrees S and 8 degrees S, from reflection/refraction seismics and gravity data: Geophysical Journal International, v. 158, p. 529–553.

Corti, G., 2009, Continental rift evolution: From rift initiation to incipient break-up in the Main Ethiopian Rift, East Africa: Earth-Science Reviews, v. 96, p. 1–53, doi: doi: DOI: 10.1016/j.earscirev.2009.06.005.

Corti, G., 2008, Control of rift obliquity on the evolution and segmentation of the main Ethiopian rift: Nature Geoscience, v. 1, p. 258–262, doi: 10.1038/ngeo160.

Corti, G., Bonini, M., Conticelli, S., Innocenti, F., Manetti, P., and Sokoutis, D., 2003, Analogue modelling of continental extension: a review focused on the relations between the patterns of deformation and the presence of magma: Earth-Science Reviews, v. 63, p. 169–247, doi: 10.1016/S0012-8252(03)00035-7.

Corti, G., Molin, P., Sembroni, A., Bastow, I.D., and Keir, D., 2018, Control of Pre‐rift Lithospheric Structure on the Architecture and Evolution of Continental Rifts: Insights From the Main Ethiopian Rift, East Africa: Tectonics, v. 37, p. 477–496, doi: 10.1002/2017TC004799.

Cowie, L., Kusznir, N., and Manatschal, G., 2015, Determining the COB location along the Iberian margin and Galicia Bank from gravity anomaly inversion, residual depth anomaly and subsidence analysis: Geophysical Journal International, v. 203, p. 1355–1372, doi: 10.1093/gji/ggv367.

Cullen, A., Reemst, P., Henstra, G., Gozzard, S., and Ray, A., 2010, Rifting of the South China Sea: new perspectives: Petroleum Geoscience, v. 16, p. 273–282, doi: 10.1144/1354-079309-908.

Daly, M.C., Chorowicz, J., and Fairhead, J.D., 1989, Rift basin evolution in Africa: the influence of reactivated steep basement shear zones: Geological Society, London, Special Publications, v. 44, p. 309–334, doi: 10.1144/GSL.SP.1989.044.01.17.

Daniels, K.A., Bastow, I.D., Keir, D., Sparks, R.S.J., and Menand, T., 2014, Thermal models of dyke intrusion during development of continent–ocean transition: Earth and Planetary Science Letters, v. 385, p. 145–153, doi: 10.1016/j.epsl.2013.09.018.

Dauteuil, O., and Brun, J.P., 1993, Oblique Rifting in a Slow-Spreading Ridge: Nature, v. 361, p. 145–148, doi: doi:10.1038/361145a0.

Davis, J.K., and Lavier, L.L., 2017, Influences on the development of volcanic and magma-poor morphologies during passive continental rifting: Geosphere, v. 13, p. 1524–1540, doi: 10.1130/GES01538.1.

Dick, H.J.B., Lin, J., and Schouten, H., 2003, An ultraslow-spreading class of ocean ridge: Nature, v. 426, p. 405–412, doi: 10.1038/nature02128.

Direen, N.G., Stagg, H.M.J., Symonds, P.A., and Norton, I.O., 2012, Variations in rift symmetry: cautionary examples from the Southern Rift System (Australia–Antarctica): Geological Society, London, Special Publications, v. 369, doi: 10.1144/SP369.4.

Duclaux, G., Huismans, R.S., and May, D., 2017, Three-dimensional frictional plastic strain partitioning during oblique rifting, *in* EGU General Assembly Conference Abstracts, v. 19, p. 4790, http://adsabs.harvard.edu/abs/2017EGUGA..19.4790D (accessed July 2018).

Duretz, T., Schmalholz, S.M., and Podladchikov, Y.Y., 2015, Shear heating-induced strain localization across the scales: Philosophical Magazine, v. 0, p. 1–16, doi: 10.1080/14786435.2015.1054327.

Ebinger, C.J., Jackson, J.A., Foster, A.N., and Hayward, N.J., 1999, Extensional basin geometry and the elastic lithosphere: Philosophical Transactions of the Royal Society of London. Series A: Mathematical, Physical and Engineering Sciences, v. 357, p. 741–765, doi: 10.1098/rsta.1999.0351.

Ebinger, C., and Scholz, C.A., 2011, Continental Rift Basins: The East African Perspective, *in* Busby, C. and Azor, A. eds., Tectonics of Sedimentary Basins, Chichester, UK, John Wiley & Sons, Ltd, p. 183–208, http://onlinelibrary.wiley.com/doi/10.1002/9781444347166.ch9/summary.

Ebinger, C.J., and Sleep, N.H., 1998, Cenozoic magmatism throughout east Africa resulting from impact of a single plume: Nature, v. 395, p. 788–791, doi: 10.1038/27417.

Ebinger, C.J., Yemane, T., Harding, D.J., Tesfaye, S., Kelley, S., and Rex, D.C., 2000, Rift deflection, migration, and propagation: Linkage of the Ethiopian and Eastern rifts, Africa: GSA Bulletin, v. 112, p. 163–176, doi: 10.1130/0016-7606(2000)112<163:RDMAPL>2.0.CO;2.

Eilon, Z., Abers, G.A., Gaherty, J.B., and Jin, G., 2015, Imaging continental breakup using teleseismic body waves: The Woodlark Rift, Papua New Guinea: Geochemistry, Geophysics, Geosystems, v. 16, p. 2529–2548, doi: 10.1002/2015GC005835.

Eldholm, O., Gladczenko, T.P., Skogseid, J., and Planke, S., 2000, Atlantic volcanic margins: a comparative study: Geological Society, London, Special Publications, v. 167, p. 411–428, doi: 10.1144/GSL.SP.2000.167.01.16.

England, P., and McKenzie, D., 1982, A thin viscous sheet model for continental deformation: Geophysical Journal of the Royal Astronomical Society, v. 70, p. 295–321, doi: 10.1111/j.1365-246X.1982.tb04969.x.

Espurt, N., Callot, J.-P., Roure, F., Totterdell, J.M., Struckmeyer, H.I.M., and Vially, R., 2012, Transition from symmetry to asymmetry during continental rifting: an example from the Bight Basin–Terre Adélie (Australian and Antarctic conjugate margins): Terra Nova, v. 24, p. 167–180, doi: 10.1111/j.1365-3121.2011.01055.x.

Faccenna, C., Becker, T.W., Lucente, F.P., Jolivet, L., and Rossetti, F., 2001, History of subduction and back-arc extension in the Central Mediterranean: Geophysical Journal International, v. 145, p. 809–820, doi: 10.1046/j.0956-540x.2001.01435.x.

Fletcher, J.M., Grove, M., Kimbrough, D., Lovera, O., and Gehrels, G.E., 2007, Ridge-trench interactions and the Neogene tectonic evolution of the Magdalena shelf and southern Gulf of California: Insights from detrital zircon U-Pb ages from the Magdalena fan and adjacent areas: Geological Society of America Bulletin, v. 119, p. 1313–1336, doi: 10.1130/B26067.1.

Foley, S.F., and Fischer, T.P., 2017, An essential role for continental rifts and lithosphere in the deep carbon cycle: Nature Geoscience, p. 1, doi: 10.1038/s41561-017-0002-7.

Forsyth, D., and Uyeda, S., 1975, On the Relative Importance of the Driving Forces of Plate Motion: Geophysical Journal of the Royal Astronomical Society, v. 43, p. 163–200.

Fournier, M., Bellahsen, N., Fabbri, O., and Gunnell, Y., 2004, Oblique rifting and segmentation of the NE Gulf of Aden passive margin: Geochemistry, Geophysics, Geosystems, v. 5, p. Q11005, doi: 10.1029/2004GC000731.

Franke, D., 2013, Rifting, lithosphere breakup and volcanism: Comparison of magma-poor and volcanic rifted margins: Marine and Petroleum Geology, v. 43, p. 63–87, doi: 10.1016/j.marpetgeo.2012.11.003.

Franke, D., Neben, S., Ladage, S., Schreckenberger, B., and Hinz, K., 2007, Margin segmentation and volcano-tectonic architecture along the volcanic margin off Argentina/Uruguay, South Atlantic RID A-5383-2011: Marine Geology, v. 244, p. 46–67, doi: 10.1016/j.margeo.2007.06.009.

Franke, D., Savva, D., Pubellier, M., Steuer, S., Mouly, B., Auxietre, J.-L., Meresse, F., and Chamot-Rooke, N., 2014, The final rifting evolution in the South China Sea: Marine and Petroleum Geology, v. 58, Part B, p. 704–720, doi: 10.1016/j.marpetgeo.2013.11.020.

Göğüş, O.H., 2015, Rifting and subsidence following lithospheric removal in continental back arcs: Geology, v. 43, p. 3–6, doi: 10.1130/G36305.1.

Guiraud, R., and Maurin, J.-C., 1992, Early Cretaceous rifts of Western and Central Africa: an overview: Tectonophysics, v. 213, p. 153–168, doi: 10.1016/0040-1951(92)90256-6.

Hamilton, W., 1987, Crustal extension in the Basin and Range Province, southwestern United States: Geological Society, London, Special Publications, v. 28, p. 155–176, doi: 10.1144/GSL.SP.1987.028.01.12.

Heine, C., and Brune, S., 2014, Oblique rifting of the Equatorial Atlantic: Why there is no Saharan Atlantic Ocean: Geology, v. 42(3), p. 211–214, doi: 10.1130/G35082.1.

Heine, C., Zoethout, J., and Müller, R.D., 2013, Kinematics of the South Atlantic rift: Solid Earth, v. 4, p. 215–253, doi: 10.5194/se-4-215-2013.

Heron, P.J., and Lowman, J.P., 2014, The impact of Rayleigh number on assessing the significance of supercontinent insulation: Journal of Geophysical Research: Solid Earth, v. 119, p. 711–733, doi: 10.1002/2013JB010484.

Hetzel, R., and Strecker, M.R., 1994, Late Mozambique Belt structures in western Kenya and their influence on the evolution of the Cenozoic Kenya Rift: Journal of Structural Geology, v. 16, p. 189–201, doi: 10.1016/0191-8141(94)90104-X.

Hodge, M.S., Fagereng, Å., Biggs, J., and Mdala, H., 2018, Controls on early-rift geometry: new perspectives from the Bilila-Mtakataka fault, Malawi: Geophysical Research Letters, doi: 10.1029/2018GL077343.

Hopper, J.R., Funck, T., Tucholke, B.E., Larsen, H.C., Holbrook, W.S., Louden, K.E., Shillington, D., and Lau, H., 2004, Continental breakup and the onset of ultraslow seafloor spreading off Flemish Cap on the Newfoundland rifted margin: Geology, v. 32, p. 93–96, doi: 10.1130/G19694.1.

Houseman, G., and England, P., 1986, A dynamical model of lithosphere extension and sedimentary basin formation: Journal of Geophysical Research: Solid Earth, v. 91, p. 719–729, doi: 10.1029/JB091iB01p00719.

Hubbert, M.K., 1937, Theory of scale models as applied to the study of geologic structures: Geological Society of America Bulletin, v. 48, p. 1459–1520, doi: 10.1130/GSAB-48-1459.

Huismans, R.S., and Beaumont, C., 2011, Depth-dependent extension, two-stage breakup and cratonic underplating at rifted margins: Nature, v. 473, p. 74–78, doi: 10.1038/nature09988.

Huismans, R.S., and Beaumont, C., 2003, Symmetric and asymmetric lithospheric extension: Relative effects of frictional-plastic and viscous strain softening: Journal of Geophysical Research-Solid Earth, v. 108, p. 2496, doi: doi:10.1029/2002JB002026.

Huismans, R.S., Podladchikov, Y.Y., and Cloetingh, S., 2001, Transition from passive to active rifting: Relative importance of asthenospheric doming and passive extension of the lithosphere: Journal of Geophysical Research: Solid Earth, v. 106, p. 11271–11291, doi: 10.1029/2000JB900424.

Jakobsson, M., Backman, J., Rudels, B., Nycander, J., Frank, M., Mayer, L., Jokat, W., Sangiorgi, F., O'Regan, M., Brinkhuis, H., King, J., and Moran, K., 2007, The early Miocene onset of a ventilated circulation regime in the Arctic Ocean: Nature, v. 447, p. 986–990, doi: 10.1038/nature05924.

Jarvis, G.T., and McKenzie, D.P., 1980, Sedimentary basin formation with finite extension rates: Earth and Planetary Science Letters, v. 48, p. 42–52, doi: 10.1016/0012-821X(80)90168-5.

Jolie, E., Klinkmueller, M., Moeck, I., and Bruhn, D., 2016, Linking gas fluxes at Earth's surface with fracture zones in an active geothermal field: Geology, v. 44, p. 187–190, doi: 10.1130/G37412.1.

Karner, G.D., Driscoll, N.W., McGinnis, J.P., Brumbaugh, W.D., and Cameron, N.R., 1997, Tectonic significance of syn-rift sediment packages across the Gabon-Cabinda continental margin: Marine and Petroleum Geology, v. 14, p. 973–1000, doi: 10.1016/S0264-8172(97)00040-8.

Katzman, R., Brink, U.S. ten, and Lin, J., 1995, Three-dimensional modeling of pull-apart basins: Implications for the tectonics of the Dead Sea Basin: Journal of Geophysical Research, v. 100, p. 6295–6312, doi: 10.1029/94JB03101.

Keir, D., Bastow, I.D., Corti, G., Mazzarini, F., and Rooney, T.O., 2015, The origin of along-rift variations in faulting and magmatism in the Ethiopian Rift: Tectonics, v. 34, p. 2014TC003698, doi: 10.1002/2014TC003698.

Keranen, K., Klemperer, S.L., Gloaguen, R., and Group, E.W., 2004, Three-dimensional seismic imaging of a protoridge axis in the Main Ethiopian rift: Geology, v. 32, p. 949–952, doi: 10.1130/G20737.1.

Kerrick, D.M., 2001, Present and past nonanthropogenic CO2 degassing from the solid earth: Reviews of Geophysics, v. 39, p. 565–585, doi: 10.1029/2001RG000105.

Kinabo, B.D., Hogan, J.P., Atekwana, E.A., Abdelsalam, M.G., and Modisi, M.P., 2008, Fault growth and propagation during incipient continental rifting: Insights from a combined aeromagnetic and Shuttle Radar Topography Mission digital elevation model investigation of the Okavango Rift Zone, northwest Botswana: Tectonics, v. 27, p. TC3013, doi: 10.1029/2007TC002154.

Kneller, E.A., Johnson, C.A., Karner, G.D., Einhorn, J., and Queffelec, T.A., 2012, Inverse methods for modeling non-rigid plate kinematics: Application to mesozoic plate reconstructions of the Central Atlantic: Computers & Geosciences, v. 49, p. 217–230, doi: http://dx.doi.org/10.1016/j.cageo.2012.06.019.

Koptev, A., Calais, E., Burov, E., Leroy, S., and Gerya, T., 2015, Dual continental rift systems generated by plume-lithosphere interaction: Nature Geoscience, v. 8, p. 388–392, doi: 10.1038/ngeo2401.

Koptev, A., Cloetingh, S., Burov, E., François, T., and Gerya, T., 2017, Long-distance impact of Iceland plume on Norway's rifted margin: Scientific Reports, v. 7, doi: 10.1038/s41598-017-07523-y.

Korchinski, M., Rey, P.F., Mondy, L., Teyssier, C., and Whitney, D.L., 2018, Numerical investigation of deep-crust behavior under lithospheric extension: Tectonophysics, v. 726, p. 137–146, doi: 10.1016/j.tecto.2017.12.029.

Lavier, L.L., and Manatschal, G., 2006, A mechanism to thin the continental lithosphere at magma-poor margins: Nature, v. 440, p. 324–328, doi: 10.1038/nature04608.

Le Pourhiet, L., Chamot-Rooke, N., Delescluse, M., May, D.A., Watremez, L., and Pubellier, M., 2018, Continental break-up of the South China Sea stalled by far-field compression: Nature Geoscience, p. 1, doi: 10.1038/s41561-018-0178-5.

Le Pourhiet, L., Huet, B., May, D.A., Labrousse, L., and Jolivet, L., 2012, Kinematic interpretation of the 3D shapes of metamorphic core complexes: Geochemistry Geophysics Geosystems, v. 13, p. Q09002, doi: 10.1029/2012GC004271.

Le Pourhiet, L., May, D.A., Huille, L., Watremez, L., and Leroy, S., 2017, A genetic link between transform and

hyper-extended margins: Earth and Planetary Science Letters, v. 465, p. 184–192, doi: 10.1016/j.epsl.2017.02.043.

Lee, H., Muirhead, J.D., Fischer, T.P., Ebinger, C.J., Kattenhorn, S.A., Sharp, Z.D., and Kianji, G., 2016, Massive and prolonged deep carbon emissions associated with continental rifting: Nature Geoscience, v. 9, p. 145–149, doi: 10.1038/ngeo2622.

Leroy, S., Razin, P., Autin, J., Bache, F., d'Acremont, E., Watremez, L., Robinet, J., Baurion, C., Denèle, Y., Bellahsen, N., Lucazeau, F., Rolandone, F., Rouzo, S., Kiel, J., et al., 2012, From rifting to oceanic spreading in the Gulf of Aden: a synthesis: Arabian Journal of Geosciences, v. 5, p. 859–901, doi: 10.1007/s12517-011-0475-4.

Liao, J., and Gerya, T., 2015, From continental rifting to seafloor spreading: Insight from 3D thermo-mechanical modeling: Gondwana Research, v. 28, p. 1329–1343, doi: 10.1016/j.gr.2014.11.004.

Liao, J., and Gerya, T., 2014, Influence of lithospheric mantle stratification on craton extension: Insight from two-dimensional thermo-mechanical modeling: Tectonophysics, doi: 10.1016/j.tecto.2014.01.020.

Lister, G.S., Etheridge, M.A., and Symonds, P.A., 1991, Detachment models for the formation of passive continental margins: Tectonics, v. 10, p. 1038–1064, doi: 10.1029/90TC01007.

Lithgow-Bertelloni, C., and Silver, P.G., 1998, Dynamic topography, plate driving forces and the African superswell: Nature, v. 395, p. 269–272, doi: 10.1038/26212.

Lizarralde, D., Axen, G.J., Brown, H.E., Fletcher, J.M., Gonzalez-Fernandez, A., Harding, A.J., Holbrook, W.S., Kent, G.M., Paramo, P., Sutherland, F., and Umhoefer, P.J., 2007, Variation in styles of rifting in the Gulf of California: Nature, v. 448, p. 466–469, doi: 10.1038/nature06035.

Logatchev, N.A., and Zorin, Y.A., 1992, Baikal rift zone: Structure and geodynamics: Tectonophysics, v. 208, p. 273–286, doi: 10.1016/0040-1951(92)90349-B.

Lundin, E.R., and Doré, A.G., 2011, Hyperextension, serpentinization, and weakening: A new paradigm for rifted margin compressional deformation: Geology, v. 39, p. 347–350, doi: 10.1130/G31499.1.

Magni, V., Faccenna, C., Hunen, J. van, and Funiciello, F., 2014, How collision triggers backarc extension: Insight into Mediterranean style of extension from 3-D numerical models: Geology, v. 42, p. 511–514, doi: 10.1130/G35446.1.

Maloney, K.T., Clarke, G.L., Klepeis, K.A., and Quevedo, L., 2013, The Late Jurassic to present evolution of the Andean margin: Drivers and the geological record: Tectonics, v. 32, p. 1049–1065, doi: 10.1002/tect.20067.

Mart, Y., and Dauteuil, O., 2000, Analogue experiments of propagation of oblique rifts: Tectonophysics, v. 316, p. 121–132, doi: 10.1016/S0040-1951(99)00231-0.

McKenzie, D., 1978, Some remarks on the development of sedimentary basins: Earth and Planetary Science Letters, v. 40, p. 25–32, doi: 10.1016/0012-821X(78)90071-7.

McQuarrie, N., and Wernicke, B.P., 2005, An animated tectonic reconstruction of southwestern North America since 36 Ma: Geosphere, v. 1, p. 147–172, doi: 10.1130/GES00016.1.

Menzies, M.A., Klemperer, S.L., Ebinger, C.J., and Baker, J., 2002, Characteristics of volcanic rifted margins: Geological Society of America Special Papers, v. 362, p. 1–14, doi: 10.1130/0-8137-2362-0.1.

Merino, M., Keller, G.R., Stein, S., and Stein, C., 2013, Variations in Mid-Continent Rift magma volumes consistent with microplate evolution: Geophysical Research Letters, v. 40, p. 1513–1516, doi: 10.1002/grl.50295.

Michon, L., and Merle, O., 2000, Crustal structures of the Rhinegraben and the Massif Central grabens: An experimental approach: Tectonics, v. 19, p. 896–904, doi: 10.1029/2000TC900015.

Minshull, T.A., Lane, C.I., Collier, J.S., and Whitmarsh, R.B., 2008, The relationship between rifting and magmatism in the northeastern Arabian Sea: Nature Geoscience, v. 1, p. 463–467, doi: 10.1038/ngeo228.

Mjelde, R., Breivik, A.J., Raum, T., Mittelstaedt, E., Ito, G., and Faleide, J.I., 2008, Magmatic and tectonic evolution of the North Atlantic: Journal of the Geological Society, v. 165, p. 31–42, doi: 10.1144/0016-76492007-018.

Mohn, G., Manatschal, G., Beltrando, M., and Haupert, I., 2014, The role of rift-inherited hyper-extension in Alpine-type orogens: Terra Nova, v. 26, p. 347–353, doi: 10.1111/ter.12104.

Molnar, N.E., Cruden, A.R., and Betts, P.G., 2017, Interactions between propagating rotational rifts and linear rheological heterogeneities: Insights from three-dimensional laboratory experiments: Tectonics, v. 36, p. 2016TC004447, doi: 10.1002/2016TC004447.

Mondy, L.S., Rey, P.F., Duclaux, G., and Moresi, L., 2017, The role of asthenospheric flow during rift propagation and breakup: Geology, v. 46, p. 103–106, doi: 10.1130/G39674.1.

Moulin, M., Aslanian, D., and Unternehr, P., 2010, A new starting point for the South and Equatorial Atlantic Ocean: Earth-Science Reviews, v. 98, p. 1–37, doi: 10.1016/j.earscirev.2009.08.001.

Muirhead, J.D., Kattenhorn, S.A., Lee, H., Mana, S., Turrin, B.D., Fischer, T.P., Kianji, G., Dindi, E., and Stamps, D.S., 2016, Evolution of upper crustal faulting assisted by magmatic volatile release during early-stage continental rift development in the East African Rift: Geosphere, v. 12, p. 1670–1700, doi: 10.1130/GES01375.1.

Müller, R.D., Cannon, J., Qin, X., Watson, R.J., Gurnis, M., Williams, S., Pfaffelmoser, T., Seton, M., Russell, S.H.J., and Zahirovic, S., 2018, GPlates – Building a Virtual Earth Through Deep Time: Geochemistry, Geophysics, Geosystems, v. (in press), doi: 10.1029/2018GC007584.

Müller, R.D., Seton, M., Zahirovic, S., Williams, S.E., Matthews, K.J., Wright, N.M., Shephard, G.E., Maloney, K.T., Barnett-Moore, N., Hosseinpour, M., Bower, D.J., and Cannon, J., 2016, Ocean Basin Evolution and Global-Scale Plate Reorganization Events Since Pangea Breakup: Annual Review of Earth and Planetary Sciences, v. 44, p. 107–138, doi: 10.1146/annurev-earth-060115-012211.

Mutter, J.C., Talwani, M., and Stoffa, P.L., 1982, Origin of seaward-dipping reflectors in oceanic crust off the Norwegian margin by "subaerial sea-floor spreading": Geology, v. 10, p. 353–357, doi: 10.1130/0091-7613(1982)10<353:OOSRIO>2.0.CO;2.

Naliboff, J.B., Buiter, S.J.H., Péron-Pinvidic, G., Osmundsen, P.T., and Tetreault, J., 2017, Complex fault interaction controls continental rifting: Nature Communications, v. 8, p. 1179, doi: 10.1038/s41467-017-00904-x.

Nemčok, M., and Rybár, S., 2017, Rift–drift transition in a magma-rich system: the Gop Rift–Laxmi Basin case study, West India: Geological Society, London, Special Publications, v. 445, p. 95–117, doi: 10.1144/SP445.5.

Nestola, Y., Storti, F., Bedogni, E., and Cavozzi, C., 2013, Shape evolution and finite deformation pattern in analog experiments of lithosphere necking:

Geophysical Research Letters, v. 40, p. 2013GL057618, doi: 10.1002/grl.50978.

Nirrengarten, M., Manatschal, G., Tugend, J., Kusznir, N., and Sauter, D., 2018, Kinematic Evolution of the Southern North Atlantic: Implications for the Formation of Hyperextended Rift Systems: Tectonics, p. 2017TC004495, doi: 10.1002/2017TC004495.

Pang, Y., Zhang, H., Gerya, T.V., Liao, J., Cheng, H., and Shi, Y., 2018, The Mechanism and Dynamics of N-S Rifting in Southern Tibet: Insight From 3-D Thermomechanical Modeling: Journal of Geophysical Research: Solid Earth, v. 123, p. 2017JB014011, doi: 10.1002/2017JB014011.

Pérez-Gussinyé, M., Morgan, J.P., Reston, T.J., and Ranero, C.R., 2006, The rift to drift transition at non-volcanic margins: Insights from numerical modelling: Earth and Planetary Science Letters, v. 244, p. 458–473, doi: 10.1016/j.epsl.2006.01.059.

Peron-Pinvidic, G., Manatschal, G., and Osmundsen, P.T., 2013, Structural comparison of archetypal Atlantic rifted margins: A review of observations and concepts: Marine and Petroleum Geology, doi: 10.1016/j.marpetgeo.2013.02.002.

Petersen, K.D., Armitage, J.J., Nielsen, S.B., and Thybo, H., 2015, Mantle temperature as a control on the time scale of thermal evolution of extensional basins: Earth and Planetary Science Letters, v. 409, p. 61–70, doi: 10.1016/j.epsl.2014.10.043.

Petersen, K.D., Nielsen, S.B., Clausen, O.R., Stephenson, R., and Gerya, T., 2010, Small-Scale Mantle Convection Produces Stratigraphic Sequences in Sedimentary Basins: Science, v. 329, p. 827–830, doi: 10.1126/science.1190115.

Petit, C., and Déverchère, J., 2006, Structure and evolution of the Baikal rift: A synthesis: Geochemistry, Geophysics, Geosystems, v. 7, p. Q11016, doi: 10.1029/2006GC001265.

Petrunin, A.G., and Sobolev, S.V., 2008, Three-dimensional numerical models of the evolution of pull-apart basins: Physics of the Earth and Planetary Interiors, v. 171, p. 387–399, doi: 10.1016/j.pepi.2008.08.017.

Philippon, M., Willingshofer, E., Sokoutis, D., Corti, G., Sani, F., Bonini, M., and Cloetingh, S., 2015, Slip re-orientation in oblique rifts: Geology, v. 43, p. 147–150, doi: 10.1130/G36208.1.

Ranero, C.R., and Pérez-Gussinyé, M., 2010, Sequential faulting explains the asymmetry and extension discrepancy of conjugate margins: Nature, v. 468, p. 294–299, doi: 10.1038/nature09520.

Reston, T.J., 2007, The formation of non-volcanic rifted margins by the progressive extension of the lithosphere: the example of the West Iberian margin: Geological Society, London, Special Publications, v. 282, p. 77–110, doi: 10.1144/SP282.5.

Ricketts, J.W., Kelley, S.A., Karlstrom, K.E., Schmandt, B., Donahue, M.S., and Wijk, J. van, 2016, Synchronous opening of the Rio Grande rift along its entire length at 25–10 Ma supported by apatite (U-Th)/He and fission-track thermochronology, and evaluation of possible driving mechanisms: GSA Bulletin, v. 128, p. 397–424, doi: 10.1130/B31223.1.

Ring, U., 2014, The East African Rift System: Austrian Journal of Earth Sciences, v. 107.

Royden, L., Sclater, J.G., and Herzen, R.P.V., 1980, Continental Margin Subsidence and Heat Flow: Important Parameters in Formation of Petroleum Hydrocarbons: AAPG Bulletin, v. 64, p. 173–187.

Schmeling, H., 2010, Dynamic models of continental rifting with melt generation: Tectonophysics, v. 480, p. 33–47.

Schreurs, G., and Colletta, B., 1998, Analogue modelling of faulting in zones of continental transpression and transtension: Geological Society, London, Special Publications, v. 135, p. 59–79.

Schumacher, M.E., 2002, Upper Rhine Graben: Role of preexisting structures during rift evolution: Tectonics, v. 21, p. 6–1, doi: 10.1029/2001TC900022.

Sdrolias, M., and Müller, R.D., 2006, Controls on back-arc basin formation: Geochemistry, Geophysics, Geosystems, v. 7, p. Q04016, doi: 10.1029/2005GC001090.

Şengör, A.M.C., and Burke, K., 1978, Relative timing of rifting and volcanism on Earth and its tectonic implications: Geophysical Research Letters, v. 5, p. 419–421, doi: 10.1029/GL005i006p00419.

Şengör, A.M.C., and Natal'in, B.A., 2001, Rifts of the World: Geological Society of America Special Papers, v. 352, p. 389–482, doi: 10.1130/0-8137-2352-3.389.

Smith, J., 2016, CO2 Flux Along Faults of the Central Rio Grande Rift, New Mexico [Master Thesis]: Master Thesis, The University of New Mexico, http://repository.unm.edu/handle/1928/32989 (accessed December 2016).

Sokoutis, D., Corti, G., Bonini, M., Brun, J.P., Cloetingh, S., Mauduit, T., and Manetti, P., 2007, Modelling the extension of heterogeneous hot lithosphere: Tectonophysics, v. 444, p. 63–79, doi: 10.1016/j.tecto.2007.08.012.

Sternai, P., Jolivet, L., Menant, A., and Gerya, T., 2014, Driving the upper plate surface deformation by slab rollback and mantle flow: Earth and Planetary Science Letters, v. 405, p. 110–118, doi: 10.1016/j.epsl.2014.08.023.

Stüwe, K., 2007, Geodynamics of the Lithosphere: An Introduction: Springer.

Sun, X., and Wang, P., 2005, How old is the Asian monsoon system?—Palaeobotanical records from China: Palaeogeography, Palaeoclimatology, Palaeoecology, v. 222, p. 181–222, doi: 10.1016/j.palaeo.2005.03.005.

Sun, Z., Zhong, Z.H., Zhou, D., Pang, X., Huang, C.J., Chen, C.M., He, M., and Xu, H.H., 2008, Dynamics analysis of the Baiyun sag in the Pearl River Mouth Basin, north of the South China sea: Acta Geologica Sinica - English Edition, v. 82, p. 73–83, doi: 10.1111/j.1755-6724.2008.tb00326.x.

Sutra, E., and Manatschal, G., 2012, How Does the Continental Crust Thin in a Hyperextended Rifted Margin? Insights from the Iberia Margin: Geology, v. 40, p. 139–142, doi: 10.1130/G32786.1.

Sutra, E., Manatschal, G., Mohn, G., and Unternehr, P., 2013, Quantification and restoration of extensional deformation along the Western Iberia and Newfoundland rifted margins: Geochemistry, Geophysics, Geosystems, p. n/a–n/a, doi: 10.1002/ggge.20135.

Svartman Dias, A.E., Lavier, L.L., and Hayman, N.W., 2015, Conjugate rifted margins width and asymmetry: The interplay between lithospheric strength and thermomechanical processes: Journal of Geophysical Research: Solid Earth, v. 120, p. 2015JB012074, doi: 10.1002/2015JB012074.

Taylor, B., Goodliffe, A., Martinez, F., and Hey, R., 1995, Continental rifting and initial sea-floor spreading in the Woodlark basin: Nature, v. 374, p. 534–537, doi: 10.1038/374534a0.

Tetreault, J.L., and Buiter, S.J.H., 2017, The influence of extension rate and crustal rheology on the evolution of passive margins from rifting to break-up: Tectonophysics, doi: 10.1016/j.tecto.2017.08.029.

Thybo, H., and Nielsen, C.A., 2009, Magma-compensated crustal thinning in continental rift zones: Nature, v. 457, p. 873–876, doi: 10.1038/nature07688.

Tirel, C., Brun, J.-P., and Burov, E., 2008, Dynamics and structural development of metamorphic core complexes: Journal of Geophysical Research: Solid Earth, v. 113, p. B04403, doi: 10.1029/2005JB003694.

Torsvik, T.H., Rousse, S., Labails, C., and Smethurst, M.A., 2009, A new scheme for the opening of the South Atlantic Ocean and the dissection of an Aptian salt basin: Geophysical Journal International, v. 177, p. 1315–1333, doi: 10.1111/j.1365-246X.2010.04727.x.

Tron, V., and Brun, J.-P., 1991, Experiments on oblique rifting in brittle-ductile systems: Tectonophysics, v. 188, p. 71–84, doi: 10.1016/0040-1951(91)90315-J.

Unternehr, P., Peron-Pinvidic, G., Manatschal, G., and Sutra, E., 2010, Hyper-extended crust in the South Atlantic: in search of a model: Petroleum Geoscience, v. 16, p. 207–215, doi: 10.1144/1354-079309-904.

Van Horne, A., Sato, H., and Ishiyama, T., 2017, Evolution of the Sea of Japan back-arc and some unsolved issues: Tectonophysics, v. 710–711, p. 6–20, doi: 10.1016/j.tecto.2016.08.020.

van Wijk, J.W., 2005, Role of weak zone orientation in continental lithosphere extension: Geophysical Research Letters, v. 32, doi: 10.1029/2004GL022192.

Wallner, H., and Schmeling, H., 2010, Rift induced delamination of mantle lithosphere and crustal uplift: a new mechanism for explaining Rwenzori Mountains' extreme elevation? International Journal of Earth Sciences, doi: 10.1007/s00531-010-0521-6.

Wang, Y., Forsyth, D.W., and Savage, B., 2009, Convective upwelling in the mantle beneath the Gulf of California: Nature, v. 462, p. 499–501, doi: 10.1038/nature08552.

Weinlich, F.H., Bräuer, K., Kämpf, H., Strauch, G., Tesař, J., and Weise, S.M., 1999, An active subcontinental mantle volatile system in the western Eger rift, Central Europe: gas flux, isotopic (He, C, and N) and compositional fingerprints: Geochimica et Cosmochimica Acta, v. 63, p. 3653–3671, doi: 10.1016/S0016-7037(99)00187-8.

Wernicke, B., 1985, Uniform-sense normal simple shear of the continental lithosphere: Canadian Journal of Earth Sciences, v. 22, p. 108–125, doi: 10.1139/e85-009.

Wessel, P., and Müller, D.R., 2015, Plate Tectonics, *in* Treatise on Geophysics Vol 6 - Crust and Lithosphere Dynamics, v. 6, p. 45–93, http://dx.doi.org/10.1016/B978-0-444-53802-4.00111-1.

Whitney, D.L., Teyssier, C., Rey, P., and Buck, W.R., 2013, Continental and oceanic core complexes: Geological Society of America Bulletin, v. 125, p. 273–298, doi: 10.1130/B30754.1.

Whittaker, J.M., Williams, S.E., and Müller, R.D., 2013, Revised tectonic evolution of the Eastern Indian Ocean: Geochemistry, Geophysics, Geosystems, v. 14, p. 1891–1909, doi: 10.1002/ggge.20120.

van Wijk, J.W., and Cloetingh, S.A.P.L., 2002, Basin migration caused by slow lithospheric extension: Earth and Planetary Science Letters, v. 198, p. 275–288, doi: 10.1016/S0012-821X(02)00560-5.

Williams, S.E., Whittaker, J.M., and Müller, R.D., 2011, Full-fit, palinspastic reconstruction of the conjugate Australian-Antarctic margins: Tectonics, v. 30, p. 21 PP., doi: 201110.1029/2011TC002912.

Wilson, J.T., 1966, Did the Atlantic Close and then Re-Open? Nature, v. 211, p. 676–681, doi: 10.1038/211676a0.

de Wit, M.J., Stankiewicz, J., and Reeves, C., 2008, Restoring Pan-African-Brasiliano connections: more Gondwana control, less Trans-Atlantic corruption: Geological Society, London, Special Publications, v. 294, p. 399–412.

Withjack, M.O., and Jamison, W.R., 1986, Deformation produced by oblique rifting: Tectonophysics, v. 126, p. 99–124, doi: 10.1016/0040-1951(86)90222-2.

Wolstencroft, M., and Davies, J.H., 2017, Breaking supercontinents; no need to choose between passive or active: Solid Earth, v. 8, p. 817–825, doi: https://doi.org/10.5194/se-8-817-2017.

Yin, A., 2010, Cenozoic tectonic evolution of Asia: A preliminary synthesis: Tectonophysics, v. 488, p. 293–325, doi: 10.1016/j.tecto.2009.06.002.

Zahirovic, S., Seton, M., and Müller, R.D., 2014, The Cretaceous and Cenozoic tectonic evolution of Southeast Asia: Solid Earth, v. 5, p. 227–273, doi: 10.5194/se-5-227-2014.

Zhou, D., and Yao, B., 2009, Tectonics and sedimentary basins of the South China Sea: Challenges and progresses: Journal of Earth Science, v. 20, p. 1–12, doi: 10.1007/s12583-009-0001-8.

Ziegler, P.A., and Cloetingh, S., 2004, Dynamic processes controlling evolution of rifted basins: Earth-Science Reviews, v. 64, p. 1–50, doi: 10.1016/S0012-8252(03)00041-2.

Zilio, L.D., Faccenda, M., and Capitanio, F., 2017, The role of deep subduction in supercontinent breakup: Tectonophysics, v. in press., doi: 10.1016/j.tecto.2017.03.006.

Zwaan, F., Schreurs, G., and Adam, J., 2017, Effects of sedimentation on rift segment and transfer zone evolution in orthogonal and oblique extension settings: Insights from analogue models analysed with 4D X-ray computed tomography and digital volume correlation techniques: Global and Planetary Change, doi: 10.1016/j.gloplacha.2017.11.002.

Zwaan, F., Schreurs, G., Naliboff, J., and Buiter, S.J.H., 2016, Insights into the effects of oblique extension on continental rift interaction from 3D analogue and numerical models: Tectonophysics, v. 693, Part B, p. 239–260, doi: 10.1016/j.tecto.2016.02.036.

Chapter II - 2D Models

Article 1

Brune, S.; Heine, C.; Perez-Gussinye, M.; Sobolev, S. V. (2014): Rift migration explains continental margin asymmetry and crustal hyper-extension. ***Nature Communications***. 5:4014. doi:10.1038/ncomms5014.

Article 2

Brune, S., Heine, C., Clift, P., Perez-Gussinye, M. (2017): Rifted Margin Architecture and Crustal Rheology: Reviewing Iberia-Newfoundland, Central South Atlantic, and South China Sea. ***Marine and Petroleum Geology***, 79, 257–281, doi: 10.1016/j.marpetgeo.2016.10.018.

Article 3

Clift, P., **Brune, S.**, Quinteros, J. (2015): Climate changes control offshore crustal structure at South China Sea continental margin. ***Earth and Planetary Science Letters*** 420, 66–72. doi:10.1016/j.epsl.2015.03.032

Article 4

Brune, S., Williams, S.E., Butterworth, N.P., Müller, R.D. (2016): Abrupt plate accelerations shape rifted continental margins. ***Nature***, 536 (7615), 201–204, doi:10.1038/nature18319.

nature COMMUNICATIONS

ARTICLE

Received 17 Dec 2013 | Accepted 30 Apr 2014 | Published 6 Jun 2014

DOI: 10.1038/ncomms5014 OPEN

Rift migration explains continental margin asymmetry and crustal hyper-extension

Sascha Brune[1,2], Christian Heine[2], Marta Pérez-Gussinyé[3] & Stephan V. Sobolev[1,4]

When continents break apart, continental crust and lithosphere are thinned until break-up is achieved and an oceanic basin is formed. The most remarkable and least understood structures associated with this process are up to 200 km wide areas of hyper-extended continental crust, which are partitioned between conjugate margins with pronounced asymmetry. Here we show, using high-resolution thermo-mechanical modelling, that hyper-extended crust and margin asymmetry are produced by steady state rift migration. We demonstrate that rift migration is accomplished by sequential, oceanward-younging, upper crustal faults, and is balanced through lower crustal flow. Constraining our model with a new South Atlantic plate reconstruction, we demonstrate that larger extension velocities may account for southward increasing width and asymmetry of these conjugate magma-poor margins. Our model challenges conventional ideas of rifted margin evolution, as it implies that during rift migration large amounts of material are transferred from one side of the rift zone to the other.

[1] Geodynamic Modelling Section, Helmholtz Centre Potsdam, GFZ German Research Centre for Geosciences, Telegrafenberg, 14473 Potsdam, Germany. [2] EarthByte Group, School of Geosciences, The University of Sydney, Sydney, New South Wales 2006, Australia. [3] Department of Earth Sciences, Royal Holloway, University of London, Egham Hill, Egham, Surrey TW20 0EX, UK. [4] O.Yu. Schmidt Institute of the Physics of the Earth, Russian Academy of Sciences, 10 ul. B. Gruzinskaya, Moscow 123995, Russia. Correspondence and requests for materials should be addressed to S.B. (email: brune@gfz-potsdam.de).

The extensively surveyed Iberia/Newfoundland and Angola/Brazil conjugates provide detailed information on magma-poor rifted margin formation. They exhibit hyper-extended (with a thickness <10 km) crustal slivers that vary in widths between 70 km offshore Iberia[1,2] and 200 km off Angola[3]. The respective conjugate margin width, however, is restricted to a few tens of kilometres[4,5], resulting in large-scale crustal asymmetry.

Observations off Iberia indicate that brittle deformation is accommodated by sequentially active normal faults[2], with very thin syn-rift deposits supporting short-lived individual fault activity, that is, in the order of a few million years[2,6]. Similarly, the wide South Atlantic margins feature undeformed, pre-break-up sediments[5,7] below Aptian salt deposits[8], which requires that extensive local rift activity, achieving crustal thinning of a factor larger than 3, was surprisingly restricted to a few million years and did not result in break-up at this location.

Despite great academic and economic interest in hyper-extended margins and instructive field-based studies[1–6,9–11], no suitable thermo-mechanically corroborated model has been presented so far. A previous numerical model[12] is problematic for several reasons: it suggests that the crust is thinned by permanent pure shear both at the proximal and distal margin; a scenario that is contradicted by observations of undisturbed, pre-break-up sediments along the African margin. A felsic flow law for the entire crust is used that is not supported by the seismically inferred mafic (that is, strong) composition of the lower crust[3]. Finally, the previous study[12] produced symmetric margins and could not explain the dominant asymmetry of the South Atlantic and Iberia/Newfoundland conjugate margins.

In this study, we propose rift migration as a key process during hyper-extended margin formation. Our numerical models indicate that steady-state rift migration is maintained by sequential faulting in the brittle crust and controlled by lower crustal flow. Thus, the extent of rift migration depends on lower crustal viscosity near the moving rift, which in turn is a function of extension velocity, lower crustal composition, intensity of strain softening and initial thermal structure. By demonstrating how lower crustal viscosity and the rate of extension affect the final margin width, we explain the formation of hyper-extended crust and the degree of asymmetry in the Central South Atlantic and Iberia/Newfoundland within a single model framework.

Results

Initiation and dynamic maintenance of rift migration. We use thermo-mechanical finite-element models to investigate lithospheric thinning. The applied rheologies, initial temperature fields and extension velocities are discussed in the Methods section, while a setup sketch and all model parameters are provided in Supplementary Fig. 1 and Supplementary Table 1, respectively. Modelled rift evolution is shown in Figs 1 and 2. Rifting starts with a fault network that distributes deformation across the whole width of the model before friction softening causes coalescence[13] into a dominant single fault with few antithetic faults[14], which is typical for narrow rifts such as the East African Rift System[15]. The time necessary for the deformation to localize into this dominant fault is a function of lower crustal rheology, with weaker rheologies showing a more prolonged phase of initial distributed faulting. At the downward tip of this normal fault, brittle and ductile deformation in crust and mantle are strongly linked. Hence, slip along the dominant initial fault results in severe lithospheric thinning and hot asthenospheric upwelling. Simultaneously, sub-horizontal ductile shear zones develop in the lower portions of both the felsic and mafic crust (Figs 1c and 2b) as described for the South Atlantic conjugates[10], the Iberian margin[16] and in previous numerical rift simulations[17].

Upwelling of hot mantle material is more pronounced near the down-dip end of the initial dominant fault, so that the 600 °C isotherm penetrates into the lower crust. Elevated temperature and viscous strain softening generate a pocket of weak lower crust at the fault tip (see white isoviscosity line of $10^{20.5}$ Pa s in Fig. 2f,g). In analogy to the subduction channel at convergent plate boundaries, we refer to this weak locus of deformation as 'exhumation channel'. At the footwall side of the exhumation channel where the upwelling mantle is shallowest, cooling and strengthening of mantle material takes place[18,19] (Fig. 2g). These two processes—softening at the tip of the active fault and strengthening at its footwall—generate a lateral strength gradient that forces migration of the rift in a steady-state manner. During migration, new rift-bounding faults are generated that become sequentially active. Ductile lower crust flows within the exhumation channel towards the down-dip end of any of these faults (Fig. 3h,i). This flow balances the faults' tendency for crustal thinning and break-up, and it promotes the formation of a single, wide margin on one rift side with crust thinned to a thickness of <10 km. Opposite to previous models of margin formation[20,21], we find that large-scale asymmetry does not form by slip on large detachment faults cross-cutting the crust or entire lithosphere, but by an array of oceanward dipping faults that act sequentially in time[2].

During migration of the rift centre, previously active faults are abandoned, whereas new faults form on top of the exhumation channel cutting into undisturbed crust of the left-hand rift side. This accretes crustal material across the migrating plate boundary zone (white region in Fig. 2i–l) to the opposite rift side. Therefore, in contradiction to the common assumption that the stretched continental crust of a passive margin consists of deformed material of the same plate, our model suggests that large parts of a hyper-extended margin originate from the formerly opposite side of the rift zone.

Despite extreme final margin widths of more than 200 km (Fig. 1e), the actively deforming plate boundary zone appears to be very narrow ($\sim$30 km; Fig. 2c). Crustal thinning in the rift is accomplished by short-lived (a few million years) sequential faults with high-slip velocities (for example, 12 mm per year slip on the fault plane for 8 mm per year full extension velocity). This implies limited available time for syn-rift sediment to accumulate and agrees well with observations off West Iberia[2,6]. At very wide margins that experience a long period of rift migration (such as the Angolan Kwanza Basin), the proximal part of the margin exhibits undisturbed sedimentary successions that are dominated by thermal subsidence[5,7], although their age is actually pre-break-up[22]. Moreover, lateral motion of the rift centre causes oceanward migrating peak heat flow, with strong implications for hydrocarbon maturation patterns.

With continued rift migration, the steady-state heat supply to the exhumation channel decreases. The crust becomes cooler, and the ductile portions of the crust strengthen to a degree that the low-viscosity pocket vanishes. The crust becomes progressively brittle and faults penetrate into the mantle (as suggested for West Iberia[1,23]). Soon after, these faults bring the crust to break-up until mantle is exhumed with very little magmatic activity (Fig. 2d).

Influence of rift velocity. The longevity of the exhumation channel, and hence the final width of the conjugate margins, is determined by the ability of the lower crust to flow into the area where active faults terminate at depth. This replenishing of lower crust depends on the lower crustal viscosity and hence on temperature distribution, crustal rheology and the operating weakening mechanisms. High rift velocities lead to more efficient

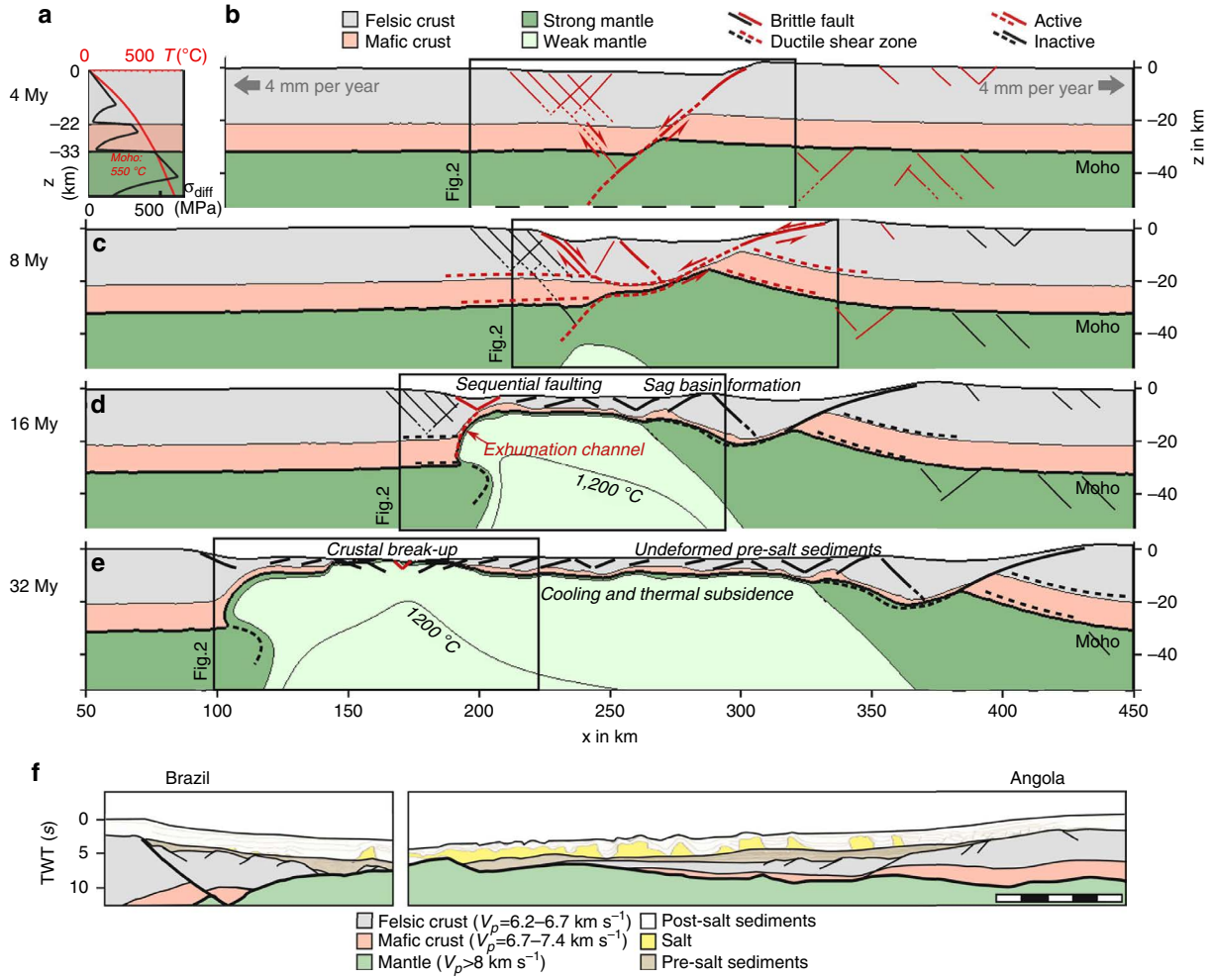

Figure 1 | The process of steady-state rift migration. (**a**–**e**) Fault kinematics of the model. Active faults are shown in red and inactive faults in black. Brittle faults are indicated with solid lines, ductile shear zones with dashed lines. The wide margin is formed through rift migration and sequentially active faulting towards the future ocean. Hence, thick undisturbed pre-salt sediments pre-dating break-up are predicted by our model to be deposited in the landward part of the margin (**d**,**e**). The final crustal structure of the model reproduces the strong asymmetry (**f**) of the conjugate Campos Basin–Angola margins (modified after ref. 5). Note that the geosection is drawn without vertical exaggeration at the same scale as the model (scale bar in the lower right corner is 50 km long). Vertical scale is in seconds two-way travel time (TWT).

heat advection and thus elevate the temperature of the exhumation channel (Fig. 3). The extent of the low-viscosity pocket is increased (Fig. 3d–f) and rift migration is maintained over a longer distance. Hence, faster extension results in wider margins with more pronounced asymmetry.

The conjugate South Atlantic margins of the central segment are an excellent test case for this model prediction as intraplate deforming zones in Africa allow to robustly reconstruct the pre-break-up kinematic history of the South Atlantic Rift[24,25]. The stage poles describing initial extension and early seafloor spreading history are located close to the northern tip of the South Atlantic Rift. Consequently, relative plate velocities between Africa and South America increase away from the stage pole, resulting in extensional velocities increasing southward along strike of the South Atlantic Rift system (Fig. 4a). This inference is also robustly featured in other reconstructions[8,26–28]. Independent evidence for opening velocities comes from seismic section restoration at the Campos and Camamu basins (M. Araujo, personal communication) yielding extension rates that correspond well with the plate kinematic model.

We find that the maximum width of the conjugate margin cross-sections increases southward almost linearly (Fig. 4b). Similarly, numerical models with varied extensional velocities exhibit a southward increase in hyper-extended margin width. In particular, our modelling indicates a linear relationship between extension velocity and margin width (Figs 3a–c and 4b). Although the polarity of the South Atlantic hyper-extended margins alternates, the width of the wider margin is very well reproduced by the numerical results. Note that the reason for the polarity switch cannot be addressed within our two-dimensional (2D) model framework. Similarly, the evolution of the Santos basin, south of Campos, that is characterized by a complicated three-dimensional tectonic and magmatic evolution[29] lies outside of our 2D modelling scope.

Influence of initial thermal profile. Lower crustal temperatures and rheology jointly affect the lower crustal viscosity and the depth of the crustal brittle-ductile transition. A cold, strong crust with a thick brittle layer effectively couples brittle deformation of crust and mantle through thin ductile shear zones producing a

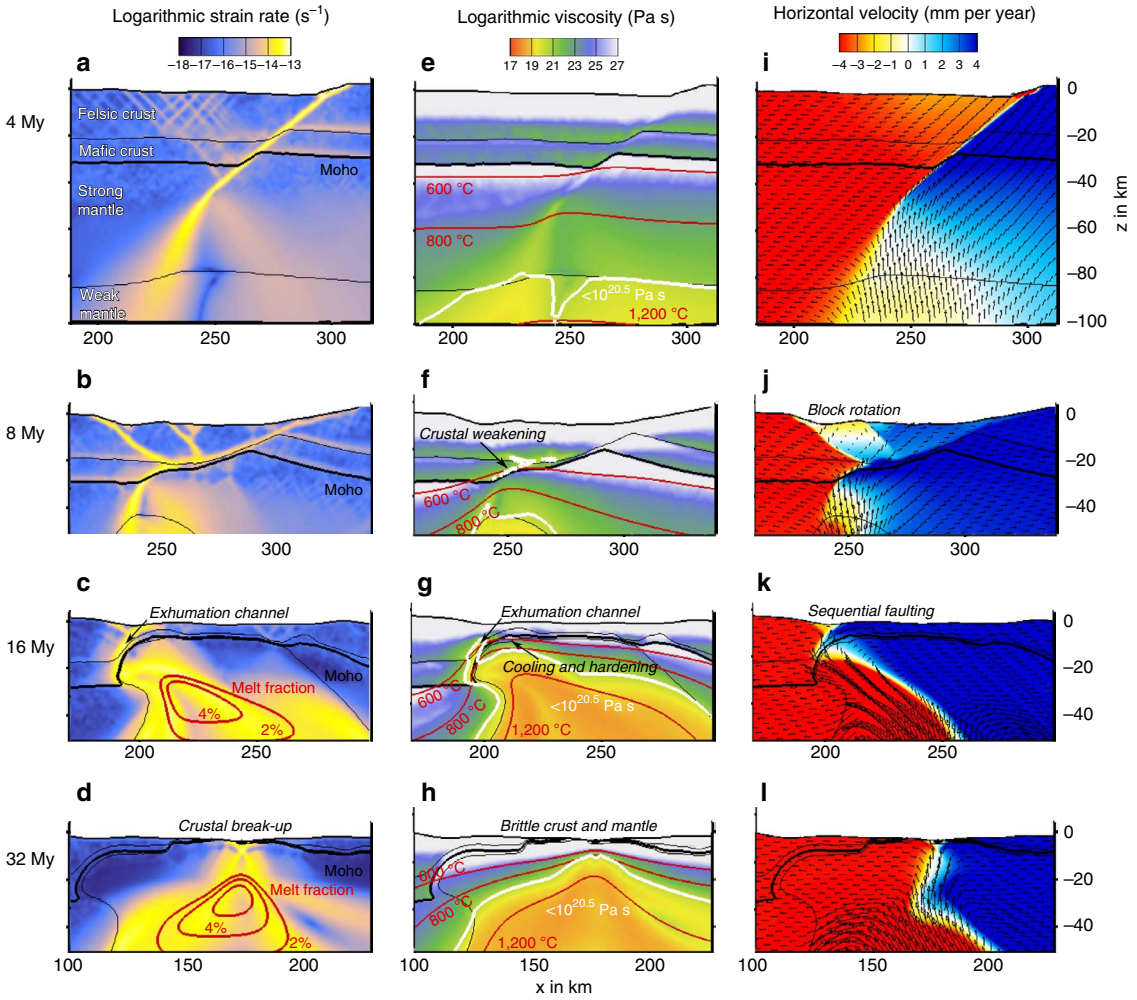

Figure 2 | Key variables of the numerical model. Shown are (**a**–**d**) strain rate, (**e**–**h**) viscosity and (**i**–**l**) horizontal velocity. A dominant fault at 4 My induces asymmetric hot mantle upwelling and subsequent asymmetric lower crustal weakening (**a**). A low-viscosity crustal pocket forms at the tip of sequential upper crustal faults, together forming the 'exhumation channel' that is visible in terms of high strain rate (**c**) and low viscosity (**g**). The existence of the low-viscosity pocket facilitates lower crustal flow towards the down-dip fault end rendering fault-induced Moho uplift less efficient. Rift migration is caused by a lateral strength gradient between the low-viscosity pocket and the cooling mantle at the fault's footwall. Rift migration stops when the lower crust becomes more viscous, followed by crustal embrittlement (**h**), and soon after crustal break-up takes place. Full extension velocity is 8 mm per year. Note that grey regions in (**e**–**h**) where viscosity is maximal, deform via brittle behaviour. The depicted x-interval varies between time steps, as shown in Fig. 1. For detailed model evolution, see animated strain rate and viscosity plots in Supplementary Fig. 3.

narrow rift[30] (Fig. 5g). Fault and shear zone weakening results in strong competition between faults, producing a single master fault in a simple shear system that leads to strong rift asymmetry[14,31]. Hot, weak lower crust, on the other hand, decouples brittle deformation between crust and mantle generating a wide rift[30] that eventually generates symmetric, wide margins[32] (see Supplementary Discussion, Supplementary Fig. 2 and Supplementary Table 2).

In between these two end members, intermediate crust–mantle coupling generates a moderately asymmetric fault pattern[14,17]. We analyse how the initial lower crustal strength influences rift migration and ultimately margin geometry by varying the initial depth of the thermal lithosphere–asthenosphere boundary (LAB; the 1,300 °C isotherm) between 90 km (Figs 5a,b and 6a), 105 km (Figs 5c,d and 6b) and 120 km (Figs 1e and 5e,f). We find that initial fault symmetry impedes rift migration while a singular normal fault leads to asymmetric mantle upwelling, which heats its hanging wall producing a low-viscosity exhumation channel enhancing rift migration. Hence, the initial fault pattern controls the extent of simultaneously and sequentially faulted areas (*cf.* blue and black arrows in Figs 3a–c and 6a,b). We note that other combinations of rheology and lithospheric thickness, as long as they result in similar lower crustal viscosity and brittle layer thickness, lead to a qualitatively identical rift evolution.

The Iberia–Newfoundland rift is best described with intermediate lithosphere thickness of 105 km (Fig. 6b,c), where an initially decoupled, moderately asymmetric fault phase is followed by crust–mantle coupling, sequential faulting and low-degree rift migration[33] (see also Supplementary Fig. 3). Our thermal setup is supported by lithospheric thickness estimates that are generally lower for Iberia–Newfoundland than for Africa–South America[34].

Discussion

We compare our results with previous numerical studies on rifted margin formation. During the initial extension phase, our models

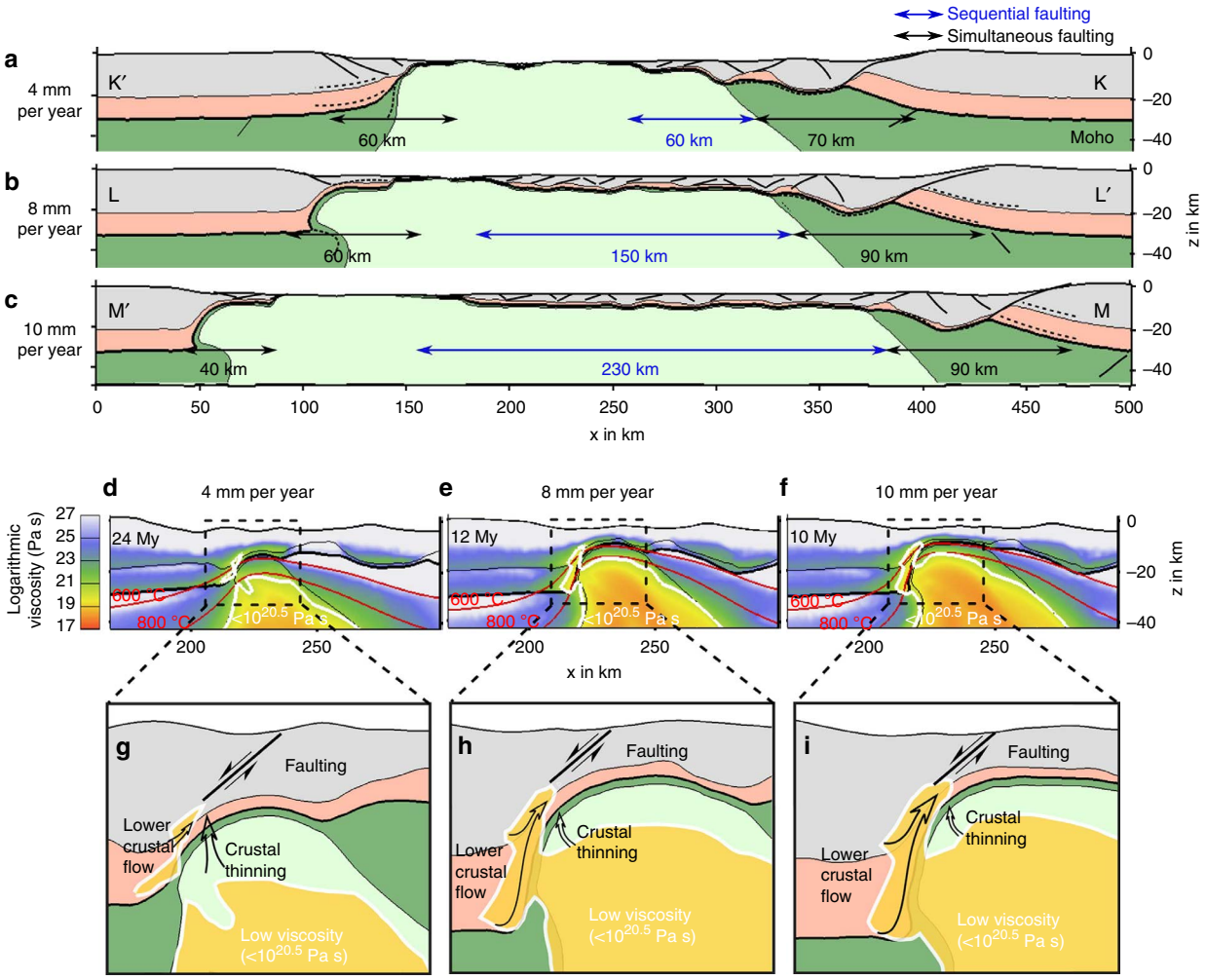

Figure 3 | Influence of rift velocity. (**a**–**c**) Conjugate margin structure for 4, 8 and 10 mm per year full rift velocities. The width of simultaneously faulted areas is indicated by black arrows, whereas sequentially faulted domains are depicted by blue arrows. The width of the wide margin increases with rift velocity. The reason for this behaviour is shown in **d**–**f**: Higher velocities lead to advection of the isotherms to shallower depths. This heats the lower crust more efficiently, forming a weaker and larger exhumation channel. (**g**–**i**) Facilitated lower crustal flow counteracts fault-controlled crustal thinning and prolongs the phase of rift migration leading to a wider margin. For animated model evolution, see Supplementary Fig. 3

agree with an earlier study[14] only that viscous strain softening in our model is considerably smaller and their models stop before hyper-extension takes place. The model with slow extension (4 mm per year; Fig. 3a) evolves very similar to previous work[17,35], generating moderately asymmetric margins. However, in our models, it is not a concave-downward detachment fault that generates the wide margin, but short-lived, sequentially active normal faults that accomplish lateral rift migration as imaged on seismic data[2]. Note that our explanation for crustal hyper-extension strongly differs from that of a previous study[12], where the crust is thinned by permanent pure shear both at the proximal and distal margin and no pronounced asymmetry is generated (see comparable scenario in Supplementary Fig. 2c,f and Supplementary Fig. 4).

We conclude that steady-state rift migration is capable of explaining the rifted margin formation of the Central South Atlantic segment and the Iberia/Newfoundland conjugates. Moreover, this process may be relevant for other hyper-extended and highly asymmetric margin pairs such as Antarctica–India[36], the North-East Atlantic[37,38], the Southern South Atlantic segment[39] and the East Australia/Lord Howe Rise conjugates[40].

Methods

Modelling techniques. Using numerical thermo-mechanical modelling techniques[41], we investigate the mechanism causing asymmetry and crustal hyper-extension during lithospheric thinning. Our models incorporate rheologies, initial temperature fields and extension velocities adequate for the Central South Atlantic segment and West Iberia–Newfoundland. Importantly, our simulations are strictly based on experimental rheological data for major rock types. By computing the degree of partial melting in the mantle, we ensure that our models are applicable to magma-poor margins: All shown models predict melt equivalent to <1.5 km of magmatic underplate before crustal break-up.

Numerical techniques. The forward models of rift evolution have been conducted using a 2D version of the finite-element code SLIM3D[41] (Semi-Lagrangian Implicit Model for 3 Dimensions), which has been successfully applied to model geodynamic processes at divergent[25,42–44], convergent[45,46] and transform[47] plate boundaries. The programme relies on the Arbitrary Lagrangian-Eulerian Method to solve the thermo-mechanically coupled conservation equations of momentum, energy and mass. Re-meshing is conducted in order to track the motion of the free surface and to avoid large grid distortion. During re-meshing, we use the particle-in-cell method in order to resolve advection of the material phases and history variables, such as accumulated plastic strain. SLIM3D involves an elasto-visco-plastic rheology formulation by adopting an additive decomposition of the deviatoric strain rate into elastic, viscous and plastic components. This approach allows to reproduce a wide range of lithospheric deformation processes such as faulting, flexure and lower crustal flow. The viscous strain rate component

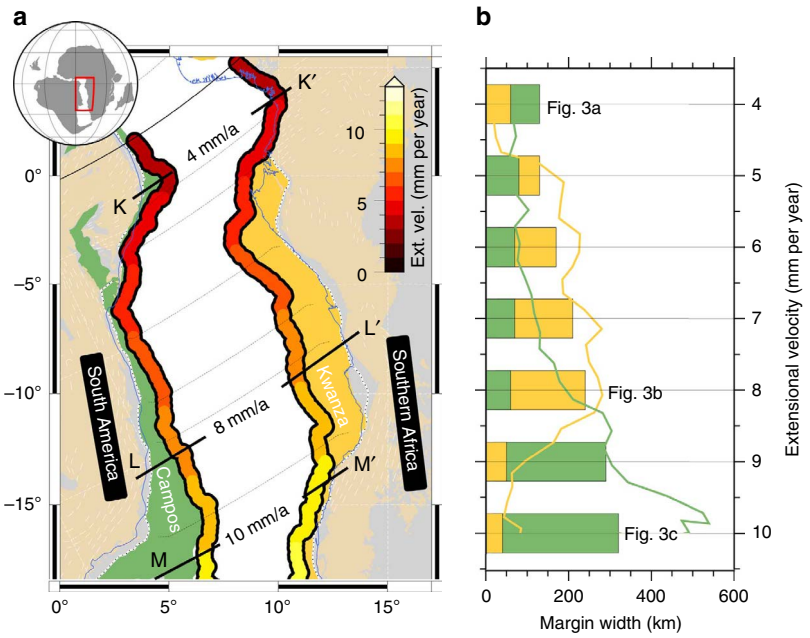

Figure 4 | Central South Atlantic extension velocities and margin width. (**a**) The Central South Atlantic segment shown in a post-break-up configuration. Extended continental crust coloured by plate (Africa: orange and South America: green). Landward limit of oceanic crust or continent–ocean boundary is defined by extensive mapping using industry-quality seismic reflection data in conjunction with high-resolution potential field data[24]. It is coloured by extension velocities (Ext. vel.) that are computed using the 127–140 Ma stage pole for South America relative to a fixed African plate. Margin widths are measured in km along flowlines (thin dashed lines). (**b**) Margin width versus extension velocity for numerical model (bars) and plate kinematic reconstruction (lines) for African (orange) and South American margins (green). In agreement with the numerical model, the width of the wider margin increases almost linearly with rift velocity. All velocities refer to full extension rates. Margin width of the numerical model (bars) represents the sum of simultaneously and sequentially faulted areas (Fig. 3). Both the green and the orange bars start from zero; that is, the bar plot is not cumulative.

simultaneously accounts for two creep mechanisms: diffusion and dislocation creep. Brittle deformation is incorporated using the Mohr–Coulomb failure model. Moreover, SLIM3D includes full compressibility, linear elasticity, shear heating, viscous and frictional strain softening, and power-law related strain rate softening. A setup sketch and a table with all model parameters are provided in Supplementary Fig. 1 and Supplementary Table 1, respectively.

All shown models are computed within a 2D domain that is 500 km wide and 150 km deep. Lateral and vertical element size is 1 km, resulting in 75,000 elements and ~150,000 nodes. We use time steps of 10 ky and let the model evolve over 40 My unless otherwise indicated. The present version of SLIM3D solves the discretized conservation equations using the direct parallel shared memory solver PARDISO[48].

Thermal model setup. The initial thermal state of the model is the equilibrated temperature distribution that results from layer-specific heat conductivity, radiogenic heat production and the following boundary conditions: the surface temperature is held constant at 0 °C. Below 120 km depth (unless otherwise indicated), the asthenosphere temperature is set to 1,300 °C. Lateral boundaries are thermally isolated. A small thermal heterogeneity is introduced in the model centre in order to avoid rift localization at the model boundaries. This heterogeneity is generated by elevating the initial 1,300 °C isotherm in form of a triangular shape with a 5-km height and 20-km width (see Supplementary Fig. 1). During subsequent model evolution, we fix the bottom boundary temperature to 1,300 °C.

The chosen depth of 120 km for the initial thermal LAB boundary (that is, the 1,300 °C isotherm) is based on compiled present day data for African Mobile belts[34]. Note that present day lithosphere thickness in Iberia and Newfoundland is somewhat smaller than at the South Atlantic conjugates[34], which is reflected in our models by using a 105-km initial lithospheric thickness. However, the low magmatic activity of the rifts indicates relatively cold pre-rift geotherms. Our models feature an initial surface heat flow of 63 and 67 mW m^{-2} for the South Atlantic and Iberia–Newfoundland setup, respectively, with corresponding initial Moho temperatures of 550 °C and 600 °C. Available quantitative inferences from an exposed Alpine magma-poor margin indicate pre-rift Moho temperatures of 550–650 °C[49].

Melt generation. We compute magma generation in a post-processing step using a batch-melting model for peridotite[50]. The solidus temperature for a given pressure is $T_{sol} = -5.1p^2 + 132.9p + 1{,}085.7$, whereas the liquidus temperature is $T_{liq} = -3.2p^2 + 80.0p + 1{,}475$. Hereby, temperatures are measured in °C and pressure p in GPa. After computing T_{sol} and T_{liq} at each element, we quantify the melt fraction of peridotite X at the temperature T as $X = ((T - T_{sol})/(T_{liq} - T_{sol}))^{3/2}$.

We account for endothermic consumption of lattice energy by computing the associated temperature change $\Delta T_{lattice} = X\Delta S/C_p$ $(T + 273)$, with the entropy change during melting[50] $\Delta S = 300\,J\,kg^{-1}\,K^{-1}$ and the heat capacity $C_p = 1{,}200\,J\,kg^{-1}\,K^{-1}$ (see Supplementary Table 1). We evaluate the melt fraction that is self-consistent with lattice energy consumption by iterative computation of X and $T = T_0 - \Delta T_{lattice}$, where T_0 is the initial temperature that does not account for energy consumption during melting.

Vertical integration over the melt-generating area allows us to approximate how much magma is produced by decompression melting. Even if we assume that all melts reach the surface, which is certainly an end member scenario, our model in Fig. 1 indicates up to 0.8 km of melt thickness before crustal break-up, thus illustrating the applicability of our model to magma-poor margins. The post-break-up melt thickness of 1.2 km agrees with observed thickness of the oceanic crust at ultra-slow (<12 mm per year full spreading rate) spreading ridges[51], especially if one considers that in reality not all melt reaches the surface.

We have tested the effect of a higher asthenosphere temperature (1,350 °C) on model evolution. Depending on extension velocity, melt thickness increases up to several kilometres, comparable to the high-velocity layer described at the Angolan margin[3]. However, the overall model outcome and particularly our conclusions concerning the influence of extension velocity, thermal LAB thickness and initial fault configuration remain robust.

Rheological model setup. Our model involves four distinct petrological layers (upper and lower crust, strong and weak mantle). The upper crustal layer is 22 km thick and deforms in accordance with a wet quartzite flow law[52]. The mafic crust between 22 and 33 km depth deforms via a wet anorthite flow law[53]. Evidence for the rheology of the lower crust derives from seismic studies that feature P-wave velocities within the lower crust >6.6 km s^{-1} at the Iberia–Newfoundland conjugates[16,54–56] and >6.7 km s^{-1} in Angola[3], which provides strong evidence for a mafic composition[57]. Independent evidence comes from Alpine geology, where the exposed lower crust of the Adriatic plate is rich in granulites and mafics[58]. The initial Moho depth of 33 km is supported by seismically inferred crustal thickness in Iberia[59], Newfoundland[54] and Brazil[60]. Thirty-three kilometres crustal thickness corresponds to pressures of 0.9 GPa at the base of the crust. This value agrees with mineral chemistry studies[49] of obducted passive margins in the Alps that indicate pre-rift Moho pressures of ~0.9 ± 0.1 GPa.

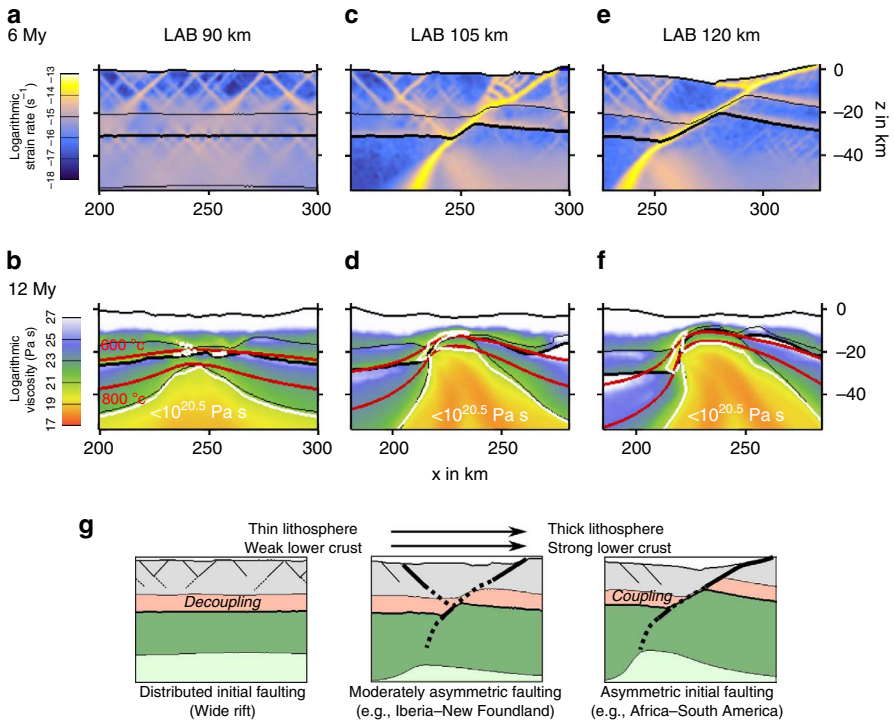

Figure 5 | Influence of initial thermal profile. (**a**,**b**) Thin (90 km) and hence hot lithosphere favours crust–mantle decoupling, pure shear deformation and distributed faulting without rift migration. (**c**,**d**) For intermediate depth of the lithosphere–asthenosphere boundary (LAB) initially pure shear straining with moderately asymmetric faulting generates a small low-viscosity pocket and a short rift migration phase. (**e**,**f**) For comparison, model results are shown with an LAB thickness of 120 km (as in Fig. 1) that involve strong crust–mantle coupling and generate a large low-viscosity pocket. Full extension velocity is 8 mm per year. We use the 1,300 °C isotherm to define the thermal LAB. Detailed model evolution is animated in Supplementary Fig. 3. (**g**) Cartoon illustrating how lithosphere thickness and crust–mantle decoupling affect initial fault pattern.

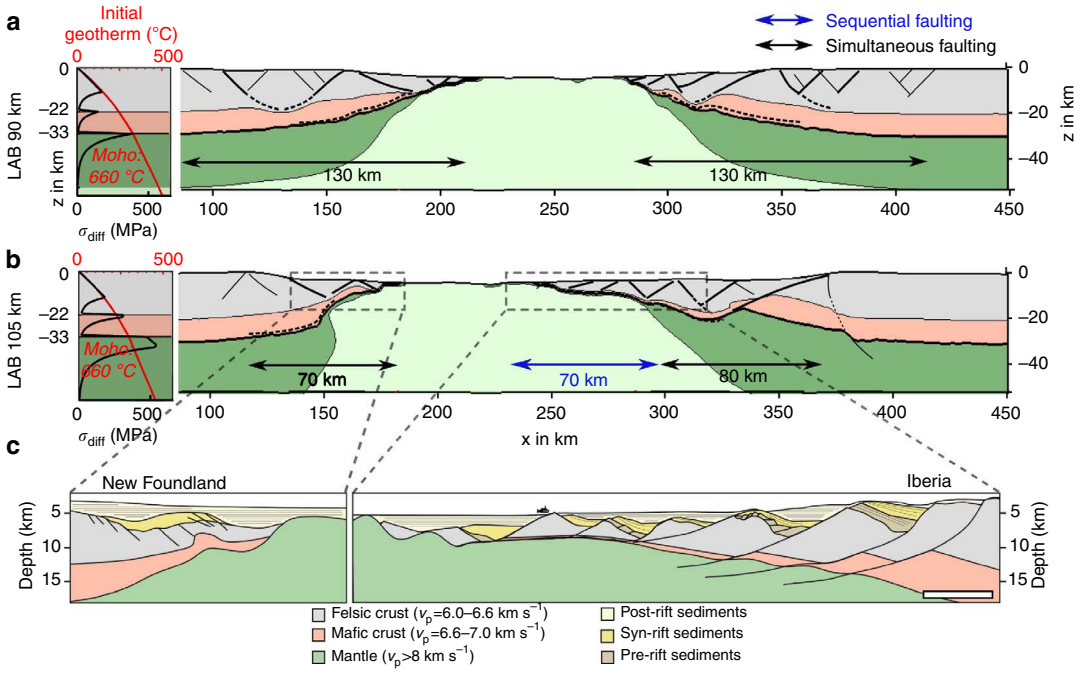

Figure 6 | Final margin widths for different initial thermal profiles. (**a**) Scenario with 90 km thick thermal lithosphere. Owing to crust–mantle decoupling (Fig. 5) symmetric rifting takes place without rift migration. (**b**) The setup with 105 km thick lithosphere generates a distinct rift migration phase. The width of simultaneously faulted areas is indicated by black arrows, whereas sequentially faulted domains are depicted by blue arrows. The model in **b** is comparable to **c** the Iberia–Newfoundland conjugates (modified after ref. 2). This geosection is drawn without vertical exaggeration and the scale bar in the lower right corner is 10 km long.

We use dry olivine rheology[61] to model deformation of the strong, depleted, subcontinental mantle, whereas we use a wet olivine (that is, 500 p.p.m. H/Si) flow law[61] for the weak, asthenospheric mantle. We assume a grain size of 6 mm that is included in the pre-exponential factors. The boundary between weak and strong mantle initially resides 30 km above the thermal LAB boundary, that is, the 1,300 °C isotherm because weak mantle material cools and attaches (freezes) onto the mechanically strong mantle layer until Rayleigh–Taylor instabilities evolve. Our initial condition is consistent with long-term thermo-mechanical equilibration[62].

Weakening mechanisms. Besides shear heating and dislocation creep-related strain rate softening, the model accounts for two mechanical weakening mechanisms that have been observed in laboratory and nature[63], namely friction softening and viscous softening that are discussed below.

Frictional softening is responsible for localization of faults[64], and is incorporated in our model by a dependency of the friction coefficient on accumulated plastic strain. The unstrained initial friction coefficient of 0.5 is thereby linearly reduced to 0.05 for accumulated plastic strain of 1. If strain exceeds 1, the friction coefficient remains constant at 0.05. In laterally homogeneous models with symmetric boundary conditions, the whole model evolution should remain symmetric. This permanent symmetry is a model artefact as lateral homogeneity does not exist in natural settings because of inherited structures such as crustal faults. In our model, we therefore introduce lateral heterogeneity by applying a small arbitrary variation to the initial friction coefficient at each numerical element. This procedure results in a random distribution of initial friction coefficients that varies between 0.4 and 0.5. In our model, the orientation of faults and thus the asymmetry of the developing rift is not prescribed and generates spontaneously.

Viscous strain softening leads to localization in ductile material. This weakening mechanism relates to the fact that large strains cause grain-size reduction in ductile shear zones[65,66] possibly via dislocation creep and dynamic recrystallization. Low grain size, however, facilitates deformation by grain-size sensitive diffusion creep leading to a switch in deformation mechanism that involves severe viscosity reduction[67,68]. We use a simple parameterization for viscous strain softening by linearly increasing the pre-exponential factor in the strain rate to stress relation of the dislocation flow law. Between a viscous strain of 0 and 1, the pre-exponential factor increases by a factor f. In our models, we use $f=30$ that implies a change in viscosity by a factor of $30^{-1/n}$, where the stress exponent n ranges between 3 (wet anorthite[53], lower crust) and 4 (wet quartzite[52], upper crust). Hence, this procedure generates a modest viscosity decrease between 0.3 and 0.4 compared with unstrained material.

Mechanical boundary conditions. Rifting is induced by prescribing a velocity of 4 mm per year at lateral boundaries, resulting in a full extension velocity of 8 mm per year, unless otherwise indicated. The free surface boundary condition at the top of the model allows self-consistent evolution of topography. At the bottom boundary, isostatic equilibrium is realized by means of the Winkler foundation[41].

Alternative numerical model setups. In order to test the robustness of our results, we conducted a series of experiments with alternative model setups where we varied the size of the computational domain and the numerical resolution, we introduced a free slip condition at the lower model boundary and applied the full extensional velocity at only one side of the model. Despite small differences between all models, the overall results of this study remain unchanged.

We also checked whether serpentinization would influence our results. We introduced a phase change from olivine to serpentine using a pressure- and temperature-dependent serpentine stability field[17,69]. We found that serpentinization does not occur near the exhumation channel owing to its elevated temperatures. According to our simulations, it takes place only before break-up and therefore does not have a qualitative influence on our conclusions.

South Atlantic plate kinematics. The South Atlantic Rift velocities and margins width (Fig. 3) have been computed using a new plate kinematic model for the separation of South America and Africa[24]. The model quantitatively integrates crustal deformation from Cretaceous African and South American intraplate deforming zones, as well as from the South Atlantic conjugate passive margins.

References

1. Whitmarsh, R. B., Manatschal, G. & Minshull, T. A. Evolution of magma-poor continental margins from rifting to seafloor spreading. *Nature* **413,** 150–154 (2001).
2. Ranero, C. R. & Perez-Gussinye, M. Sequential faulting explains the asymmetry and extension discrepancy of conjugate margins. *Nature* **468,** 294–299 (2010).
3. Contrucci, I. *et al.* Deep structure of the West African continental margin (Congo, Zaire, Angola), between 5 degrees S and 8 degrees S, from reflection/refraction seismics and gravity data. *Geophys. J. Int.* **158,** 529–553 (2004).
4. Hopper, J. R. *et al.* Continental breakup and the onset of ultraslow seafloor spreading off Flemish Cap on the Newfoundland rifted margin. *Geology* **32,** 93–96 (2004).
5. Unternehr, P., Peron-Pinvidic, G., Manatschal, G. & Sutra, E. Hyper-extended crust in the South Atlantic: in search of a model. *Pet. Geosci.* **16,** 207–215 (2010).
6. Wilson, R. C. L., Manatschal, G. & Wise, S. Rifting along non-volcanic passive margins: stratigraphic and seismic evidence from the Mesozoic successions of the Alps and western Iberia. *Geol. Soc. London Spec. Publ.* **187,** 429–452 (2001).
7. Karner, G. D. & Gambôa, L. a. P. Timing and origin of the South Atlantic pre-salt sag basins and their capping evaporites. *Geol. Soc. London Spec. Publ.* **285,** 15–35 (2007).
8. Torsvik, T. H., Rousse, S., Labails, C. & Smethurst, M. A. A new scheme for the opening of the South Atlantic Ocean and the dissection of an Aptian salt basin. *Geophys. J. Int.* **177,** 1315–1333 (2009).
9. Péron-Pinvidic, G., Manatschal, G., Minshull, T. A. & Sawyer, D. S. Tectonosedimentary evolution of the deep Iberia-Newfoundland margins: Evidence for a complex breakup history. *Tectonics* **26,** TC2011 (2007).
10. Aslanian, D. *et al.* Brazilian and African passive margins of the Central Segment of the South Atlantic Ocean: Kinematic constraints. *Tectonophysics* **468,** 98–112 (2009).
11. Mohn, G., Manatschal, G., Beltrando, M., Masini, E. & Kusznir, N. Necking of continental crust in magma-poor rifted margins: Evidence from the fossil Alpine Tethys margins. *Tectonics* **31,** TC1012 (2012).
12. Huismans, R. S. & Beaumont, C. Depth-dependent extension, two-stage breakup and cratonic underplating at rifted margins. *Nature* **473,** 74–78 (2011).
13. Cowie, P. A., Underhill, J. R., Behn, M. D., Lin, J. & Gill, C. E. Spatio-temporal evolution of strain accumulation derived from multi-scale observations of Late Jurassic rifting in the northern North Sea: A critical test of models for lithospheric extension. *Earth Planet. Sci. Lett.* **234,** 401–419 (2005).
14. Huismans, R. S. & Beaumont, C. Symmetric and asymmetric lithospheric extension: Relative effects of frictional-plastic and viscous strain softening. *J. Geophys. Res. Solid Earth* **108,** 2496 (2003).
15. Ebinger, C. J., Jackson, J. A., Foster, A. N. & Hayward, N. J. Extensional basin geometry and the elastic lithosphere. *Philos. Trans. R. Soc. Lond. A* **357,** 741–765 (1999).
16. Pérez-Gussinyé, M., Ranero, C. R., Reston, T. J. & Sawyer, D. Mechanisms of extension at nonvolcanic margins: evidence from the Galicia interior basin, west of Iberia. *J. Geophys. Res.* **108,** 2245 (2003).
17. Lavier, L. L. & Manatschal, G. A mechanism to thin the continental lithosphere at magma-poor margins. *Nature* **440,** 324–328 (2006).
18. Kusznir, N. J. & Park, R. G. The extensional strength of the continental lithosphere: its dependence on geothermal gradient, and crustal composition and thickness. *Geol. Soc. London Spec. Publ.* **28,** 35–52 (1987).
19. Van Wijk, J. W. & Cloetingh, S. A. P. L. Basin migration caused by slow lithospheric extension. *Earth Planet. Sci. Lett.* **198,** 275–288 (2002).
20. Wernicke, B. Uniform-sense normal simple shear of the continental lithosphere. *Can. J. Earth Sci.* **22,** 108–125 (1985).
21. Lister, G. S., Etheridge, M. A. & Symonds, P. A. Detachment models for the formation of passive continental margins. *Tectonics* **10,** 1038–1064 (1991).
22. Masini, E., Manatschal, G. & Mohn, G. The Alpine Tethys rifted margins: Reconciling old and new ideas to understand the stratigraphic architecture of magma-poor rifted margins. *Sedimentology* **60,** 174–196 (2013).
23. Pérez-Gussinyé, M. & Reston, T. J. Rheological evolution during extension at nonvolcanic rifted margins: Onset of serpentinization and development of detachments leading to continental breakup. *J. Geophys. Res.* **106,** 3961–3975 (2001).
24. Heine, C., Zoethout, J. & Müller, D. Kinematics of the South Atlantic rift. *Solid Earth* **4,** 215–253 (2013).
25. Heine, C. & Brune, S. Oblique rifting of the Equatorial Atlantic: Why there is no Saharan Atlantic Ocean. *Geology* **42,** 211–214 (2014).
26. Nürnberg, D. & Müller, R. D. The tectonic evolution of the South-Atlantic from Late Jurassic to present. *Tectonophysics* **191,** 27–53 (1991).
27. Eagles, G. New angles on South Atlantic opening. *Geophys. J. Int.* **168,** 353–361 (2007).
28. Moulin, M., Aslanian, D. & Unternehr, P. A new starting point for the South and Equatorial Atlantic Ocean. *Earth-Sci. Rev.* **98,** 1–37 (2010).
29. Scotchman, I. C., Gilchrist, G., Kusznir, N. J., Roberts, A. M. & Fletcher, R. The breakup of the South Atlantic Ocean: formation of failed spreading axes and blocks of thinned continental crust in the Santos Basin, Brazil and its consequences for petroleum system development. *Geol. Soc. London Pet. Geol. Conf. Ser.* **7,** 855–866 (2010).
30. Buck, W. R. Modes of continental lithospheric extension. *J. Geophys. Res. Solid Earth* **96,** 20161–20178 (1991).
31. Buiter, S. J. H., Huismans, R. S. & Beaumont, C. Dissipation analysis as a guide to mode selection during crustal extension and implications for the styles of sedimentary basins. *J. Geophys. Res. Solid Earth* **113,** B06406 (2008).
32. Clift, P., Lin, J. & Barckhausen, U. Evidence of low flexural rigidity and low viscosity lower continental crust during continental break-up in the South China Sea. *Mar. Pet. Geol.* **19,** 951–970 (2002).

33. Sutra, E. & Manatschal, G. How does the continental crust thin in a hyperextended rifted margin? insights from the Iberia margin. *Geology* **40,** 139–142 (2012).
34. Artemieva, I. M. Global 1° × 1° thermal model TC1 for the continental lithosphere: Implications for lithosphere secular evolution. *Tectonophysics* **416,** 245–277 (2006).
35. Van Avendonk, H. J. A., Lavier, L. L., Shillington, D. J. & Manatschal, G. Extension of continental crust at the margin of the eastern Grand Banks, Newfoundland. *Tectonophysics* **468,** 131–148 (2009).
36. Gaina, C., Müller, R. D., Brown, B., Ishihara, T. & Ivanov, S. Breakup and early seafloor spreading between India and Antarctica. *Geophys. J. Int.* **170,** 151–169 (2007).
37. Lundin, E. R. & Doré, A. G. Hyperextension, serpentinization, and weakening: A new paradigm for rifted margin compressional deformation. *Geology* **39,** 347–350 (2011).
38. Gerlings, J., Louden, K. E., Minshull, T. A. & Nedimović, M. R. Flemish Cap–Goban Spur conjugate margins: new evidence of asymmetry. *Geology* **40,** 1107–1110 (2012).
39. Blaich, O. A., Faleide, J. I. & Tsikalas, F. Crustal breakup and continent-ocean transition at South Atlantic conjugate margins. *J. Geophys. Res. Solid Earth* **116 (2011).**
40. Gaina, C. *et al.* The tectonic history of the Tasman Sea: A puzzle with 13 pieces. *J. Geophys. Res.* **103,** 12413–12433 (1998).
41. Popov, A. A. & Sobolev, S. V. SLIM3D: A tool for three-dimensional thermo mechanical modeling of lithospheric deformation with elasto-visco-plastic rheology. *Phys. Earth Planet. Inter.* **171,** 55–75 (2008).
42. Brune, S., Popov, A. A. & Sobolev, S. V. Modeling suggests that oblique extension facilitates rifting and continental break-up. *J. Geophys. Res.* **117,** B08402 (2012).
43. Brune, S., Popov, A. A. & Sobolev, S. V. Quantifying the thermo-mechanical impact of plume arrival on continental break-up. *Tectonophysics* **604,** 51–59 (2013).
44. Brune, S. & Autin, J. The rift to break-up evolution of the Gulf of Aden: Insights from 3D numerical lithospheric-scale modelling. *Tectonophysics* **607,** 65–79 (2013).
45. Quinteros, J., Sobolev, S. V. & Popov, A. A. Viscosity in transition zone and lower mantle: implications for slab penetration. *Geophys. Res. Lett.* **37,** L09307 (2010).
46. Quinteros, J. & Sobolev, S. V. Why has the Nazca plate slowed since the Neogene? *Geology* **41,** 31–34 (2012).
47. Popov, A. A., Sobolev, S. V. & Zoback, M. D. Modeling evolution of the San Andreas Fault system in northern and central California. *Geochem. Geophys. Geosyst.* **13,** Q08016 (2012).
48. Schenk, O. & Gärtner, K. Solving unsymmetric sparse systems of linear equations with PARDISO. *Future Gener. Comput. Syst.* **20,** 475–487 (2004).
49. Müntener, O., Hermann, J. & Trommsdorff, V. Cooling history and exhumation of lower-crustal granulite and upper mantle (Malenco, Eastern Central Alps). *J. Petrol.* **41,** 175–200 (2000).
50. Katz, R. F., Spiegelman, M. & Langmuir, C. H. A new parameterization of hydrous mantle melting. *Geochem. Geophys. Geosyst.* **4,** 1073 (2003).
51. Dick, H. J. B., Lin, J. & Schouten, H. An ultraslow-spreading class of ocean ridge. *Nature* **426,** 405–412 (2003).
52. Gleason, G. C. & Tullis, J. A flow law for dislocation creep of quartz aggregates determined with the molten-salt cell. *Tectonophysics* **247,** 1–23 (1995).
53. Rybacki, E. & Dresen, G. Dislocation and diffusion creep of synthetic anorthite aggregates. *J. Geophys. Res.* **105,** 017–26,036 (2000).
54. Funck, T. *et al.* Crustal structure of the ocean-continent transition at Flemish Cap: Seismic refraction results. *J. Geophys. Res. Solid Earth* **108,** 2531 (2003).
55. Dean, S. M., Minshull, T. A., Whitmarsh, R. B. & Louden, K. E. Deep structure of the ocean-continent transition in the southern Iberia Abyssal Plain from seismic refraction profiles: The IAM-9 transect at 40°20′N. *J. Geophys. Res. Solid Earth* **105,** 5859–5885 (2000).
56. Hopper, J. R., Funck, T. & Tucholke, B. E. Structure of the Flemish Cap margin, Newfoundland: insights into mantle and crustal processes during continental breakup. *Geol. Soc. London Spec. Publ.* **282,** 47–61 (2007).
57. Christensen, N. I. & Mooney, W. D. Seismic velocity structure and composition of the continental crust: A global view. *J. Geophys. Res.* **100,** 9761–9788 (1995).
58. Müntener, O. & Hermann, J. The role of lower crust and continental upper mantle during formation of non-volcanic passive margins: evidence from the Alps. *Geol. Soc. London Spec. Publ.* **187,** 267–288 (2001).
59. Díaz, J. & Gallart, J. Crustal structure beneath the Iberian Peninsula and surrounding waters: a new compilation of deep seismic sounding results. *Phys. Earth Planet. Inter.* **173,** 181–190 (2009).
60. Mohriak, W. U. & Dewey, J. F. Deep seismic reflectors in the Campos basin, offshore Brazil. Geophys. *J. R. Astr. Soc.* **89,** 133–140 (1987).
61. Hirth, G. & Kohlstedt, D. L. Rheology of the upper mantle and the mantle wedge: A view from the experimentalists. *Geophys. Monogr.* **138,** 83–105 (2003).
62. Sobolev, A. V., Sobolev, S. V., Kuzmin, D. V., Malitch, K. N. & Petrunin, A. G. Siberian meimechites: origin and relation to flood basalts and kimberlites. *Russ. Geol. Geophys.* **50,** 999–1033 (2009).
63. Bürgmann, R. & Dresen, G. Rheology of the lower crust and upper mantle: evidence from rock mechanics, geodesy, and field observations. *Annu. Rev. Earth Planet. Sci.* **36,** 531–567 (2008).
64. Zoback, M. D. *et al.* New evidence on the state of stress of the San Andreas fault system. *Science* **238,** 1105–1111 (1987).
65. White, S. H., Burrows, S. E., Carreras, J., Shaw, N. D. & Humphreys, F. J. On mylonites in ductile shear zones. *J. Struct. Geol.* **2,** 175–187 (1980).
66. Handy, M. R. Deformation regimes and the rheological evolution of fault zones in the lithosphere: the effects of pressure, temperature, grainsize and time. *Tectonophysics* **163,** 119–152 (1989).
67. Rybacki, E. & Dresen, G. Deformation mechanism maps for feldspar rocks. *Tectonophysics* **382,** 173–187 (2004).
68. Austin, N. & Evans, B. The kinetics of microstructural evolution during deformation of calcite. *J. Geophys. Res. Solid Earth* **114,** B09402 (2009).
69. Pérez-Gussinyé, M., Morgan, J. P., Reston, T. J. & Ranero, C. R. The rift to drift transition at non-volcanic margins: Insights from numerical modelling. *Earth Planet. Sci. Lett.* **244,** 458–473 (2006).

Acknowledgements

S.B. has been funded by SAMPLE (South Atlantic Margin Processes and Links with onshore Evolution), the German Research Foundation Priority Program 1375 and by the European Research Council, Marie Curie International Outgoing Fellowship (Project 326115). C.H. is funded by Australian Research Council Linkage Project L1759 supported by Shell International E&P and TOTAL. We thank John Armitage and Luc Lavier for commenting on an earlier version of the manuscript.

Author contributions

S.B. proposed the main concept, conducted and interpreted the thermo-mechanical models and wrote most of the paper; C.H. provided the plate kinematic aspects of the paper and model application to the South Atlantic; M.P.-G. contributed ideas on normal fault dynamics, interpretation of the model and its application to the Iberia–Newfoundland margin; and S.V.S. contributed to modelling techniques and to interpretation of modelling results. All authors contributed intellectually to the paper.

Additional information

Supplementary Information accompanies this paper at http://www.nature.com/naturecommunications

Competing financial interests: The authors declare no competing financial interests.

Reprints and permission information is available online at http://npg.nature.com/reprintsandpermissions/

How to cite this article: Brune, S. *et al.* Rift migration explains continental margin asymmetry and crustal hyper-extension. *Nat. Commun.* 5:4014 doi: 10.1038/ncomms5014 (2014).

Marine and Petroleum Geology 79 (2017) 257–281

Contents lists available at ScienceDirect

Marine and Petroleum Geology

journal homepage: www.elsevier.com/locate/marpetgeo

Review article

Rifted margin architecture and crustal rheology: Reviewing Iberia-Newfoundland, Central South Atlantic, and South China Sea

Sascha Brune [a, *], Christian Heine [b, c], Peter D. Clift [d], Marta Pérez-Gussinyé [e]

[a] Helmholtz Centre Potsdam, GFZ German Research Centre for Geosciences, Potsdam, Germany
[b] Upstream, Opportunity Identification (UPX/N/OI), Shell International Exploration & Production B.V., The Hague, Netherlands
[c] Institute for Geology, Mineralogy & Geophysics, Ruhr-University Bochum, Germany
[d] Department of Geology and Geophysics, Louisiana State University, Baton Rouge, LA, United States
[e] MARUM – Center for Marine Environmental Sciences, University of Bremen, Germany

ARTICLE INFO

Article history:
Received 23 May 2016
Received in revised form
17 October 2016
Accepted 19 October 2016
Available online 22 October 2016

Keywords:
Iberia-Newfounland
South Atlantic
South China Sea
Magma-poor margins

ABSTRACT

Crustal rheology controls the style of rifting and ultimately the architecture of rifted margins. Here we review the formation of three magma-poor margin pairs, Iberia-Newfoundland, the central segment of the South Atlantic Rift, and the South China Sea by integrating observational data into a numerical forward modelling framework. We utilise a 2D version of the finite element code SLIM3D, which includes nonlinear temperature- and stress-dependent elasto-visco-plastic rheology and is able to reproduce a wide range of rift-related deformation processes such as flexure, lower crustal flow, and faulting.

Extension in cold, strong, or thin crust is accommodated by brittle faults and ductile shear zones that facilitate narrow rifts with asymmetric fault geometries. Hot, weak, or thick continental crust is dominated by ductile deformation and often extends symmetrically into a wide rift system. This simple recipe provides the standard framework to understand initial rift geometry, however, it is insufficient to account for the dynamics of intermediate and late rift stages that shape the final margin architecture.

Asymmetric conjugate margins where one side is wide and the other narrow can be formed via both wide and narrow rift styles, which we reproduce with weak and strong crustal rheologies, respectively. Exemplified by the Iberia-Newfoundland conjugates and the Central South Atlantic, we define three characteristic rift phases: an initial phase of simultaneous faulting, an intermediate phase of rift migration that involves sequential fault activity, and finally, the breakup phase. Crustal rheology plays an overarching role in governing the dynamics of these asymmetric margins: we illustrate that weak rheologies generally prolong the phase of simultaneous faulting, while rift migration is enabled by initial fault asymmetry as well as relatively weak crust.

Formation of the predominantly symmetric and wide margins of the South China Sea was controlled by extraordinarily weak crust that extended the phase of simultaneous faulting until breakup. The weak crustal rheology of this region relates to the South China Sea's pre-rift history where plate convergence lead to crustal thickening and magmatic additions in a back-arc regime shortly before the onset of rifting.

Contents

1. Introduction 258
2. Modelling background 259
3. Iberia-Newfoundland rifting 260
 3.1. Observations 260
 3.2. Model 262
  3.2.1. Phase 1 - Simultaneous faulting 263
  3.2.2. Phase 2 – Rift migration 263
  3.2.3. Phase 3 – Breakup 264

* Corresponding author.
E-mail address: brune@gfz-potsdam.de (S. Brune).

http://dx.doi.org/10.1016/j.marpetgeo.2016.10.018
0264-8172/

4. Central South Atlantic rifting 264
4.1. Observations 264
4.2. Model 266
4.2.1. Phase 1 - Simultaneous faulting 266
4.2.2. Phase 2 – Rift migration 267
4.2.3. Phase 3 – Breakup 268
5. South China Sea rifting 269
5.1. Observations 269
5.2. Model 272
5.2.1. Phase 1 – Simultaneous faulting 272
5.2.2. No phase 2 – Rift migration 273
5.2.3. Phase 3 – Breakup 273
6. Discussion 273
7. Conclusions 274
Acknowledgements 275
Supplementary data 275
References 275

1. Introduction

With an overall length of more than 100,000 km, rifted continental margins constitute one of the major tectonic features on our planet (Bradley, 2008), two times longer than today's spreading ridges or convergent plate boundaries. Large parts of these margins are covered by thick sedimentary sequences that host a substantial part of the global hydrocarbon resources. Since proximal margins are covered by relatively shallow water, they have been extensively explored. After a series of major discoveries in the pre-salt stratigraphy in the distal part of the Brazilian Santos Basin, exploration has seen a new shift to the underexplored frontier, deep-water margins. Aided by improvements in seismic acquisition and imaging, as well as concerted research strategies, companies have been able to discover significant hydrocarbon resources in these still poorly understood outer parts of continental margins, such as the Tupi, Lula, and Libra fields offshore Brazil as well as along the conjugate, the West African margin in Angola and Gabon. Along with many on-going academic research initiatives, acquired data show that distal margin areas are underlain by highly attenuated continental crust that can be several hundred kilometres wide. Understanding the evolution and associated risks for exploration of these distal margins can unlock wide areas with potential prospectivity and large, undrilled structures.

A key element in de-risking petroleum systems is to understand maturation. Increasing pressure and temperature allow organic source rocks to mature and under certain conditions expel fluid hydrocarbons which can then migrate into reservoirs (Magoon and Dow, 1994). The ability to predict maturation thus requires a robust understanding of the temperature and pressure history of any potential source rock. Analytical solutions of the heat-flow and subsidence evolution are available for simple shear, pure shear or composite deformation mechanisms (McKenzie, 1978; Wernicke, 1985; Lister et al., 1986). These kinematic models were derived based on the study of proximal domains or failed rifts, which were the exploration focus at the time of publication about three decades ago. As our understanding of passive margins has significantly improved along with the technology to unlock resources in ultra-deepwater regions, however, the common static models of petroleum systems modelling fail to address key aspects of the evolution of hyperextended/distal margins.

Rifted margins show great variation in terms of crustal architecture, the amount of volcanism, and sedimentation patterns. Several end-member rift models have been proposed, although it is clear that most rifts display a gradual transition between these extreme cases. These end-members comprise magma-rich and magma-poor margins (Doré and Lundin, 2015; Haupert et al., 2016), wide and narrow rifts (Buck, 1991; Brun, 1999), symmetric and asymmetric crustal architectures (Lister et al., 1991; Ranero and Pérez-Gussinyé, 2010), as well as rifts forming within continents or at the tectonically active continental edges (Umhoefer, 2011). Extension within continents often appears to reactivate ancient suture zones that seem to be more prone to accommodate extensional stresses than the neighbouring cratons or continental shields (Wilson, 1966; Vauchez et al., 1997). These intra-continental rift systems may lead to separation of major landmasses thereby generating a new ocean basin. In contrast, marginal rifts often form as back-arc basins in response to subduction dynamics (Sdrolias and Müller, 2006; Schellart and Moresi, 2013). Back-arc basins are typically not as long-lived as large-scale ocean basins because the opening and closing of these basins is related to the subduction kinematics (Heine et al., 2013a).

The structural evolution of continental rifts is governed by many different factors: the rheological and thermal architecture of the lithosphere, the existence of crustal heterogeneities, anisotropies in crust and mantle, the kinematics and obliquity of the rift system, and the availability of syn-rift sediments. But the impact of each of these parameters is often difficult to estimate from observational studies, especially in the light of uncalibrated seismic data and when lacking well data. Here, forward numerical modelling provides a powerful means to isolate the key processes that control fundamental dynamic aspects of the evolving rift system. End-member scenarios can be tested and interrogated, with recent developments in computing power and resources allowing interactive animation, visualisation and a high resolution of one kilometre or less.

The research and industry communities generated ever-improving insights through decades of data acquisition and interpretation. However, a time-dependent, dynamic and evolutionary view of rifted margins is often still lacking. Geodynamic forward models and workflows offer a novel way to consistently and quantitatively link these existing local high-resolution subsurface representations, along with coarser regional data sets. Moreover, these forward models allow introducing additional constraints from rock mechanics, rheology and fundamental physical principles. We think that such coupled modelling/observational framework will significantly improve earlier conceptual models of rift evolution.

In this paper we review observations and kinematic models of three well-studied magma-poor rift systems (Fig. 1): Iberia-Newfoundland in Section 3, the Central South Atlantic in Section 4, and the South China Sea in Section 5. Beyond summarizing the academic knowledge about these margins we embed the available observations in a geodynamic forward modelling framework. By varying rheological properties of the continental lithosphere within these models we are able to reproduce the fundamental differences and similarities of these margins, thereby elucidating the geodynamic evolution of each rift system.

2. Modelling background

There are many processes thought to affect rift dynamics, mirroring the diversity of rifts and rifted margins themselves. Analogue and numerical modelling approaches allow us to isolate controlling parameters and key processes shaping margin architecture. Used in combination with detailed observations at margins, numerical models, in particular, can help us understand the tectonic, magmatic and sedimentary evolution of rifted margins.

Analogue models have been successfully applied in investigating continental extension within a single brittle layer reminiscent of the brittle upper crust (Withjack and Jamison, 1986; Tron and Brun, 1991; McClay and White, 1995; Mart and Dauteuil, 2000; Sokoutis et al., 2007). However, recent developments in lithospheric-scale analogue rift modelling, allow more advanced multi-layer models accounting for realistic crustal thinning and full isostatic balancing to be developed (Corti, 2008; Agostini et al., 2009; Autin et al., 2010, 2013; Cappelletti et al., 2013; Corti et al., 2013; Nestola et al., 2013, 2015). Analogue modelling profited greatly from introducing new materials and setups (Corti et al., 2003; Rosenau et al., 2010; Boutelier and Oncken, 2011; Duarte et al., 2013) and recent advances in imaging techniques (Leever et al., 2011; Adam et al., 2013; Philippon et al., 2015; Galland et al., 2016). Nevertheless, reproducing scalable elasto-visco-plastic rheologies and capturing the long-term temperature evolution of a tectonic system remain problematic.

Numerical modelling techniques incorporate rock properties that are often not accessible to analogue experiments, such as temperature- and stress-dependent viscosity, composite rheology, heat conduction and radiogenic heating. This has the important advantage that dynamics can be investigated not just during an initial rift phase where conductive cooling of the lithosphere can be neglected, but also during final rift phases, continental breakup, and beyond. In this late rift stage the mechanical behaviour of the lithosphere strongly depends on the balance between the increasing geothermal gradient caused by lithospheric thinning and heat conduction, which exerts a strong influence on the tectonic architecture of margins (Pérez-Gussinyé et al., 2001; Brune et al., 2014; Svartman Dias et al., 2015). During the last decade, a variety of numerical codes have been developed and 2D numerical modelling has become a standard tool for investigating rift processes (Nagel and Buck, 2004; Lavier and Manatschal, 2006; Pérez-Gussinyé et al., 2006; Gueydan et al., 2008; van Wijk et al., 2008; Jammes et al., 2010; Rosenbaum et al., 2010; Wallner and Schmeling, 2010; Huet et al., 2011; Huismans and Beaumont, 2011; Rey et al., 2011; Armitage et al., 2012; Beaumont and Ings, 2012; Choi and Buck, 2012; Chen et al., 2013; Chenin and Beaumont, 2013; Gueydan and Précigout, 2013; Watremez et al., 2013; Brune et al., 2014; Liao and Gerya, 2014; Armitage et al., 2015; Ben-Avraham and Katsman, 2015; Clift et al., 2015; Naliboff and Buiter, 2015; Petersen et al., 2015; Sharples et al., 2015; Svartman Dias et al., 2015; Jeanniot et al., 2016; Brune et al., 2016; Marotta et al., 2016; Lavecchia et al., 2016; Jammes and Lavier, 2016). Furthermore, 3D rift models have been developed with ever increasing resolution (Katzman et al., 1995; Dunbar and Sawyer, 1996; Van Wijk and Blackman, 2005; van Wijk, 2005; Gac and Geoffroy, 2009; Gerya, 2010a; Allken et al., 2012; Brune et al., 2012; Le Pourhiet et al., 2012; Brune and Autin, 2013; Brune et al., 2013; Gerya, 2013; Heine and Brune, 2014; Burov and Gerya, 2014; Le Pourhiet et al., 2014; Koopmann et al., 2014; Liao and Gerya, 2014; Brune, 2014; Koptev et al., 2015; May et al., 2015).

The underlying causes for formation of wide or narrow rifts have been investigated since the beginning of computational geodynamics in the early 1980s. Key factors have been linked to localising and delocalising processes (Buck et al., 1999). Important localising processes include: (1) Thinning of the lithosphere resulting in weakening. This has been described as the classical necking instability in horizontal layers (Zuber and Parmentier, 1986). (2) Mechanical damage of the lithosphere occurring in faults and ductile shear zones. (3) Rift-related melting generating dike intrusions that weaken the lithosphere mechanically and thermally (Buck, 2007). Important delocalising processes are: (1) Isostatic/gravitational forces work against lithospheric thinning by equilibrating lateral variations in layer thicknesses of different density (Fleitout and Froidevaux, 1982; Buck, 1991). (2) During

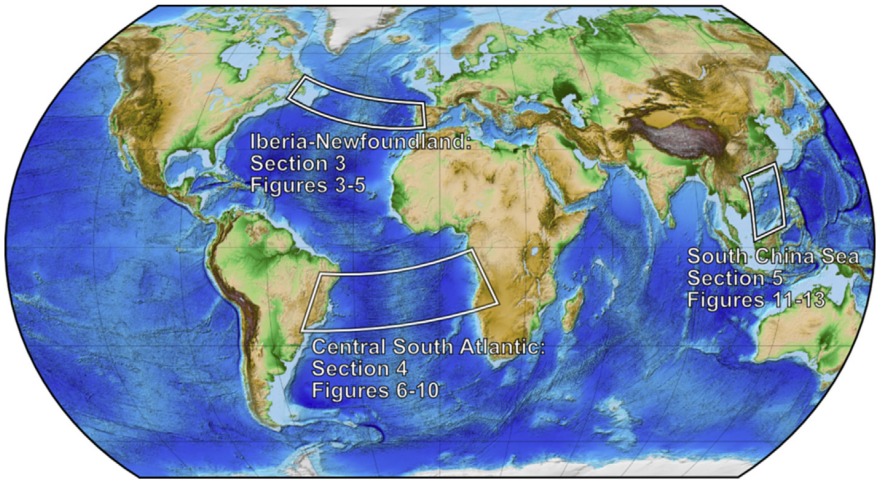

Fig. 1. Overview map. Depicted are locations of the three rifted margin pairs over a background map based on Etopo1 (Amante and Eakins, 2009).

thermal diffusion the upwelling mantle gets stronger, which strengthens the rift centre (England, 1983). The thermo-mechanical interaction of these processes is affected by material properties, extension rate and far-field stress and ultimately generates wide or narrow (Brun, 1999; Buck et al., 1999), symmetric or asymmetric (Huismans and Beaumont, 2003; Buiter et al., 2008), as well as failed, successful or migrating rifts (Kusznir and Park, 1987; van Wijk and Cloetingh, 2002; Naliboff and Buiter, 2015).

The common basis of numerical modelling studies is that they solve the partial differential equations of continuity, motion, and heat, in order to account for conservation of mass, momentum, and energy, respectively (Gerya, 2010b). Rheological rock properties enter the model through constitutive (i.e. material-specific) relations. These relations take the form of a yield criterion for brittle failure, a ductile flow law for viscous deformation that can be Newtonian or non-Newtonian, or involve a numerical representation of elasticity. Kinematic information is often prescribed in terms of lateral boundary conditions, whereas rift scenarios are usually driven by applying a constant extensional velocity.

In this study we use a two-dimensional version of the thermo-mechanical code Slim3D (Popov and Sobolev, 2008) to model geodynamic rift evolution. This software has been successfully applied to model lithospheric-scale processes in divergent (Brune et al., 2012, 2013; Brune and Autin, 2013; Brune, 2014; Heine and Brune, 2014; Koopmann et al., 2014; Clift et al., 2015; Brune et al., 2016), convergent (Quinteros et al., 2010; Quinteros and Sobolev, 2012; Duesterhoeft et al., 2014) and transform (Popov et al., 2012; Brune, 2014) plate boundaries as well as to understand centimetre-scale localisation processes (Cyprych et al., 2016). Before we apply this code to our three case examples, we shortly summarize the general numerical modelling setup.

SLIM3D is a finite element model that features a free surface at the top boundary, while at the bottom boundary isostatic equilibrium is realized by means of the Winkler foundation, where in- and outflow of material is accounted for during re-meshing. We use up to four distinct material layers: felsic crust, mafic crust, strong mantle and weak mantle (Fig. 2). For quartz-dominated felsic crust, we use the quartzite flow laws of Gleason and Tullis (1995) or Ranalli and Murphy (1987). The mafic lower crustal layer is represented by a wet anorthite flow law (Rybacki and Dresen, 2000). Further, we use dry olivine rheology (Hirth and Kohlstedt, 2003) to model deformation of the strong, depleted, subcontinental mantle, while we use a wet olivine flow law (Hirth and Kohlstedt, 2003) for the weak, asthenospheric mantle. The deformation of materials is accommodated via an elasto-visco-plastic rheology, which self-consistently reproduces diverse deformation processes like faulting, flexure and lower crustal flow. The model involves four weakening mechanisms: shear heating, power law-related strain rate softening, frictional strain softening, and viscous strain softening.

Solving the energy equation, the model's temperature field results from the material-specific heat conductivity, radiogenic heat production, dissipation of mechanical energy and the following boundary conditions: the surface temperature is held constant at 0 °C, and the bottom temperature at 1300 °C. Lateral boundaries are thermally isolated. As an initial condition, a small thermal heterogeneity is introduced in the model centre in order to avoid rift localisation at the model boundaries. We introduce a small degree of lateral heterogeneity by applying a minor variation to the initial friction coefficient at each numerical element. This procedure results in a random distribution of initial friction coefficients that varies between 0.4 and 0.5. Frictional softening is implemented through linearly reducing the friction coefficient by 90% for strain between 0 and 1, while keeping is constant for higher strains. In our model, the orientation of faults and thus the asymmetry of the developing rift is not prescribed and generates spontaneously. All models discussed in this study are computed at a horizontal and vertical resolution of 1 km. For more detailed information on the numerical setup, and listings of the applied thermo-mechanical parameter values, we refer to Brune et al. (2014).

There are several limitations to the modelling approach that have to be considered when applying the results to natural examples. (1) Extension velocity is an important parameter affecting brittle and ductile localisation processes, as well as the amount of partial melting. A recent study illustrated that rift velocities tend to evolve with a slow, and long-lived initial phase that is followed by high extension rates until continental rupture (Brune et al., 2016). This two-phase velocity evolution has been linked to the mechanical strength of the rift system, where the strength loss induces an increase of rift velocity prior to break-up (Brune et al., 2012; Heine and Brune, 2014). This time-dependent velocity evolution is not accounted for in the present models where a constant extension rate is imposed and future studies should address this important point. (2) The conducted models are two-dimensional. Here we focus on rift systems that did not involve much obliquity, which justifies the two-dimensional approach. However, when considering obliquely rifted or transform margins the 3D rift dynamics may change substantially (Brune, 2014; Basile, 2015; Mericer de Lépinay et al., 2016; Díaz-Azpiroz et al., 2016). (3) The geodynamics of rifting are sensitive to key parameters such as mantle temperature (Armitage et al., 2015; Taposeea et al., 2016), melting and volcanism (Buck, 2006; Bastow and Keir, 2011), structures inherited from pre-rift deformation (Tommasi et al., 2009; Buiter and Torsvik, 2014; Manatschal et al., 2015) as well as the brittle and ductile parameterisation of weakening (Lavier et al., 1999; Huismans and Beaumont, 2003). The degree of asymmetry for instance is far less extensive in model runs that do not include frictional strain softening. Here we focus on the impact of crustal rheology and, for reasons of limited space, do not provide a comprehensive parameter analysis. Nevertheless, we found the processes described here being robustly reproduced within a wide range of parameters.

3. Iberia-Newfoundland rifting

3.1. Observations

The conjugate Iberian Newfoundland margins have become the type example of magma-poor rifting. Over the last 30 years a wealth of geochronological, petrological, magnetic and seismic data have been acquired during four Ocean Drilling Program (ODP) and Integrated Ocean Drilling Program (IODP) drilling campaigns (103, 149, 173 and 210) and numerous marine geophysical surveys (Boillot et al., 1988; Reston et al., 1996; Whitmarsh et al., 1996; ODP Leg 173 Shipboard Scientific Party, 1998; Tucholke and Sibuet, 2007; Bayrakci et al., 2016). As a result of these studies it has been acknowledged that rifting occurred in two phases (Fig. 3): Late Triassic to Early Jurassic and Late Jurassic through Early Cretaceous (see Tucholke and Sibuet, 2007 and references therein). During the first phase, extension was distributed over a wide area and the crustal thinning was very small (Pérez-Gussinyé et al., 2006; Tucholke and Sibuet, 2007; Mohn et al., 2015). In the second phase, rifting propagated from south to north. In the south, in the Iberia Abyssal Plain, Late Jurassic-Berriasian rifting led to crustal breakup. Mantle exhumation in this sector occurred in Valanginian–Hauterivian, while extension leading to crustal breakup took place in the north (Deep Galicia Margin). During the Barremian-Aptian, extension involved exhumation of the subcontinental mantle. Seafloor spreading occurred finally around the Aptian-Albian (Tucholke and Sibuet, 2007). In this work we

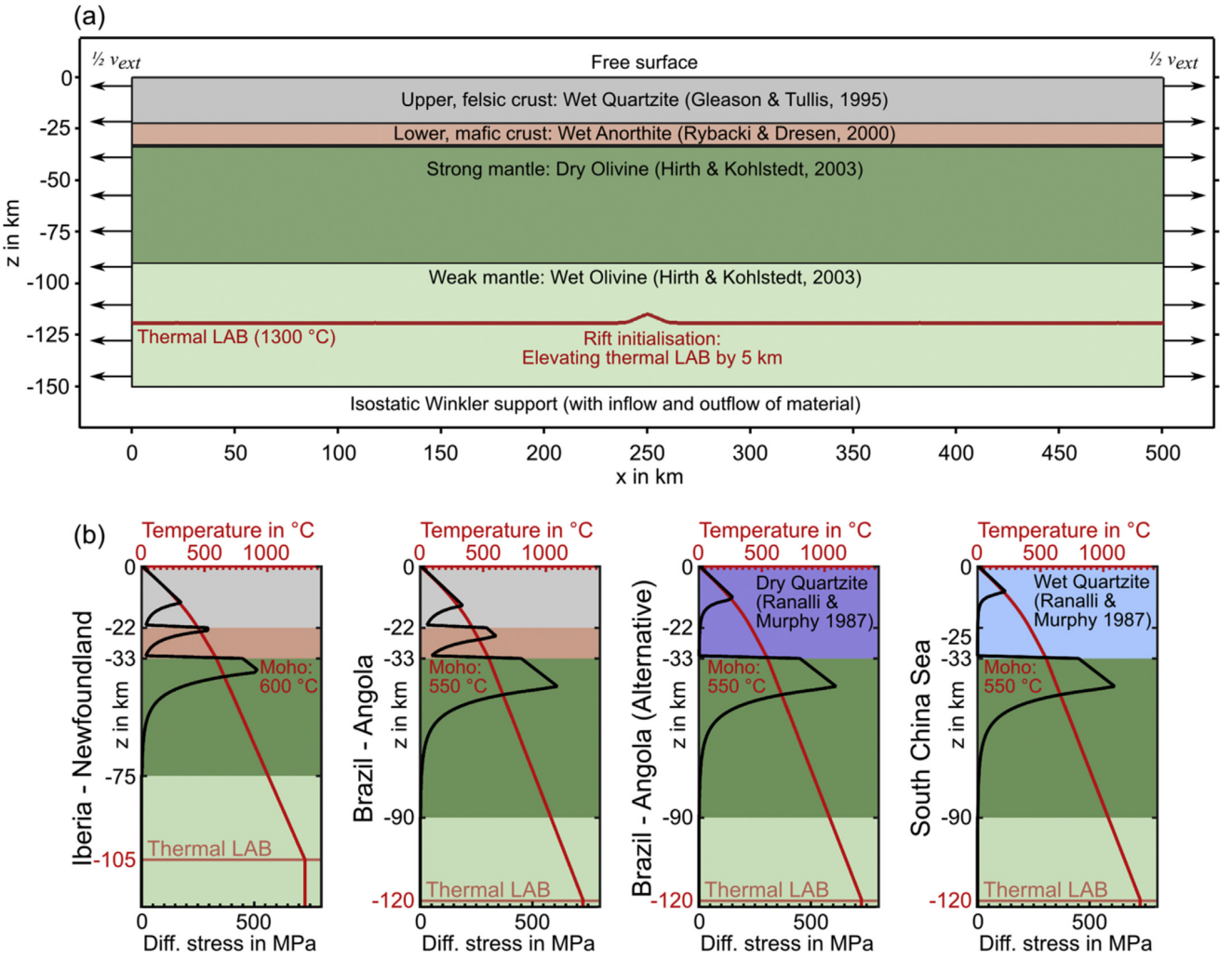

Fig. 2. Model setup and yield strength profiles. (a) Material layers and boundary conditions for the Brazil-Angola scenario. (b) Initial geotherms and yield strength profiles of all models of this paper.

describe the second phase of rifting that led to crustal breakup, exhumation of the mantle and sea-floor spreading.

We focus on the northern segment of the rift, which shows a clear tectonic asymmetry on both sides of the rift. While crustal thinning occurs gradually on the Iberian side, where the crust thins from ~18 to 0 km thickness over a horizontal distance of 80 km (see Fig. 4 adapted from Ranero and Pérez-Gussinyé, 2010), crustal thinning on the Newfoundland side is much more abrupt and crustal thinning from 18 km to 0 km occurs over a distance of ~40 km. The West Iberian side is characterized by large offset normal faults (labelled f1-f6 in Fig. 4), where offsets on the first three faults f1-f3 are 11 to 7 km. The Newfoundland conjugate in contrast, shows much less faulting. On the West Iberian margin, faults f1–f3 dip oceanward and become listric at depth. Further oceanward, with increasing extension, fault block dimensions decrease and their bounding faults merge at depth with a sub-horizontal reflector, the so-called S reflector, interpreted to be the Moho (Reston et al., 1996; Whitmarsh et al., 1996; Bayrakci et al., 2016). A similar reflector, the H reflector, which underlies highly attenuated and rotated crustal blocks has been described further southward along line LG12 in the Iberia Abyssal Plain (Krawczyk et al., 1996). Recent 3D wide-angle data, as well as older data sets, suggest that the S and H reflectors separate continental crust from serpentinised mantle below (Whitmarsh et al., 2001; Chian et al., 1999; Zelt et al., 2003; Bayrakci et al., 2016). Progressive merging of faults f1-f6 at depth with the Moho has been interpreted to reflect progressive strengthening of the lower crust. This is possible due to cooling during slow rifting that predominated during crustal thinning (Minshull et al., 2001; Pérez-Gussinyé et al., 2001, 2006). Lower crustal rocks were recovered from the deepest part of one of these rotated blocks along line LG12, where the crust is less than 6 km thick. ^{40}Ar-^{39}Ar plagioclase ages of these rocks indicate that they went through the 150 °C isotherm in the Valanginian at 136–137 Ma (ODP Sites 900 and 1067; Féraud et al., 1996). Because these rocks are within the same footwall as mantle rocks that were exhumed 2 km oceanward (and recovered from ODP Site 1068), it is inferred that they were very close to the base of the crust at the start of rifting and that they cooled and became progressively brittle during extension, as originally proposed by Pérez-Gussinyé and Reston (2001).

Synrift sediment ages recovered at ODP Sites 638, 641 and 640 (Boillot et al., 1988), suggest that faulting became younger oceanward. Focusing of the deformation oceanward has also been described for the Iberia Abyssal Plain (Péron-Pinvidic et al., 2007)

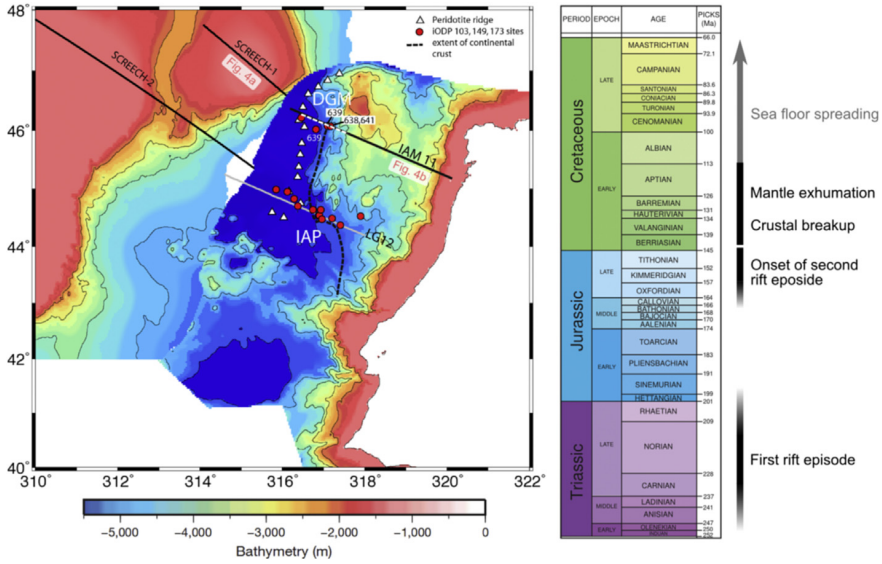

Fig. 3. Bathymetry offshore Iberia and Newfoundland, reconstructed to chron M0 (modified from Pérez-Gussinyé, 2013). Black solid lines show seismic profiles, and the curved black dashed line marks the oceanward extent of continental crust at the west Iberian margin. Abbreviations: DGM - Deep Galicia Margin; IODP, International Ocean Drilling Program; WIM - West Iberian Margin. Geological time scale is modified from Walker et al. (2013).

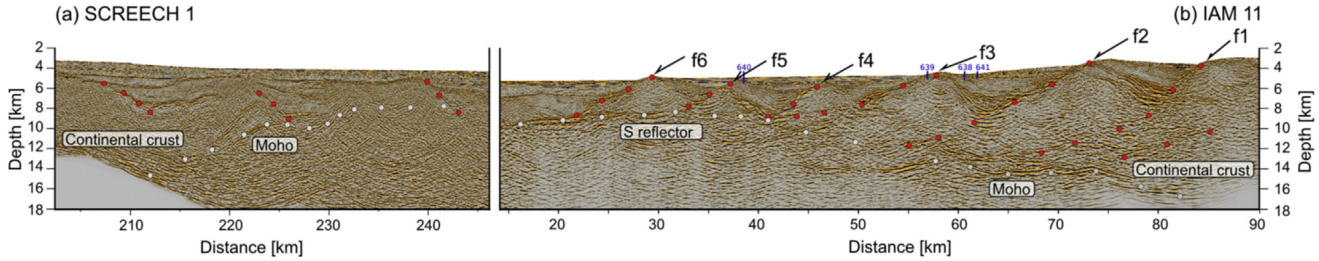

Fig. 4. Conjugate seismic profiles from Newfoundland and West Iberia (modified from Ranero and Pérez-Gussinyé, 2010). Red circles follow reflections in crust and mantle interpreted as faults. Grey circles indicate the Moho. (a) Prestack depth-migrated segment of line SCREECH-1. (b) Prestack depth-migrated segment of line IAM-11. The projection of IODP boreholes are shown in blue numbers. Locations of cross-sections are shown in Fig. 3. (For interpretation of the references to colour in this figure legend, the reader is referred to the web version of this article.)

and for many other less extended rifts and basins, as for example the Gulf of Suez (Gawthorpe et al., 2003), North Sea (Walsh et al., 2003; Cowie et al., 2005) and Gulf of Corinth (Mattei et al., 2004). Progressive coupling and embrittlement of the crust in conjunction with evidence for oceanward focusing of deformation and a reduction in brittle block size, was interpreted from faults f1 to f6 on profile IAM 11, which cut through a crust that was progressively thinner through time (Fig. 4). Ranero and Pérez-Gussinyé (2010) suggested that those faults where sequential in time and always formed in the hanging wall to the previous one, which would result in progressive younging of faulting and synrift sediments towards the basin centre. These fault kinematics would also lead to the progressive formation of tectonic asymmetry between the two conjugate margins, with the wide margin being the one where the sequential fault array was active, and the narrow one, the hanging wall to the sequential fault array (Ranero and Pérez-Gussinyé, 2010). In the following we use dynamical modelling to show how margin asymmetry and sequential faulting may emerge and under which circumstances this asymmetry does develop.

3.2. Model

Before describing the model evolution, we shortly justify the model setup. Our setting involves a felsic upper crustal layer of 22 km thickness that deforms in accordance with a wet quartzite flow law (Gleason and Tullis, 1995), while the mafic crust between 22 and 33 km depth follows a wet anorthite flow law (Rybacki and Dresen, 2000). Evidence for the rheology of the lower crust is based on seismic studies that show lower crustal P-wave velocities of >6.6 km/s within our study region (Dean et al., 2000; Funck et al., 2003; Pérez-Gussinyé et al., 2003; Hopper et al., 2007) providing strong evidence for a mafic composition (Christensen and Mooney, 1995). Additional support for use of these flow laws comes from the magma-poor margins of the Alpine Tethys that have been partially exposed during the Alpine orogeny and where the lower crust of the Adriatic plate is rich in granulites and mafics (Müntener and Hermann, 2001). The initial crustal thickness of our model is 33 km, which is based on seismically inferred Moho depth in unrifted Iberia (Díaz and Gallart, 2009). As an initial depth of the lithosphere-asthenosphere boundary, we use a value of 105 km, which agrees with the estimated present-day range of Artemieva (2006) for the Iberian peninsula.

The evolution of our geodynamic model for the Iberia-Newfoundland rift (Fig. 5) can be partitioned in three phases: Phase 1 - Simultaneous faulting, followed by Phase 2 - Rift migration and sequential faulting, and Phase 3 - Breakup. As illustrated in

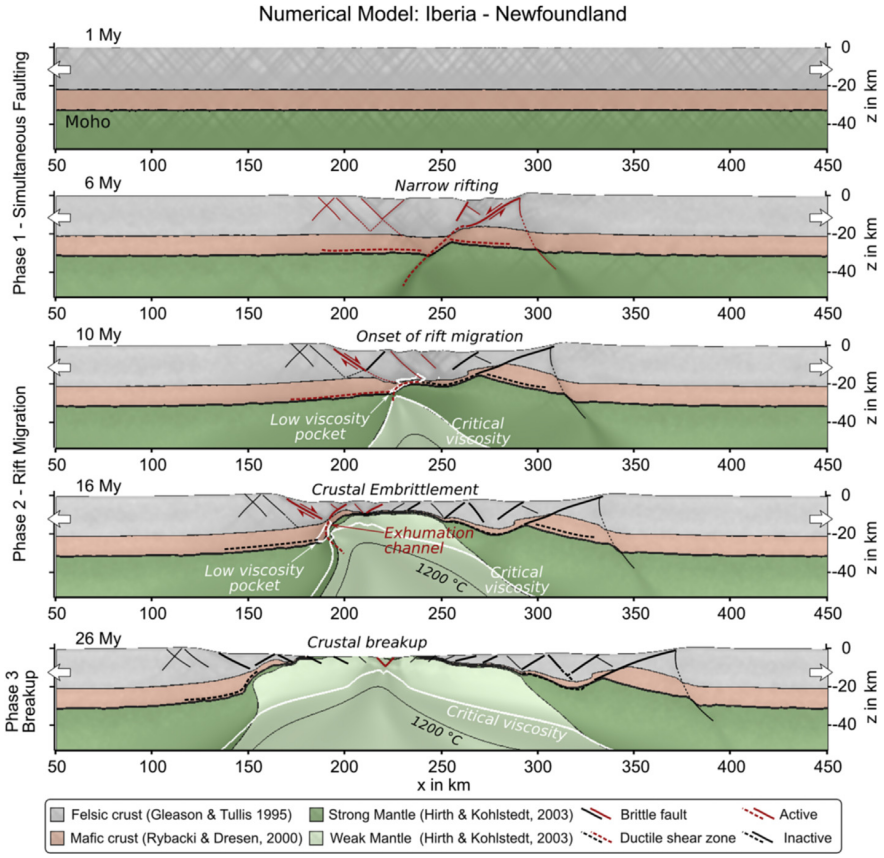

Fig. 5. Iberia-Newfoundland model. A moderately asymmetric narrow rift generates an asymmetric margin pair through rift migration. Active faults and shear zones are marked in red; those that became inactive in black. Material phases are overlain by the strain rate field in grey-shade. Critical viscosity refers to the isoviscosity line of $10^{20.5}$ Pas. The 3 phases are marked on the left. The "exhumation channel" is the concave downward deformation zone comprising the low-viscosity pocket and the upper crustal faults. An animation of this model can be found in the supplement. (For interpretation of the references to colour in this figure legend, the reader is referred to the web version of this article.)

Fig. 5, these phases are characterized by different rift widths and degree of symmetry within the actively faulted area (depicted in red). These three phases reproduce the interpreted kinematic evolution of the Iberia-Newfoundland rift systems. In the following we describe the geodynamic processes causing this three-phase behaviour. Note that animations of all models in this paper are available as supplementary materials.

3.2.1. Phase 1 - Simultaneous faulting

This phase is marked by competition between ubiquitous faults. The strength of faults reduces significantly with accommodated deformation, which is implemented in our model through a strain-dependent friction coefficient. Faults that experience slightly more strain than others, because they emerged in a dynamically favoured location or because they coincide with the trend of inherited foliations will accommodate more strain than others, and hence they will become even weaker as deformation proceeds. This localisation feedback generates a rift whose symmetry and width is controlled by the interplay of ductile and brittle deformation (Huismans and Beaumont, 2003). Ductile deformation favours symmetric thinning of the crust, while brittle deformation is energetically more efficient when fewer faults are formed, so that it favours asymmetry. Since the model consists of both ductile and brittle layers, the resulting symmetry depends on the dynamic trade off between these two deformation styles that can be understood in terms of energy dissipation (Buiter et al., 2008). In the presented model setup where brittle and ductile deformation is equally important, the energetically most efficient configuration is a narrow rift with a single border fault and few antithetic faults in an asymmetric configuration. During continued extension, the border fault experiences more strain giving rise to a moderately asymmetric rift configuration, similar to the Upper Rhine Graben (Brun et al., 1992; Michon and Merle, 2000).

3.2.2. Phase 2 – Rift migration

As the dominant border fault on the right continues to accommodate slip, the mantle is brought upwards asymmetrically under the left-hand rift side. The advected heat of the mantle reduces the crustal viscosity in this area below a critical value of $10^{20.5}$ Pas (depicted in Fig. 5 as white line) and renders it more prone to accommodate deformation. Simultaneously, the right-hand border fault rotates to about 30° and locks up, such that new faults start to form on top of the low-viscosity pocket while the width of the actively deforming area decreases significantly (Fig. 5 at 10 My). The end of activity on the right-hand border fault marks the onset of a period where new faults form in the hanging wall of this master fault as sequential faults. In this rift migration phase most of the faults dip towards the future ocean, although some minor antithetic faults are sometimes observed. In agreement with observations and kinematic modelling for the Iberian margin (Ranero and Pérez-Gussinyé, 2010), rift migration initiates in our model when the crustal thickness is reduced to less than 20 km and major faults of Phase 1 have rotated to ~30° (Fig. 5, at 10 My).

In the rift migration phase, new oceanward-dipping faults form

in the hanging wall of the previous fault, on top of the low-viscosity crust, which constitutes the weakest part of the extending lithosphere. As long as the lower crust is hot and weak, these newly formed faults are not effective in thinning the crust because vertical motion at their down-dip ends is compensated by lower crustal flow. In analogy to the "subduction channel" at convergent plate boundaries, we refer to this concave-downward deformation zone that comprises the low-viscosity pocket and the upper crustal faults as the "exhumation channel". The exhumation channel is maintained in a self-sustaining process, during which the rift centre moves sideways and creates a wide, hyper-extended margin consisting of rotated fault blocks (Fig. 5, at 16 My). Faults on top of the exhumation channel form sequentially in time, analogous to faults f1-f6 in Fig. 4. Our model reproduces multiple discrete fault blocks that are imaged in seismic data and whose size decreases towards the continent-ocean transition (Ranero and Pérez-Gussinyé, 2010).

3.2.3. Phase 3 – Breakup

The numerical modelling shows that rift migration occurs as long as there is enough weak lower crust to flow into the tip of the active fault and prevent mechanical break-up by faulting. The low-viscosity crust progressively disappears due to continuing heat loss by conduction during rifting. When the low-viscosity pocket vanishes, the entire crust becomes brittle and faults become more effective at crustal thinning and end up by inducing crustal breakup (Pérez-Gussinyé and Reston, 2001). This progressive embrittlement of the crust is observed in seismic profiles by a continuous deepening of the faults oceanwards (Fig. 4). Embrittlement is accomplished when faults reach the Moho, forming a sub-horizontal "detachment-like" surface which has been called S in the Deep Galicia Margin and H in the Iberia Abyssal Plain (Krawczyk et al., 1996; Reston et al., 1996; Sutra and Manatschal, 2012). Such a detachment-like surface forms in our model when the crust is less than 6 km thick from around 13 My onwards (Fig. 5, see also supplementary animation).

Supplementary videos related to this article can be found at http://dx.doi.org/10.1016/j.marpetgeo.2016.10.018.

Final crustal separation occurs soon after complete crustal embrittlement. During break-up, the position of faulting changes in our model: instead of cutting further into the hanging wall to the array of sequential faults, deformation jumps to a location within the wide and hyper-extended margin. This location is demarcated by the centre of the broad mantle upwelling underlying the rift (see 1200 °C isotherm in Fig. 5 at 16 My). This process is consistent with recent interpretations from the continent-ocean transition in the Australian Bight basin (Gillard et al., 2016) and marks the end of asymmetric extension during the rift migration phase, while introducing symmetric faulting during final break-up.

4. Central South Atlantic rifting

4.1. Observations

A number of unique factors make the South Atlantic a prime location for reconstructing and modelling the dynamics of lithosphere extension in a quantitative plate tectonic and geodynamic framework (Fig. 6). At the first order, the South Atlantic rift is part of a relatively simple plate kinematic system, which can be reduced to the divergence of the present-day South American and African continental lithospheric plates. At the time of inception of the South Atlantic rift system, however, the picture was more complex. Several rift branches generated a time-dependent network of Jurassic-Cretaceous rifts across Africa (West and Central African Rift systems), the Equatorial Atlantic and Northeast Brazil, and across the southern part of South America (Heine et al., 2013b). As many of these rift segments did not progress to continental breakup, they became fossilised and preserved in the subsurface, where they are directly accessible to seismic and drilling (e.g. Genik, 1992). Along with the divergence of the South American and African plates around a stage rotation pole in Northwest Africa, this complex set of intracontinental rift structures allows us to build a consistent regional model of intraplate deformation that can be used to quantitatively reconstruct the pre-breakup evolution of the South Atlantic rift in a global plate tectonic framework.

Commonly, plate tectonic models are based on oceanic magnetic anomalies and gravity data, allowing precise dating and quantitative reconstruction of the spreading history of divergent, conjugate

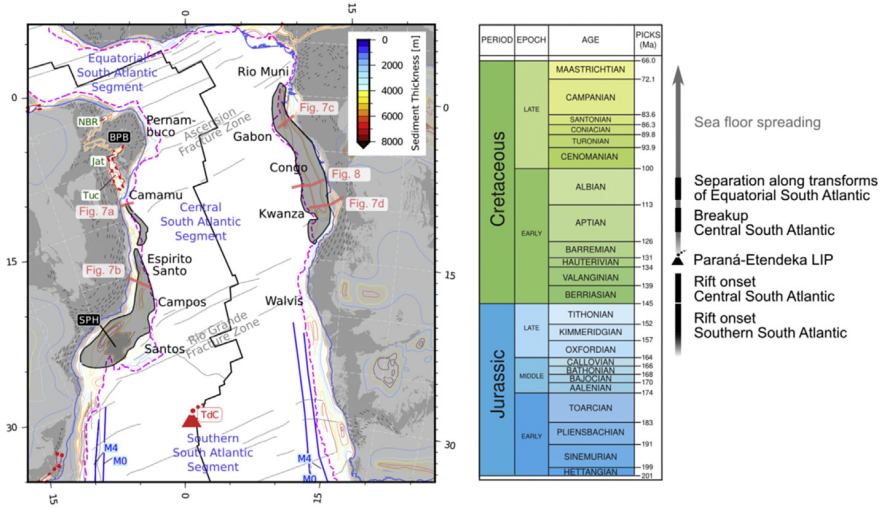

Fig. 6. Tectonic map of the Central South Atlantic. Reconstructed to 83.5 Ma position with Africa held fixed in present coordinates (modified from Heine et al., 2013b). Proterozoic rocks are shown as grey polygons, metamorphic basement grain as thin dark grey lines, and oceanic fracture zones as light grey lines. Sediment thickness contours are colour-coded. Aptian salt basins are outlined in grey shade. Pink dashed line is the landward limit of oceanic crust (LaLOC). Abbreviations: BPB – Borborema Province Block; Jat – Jatobá rift; NBR – northeast Brazilian rifts; SPH – Sào Paulo High; TdC – Tristan da Cuñha hotspot; Tuc – Tucano rift. Geological time scale is modified from Walker et al. (2013). (For interpretation of the references to colour in this figure legend, the reader is referred to the web version of this article.)

plates. In continental settings however, such markers do not exist and hence the quantification of the pre-breakup extension kinematics becomes close to impossible without good seismic, potential field, and well data calibration. While the relative simplicity of South Atlantic rifting and opening gave rise to various plate reconstructions (Wegener, 1912; Bullard et al., 1965; Unternehr et al., 1988; Nürnberg and Müller, 1991; Torsvik et al., 2009; Moulin et al., 2010; Heine et al., 2013b; Pérez-Díaz and Eagles, 2014), it has become clear that only those which consistently integrate pre-breakup observations can add the necessary extra dimension of information to our understanding of the formation of passive margins. Such quantified plate models became available for several regions worldwide (Williams et al., 2011; Kneller et al., 2012; Heine et al., 2013b; Hosseinpour et al., 2013; Barnett-Moore et al., 2016). The power of these models is that their predictions of extensional velocities and directions is not only testable against observations such as seismic data, subsidence rates derived from wells, and crustal scale fault heaves (Ranero and Pérez-Gussinyé, 2010; Cowie et al., 2015b) but they provide also an extremely promising avenue of integrating observational models with predictive, forward numerical models of lithosphere extension.

In the case of the South Atlantic, the rift axis is roughly sub-perpendicular to the extension direction. Hence, the rift axis forms a great circle through the stage pole, resulting in extensional velocities increasing from a minimum extensional rate near the stage pole to a maximum at the stage rotation equator. This setting allows the first order effects of rift velocity and lithosphere rheology to be compared on a more than 5000 km long rift that evolved into a conjugate passive margin system with a largely non-magmatic northern and central part, and a magmatic southern part (Lundin et al., 2014). Extensive Aptian evaporite sequences cover large parts of the conjugate central South Atlantic rift segments from the Santos/Benguela Basin northward to the conjugate Gabon/Camamu basins (e.g. Demercian et al., 1993; Davison, 2007), severely impacting the quality of sub-salt seismic imaging. Hence little unequivocal estimates on the amount of magmatic additions in the intra- and sub-salt sequences (or as sub-crustal magmatic underplates) exist for these rift segments. While the margins are overall considered weakly magmatic (Blaich et al., 2008, 2011) evidence for locally extensive magmatism is reported for example from the Sergipe-Alagoas margin (Fraser and Clark, 2016), the Sumbe volcanic trend in the Kwanza Basin (Marzoli et al., 1999; Quirk et al., 2013) as well as an overall trend of increasing magmatic additions towards the Santos basin/Parana-Etendeka LIP. In the Campos Basin, industry wells are reported to have finished in extensive thicknesses (>250 m) of sub-salt basaltic rocks (S. Demercian, pers. comm). However, on a first order, crustal scale, margin-wide 2D seismic surveys do not show abundant evidence of characteristic SDR-type magmatic additions along the central South Atlantic conjugate margin segments. Second order effects, such as tectono-thermal age of the lithosphere Artemieva (2006) and tectonic inheritance (e.g. Pedrosa-Soares et al., 2008), also change significantly along strike of the rift system and could exert further control on the evolution of rifting and final passive margin geometry, albeit at much shorter spatial wavelength and not continuously throughout the evolution of continental extension until breakup.

Large segments of the South Atlantic rift host considerable amounts of hydrocarbon in the syn-rift and post rift sequences, meaning that exploration industry imaging and well data have become increasingly available over the past decade. This led to further important observations characterising the evolution of rifting along the South Atlantic margins temporarily, and spatially (Mohriak et al., 1990, 2000; Chang et al., 1992; Unternehr et al., 2010; Zalán et al., 2011; Heine et al., 2013b; Quirk et al., 2013), especially through newly acquired crustal scale, long offset seismic data (as published by e.g. Unternehr et al., 2010; Zalán et al., 2011; Cowie et al., 2015a). Industry-backed research projects and multi-institutional campaigns such as the German SAMPLE project (e.g. Scheck-Wenderoth et al., 2013) have shed further light on the evolution of the South Atlantic rift basin through the acquisition and publication of new geophysical and geological data (Contrucci et al., 2004; Blaich et al., 2011; Heit et al., 2015; Ryberg et al., 2015; Dressel et al., 2016). At present, there are a number of state-of-the-art, high-resolution, deep-penetrating seismic data sets available to industry along both conjugate margins, along with numerous other seismic surveys in various marginal sub-basins with some sections successively published over the past years (Unternehr et al., 2010; Cowie et al., 2015a; Perez-Gussinye, 2015; Péron-Pinvidic et al., 2015). Global high resolution potential field data is available both to academia and specialised surveys for industry (Sandwell et al., 2014). The distribution of the surveys is correlated with hydrocarbon exploration focus areas, but in general the South Atlantic margins are relatively homogenously covered by legacy and state-of-the-art seismic surveys and are one of the densest covered conjugate Atlantic-type margin pairs globally.

The onset of continental extension in the central and northern segment of the South Atlantic dates to the Late Jurassic/Early Cretaceous (Chaboureau et al., 2013), documented by formation of the Reconcavo-Tucano-Jaitoba Rift (Ghignone and De Andrade, 1970; Magnavita et al., 1994, 2012; Poropat and Colin, 2012) in Northeast Brazil and the inner Gabon Basin (Teisserenc and Villemin, 1989; Mbina Mounguengui and Guiraud, 2009). Lacustrine basins systems developed as extension progressed at relatively low velocities (Heine et al., 2013b). By early Barremian times (~127 Ma), the central South Atlantic rift segment width had already reached around 200–250 km with extension having progressed beyond a distributed deformation phase into a necking phase. The rift widened a further 150 km until breakup along the central segment. Breakup and the transition to oceanic spreading is commonly assumed to have started during the Aptian in the Kwanza-Campos segment (~117 Ma).

The margin architecture along the eastern South American and West African seaboard is variable, however, the margin asymmetry and margin width increases from the Ascension Fracture Zone near the Equator southwards to the Walvis Ridge-Florianopolis High. Southwards of this lineament, breakup-related volcanism dominates the margin architecture, where the conjugate margin are fairly asymmetric and wide (~150–200 km) (Chang et al., 1992; Blaich et al., 2011; Heine et al., 2013b; Péron-Pinvidic et al., 2015). The conjugate margins of NE Brazil and Cameroon/Gabon are extremely narrow and characterized by steep gradients in crustal thickness. The transition from unextended continental crust to typical oceanic crust outboard of the LaLOC ("landward limit of oceanic crust", cf. Heine et al., 2013b) occurs over a distance of less than 100 km, in some parts of the Cameroon margin and the Natal margin of Northeasternmost Brazil less than 50 km. Faulting occurs along a limited number of large offset normal faults (Fainstein and Milliman, 1979; Rosendahl and Groschel-Becker, 1999; Turner et al., 2003; Blaich et al., 2009) and the overall asymmetry of the system is relatively low (cf. Brune et al., 2014). There is evidence for pre-breakup/syn-rift magmatism along the Sergipe-Alagoas margin (Caixeta et al., 2014; Fraser and Clark, 2016), likely related to a precursor of the Cardno hotspot being located in the vicinity of the evolving rift (Heine et al., 2013b). Continental breakup in this part of the margin is dated to around 117 Ma based on subsidence data of the Rio Muni-1 well (Fig. 6; Turner et al., 2003). Further south, margin width and asymmetry increase significantly in the central South Atlantic segment (Fig. 6; Brune et al., 2014). Large asymmetries developed between the narrow Camamu/Espirito Santo

margin segment on the Brazilian side and the wide Gabon/Congo margin in West Africa, with total margin width increasing from around 150 km (~50 km width Brazil, ~100 km width West Africa; Blaich et al., 2011; Cowie et al., 2015a) to more than 400 km (~100 km Campos Basin margin, ~300 km Kwanza Basin margin; Unternehr et al., 2010; Péron-Pinvidic et al., 2015) in the Campos-Kwanza Basin segment. Further south, the polarity of the asymmetry is flipped, with the Benguela part of the margin being the narrow margin and the Brazilian side being the wide margin. We treat the southern Campos Basin and Santos/Benguela Basin as separate cases, as the Cabo Frío transfer zone offsets the southern South Atlantic segment against the central segment. Here, microplate rotation and spreading ridge jumps deviate from a simple two-plate scenario (Scotchman et al., 2010; Heine et al., 2013b). Farther south, the conjugate margins become dominated by extensive syn-rift magmatism (Becker et al., 2014).

Several publications based on new long offset seismic data have highlighted the crustal structure of the hyperextended West African margin in unprecedented detail (Contrucci et al., 2004; Unternehr et al., 2010; Cowie et al., 2015a; Péron-Pinvidic et al., 2015). The margin (Figs. 7 and 8) is characterized in the proximal part by large crustal thickness gradients, offset through major normal fault systems (also described as a "necking zone"), often not more than 100 km outboard of the present-day coastline. Further outboard, crustal thickness quickly approaches values of 15–10 km, overlain by up to 5–7 km thick syn-rift and sag sediment infill underneath the base of the regionally extensive Aptian salt layer on both parts of the conjugate margins (Fig. 8; Crosby et al., 2011; Heine et al., 2013b; Norton et al., 2016). A zone of salt diapirs and chaotic outer salt (Hudec and Jackson, 2007) overlies the outermost part of the continental margin, adjacent to and partly overriding oceanic crust (Fig. 8), hampering seismic imaging of the subsalt structures. Interpretation of basement topography and structural features on available seismic data in this outer part of the margin is largely driven by conceptual/numerical models (e.g. Pérez-Gussinyé et al., 2003; Huismans and Beaumont, 2008; Péron-Pinvidic and Manatschal, 2009; Ranero and Pérez-Gussinyé, 2010; Brune et al., 2014; see also Figs. 9 and 10), however, little dispute exists that at least the more proximal parts of the highly extended crust are overlain by significant thicknesses of relatively conformable sedimentary sequences devoid of typical syn-rift structuration ("sag sequences") which continue into the Aptian evaporitic sequences (Crosby et al., 2011; Péron-Pinvidic et al., 2015; Norton et al., 2016).

4.2. Model

In this section we discuss two model setups differing in terms of crustal rheology, but that both agree with observations. Our first setup for the Brazil-Angola conjugate margins of the Central South Atlantic is very similar to the one used for Iberia-Newfoundland in Section 3.2. Again we use a felsic upper crustal flow law between the surface and 22 km and a mafic crust between 22 km and 33 km depth corresponding to regional seismic velocities patterns (Contrucci et al., 2004) and crustal thickness estimates (Mohriak and Dewey, 1987). Similarly, we apply a constant extension velocity of 8 mm/yr (full rate) in agreement with initial rift velocities in kinematic plate reconstructions for the Brazil-Angola conjugates (Heine et al., 2013b). The only difference to the Iberia-Newfoundland model lies in the initial depth of the lithosphere-asthenosphere boundary. Here we use 120 km (instead of 105 km), which is based on estimates for present-day African mobile belts (Artemieva, 2006). Note that using a deeper LAB results in the initial thermal state being cooler than for Iberia-Newfoundland case as it is computed as a 2D steady state temperature distribution.

The evolution of the model for Brazil-Angola can be partitioned in the same three phases as in the Iberia-Newfoundland model. First we describe the tectono-thermal evolution during each phase of our preferred model before we introduce an alternative model setup and discuss the differences between both simulations.

4.2.1. Phase 1 - Simultaneous faulting

Rifting starts with a fault network that distributes deformation across the entire width of the model until friction softening causes fault coalescence (Cowie et al., 2005). In the model shown in Fig. 9 an asymmetric fault configuration develops with a single dominant fault and few antithetic faults. This type of asymmetric faulting is characteristic for narrow rifts like the Baikal Rift (van der Beek, 1997), the Gulf of Corinth (Bell et al., 2008; Nixon et al., 2016) or for many locations in the East African Rift System (Ebinger et al., 1999; Chorowicz, 2005). Slip along the dominant initial fault results in severe lithospheric thinning and asymmetric asthenospheric upwelling (Fig. 9 at 8 My). Simultaneously, sub-horizontal

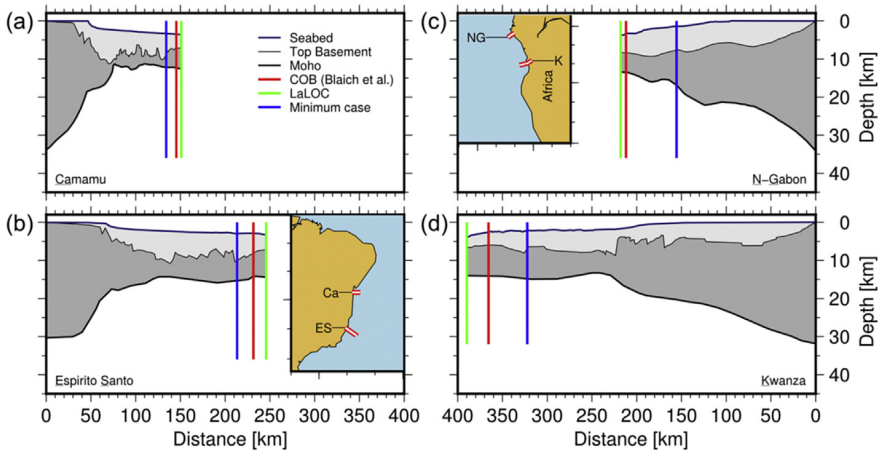

Fig. 7. Margin cross sections based on Blaich et al. (2011) and modified from Heine et al. (2013b). Extent of continental crust: LaLOC – Landward Limit of Oceanic Crust (Maximum estimate); Minimum case – conservative estimation of limit of continental crust; COB – Continent-Ocean Boundary based on Blaich et al. (2011). Locations of cross-sections are shown in Fig. 6.

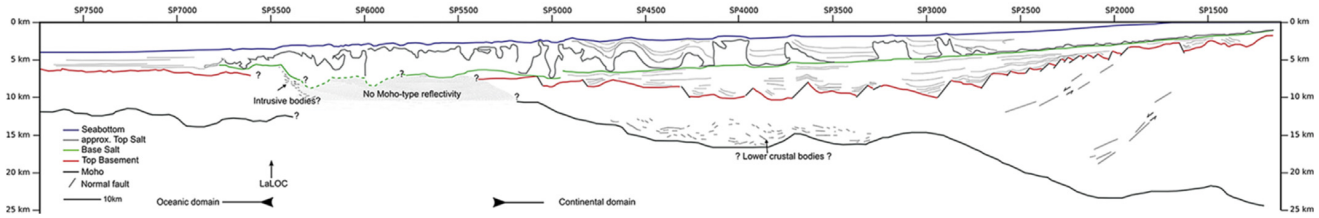

Fig. 8. Interpreted seismic profile CS2400 (courtesy of Statoil). Location of cross-section is shown in Fig. 6.

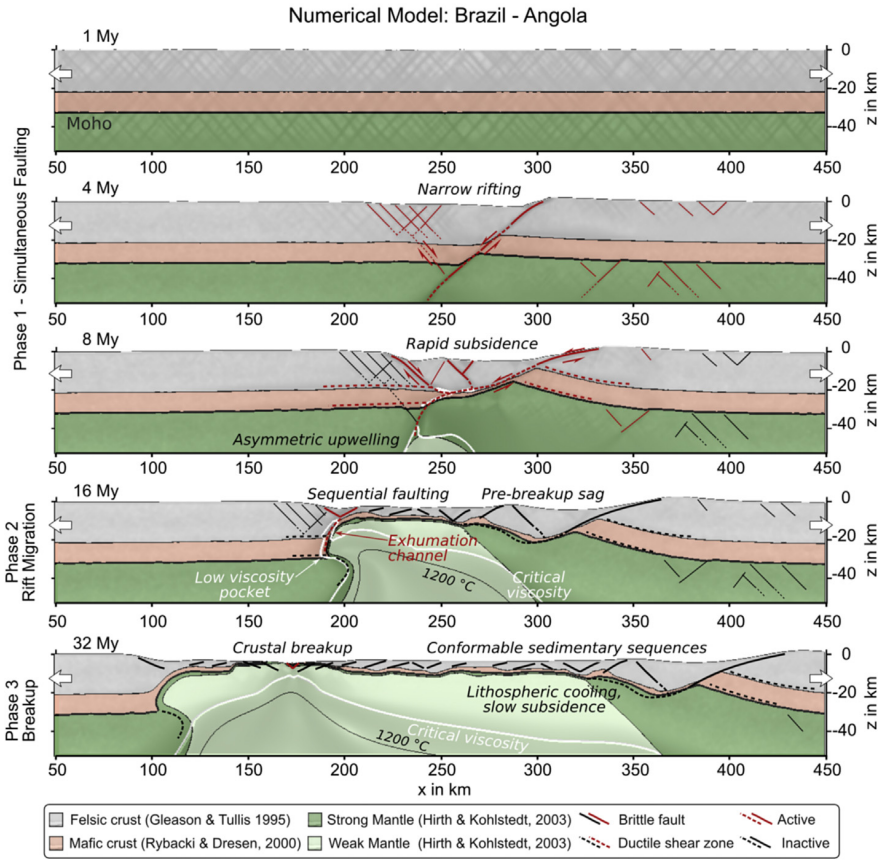

Fig. 9. Brazil-Angola model. An asymmetric narrow rift generates 150 km of hyper-extended continental crust on the right side and 20 km on the left. The rift migration phase has a duration of ~20 My. Active faults and shear zones are marked in red; those that became inactive in black. Critical viscosity refers to the isoviscosity line of $10^{20.5}$ Pas. The 3 phases are marked on the left. An animation of this model can be found in the supplement. (For interpretation of the references to colour in this figure legend, the reader is referred to the web version of this article.)

ductile shear zones develop in the lower portions of both the felsic and mafic crust, accommodating crustal flow towards the rift axis as described for the South Atlantic conjugates (Aslanian et al., 2009).

4.2.2. Phase 2 – Rift migration

This phase of sequential fault activity is caused by two processes: (i) cooling and strengthening of mantle material takes place at the footwall side of the exhumation channel, (Kusznir and Park, 1987; van Wijk and Cloetingh, 2002), while simultaneously (ii) the rift side is weakened due to conductive heat transfer from the hot asthenospheric upwelling. Both processes - softening at the tip of the active fault and strengthening at its footwall - generate a lateral strength contrast that leads to migration of the rift centre. The asthenospheric upwelling in Fig. 9 is more focussed than in Fig. 5 (i.e. in the Iberia-Newfoundland model), which heats the rift side more efficiently and generates a larger low-viscosity pocket. Hence, rift migration lasts longer and leads to a higher degree of margin asymmetry where the wide margin measures more than 200 km while the conjugate margin is only 50 km wide (Fig. 9 at 32 My). Similar results have been found in independent modelling studies (Liao and Gerya, 2014; Svartman Dias et al., 2015; Jammes and Lavier, 2016) lending additional robustness to the described process of rift migration.

Due to migrating rift activity, massive material transfer takes place across the rift detaching large crustal blocks from the future narrow margin and accreting them in the form of highly thinned continental crust to the wide margin. Note that this behaviour contradicts the common assumption that the stretched continental crust of a passive margin consists of deformed material of the same

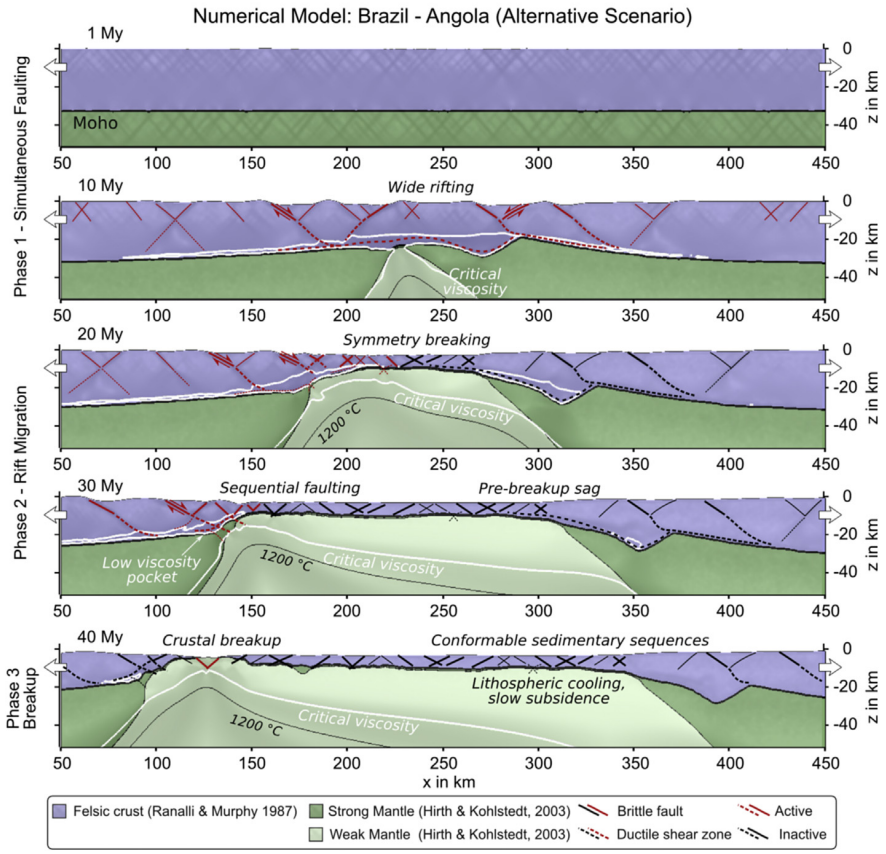

Fig. 10. Brazil-Angola - Alternative scenario. A symmetric wide rift thins through simultaneous faulting for 20 My until the crustal thickness reaches ~10 km thickness. As long as the lower crust lies within the critical viscosity contour, the entire crust undergoes pure shear extension. Once the crust in the rift centre is thin enough to become entirely brittle, the rift migration phase starts generating two highly asymmetric conjugate margins. Active faults and shear zones are marked in red; those that became inactive in black. Critical viscosity refers to the isoviscosity line of $10^{20.5}$ Pas. The 3 phases are marked on the left. An animation of this model can be found in the supplement. (For interpretation of the references to colour in this figure legend, the reader is referred to the web version of this article.)

plate (McKenzie, 1978).

Numerical modelling indicates that higher rift velocities elevate the temperature of the exhumation channel via more efficient asthenospheric heat advection. Faster rifting hence increases the extent of the low-viscosity pocket and thereby generates wider margins with more pronounced asymmetry (Brune et al., 2014). This finding is mirrored in the Central South Atlantic margins, where the extension rate was higher in the south than in the north (Moulin et al., 2010; Torsvik et al., 2009; Heine et al., 2013b) while the width of the wide margin increases southward almost linearly (Fig. 6; see also Brune et al., 2014).

Long-lasting rift migration has profound implications for sedimentation patterns on wide, hyperextended continental margins. Due to migrating rift activity, deformation at the proximal part of the wide margin may predate deformation in the distal part by more than 20 million years. This provides an alternative explanation of the existence of the observed thick and unfaulted pre-salt sediments on the wide West African margin of the Central South Atlantic where conformable sedimentary sequences have been deposited prior to break-up (Karner et al., 2003; Unternehr et al., 2010; Péron-Pinvidic et al. 2015). Our model also suggests that the sediment source might be different between proximal and distal margin: when the distal margin is formed, the closest sediment input is the opposite continent and sediments could be more easily provided by drainage systems originating on the conjugate plate. Another important implication of rift migration for hydrocarbon maturation is that the heat flow, which is highest above the exhumation channel, will be strongly time-dependent: diachronous deformation generates a peak heat flow that moves from the proximal to the distal margin over a period of many million years (Pérez-Gussinyé, 2013; Brune et al., 2014). This means that, like in the above scenario, peak heat flow at the distal part of the margin might occur more than 20 My later than in the proximal domain, with severe implications for source rock deposition, hydrocarbon maturation and migration.

4.2.3. Phase 3 – Breakup

The rift migration phase ends when the steady-state heat supply to the exhumation channel decreases. Hence, the rifting continental crust cools, which strengthens ductile areas and progressively renders the crust more brittle until faults penetrate into the mantle (Pérez-Gussinyé and Reston, 2001). When the low-viscosity pocket finally vanishes, a discrete rift jump occurs: rifting at the location of the former low-viscosity pocket stops and a new rift centre forms where the lithosphere of the foot-wall side of the rift is thinnest. This location coincides with the shallowest depth of the 1200 °C isotherm (see supplementary animation). The rift jump generates a fault pattern that switches from sequential faults where new faults form predominantly within the hanging wall of previous faults (Ranero and Pérez-Gussinyé, 2010) to “out-of-sequence” where new faults form in the foot wall (Gillard et al., 2015, 2016). Soon after, the newly formed faults lead to breakup by cutting

through the brittle crust and upper mantle portions. Following crustal breakup, mantle is exhumed to the surface with very little magmatic activity (Pérez-Gussinyé et al., 2006).

Fig. 10 shows an alternative numerical simulation that reproduces observations from the Brazil-Angola conjugates. In contrast to the model shown in Fig. 9, this simulation applies a relatively weak felsic flow law (Ranalli and Murphy, 1987) to the entire crust, while all other parameters are identical (see model with rheology R2 in Brune et al., 2014). While the three phases of simultaneous faulting, rift migration, and breakup are robustly reproduced, there are significant differences between the simulations. In the scenario with weaker crust, brittle deformation in the upper crust is decoupled from the mantle, resulting in the formation of a wide rift with extensive ductile shear zones and crustal-scale boudinage (Clerc and Lagabrielle, 2014; Clerc et al., 2015; Jammes and Lavier, 2016). Ductile decoupling of crust and mantle prolongs the initial phase of simultaneous faulting to 16 My. During this time, deformation is distributed throughout the entire width of the model, creating alternating horst and graben structures similar to the present day Basin and Range region (Stewart, 1971; Wernicke, 1981; Hamilton, 1987). At ~20 My, the wide rift mode that created a predominantly symmetric rift configuration ends. At this stage two low-viscosity regions exist under each side of the rift. In the following stage, all deformation gets focussed into the larger one on the left side, terminating active extension on the right-hand side. During the subsequent 20 My, rift migration creates more than 150 km of hyper-extended crust on the wide margin side in a diachronous fashion. Fig. 10 illustrates that more faults form above the low-viscosity pocket than in the scenario shown in Fig. 9, however the underlying self-sustaining process of rift migration is the same: as long as the low-viscosity pocket exists, the rift centre continues to migrate laterally. A final difference between both scenarios can be observed at the transition to breakup. The scenario with stronger crust (Fig. 9) features a rift jump to the location of thinnest lithosphere once the low-viscosity pocket vanishes. In the model with weaker crust, however, the place of thinnest lithosphere locates much closer to the exhumation channel, which is why the transition to breakup is much more gradual and does not involve a rift jump.

5. South China Sea rifting

5.1. Observations

The South China Sea is the largest marginal basin in Eastern Asia (Fig. 11). It was formed in the location of an active continental margin, which dominated southeastern China and northern Indochina throughout the latter part of the Mesozoic (John et al., 1990; Campbell and Sewell, 1997; Zhu et al., 2004). Subduction of the paleo-Pacific plate towards the northeast resulted in the emplacement of widespread plutons and volcanic sequences across the area where the extension in the South China Sea originated. The origins of the South China Sea have been strongly debated in the past and competing models mostly fall into two contrasting classes. In the first type extension is considered to have been driven by the relative SE motion of Indochina relative to mainland Asia, largely accommodated along the Red River Fault Zone (Peltzer and Tapponnier, 1988; Tapponnier et al., 1990). This motion is related to the indentation of a rigid Indian plate into the active margin of mainland Asia after the Eocene. If this extrusion tectonic model is applicable then there should be a close correspondence between motion on the Red River Fault and seafloor spreading in the South China Sea (Briais et al., 1993). In contrast, others have suggested that the opening of the basin was largely driven by the subduction of an earlier paleo-South China Sea towards the south under Borneo, finishing in the Middle Miocene around 16 Ma as the southern continental margin of the basin, now largely composed of the Dangerous Grounds, collided with the trench (Hamilton, 1977; Taylor and Hayes, 1983; Morley, 2002). In this type of model the primary driving force is related to slab pull towards the south. This view is supported by the observation of a fold and thrust belt along the northern coast of Borneo together with a flexural trough in the Sabah Trough region north of the island (Hinz et al., 1989; Clift et al., 2008; Franke et al., 2008). In contrast, the extrusion model would not predict such a feature but would consider this margin to be purely extensional.

There is general agreement that seafloor spreading ceased in the basin around 16 Ma based on analysis of magnetic anomalies and recently confirmed by scientific drilling near the ridge (Sites U1431, U1433 and U1434) (Li et al., 2014), despite earlier suggestions that spreading might have terminated earlier in the Early Miocene ~20 Ma (Barckhausen et al., 2014). There is less agreement about when the extension began. The presence of Cretaceous basins in southern China suggests that the earliest extension may date back into the Mesozoic (Shu et al., 2009; Wang and Shu, 2012), although consideration of offshore industrial wells, coupled with seismic data would favour the strongest phase of extension beginning in the Eocene (Ru and Pigott, 1986; Su et al., 1989; Clift and Lin, 2001), culminating in breakup and the onset of seafloor spreading in the Oligocene before or around 30 Ma (Briais et al., 1993). These estimates are based on magnetic anomalies and have yet to be confirmed by in situ sampling of the basaltic crust adjacent to the continent-ocean transition. There is some suggestion that the oldest oceanic crust, adjacent to Taiwan may date back to the Late Eocene (~37 Ma) (Hsu and Sibuet, 2005), although some geophysicists consider this region just to be extended continental material and not true oceanic lithosphere. There is however a general agreement that seafloor spreading is older in the eastern part of the basin and propagated towards the southwest through time, as there is a well-preserved propagating tip seen in the extreme southwest of the basin. Seafloor spreading appears to have jumped south from its original location within the Xisha Trough at 25 Ma (Briais et al., 1993; Barckhausen and Roeser, 2004), although the reason for this jump is unknown. Extension is believed to have ceased as a result either of the cessation of motion on the Red River Fault (Leloup et al., 2001; Gilley et al., 2003), or because of the collision of the Dangerous Grounds block with Borneo (Hutchison et al., 2000). In either case there is a regional unconformity, particularly well-developed across the southern part of the basin, which coincides with this event (Hutchison, 2010; Morley, 2016).

Since the end of extension the basin has been affected by a number of tectonic processes, most notably subduction of ocean crust towards the east under the Luzon volcanic arc (Defant et al., 1989), which itself is now in collision with mainland Asia in Taiwan (Huang et al., 2006). Within and around the basin itself there have been a number of volcanic episodes. Most prominent of these is the emplacement of flood basalts in the Central Highlands of Vietnam, which showed a rapid Late Miocene uplift after around 8 Ma during and following the main volcanic episode (Carter et al., 2000). There have also been younger uplift and volcanic events, such as those affecting Hainan island (Tu et al., 1991; Shi et al., 2011), and the neighbouring portions of mainland China, as well as a series of late Miocene to very recent seamounts that are seen throughout the basin. In particular, seamounts are common in the northeastern basin, but are also found as far Southwest as offshore the Mekong Delta (Yeh et al., 2012; Li et al., 2013). Although there has been some speculation that this magmatism is related to a mantle plume (Tu et al., 1991) there is little evidence of a focused, hot upwelling zone of the type normally associated with deep-rooted mantle plumes. Indeed, large-scale geodynamic modelling

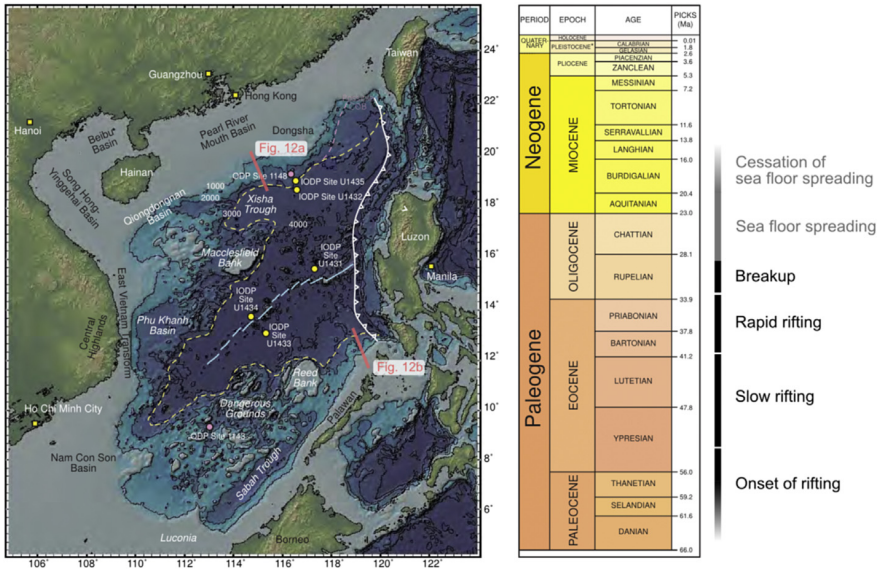

Fig. 11. Shaded bathymetric map of the South China Sea showing the major surface structures. Geological time scale is modified from Walker et al. (2013).

would indicate that this region of the asthenosphere might be cooler than normal as a result of the long-term subduction which affected this area, possibly resulting in significant depth anomalies across the basin exceeding 1 km in magnitude (Lithgow-Bertelloni and Gurnis, 1997). Debate continues as to whether these anomalies are actually present or not, with some workers suggesting that although they exist the magnitude is somewhat smaller than was originally proposed (Wheeler and White, 2002). What is clear is that the South China Sea margin is not a rifted volcanic margin of the type seen in the North Atlantic, since there is no suggestion of subaerial volcanism, or the formation of seaward-dipping reflectors. In fact, the continent-ocean boundary appears to be characterized by tilted extensional fault blocks with some localized volcanic centres (Franke et al., 2014). Scientific drilling at ODP Site 1148 showed that the syn-rift sediments were deposited in relatively deep water, precluding the presence of a significant mantle thermal anomaly at the time of breakup (Clift et al., 2001). Furthermore, more recent seismic surveys predict that there is exhumed continental mantle adjacent to the continent-ocean transition (Franke et al., 2014), which implies either a cold upper mantle and/or very slow rates of extension which allows the continental upper mantle to be exposed without excessive melting (Fig. 12).

In general the rifted margins of South China Sea are most suggestive of an origin in a setting similar to the Basin and Range province of North America. The margins are wide and have a corrugated bathymetry, best shown on the southern side in the region of the Dangerous Grounds (Fig. 11) (Hutchison and Vijayan, 2010). This is consistent with the idea of extension affecting relatively hot, weak continental lithosphere, although there are important exceptions to this. South of Hainan and offshore Palawan the continental margin is much sharper, which has been interpreted to indicate the presence of blocks of crust, with high viscosity, within the overall weak lithosphere of the region (Clift et al., 2002). Likewise two large continental blocks appear to have greater strength than most of the rifted crust in the region. The Reed and Macclesfield Banks lie almost opposite one another and have sharp continent-ocean boundaries, juxtaposing relatively weakly extended crust directly against oceanic crust (Taylor and Hayes, 1980; Cullen et al., 2010). The rifted margins are somewhat asymmetrical, with water depths and degrees of extension being higher on the southern margin under the Dangerous Grounds, than under the Pearl River Mouth Basin (PRMB) (Clift et al., 2002; see also Fig. 12).

South China Sea has been the subject of an increasing amount of scientific investigation, driven to a large extent by the expansion of the Chinese scientific community over the past 20 years, as well as increasing efforts to find hydrocarbons in these basins. Much of the earlier work in the area was based on data generated by industrial drilling and seismic surveys, especially on the northern margin. The sensitive and unresolved political status of the reefs and islands in the Dangerous Grounds/Spratley Islands means that it has often been difficult for scientific vessels to conduct detailed investigation of this area, although a number of long multichannel seismic reflection surveys have now been collected (Hinz et al., 1989; Schlüter et al., 1996; Cullen, 2014). ODP drilling in this region was however relatively shallow, only penetrating to the Upper Miocene at ODP Site 1143 (Shipboard Scientific Party, 2000), so that many of the reflectors seen in the seismic profiles are not well dated and subsidence analysis has been limited because of the lack of water depth information. What age control does exist comes from limited industrial drilling dating from the 1970s and 1980s, largely on the Reed Bank, which is not typical of the highly extended structure of this region.

The PRMB yielded early advances in the form of publicly released seismic reflection data and drilling controls, mostly done in the late 1970s. These data allowed a basic framework for the geological evolution of the basin to be established and demonstrated that extension started in the Eocene, locally accompanied by magmatism (Ru and Pigott, 1986; Su et al., 1989). A joint Chinese-American cruise collected long deep penetrating seismic reflection data, which allowed the overall crustal thickness to be estimated (Nissen et al., 1995a, 1995b) and which proposed the presence of underplated mafic igneous bodies, especially along the northern margin closer to Taiwan (Kido et al., 2001). Whether these bodies actually exist or not is rather open to question and the initial interpretation may more likely reflect the general enthusiasm for such phenomena at the time shortly after their collection in the 1990s. While it is clear that there are some higher velocity lower crustal bodies it is also possible that these are related to

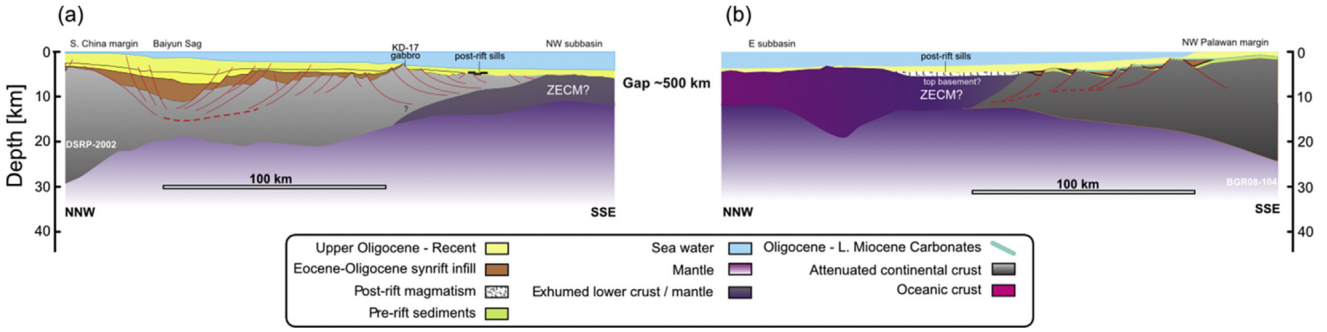

Fig. 12. Cross section showing the crustal architecture at the central South China margin. Seaward increases in extension is accompanied with a rise of the Moho. A Moho dome beneath the Baiyun Sag is observed. A major landward dipping detachment faults is interpreted as being underlain by mantle material, which is exposed further seaward. A conjugate crustal section from the NW Palawan margin images predominantly seaward dipping listric faults ramping down to a detachment fault that reaches the Moho at the continent-ocean boundary. The post-rift sills were mainly formed at an initial stage of seafloor spreading. Exhumation of continental mantle (ZECM) is possible. Modified from Franke et al. (2014). Locations of cross-sections are shown in Fig. 11.

serpentinisation of the upper mantle. Seismic images demonstrated that by the time of breakup large-scale normal faults were penetrating the entire continental crust as deep as the Moho (Hayes et al., 1995). In more recent years there has been continued industrial surveying around the northern and western sides of the basin, taking the form of both reflection seismic surveys and drilling, although much of this material has remained confidential, often only accessible to Chinese scientists and industry.

Nonetheless, it is now clear that the outermost continental margin is likely dominated by detachment faulting and large-scale extension on long, low angle normal faults (Franke et al., 2011, 2014; Ding et al., 2012). These may be related to the generation of very deep sedimentary basins along the edge of the continental margin, which exceed more than 14 km depth in extreme examples such as the Baiyun Sag (Sun et al., 2008). Such structures may also explain the apparent presence of serpentinised continental upper mantle along the continent-ocean boundary, at least along the northern margin of the basin according to interpretation of seismic reflection surveys (Franke et al., 2014), although this is yet to be demonstrated by actual sampling of the basement through drilling.

Scientific ocean drilling along the continent-ocean boundary commenced in 2014 with International Ocean Discovery Program (IODP) Expedition 349 (Li et al., 2015a). This had attempted to drill the oldest oceanic crust adjacent to the boundary (Site U1432) but this was unsuccessful for technical reasons. The drilling did however establish the presence of Eocene shallow marine sediments on a fault block adjacent to the continental margin (Site U1435), which were overlain by deep-water Oligocene and younger sediments (Li et al., 2015b). Further drilling is now planned for 2017 with a series of wells designed to penetrate a number of tectonic highs spanning the continent-ocean boundary.

Rapid extension appears to have started in the Eocene, although the precise age is not well constrained because of lack of scientific drilling sampling the deepest buried, early, rift-related sediments and because those sediments recovered from the PRMB are continental and hard to date because of the lack of marine biostratigraphy (Clift and Lin, 2001; Lin et al., 2004). What is clear is that seafloor spreading began in the Oligocene around 30 Ma, at which point subsidence began to slow in the PRMB, although rapid, synrift subsidence, contrasting with the gradual rates that occurred later, continued until at least around 24 Ma (Early Miocene) across much of the northern margin. This means that for the first 6 My of seafloor spreading there was continued, albeit reduced extension within the continental crust despite the presence of a seafloor spreading centre on which to focus much of the extensional stresses. This implies that the continental crust of the rifted margin was very weak at the time of extension, probably because of the warm thermal condition of the crust prior to extension and because of the weakening caused by brittle faulting during the early stages of that extension. This is despite the fact that seismic imaging predicts the presence of exposed upper continental mantle close to the continent-ocean boundary, where one would expect melting to occur under normal uniform extension conditions and rates. Basin modelling indicates that during the breakup there was preferential extension in the mantle lithosphere and lower crust as a result of depth dependent extension, and with a discrepancy between the lower parts of lithosphere and the upper crust increasing as the continent-ocean boundary is approached.

Extension is seen to accelerate in certain basins on the outer part of the continental margin after the end of brittle faulting (Xie et al., 2013, 2014), which has been linked to sediment loading, coupled with onshore erosion driving additional flow of the ductile middle and lower crust away from the basin centre and towards the continental interior (Westaway, 1994; Clift, 2015; Clift et al., 2015). Net flow of the ductile crust is still towards the deep water basin, but the loading of individual sub-basins on the outer continental margin appears to affect subsidence locally, as shown in several basins between the PRMB and the Song Hong-Yinggehai Basin (Yin et al., 2011; Zhao et al., 2013).

A breakup unconformity is recognized across much of the northern margin, which youngs towards the SW (Morley, 2016). There is furthermore an additional base Miocene unconformity around 24 Ma, linked to the cessation of extension within the continental crust (Clift and Lin, 2001), as well as again on the northern margin, at least in the PRMB in the Lower Miocene at ~21 Ma, coincident with the increase of sediment delivery to the outer continental margin (Xie et al., 2013). This type of unconformity is also noted in the Southwest in the Nam Con Son Basin (Matthews et al., 1997; Fyhn et al., 2009), formed immediately ahead of the propagating rift, but is not observed on the southern margin where water depths were greater, because of the larger amount of extension meaning that no subaerial exposure occurred during that initial breakup period. The most common unconformity seen on the southern margin dates to the middle Miocene, around 16 Ma, and is variously described as the Deep Regional Unconformity (DRU) in Borneo (Hutchison, 2004), possibly correlating with the "Red Unconformity" seen offshore in the Dangerous Grounds (Morley, 2016) and in the adjacent rifted margin region known as Luconia (Fig. 11). These unconformities are linked to the collision between the rifted southern margin and the trench of the Sabah Trough (Hutchison, 2005). Sediment supply is generally lower along the southern margin except on the continental margin of

Borneo itself, so that the type of loading that drives the mid crustal flow seen on the northern margin is not observed under the Dangerous Grounds. Tectonic inversion in northern Borneo, linked to the collision has driven significant sediment flux onto the margin and expose the accretionary prism that was formed during the destruction of the paleo-South China Sea (Hutchison, 1996), although the sediment flux related to the uplift of northern Borneo is mostly only preserved in Luconia and to a lesser extent in the Nam Con Son Basin (Li et al., 2013; Ding et al., 2016). Additional anomalous vertical motions are known from the post-rift period and may be related to late stage magmatic processes of unknown origin, potentially linked to the post-rift magmatism, which is widespread throughout the basin, but which has little clear explanation beyond a diffuse plume. In particular, there is Late Miocene uplift around 4.4–5.2 Ma around the Dongsha Island and again during the Liuhua movement (1.4–1.89 Ma) (Wu et al., 2003).

5.2. Model

The numerical setup for the experiment shown in Fig. 13 involves a crustal thickness of 33 km as evidenced by seismic data from the unrifted South China block (Nissen et al., 1995b). The lithosphere-asthenosphere boundary depth is probably quite heterogeneous in this complex tectonic environment with pre-rift subduction. For simplicity, we use the same LAB depth as in the Brazil-Angola scenarios (120 km) in agreement with the compilation of Artemieva (2006). The setup is overall very similar to the model for Brazil-Angola and includes a constant rift velocity of 8 mm/yr, but the key difference is that the model for the South China Sea involves a crustal rheology that is weaker than in any of the models above (Fig. 2).

In contrast to the examples discussed in the previous sections where rift history can be divided in three phases, rifting in the South China Sea exhibits continuously simultaneous faulting until breakup. The phase of rift migration that was prominent in the previous models is completely missing.

5.2.1. Phase 1 – Simultaneous faulting

The weak crust leads to very effective decoupling of deformation within the brittle crust and the mantle generating a wide rift. The evolution during the phase of simultaneous faulting is very similar to the alternative model setup of the South Atlantic shown in Fig. 10: Many small faults accommodate extension in the brittle crust. These faults extend into the underlying ductile crust as listric shear zones where lower crustal flow occurs from continent towards the basin axis. However, due to the weaker rheology in the present model, there is significantly less crustal thinning after the same amount of extension: after 20 My of rifting and altogether 160 km of extension, the crust is still more than 15 km thick in the present scenario, while it was only 7 km thick in the previous South Atlantic model (Fig. 10). This leads to a situation, where the entire mid-crust has a very low viscosity and lies within the white viscosity contour line in Fig. 13. In contrast to the previous model, there are no distinct low-viscosity pockets at the rift sides that could initiate rift migration. Instead, the weak crust continues to decouple brittle crust from the mantle, which allows for persistent pure shear deformation throughout the entire rift history until crustal breakup. As a result of the crustal viscosity being less than

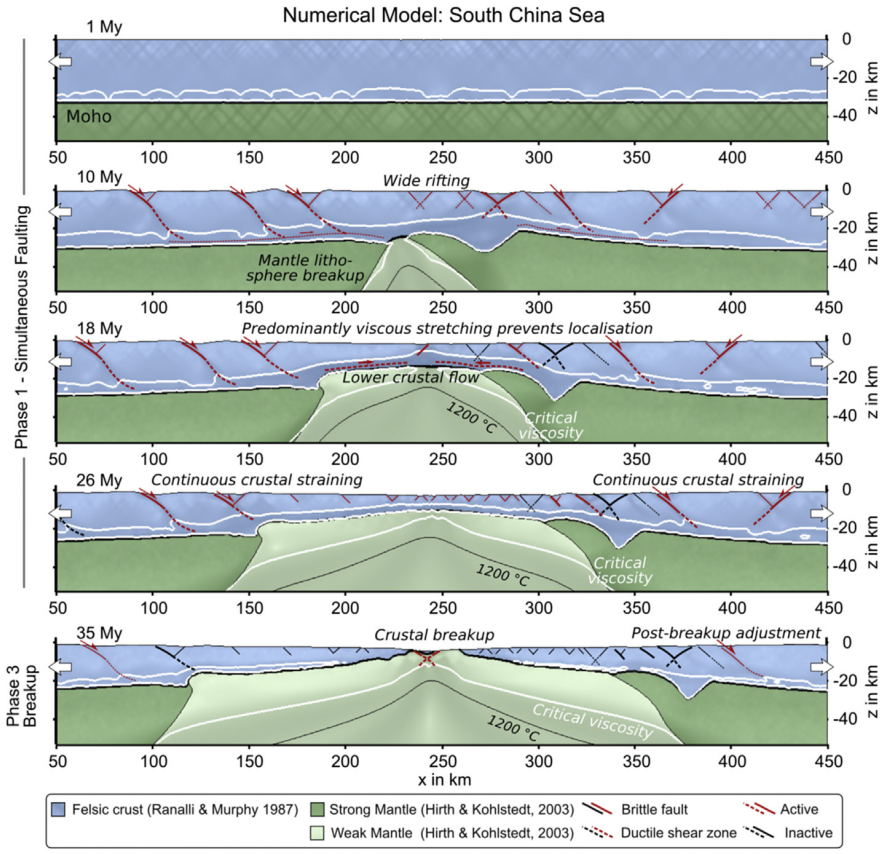

Fig. 13. South China Sea model. The very weak crust of this model decouples crust and mantle deformation throughout rift history. The rift system evolves in wide rift mode until crustal breakup. Lower crustal flow takes place towards the basin axis and compensates topographic gradients. An animation of this model can be found in the supplement.

10^{19} Pas, the mid-crust acts as an effective layer for isostatic compensation allowing for very low topographic gradients, such as observed in this region (Clift et al., 2002).

5.2.2. No phase 2 – Rift migration

Because of the low crustal viscosity, the rift centre as well as the rift sides are both very weak. The brittle crust and mantle are decoupled throughout the rift history; consequently a phase of rift migration does not exist during the formation of the South China Sea.

5.2.3. Phase 3 – Breakup

The model remains symmetric during pure shear thinning of the crust. When eventually the crustal thickness is sufficiently reduced so that upper crustal faults can reach the mantle, breakup takes place. Note that shortly after crustal breakup, the numerical model exhibits continued tectonic activity within the proximal margins (Fig. 13, at 35 My). These motions are driven by lower crustal flow that continues to level surface topography. Another interesting aspect of the post-breakup tectonic deformation arises when accounting for regional sedimentation history. Early Miocene crustal breakup in the South China Sea is accompanied by faster sediment delivery to off-shore basins (Clift, 2006; Xie et al., 2013). This increased rate of sedimentation is likely driven by a change to a more erosive, monsoonal climate around that time (Sun and Wang, 2005; Clift et al., 2014). Model viscosities in the proximal margin directly after breakup range between $10^{19.5}$ Pas and 10^{20} Pas. If the surface was depressed by a sedimentary cover, lateral mid-crustal flow could occur within a distance of more than 50 km from the loading site (Clift et al., 2015). This flow effectively thins the crust and compensates for sediment-induced surface subsidence with only minor Moho deflection. That effect has been described in the super-deep Baiyun Sag Basin (Clift et al., 2015), but also in other locations within the region: the Yinggehai-Song Hong pull-apart basin, located to the west of Hainan Island features a sharp increase in subsidence occurred at ~5 Ma even though there was only very little brittle deformation (Clift and Sun, 2006). The combination of weak crust, enhanced onshore erosion, and subsequent offshore sedimentation could even lead to post-breakup crustal flow that is directed from the rifted margin towards the continental interior. That process has to be understood as a readjustment from one state of stability (with thick crust onshore and thin sediment offshore) to another (with thinner crust onshore and a thicker sediment load offshore). This effect has been proposed for the Malay Basin (Morley and Westaway, 2006) and the northern margin of the South China Sea (Clift, 2015; Clift et al., 2015). The described crustal flow is a consequence of low-viscous crust in conjunction with extensive sediment loading. This kind of post-rift deformation would not be anticipated in passive margins with a strong rheology, low heat flow and little sedimentation.

6. Discussion

We summarize the link between crustal rheology and margin architecture in Fig. 14 and Table 1. The initial width of a rift is a function of crust-mantle coupling, which highly depends on the strength of the lower crust (Buck, 1991). While wide rifts are obvious candidates to form wide continental margins like in the South China Sea, we show that narrow rifts are also capable of forming wide continental margins in an asymmetric rift setting: the width of the actively deforming rift can be less than 50 km (cf. Fig. 9), yet the resulting hyper-extended margin can be as wide as 200 km or more. A decisive difference between wide margins formed by wide or narrow rift systems lies in the time-dependency of deformation. While in wide rifts the margin is formed by continuous pure shear stretching of the entire margin area, narrow rifts create wide margins by diachronous stretching during lateral rift migration (Brune et al., 2014).

The formation of hyper-extended margins and strong margin asymmetry through rift migration requires the formation of a low-viscosity pocket at the rift side. Formation of this weak area can be facilitated in two ways: (1) by initial asymmetry, or (2) through rheologically weak crust (Fig. 14). However, if the crust is too weak there will not be enough crust-mantle coupling to induce rift

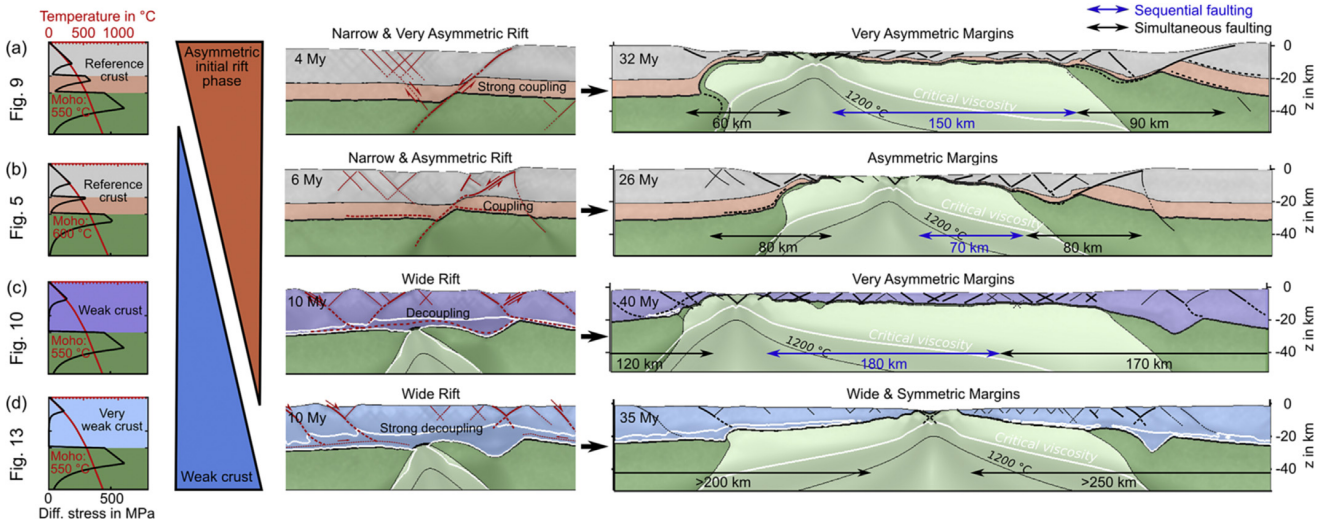

Fig. 14. Summary plot. All models shown in this study are sorted according to initial crustal strength: the strongest crust at the top, the weakest at the bottom. Strong crust generates narrow rifts with large initial asymmetry and weak crust favours wide rifts with an initially symmetric configuration. The final structure of the rifted margins is depicted on the right. The width of the margin that is formed during the simultaneous faulting phase (indicated with black arrows) and also the total margin width grows proportional to the weakness of the crust. The width of the hyperextended margin (blue arrows) depends on the duration of rift migration, which can last more than 20 My. Both narrow and wide rifts are capable of forming highly asymmetric conjugate margins. (For interpretation of the references to colour in this figure legend, the reader is referred to the web version of this article.)

Table 1
Summary table. We list the duration of phases and margin geometries of the model along with duration and final geometry of natural examples. Note how the duration of Phase 1 (Simultaneous faulting) and the margin widths increase with weaker crustal rheology.

	Iberia-Newfoundland	Brazil-Angola	Brazil-Angola (Alternative Scenario)	South China Sea
Model				
Figure No.	5	9	10	13
Crustal Rheology	Strong	Strong	Weak	Very weak
Duration Phase 1 - Simultaneous Faulting	9 My	8 My	18 My	26 My
Duration Phase 2 - Rift Migration	7 My	17 My	17 My	–
Margin Widths (Simultaneously Faulted)	80 km (left) 80 km (right)	60 km (left) 90 km (right)	120 km (left) 170 km (right)	>200 (left) >250 km (right)
Margin Widths (Sequentially Faulted)	0 (left) 70 km (right)	0 (left) 150 km (right)	0 (left) 180 km (right)	–
Initial Rift Geometry	Narrow, Asymmetric	Narrow, Very Asymmetric	Wide, Symmetric	Wide, Symmetric
Final Rifted Margin Geometry	Asymmetric	Very Asymmetric	Very Asymmetric	Wide, Symmetric
Nature				
Figure No.	3,4	6–8		11,12
Initial Tectonic Setting	Intracontinental	Intracontinental		Convergent Margin
Rift Onset Age	Late Triassic (First Episode) Late Jurassic (Final Episode)	Late Jurassic/Early Cretaceous		Paleocene
Breakup Age	Early Cretaceous (Valanginian-Barremian)	Early Cretaceous (Aptian)		Oligocene
Margin Geometry	Asymmetric	Asymmetric		Wide, Symmetric

migration and the rift will evolve in wide rift mode until breakup like in the South China Sea. Importantly, lower crustal viscosity and initial asymmetry are not independent of each other: strong crust generates more initial asymmetry than weak crust, which is why the final margin asymmetry is not a simple linear function of crustal rheology. Our results also illustrate that it is difficult to deduce rheological information from final margin configuration, because similarly asymmetric margin configurations like those shown in Figs. 9,14a and 10,14c can result from different crustal rheologies. Another important trade-off exists between crustal rheology and temperature since both affect the lower crustal viscosity and also the depth of the crustal brittle-ductile transition. Other combinations of rheology, radiogenic heat production, and initial layer thicknesses can generate qualitatively similar margin configurations, as long as they result in similar reduced crustal viscosities and brittle layer thickness.

Even though we restrict our comparison to three natural examples, our analysis holds profound implications for many other margins worldwide. Similar processes that we describe for the asymmetric rift systems of Iberia-Newfoundland and Brazil-Angola might have shaped the asymmetric margins of the Australia-Antarctica rift (Direen et al., 2012; Espurt et al., 2012), of the Southern South Atlantic (Blaich et al., 2009; Becker et al., 2014), Eastern Australia and the Lord Howe Rise (Lister et al., 1991), and the Northwest Australian Shelf (Karner and Driscoll, 1999; Heine and Müller, 2005; Reeve et al., 2016). The Northeast Atlantic margins exhibit pronounced asymmetry and long ribbons of hyper-extended crust (Lundin and Doré, 2011; Nirrengarten et al., 2014; see also Funck et al., 2016 for a review of refraction data). This large rift system evolved with a protracted kinematic history with pronounced periods of low extension rate (Lundin and Doré, 1997) or even tectonic quiescence (Færseth and Lien, 2002), which is not accounted for in our analysis. Nevertheless, the processes we describe here may be useful in understanding the formation of the North Atlantic hyper-extended domains. In agreement with our results, geological studies also revealed crustal hyperextension and asymmetric margins geometries in the pre-collisional passive margin architecture of the Pyrénées (Clerc and Lagabrielle, 2014; Tugend et al., 2014) and the European Alps (Masini et al., 2013) along with complex syn-rift heating-cooling events (Ewing et al., 2015; Seymour et al., 2016).

The South China Sea represents an important end-member where simultaneous faulting occurred throughout the entire rift evolution until breakup. The models presented above show that the duration of Phase 1 (simultaneous faulting) is a function of lower crustal rheology, with weaker rheologies showing a more prolonged phase of simultaneous faulting. A similar result could have been generated with a thinner, hotter lithosphere. In any case, the crustal viscosity in the South China Sea region must have been much lower than in the other case examples. The weak crustal rheology can be explained by the fact that the South China Sea developed in a region with significant pre-rift crustal weakening during Andean-type orogeny and the existence of a continental magmatic arc during the Mesozoic (Li et al., 2012). In this respect, the South China Sea rift resembles other rifts near continental margins such as the Basin and Range (Hamilton, 1987), the Aegean rift (Huet et al., 2011; Jolivet et al., 2013), the early Gulf of California rift (Umhoefer, 2011; Bennett and Oskin, 2014), the Woodlark rift (Mutter et al., 1996), and the Gulf of Thailand (Morley and Westaway, 2006) whose rheological weakness result from previously thickened crust, or arc magmatism, or both.

7. Conclusions

In this review we showed that the formation of asymmetric margin pairs like Iberia-Newfoundland and the Central South Atlantic conjugates can be divided in three phases: Phase 1 - Simultaneous faulting, Phase 2 - Rift migration, and Phase 3 - Breakup. In contrast to previous models of rift evolution we find that conjugate margin asymmetry results from rift migration that is accommodated by an array of sequentially active normal faults and associated ductile shear zones. Formation of the South China Sea, however, did not feature a rift migration phase and was dominated by simultaneous faulting until breakup.

Crustal rheology plays a dominant role in controlling the duration of each phase. Weak rheologies enable a prolonged phase of simultaneous faulting. The duration of the rift migration phase is controlled by the extent of a low-viscosity pocket at the side of the rift, which is enlarged in models with initial fault asymmetry and relatively weak crust. Asymmetric deformation stops shortly before breakup and the continental crust is ruptured by predominantly symmetric normal faults cutting in progressively embrittled crust and mantle. The crust of the South China Sea region appears to be significantly weaker than the crust of the Atlantic margins, which we assign to its pre-rift history where crustal thickening and magmatic additions took place in a convergent margin setting until

shortly before the onset of rifting.

Acknowledgements

SB was funded by the Marie Curie International Outgoing Fellowship 326115, the German Research Foundation Priority Program 1375 SAMPLE, and the Helmholtz Young Investigators Group CRYSTALS. CH would like to thank Statoil, in particular Ole Martinsen and Jasper Zoethout, for permission to publish Fig. 8.

Appendix A. Supplementary data

Supplementary data related to this article can be found at http://dx.doi.org/10.1016/j.marpetgeo.2016.10.018.

References

Adam, J., Klinkmüller, M., Schreurs, G., Wieneke, B., 2013. Quantitative 3D strain analysis in analogue experiments simulating tectonic deformation: integration of X-ray computed tomography and digital volume correlation techniques. J. Struct. Geol. 55, 127–149. http://dx.doi.org/10.1016/j.jsg.2013.07.011.

Agostini, A., Corti, G., Zeoli, A., Mulugeta, G., 2009. Evolution, pattern, and partitioning of deformation during oblique continental rifting: inferences from lithospheric-scale centrifuge models. Geochem. Geophys. Geosystems 10, Q11015. http://dx.doi.org/10.1029/2009GC002676.

Allken, V., Huismans, R.S., Thieulot, C., 2012. Factors controlling the mode of rift interaction in brittle-ductile coupled systems: a 3D numerical study. Geochem. Geophys. Geosystems 13, Q05010. http://dx.doi.org/10.1029/2012GC004077.

Amante, C., Eakins, B.W., 2009. ETOPO1 1 Arc-minute Global Relief Model: Procedures, Data Sources and Analysis: NOAA Technical Memorandum NESDIS NGDC-24. National Geophysical Data Center, NOAA. http://dx.doi.org/10.7289/V5C8276M.

Armitage, J.J., Collier, J.S., Minshull, T.A., 2012. The importance of rift history for volcanic margin formation. Nature 465 (7300), 913–917. http://dx.doi.org/10.1038/nature09063.

Armitage, J.J., Ferguson, D.J., Goes, S., Hammond, J.O.S., Calais, E., Rychert, C.A., Harmon, N., 2015. Upper mantle temperature and the onset of extension and break-up in Afar, Africa. Earth Planet. Sci. Lett. 418, 78–90. http://dx.doi.org/10.1016/j.epsl.2015.02.039.

Artemieva, I.M., 2006. Global 1°×°1 thermal model TC1 for the continental lithosphere: implications for lithosphere secular evolution. Tectonophysics 416 (1–4), 245–277. http://dx.doi.org/10.1016/j.tecto.2005.11.022.

Aslanian, D., Moulin, M., Olivet, J.-L., Unternehr, P., Matias, L., Bache, F., Rabineau, M., Nouzé, H., Klingelheofer, F., Contrucci, I., Labails, C., 2009. Brazilian and African passive margins of the central segment of the south Atlantic ocean: kinematic constraints. Tectonophysics 468 (1–4), 98–112. http://dx.doi.org/10.1016/j.tecto.2008.12.016.

Autin, J., Bellahsen, N., Husson, L., Beslier, M.-O., Leroy, S., d'Acremont, E., 2010. Analog models of oblique rifting in a cold lithosphere. Tectonics 29 (6), TC6016. http://dx.doi.org/10.1029/2010TC002671.

Autin, J., Bellahsen, N., Leroy, S., Husson, L., Beslier, M.-O., d'Acremont, E., 2013. The role of structural inheritance in oblique rifting: insights from analogue models and application to the Gulf of Aden. Tectonophysics 607, 51–64. http://dx.doi.org/10.1016/j.tecto.2013.05.041.

Barckhausen, U., Roeser, H.A., 2004. Seafloor Spreading Anomalies in the South China Sea Revisited. In: Clift, P., Kuhnt, W., Wang, P., Hayes, D. (Eds.), Continent-ocean Interactions within East Asian Marginal Seas. American Geophysical Union, pp. 121–125.

Barckhausen, U., Engels, M., Franke, D., Ladage, S., Pubellier, M., 2014. Evolution of the South China Sea: revised ages for breakup and seafloor spreading. Mar. Pet. Geol. 58 (Part B), 599–611. http://dx.doi.org/10.1016/j.marpetgeo.2014.02.022.

Barnett-Moore, N., Müller, R.D., Williams, S., Skogseid, J., Seton, M., 2016. A reconstruction of the North Atlantic since the earliest jurassic. Basin Res. http://dx.doi.org/10.1111/bre.12214 p. n/a-n/a.

Basile, C., 2015. Transform continental margins - part 1: concepts and models. Tectonophysics 661, 1–10. http://dx.doi.org/10.1016/j.tecto.2015.08.034.

Bastow, I.D., Keir, D., 2011. The protracted development of the continent-ocean transition in Afar. Nat. Geosci. 4 (4), 248–250. http://dx.doi.org/10.1038/ngeo1095.

Bayrakci, G., Minshull, T.A., Sawyer, D.S., Reston, T.J., Klaeschen, D., Papenberg, C., Ranero, C., Bull, J.M., Davy, R.G., Shillington, D.J., Perez-Gussinye, M., Morgan, J.K., 2016. Fault-controlled hydration of the upper mantle during continental rifting. Nat. Geosci. 9 (5), 384–388. http://dx.doi.org/10.1038/ngeo2671.

Beaumont, C., Ings, S.J., 2012. Effect of depleted continental lithosphere counterflow and inherited crustal weakness on rifting of the continental lithosphere: general results. J. Geophys. Res. Solid Earth 117 (B8), B08407. http://dx.doi.org/10.1029/2012JB009203.

Becker, K., Franke, D., Trumbull, R., Schnabel, M., Heyde, I., Schreckenberger, B., Koopmann, H., Bauer, K., Jokat, W., Krawczyk, C.M., 2014. Asymmetry of high-velocity lower crust on the South Atlantic rifted margins and implications for the interplay of magmatism and tectonics in continental breakup. Solid earth. 5 (2), 1011–1026. http://dx.doi.org/10.5194/se-5-1011-2014.

Bell, R.E., McNeill, L.C., Bull, J.M., Henstock, T.J., 2008. Evolution of the offshore western Gulf of Corinth. Geol. Soc. Am. Bull. 120 (1–2), 156–178. http://dx.doi.org/10.1130/B26212.1.

Ben-Avraham, Z., Katsman, R., 2015. The formation of graben morphology in the Dead Sea Fault, and its implications. Geophys. Res. Lett. 42 (17) http://dx.doi.org/10.1002/2015GL065111, p. 2015GL065111.

Bennett, S.E.K., Oskin, M.E., 2014. Oblique rifting ruptures continents: example from the Gulf of California shear zone. Geology 42 (3), 215–218. http://dx.doi.org/10.1130/G34904.1.

Blaich, O.A., Tsikalas, F., Faleide, J.I., 2008. Northeastern Brazilian margin: regional tectonic evolution based on integrated analysis of seismic reflection and potential field data and modelling. Tectonophysics 458 (1–4), 51–67. http://dx.doi.org/10.1016/j.tecto.2008.02.011.

Blaich, O.A., Faleide, J.I., Tsikalas, F., Franke, D., Leon, E., 2009. Crustal-scale architecture and segmentation of the Argentine margin and its conjugate off South Africa. Geophys. J. Int. 178 (1), 85–105. http://dx.doi.org/10.1111/j.1365-246X.2009.04171.x.

Blaich, O.A., Faleide, J.I., Tsikalas, F., 2011. Crustal breakup and continent-ocean transition at South Atlantic conjugate margins. J. Geophys. Research-Solid Earth 116. http://dx.doi.org/10.1029/2010JB007686.

Boillot, G., Winterer, E., others, 1988. Drilling on the Galicia Margin: Retrospect and Prospect. In: Proceedings of the Ocean Drilling Program, Scientific Results. Ocean Drilling Program College Station, TX, pp. 809–828.

Boutelier, D., Oncken, O., 2011. 3-D thermo-mechanical laboratory modeling of plate-tectonics: modeling scheme, technique and first experiments. Solid earth. 2 (1), 35–51. http://dx.doi.org/10.5194/se-2-35-2011.

Bradley, D.C., 2008. Passive margins through earth history. Earth-Science Rev. 91 (1–4), 1–26. http://dx.doi.org/10.1016/j.earscirev.2008.08.001.

Briais, A., Patriat, P., Tapponnier, P., 1993. Updated interpretation of magnetic anomalies and seafloor spreading stages in the South China Sea: implications for the Tertiary tectonics of Southeast Asia. J. Geophys. Res. Solid Earth 98 (B4), 6299–6328. http://dx.doi.org/10.1029/92JB02280.

Brun, J.-P., 1999. Narrow rifts versus wide rifts: inferences for the mechanics of rifting from laboratory experiments. philos. Trans. R. Soc. Lond. Ser. A Math. Phys. Eng. Sci. 357 (1753), 695–712. http://dx.doi.org/10.1098/rsta.1999.0349.

Brun, J.P., Gutscher, M.-A., dekorp-ecors teams, 1992. Deep crustal structure of the Rhine Graben from dekorp-ecors seismic reflection data: a summary. Tectonophysics 208 (1), 139–147. http://dx.doi.org/10.1016/0040-1951(92)90340-C.

Brune, S., 2014. Evolution of stress and fault patterns in oblique rift systems: 3-D numerical lithospheric-scale experiments from rift to breakup. Geochem. Geophys. Geosystems 15 (8), 3392–3415. http://dx.doi.org/10.1002/2014GC005446.

Brune, S., Autin, J., 2013. The rift to break-up evolution of the Gulf of Aden: insights from 3D numerical lithospheric-scale modelling. Tectonophysics 607, 65–79. http://dx.doi.org/10.1016/j.tecto.2013.06.029.

Brune, S., Popov, A.A., Sobolev, S.V., 2012. Modeling suggests that oblique extension facilitates rifting and continental break-up. J. Geophys. Res. 117 (B8), B08402. http://dx.doi.org/10.1029/2011JB008860.

Brune, S., Popov, A.A., Sobolev, S.V., 2013. Quantifying the thermo-mechanical impact of plume arrival on continental break-up. Tectonophysics 604, 51–59. http://dx.doi.org/10.1016/j.tecto.2013.02.009.

Brune, S., Heine, C., Perez-Gussinye, M., Sobolev, S.V., 2014. Rift migration explains continental margin asymmetry and crustal hyper-extension. Nat. Commun. 5 (4014) http://dx.doi.org/10.1038/ncomms5014.

Brune, S., Williams, S.E., Butterworth, N.P., Müller, R.D., 2016. Abrupt plate accelerations shape rifted continental margins. Nature 536 (7615), 201–204. http://dx.doi.org/10.1038/nature18319.

Buck, W.R., 1991. Modes of continental lithospheric extension. J. Geophys. Research-Solid Earth 96 (B12), 20161–20178. http://dx.doi.org/10.1029/91JB01485.

Buck, W.R., 2006. The role of magma in the development of the Afro-Arabian Rift System. Geol. Soc. Lond. Spec. Publ. 259 (1), 43–54. http://dx.doi.org/10.1144/GSL.SP.2006.259.01.05.

Buck, W.R., 2007. Dynamic Processes in Extensional and Compressional Settings - the Dynamics of Continental Breakup and Extension. In: Treatise on Geophysics, vol. 6. Crust and Lithosphere Dynamics.,.

Buck, W.R., Lavier, L.L., Poliakov, A.N.B., 1999. How to make a rift wide. philos. Trans. R. Soc. Lond. Ser. a-Mathematical Phys. Eng. Sci. 357 (1753), 671–690.

Buiter, S.J.H., Torsvik, T.H., 2014. A review of Wilson Cycle plate margins: a role for mantle plumes in continental break-up along sutures? Gondwana Res. 26 (2), 627–653. http://dx.doi.org/10.1016/j.gr.2014.02.007.

Buiter, S.J.H., Huismans, R.S., Beaumont, C., 2008. Dissipation analysis as a guide to mode selection during crustal extension and implications for the styles of sedimentary basins. J. Geophys. Research-Solid Earth 113 (B6), B06406. http://dx.doi.org/10.1029/2007JB005272.

Bullard, E., Everett, J.E., Smith, A.G., 1965. The fit of the continents around the Atlantic. philos. Trans. R. Soc. Lond. A Math. Phys. Eng. Sci. 258 (1088), 41–51. http://dx.doi.org/10.1098/rsta.1965.0020.

Burov, E., Gerya, T., 2014. Asymmetric three-dimensional topography over mantle plumes. Nature 513 (7516), 85–89. http://dx.doi.org/10.1038/nature13703.

Caixeta, J.M., Ferreira, T.S., Machado Jr., D.L., Teixeira, J.L., Romeiro, M.A.T., 2014. Albian Rift Systems in the Northeastern Brazilian Margin: an Example of Rifting in Hyper-extended Continental Crust. In: AAPG International Conference &

Exhibition, Search and Discovery Article #30378. AAPG, Istanbul, Turkey.
Campbell, S.D.G., Sewell, R.J., 1997. Structural control and tectonic setting of Mesozoic volcanism in Hong Kong. J. Geol. Soc. 154 (6), 1039–1052. http://dx.doi.org/10.1144/gsjgs.154.6.1039.
Cappelletti, A., Tsikalas, F., Nestola, Y., Cavozzi, C., Argnani, A., Meda, M., Salvi, F., 2013. Impact of lithospheric heterogeneities on continental rifting evolution: constraints from analogue modelling on South Atlantic margins. Tectonophysics. http://dx.doi.org/10.1016/j.tecto.2013.09.026.
Carter, A., Roques, D., Bristow, C.S., 2000. Denudation history of onshore central Vietnam: constraints on the Cenozoic evolution of the western margin of the South China Sea. Tectonophysics 322 (3–4), 265–277. http://dx.doi.org/10.1016/S0040-1951(00)00091-3.
Chaboureau, A.-C., Guillocheau, F., Robin, C., Rohais, S., Moulin, M., Aslanian, D., 2013. Paleogeographic evolution of the central segment of the South Atlantic during Early Cretaceous times: paleotopographic and geodynamic implications. Tectonophysics 604, 191–223. http://dx.doi.org/10.1016/j.tecto.2012.08.025.
Chang, H.K., Kowsmann, R.O., Figueiredo, A.M.F., Bender, A., 1992. Geodynamics of rifting, volume ii case history studies on rifts: North and south America and Africa tectonics and stratigraphy of the East Brazil rift system: an overview. Tectonophysics 213 (1), 97–138. http://dx.doi.org/10.1016/0040-1951(92)90253-3.
Chen, L., Zhang, Z., Song, H., Li, F., Franke, D., 2013. Numerical modeling of extensional sedimentary basin formation with MATLAB: application to the northern margin of the South China Sea. Comput. Geosci. 51, 153–165. http://dx.doi.org/10.1016/j.cageo.2012.07.014.
Chenin, P., Beaumont, C., 2013. Influence of offset weak zones on the development of rift basins: Activation and abandonment during continental extension and breakup. J. Geophys. Res. Solid Earth 118 (4), 1698–1720. http://dx.doi.org/10.1002/jgrb.50138.
Chian, D., Louden, K.E., Minshull, T.A., Whitmarsh, R.B., 1999. Deep structure of the ocean-continent transition in the southern Iberia Abyssal Plain from seismic refraction profiles: ocean Drilling Program (Legs 149 and 173) transect. J. Geophys. Res. Solid Earth 104 (B4), 7443–7462. http://dx.doi.org/10.1029/1999JB900004.
Choi, E., Buck, W.R., 2012. Constraints on the strength of faults from the geometry of rider blocks in continental and oceanic core complexes. J. Geophys. Res. Solid Earth 117 (B4), B04410. http://dx.doi.org/10.1029/2011JB008741.
Chorowicz, J., 2005. The East African rift system. J. Afr. Earth Sci. 43 (1–3), 379–410. http://dx.doi.org/10.1016/j.jafrearsci.2005.07.019.
Christensen, N.I., Mooney, W.D., 1995. Seismic velocity structure and composition of the continental crust: a global view. J. Geophys. Res. 100 (B6), 9761–9788. http://dx.doi.org/10.1029/95JB00259.
Clerc, C., Lagabrielle, Y., 2014. Thermal control on the modes of crustal thinning leading to mantle exhumation: insights from the Cretaceous Pyrenean hot paleomargins. Tectonics 33 (7). http://dx.doi.org/10.1002/2013TC003471, 2013TC003471.
Clerc, C., Jolivet, L., Ringenbach, J.-C., 2015. Ductile extensional shear zones in the lower crust of a passive margin. Earth Planet. Sci. Lett. 431, 1–7. http://dx.doi.org/10.1016/j.epsl.2015.08.038.
Clift, P.D., 2006. Controls on the erosion of Cenozoic Asia and the flux of clastic sediment to the ocean. Earth Planet. Sci. Lett. 241 (3–4), 571–580. http://dx.doi.org/10.1016/j.epsl.2005.11.028.
Clift, P.D., 2015. Coupled onshore erosion and offshore sediment loading as causes of lower crust flow on the margins of South China Sea. Geosci. Lett. 2 (1), 1–11. http://dx.doi.org/10.1186/s40562-015-0029-9.
Clift, P., Lin, J., 2001. Preferential mantle lithospheric extension under the South China margin. Mar. Pet. Geol. 18 (8), 929–945. http://dx.doi.org/10.1016/S0264-8172(01)00037-X.
Clift, P.D., Sun, Z., 2006. The sedimentary and tectonic evolution of the Yinggehai–Song Hong basin and the southern Hainan margin, South China Sea: implications for Tibetan uplift and monsoon intensification. J. Geophys. Res. Solid Earth 111 (B6). http://dx.doi.org/10.1029/2005JB004048 p. n/a–n/a.
Clift, P.D., Shimizu, N., Layne, G.D., Blusztajn, J.S., Gaedicke, C., Schlüter, H.-U., Clark, M.K., Amjad, S., 2001. Development of the indus fan and its significance for the erosional history of the Western Himalaya and Karakoram. Geol. Soc. Am. Bull. 113 (8), 1039–1051. http://dx.doi.org/10.1130/0016-7606(2001)113.<1039:DOTIFA>2.0.CO;2.
Clift, P., Lin, J., Barckhausen, U., 2002. Evidence of low flexural rigidity and low viscosity lower continental crust during continental break-up in the South China Sea. Mar. Pet. Geol. 19 (8), 951–970. http://dx.doi.org/10.1016/S0264-8172(02)00108-3.
Clift, P., Lee, G.H., Anh Duc, N., Barckhausen, U., Van Long, H., Zhen, S., 2008. Seismic reflection evidence for a Dangerous Grounds miniplate: No extrusion origin for the South China Sea. Tectonics 27 (3), TC3008. http://dx.doi.org/10.1029/2007TC002216.
Clift, P.D., Wan, S., Blusztajn, J., 2014. Reconstructing chemical weathering, physical erosion and monsoon intensity since 25 Ma in the northern South China Sea: a review of competing proxies. Earth-Science Rev. 130, 86–102. http://dx.doi.org/10.1016/j.earscirev.2014.01.002.
Clift, P.D., Brune, S., Quinteros, J., 2015. Climate changes control offshore crustal structure at South China Sea continental margin. Earth Planet. Sci. Lett. 420, 66–72. http://dx.doi.org/10.1016/j.epsl.2015.03.032.
Contrucci, I., Matias, L., Moulin, M., Geli, L., Klingelhofer, F., Nouze, H., Aslanian, D., Olivet, J.L., Rehault, J.P., Sibuet, J.C., 2004. Deep structure of the West African continental margin (Congo, Zaire, Angola), between 5 degrees S and 8 degrees S, from reflection/refraction seismics and gravity data. Geophys. J. Int. 158 (2), 529–553.
Corti, G., 2008. Control of rift obliquity on the evolution and segmentation of the main Ethiopian rift. Nat. Geosci. 1 (4), 258–262. http://dx.doi.org/10.1038/ngeo160.
Corti, G., Bonini, M., Conticelli, S., Innocenti, F., Manetti, P., Sokoutis, D., 2003. Analogue modelling of continental extension: a review focused on the relations between the patterns of deformation and the presence of magma. Earth-Science Rev. 63 (3–4), 169–247. http://dx.doi.org/10.1016/S0012-8252(03)00035-7.
Corti, G., Iandelli, I., Cerca, M., 2013. Experimental modeling of rifting at craton margins. Geosphere 9 (1), 138–154. http://dx.doi.org/10.1130/GES00863.1.
Cowie, P.A., Underhill, J.R., Behn, M.D., Lin, J., Gill, C.E., 2005. Spatio-temporal evolution of strain accumulation derived from multi-scale observations of Late Jurassic rifting in the northern North Sea: a critical test of models for lithospheric extension. Earth Planet. Sci. Lett. 234 (3–4), 401–419. http://dx.doi.org/10.1016/j.epsl.2005.01.039.
Cowie, L., Angelo, R.M., Kusznir, N.J., Manatschal, G., Horn, B., 2015a. The palaeobathymetry of base Aptian salt deposition on the northern Angolan rifted margin: constraints from flexural back-stripping and reverse post-break-up thermal subsidence modelling. Pet. Geosci. 2014–2087. http://dx.doi.org/10.1144/petgeo2014-087.
Cowie, L., Kusznir, N., Manatschal, G., 2015b. Determining the COB location along the Iberian margin and Galicia Bank from gravity anomaly inversion, residual depth anomaly and subsidence analysis. Geophys. J. Int. 203 (2), 1355–1372. http://dx.doi.org/10.1093/gji/ggv367.
Crosby, A.G., White, N.J., Edwards, G.R.H., Thompson, M., Corfield, R., Mackay, L., 2011. Evolution of deep-water rifted margins: testing depth-dependent extensional models. Tectonics 30 (1), TC1004. http://dx.doi.org/10.1029/2010TC002687.
Cullen, A., 2014. Reprint of: nature and significance of The West Baram and Tinjar lines, NW Borneo. Mar. Pet. Geol. 58 (Part B), 674–686. http://dx.doi.org/10.1016/j.marpetgeo.2014.01.009.
Cullen, A., Reemst, P., Henstra, G., Gozzard, S., Ray, A., 2010. Rifting of the South China Sea: new perspectives. Pet. Geosci. 16 (3), 273–282. http://dx.doi.org/10.1144/1354-079309-908.
Cyprych, D., Brune, S., Piazolo, S., Quinteros, J., 2016. Strain localization in polycrystalline material with second phase particles: Numerical modeling with application to ice mixtures. Geochem. Geophys. Geosystems. http://dx.doi.org/10.1002/2016GC006471.
Davison, I., 2007. Geology and Tectonics of the South Atlantic Brazilian Salt Basins. In: Ries, A.C., Butler, R.W.H., Graham, R.H. (Eds.), Deformation of the Continental Crust: the Legacy of Mike Coward, Special Publications 272. Geological Society, London, pp. 345–359.
Dean, S.M., Minshull, T.A., Whitmarsh, R.B., Louden, K.E., 2000. Deep structure of the ocean-continent transition in the southern Iberia Abyssal Plain from seismic refraction profiles: the IAM-9 transect at 40°20′N. J. Geophys. Res. Solid Earth 105 (B3), 5859–5885. http://dx.doi.org/10.1029/1999JB900301.
Defant, M.J., Jacques, D., Maury, R.C., Boer, J.D., and Joron, J.-L., 1989, Geochemistry and tectonic setting of the Luzon arc, Philippines: Geol. Soc. Am. Bull., v. 101, no. 5, p. 663–672, doi: http://dx.doi.org/10.1130/0016-7606(1989)101<0663:GATSOT>2.3.CO;2.
Demercian, S., Szatmari, P., Cobbold, P.R., 1993. Style and pattern of salt diapirs due to thin-skinned gravitational gliding, Campos and Santos basins, offshore Brazil. Tectonophysics 228 (3), 393–433. http://dx.doi.org/10.1016/0040-1951(93)90351-J.
Díaz, J., Gallart, J., 2009. Crustal structure beneath the Iberian Peninsula and surrounding waters: a new compilation of deep seismic sounding results. Phys. Earth Planet. inter. 173 (1–2), 181–190. http://dx.doi.org/10.1016/j.pepi.2008.11.008.
Díaz-Azpiroz, M., Brune, S., Leever, K.A., Fernández, C., Czeck, D.M., 2016. Tectonics of oblique plate boundary systems. Tectonophysics. http://dx.doi.org/10.1016/j.tecto.2016.07.028.
Ding, W., Schnabel, M., Franke, D., Aiguo, R., Zhenli, W., 2012. Crustal structure across the Northwestern margin of South China Sea: evidence for magma-poor rifting from a wide-angle seismic profile. Acta Geol. Sin. - Engl. Ed. 86 (4), 854–866. http://dx.doi.org/10.1111/j.1755-6724.2012.00711.x.
Ding, W., Li, J., Clift, P.D., 2016. Spreading dynamics and sedimentary process of the southwest sub-basin, South China Sea: constraints from multi-channel seismic data and IODP expedition 349. J. Asian Earth Sci. 115, 97–113. http://dx.doi.org/10.1016/j.jseaes.2015.09.013.
Direen, N.G., Stagg, H.M.J., Symonds, P.A., Norton, I.O., 2012. Variations in rift symmetry: cautionary examples from the Southern Rift System (Australia–Antarctica). Geol. Soc. Lond. Spec. Publ. 369 http://dx.doi.org/10.1144/SP369.4.
Doré, T., Lundin, E., 2015. Research focus: hyperextended continental margins—Knowns and unknowns. Geology 43 (1), 95–96. http://dx.doi.org/10.1130/focus012015.1.
Dressel, I., Scheck-Wenderoth, M., Cacace, M., 2016. Backward modelling of the subsidence evolution of the Colorado Basin, offshore Argentina and its relation to the evolution of the conjugate Orange Basin, offshore SW Africa. Tectonophysics. http://dx.doi.org/10.1016/j.tecto.2016.08.007.
Duarte, J.C., Schellart, W.P., Cruden, A.R., 2013. Three-dimensional dynamic laboratory models of subduction with an overriding plate and variable interplate rheology. Geophys. J. Int. http://dx.doi.org/10.1093/gji/ggt257 ggt257.

Duesterhoeft, E., Quinteros, J., Oberhänsli, R., Bousquet, R., de Capitani, C., 2014. Relative impact of mantle densification and eclogitization of slabs on subduction dynamics: a numerical thermodynamic/thermokinematic investigation of metamorphic density evolution. Tectonophysics. http://dx.doi.org/10.1016/j.tecto.2014.09.009.

Dunbar, J.A., Sawyer, D.S., 1996. Three-dimensional dynamical model of continental rift propagation and margin plateau formation. J. Geophys. Res. 101 (B12), 27,845–27,863. http://dx.doi.org/10.1029/96JB01231.

Ebinger, C.J., Jackson, J.A., Foster, A.N., Hayward, N.J., 1999. Extensional basin geometry and the elastic lithosphere: philosophical transactions of the Royal Society of London. Series a. Math. Phys. Eng. Sci. 357 (1753), 741–765. http://dx.doi.org/10.1098/rsta.1999.0351.

England, P., 1983. Constraints on extension of continental lithosphere. J. Geophys. Res. Solid Earth 88 (B2), 1145–1152. http://dx.doi.org/10.1029/JB088iB02p01145.

Espurt, N., Callot, J.-P., Roure, F., Totterdell, J.M., Struckmeyer, H.I.M., Vially, R., 2012. Transition from symmetry to asymmetry during continental rifting: an example from the Bight Basin–Terre Adélie (Australian and Antarctic conjugate margins). Terra nova. 24 (3), 167–180. http://dx.doi.org/10.1111/j.1365-3121.2011.01055.x.

Ewing, T.A., Rubatto, D., Beltrando, M., Hermann, J., 2015. Constraints on the thermal evolution of the Adriatic margin during Jurassic continental break-up: U–Pb dating of rutile from the Ivrea–Verbano Zone, Italy. Contrib. Mineral. Petrol. 169 (4), 1–22. http://dx.doi.org/10.1007/s00410-015-1135-6.

Fainstein, R., Milliman, J.D., 1979. Structure and origin of three continental-margin plateaus, Northeastern Brazil. AAPG Bull. 63 (2), 218–238.

Féraud, G., Beslier, M.-O., and Cornen, G., 1996, 40Ar/39Ar dating of gabbros from the ocean/continent transition of the western Iberia margin: preliminary results, *in* proceedings of the ocean drilling Program. Scientific results, ocean drilling Program, p. 489–495.

Fleitout, L., Froidevaux, C., 1982. Tectonics and topography for a lithosphere containing density heterogeneities. Tectonics 1 (1), 21–56. http://dx.doi.org/10.1029/TC001i001p00021.

Franke, D., Barckhausen, U., Heyde, I., Tingay, M., Ramli, N., 2008. Seismic images of a collision zone offshore NW Sabah/Borneo. Mar. Pet. Geol. 25 (7), 606–624. http://dx.doi.org/10.1016/j.marpetgeo.2007.11.004.

Franke, D., Barckhausen, U., Baristeas, N., Engels, M., Ladage, S., Lutz, R., Montano, J., Pellejera, N., Ramos, E.G., Schnabel, M., 2011. The continent-ocean transition at the southeastern margin of the South China Sea. Mar. Pet. Geol. 28 (6), 1187–1204. http://dx.doi.org/10.1016/j.marpetgeo.2011.01.004.

Franke, D., Savva, D., Pubellier, M., Steuer, S., Mouly, B., Auxietre, J.-L., Meresse, F., Chamot-Rooke, N., 2014. The final rifting evolution in the South China Sea. Mar. Pet. Geol. 58 (Part B), 704–720. http://dx.doi.org/10.1016/j.marpetgeo.2013.11.020.

Fraser, S., Clark, I., 2016. Continent-ocean Transitions, How Do They Form? An Example From Sergipe Alagoas, Brazil.

Funck, T., Hopper, J.R., Larsen, H.C., Louden, K.E., Tucholke, B.E., Holbrook, W.S., 2003. Crustal structure of the ocean-continent transition at Flemish Cap: seismic refraction results. J. Geophys. Res. Solid Earth 108 (B11), 2531. http://dx.doi.org/10.1029/2003JB002434.

Funck, T., Erlendsson, Ö., Geissler, W.H., Gradmann, S., Kimbell, G.S., McDermott, K., Petersen, U.K., 2016. A review of the NE Atlantic conjugate margins based on seismic refraction data. Geol. Soc. Lond. Spec. Publ. 447 http://dx.doi.org/10.1144/SP447.9. SP447.9.

Fyhn, M.B.W., Boldreel, L.O., Nielsen, L.H., 2009. Geological development of the central and south vietnamese margin: implications for the establishment of the South China Sea, indochinese escape tectonics and cenozoic volcanism. Tectonophysics 478 (3–4), 184–214. http://dx.doi.org/10.1016/j.tecto.2009.08.002.

Færseth, R.B., Lien, T., 2002. Cretaceous evolution in the Norwegian Sea—a period characterized by tectonic quiescence. Mar. Pet. Geol. 19 (8), 1005–1027. http://dx.doi.org/10.1016/S0264-8172(02)00112-5.

Gac, S., Geoffroy, L., 2009. 3D Thermo-mechanical modelling of a stretched continental lithosphere containing localized low-viscosity anomalies (the soft-point theory of plate break-up). Tectonophysics 468 (1–4), 158–168. http://dx.doi.org/10.1016/j.tecto.2008.05.011.

Galland, O., Bertelsen, H.S., Guldstrand, F., Girod, L., Johannessen, R.F., Bjugger, F., Burchardt, S., Mair, K., 2016. Application of open-source photogrammetric software MicMac for monitoring surface deformation in laboratory models. J. Geophys. Res. Solid Earth. http://dx.doi.org/10.1002/2015JB012564, 2015JB012564.

Gawthorpe, R.L., Jackson, C.A.-L., Young, M.J., Sharp, I.R., Moustafa, A.R., Leppard, C.W., 2003. Normal fault growth, displacement localisation and the evolution of normal fault populations: the Hammam Faraun fault block, Suez rift, Egypt. J. Struct. Geol. 25 (6), 883–895. http://dx.doi.org/10.1016/S0191-8141(02)00088-3.

Genik, G.J., 1992. Geodynamics of rifting, volume ii case history studies on rifts: North and south America and Africa regional framework, structural and petroleum aspects of rift basins in Niger, Chad and the Central African Republic (C.A.R.). Tectonophysics 213 (1), 169–185. http://dx.doi.org/10.1016/0040-1951(92)90257-7.

Gerya, T., 2010a. Dynamical instability produces transform faults at mid-ocean ridges. Science 329 (5995), 1047–1050. http://dx.doi.org/10.1126/science.1191349.

Gerya, T.V., 2010b. Introduction to Numerical Geodynamic Modelling. Cambridge University Press.

Gerya, T.V., 2013. Three-dimensional thermomechanical modeling of oceanic spreading initiation and evolution. Phys. Earth Planet. inter. 214, 35–52. http://dx.doi.org/10.1016/j.pepi.2012.10.007.

Ghignone, J.I., De Andrade, G., 1970. General Geology and Major Oil Fields of Reconcavo Basin, Brazil.

Gillard, M., Autin, J., Manatschal, G., Sauter, D., Munschy, M., Schaming, M., 2015. Tectonomagmatic evolution of the final stages of rifting along the deep conjugate Australian-Antarctic magma-poor rifted margins: constraints from seismic observations. Tectonics 34 (4). http://dx.doi.org/10.1002/2015TC003850, 2015TC003850.

Gillard, M., Manatschal, G., Autin, J., 2016. How can asymmetric detachment faults generate symmetric Ocean Continent Transitions? Terra nova. 28 (1), 27–34. http://dx.doi.org/10.1111/ter.12183.

Gilley, L.D., Harrison, T.M., Leloup, P.H., Ryerson, F.J., Lovera, O.M., Wang, J.-H., 2003. Direct dating of left-lateral deformation along the Red River shear zone, China and Vietnam. J. Geophys. Res. Solid Earth 108 (B2), 2127. http://dx.doi.org/10.1029/2001JB001726.

Gleason, G.C., Tullis, J., 1995. A flow law for dislocation creep of quartz aggregates determined with the Molten-salt cell. Tectonophysics 247 (1–4), 1–23.

Gueydan, F., Précigout, J., 2013. Modes of continental rifting as a function of ductile strain localization in the lithospheric mantle. Tectonophysics. http://dx.doi.org/10.1016/j.tecto.2013.11.029.

Gueydan, F., Morency, C., Brun, J.-P., 2008. Continental rifting as a function of lithosphere mantle strength. Tectonophysics 460 (1–4), 83–93. http://dx.doi.org/10.1016/j.tecto.2008.08.012.

Hamilton, W., 1977. Subduction in the Indonesian region, *in* Island arcs, deep sea trenches and back-arc basins. Am. Geophys. Union Maurice Ewing Ser. 15–31.

Hamilton, W., 1987. Crustal extension in the basin and range province, southwestern United States. Geol. Soc. Lond. Spec. Publ. 28 (1), 155–176. http://dx.doi.org/10.1144/GSL.SP.1987.028.01.12.

Haupert, I., Manatschal, G., Decarlis, A., Unternehr, P., 2016. Upper-plate magma-poor rifted margins: stratigraphic architecture and structural evolution. Mar. Pet. Geol. 69, 241–261. http://dx.doi.org/10.1016/j.marpetgeo.2015.10.020.

Hayes, D.E., Nissen, S.S., Buhl, P., Diebold, J., Bochu, Y., Zeng, W., Chen, Y., 1995. Throughgoing crustal faults along the northern margin of the South China Sea and their role in crustal extension. J. Geophys. Res. Solid Earth 100 (B11), 22435–22446. http://dx.doi.org/10.1029/95JB01867.

Heine, C., Brune, S., 2014. Oblique rifting of the Equatorial Atlantic: why there is no Saharan Atlantic ocean. Geology 42 (3), 211–214. http://dx.doi.org/10.1130/G35082.1.

Heine, C., Müller, R., 2005. Late Jurassic rifting along the Australian North West Shelf: margin geometry and spreading ridge configuration. Aust. J. Earth Sci. 52 (1), 27–39. http://dx.doi.org/10.1080/08120090500100077.

Heine, C., Stenzel, F., Landgrebe, T., Dietmar Müller, R., and Wasiliev, J., 2013a, The global rifts database - analysis of mesozoic-cenozic global rift patterns, *in* EGU general assembly conference abstracts.

Heine, C., Zoethout, J., Müller, R.D., 2013b. Kinematics of the south Atlantic rift. Solid earth. 4 (2), 215–253. http://dx.doi.org/10.5194/se-4-215-2013.

Heit, B., Yuan, X., Weber, M., Geissler, W., Jokat, W., Lushetile, B., Hoffmann, K.-H., 2015. Crustal thickness and Vp/Vs ratio in NW Namibia from receiver functions: evidence for magmatic underplating due to mantle plume-crust interaction. Geophys. Res. Lett. 42 (9) http://dx.doi.org/10.1002/2015GL063704, 2015GL063704.

Hinz, K., Fritsch, J., Kempter, E.H.K., Mohammad, A.M., Meyer, J., Mohamed, D., Vosberg, H., Weber, J., Benavidez, J., 1989. Thrust tectonics along the northwestern continental margin of Sabah/Borneo. Geol. Rundschau 78 (3), 705–730. http://dx.doi.org/10.1007/BF01829317.

Hirth, G., Kohlstedt, D.L., 2003. Rheology of the upper mantle and the mantle wedge: a view from the experimentalists. Geophys. Monogr. 138, 83–105.

Hopper, J.R., Funck, T., Tucholke, B.E., 2007. Structure of the Flemish Cap margin, Newfoundland: insights into mantle and crustal processes during continental breakup. Geol. Soc. Lond. Spec. Publ. 282 (1), 47–61. http://dx.doi.org/10.1144/SP282.3.

Hosseinpour, M., Müller, R.D., Williams, S.E., Whittaker, J.M., 2013. Full-fit reconstruction of the Labrador sea and Baffin Bay. Solid earth. 4 (2), 461–479. http://dx.doi.org/10.5194/se-4-461-2013.

Hsu, S.-K., Sibuet, J.-C., 2005. Continent–Ocean Transition of the Northern South China Sea and off southwestern Taiwan. Mar. Geophys. Res. 25 (1–2), 1–4. http://dx.doi.org/10.1007/s11001-005-0729-1.

Huang, C.-Y., Yuan, P.B., Tsao, S.-J., 2006. Temporal and spatial records of active arc-continent collision in Taiwan: a synthesis. GSA Bull. 118 (3–4), 274–288. http://dx.doi.org/10.1130/B25527.1.

Hudec, M.R., Jackson, M.P.A., 2007. Terra infirma: understanding salt tectonics. Earth-Science Rev. 82 (1–2), 1–28. http://dx.doi.org/10.1016/j.earscirev.2007.01.001.

Huet, B., Le Pourhiet, L., Labrousse, L., Burov, E., Jolivet, L., 2011. Post-orogenic extension and metamorphic core complexes in a heterogeneous crust: the role of crustal layering inherited from collision. Application to the Cyclades (Aegean domain). Geophys. J. Int. 184 (2), 611–625. http://dx.doi.org/10.1111/j.1365-246X.2010.04849.x.

Huismans, R.S., Beaumont, C., 2003. Symmetric and asymmetric lithospheric extension: relative effects of frictional-plastic and viscous strain softening. J. Geophys. Research-Solid Earth 108 (B10), 2496. http://dx.doi.org/10.1029/2002JB002026.

Huismans, R.S., Beaumont, C., 2008. Complex rifted continental margins explained by dynamical models of depth-dependent lithospheric extension. Geology 36

(2), 163–166.
Huismans, R.S., Beaumont, C., 2011. Depth-dependent extension, two-stage breakup and cratonic underplating at rifted margins. Nature 473 (7345), 74–78. http://dx.doi.org/10.1038/nature09988.
Hutchison, C.S., 1996. The "rajang accretionary prism" and "Lupar line" problem of Borneo. Geol. Soc. Lond. Spec. Publ. 106 (1), 247–261. http://dx.doi.org/10.1144/GSL.SP.1996.106.01.16.
Hutchison, C.S., 2004. Marginal basin evolution: the southern South China Sea. Mar. Pet. Geol. 21 (9), 1129–1148. http://dx.doi.org/10.1016/j.marpetgeo.2004.07.002.
Hutchison, C.S., 2005. Geology of North-West Borneo: Sarawak, Brunei and Sabah. Elsevier.
Hutchison, C.S., 2010. the North-West Borneo trough. Mar. Geol. 271 (1–2), 32–43. http://dx.doi.org/10.1016/j.margeo.2010.01.007.
Hutchison, C.S., Vijayan, V.R., 2010. What are the Spratly islands? J. Asian Earth Sci. 39 (5), 371–385. http://dx.doi.org/10.1016/j.jseaes.2010.04.013.
Hutchison, C.S., Bergman, S.C., Swauger, D.A., Graves, J.E., 2000. A Miocene collisional belt in north Borneo: uplift mechanism and isostatic adjustment quantified by thermochronology. J. Geol. Soc. 157 (4), 783–793. http://dx.doi.org/10.1144/jgs.157.4.783.
Jammes, S., Lavier, L.L., 2016. The effect of bimineralic composition on extensional processes at lithospheric scale. Geochem. Geophys. Geosystems 17 (8), 3375–3392. http://dx.doi.org/10.1002/2016GC006399.
Jammes, S., Lavier, L., Manatschal, G., 2010. Extreme crustal thinning in the Bay of Biscay and the western pyrenees: from observations to modeling. Geochem. Geophys. Geosystems 11 (10), Q10016. http://dx.doi.org/10.1029/2010GC003218.
Jeanniot, L., Kusznir, N., Mohn, G., Manatschal, G., Cowie, L., 2016. Constraining lithosphere deformation modes during continental breakup for the Iberia–Newfoundland conjugate rifted margins. Tectonophysics 680, 28–49. http://dx.doi.org/10.1016/j.tecto.2016.05.006.
John, B.M., Zhou, X.H., Li, J.L., 1990. Formation and tectonic evolution of Southeastern China and Taiwan: isotopic and geochemical constraints. Tectonophysics 183 (1), 145–160. http://dx.doi.org/10.1016/0040-1951(90)90413-3.
Jolivet, L., Faccenna, C., Huet, B., Labrousse, L., Le Pourhiet, L., Lacombe, O., Lecomte, E., Burov, E., Denèle, Y., Brun, J.-P., Philippon, M., Paul, A., Salaün, G., Karabulut, H., et al., 2013. Aegean tectonics: strain localisation, slab tearing and trench retreat. Tectonophysics 597–598, 1–33. http://dx.doi.org/10.1016/j.tecto.2012.06.011.
Karner, G.D., Driscoll, N.W., 1999. Style, timing and distribution of tectonic deformation across the Exmouth Plateau, northwest Australia, determined from stratal architecture and quantitative basin modelling. Geol. Soc. Lond. Spec. Publ. 164 (1), 271–311. http://dx.doi.org/10.1144/GSL.SP.1999.164.01.14.
Karner, G.D., Driscoll, N.W., Barker, D.H.N., 2003. Syn-rift regional subsidence across the West African continental margin: the role of lower plate ductile extension. Geol. Soc. Lond. Spec. Publ. 207 (1), 105–129. http://dx.doi.org/10.1144/GSL.SP.2003.207.6.
Katzman, R., Brink X, U.S., Lin, J., 1995. Three-dimensional modeling of pull-apart basins: implications for the tectonics of the Dead sea basin. J. Geophys. Res. 100 (B4), 6295–6312. http://dx.doi.org/10.1029/94JB03101.
Kido, Y., Suyehiro, K., Kinoshita, H., 2001. Rifting to spreading process along the Northern continental margin of the South China Sea. Mar. Geophys. Res. 22 (1), 1–15. http://dx.doi.org/10.1023/A:1004869628532.
Kneller, E.A., Johnson, C.A., Karner, G.D., Einhorn, J., Queffelec, T.A., 2012. Inverse methods for modeling non-rigid plate kinematics: application to mesozoic plate reconstructions of the Central Atlantic. Comput. Geosci. 49, 217–230. http://dx.doi.org/10.1016/j.cageo.2012.06.019.
Koopmann, H., Brune, S., Franke, D., Breuer, S., 2014. Linking rift propagation barriers to excess magmatism at volcanic rifted margins. Geology. http://dx.doi.org/10.1130/G36085.1. G36085.1.
Koptev, A., Calais, E., Burov, E., Leroy, S., Gerya, T., 2015. Dual continental rift systems generated by plume-lithosphere interaction. Nat. Geosci. 8 (5), 388–392. http://dx.doi.org/10.1038/ngeo2401.
Krawczyk, C.M., Reston, T.J., Beslier, M.-O., Boillot, G., 1996. Evidence for detachment tectonics on the Iberia Abyssal Plain rifted margin. Proc. Ocean Drill. Program. Sci. results 149, 603–615.
Kusznir, N.J., Park, R.G., 1987. The extensional strength of the continental lithosphere: its dependence on geothermal gradient, and crustal composition and thickness. Geol. Soc. Lond. Spec. Publ. 28 (1), 35–52.
Lavecchia, A., Beekman, F., Clark, S.R., Cloetingh, S.A.P.L., 2016. Thermo-rheological aspects of crustal evolution during continental breakup and melt intrusion: the Main Ethiopian Rift, East Africa. Tectonophysics 686, 51–62. http://dx.doi.org/10.1016/j.tecto.2016.07.018.
Lavier, L.L., Manatschal, G., 2006. A mechanism to thin the continental lithosphere at magma-poor margins. Nature 440 (7082), 324–328. http://dx.doi.org/10.1038/nature04608.
Lavier, L.L., Buck, W.R., Poliakov, A.N.B., 1999. Self-consistent rolling-hinge model for the evolution of large-offset low-angle normal faults. Geology 27 (12), 1127–1130. http://dx.doi.org/10.1130/0091-7613(1999)027. <1127:SCRHMF>2.3.CO;2.
Le Pourhiet, L., Huet, B., May, D.A., Labrousse, L., Jolivet, L., 2012. Kinematic interpretation of the 3D shapes of metamorphic core complexes. Geochem. Geophys. Geosystems 13, Q09002. http://dx.doi.org/10.1029/2012GC004271.
Le Pourhiet, L., Huet, B., Traoré, N., 2014. Links between long-term and short-term rheology of the lithosphere: insights from strike-slip fault modelling. Tectonophysics. http://dx.doi.org/10.1016/j.tecto.2014.06.034.
Leever, K.A., Gabrielsen, R.H., Sokoutis, D., Willingshofer, E., 2011. The effect of convergence angle on the kinematic evolution of strain partitioning in transpressional brittle wedges: insight from analog modeling and high-resolution digital image analysis. Tectonics 30 (2). http://dx.doi.org/10.1029/2010TC002823 p. TC2013.
Leloup, P.H., Arnaud, N., Lacassin, R., Kienast, J.R., Harrison, T.M., Trong, T.T.P., Replumaz, A., Tapponnier, P., 2001. New constraints on the structure, thermochronology, and timing of the Ailao Shan-Red River shear zone, SE Asia. J. Geophys. Res. Solid Earth 106 (B4), 6683–6732. http://dx.doi.org/10.1029/2000JB900322.
Li, Z.-X., Li, X.-H., Chung, S.-L., Lo, C.-H., Xu, X., Li, W.-X., 2012. Magmatic switch-on and switch-off along the south China continental margin since the permian: transition from an andean-type to a western Pacific-type plate boundary. Tectonophysics 532–535, 271–290. http://dx.doi.org/10.1016/j.tecto.2012.02.011.
Li, L., Clift, P.D., Nguyen, H.T., 2013. The sedimentary, magmatic and tectonic evolution of the southwestern South China Sea revealed by seismic stratigraphic analysis. Mar. Geophys. Res. 1–25. http://dx.doi.org/10.1007/s11001-013-9171-y.
Li, C.-F., Xu, X., Lin, J., Sun, Z., Zhu, J., Yao, Y., Zhao, X., Liu, Q., Kulhanek, D.K., Wang, J., Song, T., Zhao, J., Qiu, N., Guan, Y., et al., 2014. Ages and magnetic structures of the South China Sea constrained by deep tow magnetic surveys and IODP Expedition 349. Geochem. Geophys. Geosystems 15 (12), 4958–4983. http://dx.doi.org/10.1002/2014GC005567.
Li, C.-F., Lin, J., and Kulhanek, D.K., 2015a, Proceedings of the International Ocean Discovery Program, 349: South China Sea Tectonics.: International Ocean Discovery Program, College Station, TX.
Li, C., Lin, J., Kulhanek, D., Williams, T., Bao, R., Briais, A., Brown, E., Chen, Y., Clift, P., Colwell, F., and others, 2015b, Site U1435:
Liao, J., Gerya, T., 2014. Influence of lithospheric mantle stratification on craton extension: insight from two-dimensional thermo-mechanical modeling. Tectonophysics. http://dx.doi.org/10.1016/j.tecto.2014.01.020.
Lin, J., Zhang, J., Jiang, S., Wang, S., Xu, B., Wei, M., 2004. The neogene foraminiferal stratigraphy of the LH-19-4-1 bore hole: Pearl River Mouth Basin, South China Sea. J. Stratigr. 28 (2), 120–125.
Lister, G.S., Etheridge, M.A., Symonds, P.A., 1986. Detachment faulting and the evolution of passive continental margins. Geology 14 (3), 246–250. http://dx.doi.org/10.1130/0091-7613(1986)14. <246:DFATEO>2.0.CO;2.
Lister, G.S., Etheridge, M.A., Symonds, P.A., 1991. Detachment models for the formation of passive continental margins. Tectonics 10 (5), 1038–1064. http://dx.doi.org/10.1029/90TC01007.
Lithgow-Bertelloni, C., Gurnis, M., 1997. Cenozoic subsidence and uplift of continents from time-varying dynamic topography. Geology 25 (8), 735–738. http://dx.doi.org/10.1130/0091-7613(1997)025. <0735:CSAUOC>2.3.CO;2.
Lundin, E.R., Doré, A.G., 1997. A tectonic model for the Norwegian passive margin with implications for the NE Atlantic: early Cretaceous to break-up. J. Geol. Soc. 154 (3), 545–550. http://dx.doi.org/10.1144/gsjgs.154.3.0545.
Lundin, E.R., Doré, A.G., 2011. Hyperextension, serpentinization, and weakening: a new paradigm for rifted margin compressional deformation. Geology 39 (4), 347–350. http://dx.doi.org/10.1130/G31499.1.
Lundin, E.R., Redfield, T.F., and Péron-Pinvidic, G., 2014, Rifted continental margins: geometric influence on crustal architecture and melting, *in* Sedimentary basins: origin, depositional histories, and petroleum systems: 33rd Annual GCSSEPM Foundation Bob F. Perkins Conference, p. 18–53.
Magnavita, L.P., Davison, I., Kusznir, N.J., 1994. Rifting, erosion, and uplift history of the Recôncavo-Tucano-Jatobá Rift, northeast Brazil. Tectonics 13 (2), 367–388. http://dx.doi.org/10.1029/93TC02941.
Magnavita, L.P., Szatmari, P., Cupertino, J.A., Destro, N., Roberts, D., 2012. The Recôncavo Basin.
Magoon, L.B., Dow, W.G., 1994. The Petroleum System: from Source to Trap. American Association Of Petroleum Geologists, Tulsa, Oklahoma.
Manatschal, G., Lavier, L., Chenin, P., 2015. The role of inheritance in structuring hyperextended rift systems: some considerations based on observations and numerical modeling. Gondwana Res. 27 (1), 140–164. http://dx.doi.org/10.1016/j.gr.2014.08.006.
Marotta, A.M., Roda, M., Conte, K., Spalla, M.I., 2016. Thermo-mechanical numerical model of the transition from continental rifting to oceanic spreading: the case study of the Alpine Tethys. Geol. Mag. 1–30. http://dx.doi.org/10.1017/S0016756816000856.
Mart, Y., Dauteuil, O., 2000. Analogue experiments of propagation of oblique rifts. Tectonophysics 316 (1–2), 121–132. http://dx.doi.org/10.1016/S0040-1951(99)00231-0.
Marzoli, A., Melluso, L., Morra, V., Renne, P.R., Sgrosso, I., D'Antonio, M., Duarte Morais, L., Morais, E.A.A., Ricci, G., 1999. Geochronology and petrology of Cretaceous basaltic magmatism in the Kwanza basin (western Angola), and relationships with the Paranà-Etendeka continental flood basalt province. J. Geodyn. 28 (4–5), 341–356. http://dx.doi.org/10.1016/S0264-3707(99)00014-9.
Masini, E., Manatschal, G., Mohn, G., 2013. The Alpine Tethys rifted margins: reconciling old and new ideas to understand the stratigraphic architecture of magma-poor rifted margins. Sedimentology 60 (1), 174–196. http://dx.doi.org/10.1111/sed.12017.
Mattei, M., D'Agostino, N., Zananiri, I., Kondopoulou, D., Pavlides, S., Spatharas, V., 2004. Tectonic evolution of fault-bounded continental blocks: comparison of paleomagnetic and GPS data in the Corinth and Megara basins (Greece). J. Geophys. Res. Solid Earth 109 (B2), B02106. http://dx.doi.org/10.1029/2003JB002506.

Matthews, S., Fraser, A., Lowe, S., Todd, S., Peel, F., 1997. Structure, stratigraphy and petroleum geology of the SE Nam Con Son Basin, offshore Vietnam. Geol. Soc. Lond. Spec. Publ. 126 (1), 89–106.
May, D.A., Brown, J., Le Pourhiet, L., 2015. A scalable, matrix-free multigrid preconditioner for finite element discretizations of heterogeneous Stokes flow. Comput. Methods Appl. Mech. Eng. 290, 496–523. http://dx.doi.org/10.1016/j.cma.2015.03.014.
Mbina Mounguengui, M., Guiraud, M., 2009. Neocomian to early Aptian syn-rift evolution of the normal to oblique-rifted North Gabon margin (interior and N'Komi basins). Mar. Pet. Geol. 26 (6), 1000–1017. http://dx.doi.org/10.1016/j.marpetgeo.2008.11.001.
McClay, K.R., White, M.J., 1995. Analogue modelling of orthogonal and oblique rifting. Mar. Pet. Geol. 12 (2), 137–151. http://dx.doi.org/10.1016/0264-8172(95)92835-K.
McKenzie, D., 1978. Some remarks on the development of sedimentary basins. Earth Planet. Sci. Lett. 40 (1), 25–32. http://dx.doi.org/10.1016/0012-821X(78)90071-7.
Mericer de Lépinay, M., Loncke, L., Basile, C., Roest, W.R., Patriat, M., Maillard, A., De Clarens, P., 2016. Transform continental margins - Part 2: a worldwide review. Tectonophysics. http://dx.doi.org/10.1016/j.tecto.2016.05.038.
Michon, L., Merle, O., 2000. Crustal structures of the Rhinegraben and the Massif Central grabens: an experimental approach. Tectonics 19 (5), 896–904. http://dx.doi.org/10.1029/2000TC900015.
Minshull, T.A., Dean, S.M., White, R.S., Whitmarsh, R.B., 2001. Anomalous melt production after continental break-up in the southern Iberia Abyssal Plain. Geol. Soc. Lond. Spec. Publ. 187 (1), 537–550. http://dx.doi.org/10.1144/GSL.SP.2001.187.01.26.
Mohn, G., Karner, G.D., Manatschal, G., Johnson, C.A., 2015. Structural and stratigraphic evolution of the Iberia–Newfoundland hyper-extended rifted margin: a quantitative modelling approach. Geol. Soc. Lond. Spec. Publ. 413 http://dx.doi.org/10.1144/SP413.9 p. SP413.9.
Mohriak, W.U., Dewey, J.F., 1987. Deep seismic reflectors in the Campos basin, offshore Brazil. Geophys. J. R. astron. Soc. 89 (1), 133–140. http://dx.doi.org/10.1111/j.1365-246X.1987.tb04399.x.
Mohriak, W.U., Mello, M.R., Dewey, J.F., Maxwell, J.R., 1990. Petroleum geology of the Campos Basin, offshore Brazil. Geol. Soc. Lond. Spec. Publ. 50 (1), 119–141. http://dx.doi.org/10.1144/GSL.SP.1990.050.01.07.
Mohriak, W.U., Bassetto, M., Vieira, I.S., 2000. Tectonic Evolution of the Rift Basins in the Northeastern Brazilian Region. In: Mohriak, W., Taiwani, M. (Eds.), Atlantic Rifts and Continental Margins. American Geophysical Union, pp. 293–315.
Morley, C.K., 2002. A tectonic model for the Tertiary evolution of strike–slip faults and rift basins in SE Asia. Tectonophysics 347 (4), 189–215. http://dx.doi.org/10.1016/S0040-1951(02)00061-6.
Morley, C.K., 2016. Major unconformities/termination of extension events and associated surfaces in the South China Seas: review and implications for tectonic development. J. Asian Earth Sci. 120, 62–86. http://dx.doi.org/10.1016/j.jseaes.2016.01.013.
Morley, C.K., Westaway, R., 2006. Subsidence in the super-deep Pattani and Malay basins of Southeast Asia: a coupled model incorporating lower-crustal flow in response to post-rift sediment loading. Basin Res. 18 (1), 51–84. http://dx.doi.org/10.1111/j.1365-2117.2006.00285.x.
Moulin, M., Aslanian, D., Unternehr, P., 2010. A new starting point for the south and Equatorial Atlantic ocean. Earth-Science Rev. 98 (1–2), 1–37. http://dx.doi.org/10.1016/j.earscirev.2009.08.001.
Müntener, O., Hermann, J., 2001. The role of lower crust and continental upper mantle during formation of Non-volcanic passive margins: evidence from the Alps. Geol. Soc. Lond. Spec. Publ. 187 (1), 267–288. http://dx.doi.org/10.1144/GSL.SP.2001.187.01.13.
Mutter, J.C., Mutter, C.Z., Fang, J., 1996. Analogies to oceanic behaviour in the continental breakup of the western Woodlark basin. Nature 380 (6572), 333–336. http://dx.doi.org/10.1038/380333a0.
Nagel, T.J., Buck, W.R., 2004. Symmetric alternative to asymmetric rifting models. Geology 32 (11), 937–940.
Naliboff, J., Buiter, S.J.H., 2015. Rift reactivation and migration during multiphase extension. Earth Planet. Sci. Lett. 421, 58–67. http://dx.doi.org/10.1016/j.epsl.2015.03.050.
Nestola, Y., Storti, F., Bedogni, E., Cavozzi, C., 2013. Shape evolution and finite deformation pattern in analog experiments of lithosphere necking. Geophys. Res. Lett. 40 (19) http://dx.doi.org/10.1002/grl.50978, p. 2013GL057618.
Nestola, Y., Storti, F., Cavozzi, C., 2015. Strain rate-dependent lithosphere rifting and necking architectures in analog experiments. J. Geophys. Res. Solid Earth 120 (1). http://dx.doi.org/10.1002/2014JB011623, p. 2014JB011623.
Nirrengarten, M., Gernigon, L., Manatschal, G., 2014. Lower crustal bodies in the Møre volcanic rifted margin: geophysical determination and geological implications. Tectonophysics 636, 143–157. http://dx.doi.org/10.1016/j.tecto.2014.08.004.
Nissen, S.S., Hayes, D.E., Bochu, Y., Zeng, W., Chen, Y., Nu, X., 1995a. Gravity, heat flow, and seismic constraints on the processes of crustal extension: Northern margin of the South China Sea. J. Geophys. Res. Solid Earth 100 (B11), 22447–22483. http://dx.doi.org/10.1029/95JB01868.
Nissen, S.S., Hayes, D.E., Buhl, P., Diebold, J., Bochu, Y., Zeng, W., Chen, Y., 1995b. Deep penetration seismic soundings across the northern margin of the South China Sea. J. Geophys. Res. Solid Earth 100 (B11), 22407–22433. http://dx.doi.org/10.1029/95JB01866.
Nixon, C.W., McNeill, L.C., Bull, J.M., Bell, R.E., Gawthorpe, R.L., Henstock, T.J., Christodoulou, D., Ford, M., Taylor, B., Sakellariou, D., Ferentinos, G., Papatheodorou, G., Leeder, M.R., Collier, R.E.L., et al., 2016. Rapid spatiotemporal variations in rift structure during development of the Corinth Rift, central Greece. Tectonics. http://dx.doi.org/10.1002/2015TC004026, p. 2015TC004026.
Norton, I.O., Carruthers, D.T., Hudec, M.R., 2016. Rift to drift transition in the South Atlantic salt basins: a new flavor of oceanic crust. Geology 44 (1), 55–58. http://dx.doi.org/10.1130/G37265.1.
Nürnberg, D., Müller, R.D., 1991. The tectonic evolution of the south-Atlantic from late jurassic to present. Tectonophysics 191 (1–2), 27–53. http://dx.doi.org/10.1016/0040-1951(91)90231-G.
ODP Leg 173 Shipboard Scientific Party, 1998. Drilling reveals transition from continental breakup to early magmatic crust: Eos. Trans. Am. Geophys. Union 79 (14). http://dx.doi.org/10.1029/98EO00127.
Pedrosa-Soares, A.C., Alkmim, F.F., Tack, L., Noce, C.M., Babinski, M., Silva, L.C., Martins-Neto, M.A., 2008. Similarities and differences between the Brazilian and African counterparts of the neoproterozoic Araçuaí-west Congo orogen. Geol. Soc. Lond. Spec. Publ. 294 (1), 153–172. http://dx.doi.org/10.1144/SP294.9.
Peltzer, G., Tapponnier, P., 1988. Formation and evolution of strike-slip faults, rifts, and basins during the India-Asia Collision: an experimental approach. J. Geophys. Res. Solid Earth 93 (B12), 15085–15117. http://dx.doi.org/10.1029/JB093iB12p15085.
Pérez-Díaz, L., Eagles, G., 2014. Constraining South Atlantic growth with seafloor spreading data. Tectonics. http://dx.doi.org/10.1002/2014TC003644, p. 2014TC003644.
Pérez-Gussinyé, M., 2013. A tectonic model for hyperextension at magma-poor rifted margins: an example from the West Iberia–Newfoundland conjugate margins. Geol. Soc. Lond. Spec. Publ. 369 (1), 403–427. http://dx.doi.org/10.1144/SP369.19.
Perez-Gussinye, M., 2015, Modes of extension and oceanization at magma-poor margins: an example from the Brazilian-African margins, *in* agu.
Pérez-Gussinyé, M., Reston, T.J., 2001. Rheological evolution during extension at nonvolcanic rifted margins: onset of serpentinization and development of detachments leading to continental breakup. J. Geophys. Res. 106 (B3), 3961–3975. http://dx.doi.org/10.1029/2000JB900325.
Pérez-Gussinyé, M., Reston, T.J., Morgan, J.P., 2001. Serpentinization and magmatism during extension at non-volcanic margins: the effect of initial lithospheric structure. Geol. Soc. Lond. Spec. Publ. 187 (1), 551–576. http://dx.doi.org/10.1144/GSL.SP.2001.187.01.27.
Pérez-Gussinyé, M., Ranero, C.R., Reston, T.J., Sawyer, D., 2003. Mechanisms of extension at nonvolcanic margins: evidence from the Galicia interior basin, west of Iberia. J. Geophys. Res. 108 (B5), 2245. http://dx.doi.org/10.1029/2001JB000901.
Pérez-Gussinyé, M., Morgan, J.P., Reston, T.J., Ranero, C.R., 2006. The rift to drift transition at non-volcanic margins: insights from numerical modelling. Earth Planet. Sci. Lett. 244 (1–2), 458–473. http://dx.doi.org/10.1016/j.epsl.2006.01.059.
Péron-Pinvidic, G., Manatschal, G., 2009. The final rifting evolution at deep magma-poor passive margins from Iberia-Newfoundland: a new point of view. Int. J. Earth Sci. 98 (7), 1581–1597. http://dx.doi.org/10.1007/s00531-008-0337-9.
Péron-Pinvidic, G., Manatschal, G., Minshull, T.A., Sawyer, D.S., 2007. Tectonosedimentary evolution of the deep Iberia-Newfoundland margins: evidence for a complex breakup history. Tectonics 26 (2). http://dx.doi.org/10.1029/2006TC001970 p. TC2011.
Péron-Pinvidic, G., Manatschal, G., Masini, E., Sutra, E., Flament, J.M., Haupert, I., Unternehr, P., 2015. Unravelling the along-strike variability of the Angola–Gabon rifted margin: a mapping approach. Geol. Soc. Lond. Spec. Publ. 438 http://dx.doi.org/10.1144/SP438.1 p. SP438.1.
Petersen, K.D., Armitage, J.J., Nielsen, S.B., Thybo, H., 2015. Mantle temperature as a control on the time scale of thermal evolution of extensional basins. Earth Planet. Sci. Lett. 409, 61–70. http://dx.doi.org/10.1016/j.epsl.2014.10.043.
Philippon, M., Willingshofer, E., Sokoutis, D., Corti, G., Sani, F., Bonini, M., Cloetingh, S., 2015. Slip re-orientation in oblique rifts. Geology 43 (2), 147–150. http://dx.doi.org/10.1130/G36208.1.
Popov, A.A., Sobolev, S.V., 2008. SLIM3D: a tool for three-dimensional thermo mechanical modeling of lithospheric deformation with elasto-visco-plastic rheology. Phys. Earth Planet. inter. 171 (1–4), 55–75.
Popov, A.A., Sobolev, S.V., Zoback, M.D., 2012. Modeling evolution of the San Andreas Fault system in northern and central California. Geochemistry, Geophysics, Geosystems 13 (8). http://dx.doi.org/10.1029/2012GC004086 p. Q08016.
Poropat, S.F., Colin, J.-P., 2012. Early Cretaceous ostracod biostratigraphy of eastern Brazil and western Africa: an overview. Gondwana Res. 22 (3–4), 772–798. http://dx.doi.org/10.1016/j.gr.2012.06.002.
Quinteros, J., Sobolev, S.V., 2012. Why has the Nazca plate slowed since the Neogene? Geology 41 (1), 31–34. http://dx.doi.org/10.1130/G33497.1.
Quinteros, J., Sobolev, S.V., Popov, A.A., 2010. Viscosity in transition zone and lower mantle: implications for slab penetration. Geophys. Res. Lett. 37 p. L09307.
Quirk, D.G., Hertle, M., Jeppesen, J.W., Raven, M., Mohriak, W.U., Kann, D.J., Nørgaard, M., Howe, M.J., Hsu, D., Coffey, B., Mendes, M.P., 2013. Rifting, subsidence and continental break-up above a mantle plume in the central South Atlantic. Geol. Soc. Lond. Spec. Publ. 369 (1), 185–214. http://dx.doi.org/10.1144/SP369.20.
Ranalli, G., Murphy, D.C., 1987. Rheological stratification of the lithosphere. Tectonophysics 132 (4), 281–295. http://dx.doi.org/10.1016/0040-1951(87)90348-9.
Ranero, C.R., Pérez-Gussinyé, M., 2010. Sequential faulting explains the asymmetry

and extension discrepancy of conjugate margins. Nature 468 (7321), 294–299. http://dx.doi.org/10.1038/nature09520.
Reeve, M.T., Jackson, C.A.L., Bell, R.E., Magee, C., Bastow, I.D., 2016. The stratigraphic record of pre-breakup geodynamics: evidence from the barrow Delta, offshore Northwest Australia. Tectonics. http://dx.doi.org/10.1002/2016TC004172, p. 2016TC004172.
Reston, T.J., Krawczyk, C.M., Klaeschen, D., 1996. The S reflector west of Galicia (Spain): evidence from prestack depth migration for detachment faulting during continental breakup. J. Geophys. Res.: Solid earth. 101 (B4), 8075–8091. http://dx.doi.org/10.1029/95JB03466.
Rey, P.F., Teyssier, C., Kruckenberg, S.C., Whitney, D.L., 2011. Viscous collision in channel explains double domes in metamorphic core complexes. Geology 39 (4), 387–390. http://dx.doi.org/10.1130/G31587.1.
Rosenau, M., Nerlich, R., Brune, S., Oncken, O., 2010. Experimental insights into the scaling and variability of local tsunamis triggered by giant subduction megathrust earthquakes. J. Geophys. Res. Solid Earth 115 (B9), B09314. http://dx.doi.org/10.1029/2009JB007100.
Rosenbaum, G., Regenauer-Lieb, K., Weinberg, R.F., 2010. Interaction between mantle and crustal detachments: a nonlinear system controlling lithospheric extension. J. Geophys. Res. 115, 16. http://dx.doi.org/10.1029/2009JB006696.
Rosendahl, B.R., Groschel-Becker, H., 1999. Deep seismic structure of the continental margin in the Gulf of Guinea: a summary report. Geol. Soc. Lond. Spec. Publ. 153 (1), 75–83. http://dx.doi.org/10.1144/GSL.SP.1999.153.01.05.
Ru, K., Pigott, J.D., 1986. Episodic rifting and subsidence in the South China Sea. AAPG Bull. 70 (9), 1136–1155.
Rybacki, E., Dresen, G., 2000. Dislocation and diffusion creep of synthetic anorthite aggregates. J. Geophys. Res. 105 (B11), 26,017–26,036. http://dx.doi.org/10.1029/2000JB900223.
Ryberg, T., Haberland, C., Haberlau, T., Weber, M.H., Bauer, K., Behrmann, J.H., Jokat, W., 2015. Crustal structure of northwest Namibia: evidence for plume-rift-continent interaction. Geology 43 (8), 739–742. http://dx.doi.org/10.1130/G36768.1.
Sandwell, D.T., Müller, R.D., Smith, W.H.F., Garcia, E., Francis, R., 2014. New global marine gravity model from CryoSat-2 and Jason-1 reveals buried tectonic structure. Science 346 (6205), 65–67. http://dx.doi.org/10.1126/science.1258213.
Scheck-Wenderoth, M., Roure, F., Bunge, H.-P., Glasmacher, U.A., 2013. Editorial. Tectonophysics 604, 1–3. http://dx.doi.org/10.1016/j.tecto.2013.07.011.
Schellart, W.P., Moresi, L., 2013. A new driving mechanism for backarc extension and backarc shortening through slab sinking induced toroidal and poloidal mantle flow: results from dynamic subduction models with an overriding plate. J. Geophys. Res. Solid Earth 118 (6), 3221–3248. http://dx.doi.org/10.1002/jgrb.50173.
Schlüter, H.U., Hinz, K., Block, M., 1996. Tectono-stratigraphic terranes and detachment faulting of the South China Sea and Sulu sea. Mar. Geol. 130 (1), 39–78. http://dx.doi.org/10.1016/0025-3227(95)00137-9.
Scotchman, I.C., Gilchrist, G., Kusznir, N.J., Roberts, A.M., Fletcher, R., 2010. The breakup of the South Atlantic Ocean: formation of failed spreading axes and blocks of thinned continental crust in the Santos Basin, Brazil and its consequences for petroleum system development. Geol. Soc. Lond. Pet. Geol. Conf. Ser. 7, 855–866. http://dx.doi.org/10.1144/0070855.
Sdrolias, M., Müller, R.D., 2006. Controls on back-arc basin formation. Geochem. Geophys. Geosystems 7 (4), Q04016. http://dx.doi.org/10.1029/2005GC001090.
Seymour, N.M., Stockli, D.F., Beltrando, M., Smye, A.J., 2016. Tracing the thermal evolution of the corsican lower crust during Tethyan rifting. Tectonics. http://dx.doi.org/10.1002/2016TC004178, p. 2016TC004178.
Sharples, W., Moresi, L.-N., Jadamec, M.A., Revote, J., 2015. Styles of rifting and fault spacing in Numerical models of crustal extension. J. Geophys. Res. Solid Earth. http://dx.doi.org/10.1002/2014JB011813, p. 2014JB011813.
Shi, X., Kohn, B., Spencer, S., Guo, X., Li, Y., Yang, X., Shi, H., Gleadow, A., 2011. Cenozoic denudation history of southern Hainan Island, South China Sea: constraints from low temperature thermochronology. Tectonophysics 504 (1–4), 100–115. http://dx.doi.org/10.1016/j.tecto.2011.03.007.
Shipboard Scientific Party, 2000. Site 1143.
Shu, L.S., Zhou, X.M., Deng, P., Wang, B., Jiang, S.Y., Yu, J.H., Zhao, X.X., 2009. Mesozoic tectonic evolution of the Southeast China Block: New insights from basin analysis. J. Asian Earth Sci. 34 (3), 376–391. http://dx.doi.org/10.1016/j.jseaes.2008.06.004.
Sokoutis, D., Corti, G., Bonini, M., Brun, J.P., Cloetingh, S., Mauduit, T., Manetti, P., 2007. Modelling the extension of heterogeneous hot lithosphere. Tectonophysics 444 (1–4), 63–79. http://dx.doi.org/10.1016/j.tecto.2007.08.012.
Stewart, J.H., 1971, basin and range structure: a system of horsts and grabens produced by deep-seated extension: Geol. Soc. Am. Bull., v. 82, no. 4, p. 1019–1044, doi: http://dx.doi.org/10.1130/0016-7606(1971)82[1019:BARSAS]2.0.CO;2.
Su, D., White, N., McKenzie, D., 1989. Extension and subsidence of the Pearl River Mouth Basin, northern South China Sea. Basin Res. 2 (4), 205–222. http://dx.doi.org/10.1111/j.1365-2117.1989.tb00036.x.
Sun, X., Wang, P., 2005. How old is the Asian monsoon system?—Palaeobotanical records from China. Palaeogeogr. Palaeoclimatol. Palaeoecol. 222 (3–4), 181–222. http://dx.doi.org/10.1016/j.palaeo.2005.03.005.
Sun, Z., Zhong, Z.H., Zhou, D., Pang, X., Huang, C.J., Chen, C.M., He, M., Xu, H.H., 2008. Dynamics analysis of the Baiyun sag in the Pearl River Mouth Basin, north of the South China Sea. Acta Geol. Sin. - Engl. Ed. 82 (1), 73–83. http://dx.doi.org/10.1111/j.1755-6724.2008.tb00326.x.
Sutra, E., Manatschal, G., 2012. How does the continental crust thin in a hyperextended rifted Margin? Insights from the Iberia margin. Geology 40 (2), 139–142. http://dx.doi.org/10.1130/G32786.1.
Svartman Dias, A.E., Lavier, L.L., Hayman, N.W., 2015. Conjugate rifted margins width and asymmetry: the interplay between lithospheric strength and thermomechanical processes. J. Geophys. Res. Solid Earth 120 (12). http://dx.doi.org/10.1002/2015JB012074, p. 2015JB012074.
Taposeea, C.A., Armitage, J.J., Collier, J.S., 2016. Asthenosphere and lithosphere structure controls on early onset oceanic crust production in the southern South Atlantic. Tectonophysics. http://dx.doi.org/10.1016/j.tecto.2016.06.026.
Tapponnier, P., Lacassin, R., Leloup, P.H., Schärer, U., Dalai, Z., Haiwei, W., Xiaohan, L., Shaocheng, J., Lianshang, Z., Jiayou, Z., 1990. The ailao Shan/Red River metamorphic belt: Tertiary left-lateral shear between Indochina and south China. Nature 343 (6257), 431–437. http://dx.doi.org/10.1038/343431a0.
Taylor, B., Hayes, D.E., 1980. The Tectonic Evolution of the South China Basin. In: Hayes, D.E. (Ed.), The Tectonic and Geologic Evolution of Southeast Asian Seas and Islands. American Geophysical Union, pp. 89–104.
Taylor, B., Hayes, D.E., 1983. Origin and History of the South China Sea Basin. In: Hayes, D.E. (Ed.), The Tectonic and Geologic Evolution of Southeast Asian Seas and Islands: Part 2. American Geophysical Union, pp. 23–56.
Teisserenc, P., Villemin, J., 1989. Sediment. Basin Gabon–Geology Oil Syst. 132, 117–199.
Tommasi, A., Knoll, M., Vauchez, A., Signorelli, J., Thoraval, C., Loge, R., 2009. Structural reactivation in plate tectonics controlled by olivine crystal anisotropy. Nat. Geosci. 2 (6), 422–426.
Torsvik, T.H., Rousse, S., Labails, C., Smethurst, M.A., 2009. A new scheme for the opening of the South Atlantic Ocean and the dissection of an Aptian salt basin. Geophys. J. Int. 177 (3), 1315–1333.
Tron, V., Brun, J.-P., 1991. Experiments on oblique rifting in brittle-ductile systems. Tectonophysics 188 (1–2), 71–84. http://dx.doi.org/10.1016/0040-1951(91)90315-J.
Tu, K., Flower, M.F.J., Carlson, R.W., Zhang, M., Xie, G., 1991. Sr, Nd, and Pb isotopic compositions of Hainan basalts (south China): implications for a subcontinental lithosphere Dupal source. Geology 19 (6), 567–569. http://dx.doi.org/10.1130/0091-7613(1991)019. <0567:SNAPIC>2.3.CO;2.
Tucholke, B.E., and Sibuet, J.-C., 2007, Leg 210 synthesis: tectonic, magmatic, and sedimentary evolution of the Newfoundland-Iberia rift, in Proceedings of the Ocean Drilling Program, Scientific Results, Ocean Drilling Program College Station, TX, p. 1–56.
Tugend, J., Manatschal, G., Kusznir, N.J., Masini, E., Mohn, G., Thinon, I., 2014. Formation and deformation of hyperextended rift systems: insights from rift domain mapping in the Bay of Biscay-Pyrenees. Tectonics 33 (7). http://dx.doi.org/10.1002/2014TC003529, p. 2014TC003529.
Turner, J.P., Rosendahl, B.R., Wilson, P.G., 2003. Structure and evolution of an obliquely sheared continental margin: Rio Muni, West Africa. Tectonophysics 374 (1–2), 41–55. http://dx.doi.org/10.1016/S0040-1951(03)00325-1.
Umhoefer, P.J., 2011. Why did the Southern Gulf of California rupture so rapidly?—Oblique divergence across hot, weak lithosphere along a tectonically active margin. GSA Today 21 (11), 4–10. http://dx.doi.org/10.1130/G133A.1.
Unternehr, P., Curie, D., Olivet, J.L., Goslin, J., Beuzart, P., 1988. 8th geodynamics symposium, “mesozoic and cenozoic plate reconstructions”South Atlantic fits and intraplate boundaries in Africa and south America. Tectonophysics 155 (1), 169–179. http://dx.doi.org/10.1016/0040-1951(88)90264-8.
Unternehr, P., Peron-Pinvidic, G., Manatschal, G., Sutra, E., 2010. Hyper-extended crust in the South Atlantic: in search of a model. Pet. Geosci. 16 (3), 207–215. http://dx.doi.org/10.1144/1354-079309-904.
van der Beek, P., 1997. Flank uplift and topography at the central Baikal Rift (SE Siberia): a test of kinematic models for continental extension. Tectonics 16 (1), 122–136. http://dx.doi.org/10.1029/96TC02686.
van Wijk, J.W., 2005. Role of weak zone orientation in continental lithosphere extension. Geophys. Res. Lett. 32 (2) http://dx.doi.org/10.1029/2004GL022192.
Van Wijk, J.W., Blackman, D.K., 2005. Dynamics of continental rift propagation: the end-member modes. Earth Planet. Sci. Lett. 229 (3–4), 247–258. http://dx.doi.org/10.1016/j.epsl.2004.10.039.
van Wijk, J.W., Cloetingh, S.A.P.L., 2002. Basin migration caused by slow lithospheric extension. Earth Planet. Sci. Lett. 198 (3–4), 275–288.
van Wijk, J., van Hunen, J., Goes, S., 2008. Small-scale convection during continental rifting: evidence from the Rio Grande rift. Geology 36 (7), 575–578. http://dx.doi.org/10.1130/G24691A.1.
Vauchez, A., Barruol, G., Tommasi, A., 1997. Why do continents break-up parallel to ancient orogenic belts? Terra nova. 9 (2), 62–66. http://dx.doi.org/10.1111/j.1365-3121.1997.tb00003.x.
Walker, J.D., Geissman, J.W., Bowring, S.A., Babcock, L.E., 2013. The geological society of America geologic time scale. Geol. Soc. Am. Bull. 125 (3–4), 259–272. http://dx.doi.org/10.1130/B30712.1.
Wallner, H., Schmeling, H., 2010. Rift induced delamination of mantle lithosphere and crustal uplift: a new mechanism for explaining Rwenzori Mountains' extreme elevation? Int. J. Earth Sci. http://dx.doi.org/10.1007/s00531-010-0521-6.
Walsh, J.J., Childs, C., Imber, J., Manzocchi, T., Watterson, J., Nell, P.A.R., 2003. Strain localisation and population changes during fault system growth within the inner Moray Firth, Northern North Sea. J. Struct. Geol. 25 (2), 307–315. http://dx.doi.org/10.1016/S0191-8141(02)00028-7.
Wang, D., Shu, L., 2012. Late Mesozoic basin and range tectonics and related magmatism in Southeast China. Geosci. Front. 3 (2), 109–124. http://dx.doi.org/10.1016/j.gsf.2011.11.007.

Watremez, L., Burov, E., d'Acremont, E., Leroy, S., Huet, B., Le Pourhiet, L., Bellahsen, N., 2013. Buoyancy and localizing properties of continental mantle lithosphere: insights from thermomechanical models of the eastern Gulf of Aden. Geochem. Geophys. Geosystems 14 (8), 2800–2817. http://dx.doi.org/10.1002/ggge.20179.

Wegener, D.A., 1912. Die Entstehung der Kontinente. Geol. Rundschau 3 (4), 276–292. http://dx.doi.org/10.1007/BF02202896.

Wernicke, B., 1981. Low-angle normal faults in the Basin and Range Province: nappe tectonics in an extending orogen. Nature 291 (5817), 645–648. http://dx.doi.org/10.1038/291645a0.

Wernicke, B., 1985. Uniform-sense normal simple shear of the continental lithosphere. Can. J. Earth Sci. 22 (1), 108–125. http://dx.doi.org/10.1139/e85-009.

Westaway, R., 1994. Re-evaluation of extension across the Pearl River Mouth Basin, South China Sea: implications for continental lithosphere deformation mechanisms. J. Struct. Geol. 16 (6), 823–838. http://dx.doi.org/10.1016/0191-8141(94)90148-1.

Wheeler, P., White, N., 2002. Measuring dynamic topography: an analysis of Southeast Asia. Tectonics 21 (5), 1040. http://dx.doi.org/10.1029/2001TC900023.

Whitmarsh, R.B., White, R.S., Horsefield, S.J., Sibuet, J.-C., Recq, M., Louvel, V., 1996. The ocean-continent boundary off the western continental margin of Iberia: crustal structure west of Galicia Bank. J.Geophys. Res.: Solid Earth. 101 (B12), 28291–28314. http://dx.doi.org/10.1029/96JB02579.

Whitmarsh, R.B., Manatschal, G., Minshull, T.A., 2001. Evolution of magma-poor continental margins from rifting to seafloor spreading. Nature 413 (6852), 150–154. http://dx.doi.org/10.1038/35093085.

Williams, S.E., Whittaker, J.M., Müller, R.D., 2011. Full-fit, palinspastic reconstruction of the conjugate Australian-Antarctic margins. Tectonics 30, 21. http://dx.doi.org/10.1029/2011TC002912.

Wilson, J.T., 1966. Did the Atlantic close and then Re-Open? Nature 211 (5050), 676–681. http://dx.doi.org/10.1038/211676a0.

Withjack, M.O., Jamison, W.R., 1986. Deformation produced by oblique rifting. Tectonophysics 126 (2–4), 99–124. http://dx.doi.org/10.1016/0040-1951(86)90222-2.

Wu, S., Liu, Z., Wang, W., Guo, J., Lüdmann, T., Wong, H.K., 2003. Late cenozoic tectonic deformation in the Dongsha Islands and adjacent sea area. Chin. J. Oceanol. Limnol. 21, 377–388. http://dx.doi.org/10.1007/BF02860434.

Xie, H., Zhou, D., Pang, X., Li, Y., Wu, X., Qiu, N., Li, P., Chen, G., 2013. Cenozoic sedimentary evolution of deepwater sags in the Pearl River Mouth Basin, northern South China Sea. Mar. Geophys. Res. 34 (3–4), 159–173. http://dx.doi.org/10.1007/s11001-013-9183-7.

Xie, H., Di, Z., Li, Y., Pang, X., Li, P., Chen, G., Li, F., Cao, J., 2014. Cenozoic tectonic subsidence in deepwater sags in the Pearl River Mouth Basin, Northern South China Sea. Tectonophysics. http://dx.doi.org/10.1016/j.tecto.2014.01.010.

Yeh, Y.-C., Hsu, S.-K., Doo, W.-B., Sibuet, J.-C., Liu, C.-S., Lee, C.-S., 2012. Crustal features of the northeastern South China Sea: insights from seismic and magnetic interpretations. Mar. Geophys. Res. 33 (4), 307–326. http://dx.doi.org/10.1007/s11001-012-9154-4.

Yin, X., Ren, J., Lei, C., Wang, S., Zhang, J., 2011. Postrift rapid subsidence characters in Qiongdongnan basin, South China Sea. J. Earth Sci. 22 (2), 273–279. http://dx.doi.org/10.1007/s12583-011-0180-y.

Zalán, P.V., Severino, M., do, C.G., Rigoti, C.A., Magnavita, L.P., Oliveira, J.A.B., Vianna, A.R., 2011. An Entirely New 3D-view of the Crustal and Mantle Structure of a South Atlantic Passive Margin-Santos. In: Americal Association of Petroleum Geology, Annual Convention and Exhibition. Campos and Espírito Santo basins, Brazil.

Zelt, C.A., Sain, K., Naumenko, J.V., Sawyer, D.S., 2003. Assessment of crustal velocity models using seismic refraction and reflection tomography. Geophys. J. Int. 153 (3), 609–626. http://dx.doi.org/10.1046/j.1365-246X.2003.01919.x.

Zhao, Z., Sun, Z., Wang, Z., Sun, Z., Liu, J., Wang, Z., Sun, L., 2013. The dynamic mechanism of post-rift accelerated subsidence in Qiongdongnan Basin, northern South China Sea. Mar. Geophys. Res. 34 (3–4), 295–308. http://dx.doi.org/10.1007/s11001-013-9188-2.

Zhu, B.-Q., Wang, H.-F., Chen, Y.-W., Chang, X.-Y., Hu, Y.-G., Xie, J., 2004. Geochronological and geochemical constraint on the Cenozoic extension of Cathaysian lithosphere and tectonic evolution of the border sea basins in East Asia. J. Asian Earth Sci. 24 (2), 163–175. http://dx.doi.org/10.1016/j.jseaes.2003.10.006.

Zuber, M.T., Parmentier, E.M., 1986. Lithospheric necking: a dynamic model for rift morphology. Earth Planet. Sci. Lett. 77 (3–4), 373–383. http://dx.doi.org/10.1016/0012-821X(86)90147-0.

Earth and Planetary Science Letters 420 (2015) 66–72

Contents lists available at ScienceDirect

Earth and Planetary Science Letters

www.elsevier.com/locate/epsl

Climate changes control offshore crustal structure at South China Sea continental margin

Peter D. Clift [a,*], Sascha Brune [b,c], Javier Quinteros [c]

[a] Department of Geology and Geophysics, Louisiana State University, Baton Rouge, LA 70803, USA
[b] EarthByte Group, School of Geosciences, University of Sydney, NSW 2006, Australia
[c] German Research Centre for Geosciences GFZ, 14473 Potsdam, Germany

ARTICLE INFO

Article history:
Received 6 November 2014
Received in revised form 12 March 2015
Accepted 15 March 2015
Available online 3 April 2015
Editor: A. Yin

Keywords:
South China Sea
tectonics
extension
erosion

ABSTRACT

Rifted continental lithosphere subsides as a consequence of combined crustal thinning and mantle lithosphere cooling yet basins on some continental margins experience anomalous subsidence events that postdate active extension. Deep basins on the northern margin of the South China Sea, notably the Baiyun Sag, show basement subsidence accelerating after ~21 Ma, postdating extension by several million years. We combine geophysical observations and numerical forward modeling to show that loading of the offshore basins by increased sediment flux caused by faster onshore erosion following Early Miocene monsoon intensification is a viable trigger for ductile flow after the cessation of active extension. This illustrates that offshore basin dynamics at continental margins with weak crust can be controlled by onshore surface processes in a newly recognized form of climate–tectonic coupling.

1. Introduction

Crustal thickness in rifted continental margins largely reflects the processes of extension that are driven by plate tectonic forces. Initial crustal thicknesses are reduced by extension during continental break-up, resulting in subsidence mostly due to isostatic compensation (McKenzie, 1978). However, in certain tectonic settings significant portions of the continental crust can act in a ductile fashion (Kruse et al., 1991; Wernicke, 1990), resulting in flow away from areas of thickened crust (Clark and Royden, 2000). A flattened Moho under some extensional terrains demonstrates that flow may be important in accommodating strain and that isostatic equilibrium is not always achieved in the asthenosphere (Zuber et al., 1986). In particular, areas with higher heatflow and thicker crust tend to exhibit significant viscous mechanical behavior below the crustal brittle–ductile transition (Block and Royden, 1990; Kruse et al., 1991; Zuber et al., 1986). In this study we model the importance of ductile flow during the break-up of the South China Sea (Fig. 1), whose affected crust originally located within a Mesozoic magmatic arc that began to extend no later than the Eocene (Franke et al., 2014; Morley, 2012), and culminating in seafloor spreading around 30 Ma (Barckhausen et al., 2014; Briais et al., 1993). We show that sediment loading caused by faster erosion onshore following the onset of wetter climatic conditions can result in thinning of the crust under super-deep offshore basins after the end of tectonic extension.

2. Geological setting

The South China Sea is the largest of a series of marginal seas fringing SE and Eastern Asia and whose development has variously been ascribed to plate tectonic forces related to subduction in Indonesia and the Pacific (Morley, 2002; Taylor and Hayes, 1983) and to the relative extrusion of Indochina as a rigid block away from the India–Eurasia collision zone (Peltzer and Tapponnier, 1988). Whatever the original cause of the extension a number of subbasins have formed on the margins of this oceanic tract and whose vertical tectonics does not follow standard models for continental extension.

Backstripping analysis has shown that the amount of subsidence observed along the northern margin of the South China Sea is much greater than that predicted from the degree of brittle upper crustal extension seen in seismic profiles (Clift et al., 2002; Davis and Kusznir, 2004). Some studies have argued that the additional subsidence is in part caused by the location of the South China Sea overlying a region of colder than normal mantle (Lithgow-Bertelloni and Gurnis, 1997), but other evidence suggests that such dynamic subsidence is <300 m in this area and cannot be responsible for short wavelength and/or rapid subsidence events (Petersen et al., 2010; Wheeler and White, 2002). If we are

* Corresponding author.
E-mail address: pclift@lsu.edu (P.D. Clift).

http://dx.doi.org/10.1016/j.epsl.2015.03.032
0012-821X/

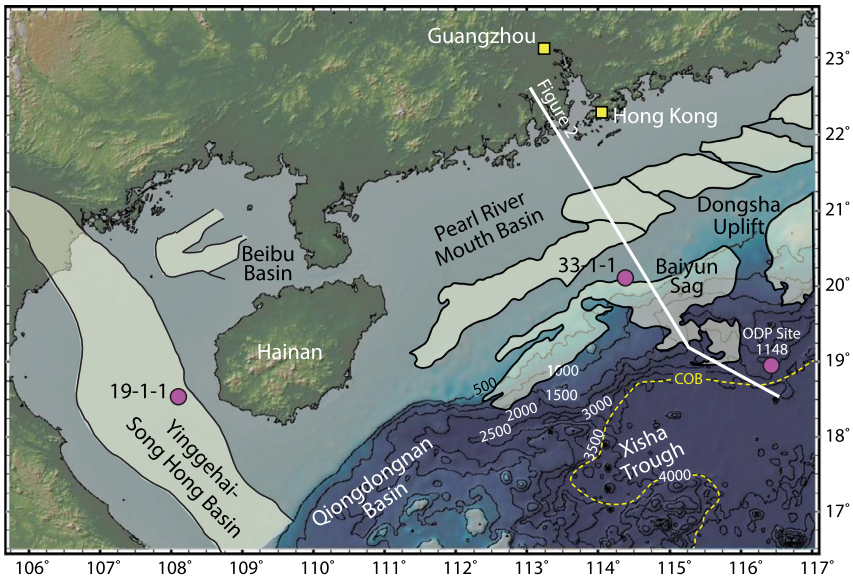

Fig. 1. Shaded bathymetric maps of the study area showing the location of features mentioned in the text. Light shaded areas show deeper areas of subsidence separated by structural highs.

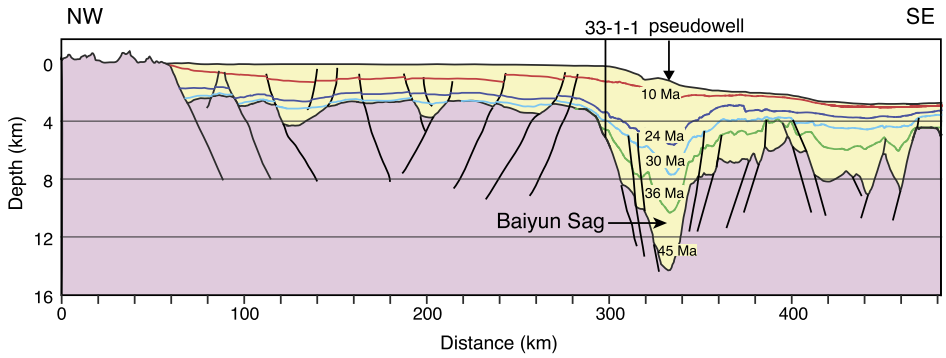

Fig. 2. Structural section across the South China margin and the Baiyun Sag compiled from Sun et al. (2008) and depth converted using drilling data from wells in the Pearl River Mouth Basin and stacking velocities from the central Baiyun Sag.

to explain the excess subsidence by crustal thinning then the extra attenuation must be assigned to the ductile part of the crust because the upper crust is well defined. Preferential lower crustal extension increases towards the continent–ocean boundary (COB) (Clift et al., 2002; Davis and Kusznir, 2004), consistent with ductile lower crustal flow from areas of thick crust towards zones of crustal thinning, as has been proposed for the Tibetan Plateau (Clark and Royden, 2000) and the rifts of the Basin and Range (Kruse et al., 1991; Zuber et al., 1986).

In order to assess the potential role of crustal flow in governing subsidence anomalies in the South China Sea we use a combination of reverse modeling of geologic data and finite element modeling to explore how post-rift subsidence can be accelerated.

3. Subsidence anomalies

A range of observations indicate anomalous subsidence at the northern continental margin of the South China Sea. In the Yinggehai–Song Hong pull-apart basin (YSHB), located to the west of Hainan Island (Fig. 1), a sharp increase in subsidence occurred at ~5 Ma (Fig. 3A) when there was very little brittle deformation (Clift and Sun, 2006). Moreover, the largest subsidence anomaly in the YSHB was spatially related to the region of fastest sedimentation, suggesting that the two might be linked. Mismatch between total subsidence and the observed degree of brittle extension is particularly noteworthy in some deep basins on the outer continental shelf, especially the Baiyun Sag (Fig. 1), where brittle faulting shows only modest degrees of horizontal extension (Sun et al., 2008; Zhao et al., 2011) (Fig. 2). In this case high degrees of crustal flow would be required to explain the total basin depths, regardless of when the extension occurred.

Analysis of tectonically driven basement motion in the Baiyun Sag accounts for sediment loading, sediment compaction and water depths of sedimentation. We applied standard backstripping methods (Sclater and Christie, 1980) to a “pseudowell” (i.e., a section which has not actually been drilled) in the center of Baiyun Sag, assuming local isostatic equilibrium in order to isolate the subsidence driven by tectonic processes. The greatest uncertainty is the assignment of palaeo-water depths of sedimentation. Modern water depths are ~1200 m in the basin center, but otherwise we follow the water depth reconstructions from a recent synthesis of drilling data (Xie et al., 2013). Well 33-1-1, which is positioned on the landward edge of the basin, is used for age control (Fig. 1; Table 1). This well is also used as a guide to lithological information, which is used to correct for the effects of sediment compaction.

Because Well 33-1-1 is located landward of the basin center we estimate that the sediment in the pseudowell would be slightly

Table 1
Age, depth and lithology data from Well 33-1-1, located at 20°5′16.7″, 114°22′21.6″ used for estimating age and lithology in the pseudowell section located in the axis of the Baiyun Sag basin.

Depth below sealevel (m)	Lithology			Water depths of sedimentation		
	Age (Ma)	Shale (%)	Siltstone (%)	Sandstone (%)	Maximum (m)	Minimum (m)
Panyu 33-1-1						
216	0	40	40	20	188	188
1029	5.5	40	40	20	200	75
1029	6.0	45	45	10	200	75
1488	11.3	40	40	20	100	75
2184	12.9	30	30	40	100	75
3115	21	30	30	40	50	0
3551	24.6	40	40	20	50	0
3860	26.5	40	40	20	50	−50
4213	38	10	10	80	25	−100
5100	50	Basement			0	0
Baiyun Sag Pseudowell						
1230	0	50	40	10	1230	1230
2390	10.5	50	40	10	1750	250
2890	12.5	50	40	10	1750	250
3410	13.8	50	40	10	1750	250
3650	15.5	50	40	10	1750	250
4020	16.5	50	40	10	1750	250
4380	17.5	50	40	10	1750	250
5630	21	50	40	10	100	0
7700	30	50	40	10	100	0
10 330	36	30	30	50	100	0
14 350	45	Basement			0	0

finer grained than that found at Well 33-1-1. Compared to water depth uncertainties moderate changes in the relative proportions of silt to shale that dominate the backstripped sections are insignificant as a source of uncertainty to the subsidence analysis. Well 33-1-1 reached basement at a depth of 5104 m below sealevel and accumulated a sandstone-dominated Eocene section, followed by a silty–muddy section of Oligocene which is still of fluvial–lacustrine facies. Marine sedimentation started in the Miocene and remained dominated by clayey siltstone throughout. A deepening to outer shelf and then upper slope conditions occurred in the Late Miocene (Table 1).

Most conceptual models predict a slowing of subsidence after the end of active extension, but on the South China margin subsidence accelerated ~4 m.y. after the end of brittle extension. Our backstripping of the Baiyun Sag shows that subsidence was rapid after ~21–24 Ma (Fig. 3B). In particular, water depths rapidly increased from shallow shelf to bathyal (>250 m) in the Early Miocene (24 and 21 Ma) (Fig. 3B) (Pang et al., 2009). The basin developed an unconformity at ~24 Ma. Older Oligocene sedimentary rocks are interpreted to be of lacustrine facies, at least at Well 33-1-1, meaning that the central Baiyun Sag was likely not deeper than shelf depths until 24 Ma, after which a major change occurred. Fast post-rift subsidence after 21 Ma generated ~1200 m of anomalous subsidence in Baiyun Sag (Xie et al., 2014) despite the lack of any evidence for synchronous faulting (Fig. 2). Analysis of seismic profiles has also identified a late stage of faster subsidence at 17 to 11 Ma (Chen, 2014), although the degree of brittle extension seen on reflection profiles was minimal at that time (Sun et al., 2008).

Fig. 3B compares the reconstructed subsidence with two theoretical curves based on a uniform extension model (McKenzie, 1978) and the assumption that rapid extension finished at 30 Ma, at the onset of seafloor spreading. The total amount of syn-rift subsidence was used to predict the amount of post-rift, thermal subsidence. The observed subsidence is far in excess of the prediction after 21 Ma requiring additional tectonism to account for the basin depth.

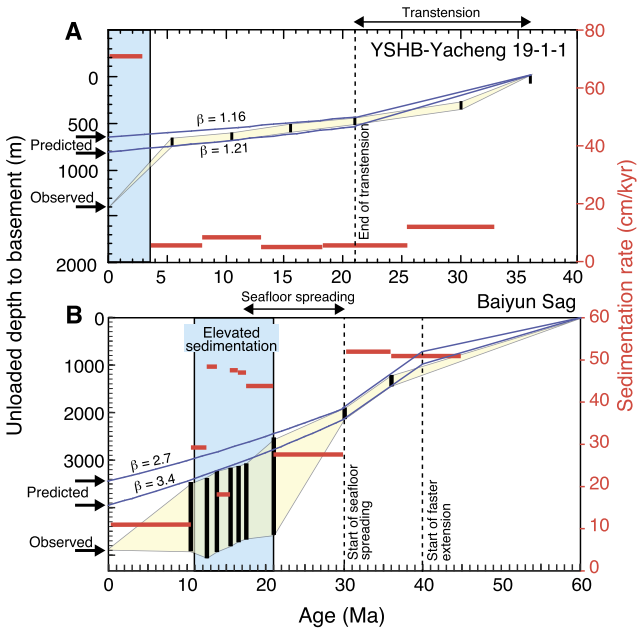

Fig. 3. Backstripped tectonic subsidence curve for two wells (A) Yacheng 19-1-1 in the YSHB (Clift and Sun, 2006), as well as (B) a pseudowell derived from seismic data and a nearby well from the Baiyun Sag. Vertical black bars indicate uncertainties in water depth of sedimentation, with yellow shading shows the range of basement depths through time. Each reconstruction is compared with maximum and minimum theoretical subsidence curves (dark blue) that are calculated from the amount of syn-rift subsidence. Arrows on the left of the figures show the modern day sediment unloaded depth to basement and the depth predicted from the syn-rift. (B) compares the Baiyun Sag with models with major extension ending at 30 Ma, at the start of seafloor spreading. Horizontal red bars indicate average rates of sedimentation and correspond to the scale on the right side of each figure. Light blue area shows timing of accelerated subsidence derived from regional seismic profiles (Chen, 2014).

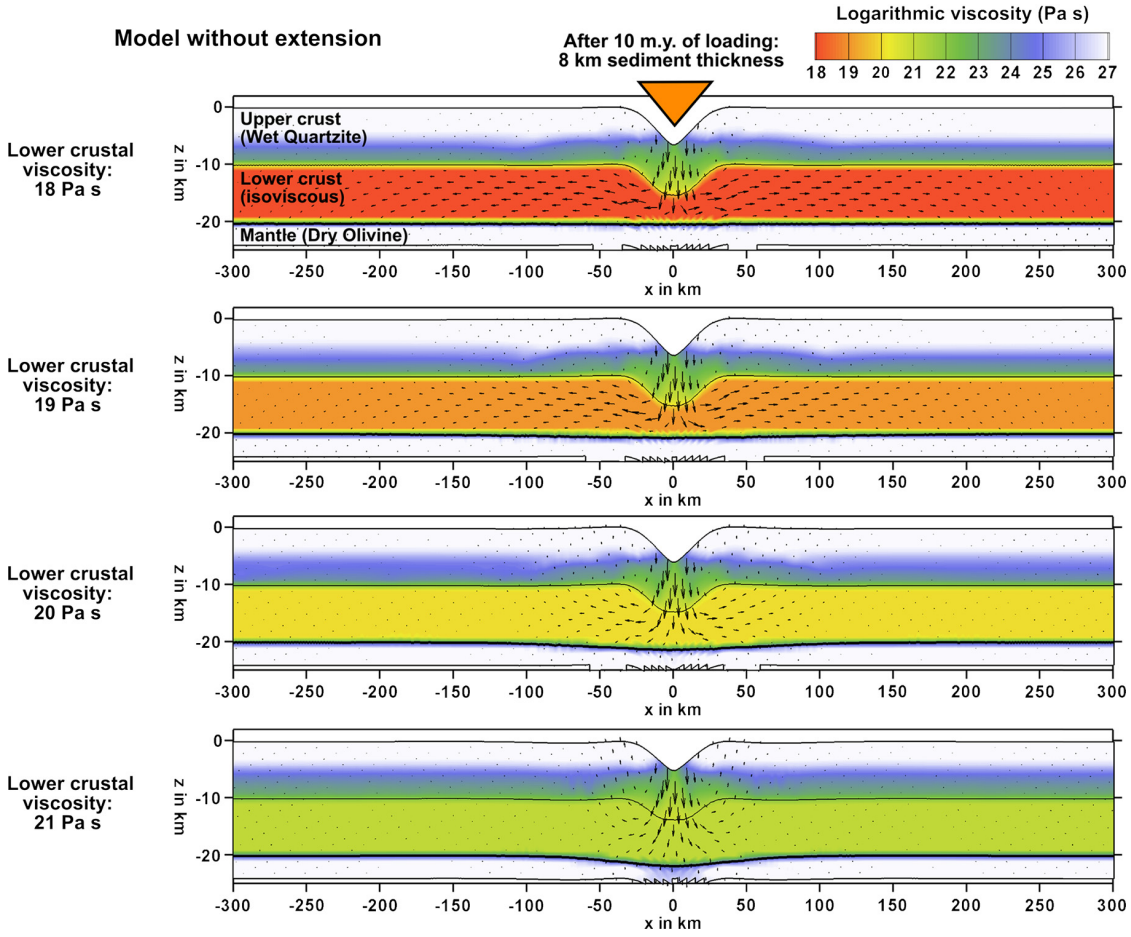

Fig. 4. Effect of lower crustal viscosity in the simplified model without extension. Images show crustal structure, logarithmic viscosities and material flow when the maximum sediment load is reached, 10 m.y. after sedimentation started. For weak lower crust, the load-induced vertical motion of the upper crust is translated to lower crustal flow, while for strong lower crust it leads to Moho subsidence. Lateral lower crustal flow can exceed 100 km if viscosity is sufficiently low.

4. Miocene climate change. Monsoon. Erosion and sedimentation

Here we argue that climatically modulated erosion is a viable mechanism for driving the sediment loading and crustal flow under the rifted margin during the Early and Middle Miocene. Although debate continues about the history of the East Asian Summer Monsoon, there is increasing evidence that initial intensification of this phenomenon began around the start of the Miocene, ~23 Ma. Changes in the flora of continental China (Sun and Wang, 2005) date from around this time and sedimentation rates across continental margins and deltas in South and SE Asia increased, as might be expected under the influence of heavier precipitation driving faster erosion in the source regions (Clift, 2006). Although it has been suggested that stronger monsoons might reduce erosion by encouraging greater vegetation growth (Castillo et al., 1997; Morgan, 2005) and that this in turn would impede erosion of soils, this reaction appears to mostly apply to semi-arid settings or mountain regions (Burbank et al., 2003), unlike the source regions of southern China. More recent evidence from modern river systems shows that precipitation is positively correlated with faster erosion and that this likely reflects the crucial role of rainfall in fostering landsliding, which is the most effective sediment producing process (Bookhagen et al., 2005). Recent analysis of the chemical weathering history in the South China Sea also supports increased weathering after ~23 Ma, consistent with an increase in humidity and seasonality under the influence of a strengthening monsoon (Clift et al., 2014; Wan et al., 2007). This monsoon is responsible for delivering extra sediment to the Pearl River offshore in the absence of major tectonic activity in the drainage basin at that time.

We discount tectonically driven rock uplift as a trigger for the faster erosion because active rifting is finished in the Pearl River Mouth Basin about around 25 Ma (Clift and Lin, 2001; Sun et al., 2008), so that the continental margin was a state of passive thermal subsidence at the time that the anomalous subsidence occurs. The headwater of the Pearl River today extend into the lower slopes of the Tibetan Plateau and there is evidence that some surface uplift was occurring in SW China at this time (Wang et al., 2012), which could be the trigger for an erosional pulse. However, drainage models for SE Asia suggest that the Pearl River basin was smaller than it is today at the time (Hoang et al., 2009) and since this pulse is something recognized in many basins across the region at this time (Clift, 2006), coincident with climate change, the most likely explanation for the faster sediment delivery is a climate trigger.

5. Numerical modeling

Using numerical forward modeling, we test under which circumstances monsoon induced sedimentation can lead to significant crustal thinning during the post-rift phase. This is accomplished using two model setups: a simple generic experiment (Fig. 4) and a more complex model setup accounting for the tectonic history of the South China Sea (Fig. 5). In both cases,

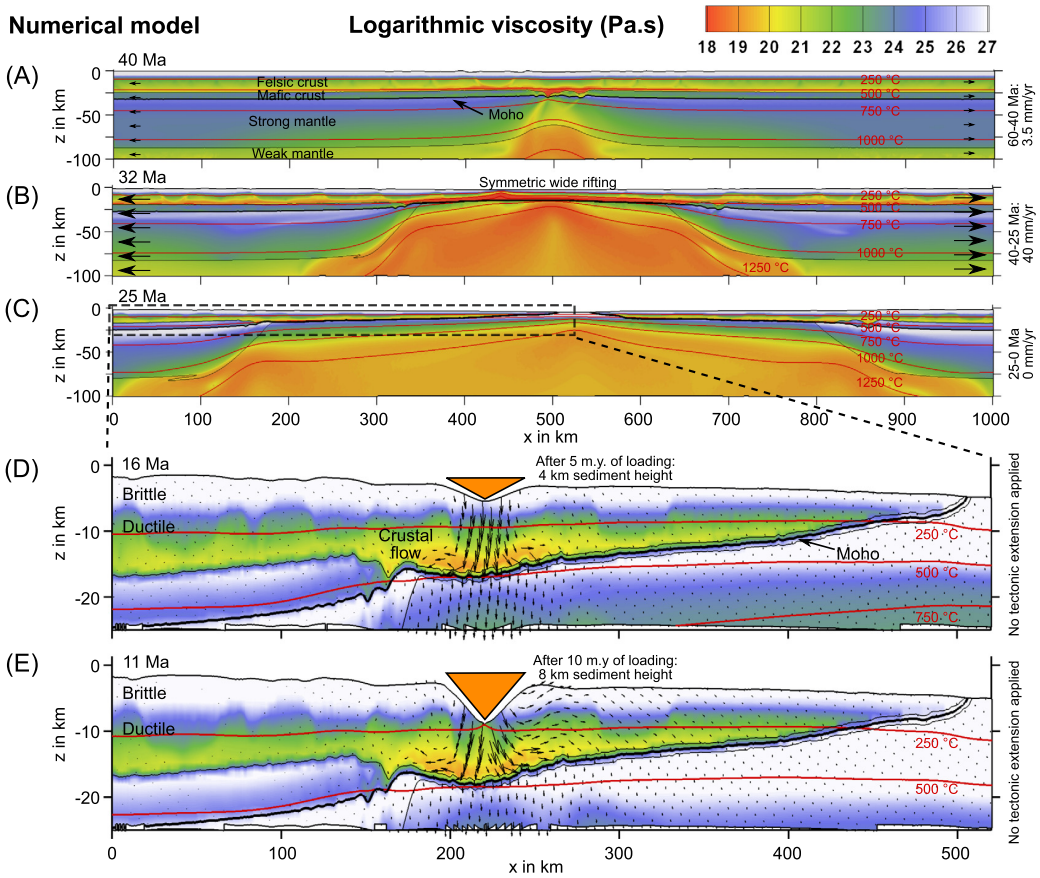

Fig. 5. Crustal structure, temperature, viscosity and direction of flow based on the numerical model as outlined in the text. Model has sediment loading starting at 21 Ma and increasing to full load until 11 Ma. Sediment distribution is indicated by orange triangle. (A)–(C) The weak crust decouples deformation of crust and mantle. A wide rift develops into two symmetric margins. (D)–(E) Post-breakup sediment loading is accommodated by lateral flow of the low-viscosity ($\sim 10^{19.5}$–10^{20} Pa s) crust.

we quantify how lower crustal flow accommodates strain in a sediment-loaded rifted margin setting. For simplicity, we approximate the sedimentation distribution of the Baiyun Sag basin through a triangular shape of 50 km width and 8 km height (orange triangle in Figs. 4 and 5). Assuming a constant sedimentation rate, the sediment thickness increases linearly from zero to 8 km within 10 m.y. Instead of introducing sediments as a proper material phase, we prescribe a local boundary stress corresponding to the triangular sediment distribution. This procedure robustly incorporates the effect of a space- and time-dependent sediment load on the crystalline basement, even though the internal structure of the sediments is not resolved. We account for thermal insulation of the sediments by correlating model surface temperature with sediment thickness through a constant thermal gradient of 30 °C/km, which yields a final peak temperature of 250 °C at the bottom of the basin.

The applied numerical finite-element code is a two-dimensional version of the thermo-mechanical forward modeling software SLIM3D (Popov and Sobolev, 2008). The elasto–visco–plastic model allows to address a wide range of rift-related deformation processes such as flexure, lower crustal flow, and faulting (Brune, 2014; Brune et al., 2014). Details on the numerical, thermal, and rheological setup including all model parameters are given in the Supporting Information.

First we conduct a simple experiment without extension. A laterally homogeneous lithosphere with two crustal and a mantle layer is exposed to the aforementioned time-dependent sediment load. The lower crust has a prescribed viscosity while the upper crustal and mantle layer deform via a laboratory-derived wet quartzite and dry olivine flow law involving temperature- and stress-dependent viscosity. Fig. 4 shows the flow field of four models with different lower crustal viscosities of 18 to 21 Pa s after 10 m.y. of continuous sedimentation. For the weakest lower crust (10^{18} Pa s), all vertical surface motion is compensated by lower crustal flow. The Moho discontinuity remains flat and no elastic bulge occurs adjacent to the load. In this model the distance at which lateral crustal flow takes place is limited by the left and right model boundary. For a crustal viscosity of 10^{19} Pa s, the result is nearly identical. Note that analytical estimates of crustal viscosity in the South China Sea (Clift et al., 2002) based on regional slope range between 10^{18} and 10^{19} Pa s. With a viscosity of 10^{20} Pa s, lateral flow occurs within a distance of about 75 km to each side of the load. Within the same distance, a small amount of Moho subsidence can be observed. For a high viscosity of 10^{21} Pa s, lateral flow does not exceed 50 km distance from the load center and is compensated by Moho subsidence. Additionally, upward directed flow occurs throughout the crust in close proximity to the loading area leading to surface uplift.

We extend the previous model accounting for the tectonic environment of the South China Sea and by using temperature- and stress-dependent viscosity in all layers. In order to reproduce the time-dependent structure of the northern margin of the South China Sea we model the entire rift process by applying extensional velocities at the lateral boundaries of an initially layered setup. Based on a recent plate tectonic reconstruction (Zahirovic et al., 2014), we approximate the kinematic evolution of the South China Sea extension in a three-stage history: (i) Full extension velocities of 3.5 mm/yr between 60 Ma and 40 Ma, (ii) 40 mm/yr

between 40 Ma and 25 Ma, and (iii) after 25 Ma, the rifted margin remains without extension, although we recognize that there has been small degrees of extension of the shelf since that time (Lüdmann and Wong, 1999). Ongoing debate about the timing of seafloor spreading (Chang et al., 2015) do not affect the mode because all model agree that the passive margin was in a state of passive subsidence at the point and our model is not sensitive to the rate of seafloor spreading in the basin center at this time. The initial configuration has a 25-km-thick felsic upper crust, an 8-km-thick mafic lower crust, a sub-continental lithospheric mantle that extends down to 90 km and weak asthenospheric mantle below. Sediment loading starts at 21 Ma and increases linearly to full load until 11 Ma.

The model reproduces wide rifting where felsic crustal viscosities as low as 10^{18} Pa s decouple crust and mantle deformation, which ultimately generates two wide, symmetric margins with low topographic gradients, such as observed in this region (Clift et al., 2002). Enhanced sediment loading reminiscent of the Baiyun Sag basin (orange triangle in Fig. 5) commences during the post-rift phase. At this time, self-consistently evolving viscosities in the area of sedimentation range between $10^{19.5}$ Pa s and 10^{20} Pa s. In agreement with the simplified model set-up presented above, lateral flow occurs within a distance of more than 50 km from the loading site. This flow effectively thins the crust and compensates the surface subsidence with only minor Moho deflection.

6. Role of crustal flow

Although there is common understanding that post-rift subsidence acceleration has occurred in the South China Sea, there is little agreement about what caused this. Some have suggested that subsidence could be caused by emplacement of a dense intrusive body into the lower crust at ~17 Ma (Shi et al., 2005; Xie et al., 2006), followed by thermal cooling. However, magmatic thickening of crust results in uplift rather than subsidence, e.g., North Atlantic Tertiary (Brodie and White, 1994). Only if gabbroic melt is trapped at >50 km in the lithosphere and eclogitized then it may have potential to drive local subsidence (Hall and White, 1994). In any case no strong evidence exists to support intrusive magmatism into the base of the Baiyun Sag at 17 Ma, beyond some poorly defined seismic reflections in the lower crust in that region, but precisely what these represent is unknown.

Our finite element model indicates that rapid subsidence after 21 Ma reflects the influence of ductile flow in the post-rift period. As with the Plio-Pleistocene in the YSHB, the Early Miocene in the South China Sea is associated with faster sediment delivery to offshore basins (Clift, 2006; Xie et al., 2013) driven by a change to a more erosive, monsoonal climate around that time (Clift et al., 2014; Sun and Wang, 2005). In the Malay Basin a combination of onshore erosion and offshore sedimentation resulted in a reverse flow of ductile lower crust away from the basin center and toward the continental margin after the end of extension (Morley and Westaway, 2006). This requires the flow of crust towards regions of thicker crust, which is only explicable when understood as a readjustment from one state of stability (with thick crust under the margin and thin sediment offshore) to another (with thinner crust onshore and a thicker sediment load offshore). Removal of rock from onshore by erosion results in isostatic uplift, while at the same time increasing loads in the offshore act to change the pressure gradient across the coast, driving ductile material away from the basin axis and towards the continental interior. Net flow is still from thick to thin crustal regions achieved during active extension.

This process may be understood by considering where isostatic equilibrium is achieved. Mid crustal viscosity estimates based on the regional slope on the margin basement range from 10^{19} to 10^{18} Pa s within a hypothetical 5 km-wide mid crustal channel (Clift et al., 2002). While the lithosphere is generally estimated to have a viscosity of 10^{23} Pa s, the asthenosphere can have values of 10^{19} Pa s or lower, depending on water contents and temperature (Doglioni et al., 2011). These values overlap with those from the lower crust in South China and raise the possibility that loads on the continental margin might be compensated within the crust rather than on the lithospheric scale. We argue, based on the finite element modeling that loading of the continental margin during the Early Miocene drove the flow of ductile crust away from the basin axis, largely northwards under the Chinese margin, as first argued by Westaway (1994). Southward flow is impossible because the southern edge of Baiyun Sag abuts the oceanic, and therefore rigid, crust of the deep South China Sea.

Lateral crustal flow is a consequence of the weakness of the crust, caused by high heatflow, a weak quartz-rheology and is triggered by sediment loading. This type of deformation would not be anticipated in rifted margins where heatflow was low or little sedimentation was occurring. This is a new form of climate–tectonic interaction in which weak crust affected by extension can continue to deform and flow in the post-rift period as a result of changing erosion rates on the basin flanks delivering increased sediment loads to the basin center and altering the crustal structure offshore. We suggest that super-deep rift basins, like Baiyun Sag, are likely often linked to the flow of ductile crust in this fashion and would not be expected in cooler rift settings, such as found along the Atlantic margins.

7. Conclusions

Subsidence anomalies have been identified on continental margins in different parts of the world and of different ages, yet those of the South China Sea are of especially large magnitude and cannot be linked to many of the common cited processes, such as magmatic underplating or mantle circulation. We propose that flow of ductile mid and lower crust, inherited from an earlier phase of active margin magmatism, is the cause of this subsidence. While this crust flows towards the rift axis during break-up, causing an earlier phase of excess subsidence compared to the amount of brittle faulting, the flow reverses during the Early Miocene as a strengthening summer monsoon increased continental erosion and rapidly loaded the deep sub-basins on the margin with several kilometers of material. Numerical modeling shows that emplacement of such a load has the potential to drive flow away from the basin center and decrease the thickness of crystalline crust in the offshore. This is a newly recognized form of climate–tectonic interaction that might be recognized in any thermally juvenile continental margin that is subject to a strong erosional flux. Since monsoon-modulated erosion increased across the whole of SE Asia in the Early Miocene such subsidence pulses may be predicted in other Asian marginal basins at the same time, where sedimentation rates spike (Clift, 2006). This not only has implications for crustal structure in rifted margins but also for hydrocarbon exploration because simple measurement of extension factor based on modern basement depths will provide an inappropriate model of the thermal evolution.

Acknowledgements

P.C. thanks Chris Morley for discussing these topics and for support from the Charles T. McCord chair at LSU. S.B. has been funded by the European Research Council, Marie Curie International Outgoing Fellowship (Project 326115) and by SAMPLE (South Atlantic Margin Processes and Links with onshore Evolution), the German Research Foundation Priority Program 1375. J.Q. has been partially

funded by the Helmholtz Association as Head of a Helmholtz International Research Group (HIRG-008).

Appendix A. Supplementary material

Supplementary material related to this article can be found online at http://dx.doi.org/10.1016/j.epsl.2015.03.032.

References

Barckhausen, U., Engels, M., Franke, D., Ladage, S., Pubellier, M., 2014. Evolution of the South China sea: revised ages for breakup and seafloor spreading. Mar. Pet. Geol. http://dx.doi.org/10.1016/j.marpetgeo.2014.02.022.

Block, L., Royden, L.H., 1990. Core complex geometries and regional scale flow in the lower crust. Tectonics 9, 557–567.

Bookhagen, B., Thiede, R.C., Strecker, M.R., 2005. Late quaternary intensified monsoon phases control landscape evolution in the northwest Himalaya. Geology 33 (2), 149–152.

Briais, A., Patriat, P., Tapponnier, P., 1993. Updated interpretation of magnetic anomalies and seafloor spreading stages in the South China Sea: implications for the Tertiary tectonics of Southeast Asia. J. Geophys. Res. 98, 6299–6328.

Brodie, J., White, N., 1994. Sedimentary basin inversion caused by igneous underplating: Northwest European continental shelf. Geology 22, 147–150.

Brune, S., 2014. Evolution of stress and fault patterns in oblique rift systems: 3-D numerical lithospheric-scale experiments from rift to breakup. Geochem. Geophys. Geosyst. 15, 3392–3415.

Brune, S., Heine, C., Perez-Gussinye, M., Sobolev, S.V., 2014. Rift migration explains continental margin asymmetry and crustal hyper-extension. Nat. Commun. 5 (4014). http://dx.doi.org/10.1038/ncomms5014.

Burbank, D.W., Blythe, A.E., Putkonen, J., Pratt-Sitaula, B., Gabet, E., Oskins, M., Barros, A., Ojha, T.P., 2003. Decoupling of erosion and precipitation in the Himalayas. Nature 426, 652–655.

Castillo, V.M., Martinez-Mena, M., Albaladejo, J., 1997. Runoff and soil loss response to vegetation removal in a semiarid environment. Soil Sci. Soc. Am. J. 61, 1116–1121.

Chang, J.-H., Lee, T.-Y., Hsu, H.-H., Liu, C.-S., 2015. Comment on Barckhausen et al., 2014 – Evolution of the South China Sea: revised ages for breakup and seafloor spreading. Mar. Pet. Geol. 59, 676–678.

Chen, L., 2014. Stretching factor estimation for the long-duration and multi-stage continental extensional tectonics: application to the Baiyun Sag in the northern margin of the South China Sea. Tectonophysics 611, 167–180.

Clark, M.K., Royden, L.H., 2000. Topographic ooze: building the eastern margin of Tibet by lower crustal flow. Geology 28, 703–706.

Clift, P., Lin, J., 2001. Preferential mantle lithospheric extension under the South China margin. Mar. Pet. Geol. 18 (8), 929–945.

Clift, P., Lin, J., Barckhausen, U., 2002. Evidence of low flexural rigidity and low viscosity lower continental crust during continental break-up in the South China Sea. Mar. Pet. Geol. 19 (8), 951–970.

Clift, P.D., 2006. Controls on the erosion of Cenozoic Asia and the flux of clastic sediment to the ocean. Earth Planet. Sci. Lett. 241 (3–4), 571–580.

Clift, P.D., Sun, Z., 2006. The sedimentary and tectonic evolution of the Yinggehai–Song Hong Basin and the southern Hainan margin, South China Sea; implications for Tibetan uplift and monsoon intensification. J. Geophys. Res. 111 (B6), 28.

Clift, P.D., Wan, S., Blusztajn, J., 2014. Reconstructing chemical weathering, physical erosion and monsoon intensity since 25 Ma in the northern South China Sea: a review of competing proxies. Earth-Sci. Rev. 130, 86–102.

Davis, M., Kusznir, N.J., 2004. Depth-dependent lithospheric stretching at rifted continental margins. In: Karner, G.D. (Ed.), Proceedings of NSF Rifted Margins Theoretical Institute. Columbia University Press, New York, pp. 92–136.

Doglioni, C., Ismail-Zadeh, A., Panza, G., Riguzzi, F., 2011. Lithosphere–asthenosphere viscosity constrast and decoupling. Phys. Earth Planet. Inter. 189 (1–2), 1–8.

Franke, D., Savva, D., Pubellier, M., Steuer, S., Mouly, B., Auxietre, J.-L., Meresse, F., Chamot-Rooke, N., 2014. The final rifting evolution in the South China Sea. Mar. Pet. Geol. 58B, 704–720. http://dx.doi.org/10.1016/j.marpetgeo.2013.11.020.

Hall, B.D., White, N., 1994. Origin of anomalous Tertiary subsidence adjacent to North Atlantic continental margins. Mar. Pet. Geol. 11 (6), 702–714.

Hoang, L.V., Wu, F.Y., Clift, P.D., Wysocka, A., Swierczewska, A., 2009. Evaluating the evolution of the Red River system based on in-situ U–Pb dating and Hf isotope analysis of zircons. Geochem. Geophys. Geosyst. 10, Q11008.

Kruse, S., McNutt, M.K., Phipps-Morgan, J., Royden, L., Wernicke, B.P., 1991. Lithospheric extension near Lake Mead, Nevada; a model for ductile flow in the lower crust. J. Geophys. Res. 96 (3), 4435–4456.

Lithgow-Bertelloni, C., Gurnis, M., 1997. Cenozoic subsidence and uplift of continents from time-varying dynamic topography. Geology 25, 735–738.

Lüdmann, T., Wong, H.K., 1999. Neotectonic regime on the passive continental margin of the northern South China Sea. Tectonophysics 311, 113–138.

McKenzie, D.P., 1978. Some remarks on the development of sedimentary basins. Earth Planet. Sci. Lett. 40, 25–32.

Morgan, R.P.C., 2005. Soil Erosion and Conservation. Blackwell, Oxford. 325 pp.

Morley, C.K., 2002. A tectonic model for the Tertiary evolution of strike-slip faults and rift basins in SE Asia. Tectonophysics 347 (4), 189–215.

Morley, C.K., Westaway, R., 2006. Subsidence in the super-deep Pattani and Malay basins of Southeast Asia: a coupled model incorporating lower-crustal flow in response to post-rift sediment loading. Basin Res. 18, 51–84.

Morley, C.K., 2012. Late Cretaceous–Early Palaeogene tectonic development of SE Asia. Earth-Sci. Rev. 115 (1), 37–75.

Pang, X., Chen, C., Zhu, M., He, M., Shen, J., Lian, S., Wu, X., Shao, L., 2009. Baiyun movement: a significant tectonic event on Oligocene/Miocene boundary in the Northern South China Sea and its regional implications. J. Earth Sci. 20 (1), 49–56.

Peltzer, G., Tapponnier, P., 1988. Formation and evolution of strike-slip faults, rifts, and basins during the India–Asia Collision: an experimental approach. J. Geophys. Res. 93, 15085–15117.

Petersen, K.D., Nielsen, S.B., Clausen, O.R., Stephenson, R., Gerya, T., 2010. Small-scale mantle convection produces stratigraphic sequences in sedimentary basins. Science 329, 827–830.

Popov, A.A., Sobolev, S.V., 2008. SLIM3D: a tool for three-dimensional thermo mechanical modeling of lithospheric deformation with elasto–visco–plastic rheology. Phys. Earth Planet. Inter. 171, 55–75.

Sclater, J.G., Christie, P.A.F., 1980. Continental stretching: an explanation of the post Mid-Cretaceous subsidence of the central North Sea basin. J. Geophys. Res. 85, 3711–3739.

Shi, X., Burov, E., Leroy, S., Qiu, X., Xia, B., 2005. Intrusion and its implication for subsidence: a case from the Baiyun Sag, on the northern margin of the South China Sea. Tectonophysics 407 (1–2), 117–134.

Sun, X., Wang, P., 2005. How old is the Asian monsoon system? Palaeobotanical records from China. Palaeogeogr. Palaeoclimatol. Palaeoecol. 222 (3–4), 181–222.

Sun, Z., Zhong, Z., Zhou, D., Pang, X., Huang, C.C., Chen, C., He, M., Xu, H., 2008. Dynamics analysis of the Baiyun Sag in the Pearl River Mouth Basin. North of the South China Sea. Acta Geol. Sin. 82 (1), 73–83.

Taylor, B., Hayes, D.E., 1983. Origin and history of the South China Sea basin. In: Hayes, D.E. (Ed.), The Tectonic and Geologic Evolution of the Southeast Asian Seas and Islands. American Geophysical Union, Washington, DC, pp. 23–56.

Wan, S., Li, A., Clift, P.D., Stuut, J.-B.W., 2007. Development of the East Asian monsoon: mineralogical and sedimentologic records in the northern South China Sea since 20 Ma. Palaeogeogr. Palaeoclimatol. Palaeoecol. 254 (3–4), 561–582.

Wang, E., Kirby, E., Furlong, K.P., Soest, M.v., Xu, G., Shi, X., Kamp, P.J.J., Hodges, K.V., 2012. Two-phase growth of high topography in eastern Tibet during the Cenozoic. Nat. Geosci. 5, 640–645.

Wernicke, B.P., 1990. The fluid crustal layer and its implications for continental dynamics. In: Salisbury, M.H., Fountain, D.M. (Eds.), Exposed Cross-Sections of the Continental Crust. In: NATO ASI Series. Kluwer Academic Publishers, Dordrecht, The Netherlands, pp. 509–544.

Westaway, R., 1994. Re-evaluation of extension across the Pearl River Mouth Basin, South China Sea: implications for continental lithosphere deformation mechanisms. J. Struct. Geol. 16, 823–838.

Wheeler, P., White, N., 2002. Measuring dynamic topography: an analysis of Southeast Asia. Tectonics 21 (5), 1040.

Xie, X.N., Müller, R.D., Li, S.T., Gong, Z.S., Steinberger, B., 2006. Origin of anomalous subsidence along the Northern South China Sea margin and its relationship to dynamic topography. Mar. Pet. Geol. 23 (7), 745–765.

Xie, H., Zhou, D., Pang, X., Li, Y., Wu, X., Qiu, N., Li, P., Chen, G., 2013. Cenozoic sedimentary evolution of deepwater sags in the Pearl River Mouth Basin, northern South China Sea. Mar. Geophys. Res. 34, 159–173. http://dx.doi.org/10.1007/s11001-013-9183-7.

Xie, H., Zhou, D., Li, Y., Pang, X., Li, P., Chen, G., Li, F., Cao, J., 2014. Cenozoic tectonic subsidence in deepwater sags in the Pearl River Mouth Basin, northern South China Sea. Tectonophysics 615–616, 182–198.

Zahirovic, S., Seton, M., Müller, R.D., 2014. The Cretaceous and Cenozoic tectonic evolution of Southeast Asia. Solid Earth Discuss. 5, 227–273.

Zhao, Z.X., Sun, Z., Xie, H., Yan, C.Z., Li, Y.P., 2011. Cenozoic subsidence and lithospheric stretching deformation of the Baiyun deepwater area. Chin. J. Geophys. 54 (6), 1159–1166.

Zuber, M.T., Parmentier, E.M., Fletcher, R.C., 1986. Extension of continental lithosphere: a model for two scales of basin and range deformation. J. Geophys. Res. 91, 4826–4838.

LETTER

doi:10.1038/nature18319

Abrupt plate accelerations shape rifted continental margins

Sascha Brune[1,2], Simon E. Williams[2], Nathaniel P. Butterworth[2] & R. Dietmar Müller[2]

Rifted margins are formed by persistent stretching of continental lithosphere until breakup is achieved. It is well known that strain-rate-dependent processes control rift evolution[1,2], yet quantified extension histories of Earth's major passive margins have become available only recently. Here we investigate rift kinematics globally by applying a new geotectonic analysis technique to revised global plate reconstructions. We find that rifted margins feature an initial, slow rift phase (less than ten millimetres per year, full rate) and that an abrupt increase of plate divergence introduces a fast rift phase. Plate acceleration takes place before continental rupture and considerable margin area is created during each phase. We reproduce the rapid transition from slow to fast extension using analytical and numerical modelling with constant force boundary conditions. The extension models suggest that the two-phase velocity behaviour is caused by a rift-intrinsic strength–velocity feedback, which can be robustly inferred for diverse lithosphere configurations and rheologies. Our results explain differences between proximal and distal margin areas[3] and demonstrate that abrupt plate acceleration during continental rifting is controlled by the nonlinear decay of the resistive rift strength force. This mechanism provides an explanation for several previously unexplained rapid absolute plate motion changes, offering new insights into the balance of plate driving forces through time.

Rifted continental margins, with an overall length of more than 100,000 km, are the longest tectonic features on our planet, two times longer than spreading ridges or convergent plate boundaries. During formation of rifted margins, new continental surface area is generated by normal faulting and volcanic intrusions. Both processes are dependent on extension velocity, which governs the thermal configuration of the rift and hence the depth of the brittle–ductile transition and the length of normal faults[1], as well as the degree of decompression melting and serpentinization[4]. Moreover, rift velocity has been shown to control rift symmetry and the formation of hyper-extended crust[5].

Quantifying the history of extension velocity at rifted margins requires knowledge of the motions between diverging plates and of the timing of continental breakup. Recently, revised regional syn-rift plate models for the opening of the Atlantic, South China Sea, Gulf of California and Australia–Antarctica rifting have become available (see Supplementary Table 1). Here, we incorporate these regional studies in a global plate kinematic model[6] and use an updated, simplified global set of boundaries between continental and oceanic crust (COBs) to explore continental breakup processes. We exploit the fact that in a pre-rift reconstruction, present-day COBs from conjugate passive margins will show substantial overlap, since the plate tectonic models do not explicitly incorporate lithospheric deformation. As the plates move apart the overlap decreases, and the time when conjugate COBs disconnect defines breakup, the transition from rifting to sea-floor spreading (Fig. 1).

We extracted the local rift velocity via pyGPlates, a novel Python library that allows script-based access to the plate reconstruction software GPlates. We subdivided each COB in segments of ~50 km length, and computed the relative velocity between the two contributing plates at each segment (Fig. 1c). First we address the question of whether there is a systematic trend in the temporal evolution of extension velocity within entire rift systems. We visualize the velocity evolution of the rift system in a single diagram by displaying the integrated rift axis length of all segments that deform within a certain velocity range in 1 million year (Myr) time intervals (Fig. 1d). We discarded any segment where breakup is accomplished, that is, where COBs do not overlap anymore. Hence, the analysed plate boundary length declines through time (see dashed grey line in Fig. 1e) and reduces to zero at final continental separation. We explicitly excluded failed rifts from our analysis, because they do not contribute to passive margin formation.

In addition to rift velocity we computed the rate of rifted margin formation, that is, the product of the extension velocity and the velocity-orthogonal length of each COB segment. Integration along both conjugate margins and division by 2 yields the overall rate of rifted margin formation F. The formation rate F increases with extension velocity and decreases when individual segments are discarded during diachronous breakup (Fig. 1e). Note that F is independent of the distance between hinge line and COB, instead representing the newly created margin surface. This allows us to draw robust conclusions on rifted margin growth as no assumptions about previous rift phases, or initial crustal and lithospheric thickness have to be made.

With a rift length of more than 10,000 km, the South Atlantic Rift (Fig. 1) generated 2.1×10^6 km^2 of rifted margin area, more than any other Phanerozoic continental rift. During the first 25 Myr of extension, the Euler pole is located close to the equatorial Atlantic Rift[7,8]; therefore rifting is faster in the southern South Atlantic. The mean rift velocity remains relatively low (<10 mm yr^{-1}, full rate) until it increases rapidly to more than 35 mm yr^{-1} within 6 Myr. This speed-up at ~126–120 Myr ago coincides with severe loss of strength in the equatorial Atlantic Rift[9], suggesting rift weakening as a controlling parameter. Both rift phases shape the rifted margins: about one-third of the South Atlantic margin area was formed during the slow, and two-thirds during the fast phase (Fig. 1e).

This two-phase velocity history is a common feature of many other rift systems, illustrated for the central North Atlantic, North America–Iberia, Australia–Antarctica and South China Sea rifting in Fig. 2 and for the Gulf of California, the northeast Atlantic and North America–Greenland in Extended Data Figs 3 and 4. Consistently, the fast rift phase starts ~10 Myr before inception of breakup and persists until plate separation is complete. Both the slow and the fast phase contribute markedly to shaping the rifted margins. All regional tectonic reconstructions used here, compiled from a range of independent studies, result in the same two-phase pattern, underlining the robustness of our results. Moreover, using alternative reconstructions for the South Atlantic does not change our conclusions (Extended Data Fig. 8).

We conducted robustness tests for all case studies using alternative COBs defined by the extreme landward limit of basement that is not clearly continental crust. These COB polygons are located closer to the coastline, which shortens the duration of rifting by several million

[1]GFZ German Research Centre for Geosciences, Telegrafenberg, 14473 Potsdam, Germany. [2]EarthByte Research Group, School of Geosciences, 2006 University of Sydney, Sydney, Australia.

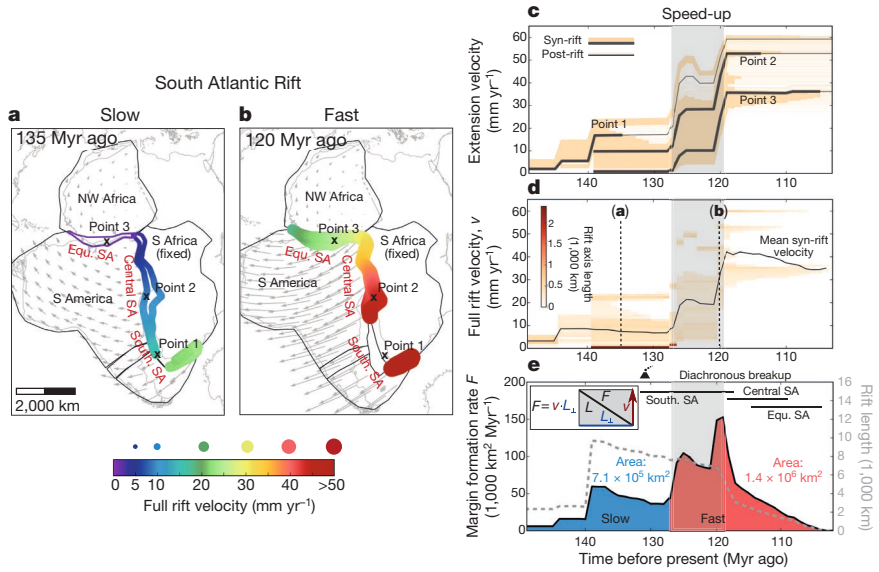

Figure 1 | Rift velocity evolution of the South Atlantic. a, **b**, Rift velocities (coloured circles) are evaluated at overlapping plate polygons (black) with rift-ward polygon boundaries being defined through present-day COBs. Central SA, Central South Atlantic; Equ. SA, equatorial South Atlantic; NW Africa, Northwest Africa; S Africa, South Africa; S America, South America; South. SA, southern South Atlantic. **c**, Extension velocity evolution of all rift points showing the syn-rift and post-rift phase (thick and thin lines, respectively). **d**, Frequency of syn-rift velocities in terms of rift axis length. Colours display the integrated length of all rift segments deforming at the same velocity. The black line shows mean velocity of all syn-rift segments. The fast rift phase starts ~126 Myr ago. **e**, The margin formation rate F at each rift segment of length L is computed by multiplying rift velocity v and velocity-orthogonal length of the segment $L_\perp$. Total rift length is shown as grey dashed line. Timing of Paraná–Etendeka flood basalts is depicted by volcano symbol. Black horizontal bars indicate diachronous breakup. For an animation of the kinematic evolution, see Supplementary Video 1.

years. Nevertheless, the contributions of both phases in shaping the rifted margins remain substantial (Extended Data Figs 5 and 6).

To evaluate the geodynamic response of a rift zone to plate driving forces, we used two-dimensional analytical and numerical models. While the most common modelling approach is to prescribe a constant velocity at the model boundary[5,10], here we use a force boundary condition[11–13] allowing for self-consistent computation of velocity evolution. The force boundary condition is applicable to major rifts where the integrated strength of the entire rift system is comparable to the plate driving forces, such as those considered here.

First, we developed an analytical model of a homogeneous lithospheric layer that deforms according to power law rheology under a constant force. For simplicity, we neglect depth-dependent thinning, non-constant temperature and compressibility; however, these processes are incorporated within the numerical models described later. The resulting velocity is $v = L/(n\,t_r) \times (1 - t/t_r)^{-1}$, where L is the width of the necking zone, n the dislocation creep stress-exponent, t_r the duration of rifting and t is time (see Methods for derivation). The formula is plotted in Fig. 3c using typical parameter values of $L = 100$ km and $t_r = 20$ Myr. Realistic values[14] for n range between 3 and 4, hence we approximate a purely viscous lithosphere by $n = 3.5$ (model A1). Introducing brittle failure as a highly nonlinear end-member of power law creep[12], we also show solutions for $n = 10$ (model A2) and $n = 30$ (model A3). In all cases, rifting commences slowly, yet velocities increase within a few million years, where the short duration of speed-up is caused by the power law rheology of the lithosphere.

Numerical modelling accounts for more realistic evolution of deformation, temperature and buoyancy, but the resulting velocity evolution is very similar to the analytical solution (Fig. 3c). The reason for the acceleration is a feedback mechanism that we term dynamic rift weakening: as long as the rift is strong, the extension rate is low (Fig. 3a), but with continued deformation the rift centre becomes successively weaker due to necking and strain softening (Fig. 3b). Loss of strength accelerates rifting, which results in new strength loss

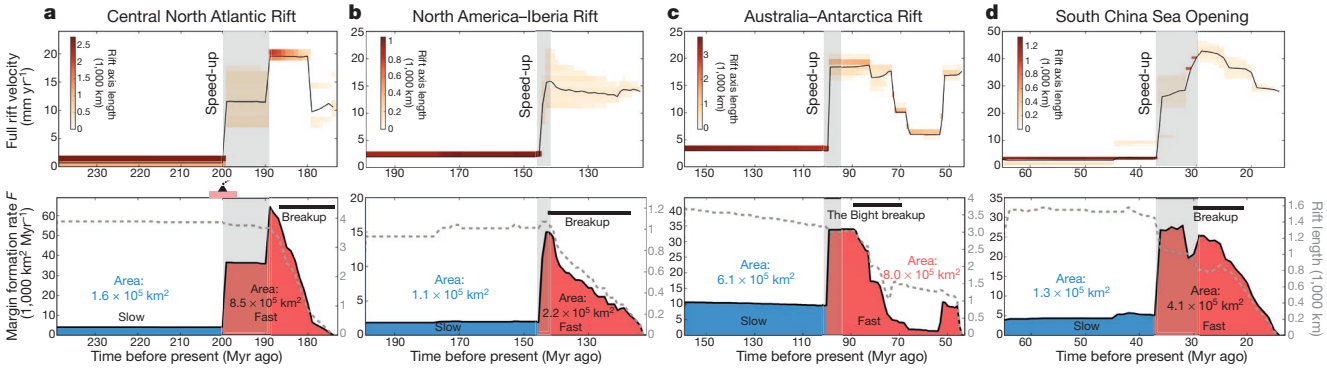

Figure 2 | Other rift systems. a–**d**, All depicted rifts exhibit a two-phase velocity history. A rapid plate acceleration precedes inception of breakup by ~10 Myr. Timing of Central Atlantic Magmatic Province is depicted by volcano symbol in **a**. Corresponding map views are shown in Extended Data Figs 1–3. For an animation of each rift kinematic evolution, see Supplementary Videos 2–5.

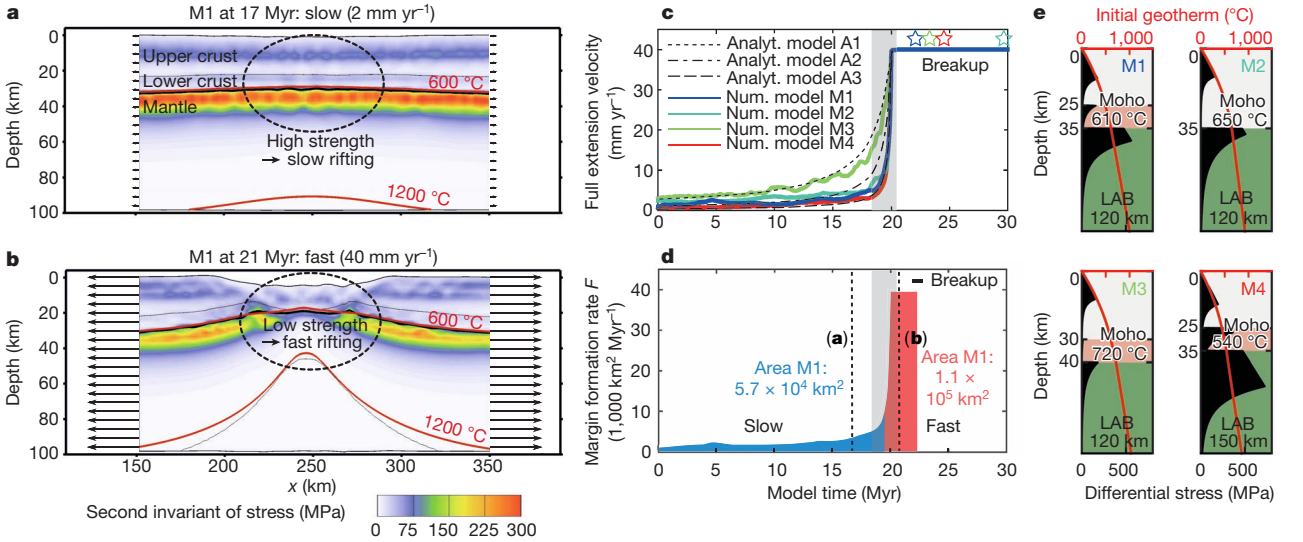

Figure 3 | Analytical and numerical model with force boundary conditions. a, **b**, Strength evolution of two-dimensional numerical rift model. Arrows at lateral model sides indicate extension velocity. **c**, Velocity evolution of analytical (Analyt.) models (A1–A3) and numerical (Num.) experiments (M1–M4). Analytical solution A1 employs a stress-exponent of $n = 3.5$, assuming an entirely viscous lithosphere, while A2 and A3 also account for brittle crustal deformation by using $n = 10$ and $n = 30$, respectively. Numerical reference model M1 is described in Methods and Extended Data Table 1. Other models are identical to M1, but apply a fully felsic crust (M2), a comparably thick crust (M3), or a thick lithosphere (M4), respectively. The duration of plate speed-up is a few million years for any of these configurations. The generated margin structures of M1–M4 are displayed along with six alternative models in Extended Data Fig. 7. **d**, The margin area of M1 consists of two major parts, formed during the slow and the fast phase, respectively. A constant rift length of 1,000 km is assumed. **e**, Rheological setup of models M1–M4. LAB, lithosphere–asthenosphere boundary; Moho, crust–mantle boundary.

and causes conjugate rift sides to accelerate rapidly[15,16]. We show ten models with varying rheological flow laws, thermal configurations, layer thicknesses, frictional softening and thermal expansivity (Fig. 3), which reproduce a large variety of rifted margin configurations (Extended Data Fig. 7). The two-phase behaviour and the abruptness of speed-up are robustly represented by any of these models. The numerical experiments also demonstrate that a variation of the extensional tectonic forces applied at the model boundaries affects the duration of the first, slow rift phase. Increasing the boundary force leads to earlier rift acceleration and breakup, while reducing the force prolongs the slow rift phase, or even generates a failed rift where conductive cooling and thermal strengthening decrease the extension rate until the rift becomes abandoned (Extended Data Fig. 7). We conclude that our plate kinematic and theoretical analyses independently suggest two-phase velocity behaviour as a key feature of successful rifts, which should have affected any rifted continental margin. Numerical modelling with realistic material properties as conducted here brackets the duration of rift-induced plate speed-up to between 2 and 10 million years.

Our results have profound implications for the interpretation of passive margin structures. A variety of studies illustrate striking differences between proximal and distal rifted margin domains[3,10]. This dichotomy can be attributed to the suggested two-phase velocities during basinward localization: the slow phase shapes the proximal margin, while the fast phase dominates the distal margin where our analysis predicts larger fault-slip rates, faster subsidence, higher heat flow, enhanced partial melting and associated underplating or volcanism.

This study provides an alternative explanation for the often enigmatic lack of extension interpreted from the tectono-stratigraphic record along many rifted margins[17]. Both reconstructions and modelling suggest that most of the new area of crust formed during rifting is created in a comparably short period of time towards the end of the syn-rift phase, when strain is likely to have localized to the distal part of the margins. This may explain why extension estimates from syn-rift faulting, typically biased towards the proximal margin areas, and interpreted using concepts borrowed from failed rifts where the feedback process we describe never occurred, commonly underestimate the total extension indicated by whole-crustal thinning.

Our results are applicable to any rifted margin, whether volcanic or magma-poor. Yet, the evolution of specific rifts will be modulated by other factors affecting the force budget and the rift strength such as lithospheric heterogeneity, rift obliquity[13], active rifting due to asthenospheric upwelling[18] and diking, as well as plume arrival[19]. Plumes contribute to breakup by reducing the strength of the rift[19], however, there can be a considerable delay between plume arrival and abrupt plate acceleration[20]. While any combination of these processes may influence how lithospheric strength evolves within individual rift systems, all successful rifts are expected to experience the proposed strength–velocity feedback before breakup.

Owing to the high viscosity of the lower mantle, only lithospheric and upper mantle processes can affect plate movements at timescales of a few million years[21]. It has been proposed that abrupt plate accelerations can be caused by plume–lithosphere interaction[22], subduction initiation[23], and slab detachment[24] possibly induced by ridge subduction[25]. However, none of these mechanisms explain our result that plate speed-up systematically precedes continental breakup. While the present motions of Earth's plates are governed by slab pull, basal drag and ridge push, we propose that abrupt plate acceleration during continental rifting is controlled by the rapid decrease of rift strength.

Dynamic rift weakening presents a new explanation for several previously unexplained rapid absolute plate motion changes, often appearing as cusps or kinks in apparent polar wander (APW) paths. A recent review[26] found four cusps in global APW paths during the last 200 Myr and each of them can be associated with rift velocity speed-up during major continental rifting events: (1) 190 Myr ago—central North Atlantic opening; (2) 150 Myr ago—separation of East and West Gondwana; (3) 125 Myr ago—South Atlantic Rift and the split between India and Antarctica; and (4) 50 Myr ago—northeast Atlantic opening. A global-scale plate reorganization at ~100 Myr ago (ref. 27) corresponds to an increase in rift velocity between Australia and Antarctica, and the end of a standstill in the APW path for South

America as the final continental connection with Africa is broken[8]. We suggest that absolute plate motion changes are strongly related to continental breakup, allowing a linkage between palaeomagnetic data and geological evidence in reconstructing the dynamics of previous supercontinents such as Pangea, Rodinia and Nuna.

Online Content Methods, along with any additional Extended Data display items and Source Data, are available in the online version of the paper; references unique to these sections appear only in the online paper.

Received 2 February; accepted 5 May 2016.
Published online 18 July 2016.

1. Burov, E. B. in *Treatise on Geophysics* Vol. 6 (ed. Schubert, G.) 99–151 (Elsevier, 2007).
2. Whitmarsh, R. B., Manatschal, G. & Minshull, T. A. Evolution of magma-poor continental margins from rifting to seafloor spreading. *Nature* **413,** 150–154 (2001).
3. Péron-Pinvidic, G. & Manatschal, G. The final rifting evolution at deep magma-poor passive margins from Iberia-Newfoundland: a new point of view. *Int. J. Earth Sci.* **98,** 1581–1597 (2009).
4. Pérez-Gussinyé, M., Morgan, J. P., Reston, T. J. & Ranero, C. R. The rift to drift transition at non-volcanic margins: insights from numerical modelling. *Earth Planet. Sci. Lett.* **244,** 458–473 (2006).
5. Brune, S., Heine, C., Perez-Gussinye, M. & Sobolev, S. V. Rift migration explains continental margin asymmetry and crustal hyper-extension. *Nature Commun.* **5,** 4014 (2014).
6. Seton, M. *et al.* Global continental and ocean basin reconstructions since 200 Ma. *Earth Sci. Rev.* **113,** 212–270 (2012).
7. Heine, C., Zoethout, J. & Müller, R. D. Kinematics of the South *Atlantic rift. Solid Earth* **4,** 215–253 (2013).
8. Granot, R. & Dyment, J. The Cretaceous opening of the South Atlantic Ocean. *Earth Planet. Sci. Lett.* **414,** 156–163 (2015).
9. Heine, C. & Brune, S. Oblique rifting of the Equatorial Atlantic: why there is no Saharan Atlantic Ocean. *Geology* **42,** 211–214 (2014).
10. Lavier, L. L. & Manatschal, G. A mechanism to thin the continental lithosphere at magma-poor margins. *Nature* **440,** 324–328 (2006).
11. Kusznir, N. J. & Park, R. G. The extensional strength of the continental lithosphere: its dependence on geothermal gradient, and crustal composition and thickness. *Geol. Soc. Lond. Spec. Publ.* **28,** 35–52 (1987).
12. Christensen, U. R. An Eulerian technique for thermomechanical modeling of lithospheric extension. *J. Geophys. Res. Solid Earth* **97,** 2015–2036 (1992).
13. Brune, S., Popov, A. A. & Sobolev, S. V. Modeling suggests that oblique extension facilitates rifting and continental breakup. *J. Geophys. Res.* **117,** B08402 (2012).
14. Bürgmann, R. & Dresen, G. Rheology of the lower crust and upper mantle: evidence from rock mechanics, geodesy, and field observations. *Annu. Rev. Earth Planet. Sci.* **36,** 531–567 (2008).
15. Takeshita, T. & Yamaji, A. Acceleration of continental rifting due to a thermomechanical instability. *Tectonophysics* **181,** 307–320 (1990).
16. Hopper, J. R. & Buck, W. R. The initiation of rifting at constant tectonic force: role of diffusion creep. *J. Geophys. Res. Solid Earth* **98,** 16213–16221 (1993).
17. Reston, T. J. The structure, evolution and symmetry of the magma-poor rifted margins of the North and Central Atlantic: a synthesis. *Tectonophysics* **468,** 6–27 (2009).
18. Huismans, R. S., Podladchikov, Y. Y. & Cloetingh, S. Transition from passive to active rifting: relative importance of asthenospheric doming and passive extension of the lithosphere. *J. Geophys. Res. Solid Earth* **106,** 11271–11291 (2001).
19. Buiter, S. J. H. & Torsvik, T. H. A review of Wilson Cycle plate margins: a role for mantle plumes in continental breakup along sutures? *Gondwana Res.* **26,** 627–653 (2014).
20. Brune, S., Popov, A. A. & Sobolev, S. V. Quantifying the thermo-mechanical impact of plume arrival on continental breakup. *Tectonophysics* **604,** 51–59 (2013).
21. Iaffaldano, G. & Bunge, H.-P. Rapid plate motion variations through geological time: observations serving geodynamic interpretation. *Annu. Rev. Earth Planet. Sci.* **43,** 571–592 (2015).
22. Cande, S. C. & Stegman, D. R. Indian and African plate motions driven by the push force of the Reunion plume head. *Nature* **475,** 47–52 (2011).
23. Gurnis, M., Hall, C. & Lavier, L. Evolving force balance during incipient subduction. *Geochem. Geophys. Geosystems* **5,** Q07001 (2004).
24. Bercovici, D., Schubert, G. & Ricard, Y. Abrupt tectonics and rapid slab detachment with grain damage. *Proc. Natl Acad. Sci. USA* **112,** 1287–1291 (2015).
25. Seton, M. *et al.* Ridge subduction sparked reorganization of the Pacific plate-mantle system 60–50 million years ago. *Geophys. Res. Lett.* **42,** 1732–1740 (2015).
26. Torsvik, T. H., Muller, R. D., Van der Voo, R., Steinberger, B. & Gaina, C. Global plate motion frames: toward a unified model. *Rev. Geophys.* **46,** RG3004 (2008).
27. Matthews, K. J., Seton, M. & Müller, R. D. A global-scale plate reorganization event at 105–100 Ma. *Earth Planet. Sci. Lett.* **355–356,** 283–298 (2012).

Supplementary Information is available in the online version of the paper.

Acknowledgements S.B. was funded by the Marie Curie International Outgoing Fellowship 326115, the German Research Foundation Priority Program 1375 SAMPLE, and the Helmholtz Young Investigators Group CRYSTALS. S.E.W., N.P.B. and R.D.M. were supported by Science and Industry Endowment Fund project RP 04-174 and Australian Research Council grant IH130200012. Simulations were performed on the cluster facilities of the German Research Centre for Geosciences. Figures were created using matplotlib, Tecplot and Matlab. We thank X. Qin and J. Cannon for their efforts developing the GPlates portal and pyGPlates infrastructure.

Author Contributions S.B. and S.E.W. conceived the plate tectonic analysis. S.B. designed and conducted the thermo-mechanical modelling. S.B., S.E.W. and N.P.B. developed the pyGPlates workflow. S.B., S.E.W. and R.D.M. discussed and integrated the results. The paper was written by S.B. with contributions from all authors.

Author Information The rift velocity database is accessible via an open-access virtual-globe web interface through http://portal.gplates.org/cesium/?view=rift_v. Reprints and permissions information is available at www.nature.com/reprints. The authors declare no competing financial interests. Readers are welcome to comment on the online version of the paper. Correspondence and requests for materials should be addressed to S.B. (sascha.brune@gfz-potsdam.de).

Reviewer Information *Nature* thanks S. Buiter and R. Granot for their contribution to the peer review of this work.

METHODS

Rift kinematics. Quantitative restoration of continents to their pre-rift configuration during Pangea breakup involves estimating the amount of syn-rift extension from present-day crustal thickness, and accounting for uncertainties in these estimates[28,29]. The time of onset of rifting between two plates is constrained by geological evidence such as the ages of oldest syn-rift sediments and rift-associated volcanism. The direction and rate of divergence during rifting can be reconstructed by careful consideration of a diverse range of geological indicators such as seismic tectono-stratigraphy, dating of exhumed and volcanic rocks dredged/drilled within continent–ocean transitions, and fitting constraints from sections of the plate boundaries beyond the rift zone[7,30,31]. Note that in Mesozoic/Cenozoic tectonic reconstructions, plate rotations have to be discretized, whereas typical stage lengths are 5–10 Myr or even longer as observations usually do not permit building plate kinematic models with smaller stages. Our analysis combines independently conducted reconstructions (Supplementary Table 1) that account for recent geological and geophysical data sets.

COBs. The definition of COBs contains considerable uncertainties for many margins—indeed, the definition of a COB as a sharp boundary is conceptually problematic, with interpretations of geophysical data highlighting the complex crustal architecture within the transition from continental to oceanic domains[2,32]. Regions of transition can be several tens of kilometres wide, with complexities that vary between margins closer to volcanic or non-volcanic end-member scenarios. Our starting point for defining COBs were the geometries defined by Seton *et al.*[6]. We modified these using a synthesis of COB interpretations compiled from published crustal-scale geophysical data sets (see Supplementary Table 2). These data are primarily derived from seismic refraction experiments, but interpretations of crustal structure based on seismic reflection and gravity modelling are also included for regions where refraction data are sparse. Additional seismic constraints come from the data set of Winterbourne *et al.*[33], who identified unequivocal oceanic crust adjacent to continental margins along seismic profiles including some industry data, which are otherwise unavailable. The synthesis of margin-perpendicular profiles gives us a series of tie points along each margin, with which our COBs must be broadly consistent. To define COB polylines, we must interpolate between these tie points, which we did guided by first-order trends in maps of gravity derivatives and magnetic anomalies[29]. However, for the specific purposes of this study, an important consideration is that we use the COBs to define the orientation of the rift. For this reason, we have used deliberately simplified COB geometries with orientations that represent the first-order trend of each rifted margin. Using these constraints, we generated alternative COB geometries to define a range of possible COB locations. Our preferred COB set lies relatively ocean-ward, so that it includes areas where the basement is interpreted to comprise exhumed mantle or seaward dipping reflectors, but not basement formed by sea-floor spreading processes. To test how sensitive our results are to our COB interpretation, we generated a second set of COB geometries, defining the extreme landward limit of basement that is not clearly continental crust (see Extended Data Figs 5 and 6). We stress that the COBs used in this study define an envelope of possible COB locations suitable for our sensitivity tests, and are not a natural replacement for 'best-fitting' COB locations interpreted in other studies.

Observational evidence for timing of rift initiation. Our results, and particularly the occurrence of a two-phase, 'slow–fast' pattern in reconstructions of continental rifting, is sensitive to the age assigned to the onset of rifting. The condition for the slow–fast trend to disappear would be if the rift onset ages in our reconstruction model are erroneously old, such that rifting began later and proceeded (from the same full-fit configuration) at a faster rate. Hence, to establish the robustness of the slow–fast trend, we summarize geological evidence for the minimum age at which rifting began in each of the rift systems illustrated in our study, as well as observational evidence for accelerations in rift velocity that lend weight to our kinematic reconstructions.

South Atlantic Rift. We model South Atlantic rifting using the reconstruction of Heine *et al.*[7], with onset of slow rifting at ~150 Myr ago followed by acceleration at ~125 Myr ago. An extensive study linking biostratigraphy, lithostratigraphy and timing of deformation within basins along both African and South Atlantic conjugate margins north of the Walvis Fracture Zone[34] indicates that rifting was established by Berriasian times (>140 Myr ago). South of the Walvis Fracture Zone, the main phase of rifting between South America and southern Africa probably began earlier, in the Late Jurassic, following widespread, isolated Triassic–Jurassic rift basin development within southern South America[35]. The timing of slow rift onset and subsequent acceleration are consistent with earlier reconstructions[36]. A reconstruction invoking later, post-Aptian age of breakup between salt basins on the Brazilian and Angolan conjugate margins[37] has been proposed, but detailed seismic imaging and drilling of syn-rift sediments within the rifted margins, combined with basin subsidence histories[38] argue against this later breakup scenario. Further supporting our model, recent interpretation of magnetic anomalies in the southern South Atlantic within crust formed during the Cretaceous Normal Superchron constrains changes in the rate and direction of plate motions during breakup[8], showing rapid acceleration of plate divergence during initial breakup in the southernmost South Atlantic, contemporaneous with the final stages of rifting further north.

Central North Atlantic Rift. Our base reconstruction follows the work of Kneller *et al.*[28], who assigned a rifting onset age of 240 Myr ago, and predicts a speed-up at ~200 Myr ago. The speed-up occurs around the time of Central Atlantic Magmatic Province (CAMP) volcanism, which represents an important time marker within the rift evolution. Stratigraphic evidence from syn-rift sediments within basins along the eastern margins of North America[39,40] and the conjugate Northwest African margins[41] shows that continental rifting was active for at least 25 Myr before CAMP magmatism. Rapid speed-up of rifting is evidenced by a rate of sediment accumulation within these basins that increases drastically within 1–5 Myr before 200 Myr ago[39].

North America–Iberia. Our reconstruction proceeds from onset of rifting at 200 Myr ago with a speed-up at ~145 Myr ago. Recent, alternative reconstructions[42] show a similar increase in extension velocities at the end of the Jurassic, but with a slightly earlier initiation of rifting (~203 Myr ago). Evidence for widespread rifting is recorded in basins along the Newfoundland and Iberian margins beginning in the late Triassic, but resulting in little crustal thinning; a second phase beginning in the late Jurassic led to marked thinning and breakup in the Early Cretaceous[3,43]. Sequential restoration[30] yields post-145 Myr ago extension velocities of 1–2 mm yr^{-1}, consistent with our reconstructions. The rift velocity before ~145 Myr ago depends on the assumed age of rift onset. Taking the latest possible onset of rifting, Oxfordian (~161 Myr ago), modelled extension rates remain fairly constant throughout rifting. However, any earlier onset of rifting (for example, Triassic–Early Jurassic) as indicated by evidence listed above, would result in slower initial rifting followed by a Late Jurassic acceleration, consistent with our reconstruction model. The slow–fast velocity evolution is further supported by a study[44] that uses previously unpublished seismic and borehole data to show continuous rifting in the basins along western Iberia beginning in the Triassic (>210 Myr ago), with three rift cycles, ending at 144 Myr ago. These authors find that the subsidence is relatively slow in the first two rift phases, then increases rapidly in rate during a rift climax in Late Oxfordian–Kimmeridgian times (~160–152 Myr ago) coinciding with the timing of our speed-up.

Australia–Antarctica. Our reconstruction places the onset of rifting between Australia and Antarctica in the late Jurassic (~165–155 Myr ago), with an increase in rift velocity around 100 Myr ago. The earliest rift-fill comprises Callovian–Early Berriasian sediments (>160 to ~140 Myr ago), constrained by palynological dating of samples from the Polda, Bremer and Eyre basin[45]. Detailed tectono-stratigraphic analysis[45] and sequential structural restoration of interpreted seismic sections[46] point towards slow rifting during the Jurassic–Early Cretaceous, followed by a rapid acceleration in crustal thinning and subsidence at the beginning of the Late Cretaceous (beginning around 102 or 93.5 Myr ago)[46,47]. Shortly thereafter, breakup begins in the westernmost part of the rift system (dated by exhumation fabrics and volcanics), propagating eastwards over tens of millions of years[48].

South China Sea. Reconstructions of the South China margins indicate rapid extension and breakup beginning in the late Eocene[49]. Earlier extension developed from ~60 Myr ago within a former Andean-style margin, while onset of slow extension before the late Eocene speed-up is recorded by minor volcanism in rift-related basins[50]. This is further supported by subsidence and strain-rate analyses of wells and stratigraphic sections for basins within the northern margin of the South China Sea[51].

Gulf of California. The speed-up in our reconstruction occurs around 12 Myr ago, corresponding to a phase of abruptly increased rift velocity and obliquity inferred from widespread structural markers[52]. Phases of continental extension before the mid-Miocene are recorded by tectono-stratigraphic relationships and dating of rift-related volcanics and plutons[53,54]. These data indicate more diffuse extension at significantly lower rates: Ferrari *et al.*[53] estimate that the relative motion between the conjugate margins of the Gulf of California proceeded at an average of 7.7 mm yr^{-1} from ~30–18 Myr ago, and 8.3 mm yr^{-1} from ~18–12 Myr ago, consistent with our computed values.

North America–Greenland. Initiation of rifting by ~140 Myr ago is substantiated by dating of rift-related volcanics and biostratigraphy[55]. Starting from ~120 Myr ago, rift basin sedimentation is evident throughout the Cretaceous[56]. Rifting and subsidence rates were slow until a rapid increase around 70–80 Myr ago[55,57], around the time of an increase in rift velocity and subsequent initiation of sea-floor spreading.

Northeast Atlantic. Our reconstruction of relative motion between Greenland and Eurasia before the oldest sea-floor spreading magnetic anomalies in the northeast Atlantic (C24, ~53 Myr ago[58]) incorporates plate circuit computations using

constraints from the rift systems between Greenland, North America and Eurasia. The reconstruction shows slow extension in the Jurassic to Early Cretaceous followed by tectonic quiescence or modest mid-Cretaceous extension[59,60], and a pronounced speed-up in the Late Cretaceous. The acceleration in Late Cretaceous rifting indicated by the reconstructions is more tightly constrained from spreading histories in the adjacent basins. The most important phase of rifting that ultimately led to breakup is constrained to the Latest Cretaceous–Early Paleocene. Skogseid[61] proposed that enhanced syn-rift deposition took place between 75 and 62 Myr ago based on tectono-stratigraphy and subsidence analysis from seismic and well data from the Vøring margin.

End-member models of the South Atlantic Rift. We performed our analysis on several end-member models for the South Atlantic Rift (Extended Data Fig. 8). These models differ in terms of the timing of final South Atlantic breakup, which is difficult to constrain due to the Cretaceous superchron. However, models that feature a late breakup[8,37,62] also show a late speed-up at 110 Myr ago. Models with an earlier breakup, however[7,36] depict an earlier speed-up at 120 Myr ago. In all cases, initially slow rift velocities are followed by large plate accelerations that precede the final breakup by 10–15 Myr.

Another major difference between these models is the plate-internal deformation within South America: the Heine *et al.* model[7] uses a largely intact South American plate where deformation occurs only along the border to Patagonia, while Moulin *et al.*[62] separate South America in eight individual plates. We apply our analysis under two premises: (1) assuming a three-plate scenario (West Africa, South Africa, South America) shown in the upper panel of rift velocity diagrams (Extended Data Fig. 8b), and (2) we account for South America-internal deformation in a four-plate analysis where the northern and the southern part of South America are evaluated independently within the two bottommost panels in Extended Data Fig. 8b.

We find that plate models, which feature large intra-plate deformation[36,37,62] display two distinct speed-up events: first the Southern plates accelerate several million years before breakup in the southern South Atlantic and second the northern plates accelerate before breakup in the equatorial Atlantic. Plate models with less internal deformation, such as the Heine *et al.* model, display only a minor acceleration before southern South Atlantic opening whereas the largest speed-up occurs at 120 Myr ago before equatorial Atlantic breakup. While the relative importance of each speed-up depends on the amount of South America-internal deformation, all models illustrate plate acceleration before breakup of the controlling rift segment.

Database. The entire rift velocity database is accessible via an open-access virtual-globe web interface through http://portal.gplates.org/cesium/?view=rift_v. This database contains the rift velocity history of any point at a major post-Pangea rifted margin. The velocity history can be visualized online and downloaded, lending itself as a source of tectonic boundary conditions for basin analysis software and geodynamic forward models.

Numerical model setup. We apply the finite element code SLIM3D[63] to solve the coupled system of conservation equations for momentum, thermal energy and constitutive equations. The reference model M1 consists of four distinct petrological layers: 25 km of felsic upper crust[64], 10 km of mafic lower crust[65], and a lithospheric mantle dominated by dry olivine rheology[66] that extends to a depth of 120 km. The weak asthenospheric material below 120 km depth is represented through wet (that is, 1,000 p.p.m. H/Si) olivine rheology[66]. The entire model comprises a rectangular domain of 150 km depth and 500 km width, with 2 km resolution.

We apply dynamic boundary conditions at the lateral model sides, such that during rifting, the boundary force is kept constant, allowing for self-consistent evolution of extensional velocities. This approach is feasible if the model domain represents a large region whose strength is a major component in the overall force balance of the involved plates. The constant boundary force is maintained in our model until extensional velocities reach typical sea-floor spreading rates. Hereafter, the low rift strength becomes neglectable in the force balance, and we use velocity boundary conditions with a rate of 40 mm yr^{-1}. At the top boundary we use a free surface while at the bottom side isostatic equilibrium is realized by means of the Winkler foundation, where in- and outflow of material is accounted for during re-meshing. Deformation is accommodated by elasto-visco-plastic rheology so that the model self-consistently reproduces diverse lithospheric-scale deformation processes such as faulting, flexure and lower crustal flow. Viscous flow occurs via two creep mechanisms: diffusion and dislocation creep. The Mohr–Coulomb failure model is implemented for brittle deformation.

The thermal state at the model start is a steady-state temperature distribution resulting from each layer's heat conductivity, radiogenic heat production and the following boundary conditions: (1) lateral boundaries are thermally isolated, (2) the temperature at the surface is 0 °C, (3) below the lithosphere asthenosphere boundary the temperature is set to 1,350 °C. To avoid rift localization at the model boundaries, a small thermal heterogeneity is introduced in the model centre. We introduce this heterogeneity of triangular shape and 20 km width by elevating the initial 1,350 °C isotherm up to 10 km before thermal equilibration[5]. All rheological and thermal parameters are given in Extended Data Table 1.

Analytical solution. Here we derive a transparent analytical solution for finite amplitude necking of a homogeneous viscous layer consisting of a power-law material. A horizontal layer of initial thickness D_0 is extended by a constant line force F that is applied parallel to the layer. In an incompressible, free layer the mean layer-parallel deviatoric stress τ is half of the total stress, F/D_0 (ref. 67), that is, $\tau = \frac{1}{2}F/D_0$. The deviatoric stress further relates to the strain rate through the power law $\dot{\varepsilon} = B\tau^n$ where the pre-exponential factor B and the stress exponent n are material parameters. Note that B is often considered to be temperature-dependent with $B = A \times \exp(-E/(RT))$. On the basis of these relations a characteristic viscosity $\eta_c = \tau/\dot{\varepsilon} = \tau^{(1-n)}/B$ and a characteristic time $t_c = \eta_c/\tau = 1/B \times (\frac{1}{2}F/D_0)^{-n}$ can be defined[68].

Owing to mass conservation and incompressible flow, the horizontal stretching of the layer has to be balanced by vertical thinning: $1/L \times \mathrm{d}L/\mathrm{d}t = -1/D \times \mathrm{d}D/\mathrm{d}t$, where L is the length of the layer. The resulting extensional velocity $v = \mathrm{d}L/\mathrm{d}t$ can thus be written as

$$v = -L/D \times \mathrm{d}D/\mathrm{d}t \quad (1)$$

We assume that the upper and lower boundaries are traction-free and that no depth-dependent thinning occurs. These assumptions allowed derivation of closed analytical solutions for necking instabilities in boudinage mechanics and slab detachment[68] involving the time-dependent layer thickness D that can be expressed as:

$$D = D_0(1 - t/t_r)^{(1/n)} \quad (2)$$

where the time until rupture t_r relates to the aforementioned characteristic time[68] t_c such that $t_r = t_c/n$.

Combining equation (1) and equation (2) yields the formula for the time-dependent extension velocity:

$$v = L/(nt_r) \times (1 - t/t_r)^{-1} \quad (3)$$

To apply the analytical results to continental rifting, we use parameters that describe a typical rift configuration (lithospheric thickness 100 km; mean lithospheric temperature $T = 600$ °C; applied tectonic force 8 TN m^{-1}; width of the necking zone $L = 100$ km; duration of rifting $t_r = 20$ Myr). The stress exponents of lithospheric materials range between 3 and 4, hence a purely viscous lithosphere can be approximated by $n = 3.5$. However, this approach neglects the existence of brittle deformation that is evidenced at real plate boundaries by ubiquitous faulting. Brittle failure can be represented as an end-member of power law creep, if stress exponents up to 30 are used[12]. The analytical solution is plotted in Fig. 3 for three cases: $n = 3.5$ (A1), $n = 10$ (A2), $n = 30$ (A3). Despite the simplicity of the analytical model, the numerical solutions of lithospheric necking are very similar to analytical solutions (Fig. 3). Hence, the analytical calculation corroborates our conclusion that it is the rapid loss of lithospheric strength during continental rifting, which is responsible for the abrupt increase of extension velocity.

28. Kneller, E. A., Johnson, C. A., Karner, G. D., Einhorn, J. & Queffelec, T. A. Inverse methods for modeling non-rigid plate kinematics: application to mesozoic plate reconstructions of the Central Atlantic. *Comput. Geosci.* **49,** 217–230 (2012).
29. Williams, S. E., Whittaker, J. M. & Müller, R. D. Full-fit, palinspastic reconstruction of the conjugate Australian-Antarctic margins. *Tectonics* **30,** TC6012 (2011).
30. Sutra, E., Manatschal, G., Mohn, G. & Unternehr, P. Quantification and restoration of extensional deformation along the Western Iberia and Newfoundland rifted margins. *Geochem. Geophys. Geosyst.* **14,** 2575–2597 (2013).
31. Whittaker, J. M., Williams, S. E. & Müller, R. D. Revised tectonic evolution of the Eastern Indian Ocean. *Geochem. Geophys. Geosyst.* **14,** 1891–1909 (2013).
32. Dean, S. L., Sawyer, D. S. & Morgan, J. K. Galicia Bank ocean–continent transition zone: new seismic reflection constraints. *Earth Planet. Sci. Lett.* **413,** 197–207 (2015).
33. Winterbourne, J., Crosby, A. & White, N. Depth, age and dynamic topography of oceanic lithosphere beneath heavily sedimented Atlantic margins. *Earth Planet. Sci. Lett.* **287,** 137–151 (2009).
34. Chaboureau, A.-C. *et al.* Paleogeographic evolution of the central segment of the South Atlantic during Early Cretaceous times: paleotopographic and geodynamic implications. *Tectonophysics* **604,** 191–223 (2013).
35. Loegering, M. J. *et al.* Tectonic evolution of the Colorado Basin, offshore Argentina, inferred from seismo-stratigraphy and depositional rates analysis. *Tectonophysics* **604,** 245–263 (2013).
36. Nürnberg, D. & Müller, R. D. The tectonic evolution of the South-Atlantic from Late Jurassic to present. *Tectonophysics* **191,** 27–53 (1991).

37. Torsvik, T. H., Rousse, S., Labails, C. & Smethurst, M. A. A new scheme for the opening of the South Atlantic Ocean and the dissection of an Aptian salt basin. *Geophys. J. Int.* **177,** 1315–1333 (2009).
38. Quirk, D. G. *et al.* Rifting, subsidence and continental breakup above a mantle plume in the central South Atlantic. *Geol. Soc. Lond. Spec. Publ.* **369,** 185–214 (2013).
39. Schlische, R. W., Withjack, M. O. & Olsen, P. E. Relative timing of CAMP, rifting, continental breakup, and basin inversion: tectonic significance. *Geophys. Monogr.* **136,** 33–59 (2003).
40. Withjack, M. O., Schlische, R. W., Malinconico, M. L. & Olsen, P. E. Rift-basin development: lessons from the Triassic–Jurassic Newark Basin of eastern North America. *Geol. Soc. Lond. Spec. Publ.* **369,** 301–321 (2013).
41. Davison, I. Central Atlantic margin basins of North West Africa: geology and hydrocarbon potential (Morocco to Guinea). *J. Afr. Earth Sci.* **43,** 254–274 (2005).
42. Vissers, R. L. M., van Hinsbergen, D. J. J., Meijer, P. T. & Piccardo, G. B. Kinematics of Jurassic ultra-slow spreading in the Piemonte Ligurian ocean. *Earth Planet. Sci. Lett.* **380,** 138–150 (2013).
43. Alves, T. M. *et al.* Diachronous evolution of Late Jurassic–Cretaceous continental rifting in the northeast Atlantic (west Iberian margin). *Tectonics* **28,** TC4003 (2009).
44. Pereira, R. & Alves, T. M. Tectono-stratigraphic signature of multiphased rifting on divergent margins (deep-offshore southwest Iberia, North Atlantic). *Tectonics* **31,** TC4001 (2012).
45. Ball, P., Eagles, G., Ebinger, C., McClay, K. & Totterdell, J. The spatial and temporal evolution of strain during the separation of Australia and Antarctica. *Geochem. Geophys. Geosyst.* **14,** 2771–2799 (2013).
46. Espurt, N. *et al.* Transition from symmetry to asymmetry during continental rifting: an example from the Bight Basin–Terre Adélie (Australian and Antarctic conjugate margins). *Terra Nova* **24,** 167–180 (2012).
47. Veevers, J. J. Change of tectono-stratigraphic regime in the Australian plate during the 99 Ma (mid-Cretaceous) and 43 Ma (mid-Eocene) swerves of the Pacific. *Geology* **28,** 47–50 (2000).
48. Direen, N. G., Stagg, H. M. J., Symonds, P. A. & Norton, I. O. Variations in rift symmetry: cautionary examples from the Southern Rift System (Australia–Antarctica). *Geol. Soc. Lond. Spec. Publ.* **369,** 453–475 (2013).
49. Lee, T.-Y. & Lawver, L. A. Cenozoic plate reconstruction of the South China Sea region. *Tectonophysics* **235,** 149–180 (1994).
50. Yan, Q., Shi, X. & Castillo, P. R. The late Mesozoic–Cenozoic tectonic evolution of the South China Sea: a petrologic perspective. *J. Asian Earth Sci.* **85,** 178–201 (2014).
51. Xie, H. *et al.* Cenozoic tectonic subsidence in deepwater sags in the Pearl River Mouth Basin, Northern South China Sea. *Tectonophysics* **615–616,** 182–198 (2014).
52. Bennett, S. E. K. & Oskin, M. E. Oblique rifting ruptures continents: example from the Gulf of California shear zone. *Geology* **42,** 215–218 (2014).
53. Ferrari, L. *et al.* Late Oligocene to Middle Miocene rifting and synextensional magmatism in the southwestern Sierra Madre Occidental, Mexico: the beginning of the Gulf of California rift. *Geosphere* **9,** 1161–1200 (2013).
54. Duque-Trujillo, J. *et al.* Timing of rifting in the southern Gulf of California and its conjugate margins: insights from the plutonic record. *Geol. Soc. Am. Bull.* **127,** 702–736 (2015).
55. Dickie, K., Keen, C. E., Williams, G. L. & Dehler, S. A. Tectonostratigraphic evolution of the Labrador margin, Atlantic Canada. *Mar. Petrol. Geol.* **28,** 1663–1675 (2011).
56. Chalmers, J. A. & Pulvertaft, T. C. R. Development of the continental margins of the Labrador Sea: a review. *Geol. Soc. Lond. Spec. Publ.* **187,** 77–105 (2001).
57. McGregor, E. D., Nielsen, S. B., Stephenson, R. A. & Haggart, J. W. Basin evolution in the Davis Strait area (West Greenland and conjugate East Baffin/Labrador passive margins) from thermostratigraphic and subsidence modelling of well data: implications for tectonic evolution and petroleum systems. *Bull. Can. Petrol. Geol.* **62,** 311–329 (2014).
58. Gaina, C., Gernigon, L. & Ball, P. Palaeocene–recent plate boundaries in the NE Atlantic and the formation of the Jan Mayen microcontinent. *J. Geol. Soc. Lond.* **166,** 601–616 (2009).
59. Tsikalas, F., Faleide, J. I., Eldholm, O. & Wilson, J. Late Mesozoic–Cenozoic structural and stratigraphic correlations between the conjugate mid-Norway and NE Greenland continental margins. *Geol. Soc. Lond. Pet. Geol. Conf. Ser.* **6,** 785–801 (2005).
60. Færseth, R. B. & Lien, T. Cretaceous evolution in the Norwegian Sea—a period characterized by tectonic quiescence. *Mar. Petrol. Geol.* **19,** 1005–1027 (2002).
61. Skogseid, J. Dimensions of the Late Cretaceous-Paleocene Northeast Atlantic rift derived from Cenozoic subsidence. *Tectonophysics* **240,** 225–247 (1994).
62. Moulin, M., Aslanian, D. & Unternehr, P. A new starting point for the South and Equatorial Atlantic Ocean. *Earth Sci. Rev.* **98,** 1–37 (2010).
63. Popov, A. A. & Sobolev, S. V. SLIM3D: A tool for three-dimensional thermo mechanical modeling of lithospheric deformation with elasto-visco-plastic rheology. *Phys. Earth Planet. Inter.* **171,** 55–75 (2008).
64. Gleason, G. C. & Tullis, J. A flow law for dislocation creep of quartz aggregates determined with the molten-salt cell. *Tectonophysics* **247,** 1–23 (1995).
65. Rybacki, E. & Dresen, G. Dislocation and diffusion creep of synthetic anorthite aggregates. *J. Geophys. Res.* **105,** 26017–26036 (2000).
66. Hirth, G. & Kohlstedt, D. L. Rheology of the upper mantle and the mantle wedge: a view from the experimentalists. *Geophys. Monogr.* **138,** 83–105 (2003).
67. Turcotte, D. L. & Schubert, G. *Geodynamics* (Cambridge Univ. Press, 2002).
68. Schmalholz, S. M. A simple analytical solution for slab detachment. *Earth Planet. Sci. Lett.* **304,** 45–54 (2011).
69. Andersen, O. B., Knudsen, P. & Berry, P. A. M. The DNSC08GRA global marine gravity field from double retracked satellite altimetry. *J. Geodyn.* **84,** 191–199 (2010).
70. Ranalli, G. & Murphy, D. C. Rheological stratification of the lithosphere. *Tectonophysics* **132,** 281–295 (1987).

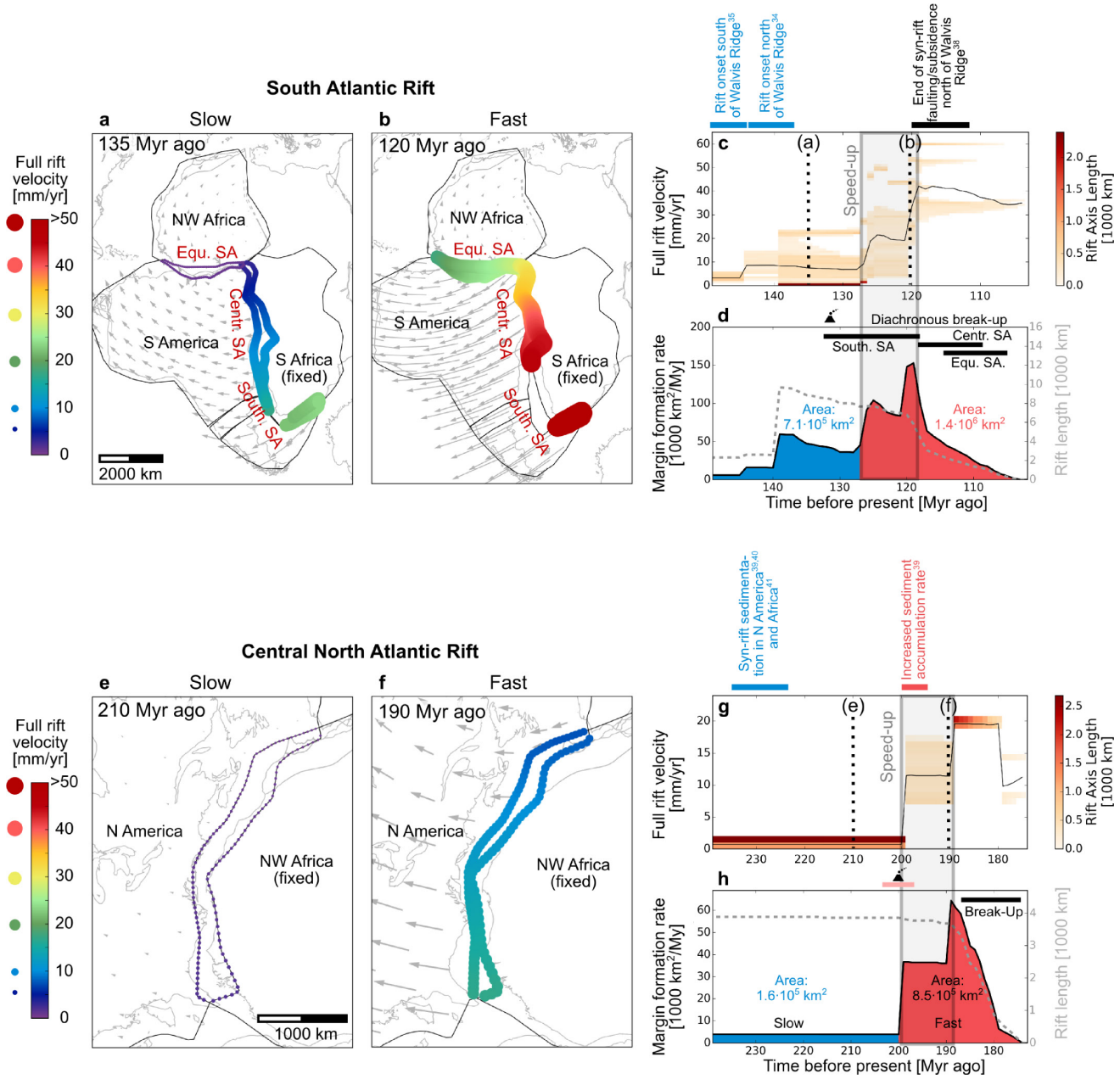

Extended Data Figure 1 | South Atlantic Rift and the central North Atlantic Rift. a–h, The maps depict snapshots of the slow and fast rift phase in the South Atlantic Rift (**a**, **b**) and central North Atlantic Rift (**e**, **f**). We corroborate the inferred velocity history with key temporal constraints[34,35,38–41] from geological and geophysical observations (**c**, **g**). For animations of the kinematic evolution, see Supplementary Videos 1 and 2.

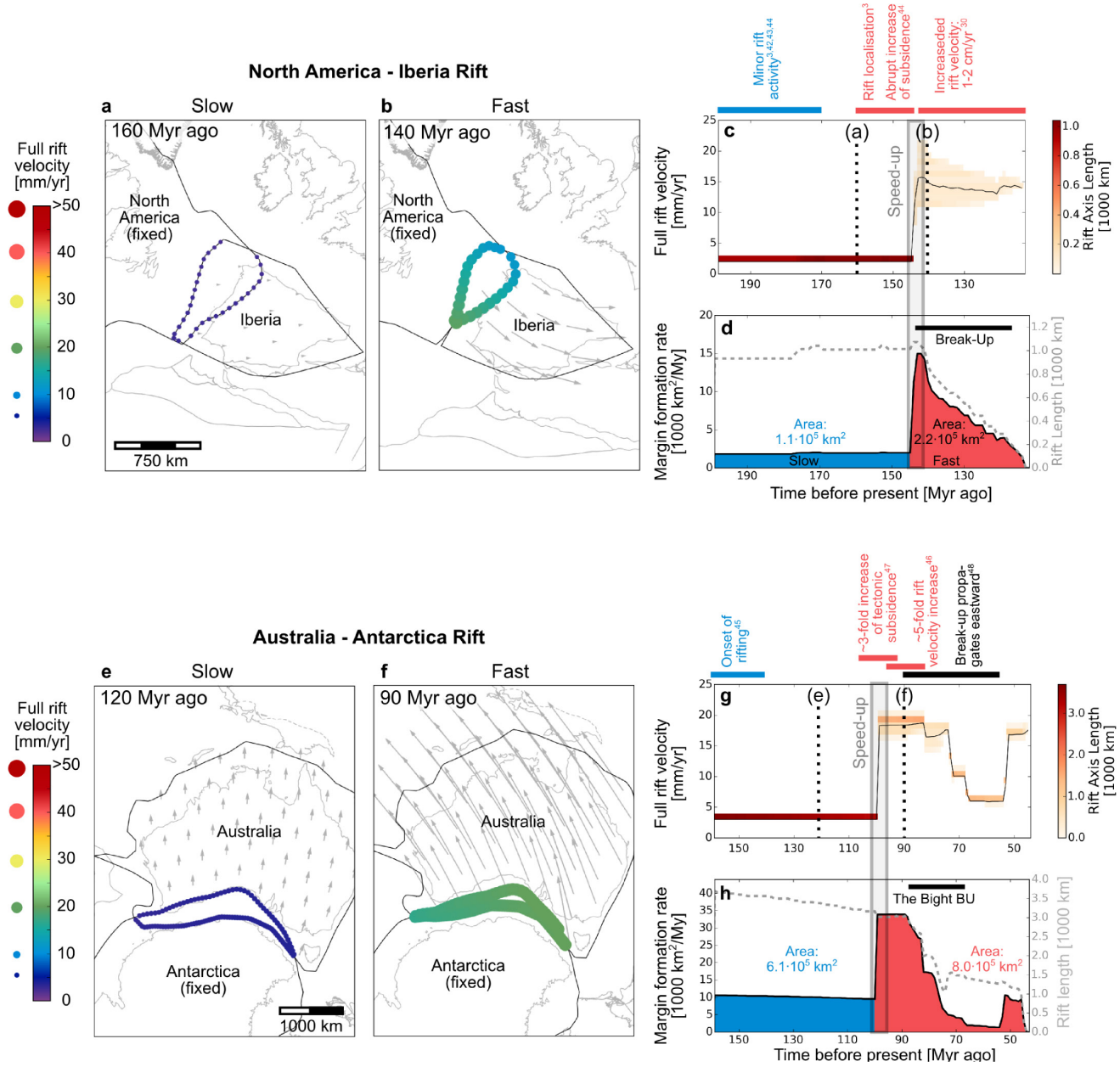

Extended Data Figure 2 | North America–Iberia Rift and the Australia–Antarctica Rift. a–h, The maps depict snapshots of the slow and fast rift phase in the North America–Iberia Rift (**a**, **b**) and the Australia–Antarctica Rift (**e**–**h**). We corroborate the inferred velocity history with key temporal constraints[3,30,42–48] from geological and geophysical observations (**c**, **g**). For animations of the kinematic evolution, see Supplementary Videos 3 and 4.

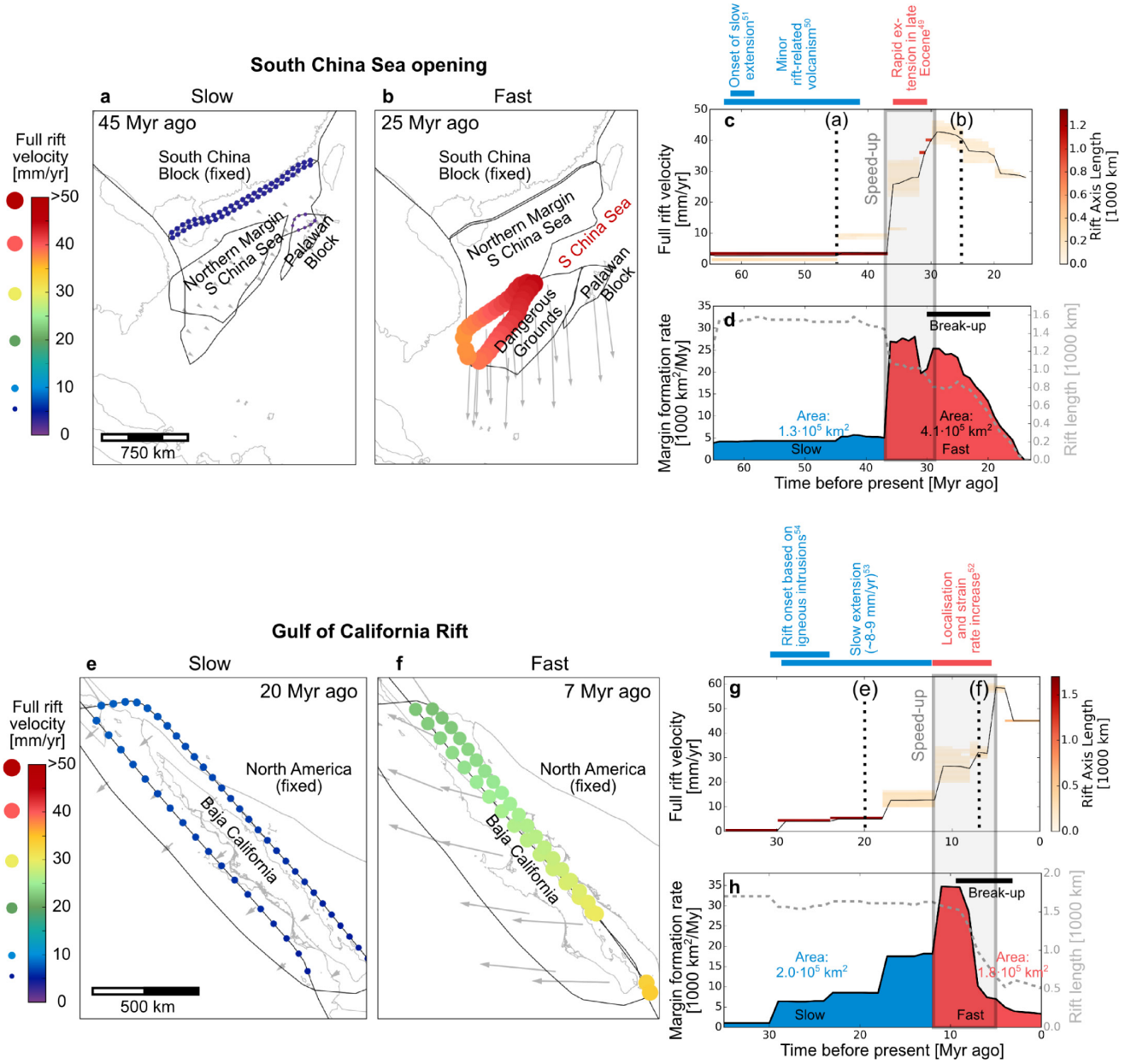

Extended Data Figure 3 | South China Sea opening and the Gulf of California Rift. a–h, The maps depict snapshots of the slow and fast rift phase in the South China Sea opening (**a**, **b**) and the Gulf of California Rift (**e**, **f**). We corroborate the inferred velocity history with key temporal constraints from[49–54] geological and geophysical observations (**c**, **g**). For animations of the kinematic evolution, see Supplementary Videos 5 and 6.

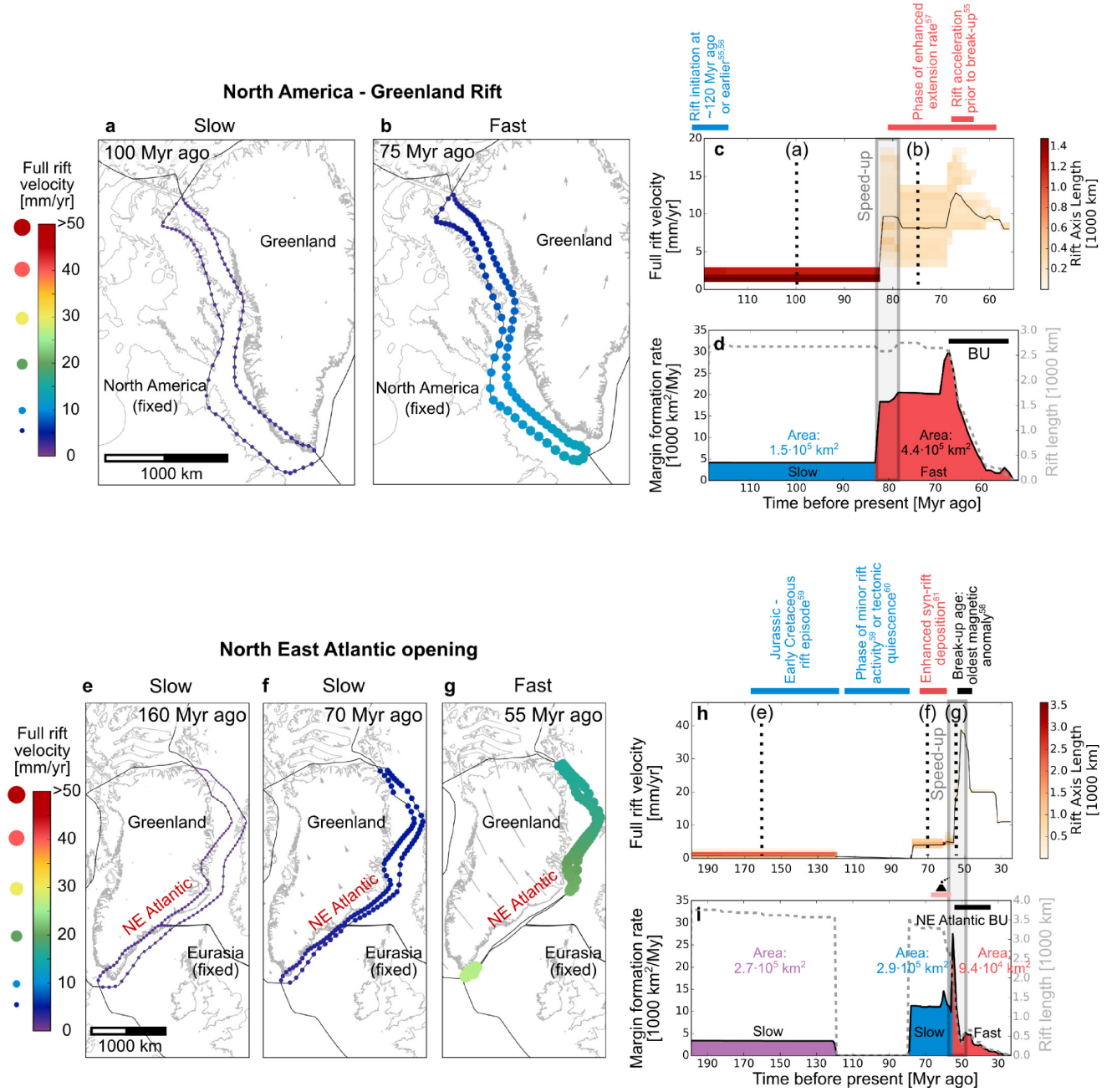

Extended Data Figure 4 | North America–Greenland Rift and the northeast Atlantic opening. a–i, The maps depict snapshots of the slow and fast rift phase in the North America–Greenland Rift (**a**, **b**) and the northeast Atlantic opening (**e**–**g**). We corroborate the inferred velocity history with key temporal constraints[55–61] from geological and geophysical observations (**c**, **h**). For animations of the kinematic evolution, see Supplementary Videos 7 and 8.

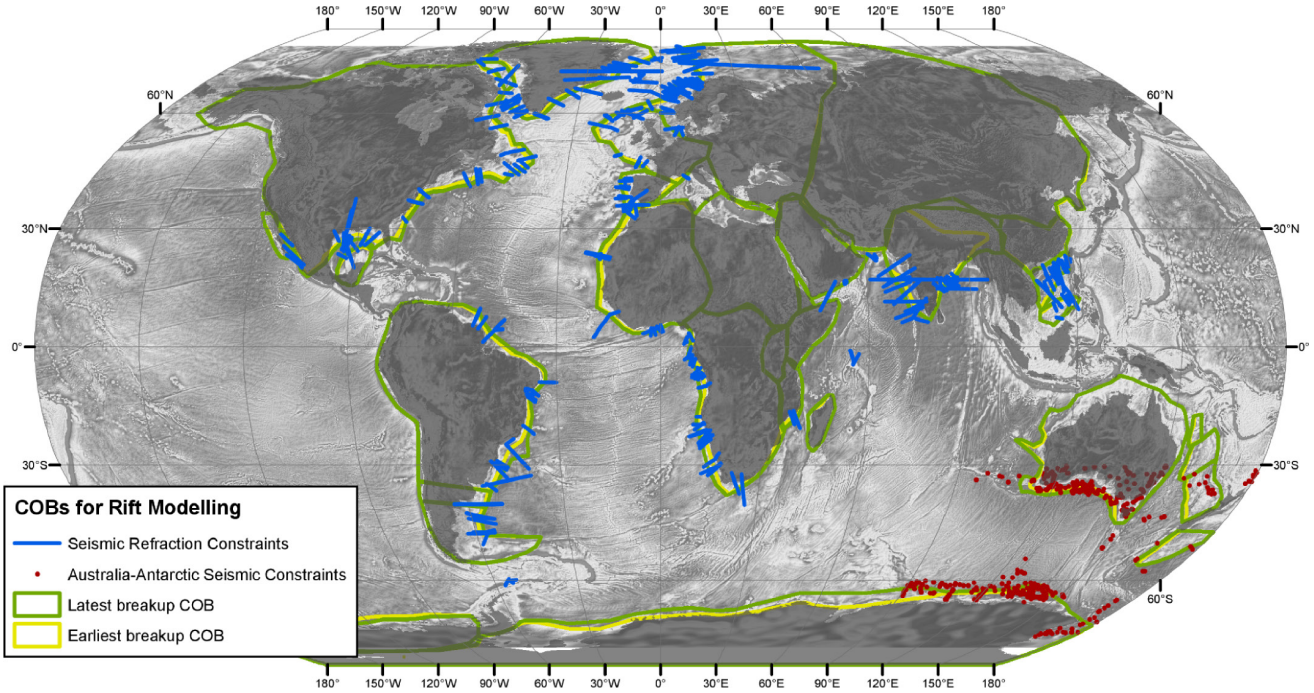

Extended Data Figure 5 | Data coverage for construction of COBs. We restrict our analysis to regions where seismic refraction data for both conjugate margins is available. Seismic refraction profiles are shown in blue, together with 'point' deep crustal seismic soundings linked together by gravity modelling. Red points represent a mixture of sonobuoys and deep reflection profiles. All references for displayed data are listed in Supplementary Table 2. Our preferred set of COBs (green) includes some areas where the basement is interpreted to comprise exhumed mantle or seaward dipping reflectors, but not basement formed by sea-floor spreading processes. The alternative set of COB geometries, defining the extreme landward limit of what basement that is not clearly continental crust, is shown in yellow. Underlying image shows global free-air gravity field[69].

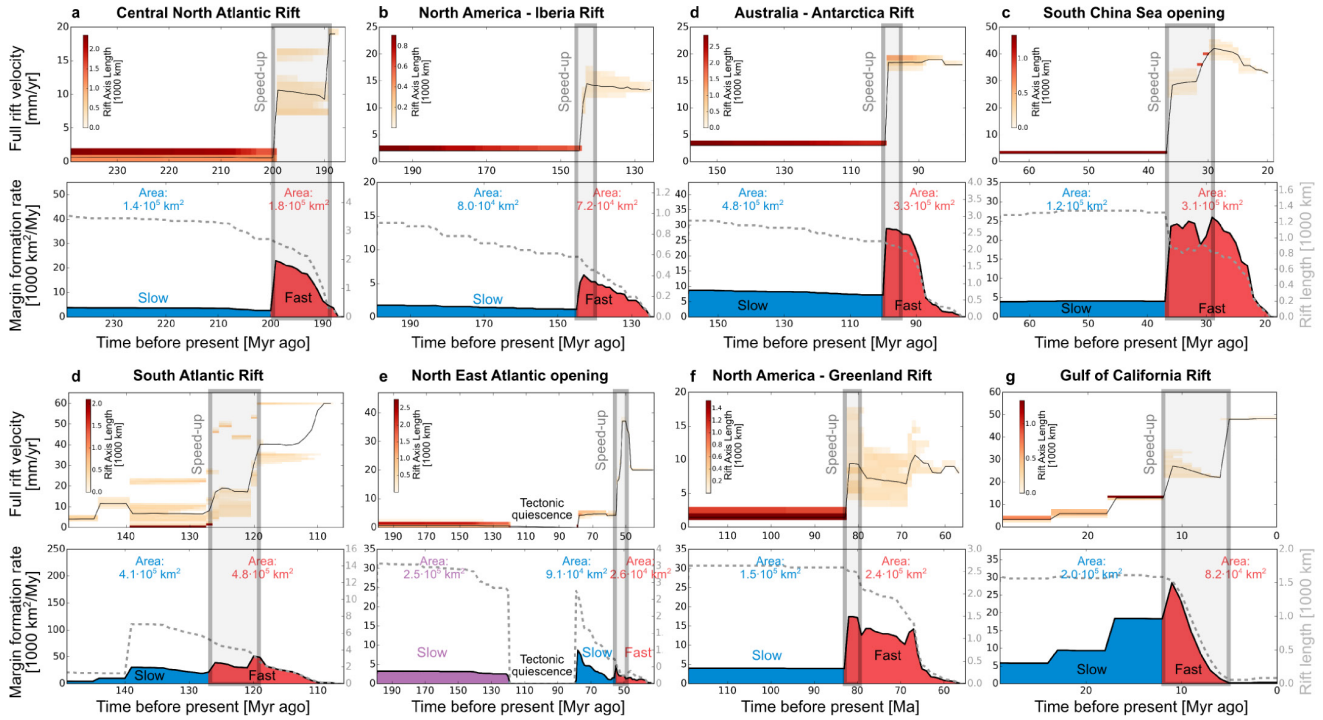

Extended Data Figure 6 | Results using alternative, continent-ward set of COBs. The COB set is shown in Extended Data Fig. 5 as yellow polygons. Breakup takes place earlier, yet the two-phase evolution is robustly represented in this end-member scenario.

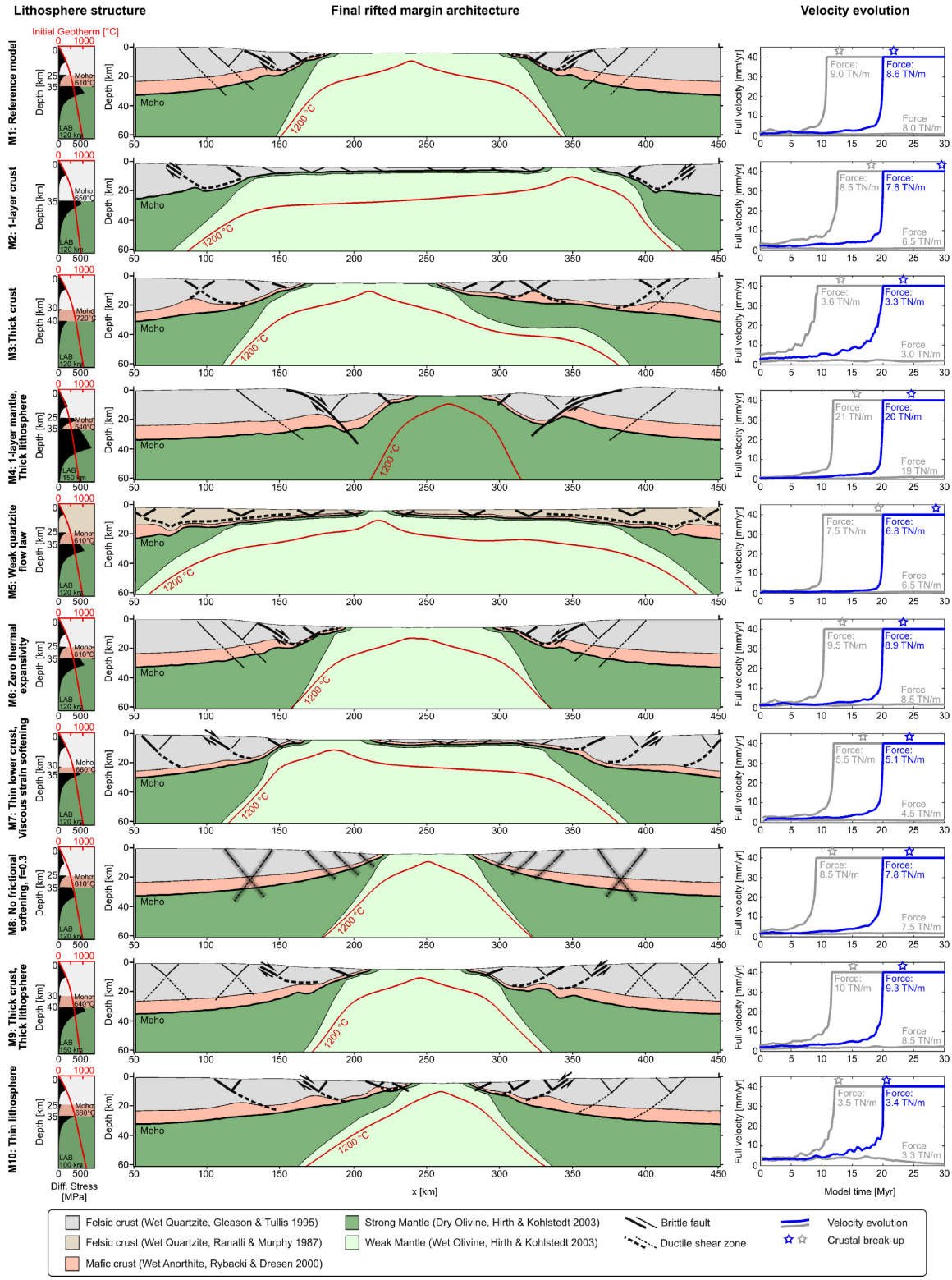

Extended Data Figure 7 | Final margin structures of numerical experiments. Using model M1 as our reference model, we vary layer thickness, rheological flow laws, the thermal configuration, frictional softening, and thermal expansivity to compute models M2–M10. M5 uses a comparatively weak quartzite flow law[70]. The final margin structures feature a wide range of rifted margin geometries reproducing all observed configurations of wide, narrow, symmetrical and asymmetrical margins. Depending on rheological evolution, extension is accommodated by brittle faults, ductile shear zones or both. For all cases, the associated time-dependent extension velocity (shown on the right in blue) exhibits the characteristic two-phase behaviour of slow rifting during the first rift phase, speed-up during lithospheric necking and fast rifting before breakup. Blue lines correspond to the final margin structures on the left and represent model runs where the boundary force coincides with the integrated strength of the yield strength profiles. Grey lines depict parameter variations where the boundary force is larger or smaller than the lithospheric strength resulting in two-phase velocities with an earlier speed-up, or decreasing rift activity reproducing failed rifts, respectively.

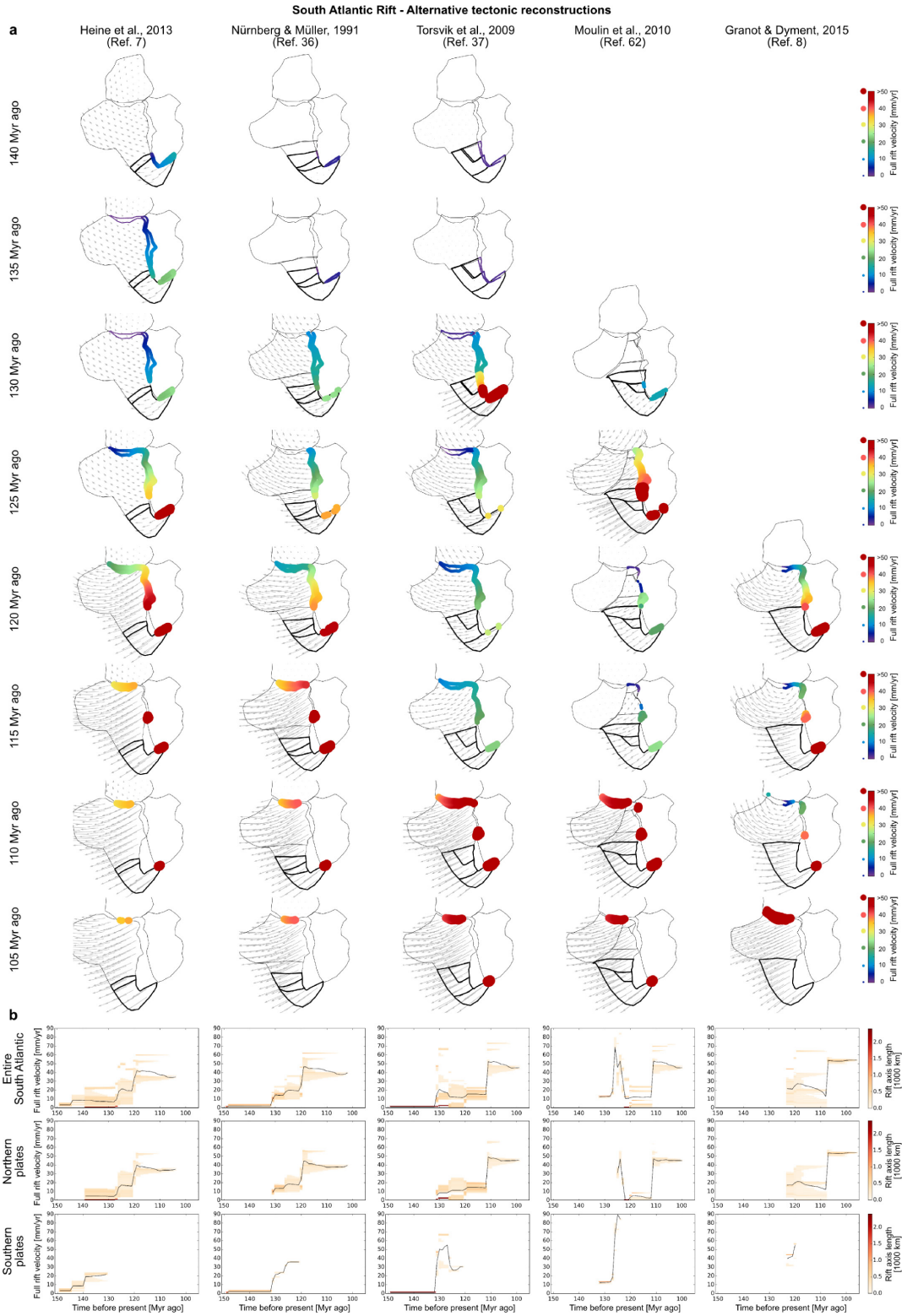

Extended Data Figure 8 | Alternative South Atlantic plate tectonic reconstructions. **a**, **b**, Several end-member models are shown that differ in terms of the timing of final South Atlantic breakup, and intra-plate deformation. **a**, Map view evolution. **b**, Frequency of extension velocity considering the entire South Atlantic (top) or only the Northern and Southern Plates (middle and bottom, respectively). Southern plates are depicted as bold polygons in the map view (**a**). Plate models[7,36] with a final breakup at ~110 Myr ago depict a speed-up at 125–120 Myr ago, while models with a later breakup[8,37,62] at ~100 Myr ago also involve a later rift acceleration at ~110 Myr ago. Reconstructions in which large intra-plate deformation[36,37,62] decouples northern and southern South America display first a speed-up of southern South America followed by a distinct speed-up of northern South America. Plate models with less internal deformation (for example, ref. 7) exhibit a minor acceleration of the southern plates followed by a large acceleration of entire South America. In all cases, plate kinematics show major speed-up about 10 Myr before breakup of the controlling rift segment.

Extended Data Table 1 | Thermo-mechanical reference parameters

Parameter	Units	Upper Crust		Lower Crust	Strong Mantle	Weak Mantle
Density	kg m^{-3}	2700		2850	3280	3300
Thermal expansivity	10^{-5} K^{-1}	2.7		2.7	3.0	3.0
Bulk modulus	GPa	55		63	122	122
Shear modulus	GPa	36		40	74	74
Heat capacity	J $kg^{-1}K^{-1}$	1200		1200	1200	1200
Heat conductivity	W $K^{-1}m^{-1}$	2.5		2.5	3.3	3.3
Radiogenic heat production	μW m^{-3}	1.5		0.2	0.0	0.0
Initial friction coefficient*	-	0.5		0.5	0.5	0.5
Cohesion	MPa	5.0		5.0	5.0	5.0
Rheology		Wet Quartzite	Wet Quartzite	Wet Anorthite	Dry Olivine	Wet Olivine
Flow law reference		64	70	65	66	66
Pre-exponential constant for diffusion creep	$Pa^{-1}s^{-1}$	-	-	-	2.25e-09	1.5e-09
Activation energy for diffusion creep	kJ/mol	-	-	-	375	335
Activation volume for diffusion creep	cm^{-3}/mol	-	-	-	6	4
Pre-exponential constant for dislocation creep	$Pa^{-n}s^{-1}$	8.57e-28	1.54e-17	1.79e-15	6.51e-16	2.12e-15
Power law exponent for dislocation creep	-	4.0	2.3	3.0	3.5	3.5
Activation energy for dislocation creep	kJ/mol	223	154	356	530	480
Activation volume for dislocation creep	cm^{-3}/mol	0	0	0	13	11

These listed parameters are used unless indicated otherwise. Pre-exponential constants of the flow laws[64–66,70] have been recalculated to account for flow laws written as a function of second invariants of stress and strain rate.
*During frictional strain softening, the friction coefficient reduces linearly from 0.5 to 0.05 for brittle strain between 0 and 1. For strains larger than 1, it remains constant at 0.05.

Chapter III - 3D Models

Article 5

Brune, S., Corti, G., and Ranalli, G. (2017): Controls of inherited lithospheric heterogeneity on rift linkage: Numerical and analogue models of interaction between the Kenyan and Ethiopian rifts across the Turkana depression. ***Tectonics***, p. 2017TC004739, doi: 10.1002/2017TC004739.

Article 6

Brune, S.; Popov, A. A.; Sobolev, S. V. (2012): Modelling suggests that oblique extension facilitates rifting and continental break-up. ***Journal of Geophysical Research***, 117, B08402, doi:10.1029/2011JB008860.

Article 7

Heine, C.; **Brune, S.** (2014): Oblique rifting of the Equatorial Atlantic: Why there is no Saharan Atlantic Ocean. ***Geology***, 42, 211-214. doi:10.1130/G35082.1.

Article 8

Brune, S. (2014): Evolution of stress and fault patterns in oblique rift systems: 3D numerical lithospheric-scale experiments from rift to breakup. ***Geochemistry Geophysics Geosystems***, 15:8, 3392–3415. doi:10.1002/2014GC005446.

AGU PUBLICATIONS

Tectonics

RESEARCH ARTICLE
10.1002/2017TC004739

Key Points:
- Combined analog and numerical geodynamic modeling of the Turkana region elucidates the impact of tectonic inheritance on rift architecture
- The anomalously wide Turkana rift zone is due to a transversal region of thinned crust resulting from Mesozoic rifting
- Kenyan and Ethiopian rifts avoid a straight link through the Turkana region due to inherited mantle lithospheric strength variations

Supporting Information:
- Supporting Information S1
- Movie S1
- Movie S2
- Movie S3
- Movie S4
- Movie S5
- Movie S6

Correspondence to:
S. Brune,
brune@gfz-potsdam.de

Citation:
Brune, S., G. Corti, and G. Ranalli (2017), Controls of inherited lithospheric heterogeneity on rift linkage: Numerical and analog models of interaction between the Kenyan and Ethiopian rifts across the Turkana depression, *Tectonics*, *36*, 1767–1786, doi:10.1002/2017TC004739.

Received 23 MAR 2017
Accepted 29 JUL 2017
Accepted article online 10 AUG 2017
Published online 13 SEP 2017

Controls of inherited lithospheric heterogeneity on rift linkage: Numerical and analog models of interaction between the Kenyan and Ethiopian rifts across the Turkana depression

Sascha Brune[1,2], Giacomo Corti[3], and Giorgio Ranalli[4]

[1]German Research Centre for Geosciences GFZ, Potsdam, Germany, [2]Institute of Earth and Environmental Sciences, University of Potsdam, Potsdam, Germany, [3]Istituto di Geoscienze e Georisorse, Consiglio Nazionale delle Ricerche, Florence, Italy, [4]Department of Earth Sciences and Ottawa-Carleton Geoscience Centre, Carleton University, Ottawa, Ontario, Canada

Abstract Inherited rheological structures in the lithosphere are expected to have large impact on the architecture of continental rifts. The Turkana depression in the East African Rift connects the Main Ethiopian Rift to the north with the Kenya rift in the south. This region is characterized by a NW-SE trending band of thinned crust inherited from a Mesozoic rifting event, which is cutting the present-day N-S rift trend at high angle. In striking contrast to the narrow rifts in Ethiopia and Kenya, extension in the Turkana region is accommodated in subparallel deformation domains that are laterally distributed over several hundred kilometers. We present both analog experiments and numerical models that reproduce the along-axis transition from narrow rifting in Ethiopia and Kenya to a distributed deformation within the Turkana depression. Similarly to natural observations, our models show that the Ethiopian and Kenyan rifts bend away from each other within the Turkana region, thus forming a right-lateral step over and avoiding a direct link to form a continuous N-S depression. The models reveal five potential types of rift linkage across the preexisting basin: three types where rifts bend away from the inherited structure connecting via a (1) wide or (2) narrow rift or by (3) forming a rotating microplate, (4) a type where rifts bend towards it, and (5) straight rift linkage. The fact that linkage type 1 is realized in the Turkana region provides new insights on the rheological configuration of the Mesozoic rift system at the onset of the recent rift episode.

Plain Language Summary The Turkana depression in the Kenya/Ethiopia borderland is most famous for its several million years old human fossils, but it also holds a rich geological history of continental separation. The Turkana region is a lowland located between the East African and Ethiopian domes because its crust and mantle have been stretched in a continent-wide rift event during Cretaceous times about 140-120 Ma ago. This thin lithosphere exerted paramount control on the dynamics of East African rifting in this area, which commenced around 15 Ma ago and persists until today. Combining analog "sandbox" experiments with numerical geodynamic modeling, we find that inherited rift structures explain the dramatic change in rift style from deep, narrow rift basins north and south of the Turkana area to wide, distributed deformation within the Turkana depression. The failed Cretaceous rift is also responsible for the eastward bend of the Ethiopian rift and the westward bend of the Kenyan rift when entering the Turkana depression, which generated the characteristic hook-shaped form of present-day Lake Turkana. Combing two independent modeling techniques - analog and numerical experiments - is a very promising approach allowing to draw robust conclusions about the processes that shape the surface of our planet.

1. Introduction

The evolution and architecture of continental rifts is controlled by the interaction among several parameters, including the rate of plate divergence, the thermal state of the lithosphere, and the presence and volumes of magmatic products [e.g., *Ziegler and Cloetingh*, 2004; *Brune*, 2016]. However, almost all continental rifts form in predeformed, and thus already structured, anisotropic lithosphere and reactivate preexisting weak zones, such as mobile belts, while avoiding stronger regions, such as cratons [e.g., *Dunbar and Sawyer*, 1988; *Versfelt and Rosendahl*, 1989]. The prerift lithospheric rheological structure and in particular its along-axis variations play one of the most important roles during continental extension.

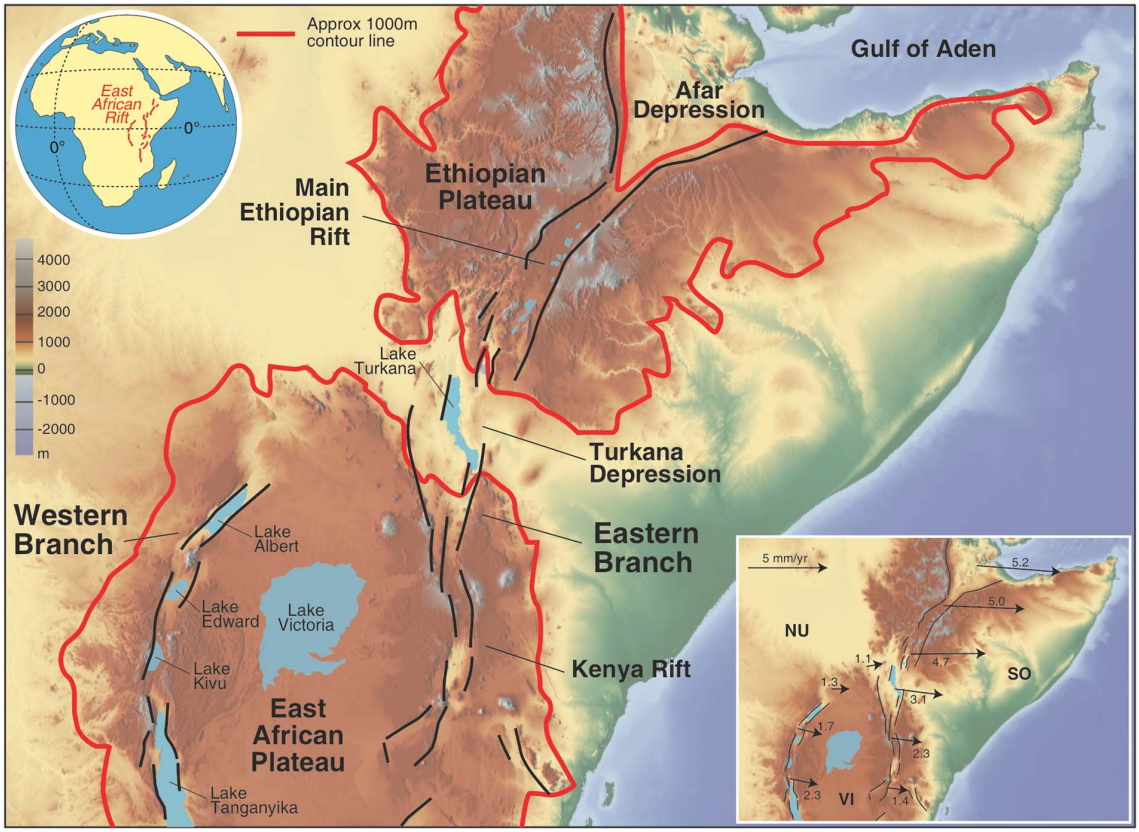

Figure 1. Tectonic setting of the East African Rift. Schematic fault pattern and present-day plate kinematics (inset). Black arrows show relative motions with respect to a stable Nubian reference frame according to the best fit model of *Saria et al.* [2014]. Values besides arrows indicate motion in mm/yr. NU: Nubian plate; SO: Somalian plate; VI: Victoria microplate.

The East African Rift (EAR) is a classical example where rifts are guided by inherited structures. The rift system developed within a region that has experienced several deformation events, from different phases of collision during the Precambrian to Mesozoic extension [*Chorowicz*, 2005]. This complex tectonic history has given rise to significant lateral variations in the rheological structure of the lithosphere [*Ebinger et al.*, 1997], which in turn have played a major role in rift evolution. This is clearly testified by the localization and propagation of major rift segments within weak Proterozoic mobile belts, which surround the undeformed Tanzania Craton [*Chorowicz*, 2005, and references therein]. Linking and mechanical interaction between adjacent rift segments has typically occurred in correspondence to transverse preexisting fabrics, where structurally complex areas (transfer zones) have allowed significant along-axis variations in subsidence of grabens and elevation of uplifted flanks [*Rosendahl*, 1987; *Morley et al.*, 1990; *Faulds and Varga*, 1998; *Morley*, 1999].

One of these complex areas is the Turkana depression, the region of interaction between the Ethiopian and Kenyan rifts, which is characterized by anomalous morphology and architecture with respect to the rift valleys in Kenya and Ethiopia. In this paper we test the hypothesis that these anomalies result from the presence of a preexisting rift, transverse to the trend of the rift valleys, and characterized by thin crust and lithosphere. To this aim, we complement crustal-scale centrifuge analog models with lithospheric-scale numerical modeling.

2. Tectonic Setting

The Turkana depression is a lowland located between the uplifted East African and Ethiopian domes (Figure 1). The tectonic setting of this area is controlled by long-term divergence between the Nubian and Somalian plates, which is currently occurring in a roughly E-W direction at rates of a few

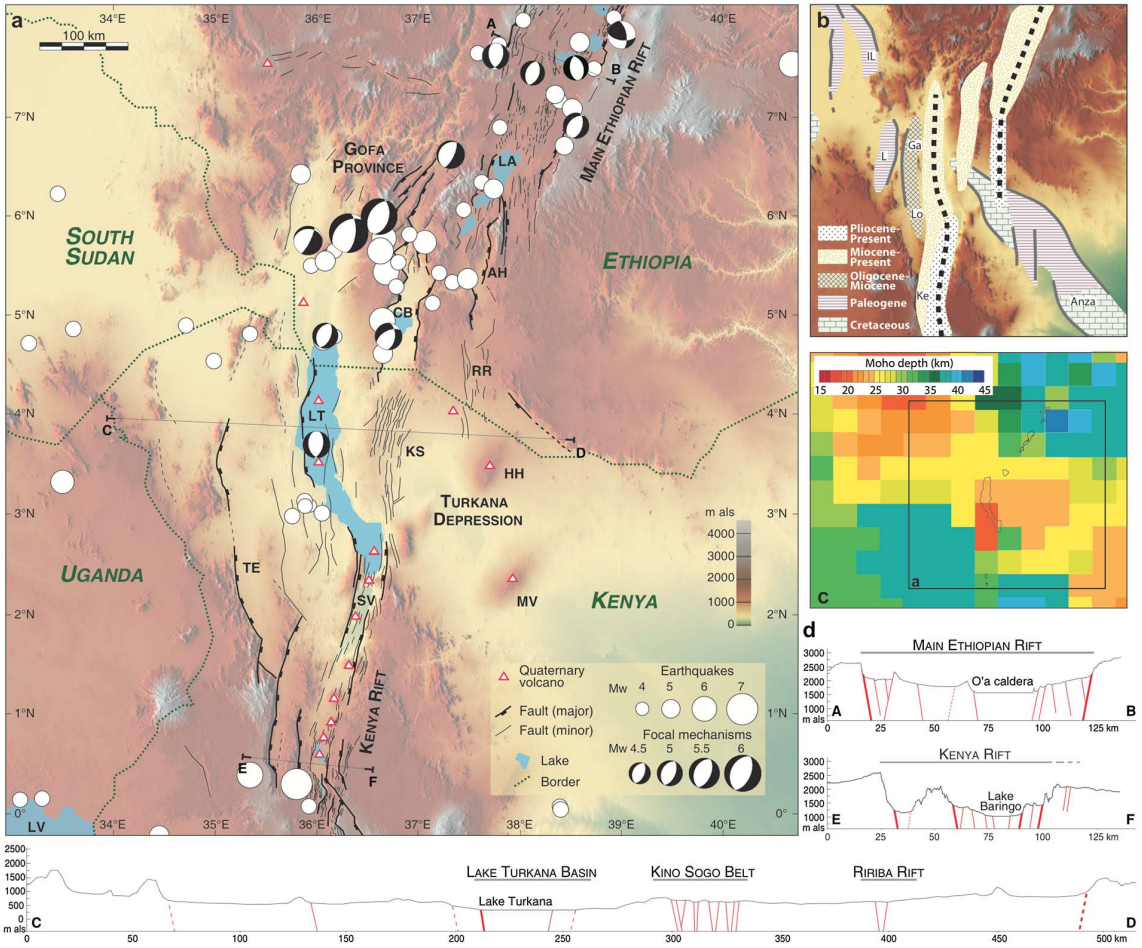

Figure 2. Detailed tectonics of the study area. (a) Quaternary faults, seismicity, and Quaternary volcanoes in the Turkana depression and surrounding regions superimposed on a SRTM (Nasa Shuttle Radar Topography Mission) digital elevation model. Seismicity from U.S. Geological Survey National Earthquake Information Center catalog (1900 to present); focal mechanisms from the global centroid moment tensor project; volcanoes from the Smithsonian Institution, Global Volcanism Program database. Fault pattern modified from *Moore and Davidson* [1978], *Ebinger et al.* [2000], *Hautot et al.* [2000], *Morley* [2002], *Vetel et al.* [2005], *Melnick et al.* [2012], and *Philippon et al.* [2014]. AH: Amaro Horst; CB: Chew Bahir basin; HH: Hurri Hills; KS: Kino Sogo belt; LA: Lake Abaya; LT: Lake Turkana; LV: Lake Victoria; MV: Marsabit volcano; RR: Ririba Rift; SV: Suguta Valley; TE: Turkwell Escarpment. (b) Ages of basins within the Turkana depression and simplified patterns of interaction between the Kenyan and Ethiopian rifts (black dashed lines indicate the rift axis). Basins are labeled as follows: Ga, Gatome; IL, Ilubabor; Ke, Kerio; L, Lokitipi; and Lo, Lokichar. Dark gray lines represent Cretaceous and Paleogene faults. (c) Map of crustal thickness in the region [from *Benoit et al.*, 2006]. (d) Simplified cross sections highlighting the different style and distribution of deformation in the Turkana depression with respect to the Kenyan and Ethiopian rifts.

millimeters per year [*Saria et al.*, 2014; *Stamps et al.*, 2014]. Recent plate motion models [*Iaffaldano et al.*, 2014; *DeMets and Merkouriev*, 2016] suggest that this direction of extension has likely remained steady during rift development (i.e., in the last 10–12 Myr).

The Main Ethiopian Rift (MER) and the Kenya rift are part of the Eastern Branch of the EAR (Figure 1) [*Chorowicz*, 2005]. North of the Turkana region, in the MER and southern portion of the Afar depression, extensional deformation is characterized by a typical narrow rift morphology exhibiting large fault escarpments with vertical displacement of >1 km, which bound a roughly 80–100 km wide rift valley and separate two uplifted plateaus [*Mohr*, 1983]. South of the Turkana depression, deformation in the Kenya rift is, similarly to the MER, characterized by large marginal fault systems, which separate a narrow rift valley (about 60–80 km in width) from surrounding uplifted plateaus. The MER and Kenya rift interact within the Turkana depression, which is characterized by a style of deformation where faulting, seismicity, and Quaternary-Holocene volcanic centers are widespread over a width of more than 300 km (Figure 2). This testifies a wide region of ongoing rift-related tectono-magmatic activity, which is in striking contrast with the two narrow

rifts to the north and south. Similarly, the Turkana region lacks the typical rift valley morphology dominated by large fault escarpments. Instead, extension is accommodated by numerous faults with limited vertical offset clustered within different subparallel deformation domains (Figures 2a and 2d) [see also *Ebinger et al.*, 2000], where the main domains are (i) the Turkana Basin, (ii) the Kino Sogo fault belt, and (iii) the Ririba Rift. The Turkana Basin corresponds to the northwestward propagation of the Kenya rift via the Suguta Valley, whereas the Ririba Rift (and the Hurri Hills and Marsabit volcanic lineaments) is believed to represent the southeastward propagation of the Ethiopian rift [*Ebinger et al.*, 2000; *Bonini et al.*, 2005]. The Kino Sogo belt, a 30 km wide system of small horsts and grabens located between the Turkana Basin and the Ririba Rift, accommodates a minor part of the extensional deformation [*Vetel et al.*, 2005]. To the north, this fault system links with the Chew Bahir basin, which is part of the complex Broadly Rifted Zone of South Ethiopia [*Ebinger et al.*, 2000; *Vetel and Le Gall*, 2006].

The deformation events that preceded the main Cenozoic rift phase have been suggested to have largely controlled the structural pattern and the physiography of the area, both at a regional scale [*Ebinger et al.*, 2000; *Benoit et al.*, 2006] and at the scale of individual faults and fault arrays [*Vetel et al.*, 2005; *Vetel and Le Gall*, 2006]. In particular, the area has been affected by a significant Mesozoic rift event, which created a system of NW-SE grabens (such as the Anza graben in Ethiopia) at a high angle to the Cenozoic Ethiopian/Kenyan rift valleys (Figure 2b). Geophysical data provide evidence for significant crustal thinning beneath the Turkana depression, where a crustal thickness $<$25 km has been imaged (Figure 2c) [*Woldetinsae and Götze*, 2005; *Benoit et al.*, 2006; *Sippel et al.*, 2017]. The inherited thin crust related to this Mesozoic event was suggested to cause the low topography of the region with respect to the surrounding uplifted plateaus [*Benoit et al.*, 2006]. As a consequence, the Turkana depression is one of the few places with elevations below 1 km that belongs to the region of anomalously elevated topography characterizing eastern and southern Africa.

The complex, pre-Miocene tectonic history within the Turkana depression is testified by the continuation of sedimentation in the Anza graben during the Paleogene and by the roughly coeval development of N-S trending sedimentary basins (e.g., Lotikipi and Lokichar) west of Lake Turkana (Figure 2b) [*Morley et al.*, 1992; *Morley*, 1999; *Ebinger et al.*, 2000]. These basins started developing during the Oligocene-early Miocene [*Morley et al.*, 1992; *Hendrie et al.*, 1994; *Morley*, 1999] before the beginning of Nubia-Somalia divergence and after the earliest manifestation of flood magmatism at ~45 Ma in the Broadly Rifted Zone of South Ethiopia [*Davidson and Rex*, 1980; *George et al.*, 1998]. During early Miocene times, extension started in the Chew Bahir basin, contemporaneous with a first, minor phase of extensional deformation in the Southern MER [*Bonini et al.*, 2005; *Pik et al.*, 2008]. Basin development began in the Lake Turkana region at around 15 Ma, followed by activation of large boundary faults at around 12 Ma in the Broadly Rifted Zone of South Ethiopia and at 8–10 Ma in the Amaro Horst region of the Southern MER [*Balestrieri et al.*, 2016]. During the Pliocene-Quaternary, the volcano-tectonic activity focused in the Lake Turkana Basin, now a direct continuation of the Kenya rift, whereas the extensional deformation related to the MER propagated southward into the Eastern Turkana depression (Ririba Rift, Hurri Hills, and Marsabit volcanic lineaments) [*Bonini et al.*, 2005].

Overall, a progressive eastward migration of Oligocene-recent deformation within the Turkana depression has been suggested [*Ebinger et al.*, 2000, and references therein]. This migration, together with a northward propagation of rifting in the Kenya rift and a southward propagation of the Main Ethiopian Rift to the Ririba and Marsabit volcanic lineaments, is considered responsible for the anomalous breadth of the zone of deformation in the region [*Ebinger et al.*, 2000]. Strain hardening between episodes of extension [*Morley et al.*, 1992] or deep-seated asthenospheric processes such as plume impingement at the base of the lithosphere [*Ebinger et al.*, 2000] has been considered responsible for the progressive eastward migration in the Turkana depression.

3. Initial and Boundary Conditions for Modeling

We conduct both analog and numerical experiments in order to investigate the interaction between the Ethiopian and Kenyan rifts across the Turkana depression. These modeling approaches complement each other since analog models are powerful in analyzing brittle deformation and the surface fault pattern at a very high resolution (here: ~800 m) but are limited in that they normally cannot account for complex

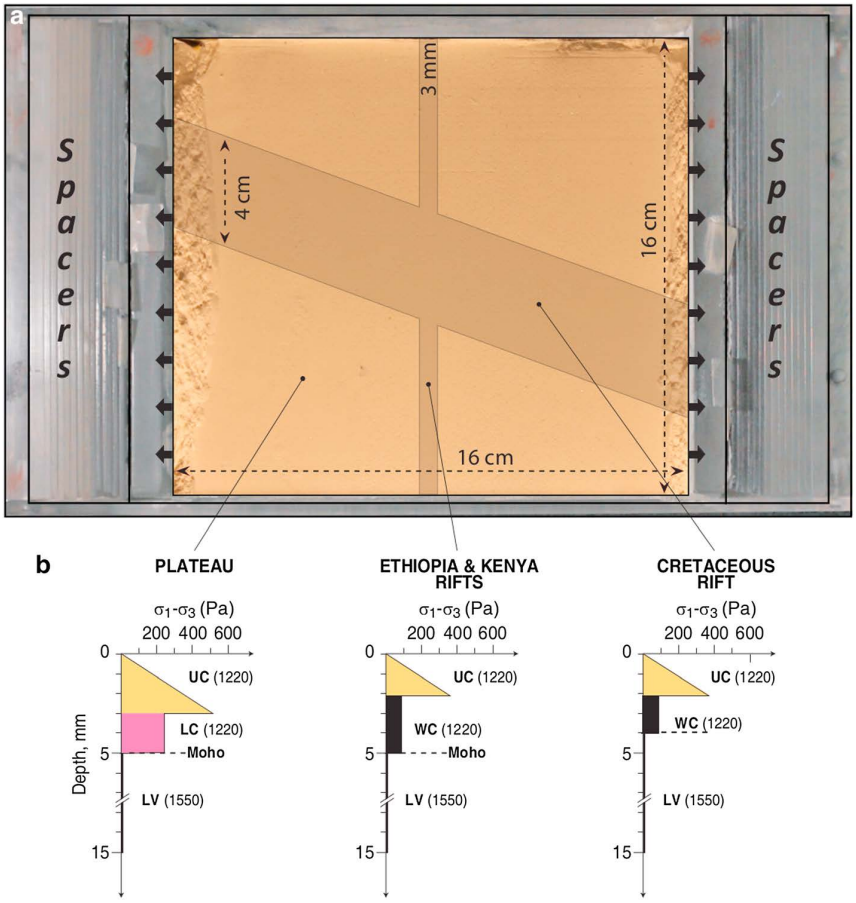

Figure 3. Analog modeling setup. (a) Top view of the experimental apparatus (see text for details). (b) Strength profiles in the different model domains. LC: lower crust; LV: low-viscosity mixture providing isostatic support to the overlying crust; UC: upper crust; WC: weak lower crust.

rheologies and thermal variations during deformation and related processes. These complexities are instead well reproduced and analyzed in numerical models, which, however, are more limited in model resolution (here: 7 km). In the following we outline the general model framework, while the specific setup for analog and numerical models is discussed in sections 4 and 5, respectively.

We capture the first-order regional plate tectonic setup by subdividing the region into three different domains, namely, Turkana depression, Kenya/Ethiopia rifts, and plateaus outside of any rift (Figure 3). The main starting point for our modeling is the presence of thin crust beneath the NW-SE trending domain of Mesozoic extension (section 2). We set the initial crustal thickness in this area to 30 km, which represents the initial Moho depth before the onset of Neogene rifting. This value corresponds to the thickness of crystalline crust within parts of the Anza graben that have not been reactivated (Figure 2c) [see also *Benoit et al.*, 2006; *Sippel et al.*, 2017]. The stable plateaus and the rift valleys are characterized instead by an initial thickness of about 40 km, which is the average Moho depth of today's plateaus in both domains [*Keranen et al.*, 2009; *Sippel et al.*, 2017]. For the thickness of the felsic upper crustal layer at the onset of Neogene rifting we use a value of 20 km. This is justified through Kenyan and Ethiopian seismic refraction surveys that exhibit v_p larger than 6.5 km/s at depths of 20 km alongside the main grabens [*Keller et al.*, 1994; *Maguire et al.*, 2006]. These velocities further indicate that the lower crust is composed of mafic lithologies [*Christensen and Mooney*, 1995]. We have also assumed a strength contrast between plateaus and Turkana depression and Kenyan/Ethiopian rift valleys. Both domains have been likely influenced by channeling and ponding of plume material in the Oligocene/Miocene

[*Ebinger and Sleep*, 1998; *Ebinger et al.*, 2000], resulting in an elevated lithosphere-asthenosphere boundary (LAB) with respect to the surrounding plateaus. In the numerical models this is represented directly through different thermal LAB depths in each domain, while in the analog model we implement the strength contrast through different materials and layer thicknesses.

According to recent geodetical estimates [*Saria et al.*, 2014; *Stamps et al.*, 2014], extension in the models has been considered to be orthogonal to the Ethiopian/Kenyan rift valleys, i.e., roughly E-W (Figure 1). Note that our models are focused on the Eastern Branch of the EAR and do not consider the transfer of deformation from the latter to the Western Branch. The amount of total extension, the velocity of plate motion in the past, and the timing of initiation of Nubia-Somalia motion are not well constrained, as different plate motion models predict different values. Plate tectonic models that integrate seafloor spreading reconstructions into plate circuits indicate that divergence between the major plates started before 16 Ma [*DeMets and Merkouriev*, 2016], likely at ~20 Ma [*Iaffaldano et al.*, 2014], with maximum values of extension of approximately 80 km [*Iaffaldano et al.*, 2014]. Geological data, however, seem to point to a later rift activation (at 10–12 Ma) [see *Balestrieri et al.*, 2016, and references therein] and lower amount of total extension (~30–40 km) [*Corti*, 2009, and references therein]. In this study we incorporated 15 Myr of symmetric extension at rates of ~4 mm/yr, resulting in a total amount of extension of 60 km.

4. Analog Modeling

4.1. Model Setup

The analog models were performed in an artificial gravity field of ~18 g using the large-capacity centrifuge available at the Tectonic Modelling Laboratory of the Institute of Geosciences and Earth Resources (National Research Council of Italy) and the Department of Earth Sciences of the University of Florence. The models simulated a simplified rheological layering composed of brittle-ductile crust floating above a low-viscosity material (Figure 3). The use of the centrifuge technique to perform experiments is based on the principle that the centrifugal force plays the same role in the models as does the force of gravity in natural geologic processes [*Ramberg*, 1981]. In the centrifuge, the models thin vertically and expand laterally in response to the centrifugal body force field that act during a centrifuge run. More specifically, the models, with dimensions of $16 \times 16 \times 1.5$ cm, were built inside a rectangular Plexiglas box and were laterally confined by rectangular blocks (spacers) that were removed before running the model for a given time interval in the centrifuge (Figure 3a). During the centrifuge run, the models expanded to fill the empty space at their sides, simulating extensional tectonics in nature; sequential removal of spacers during successive runs in the centrifuge allowed controlling the amount and rate of extension. Top view photos and laser scans of the models were taken after the end of each centrifuge run in order to monitor the evolution of surface deformation. The models were frozen before taking a number of cross sections to study their internal geometry. This modeling technique has been extensively tested and employed in different settings [see, e.g., *Ramberg*, 1981; *Corti et al.*, 2003; *Corti*, 2012].

4.2. Rheological Layering, Materials, and Geometry

The two-layer models are composed of an upper brittle layer simulating the upper crust that, as in several previous centrifuge experiments [e.g., *Agostini et al.*, 2009; *Corti*, 2012], was modeled by using a K-feldspar powder characterized by a linear increase in strength with depth to reproduce natural brittle behavior (Figure 3b). The underlying ductile lower crust in the plateau domains was modeled with a mixture of plasticine (Pongo Fantasia modeling dough, distributed by FILA) and PDMS-Polydimethylsiloxane (Dow Corning, SGM36), with proportions of 100:80% in weight. The lower crust beneath the rift valleys and the Turkana domain was reproduced by using a similar weak mixture of silicone (Dow Corning DC3179), corundum sand, and oleic acid (100:20:5% in weight). The models involved a thinner crust beneath the Turkana depression with respect to the surrounding domains. Considering the absence of the underlying lithospheric mantle, this makes the Turkana depression slightly weaker than the Ethiopia/Kenya rifts. However, we tested other conditions in which the Turkana domain had the same strength or was slightly stronger than the rifts (see below and supporting information Figure S1). All these crustal layers rested on a low-viscosity mixture of DC3179, corundum sand, and oleic acid (100:80:15% in weight), which provided isostatic support to the extending, overlying crust (Figure 3).

The geometry of the models mimicked that of the natural prototype at a scale of ~1.3×10^{-7}, such that 1 cm in the experiments corresponded to ~80 km in nature. This allowed modeling ~60 km of total extension. Dynamic-kinematic similarity of gravitational, viscous, and frictional stresses acting in the system [*Ramberg*, 1981] ensured that the velocity of lateral displacement in the models ~2.5×10^{-5} m/s scaled to natural values of ~3–5 mm/yr.

4.3. Analog Modeling Results

Upon extension, deformation localized within the rift domains, giving rise to major fault escarpments bounding a subsiding narrow depression (Figure 4). These major faults formed at the rift/plateau boundaries, whereas systems of internal normal faults with more limited vertical displacement affected the rift floor. In both Kenyan/Ethiopian rift domains, deformation was entirely localized within the narrow depressions, i.e., in an area, which was ~1.4 cm (~110 km) wide after 4 mm (~30 km) of bulk extension (Figure 4a). The Turkana domain was instead characterized by a much wider region affected by deformation (up to ~7 cm —i.e., ~550 km—in width). Within this region, extension was accommodated by a much higher number of normal faults characterized by a limited vertical displacement and a general N-S trend.

During progressive extension, this overall architecture did not change significantly. Owing to an increase in slip on the boundary fault systems, the rift depression progressively increased its subsidence; the width of the rift valley increased to ~1.8 cm (~140 km), indicating that extension was entirely accommodated within it. In contrast, deformation within the Turkana depression was still distributed over a wide region (~8 cm—i.e., ~640 km—in width) and accommodated by a large number of small-offset normal faults (Figure 4). These faults were locally characterized by a zigzag pattern and by a trend that—although generally N-S—displayed local deviations to a more NNW-SSE orientation. Reactivation of the NW-SE-trending boundary between the weak Turkana depression and the strong surrounding plateaus occurred locally, as observed at the NW termination of the Kenyan rift valley (Figure 4).

Observation of the fault pattern and the topography of the model surface at the end of deformation (Figure 4b) indicates that entering the Turkana domain, the region of maximum subsidence (i.e., highest fault activity) related to the Ethiopian domain propagated toward the SE, whereas that of the Kenyan domain propagated toward the NW. Instead of linking directly to form a throughgoing N-S depression, the rift valleys propagated away from each other within the Turkana depression giving rise to a right-lateral step over of interacting rifts.

In different models we have tested different rheologies for the Turkana domain, rendering it slightly stronger or characterized by a similar strength with respect to the Kenyan/Ethiopian rifts. The model results are at a first order similar to the one described above in terms of distribution and characteristics of deformation (see supporting information Figure S1), underlining the robustness of our results.

5. Numerical Modeling

In addition to the analog experiments presented in section 4, the numerical model captures also the thermal evolution of the system taking into account radiogenic heating of the crust and thermal equilibration of the lithosphere. Hence, the brittle layer thickness and thus the degree of crust-mantle coupling is a dynamically evolving component of the model.

5.1. Model Setup

In the following we apply the finite element code SLIM3D [*Popov and Sobolev*, 2008], which solves the conservation equations of momentum, energy, and mass using an Arbitrary Lagrangian-Eulerian formulation involving the particle-in-cell technique. The deformation of materials is accommodated via an elastoviscoplastic rheology, which self-consistently reproduces diverse deformation processes like faulting, flexure, and lower crustal flow. SLIM3D has been extensively benchmarked and applied to model lithospheric-scale processes in divergent [*Brune et al.*, 2012, 2013; *Brune and Autin*, 2013; *Brune*, 2014; *Heine and Brune*, 2014; *Koopmann et al.*, 2014; *Clift et al.*, 2015; *Brune et al.*, 2016, 2017], convergent [*Quinteros et al.*, 2010; *Quinteros and Sobolev*, 2012; *Duesterhoeft et al.*, 2014], and transform [*Popov et al.*, 2012; *Brune*, 2014] plate boundaries and in a centimeter-scale study of localization dynamics [*Cyprych et al.*, 2016].

The model has a free surface at the top boundary, while at the bottom boundary we apply an isostatic Winkler boundary condition, where inflow and outflow of material are accounted for during remeshing. We use a

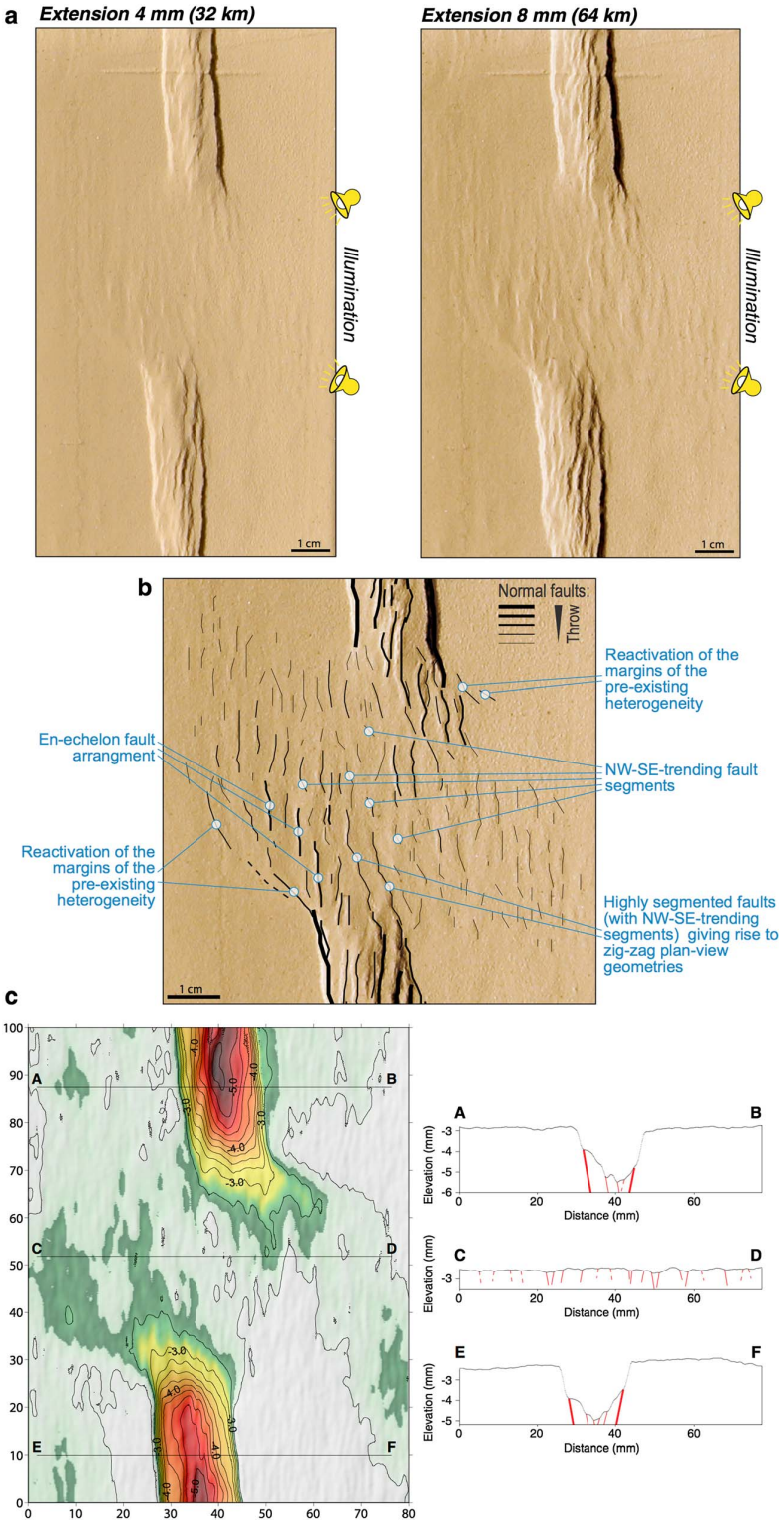

Figure 4. Analog modeling results. (a) Top view photos of the analog model for 4 mm and 8 mm bulk extension. (b) Line drawing of structures with examples of deformation features affecting the central part of the model. (c) Digital elevation model of the surface and topographic profiles at the end of deformation (8 mm bulk extension).

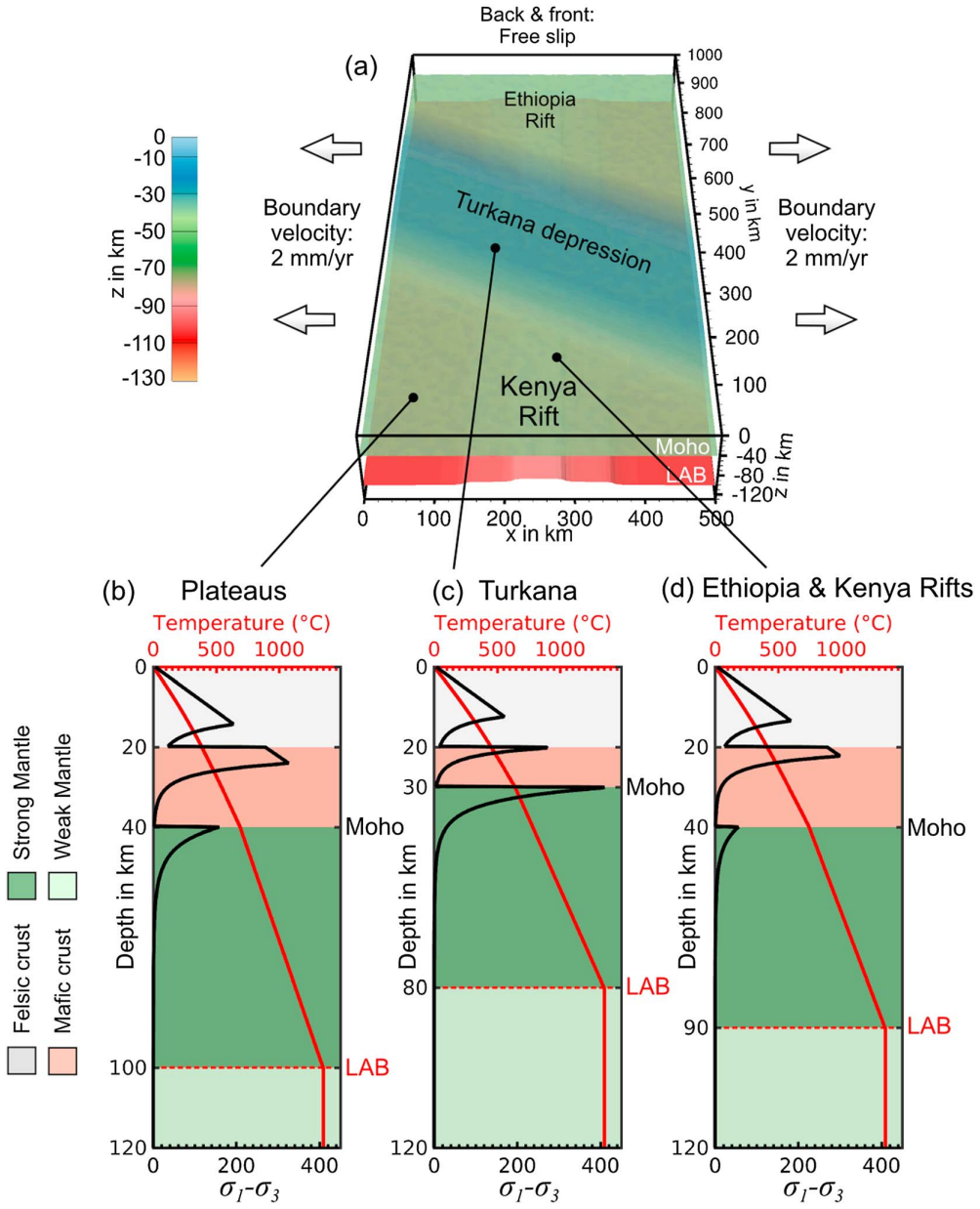

Figure 5. Numerical model setup. (a) Boundary conditions and domain locations. (b–d) Thermal profile and yield strength profiles computed for the initial bulk extension rate of the models, i.e., $2.7 \cdot 10^{-16}$ 1/s. For numerical parameters see supporting information Table S1.

constant rift velocity of 4 mm/yr (full rate) so that a 2 mm/yr velocity is prescribed orthogonal to both model boundaries facing in *x* direction (Figure 5). Front and back boundaries feature free slip. The numerical model comprises a domain of 500 × 1000 × 130 km in *x* (cross rift), *y* (along strike), and *z* direction (depth) and a resolution of ~7 km in all directions.

Temperature boundary conditions are as follows: the surface temperature is held constant at 0°C and the bottom temperature at 1350°C. Lateral boundaries are thermally isolated. At the model start, the temperature field results from the thermal equilibrium governed by the boundary conditions, the crustal radiogenic heat contribution, and by the initial depth of the LAB, defined through the 1300°C potential temperature isotherm,

which locates at 100 km depth under the plateaus, 80 km depth beneath the Turkana depression, and 90 km depth beneath the Ethiopia and Kenya rifts (Figure 5) unless otherwise indicated. The slightly shallower LAB beneath the rifts is used to seed strain localization without imposing crustal fault locations. Note that due to radiogenic heat production, domains with thin crust generate less heat than those with thick crust. For simplicity, we focus on lithospheric processes and do not implement heterogeneities in the deeper parts of the mantle such as the Afar plume [*Ebinger and Sleep*, 1998; *Hansen and Nyblade*, 2013] or the northward shallowing of the LAB under East Africa [*Fishwick and Bastow*, 2011].

The model accounts for four material layers: felsic crust, mafic crust, strong mantle, and weak mantle (Figure 5b). For the quartz-dominated felsic upper crust, we use the wet quartzite flow law of *Gleason and Tullis* [1995]. The mafic lower crustal layer is represented by a wet anorthite flow law [*Rybacki and Dresen*, 2000]. We use dry olivine rheology [*Hirth and Kohlstedt*, 2003] to model deformation of the strong, depleted, subcontinental mantle, while a wet (i.e., 1000 ppm H/Si) olivine flow law [*Hirth and Kohlstedt*, 2003] is applied for the weak, asthenospheric mantle. All rheological parameters are listed in supporting information Table S1. The model involves linearized frictional strain softening, a standard strategy to parameterize fault weakening [*Bos and Spiers*, 2002] in numerical models [*Huismans and Beaumont*, 2011; *Naliboff and Buiter*, 2015; *Le Pourhiet et al.*, 2017]. Here we linearly reduce the friction coefficient from 0.5 to 0.05 for brittle strain between 0 and 0.5. For strains larger than 0.5, it remains constant at 0.05. Similarly, we reproduce viscous strain softening [*Bürgmann and Dresen*, 2008] by increasing the preexponential factor of the ductile flow law by 10 times between viscous strains 0 and 0.5, which results in a moderate viscosity reduction of ~0.5.

5.2. Numerical Modeling Results

In numerical model A1 the rift exhibits a distinct northern, central, and southern segment (Figures 6a–6c). After 5 Myr model time, high tectonic strain rates of more than 10^{-15} 1/s are encountered in the northern and southern segments in a narrow band of roughly 100 km width. At the transition to the central segment, the rift arms bend away left laterally from the transversal central region, giving rise to a right-lateral step over geometry. Simultaneously, the rifts connect with each other such that the lateral extent of the rift in the central domain increases almost to the entire model width of 500 km. During subsequent model evolution, the northern and southern segments localize toward the basin center finally reaching a width of ~70 km at 15 Myr model time, while the N-S trending deformation domains inside the central segment are distributed with a width of about 300 km.

Next we focus on the final structure of the model after 15 Myr model time. The northern and southern rifts feature a deep basin of up to 100 km width (Figure 6g), whereas the central domain consists of a wide plain with N-S oriented horst and grabens and relatively low relief. The final topographic pattern primarily results from the isostatic response to crustal thinning, which is why surface topography mirrors Moho depth (Figure 6f) except for local horsts and grabens. Both topography and Moho depth exhibit left-lateral bending where the north/south rifts merge into the central domain. However, the LAB topography does not show this pattern indicating the lateral strength contrast in the shallow lithosphere as the main control for this pattern. The surface velocity field clearly shows the transition from narrow to wide rifting in the *x* component of velocity (Figure 6i). The right-lateral step over from the northern to the southern segments creates a specific tectonic strain field that leads to northward velocities in the eastern part of the Mesozoic rift basin and southward movement in its western part (Figure 6j) predicting minor counterclockwise rotation of the central domain. These velocities of less than 0.4 mm/yr are a magnitude smaller than the overall extension velocity and do not generate any indication of strike-slip deformation. However, the direction of motion compares well with observations and models of other extensional plate boundaries with step over geometries, such as in the western branch of the EAR [*Koehn et al.*, 2008].

In the previous analog and numerical models we find a left-lateral bend (resulting in a right-lateral step over) of the narrow rifts at the transition to the transversal central domain. In the following we investigate the rheological configurations that enable this type of rift connectivity. To this aim, we modify layer thicknesses and thereby the thermal profile within the inherited Mesozoic rift (see supporting information Table S2) while the other model domains remain unchanged. Note that the thicknesses of crust and mantle at the onset of Cenozoic rifting cannot be deduced directly. Hence, we define a range of plausible layer thicknesses for the Turkana region by considering those parts of the Mesozoic African rift systems that have not been reactivated. One such example is the Anza graben in northeast Kenya with 25 to 30 km thick crust [*Sippel et al.*,

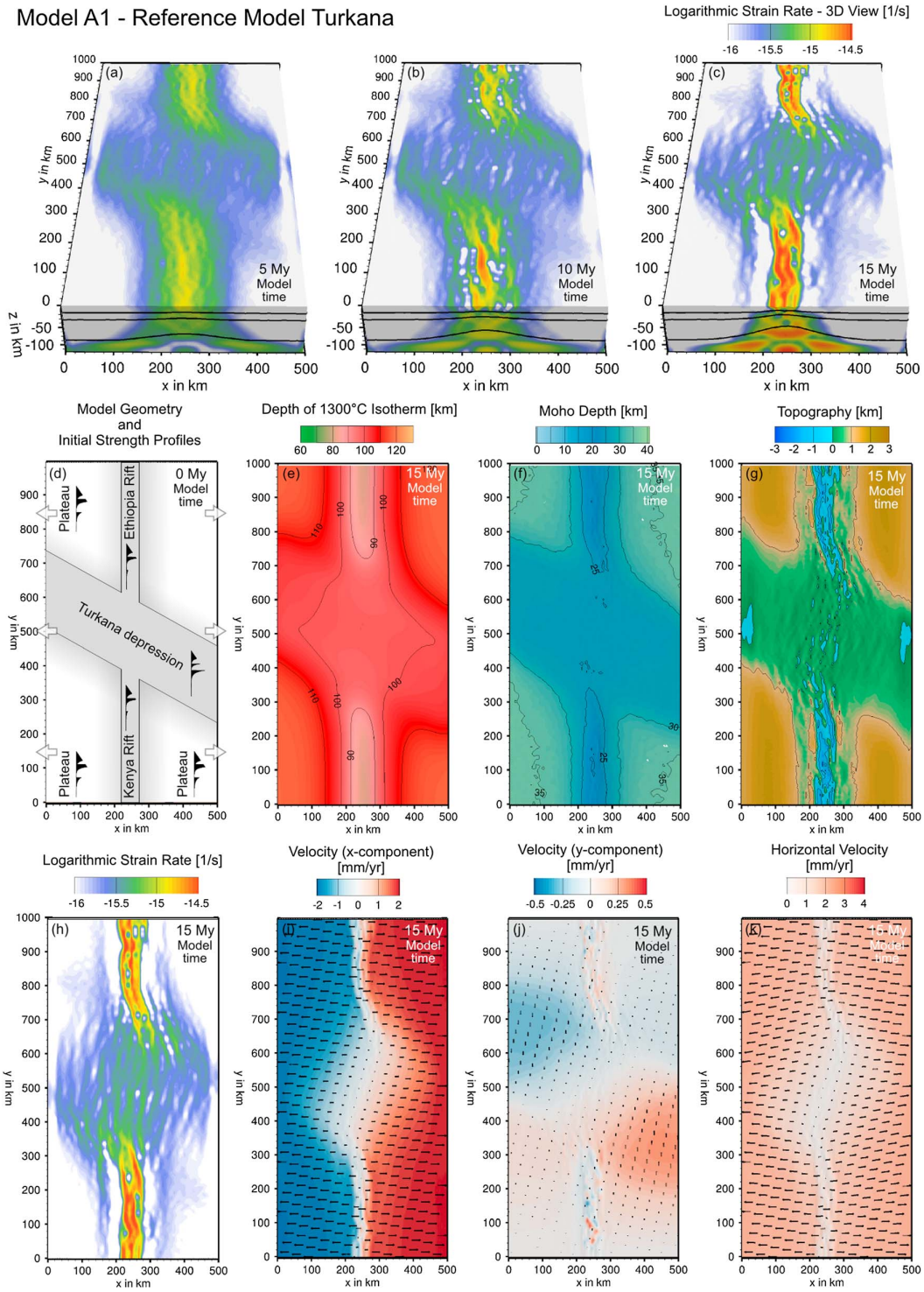

Figure 6. Numerical reference model. (a–c) Evolution of deformation pattern (second invariant of strain rate) in 3-D view. Numerical simulations at 15 Myr are comparable to the present-day structure of the study region. Note the left-bending rift tips (and thus right-stepping rift segments) where the northern and southern rifts interact with the central domain. (d) Initial model geometry in map view. (e) Final lithosphere-asthenosphere boundary (LAB). (f) Final Moho depth. (g) Final surface topography. (h) Final deformation pattern in map view. (i, j) N-S and E-W directed components of surface velocity. (k) Full horizontal velocity field. Seerendering supporting information Movie S1 for detailed model evolution.

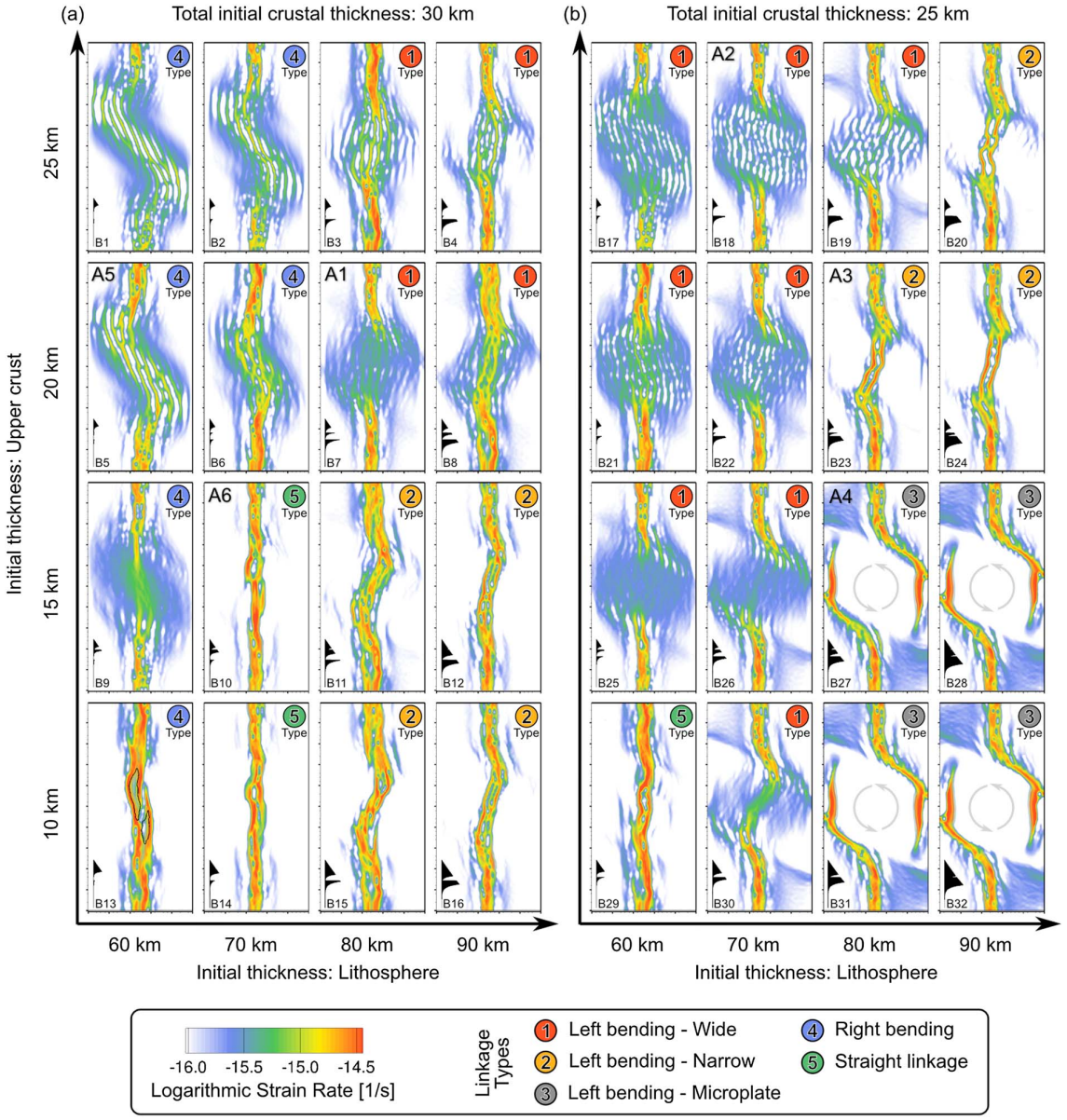

Figure 7. Alternative model results. We vary the initial conditions by scanning through different configuration of initial thicknesses of lithosphere, full crust, and upper crust within the transverse inherited domain of the Turkana region. (a) Initial crustal thickness of 30 km. (b) Initial crustal thickness of 25 km. All other parameters and layer thicknesses are kept identical to model A1. Images show strain rate patterns after 15 Myr of stretching, equivalent to 60 km of extension. In the lower left corner of each image we plot the yield strength profile of the transverse central region at the onset of rifting. Lithospheric strength is controlled by the interplay of lithospheric thickness and radiogenic heat production within the upper crust. The initial strength controls rift localization and leads to five different types of rift linkage after 15 Myr indicated in the upper right corner of each image. Initial strength of each layer within the central domain of all models is also provided in supporting information Table S2. Animations of six characteristic models representing key aspects of rift linkage are given in the supporting information as Movies S1 to S6.

2017] and a lithosphere thickness of 60 to 90 km [*Fishwick*, 2010]. Similar present-day thicknesses have also been found in the Central and West African Rift System for both lithospheric [*Fishwick and Bastow*, 2011] and crustal [*Pasyanos et al.*, 2014] layers.

The resulting deformation patterns after 15 Myr model time are depicted along with initial vertical strength profiles of the central transversal domain in Figure 7. We find a large variety of rift patterns that are solely due

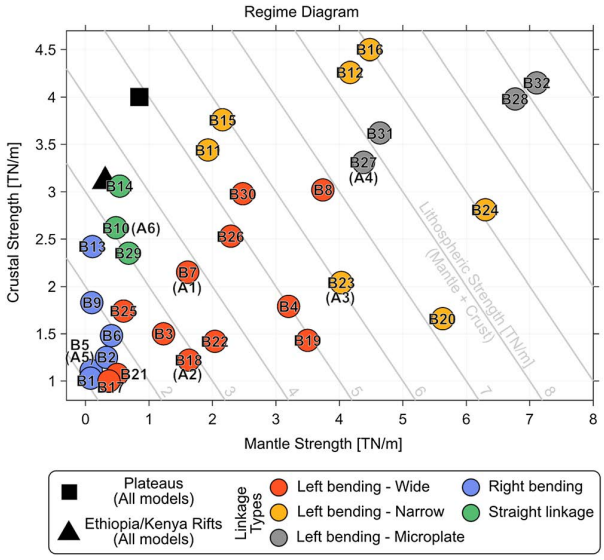

Figure 8. Regime diagram. All models of Figure 7 are represented in terms of initial crustal and mantle strength within the Turkana depression. Initial strength of other model domains such as plateaus, and Ethiopia/Kenya rifts are shown as black square and triangle, respectively. The five linkage types are identified by colored circles. Gray, diagonal lines indicate total lithospheric strength. For characteristic models S1 to S6 we provide supporting information movies of the model evolution.

to the rheological configuration of the central domain. The patterns can be classified into five distinct types: a group of three left-lateral bending types (i.e., right-stepping rift segments) where rifting in the central domain occurs (1) as a wide rift like in the Turkana region and as in model A1, (2) in narrow rift mode, and (3) through microplate formation. Further, we identify (4) a right-lateral bending type and (5) a type with straight segment linkage. Representative model animations for the evolution of each linkage type can be found in the supporting information.

The existence of these five types can be explained at first order by considering the strength contrast between crust and mantle in each model (Figure 8). In most cases where the strength of the mantle in the central domain is larger than that of the plateaus outside of the rift zones, the northern and southern segments avoid a direct connection by forming the left-lateral bend near the central segment (Types 1–3). Hence, the left-lateral bend results from minimizing the mechanical work that is required to deform the central domain. This further indicates that mantle strength exerts first-order control on surficial deformation pattern by controlling the location of lithospheric necking. Wide rifting (Type 1) dominates for integrated lithospheric strengths below ~4–6 TN/m (gray diagonal lines in Figure 6c), while narrow rifting (Type 2) and microplate formation (Type 3) prevail for higher lithospheric strengths. This can be understood when considering that in this high-strength regime brittle deformation leads to more rapid localization so that lithospheric necking occurs faster which promotes narrow rifting. In fact, left-bending wide rifts (Type 1) eventually localize into narrow rifts (Type 2), while the initial stages of narrow rifts (Type 2) feature wide rift characteristics (see supporting information Movies S1–S3); hence, the difference between these types is time dependent. Microplate formation occurs for high-strength end-members within the left-bending regime. In these scenarios, the central domain behaves like an almost undeformable block that diverts strain to the lateral model boundaries. In agreement with continental and oceanic microplate rotations, the right-lateral step over geometry generates a counterclockwise rotating microplate [*Katz et al.*, 2005; *Koehn et al.*, 2008]. Right-lateral bending (i.e., left stepping) of the northern and southern rifts (Type 4) occurs if the mantle strength in the central domain is less or similar to that of these segments. In this case the mantle beneath the central rift is so weak that it governs the necking process and forces crustal localization to bend right laterally into the central segment. This case is reminiscent to recent analog models of propagating rotational rifts interacting with linear rheological heterogeneities cutting the rift at moderate and high obliquity [*Molnar et al.*, 2017]. If the rheological configuration of the central domain is very similar to the rift valleys to the north and south, the model virtually does not notice the inherited heterogeneity and straight linkage (Type 5) occurs. While these explanations hold at first order, the strength diagram also shows that the transition from one regime to the other does not occur as an abrupt boundary.

5.3. Model Limitations and Robustness

The numerical model includes only the lithosphere and shallow asthenosphere; hence, it does not account for mantle-related topographic changes caused by asthenospheric flow [*Emishaw et al.*, 2017], small-scale convection [*van Wijk et al.*, 2008], or whole-mantle convection [*Flament et al.*, 2013; *Rubey et al.*, 2017].

These dynamic topography contributions add to the isostatically compensated topography, especially above regions of focused upwelling. For the Ethiopian dome, independent studies attributed amplitudes of ~1.5 km to this kind of dynamic mantle support [*Hoggard et al.*, 2016; *Sembroni et al.*, 2016], which is why we chose this value for our initial topographic baseline.

When comparing numerical results to regional geophysical models of Moho and LAB depth, one has to keep in mind that our numerical model locally conserves crustal mass. This means that we do not account for magmatic underplating or basin sedimentation leading to replenishment of crustal thickness. The contributions of these processes to crustal rethickening beneath EAR rift valleys are up to 3 km for sedimentation [*Ebinger et al.*, 1999; *Sippel et al.*, 2017] and about 4 km for underplating in the Kenya rift [*Thybo et al.*, 2000].

Values of experimentally determined creep parameters for the chosen compositions vary slightly in the literature. We therefore tested the influence of alternative flow laws for upper crust [*Rutter and Brodie*, 2004], lower crust [*Rybacki et al.*, 2006], and mantle [*Karato and Jung*, 2003] and found that despite minor structural differences, our conclusions were robustly reproduced. The model results did not change when we simultaneously applied dislocation and diffusion creep within the mantle [*Hirth and Kohlstedt*, 2003] instead of only dislocation creep as in the models above. We used 1 mm and 10 mm grain size, and even though the mantle viscosity dropped from a minimum of 10^{19} Pa s to below 10^{18} Pa s, the strain rate field at the surface remained identical. We also tested asymmetric boundary conditions, where we applied the full extension rate to one model side while keeping the opposite side fixed. Since there are no shear tractions allowed across the bottom, top, front, and back boundaries, the results are invariant with respect to asymmetric boundary conditions.

Localization dynamics of faults and shear zones depend on the included weakening mechanisms and the employed numerical resolution [*Buiter et al.*, 2006, 2016]. Reducing the element size to 10 km and/or switching off strain softening for model A1 indeed changes the temporal evolution of the rift. However, after sufficient model time the resulting deformation patterns are qualitatively similar to the reference model (Figure 6). We conducted models where we used rift velocities of 3 mm/yr and 5 mm/yr (full rate) covering the plausible range from plate reconstructions and geological indicators (cf. section 3). The deformation pattern after the same amount of extension featured some small differences, but qualitatively, the structures remained the same. Finally, we varied the obliquity of the inherited Mesozoic rift between 0 and 60° (measured between the domain trend and the extension normal), while all other parameters were identical to model A1. For higher obliquities, the effect that the rifts avoid cutting into the transversal domain is enhanced. For low obliquities, the effect is less pronounced and at no obliquity it disappears (supporting information Figure S2).

6. Discussion

6.1. Along-Strike Differences in Deformation Style

The two independent modeling approaches, crustal-scale analog experiments and numerical lithospheric-scale models, were able to reproduce the significant along-axis differences in style and distribution of deformation between the Ethiopia/Kenya rift valleys and the Turkana depression. In particular, both modeling approaches showed a transition from localized deformation in the rift valley domains characterized by large marginal escarpments to a diffuse deformation within the Mesozoic rift, accommodated by a large number of minor faults with limited vertical displacement. Our results therefore highlight the important role of the transversal preexisting heterogeneity with thinned crust and lithosphere in the Turkana region on the style and distribution of deformation during Cenozoic rifting.

Our findings confirm previous works [*Ebinger et al.*, 2000] in that the width of deformation within the Turkana depression has no similarity to patterns in broad rift zones that developed in relatively hot lithosphere, such as the Basin and Range and Aegean extensional provinces [*Buck*, 1991, 1999; *Labrousse et al.*, 2016]. Instead, the anomalously wide rift zone is caused by the N-S propagation of the Main Ethiopian and Kenya rift systems into a region of thinned crust, with mantle lithosphere that is stronger than that next to the inherited Mesozoic heterogeneity.

Highly oblique rifts are typically characterized by a wider deformation zone than more orthogonal rifts [e.g., *Corti*, 2012; *Brune*, 2014]; since the reactivation of the NW-SE trending heterogeneity under

roughly E-W extension results in a high obliquity of 60°, this may indicate a control exerted by rift obliquity on the anomalously wide deformation domain in the Turkana depression. However, highly oblique rifts feature complex fault patterns that are typically dominated by faults which are not orthogonal or suborthogonal to extension but are instead oblique or highly oblique to this direction [see, e.g., *Agostini et al.*, 2009]. These patterns are very different from what is observed in the Turkana depression, where deformation is characterized by subparallel fault domains trending roughly N-S (i.e., roughly extension-orthogonal). This indicates that faults in the Turkana depression respond directly to the roughly E-W Nubia-Somalia motion and that the high rift obliquity does not play a major role in controlling the style and distribution of deformation. Moreover, the very good correspondence between our model results and the distribution and characteristics of deformation in the Turkana depression suggests a negligible influence exerted by the Western Branch on the interaction between the Kenyan and Ethiopian rifts. This is also supported by the lack of significant volcano-tectonic activity in a large region close to the border between South Sudan and Kenya, west of Lake Turkana.

The numerical models predict a progressive narrowing of deformation within the preexisting Mesozoic rift, which is in agreement with the eastward migration of deformation from basins in the western portion of the Turkana depression to more central domains (e.g., Lake Turkana itself and surrounding areas) [*Ebinger et al.*, 2000, and references therein]. However, the sedimentary basins west of Lake Turkana, which started developing prior to ~25 Ma, likely predate Nubia-Somalia divergence [*Iaffaldano et al.*, 2014; *DeMets and Merkouriev*, 2016] and therefore were not strictly related to the Tertiary rifting event in a strict sense. Consequently, other processes, such as deep-seated asthenospheric processes (plume impingement at the base of the lithosphere) [*Ebinger et al.*, 2000] or strain hardening between episodes of extension [*Morley et al.*, 1992], likely contributed to the observed evolution.

6.2. Characteristics of Rift Linkage Within the Turkana Depression

Both our analog model and Types 1–3 of the numerical models depict the tendency of the rift valleys to propagate preferentially to SE (Ethiopia) or to the NW (Kenya) instead of linking up directly. As explained in section 2, this reproduces a key natural observation. In fact, extensional deformation related to the Kenya rift is shifted to the NW to form the narrow depression hosting Lake Turkana; similarly, the Ethiopian rift is progressively shifted to the SE forming the Ririba Rift and Hurri Hills [*Ebinger et al.*, 2000; *Bonini et al.*, 2005].

What is the tectonic reason for diverting the Ethiopian and Kenya rifts toward the east and west, respectively? Our models show that this pattern occurs during the very beginning of deformation (Figure 6a), so it cannot be related to evolving variables such as strain softening or crustal thinning, as evoked for 2-D rift migration [*Kusznir and Park*, 1987; *van Wijk and Cloetingh*, 2002; *Brune et al.*, 2014; *Svartman Dias et al.*, 2015; *Jammes and Lavier*, 2016]. We find that strength variations in crust and mantle play a first-order role in controlling the regional rift architecture. However, mode selection is not controlled by the vertically integrated lithosphere strength. If this was the case, models where the central domain is weaker than the plateaus outside of the rift zones, such as the analog model and numerical models A1, B3, B17, B18, B21, B22, B25, and B26, would not feature the left-lateral bend at the segment boundary. Therefore, we suggest that there is a hierarchy of dominating processes:

1. On crustal level, localization is solely controlled by brittle localization dynamics and stress focusing due to rift propagation into the transversal preexisting heterogeneity. This agrees with previous modeling [*Acocella et al.*, 1999] that in conditions of orthogonal rifting (i.e., the extension direction is perpendicular to the rift trend) when the angle between the rift margins and the margins of the preexisting heterogeneity is $>90°$, reactivation of its boundaries is favored; conversely, when the angle is $<90°$, reactivation is less probable (Figure 9).
2. If the existence of lithospheric and asthenospheric mantle is accounted for, the crustal processes are largely overruled by lithospheric thinning. In this case, it is the mantle strength that has first-order control on the transition from left-bending type to straight linkage and right-bending type, while second-order deviations of this rule are due to crustal processes.
   When applying our results to nature, we suggest that both processes facilitate localization of deformation at the NW termination of the Kenya rift and at the SE tip of the Ethiopian rift (Figure 9), promoting the propagation of this latter to the SE and that of the Kenyan domain toward the NW.

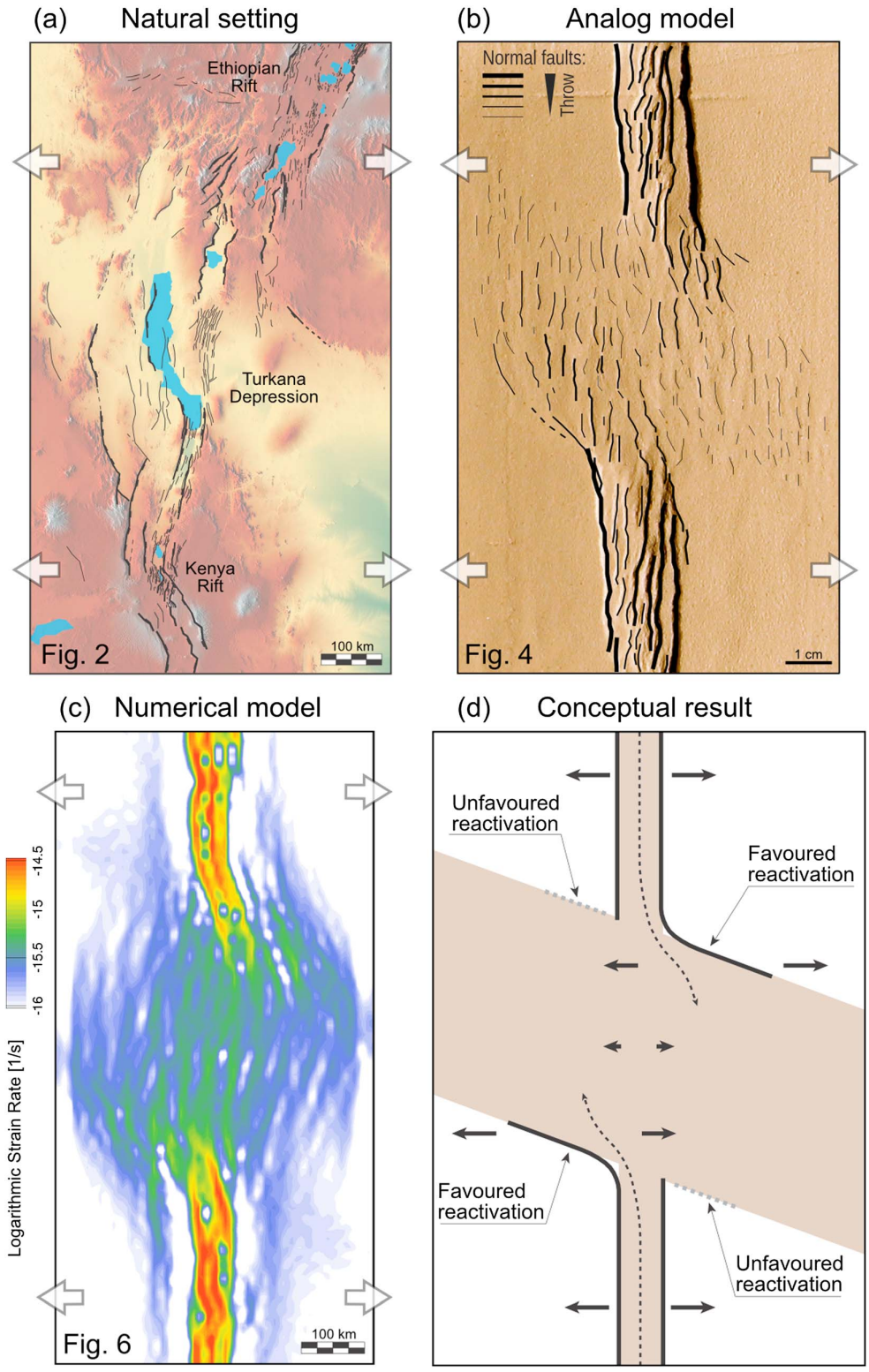

Figure 9. Summary plot. (a) Major faults of the study area. (b) Key features of the analog model. (c) Final deformation pattern of numerical reference model A1. (d) Summarizing interpretation (see text for details).

6.3. Influence of the Preexisting Lithospheric Structure on the Local Fault Pattern

Besides capturing the large-scale picture of rift interaction, our analog modeling indicates that the preexisting variations in strength of the different domains have an important control on the fault pattern at a more local scale. For instance, the models indicate significant reactivation of the boundaries between the Turkana domain and the strong surrounding plateaus, giving rise to NW-SE faults at the margins of the preexisting transversal heterogeneity, which are a continuation of the boundary faults of the main rift valleys. A similar feature can be hypothesized in nature at both the southern tip of the Ethiopian rift (where NW-SE faults characterize the margins of the preexisting Anza graben, east of the Ririba Rift) and the NW termination of the Kenya rift (where NW-SE to NNW-SSE trending faults give rise to the large Turkwell escarpment; Figures 2 and 9). In this latter case, the NW-SE faults typically curve at their tip to acquire a more N-S to NNE-SSW trend, a characteristic that is observed in the analog models. This feature resembles the horse-tail splays at the termination of transcurrent faults and likely result from the component of strike-slip motion at the margins of the Turkana depression imposed by the relative orientation between the boundary of the preexisting transversal heterogeneity and the extension direction (Figure 9).

Another interesting feature within the fault pattern is the presence of numerous NW-SE trending minor faults or fault segments, which develop with a high obliquity to the extension direction but subparallel to the transversal preexisting domain (Figure 4b). In places, these segments tend to connect N-S structures, resulting in highly segmented NNW-SSE trending normal faults with a typical zigzag plan view geometry. In turn, these fault systems bound highly segmented basins, which result from the coalescence of en echelon N-S trending subbasins connected by NW-SE segments. This geometry strikingly resembles the typical "staircase" pattern of the basin hosting Lake Turkana. Although this architecture has been suggested to be controlled by the reactivation of preexisting, discrete upper crustal fabrics [*Vetel and Le Gall*, 2006], our laterally homogenous models indicate that this architecture may result from the complex stress field developing within the area of wide deformation, which is controlled by rift propagation, the geometry of the preexisting domains, and the direction of extension (Figure 9). We cannot, however, exclude that on a local scale preexisting discrete heterogeneities may have controlled fault development and architecture [*Vetel and Le Gall*, 2006].

7. Conclusions

In order to elucidate the interaction between the Ethiopian and Kenyan rift valleys within the Turkana depression, we have integrated crustal-scale, isothermal analog experiments with lithospheric-scale, thermomechanical numerical models. This integration and the comparison of the results with nature lead us to draw the following conclusions:

1. The along-axis transition from narrow rift valleys in Ethiopia/Kenya to a distributed deformation within the Turkana depression results from inherited lithospheric strength variations. In particular, the anomalously wide rift zone is controlled by the presence of a NW-SE region of thinned crust resulting from Mesozoic rifting.
2. Within the Turkana region, the Kenyan and Ethiopian rift valleys are deflected left laterally away from one another, avoiding a direct link to form a throughgoing N-S depression. We find that this is primarily linked to the mantle lithospheric strength of the transversal preexisting heterogeneity and also influenced by stress focusing effects and upper crustal fault dynamics.
3. Local-scale characteristics of the fault pattern, such as the occurrence of horse-tail splays at fault terminations or the presence of faults with zigzag plan view geometry giving rise to basins with a staircase pattern as in the case of Lake Turkana, may result from a minor component of strike-slip motion controlled by relative orientation between the geometry of the preexisting domains and the direction of extension.

Acknowledgments
We thank two anonymous reviewers and the Associate Editor for their useful suggestions, which helped to improve the paper. S. Brune was funded through the Helmholtz Young Investigators Group CRYSTALS (VH-NG-1132).

References

Acocella, V., C. Faccenna, R. Funiciello, and F. Rossetti (1999), Sand-box modelling of basement-controlled transfer zones in extensional domains, *Terra Nova*, *11*(4), 149–156, doi:10.1046/j.1365-3121.1999.00238.x.

Agostini, A., G. Corti, A. Zeoli, and G. Mulugeta (2009), Evolution, pattern, and partitioning of deformation during oblique continental rifting: Inferences from lithospheric-scale centrifuge models, *Geochem. Geophys. Geosyst.*, *10*, Q11015, doi:10.1029/2009GC002676.

Balestrieri, M. L., M. Bonini, G. Corti, F. Sani, and M. Philippon (2016), A refinement of the chronology of rift-related faulting in the Broadly Rifted Zone, southern Ethiopia, through apatite fission-track analysis, *Tectonophysics*, *671*, 42–55, doi:10.1016/j.tecto.2016.01.012.

Benoit, M. H., A. A. Nyblade, and M. E. Pasyanos (2006), Crustal thinning between the Ethiopian and East African Plateaus from modeling Rayleigh wave dispersion, *Geophys. Res. Lett.*, *33*, L13301, doi:10.1029/2006GL025687.

Bonini, M., G. Corti, F. Innocenti, P. Manetti, F. Mazzarini, T. Abebe, and Z. Pecskay (2005), Evolution of the Main Ethiopian Rift in the frame of Afar and Kenya rifts propagation, *Tectonics*, *24*, TC1007, doi:10.1029/2004TC001680.
Bos, B., and C. J. Spiers (2002), Frictional-viscous flow of phyllosilicate-bearing fault rock: Microphysical model and implications for crustal strength profiles, *J. Geophys. Res.*, *107*(2), 1-1-1–1-113, doi:10.1029/2001JB000301.
Brun, J.-P. (1999), Narrow rifts versus wide rifts: Inferences for the mechanics of rifting from laboratory experiments, *Philos. Trans. R. Soc. Lond. Ser. Math. Phys. Eng. Sci.*, *357*(1753), 695–712, doi:10.1098/rsta.1999.0349.
Brune, S. (2014), Evolution of stress and fault patterns in oblique rift systems: 3-D numerical lithospheric-scale experiments from rift to breakup, *Geochem. Geophys. Geosyst.*, *15*, 3392–3415, doi:10.1002/2014GC005446.
Brune, S. (2016), Rifts and rifted margins: A review of geodynamic processes and natural hazards, edited by J. C. Duarte and W. P. Schellart, *Plate Boundaries Nat. Hazards*, *11–37*, doi:10.1002/9781119054146.ch2.
Brune, S., and J. Autin (2013), The rift to break-up evolution of the Gulf of Aden: Insights from 3D numerical lithospheric-scale modelling, *Tectonophysics*, *607*, 65–79, doi:10.1016/j.tecto.2013.06.029.
Brune, S., A. A. Popov, and S. V. Sobolev (2012), Modeling suggests that oblique extension facilitates rifting and continental break-up, *J. Geophys. Res.*, *117*, B08402, doi:10.1029/2011JB008860.
Brune, S., A. A. Popov, and S. V. Sobolev (2013), Quantifying the thermo-mechanical impact of plume arrival on continental break-up, *Tectonophysics*, *604*, 51–59, doi:10.1016/j.tecto.2013.02.009.
Brune, S., C. Heine, M. Perez-Gussinye, and S. V. Sobolev (2014), Rift migration explains continental margin asymmetry and crustal hyper-extension, *Nat. Commun.*, *5*(4014), doi:10.1038/ncomms5014.
Brune, S., S. E. Williams, N. P. Butterworth, and R. D. Müller (2016), Abrupt plate accelerations shape rifted continental margins, *Nature*, *536*(7615), 201–204, doi:10.1038/nature18319.
Brune, S., C. Heine, P. D. Clift, and M. Pérez-Gussinyé (2017), Rifted margin architecture and crustal rheology: Reviewing Iberia-Newfoundland, Central South Atlantic, and South China Sea, *Mar. Pet. Geol.*, *79*, 257–281, doi:10.1016/j.marpetgeo.2016.10.018.
Buck, W. R. (1991), Modes of continental lithospheric extension, *J. Geophys. Res.*, *96*(B12), 20161–20178, doi:10.1029/91JB01485.
Buiter, S. J. H., A. Y. Babeyko, S. Ellis, T. V. Gerya, B. J. P. Kaus, A. Kellner, G. Schreurs, and Y. Yamada (2006), The numerical sandbox: Comparison of model results for a shortening and an extension experiment, *Geol. Soc. Lond. Spec. Publ.*, *253*(1), 29–64, doi:10.1144/GSL.SP.2006.253.01.02.
Buiter, S. J. H., et al. (2016), Benchmarking numerical models of brittle thrust wedges, *J. Struct. Geol.*, *92*, 140–177, doi:10.1016/j.jsg.2016.03.003.
Bürgmann, R., and G. Dresen (2008), Rheology of the lower crust and upper mantle: Evidence from rock mechanics, geodesy, and field observations, *Annu. Rev. Earth Planet. Sci.*, *36*(1), 531–567.
Chorowicz, J. (2005), The east African rift system, *J. African Earth Sci.*, *43*(1–3), 379–410, doi:10.1016/j.jafrearsci.2005.07.019.
Christensen, N. I., and W. D. Mooney (1995), Seismic velocity structure and composition of the continental crust: A global view, *J. Geophys. Res.*, *100*(B6), 9761–9788, doi:10.1029/95JB00259.
Clift, P. D., S. Brune, and J. Quinteros (2015), Climate changes control offshore crustal structure at South China Sea continental margin, *Earth Planet. Sci. Lett.*, *420*, 66–72, doi:10.1016/j.epsl.2015.03.032.
Corti, G. (2009), Continental rift evolution: From rift initiation to incipient break-up in the Main Ethiopian Rift, East Africa, *Earth Sci. Rev.*, *96*(1–2), 1–53, doi:10.1016/j.earscirev.2009.06.005.
Corti, G. (2012), Evolution and characteristics of continental rifting: Analog modeling-inspired view and comparison with examples from the East African Rift System, *Tectonophysics*, *522–523*, 1–33, doi:10.1016/j.tecto.2011.06.010.
Corti, G., M. Bonini, S. Conticelli, F. Innocenti, P. Manetti, and D. Sokoutis (2003), Analogue modelling of continental extension: A review focused on the relations between the patterns of deformation and the presence of magma, *Earth Sci. Rev.*, *63*(3–4), 169–247, doi:10.1016/S0012-8252(03)00035-7.
Cyprych, D., S. Brune, S. Piazolo, and J. Quinteros (2016), Strain localization in polycrystalline material with second phase particles: Numerical modeling with application to ice mixtures, *Geochem. Geophys. Geosyst.*, *17*, 3608–3628, doi:10.1002/2016GC006471.
Davidson, A., and D. C. Rex (1980), Age of volcanism and rifting in southwestern Ethiopia, *Nature*, *283*(5748), 657–658, doi:10.1038/283657a0.
DeMets, C., and S. Merkouriev (2016), High-resolution estimates of Nubia–Somalia plate motion since 20 Ma from reconstructions of the Southwest Indian Ridge, Red Sea and Gulf of Aden, *Geophys. J. Int.*, *207*(1), 317–332, doi:10.1093/gji/ggw276.
Duesterhoeft, E., J. Quinteros, R. Oberhänsli, R. Bousquet, and C. de Capitani (2014), Relative impact of mantle densification and eclogitization of slabs on subduction dynamics: A numerical thermodynamic/thermokinematic investigation of metamorphic density evolution, *Tectonophysics*, doi:10.1016/j.tecto.2014.09.009.
Dunbar, J. A., and D. S. Sawyer (1988), Continental rifting at pre-existing lithospheric weaknesses, *Nature*, *333*(6172), 450–452, doi:10.1038/333450a0.
Ebinger, C., Y. P. Djomani, E. Mbede, A. Foster, and J. B. Dawson (1997), Rifting Archaean lithosphere: The Eyasi-Manyara-Natron rifts, East Africa, *J. Geol. Soc. London*, *154*(6), 947–960, doi:10.1144/gsjgs.154.6.0947.
Ebinger, C. J., and N. H. Sleep (1998), Cenozoic magmatism throughout east Africa resulting from impact of a single plume, *Nature*, *395*(6704), 788–791, doi:10.1038/27417.
Ebinger, C. J., J. A. Jackson, A. N. Foster, and N. J. Hayward (1999), Extensional basin geometry and the elastic lithosphere, *Philos. Trans. R. Soc. Lond. Ser. Math. Phys. Eng. Sci.*, *357*(1753), 741–765, doi:10.1098/rsta.1999.0351.
Ebinger, C. J., T. Yemane, D. J. Harding, S. Tesfaye, S. Kelley, and D. C. Rex (2000), Rift deflection, migration, and propagation: Linkage of the Ethiopian and eastern rifts, Africa, *GSA Bull.*, *112*(2), 163–176, doi:10.1130/0016-7606(2000)112<163:RDMAPL>2.0.CO;2.
Emishaw, L., D. A. Laó-Dávila, M. G. Abdelsalam, E. A. Atekwana, and S. S. Gao (2017), Evolution of the broadly rifted zone in southern Ethiopia through gravitational collapse and extension of dynamic topography, *Tectonophysics*, *699*, 213–226, doi:10.1016/j.tecto.2016.12.009.
Faulds, J. E., and R. J. Varga (1998), The role of accommodation zones and transfer zones in the regional segmentation of extended terranes, *Geol. Soc. Am. Spec. Pap.*, *323*, 1–45, doi:10.1130/0-8137-2323-X.1.
Fishwick, S. (2010), Surface wave tomography: Imaging of the lithosphere–asthenosphere boundary beneath central and southern Africa? *Lithos*, *120*(1–2), 63–73, doi:10.1016/j.lithos.2010.05.011.
Fishwick, S., and I. D. Bastow (2011), Towards a better understanding of African topography: A review of passive-source seismic studies of the African crust and upper mantle, *Geol. Soc. Lond. Spec. Publ.*, *357*(1), 343–371, doi:10.1144/SP357.19.
Flament, N., M. Gurnis, and R. D. Müller (2013), A review of observations and models of dynamic topography, *Lithosphere*, *5*(2), 189–210, doi:10.1130/L245.1.
George, R., N. Rogers, and S. Kelley (1998), Earliest magmatism in Ethiopia: Evidence for two mantle plumes in one flood basalt province, *Geology*, *26*(10), 923–926, doi:10.1130/0091-7613(1998)026<0923:EMIEEF>2.3.CO;2.

Gleason, G. C., and J. Tullis (1995), A flow law for dislocation creep of quartz aggregates determined with the molten salt cell, *Tectonophysics*, *247*(1–4), 1–23.
Hansen, S. E., and A. A. Nyblade (2013), The deep seismic structure of the Ethiopia/Afar hotspot and the African superplume, *Geophys. J. Int.*, *194*(1), 118–124, doi:10.1093/gji/ggt116.
Hautot, S., P. Tarits, K. Whaler, B. Le Gall, J.-J. Tiercelin, and C. Le Turdu (2000), Deep structure of the Baringo Rift Basin (central Kenya) from three-dimensional magnetotelluric imaging: Implications for rift evolution, *J. Geophys. Res.*, *105*(B10), 23493–23518, doi:10.1029/2000JB900213.
Heine, C., and S. Brune (2014), Oblique rifting of the equatorial Atlantic: Why there is no Saharan Atlantic Ocean, *Geology*, *42*(3), 211–214, doi:10.1130/G35082.1.
Hendrie, D. B., N. J. Kusznir, C. K. Morley, and C. J. Ebinger (1994), Cenozoic extension in northern Kenya: A quantitative model of rift basin development in the Turkana region, *Tectonophysics*, *236*(1), 409–438, doi:10.1016/0040-1951(94)90187-2.
Hirth, G., and D. L. Kohlstedt (2003), Rheology of the upper mantle and the mantle wedge: A view from the experimentalists, *Geophys. Monogr.*, *138*, 83–105.
Hoggard, M. J., N. White, and D. Al-Attar (2016), Global dynamic topography observations reveal limited influence of large-scale mantle flow, *Nat. Geosci.*, *9*(6), 456–463, doi:10.1038/ngeo2709.
Huismans, R. S., and C. Beaumont (2011), Depth-dependent extension, two-stage breakup and cratonic underplating at rifted margins, *Nature*, *473*(7345), 74–78, doi:10.1038/nature09988.
Iaffaldano, G., R. Hawkins, and M. Sambridge (2014), Bayesian noise-reduction in Arabia/Somalia and Nubia/Arabia finite rotations since ~20 Ma: Implications for Nubia/Somalia relative motion, *Geochem. Geophys. Geosyst.*, *15*, 845–854, doi:10.1002/2013GC005089.
Jammes, S., and L. L. Lavier (2016), The effect of bimineralic composition on extensional processes at lithospheric scale, *Geochem. Geophys. Geosyst.*, *17*, 3375–3392, doi:10.1002/2016GC006399.
Karato, S.-I., and H. Jung (2003), Effects of pressure on high-temperature dislocation creep in olivine, *Philos. Mag.*, *83*(3), 401–414, doi:10.1080/0141861021000025829.
Katz, R. F., R. Ragnarsson, and E. Bodenschatz (2005), Tectonic microplates in a wax model of sea-floor spreading, *New J. Phys.*, *7*, 37–37, doi:10.1088/1367-2630/7/1/037.
Keller, G. R., et al. (1994), Crustal and upper mantle structure of the Kenya rift the east African rift system in the light of KRISP 90, *Tectonophysics*, *236*(1), 465–483, doi:10.1016/0040-1951(94)90190-2.
Keranen, K. M., S. L. Klemperer, J. Julia, J. F. Lawrence, and A. A. Nyblade (2009), Low lower crustal velocity across Ethiopia: Is the Main Ethiopian Rift a narrow rift in a hot craton?, *Geochem. Geophys. Geosyst.*, *10*, Q0AB01, doi:10.1029/2008GC002293.
Koehn, D., K. Aanyu, S. Haines, and T. Sachau (2008), Rift nucleation, rift propagation and the creation of basement micro-plates within active rifts, *Tectonophysics*, *458*(1–4), 105–116, doi:10.1016/j.tecto.2007.10.003.
Koopmann, H., S. Brune, D. Franke, and S. Breuer (2014), Linking rift propagation barriers to excess magmatism at volcanic rifted margins, *Geology*, G36085, 1, doi:10.1130/G36085.1.
Kusznir, N. J., and R. G. Park (1987), The extensional strength of the continental lithosphere: Its dependence on geothermal gradient, and crustal composition and thickness, *Geol. Soc. Lond. Spec. Publ.*, *28*(1), 35–52.
Labrousse, L., B. Huet, L. Le Pourhiet, L. Jolivet, and E. Burov (2016), Rheological implications of extensional detachments: Mediterranean and numerical insights, *Earth Sci. Rev.*, *161*, 233–258, doi:10.1016/j.earscirev.2016.09.003.
Le Pourhiet, L., D. A. May, L. Huille, L. Watremez, and S. Leroy (2017), A genetic link between transform and hyper-extended margins, *Earth Planet. Sci. Lett.*, *465*, 184–192, doi:10.1016/j.epsl.2017.02.043.
Maguire, P. K. H., et al. (2006), Crustal structure of the northern Main Ethiopian Rift from the EAGLE controlled-source survey; a snapshot of incipient lithospheric break-up, *Geol. Soc. Lond. Spec. Publ.*, *259*(1), 269–292, doi:10.1144/GSL.SP.2006.259.01.21.
Melnick, D., Y. Garcin, J. Quinteros, M. R. Strecker, D. Olago, and J.-J. Tiercelin (2012), Steady rifting in northern Kenya inferred from deformed Holocene lake shorelines of the Suguta and Turkana basins, *Earth Planet. Sci. Lett.*, *331–332*, 335–346, doi:10.1016/j.epsl.2012.03.007.
Mohr, P. (1983), Volcanotectonic aspects of the Ethiopian Rift evolution, *Bull Cent Rech Explor Prod Elf-Aquitaine*, *7*, 175–189.
Molnar, N. E., A. R. Cruden, and P. G. Betts (2017), Interactions between propagating rotational rifts and linear rheological heterogeneities: Insights from three-dimensional laboratory experiments, *Tectonics*, *36*, 420–443, doi:10.1002/2016TC004447.
Moore, J. M., and A. Davidson (1978), Rift structure in southern Ethiopia, *Tectonophysics*, *46*, 159–173, doi:10.1016/0040-1951(78)90111-7.
Morley, C. K. (1999), Influence of preexisting fabrics on rift structure, 151–160.
Morley, C. K. (2002), Evolution of large normal faults: Evidence from seismic reflection data, *AAPG Bull.*, *86*(6), 961–978, doi:10.1306/61EEDBFC-173E-11D7-8645000102C1865D.
Morley, C. K., R. A. Nelson, T. L. Patton, and S. G. Munn (1990), Transfer zones in the East African rift system and their relevance to hydrocarbon exploration in rifts (1), *AAPG Bull.*, *74*(8), 1234–1253.
Morley, C. K., W. A. Wescott, D. M. Stone, R. M. Harper, S. T. Wigger, and F. M. Karanja (1992), Tectonic evolution of the northern Kenyan Rift, *J. Geol. Soc. London*, *149*(3), 333–348, doi:10.1144/gsjgs.149.3.0333.
Naliboff, J., and S. J. H. Buiter (2015), Rift reactivation and migration during multiphase extension, *Earth Planet. Sci. Lett.*, *421*, 58–67, doi:10.1016/j.epsl.2015.03.050.
Pasyanos, M. E., T. G. Masters, G. Laske, and Z. Ma (2014), LITHO1.0: An updated crust and lithospheric model of the Earth, *J. Geophys. Res. Solid Earth*, *119*, 2153–2173, doi:10.1002/2013JB010626.
Philippon, M., G. Corti, F. Sani, M. Bonini, M.-L. Balestrieri, P. Molin, E. Willingshofer, D. Sokoutis, and S. Cloetingh (2014), Evolution, distribution, and characteristics of rifting in southern Ethiopia, *Tectonics*, *33*, 485–508, doi:10.1002/2013TC003430.
Pik, R., B. Marty, J. Carignan, G. Yirgu, and T. Ayalew (2008), Timing of East African Rift development in southern Ethiopia: Implication for mantle plume activity and evolution of topography, *Geology*, *36*(2), 167–170, doi:10.1130/G24233A.1.
Popov, A. A., and S. V. Sobolev (2008), SLIM3D: A tool for three-dimensional thermomechanical modeling of lithospheric deformation with elasto-visco-plastic rheology, *Phys. Earth Planet. In.*, *171*(1–4), 55–75, doi:10.1016/j.pepi.2008.03.007.
Popov, A. A., S. V. Sobolev, and M. D. Zoback (2012), Modeling evolution of the San Andreas Fault system in northern and central California, *Geochem. Geophys. Geosyst.*, *13*, Q08016, doi:10.1029/2012GC004086.
Quinteros, J., and S. V. Sobolev (2012), Why has the Nazca plate slowed since the Neogene?, *Geology*, *41*(1), 31–34, doi:10.1130/G33497.1.
Quinteros, J., S. V. Sobolev, and A. A. Popov (2010), Viscosity in transition zone and lower mantle: Implications for slab penetration, *Geophys. Res. Lett.*, *37*, L09307, doi:10.1029/2010GL043140.
Ramberg, H. (1981), *Gravity, Deformation, and the Earth's Crust: In Theory, Experiments, and Geological Application*, Academic Press, London.
Rosendahl, B. R. (1987), Architecture of continental rifts with special reference to East Africa, *Annu. Rev. Earth Planet. Sci.*, *15*(1), 445–503, doi:10.1146/annurev.ea.15.050187.002305.

Rubey, M., S. Brune, C. Heine, D. R. Davies, S. E. Williams, and R. D. Müller (2017), Global patterns of Earth's dynamic topography since the Jurassic, *Solid Earth Discuss.*, *1–34*, doi:10.5194/se-2017-26.

Rutter, E. H., and K. H. Brodie (2004), Experimental grain size-sensitive flow of hot-pressed Brazilian quartz aggregates, *J. Struct. Geol.*, *26*(11), 2011–2023, doi:10.1016/j.jsg.2004.04.006.

Rybacki, E., and G. Dresen (2000), Dislocation and diffusion creep of synthetic anorthite aggregates, *J. Geophys. Res.*, *105*(B11), 26,017–26,036, doi:10.1029/2000JB900223.

Rybacki, E., M. Gottschalk, R. Wirth, and G. Dresen (2006), Influence of water fugacity and activation volume on the flow properties of fine-grained anorthite aggregates, *J. Geophys. Res.*, *111*, B03203, doi:10.1029/2005JB003663.

Saria, E., E. Calais, D. S. Stamps, D. Delvaux, and C. J. H. Hartnady (2014), Present-day kinematics of the East African Rift, *J. Geophys. Res. Solid Earth*, *119*, 3584–3600, doi:10.1002/2013JB010901.

Sembroni, A., C. Faccenna, T. W. Becker, P. Molin, and B. Abebe (2016), Long-term, deep-mantle support of the Ethiopia-Yemen Plateau, *Tectonics*, *35*, 469–488, doi:10.1002/2015TC004000.

Sippel, J., C. Meeßen, M. Cacace, J. Mechie, S. Fishwick, C. Heine, M. Scheck-Wenderoth, and M. R. Strecker (2017), The Kenya rift revisited: Insights into lithospheric strength through data-driven 3-D gravity and thermal modelling, *Solid Earth*, *8*(1), 45–81, doi:10.5194/se-8-45-2017.

Stamps, D. S., L. M. Flesch, E. Calais, and A. Ghosh (2014), Current kinematics and dynamics of Africa and the East African Rift System, *J. Geophys. Res. Solid Earth*, *119*, 5161–5186, doi:10.1002/2013JB010717.

Svartman Dias, A. E., L. L. Lavier, and N. W. Hayman (2015), Conjugate rifted margins width and asymmetry: The interplay between lithospheric strength and thermomechanical processes, *J. Geophys. Res. Solid Earth*, *120*, 8672–8700, doi:10.1002/2015JB012074.

Thybo, H., P. K. H. Maguire, C. Birt, and E. Perchuć (2000), Seismic reflectivity and magmatic underplating beneath the Kenya Rift, *Geophys. Res. Lett.*, *27*(17), 2745–2748, doi:10.1029/1999GL011294.

Versfelt, J., and B. R. Rosendahl (1989), Relationships between pre-rift structure and rift architecture in Lakes Tanganyika and Malawi, East Africa, *Nature*, *337*(6205), 354–357, doi:10.1038/337354a0.

Vetel, W., and B. Le Gall (2006), Dynamics of prolonged continental extension in magmatic rifts: The Turkana Rift case study (North Kenya), *Geol. Soc. Lond. Spec. Publ.*, *259*(1), 209–233, doi:10.1144/GSL.SP.2006.259.01.17.

Vetel, W., B. Le Gall, and J. J. Walsh (2005), Geometry and growth of an inner rift fault pattern: The Kino Sogo Fault Belt, Turkana Rift (North Kenya), *J. Struct. Geol.*, *27*(12), 2204–2222, doi:10.1016/j.jsg.2005.07.003.

van Wijk, J., J. van Hunen, and S. Goes (2008), Small-scale convection during continental rifting: Evidence from the Rio Grande rift, *Geology*, *36*(7), 575–578, doi:10.1130/G24691A.1.

van Wijk, J. W., and S. A. P. L. Cloetingh (2002), Basin migration caused by slow lithospheric extension, *Earth Planet. Sci. Lett.*, *198*(3–4), 275–288, doi:10.1016/S0012-821X(02)00560-5.

Woldetinsae, G., and H.-J. Götze (2005), Gravity field and isostatic state of Ethiopia and adjacent areas, *J. African Earth Sci.*, *41*(1–2), 103–117, doi:10.1016/j.jafrearsci.2005.02.004.

Ziegler, P. A., and S. Cloetingh (2004), Dynamic processes controlling evolution of rifted basins, *Earth Sci. Rev.*, *64*(1–2), 1–50, doi:10.1016/S0012-8252(03)00041-2.

Modeling suggests that oblique extension facilitates rifting and continental break-up

Sascha Brune,[1] Anton A. Popov,[1,2] and Stephan V. Sobolev[1]

Received 12 September 2011; revised 27 March 2012; accepted 5 June 2012; published 2 August 2012.

[1] In many cases the initial stage of continental break-up was and is associated with oblique rifting. That includes break-up in the Southern and Equatorial Atlantic, separation from eastern and western Gondwana as well as many recent rift systems, like Gulf of California, Ethiopia Rift and Dead Sea fault. Using a simple analytic mechanical model and advanced numerical, thermomechanical modeling techniques we investigate the influence of oblique extension on the required tectonic force in a three-dimensional setting. While magmatic processes have been already suggested to affect rift evolution, we show that additional mechanisms emerge due to the three-dimensionality of an extensional system. Focusing on non-magmatic rift settings, we find that oblique extension significantly facilitates the rift process. This is due to the fact that oblique deformation requires less force in order to reach the plastic yield limit than rift-perpendicular extension. The model shows that in the case of two competing non-magmatic rifts, with one perpendicular and one oblique to the direction of extension but otherwise having identical properties, the oblique rift zone is mechanically preferred and thus attracts more strain.

Citation: Brune, S., A. A. Popov, and S. V. Sobolev (2012), Modeling suggests that oblique extension facilitates rifting and continental break-up, *J. Geophys. Res.*, *117*, B08402, doi:10.1029/2011JB008860.

1. Introduction

[2] Rifting and continental break-up belong to the fundamental features of plate tectonics. Continental rifting has been studied extensively using mathematical models [e.g., *McKenzie*, 1978; *Royden and Keen*, 1980; *Braun and Beaumont*, 1989; *Huismans and Beaumont*, 2003; *Regenauer-Lieb et al.*, 2008; *Huismans and Beaumont*, 2011]; however, the conditions which allow rifting to result in continental break-up remain poorly understood. Several mechanism exist that are thought to facilitate break-up: Inherited weak zones originate from the amalgamation of distinct tectonic plates that are reactivated by the rift process [*Ziegler and Cloetingh*, 2004]. Stress focusing occurs when break-up does not take place simultaneously in a rift zone, but propagates in a certain direction, as was the case for the opening of the South Atlantic [*Torsvik et al.*, 2009]. Melt generation and magma transport weaken the lithosphere both by efficient heating, and by mechanical strength reduction [*Buck*, 2007]. The impingement of mantle plumes on active rift zones plays an important role in triggering continental break-up [*Ziegler and Cloetingh*, 2004]. Here we focus at another possible rift-intensifying process that was to our knowledge never discussed in this aspect in the literature: extension with a direction that is strongly oblique to the rift axis.

[3] Oblique rifting was associated with break-up at many places in the world (Figure 1). The separation of Africa and South America featured significantly oblique separation angles [*Nürnberg and Müller*, 1991; *Macdonald et al.*, 2003; *Torsvik et al.*, 2009; *Moulin et al.*, 2010], especially the North Falkland-South African section [*Parsiegla et al.*, 2009] and the Equatorial Atlantic [*Edwards et al.*, 1997]. In the Indian Ocean region, oblique break-up separated Africa and Madagascar [*de Wit*, 2003], Madagascar and India [*Storey et al.*, 1995], Sri Lanka and South India from Antarctica [*Gaina et al.*, 2007], Antarctica and Australia [*Whittaker et al.*, 2007], opened the Gulf of Aden [*Bellahsen et al.*, 2003] and the Red Sea [*Hempton*, 1987]. In the North Atlantic, the formation of the Davis Strait involved highly oblique rifting [*Suckro et al.*, 2012] while the Fram Strait separates two sheared conjugate margins [*Engen et al.*, 2008]. Moreover, several currently active rifts exhibit an oblique component, like in the Gulf of California [*Lizarralde et al.*, 2007], the Dead Sea Fault [*Weber et al.*, 2009], and the Ethiopian Rift [*Corti*, 2008]. The locus and the orientation of a developing rift zone is controlled by the complex interplay of tectonic forces, lithospheric inheritance and overall plate geometry. The impact of individual contributions from e.g. slab pull, mantle drag, inherited faults, mantle anisotropy and rift orientation strongly depend on individual plate configurations and are often poorly known. Thus, it can not be excluded that some or all of the rifts mentioned before are oblique because the tectonic system simply had no other

[1]Geodynamic Modelling Section, Helmholtz Centre Potsdam, GFZ German Research Centre for Geosciences, Potsdam, Germany.
[2]Now at Institute of Geosciences, Johannes Gutenberg University Mainz, D-55099 Mainz, Germany.

Corresponding author: S. Brune, Geodynamic Modelling Section, Helmholtz Centre Potsdam, GFZ German Research Centre for Geosciences, Telegrafenberg, Potsdam D-14473, Germany. (brune@gfz-potsdam.de)

0148-0227/12/2011JB008860

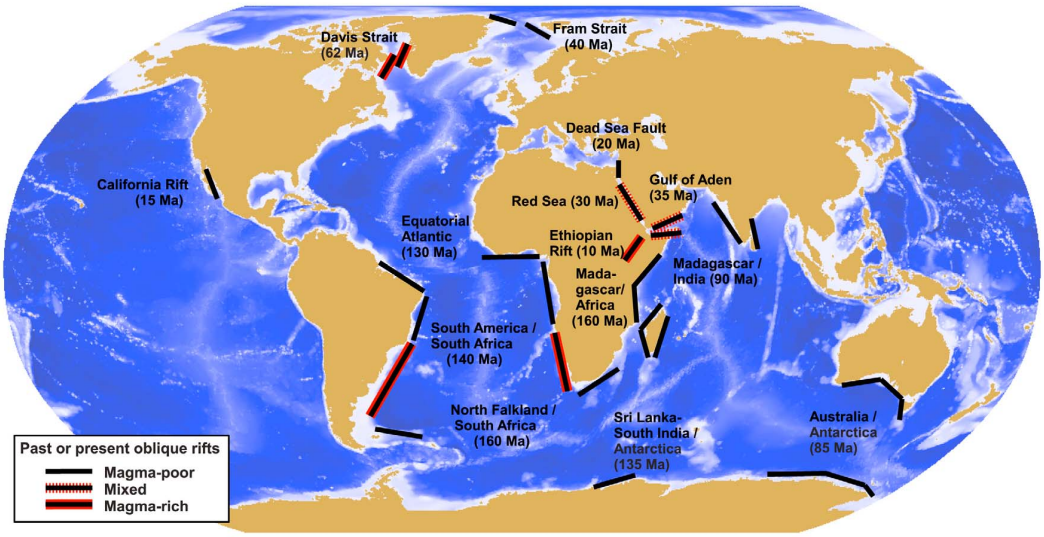

Figure 1. Worldwide compilation of obliquely rifted conjugate margins and presently active oblique rifts. Numbers indicate approximate times of rift initiation. Magma-rich margins and rifts are indicated in red. If some segments of the same rift are magma-rich and others magma-poor the rift type is designated as mixed (for references see text).

choice. Keeping this in mind, this study shows that oblique rift zones require less tectonic force than perpendicular rifts so that plate motions involving significant rift obliquity appear to be mechanically preferred.

[4] Many analog experiments successfully addressed the topic of continental rifting and the fault patterns caused by oblique extension [*Withjack and Jamison*, 1986; *Tron and Brun*, 1991; *Clifton et al.*, 2000; *Chemenda et al.*, 2002; *Corti et al.*, 2003; *Sokoutis et al.*, 2007; *Autin et al.*, 2010]. The advantage of analog models is that they are three-dimensional by default so that oblique rift models are relatively straightforward to obtain. However, analog models necessitate important simplifications, particularly realistic elasto-visco-plastic rheology and temperature dependency are hard to implement. While present-day numerical codes include these features, models of oblique rifting intrinsically require computationally expensive calculations in three dimensions which is why only two numerical model have been published to our knowledge so far [*van Wijk*, 2005; *Allken et al.*, 2011]. Neither analog nor numerical publications, however, addressed the impact of rift obliquity on the tectonic force that is required to allow extension.

[5] In this study, we investigate how oblique rifting influences the effective strength of the lithosphere. To this aim, we first conduct simplified analytic modeling followed by three-dimensional numerical experiments that comprise a layered lithosphere of elasto-visco-plastic, stress- and temperature-dependent rheology. Presenting two distinct numerical model setups, we induce obliqueness by applying boundary velocities that are not perpendicular to the prospective rift zone. In the first setup, we compute the force required to maintain a certain rift velocity and evaluate its dependency on the extensional direction. In the other setting, two possible rift zones of different angles evolve under uniform extension. Finally, we apply dynamic boundary condition by prescribing boundary forces and observe the kinematic behavior of the system. In all cases, we find that oblique rifting is preferred.

2. Analytical Considerations

[6] Fundamental insights can be drawn from an analytical solution of a simplified formulation of the problem. We therefore consider a homogeneous and isotropic plate to consist of a linearly elastic material that becomes perfectly plastic when von Mises yield stress is reached. Gravity is neglected. The plate is deformed by displacing the plate edge by the distance u in a direction defined by the angle of obliquity α (Figure 2a).

[7] We build our analytics on the work of *Withjack and Jamison* [1986] who solved the elastic part of the problem, i.e. stress as a function of displacement. Note that they used the notation that tensile stresses are positive, while we apply the geophysical notation where compressive stresses have positive sign. Furthermore, their definition of α is opposite to ours, so that our α equals to 90° minus theirs. The solution of *Withjack and Jamison* [1986] in the principal coordinate system yields two horizontal stresses

$$\sigma_{H1} = -\frac{E}{2}\frac{u}{L_x}\left[\frac{1}{1-\nu}\cos(\alpha) + \frac{1}{1+\nu}\right] \quad (1)$$

$$\sigma_{H2} = -\frac{E}{2}\frac{u}{L_x}\left[\frac{1}{1-\nu}\cos(\alpha) - \frac{1}{1+\nu}\right] \quad (2)$$

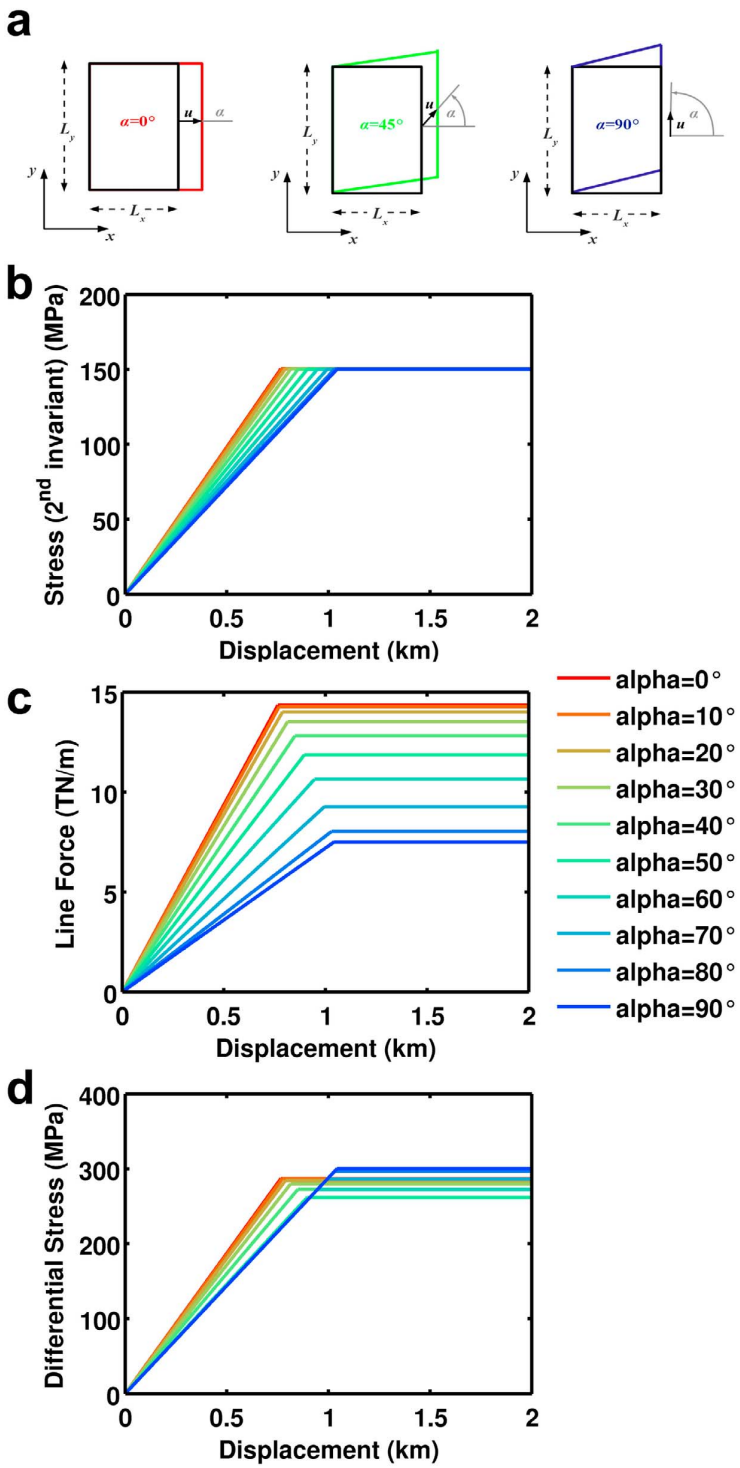

Figure 2. (a) Analytical setup and (b–d) solutions using upper crustal elastic parameters as shown in Table 1 (Young's modulus $E = \frac{9KG}{3K+G} = 88.6$ GPa, Poisson ratio $\nu = \frac{3K-2G}{2(3K+G)} = 0.23$).

and the vertical stress

$$\sigma_V = \sigma_{zz} = 0 \tag{3}$$

at which our notation is used and E is the Young's modulus, ν the Poisson ratio, u displacement and L_x the length of the model domain in x-direction.

[8] We compute the individual components of the stress tensor σ_{ij} in the xyz-coordinate system by classical rotational coordinate transformation.

$$\sigma_{xx} = -\frac{Eu}{L_x}\cos\alpha\frac{1}{1-\nu^2} \tag{4}$$

$$\sigma_{yy} = -\frac{Eu}{L_x}\cos\alpha\frac{\nu}{1-\nu^2} \tag{5}$$

$$\sigma_{zz} = 0 \tag{6}$$

$$\sigma_{xy} = -\frac{1}{2}\frac{Eu}{L_x}\sin\alpha\frac{1}{1+\nu} \tag{7}$$

$$\sigma_{xz} = 0 \tag{8}$$

$$\sigma_{yz} = 0 \tag{9}$$

Based on σ_{ij}, we evaluate the second invariant of deviatoric stress tensor τ_{II}:

$$\tau_{II} = \sqrt{\frac{1}{2}(\sigma_{xx}-p)^2 + \frac{1}{2}(\sigma_{yy}-p)^2 + \frac{1}{2}(\sigma_{zz}-p)^2 + \sigma_{xy}^2 + \sigma_{xz}^2 + \sigma_{yz}^2} \tag{10}$$

with pressure

$$p = \frac{1}{3}(\sigma_{xx} + \sigma_{yy} + \sigma_{zz}). \tag{11}$$

[9] Since τ_{II} depends on the displacement u via the stress tensor, we can compute the critical displacement u_{yield} that is required to reach von Mises yield stress τ_{yield}:

$$\tau_{II}(u_{yield}) = \tau_{yield}. \tag{12}$$

[10] Finally, we evaluate the line force F at the displaced plate edge that has to be applied in order to realize the given displacement. This force results from Pythagorean addition of the stress components facing in x-direction:

$$F(u) = \sqrt{\sigma_{xx}^2 + \sigma_{xy}^2 + \sigma_{xz}^2}\cdot L_z. \tag{13}$$

[11] This formula holds true, since the vertical stress σ_{zz} vanishes. If this was not the case, computed tectonic forces would have to be corrected for the vertical stress component as discussed in section 4.1 (see equation (31)). Applying equations (4), (7), and (8) and setting u to u_{yield} results in the force at the plastic limit:

$$F_{yield} = \tau_{yield}L_z\sqrt{\frac{\cos^2\alpha + \frac{1}{4}\sin^2\alpha(1-\nu)^2}{\frac{1}{3}\cos^2\alpha(\nu^2-\nu+1) + \frac{1}{4}\sin^2\alpha(1-\nu)^2}}. \tag{14}$$

[12] A similar solution can be obtained if we do not consider an elastic material, but an incompressible viscous fluid. By using the analogy of linear viscous flow and elastic deformation we assume in equations (1) to (13) a Poisson ratio of $\nu = 0.5$ (incompressibility) and we substitute displacements u by velocities $\dot{u}$ as well as the shear modulus G by viscosity η (note that $E = 2G(1+\nu)$ must be replaced by 3η). In this case, the force at plastic yield will be given by the simple relation:

$$F_{yield} = \tau_{yield}L_z\sqrt{\frac{1+15\cos^2\alpha}{1+3\cos^2\alpha}}. \tag{15}$$

[13] From the more general equation (14), we derive two end-member cases, i.e. strike-slip ($\alpha = 90^\circ$) and pure extension ($\alpha = 0^\circ$) with fairly simple expressions:

$$F_{strike-slip} = \tau_{yield}L_z \tag{16}$$

and

$$F_{extension} = \frac{\tau_{yield}L_z}{\sqrt{\frac{1}{3}(\nu^2-\nu+1)}}. \tag{17}$$

[14] In the visco-plastic limit and for incompressible elastic materials, equation (16) does not change while equation (17) simplifies to:

$$F_{extension} = 2\tau_{yield}L_z. \tag{18}$$

[15] The ratio of $F_{extension}$ to $F_{strike\text{-}slip}$ is exactly 2 for incompressible media where the Poisson ratio ν is 0.5. For more realistic materials with $\nu \approx 0.25$, the force ratio amounts to 1.9. Hence, it is a general feature of Earth-relevant elasto-plastic and visco-plastic materials that the yield force is ~2 times higher for pure extension than for strike-slip.

[16] We plot the analytical solutions of the problem's key variables τ_{II}, F, and $\sigma_1 - \sigma_3$ in Figure 2. We thereby use upper crustal values for the elastic parameters (see Table 1), a realistic value for von Mises yield stress ($\tau_{yield} \sim$ 150 MPa), a model width L_x of 250 km and identify L_z with the depth of typical brittle-ductile transition in the mantle (50 km). During elastic deformation, all variables increase linearly with displacement. Plastic deformation commences when τ_{II} reaches τ_{yield} and is characterized by constant values for the considered variables. Note that for pure extension, the yield limit is reached with least displacement. The tectonic force F depends non-linearly on α showing clearly that oblique extension is favored mechanically over perpendicular extension.

[17] From the classical fault mechanics point of view this result seems counterintuitive, since strike-slip motion is an intermediate case between extension and compression, with compression requiring highest and extension least differential stress [e.g., *Sibson*, 1974]. The apparent contradiction however resolves when we compute the differential stress $\sigma_1 - \sigma_3$ in the plastic deformation phase. The smallest principal stress σ_3 is equal to σ_{H1} of equation (1) as it is negative (tensile) and smaller than both σ_{H2} and σ_V for all α. The largest principal stress σ_1 can be identified with σ_{H2} which is positive (compressive) if α exceeds a certain critical

Table 1. Parameters[a]

Parameter	Upper Crust	Lower Crust	Strong Mantle	Weak Mantle
Density, ρ (kg m^{-3})	2700	2850	3300	3300
Thermal expansivity, α (10^{-5} K^{-1})	2.7	2.7	3.0	3.0
Bulk modulus, K (GPa)	55	63	122	122
Shear modulus, G (GPa)	36	40	74	74
Heat capacity, C_p (J kg^{-1} K^{-1})	1200	1200	1200	1200
Heat conductivity, λ (W K^{-1} m^{-1})	2.5	2.5	3.3	3.3
Radiogenic heat production, A (μW m^{-3})	1.3	0.2	0	0
Initial friction coefficient, μ (-)	0.6	0.6	0.6	0.6
Maximum plastic friction softening[b]	90 %	90%	none	none
Cohesion, c (MPa)	5.0	5.0	5.0	5.0
Pre-exponential constant for diffusion creep, log(B_{Diff}) (Pa^{-1} s^{-1})	-	-	−8.65	−8.65
Activation energy for diffusion creep, E_{Diff} (kJ mol^{-1})	-	-	375	335
Activation volume for diffusion creep, V_{Diff} (10^{-6} m^3/mol)	-	-	6	4
Pre-exponential constant for dislocation, creep , log(B_{Disloc}) (Pa^{-n} s^{-1})	−28.0	−21.05	−15.56	−15.05
Power law exponent for dislocation, creep, n	4.0	4.2	3.5	3.5
Activation energy for dislocation creep, E_{Disloc} (kJ mol^{-1})	223	445	530	480
Activation volume for dislocation creep, V_{Disloc} (10^{-6} m^3/mol)	0	0	13	10
Pre-exponential constant for Peierls creep, log($B_{Peierls}$) (Pa^{-n} s^{-1})	-	-	11.76	-
Activation energy for Peierls creep, $E_{Peierls}$ (kJ mol^{-1})	-	-	540	-
Peierls stress, $\tau_{Peierls}$ (GPa)	-	-	8.5	-

[a]Dislocation creep parameters for upper crust: wet quartzite [*Gleason and Tullis*, 1995], lower crust: mafic Pikwitonei granulite [*Wilks and Carter*, 1990], strong mantle: dry olivine [*Hirth and Kohlstedt*, 2003], weak mantle: wet olivine, i.e., 500 ppm H/Si [*Hirth and Kohlstedt*, 2003] which is included in the pre-exponential factor. In diffusion creep parameters for strong mantle and weak mantle [*Hirth and Kohlstedt*, 2003], the grain size is held constant at 6 mm and is included in the pre-exponential factors. Peierls creep parameters for strong mantle [*Kameyama et al.*, 1999]. Weak mantle never reaches the required stress level of ≈500 MPa which is why we do not implement Peierls in the asthenospheric mantle.

[b]Linear decrease of μ from 0.6 to 0.06 between strain values of 0 and 1.

value α_{crit}, and $\sigma_V = 0$ otherwise. The exact value of α_{crit} depends on the Poisson ratio (for incompressible materials with $\nu = 0.5$, α_{crit} equals 71°, in more realistic cases where $\nu = 0.25$, α_{crit} equals 53°). Figure 2d depicts the differential stress evolution for all α. We find that $\sigma_1 - \sigma_3$ is indeed lower for pure extension than for strike-slip, as soon as the plastic limit is exceeded. The underlying reason are: (i) The largest principal stress σ_{H1} is a discontinuous function of α as it switches between the vertical σ_V and horizontal σ_{H2} at α_{crit}. (ii) Pure extension and low-obliquity deformation reach the yield limit at less displacement than strike-lip motion so that the differential stress remains at a lower level. This behavior is robust for all relevant parameter variations that are realized in the lithosphere (Table 1). Our results are thus in good agreement with long-known observations from fault mechanics.

[18] In order to allow analytic solution, a number of assumption such as simple elasto-plastic rheology, material homogeneity and zero gravity have to be made. With the following numerical solutions, we show that the characteristic dependency of the force on α is independent of these assumptions.

3. Modeling Approach

3.1. Experimental Setup

[19] In the numerical part of this study we can avoid the simplifications that where made for our analytic solutions. Namely, we apply realistic elasto-visco-plastic rheology with depth-dependent Drucker-Prager failure criterion to a layered Earth model under non-zero gravity.

[20] Our model consists of a rectangular segment of 750 km length, 250 km width and 150 km depth (Figure 3h) that includes a 20 km thick upper crustal layer of wet quartzite rheology [*Gleason and Tullis*, 1995], a lower crustal layer of 15 km thickness with mafic granulite properties [*Wilks and Carter*, 1990], and a 45 km thick layer of strong mantle material with dry olivine rheology [*Hirth and Kohlstedt*, 2003]. Taking into account the higher water content of the asthenosphere, we use rheological parameters of wet (i.e. 500 ppm H/Si) olivine in the lowermost layer below 80 km depth [*Hirth and Kohlstedt*, 2003]. All rheological parameters are listed in Table 1.

[21] A constant temperature is prescribed for the top and bottom surfaces of the model (0 °C and 1350 °C, respectively), while zero heat flow conditions are adopted for lateral boundaries. Numerical experiments are started with an equilibrium temperature distribution such that the 1350 °C isotherm is situated at 100 km depth, which accounts for thermal lithospheric thickness within mobile belts like the Damara Belt or the Pan-African Belt of Central Africa [*Artemieva*, 2006]. Moreover, a setting where the thermal lithosphere-asthenosphere boundary is located 20–30 km below the chemical lithosphere-asthenosphere boundary (here initially at 80 km) remains stable for several 100 Ma if small-scale convection is taken into account [*Sobolev et al.*, 2009]. The setup is applied to mobile belts since rifting often localizes along former plate sutures. A thicker chemical and thermal lithosphere that is encountered for rifts in undeformed continents will affect the magnitude of the involved tectonic forces but not the main outcome of this publication. After the first time step the thermal initial condition is relaxed and only the bottom temperature is prescribed. From that moment on, the thermal lithosphere-asthenosphere boundary results self-consistently from the combined effects of heat conduction and advection. The prospective rift zone is introduced in the thermal initial condition by a small temperature deviation along strike: the 1350 °C isotherm is elevated from 100 km to 80 km in a narrow zone of 20 km width (Figure 3). This setup essentially anticipates a small

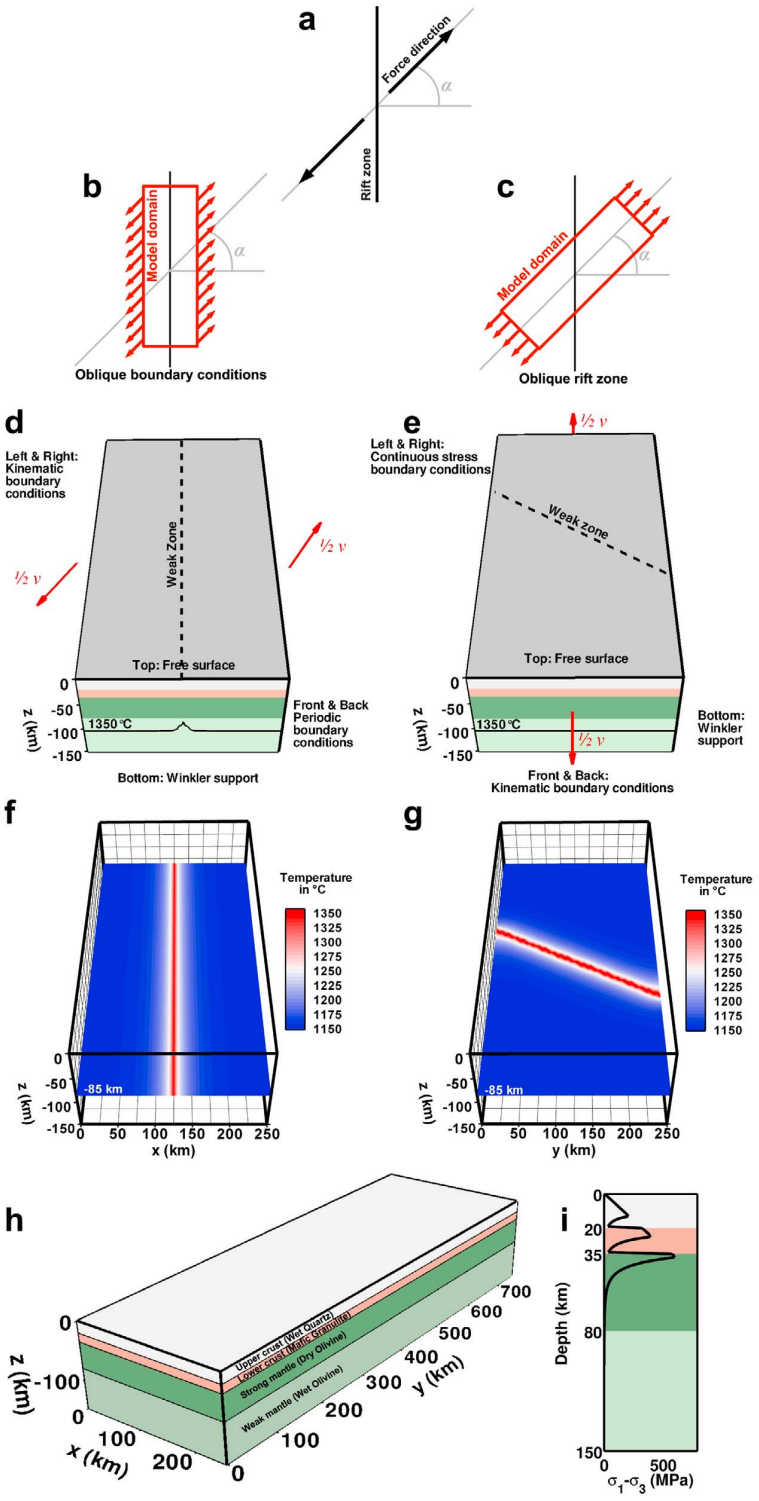

Figure 3. (a) Schematic view of oblique rifting where α designates the angle of obliquity. (b) General setup with oblique boundary conditions. (c) General setup with a rift zone that is oblique to the boundaries. (d, e) Boundary conditions for both setups. Extensional velocities are marked as red arrows. (f, g) Horizontal slice in 85 km depth depicting the initial thermal perturbation to localize rifting. (h) Rheological setup. (i) Yield strength profile (differential stress) for a strain rate of 1.3 10^{-15} s^{-1} that corresponds to the model description in Section 3.2.

amount of lithospheric necking which focuses the extensional deformation into the desired rift axis. This is one way of representing a weak zone. Alternative approaches are crustal thickening [*van Wijk*, 2005], implementation of a weak plastic seed [*Huismans and Beaumont*, 2003], or mechanical anisotropy [*Tommasi and Vauchez*, 2001]. Please note that all of these techniques will result in lithospheric necking comparable to our initial condition after a small amount of extension.

[22] As mentioned before, the locus and orientation of Earth's rift zones is controlled by the magnitude and direction of the plate-driving forces as well as by the location of inherited suture zones. In this study, we reduce complexity by considering a lithospheric segment of several hundred kilometers in width and length that is small compared to Earth's tectonic plates. Hence, tectonic forces that act on entire plates (ridge push, mantle drag) or plate boundaries (slab pull) will enter our model domain via the lateral boundaries. At any real rift zone, the direction of the extensional force will be constrained by the overall plate configuration. In order to investigate the role of rift obliquity, however, we vary the extensional direction between 0° and 90° with respect to the rift axis. In nature, the interaction between the obliquity-dependent rift force and the large scale plate forces will result in the overall plate kinematics.

[23] In this study, we model oblique extensional settings using two distinct kinds of models differing in the positioning of the model domain: (i) The model sides are parallel to the prospective rift zone while oblique boundary conditions are applied along strike. The front and back side are thereby connected via periodic boundary conditions (Figures 3b, 3d, and 3f). (ii) The initial weak zone is situated obliquely to the boundaries where face-perpendicular velocities are applied at the front and backside, whereby on the left and right boundary, continuous stress boundary conditions (described in next section) are implemented (Figures 3c, 3e, and 3g). The reason why two setups are chosen is of numerical nature: Prescribing the velocity distribution across a zone of deformation inhibits localization feedbacks and results in a zone of deformation which does not evolve self-consistently. We prescribe extensional velocities at the boundaries in x-direction which means that we have to avoid contact between a fault zone and these boundaries. By applying oblique boundary conditions the prospective rift zone lies parallel to the x-axis and the angle of obliquity can be varied freely between 0° (pure extension) and 90° (strike-slip). Within the oblique weak zone setup the location of the prospective rift zone varies with the angle of obliquity. Since the deformation zone is not allowed to touch the extending boundaries, the angle of obliquity is confined to a certain range. Thus, our geometry of 750 km length and 250 km width limits the rift angle to maximal 60°. Only one shear zone can be introduced for oblique boundary conditions, due to the periodic boundaries used in y-directions. Here lies the advantage of the oblique weak zone setup, where multiple rift zones with different angles of obliquity may be studied within the same model domain.

3.2. Numerical Modeling Techniques

[24] We use the implicit, Arbitrary Lagrangian-Eulerian (ALE), three-dimensional FEM code SLIM3D (Semi-Lagrangian Implicit Model for 3 Dimensions) [*Popov and Sobolev*, 2008] to solve the thermomechanically coupled conservation equations of momentum

$$-\frac{\partial p}{\partial x_i}+\frac{\partial \tau_{ij}}{\partial x_j}+\rho g_i=0 \tag{19}$$

energy

$$\rho C_p\frac{\mathrm{D}T}{\mathrm{D}t}-\frac{\partial}{\partial x_i}\left(\lambda\frac{\partial T}{\partial x_i}\right)-\tau_{ij}\dot{\varepsilon}_{ij}-\rho A=0 \tag{20}$$

and mass

$$\frac{1}{K}\frac{\mathrm{D}p}{\mathrm{D}t}-\alpha_T\frac{\mathrm{D}T}{\mathrm{D}t}+\frac{\partial v_i}{\partial x_i}=0 \tag{21}$$

with pressure p (defined as mean stress), coordinates x_i, time t, stress deviator τ_{ij}, density ρ, gravity vector g_i, heat capacity C_p, temperature T, material time derivative D/Dt, heat conductivity λ, strain rate deviator $\dot{\varepsilon}_{ij}$, radioactive heat production A, bulk modulus K, thermal expansivity α_T, and velocities v_i. Parameter values are given in Table 1. The Einstein summation rule applies for repeated indices.

[25] The Lagrangian formulation is used to solve the system of equations for the primary variables, namely incremental displacement (Δu), and temperature (T) using the Galerkin procedure of the Finite Element Method. Remeshing is used to prevent large grid distortion and to track motion of the free surface. During the remeshing phase we use the marker-in-cell technique to resolve the advection of the material phases and history variables, such as Cauchy stress and accumulated plastic strain.

[26] The conservation equations are solved with simultaneous consideration of the constitutive laws that relate deformation and stress. An elasto-visco-plastic rheology is implemented adopting additive decomposition of the deviatoric strain rate into elastic, viscous, and plastic components [*Simo and Hughes*, 2000].

$$\dot{\varepsilon}_{ij}=\dot{\varepsilon}_{ij}^{el}+\dot{\varepsilon}_{ij}^{vs}+\dot{\varepsilon}_{ij}^{pl}=\frac{1}{2G}\hat{\tau}_{ij}+\frac{1}{2\eta_{eff}}\tau_{ij}+\dot{\gamma}\frac{\partial Q}{\partial \tau_{ij}} \tag{22}$$

[27] Where G is the elastic shear modulus, $\hat{\tau}_{ij}$ the objective stress rate, η_{eff} the effective creep viscosity, $\dot{\gamma}$ the plastic multiplier, and Q is the plastic potential function.

[28] Following the approach of *Kameyama et al.* [1999], we use three types of creep mechanisms: diffusion, dislocation, and Peierls:

$$\eta_{eff}=\frac{1}{2}\tau_{II}\left(\dot{\varepsilon}_{Diff}+\dot{\varepsilon}_{Disloc}+\dot{\varepsilon}_{Peierls}\right)^{-1} \tag{23}$$

with τ_{II} being the second invariant of deviatoric stress and $\dot{\varepsilon}_{Diff}$, $\dot{\varepsilon}_{Disloc}$, as well as $\dot{\varepsilon}_{Peierls}$ the second invariant of strain rate for the respective creep mechanism. The latter are computed as follows:

[29] Diffusion creep

$$\dot{\varepsilon}_{Diff}=B_{Diff}\tau_{II}\exp\left(-\frac{E_{Diff}+pV_{Diff}}{RT}\right) \tag{24}$$

[30] Dislocation creep

$$\dot{\varepsilon}_{Disloc} = B_{Disloc}(\tau_{II})^n \exp\left(-\frac{E_{Disloc} + pV_{Disloc}}{RT}\right) \quad (25)$$

[31] Peierls creep

$$\dot{\varepsilon}_{Peierls} = B_{Peierls}\left(\frac{\tau_{II}}{\beta\tau_{Peierls}}\right)^s \exp\left[\frac{-E_{Peierls}}{RT}(1-\beta)^2\right] \quad (26)$$

where

$$s = 2\beta(1-\beta)\frac{E_{Peierls}}{RT} \quad (27)$$

[32] In the above equations B_{Diff}, B_{Disloc}, $B_{Peierls}$ and E_{Diff}, E_{Disloc}, $E_{Peierls}$ denote the creep parameter and activation enthalpy, respectively, of each correspondent mechanism. R is the gas constant, n the power law exponent, $\tau_{Peierls}$ the Peierls stress, and $0 < \beta < 1$ is an adjustable approximation parameter [see *Popov and Sobolev*, 2008, and references therein].

[33] Brittle deformation is implemented by means of the standard Mohr-Coulomb plasticity model:

$$f = \frac{1}{2}(\sigma_{\max} - \sigma_{\min}) + \frac{1}{2}(\sigma_{\max} + \sigma_{\min})\sin\varphi - c\cos\varphi \le 0 \quad (28)$$

where f defines the yield surface, $\sigma_{\max}$ and $\sigma_{\min}$ are maximum and minimum principal stresses, φ is the friction angle, and c cohesion. During every computational step, a visco-elastic trial stress is calculated assuming constant viscosity. If the trial stress locates beyond the yield surface, plastic failure takes place. In this case, the stress point is projected onto the yield surface under application of the Prandtl-Reuss flow rule and plastic strain is increased accordingly.

[34] Several weakening mechanisms exist in the model that tend to localize deformation in the lithosphere:

[35] 1. The ongoing shear deformation within a fault zone leads to a reduction of crustal fault strength [*Zoback et al.*, 1987; *Provost and Houston*, 2003]. This process is strongly influenced by the presence of fluids within the crust that are required to generate weak fault rocks. Fluids can not easily advance into the mantle which is why we apply friction softening only in the crust. The process itself is approximated here using a plastic strain-dependent friction angle. In our experiments, the friction angle decreases linearly by 90 % of the initial value when plastic strain reaches 1, and remains constant for larger strains.

[36] 2. Another inherent weakening mechanism is shear heating that is proportional to $\tau_{II}\dot{\varepsilon}_{II}$ (equation (20)): Large strain rates lead to increased temperature which lowers the effective viscosity. A smaller viscosity attracts deformation and thus increases the strain rate.

[37] 3. Dislocation creep features a power law dependency between strain rate and stress. For constant strain rate, this causes a decreasing viscosity if stresses increase (i.e. stress softening). On the other hand, if stress is assumed constant, the power law dependency results in lower viscosity for an increase in strain rate (i.e. strain rate softening).

[38] The extensional setting is represented here using appropriate Dirichlet boundary conditions prescribing the velocities over the entire sides. Unless otherwise indicated, the extension velocities in this publication refer to full spreading rates, so that extension of 10 mm/yr is applied by prescribing boundary velocities of 5 mm/yr at each side. Mechanical boundary conditions for upper and lower faces consist of a free surface at the top and Winkler support at the bottom. The lower boundary moves upward during extension, however during each remeshing it is reset to 150 km while new asthenospheric markers are introduced. The straightforward implementation of these boundary conditions constitutes a major advantage of the deformable mesh within the Finite Element framework. Two additional implementations can be used for lateral boundaries: (i) In the oblique boundary condition setup, periodic boundaries equalize all variables at one side of the model to the opposite boundary. The periodicity resembles that of a circle, however in Cartesian coordinates. (ii) The continuous stress boundary conditions used in the oblique weak zone setup constitute an extension of the free slip boundary. While volumetric stresses for the free slip formulation do not change across the boundary, shear stresses are assumed to be zero. The analogon of free-slip boundaries in nature would be very weak, vertical faults that cut through the whole lithosphere. By assuming that both volumetric and face-parallel shear components of the stress tensor remain identical across the boundary, we extend the free slip boundary condition. Note that velocities that are perpendicular to the boundary remain zero like for the free-slip condition.

[39] We use cubic finite elements with 8 displacement nodes and volume-averaged derivatives of the shape function. The closest mixed-finite element discretization would be Q1P0. An ad-hoc stabilization of pressure oscillations is implemented [*Popov and Sobolev*, 2008]. Unless otherwise indicated, elements have 5 km edge length resulting in 225000 elements within the domain. The implicit time stepping allows for a step size of 20 ky so that 500 steps suffice to compute 10 My evolution. The current version of SLIM3D solves the discretized conservation equations using the direct parallel shared memory solver PARDISO [*Schenk and Gärtner*, 2004].

4. Results

4.1. Oblique Boundary Conditions

[40] First, we focus on the setup with oblique boundary condition (Figures 3b, 3d, and 3f). In the following, we study three distinct cases with angle of obliquity $\alpha = 0°$, $60°$, $90°$, corresponding to pure extension, high obliquity, and strike-slip deformation, respectively (Figure 4; corresponding animations can be found in the auxiliary material).[1]

[41] All models exhibit strain localization at the center of the computational domain above the prescribed thermal perturbation. However, the models differ significantly with respect to shear zone geometry, evolution of lithospheric thinning and mechanical strength of the domain.

[42] During pure extension ($\alpha = 0°$), the uppermost mantle and crust undergo necking (Figures 4a and 4b). Below the rift center, lithospheric material is replaced by hot advective upwelling. Cooling of this upwelling takes place much

[1] Auxiliary materials are available in the HTML. doi:10.1029/2011JB008860.

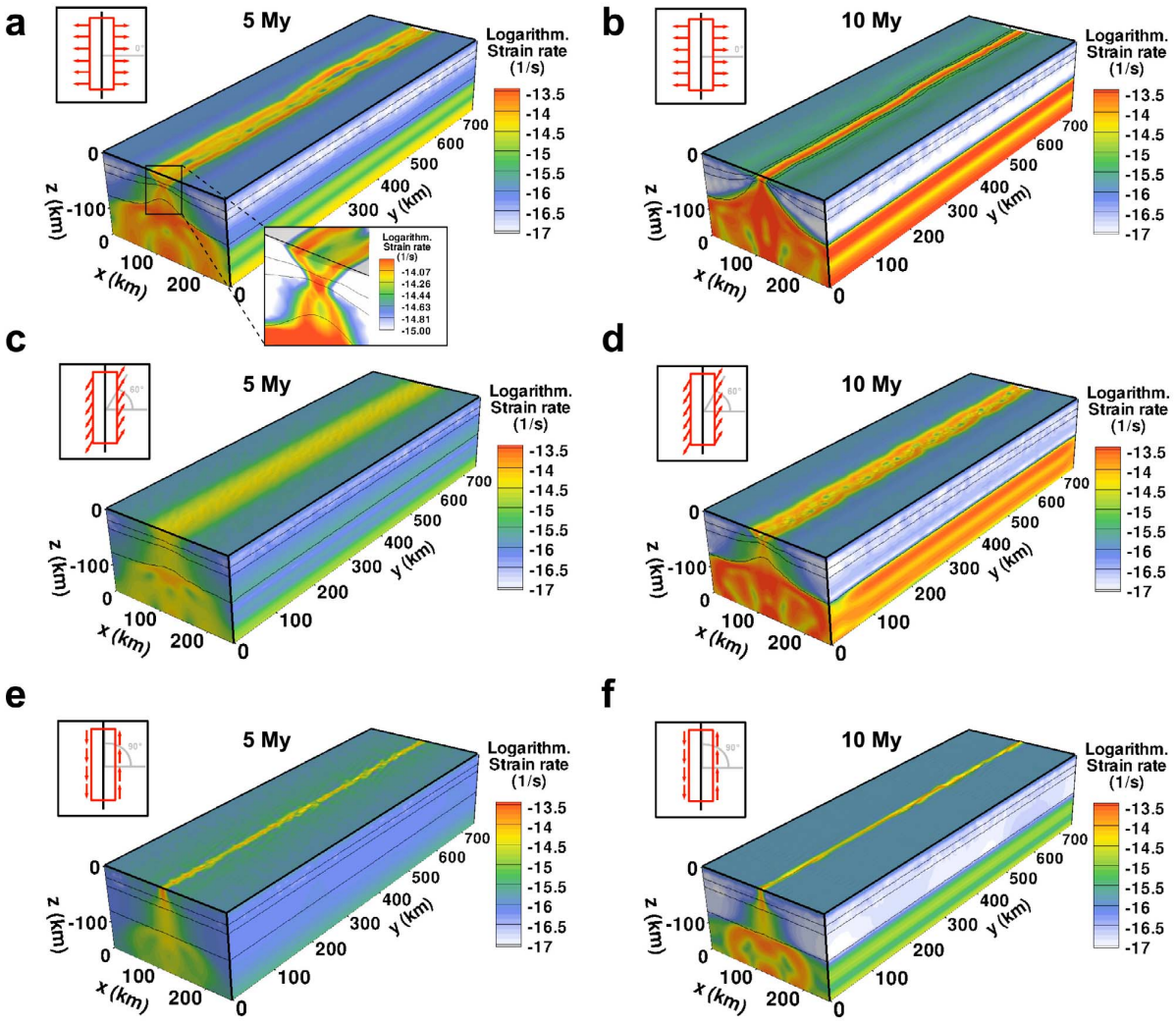

Figure 4. Oblique boundary conditions. Shown is the second invariant of strain rate $\dot{\varepsilon}_{II}$ at 5 My and 10 My. Black lines designate phase boundaries between upper and lower crust as well as strong and weak mantle. (a, b) Pure extension ($\alpha = 0°$). (c, d) High obliquity ($\alpha = 60°$). (e, f) Strike-slip deformation ($\alpha = 90°$). Corresponding animations can be found in the supplementary material.

slower than its intrusion leading to a loss of strength in the center of the domain. A set of shear zones evolves in the rift zone of which two large normal faults cut through the crust. After roughly 10 My, mantle material reaches the surface which finalizes break-up and initiates seafloor spreading. The small along-strike variations that occur during the highly non-linear localization process are due to numerical noise that derives from a random marker distribution.

[43] The highest possible angle of obliquity ($\alpha = 90°$) results in strike-slip deformation of the domain (Figures 4e and 4f). Neither crustal nor lithospheric necking takes place, because the boundary velocity contains no rift-perpendicular extensional component. One large strike-slip zone emerges shortly after the model start that is underlain by a broad zone of deformation in the viscous domain. Due to the intrinsic weakening mechanisms, the frictional resistance decreases with ongoing strain which attracts further deformation. After 10 My the mature system focuses most strain into the strike-slip zone.

[44] Oblique rifting features many characteristics of both pure extension and strike-slip deformation (Figures 4c and 4d). In the oblique models, the zone of deformation is much more diffuse than in the end-member cases 0° and 90°, until it localizes into distinct shear zones that strike at a certain angle to the boundary velocity, comparable to en-echelon faulting. This behavior has also been observed in many analog models [*Corti et al.*, 2003; *Agostini et al.*, 2009; *Autin et al.*, 2010] and in some numerical experiments [*van Wijk*, 2005; *Popov and Sobolev*, 2008]. The angle of the individual shear zones with respect to the model boundaries reflects the direction of the principal stress directions as discussed in *Withjack and Jamison* [1986].

[45] The general structure of the models does not vary significantly along strike, and remains identical if the model length in that direction is varied. Note that periodic boundary conditions along strike avoid any otherwise occurring boundary effects. Moreover, the temporal history of mechanical variables is not influenced, if the model domain in *y*-direction is reduced to the size of one element. Although the domain is in this case essentially two-dimensional, the velocities still bear three components, which results in a model that we use to call 2.5-dimensional [*Sobolev et al.*, 2005]. A major advantage of the domain shortening is that much less computational effort is necessary if elements keep their size of 5 km. Alternatively, we have the opportunity to increase the resolution significantly at comparable computation times. Below we use element sizes of 1 km.

[46] In the above models, we apply a constant velocity at the lateral boundaries. Keeping the velocity constant requires a specific boundary force F that can be computed from stress components σ_{ij} at the boundary. For that purpose, we first compute the integrated stress tensor S_{ij}:

$$S_{ij} = \frac{1}{L_y L_z} \int\int \sigma_{ij} \; dydz \tag{29}$$

where the length of the model domain in y and z direction are denoted L_y and L_z, respectively. The full boundary force F_{full} results from the Pythagorean addition of those stress components S_{ij} that locate on the face of the box with normal in x-direction (S_{xx}, S_{xy}, and S_{xz}):

$$F_{full} = \sqrt{S_{xx}^2 + S_{xy}^2 + S_{xz}^2} \cdot L_z \tag{30}$$

[47] If the extensional velocity was zero, the horizontal stress S_{xx} would be equal to the non-zero, lithostatic stress S_{zz}, while S_{xy} and S_{xz} would vanish [*Turcotte and Schubert*, 2002]. This means that F_{full} is not appropriate to measure the tectonic force since it is non-zero although no deformation takes place. In order to calculate the correct tectonic force we introduce the tectonic stress ΔS [*Artyushkov*, 1973]: Applied boundary velocities increase S_{xx} by ΔS so that $S_{xx} = S_{zz} + \Delta S$, whereas the shear components S_{xy} and S_{xz} remain unchanged. In the following, we compute the tectonic force F due to the tectonic stress contribution:

$$\begin{aligned} F &= \sqrt{(\Delta S)^2 + S_{xy}^2 + S_{xz}^2} \cdot L_z \\ &= \sqrt{(S_{xx} - S_{zz})^2 + S_{xy}^2 + S_{xz}^2} \cdot L_z. \end{aligned} \tag{31}$$

[48] That formula is the three-dimensional analog of the commonly used two-dimensional definition of the tectonic extensional force [e.g., *Bialas et al.* 2010].

[49] F reflects the integrated material strength and thus strongly depends on the internal thermomechanical structure of the model. As we showed in the previous paragraph, this structure is decisively influenced by the direction of the boundary velocity. In a set of experiments, we evaluate the boundary force for a constant boundary velocity of 10 mm/yr (full extension rate) whose direction varied between $\alpha = 0^\circ$ (pure extension) and $\alpha = 90^\circ$ (strike-slip) (Figure 5a). First, we consider the regime of pure extension (red curve): Within the first time steps, stresses are propagated elastically, and the force grows linear with time, until yield strength is reached at 13 TN/m. Due to lithospheric necking, the strength of the lithosphere decreases with time to 1.5 TN/m at around 10 My, where mantle material reaches the surface and break-up is completed. In the case of strike-slip deformation (blue curve in Figure 5a), following the period of elastic stress propagation, yield strength is reached at 7 TN/m. Due to the lack of lithospheric necking, the force decreases much slower than for the case of pure extension until it reaches 4 TN/m at 10 My. The weakening is caused solely by shear heating and strain softening, which will be investigated later on. Oblique rifting ($10^\circ \leq \alpha \leq 80^\circ$) constitutes a mixture of both end-member cases. Especially the maximum force varies smoothly, although nonlinear with the rift angle.

[50] The absolute value of the extensional velocities can be expected to have distinct control on the tectonic force. We investigate that issue by varying the extensional velocity by a factor of 2 and 0.5. Correspondingly, we use different calculation times (5 My and 20 My) so that the absolute extension remains identical. For simplicity, we investigate only the cases where α equals 0° and 90° (Figure 5b). Two primary effects can be observed: (i) Since higher velocities (20 mm/yr) imply higher strain rates, the viscous domains exhibit higher stress values and the integrated lithospheric strength is elevated. This explains why the maximum force increases when faster extension is applied. The opposite is true for low velocities of 5 mm/yr. (ii) Thermal equilibration of the lithosphere counteracts the weakening effect of lithospheric necking. If extensional rates are small, there is more time for conductive lithospheric cooling which is why the effective strength of the lithosphere decreases more slowly [e.g., *Kusznir and Park*, 1987]. This effect is relevant only for slow extension (5 mm/yr) illustrated by the fact that here the force at 20 My is distinctly larger than the final force for both the 10 mm/yr and 20 mm/yr experiments.

[51] The maximum force value is measured at the yield limit before any weakening mechanisms play a role. This value can be compared directly to the yield force computed in the analytical solution of section 2. Figure 5c displays the dependence of yield force F on the angle of obliquity α. Despite the severe assumptions of the analytical approach, the correspondence between the analytical curve (with $\nu = 0.23$ and $L_z = 47$ km) and the numerical results is very good, ensuring the robustness of our results.

[52] The temporal behavior of the force in Figure 5a is dominated by diverse weakening effects like lithospheric necking, crustal strain-dependent friction softening, shear heating, and power law rheology in the viscous domain. We study the effect of friction softening and shear heating by successively switching these effects on or off (Figure 6). Lithospheric necking and Non-Newtonian dislocation creep, however, are so strongly inherent that it is not feasible to disable them. Both strain softening and shear heating become effective only after a few My, when either deformation or strain rate is high enough. In the case of pure extension, lithospheric necking is the major weakening mechanism, although it is enhanced by shear heating and friction softening. After 9 My when break-up is complete, stresses and crustal deformation in the rift center become very small so that the force becomes independent of friction softening and shear heating. In the strike-slip setting, no

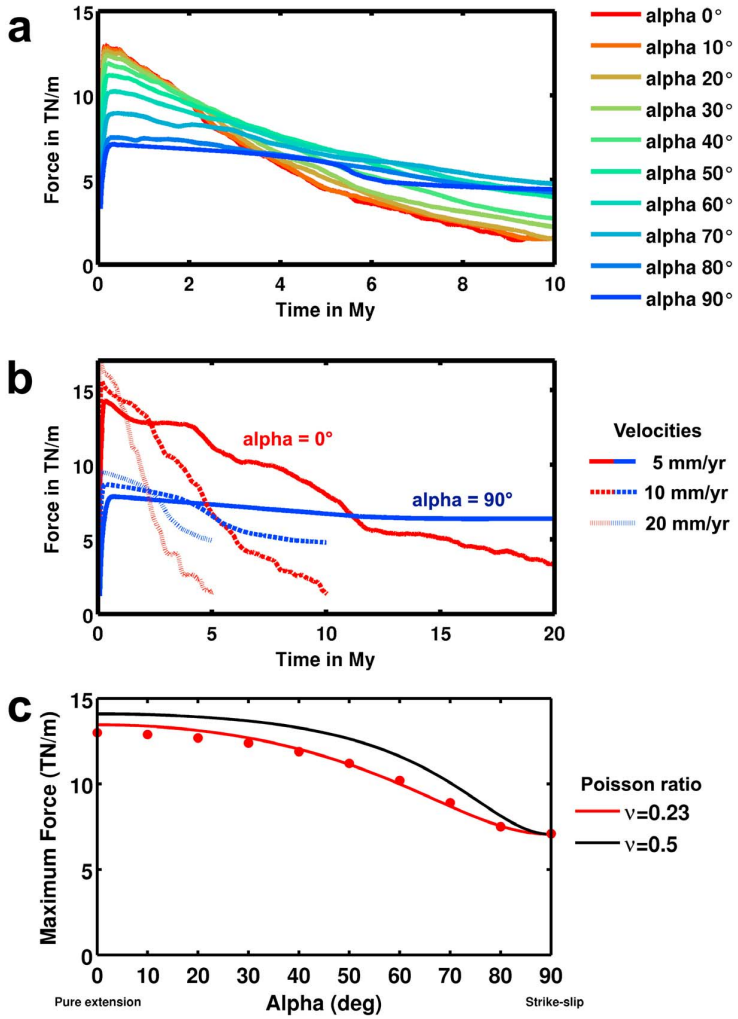

Figure 5. Tectonic force evolution in numerical experiments. (a) The required force to maintain extensional velocities. (b) Influence of extension velocity. (c) Comparison between maximum force values of numerical experiments (red dots) and analytic calculations for volume-conserving (ν = 0.5, blue curve) and realistic (ν = 0.23, red curve) values of the Poisson ratio. The layer thickness for the analytical solutions is L_z = 47 km.)

upwelling takes place and weakening is controlled by shear heating and friction softening. If both mechanism are switched off, the force remains constant or even increases slightly due to lithosphere cooling. For this setup and the applied parameterizations, we find that friction softening is more important than shear heating and the influence of both effects is responsible for about 2 to 3 TN/m force reduction.

4.2. Oblique Rift Zone

[53] If oblique rifting requires less force, what happens if two prospective rift zones of different obliquity compete in the same tectonic setting? In this section, we address that question using an alternative setup to oblique boundary conditions by implementing a rift zone that is oblique to the boundaries (Figures 3c, 3e, and 3g). We first display the evolution of an oblique and a perpendicular rift zone before we investigate a setting with both rifts simultaneously. Again, we use a small temperature perturbation at the bottom of the lithosphere to prescribe the orientation of a prospective rift zone. This perturbation has the same height, width and average cross section as in the previous setting. While the rift zone is oblique, the boundary velocities are now perpendicular to the sides of the domain. We apply extension at the front and back of the model, while the lateral sides feature continuous stress boundary conditions. As in the previous setup, we look at rift angles $\alpha = 0°$ and 60°. The case of $\alpha = 90°$ can not be implemented for this setting, as this would mean to prescribe velocities within the shear zone which inhibits the natural localization process.

[54] Pure extension ($\alpha = 0°$) results in the formation of two finite-width normal faults, lithospheric and crustal necking (Figures 7a and 7b), just as in the setting of oblique boundary conditions. Oblique rifting ($\alpha = 60°$) again shows distinct shear zones that cut through the rift zone, striking

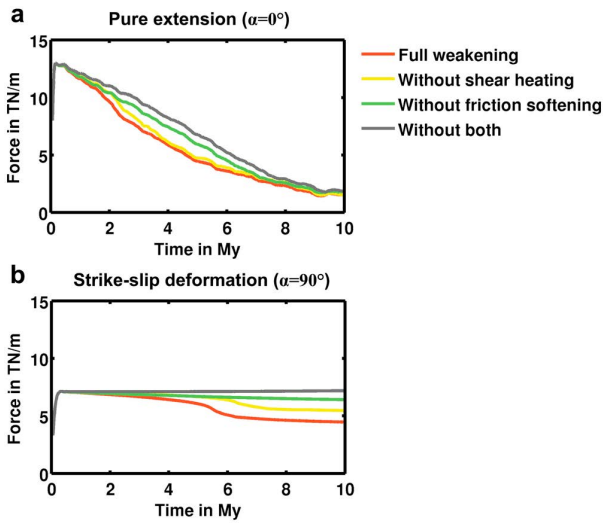

Figure 6. Influence of weakening processes: Shear heating $(\sim\tau_{II}\dot{\varepsilon}_{II})$ and friction softening $(\sim\varepsilon_{II})$. Please refer to the text for more details on the weakening mechanisms. (a) Weakening for pure extension is dominated by lithosphere necking. (b) The strike slip setting is controlled by shear heating and friction softening.

subparallel to the weak zone (Figures 7c and 7d). However, some discrepancies to Figure 4 are visible. The boundaries somewhat affect the form of the rift so that the endings of the shear zone are slightly bent. Furthermore, as the model length in extensional direction is larger in the present setting, but spreading velocities remained identical, the mean strain rate in the present setup is smaller than that of the previous section. Nevertheless, as soon as deformation is localized into the rift zone of approximately the same width, rift-relevant strain rates become effectively identical to the setup with oblique boundary conditions which is why the general dynamics of both setups is very similar. These differences have only minor effects on the temporal evolution of the required boundary force. The maximum forces for the oblique boundary setting and the oblique weak zone setup are the same; only the timing is slightly different, due to different strain rates.

[55] Finally, we introduce two prospective rift zones of distinct orientation ($\alpha_1 = 0°$ and $\alpha_2 = 60°$) into the model (Figures 7e and 7f), while all other parameters and boundary conditions remain the same. Essentially, both setups of Figures 7a and 7b and Figures 7c and 7d are appended in a row, whereby the length of the computational domain is increased to 900 km. During the first several million years, both weak zones are simultaneously active, while the strain rate of the oblique rift grows steadily at the expense of the perpendicular zone. The oblique rift zone attracts successively more strain until the boundary-perpendicular zone of deformation becomes extinct at roughly 8 My. This result is independent of the specific implementation. Variations in width and height of the initial temperature heterogeneity, the extensional velocity or the size of the model domain did not change the overall behavior. Moreover, the outcome can be related to *Chemenda et al.* [2002] who showed that in analog models of extending, homogeneous lithosphere faults develop preferentially at an angle of ≈60° toward the extensional direction. Although our lithosphere is not homogeneous, and the boundary conditions differ, both experiments show that rift obliquity is mechanically preferred.

4.3. Dynamic Boundary Conditions

[56] Interaction between a rift zone and the forces that drive plate motion can be of two distinct kinds: Either dynamics of the rift zone influence the overall force balance, or they do not. Velocity boundary conditions are best applicable in the latter case when the integrated strength of the rift zone is small compared to the plate-driving forces. In this case, the extensional velocity of the rift will depend only on the large-scale force balance and plate geometries. If the rift's strength, however, is comparable to the plate-driving forces, it will feed back on the extensional velocities. This is the case for the opening of large oceanic basin, where the length of the rift zones exceeds several 1000 kilometers.

[57] In the previous sections, we held the boundary velocities constant and computed the required force. Here, we reverse that approach and prescribe the boundary force and its direction in order to compute resulting velocities. We showed beforehand that oblique rifting is mechanically preferred, however higher obliquity results in less rift-perpendicular extension. Strike-slip motion for instance may require least force, but it does not result in break-up since the plates do not separate. In this section we investigate whether an optimal extensional angle exists that maximizes rift-perpendicular extension for a given boundary force.

[58] Under the application of a constant force to any brittle material, three dynamic regimes can be anticipated: (i) If forces are too low they can not induce plastic failure so that deformation stops according to the purely elastic response. (ii) The applied force overcomes the plastic yields strength. The system deforms according to its internal structure resulting in boundary velocities that can be regarded as an integrated response to the external load. (iii) Weakening processes like lithospheric necking dominate the mechanical behavior. The decreasing strength of a maturing rift is compensated by rising velocities in order to fulfill the constant force boundary condition. Increasing velocities lead to even more weakening and a runaway process is induced. Rift zones bear a certain strength, while mid-oceanic ridges are extremely weak. During the transition between rifting and seafloor spreading, the runaway process stops when the extensional velocity becomes independent of lithospheric strength and finally reflects the interplay of plate boundary forces and mantle drag. We address this issue in our model by implementing an upper limit to velocities of 50 mm/yr that agrees well with typical values for ocean floor spreading rates in the Atlantic [*Müller et al.*, 2008]. Once this velocity limit is reached, constant velocity boundary conditions are used like in the previous subsections. These mixed force-velocity boundary conditions allow to model the whole process from rifting to break-up until seafloor spreading is initiated and they reproduce the observed rift velocities of 5 to 20 mm/yr [*Buck*, 1991] together with typical seafloor spreading rates in the order of 40 to 100 mm/yr [*Müller et al.*, 2008].

[59] Using the same setting of oblique boundary conditions as in section 3.1, we apply forces of 8 TN/m and 11 TN/m that are high enough to induce plastic failure for

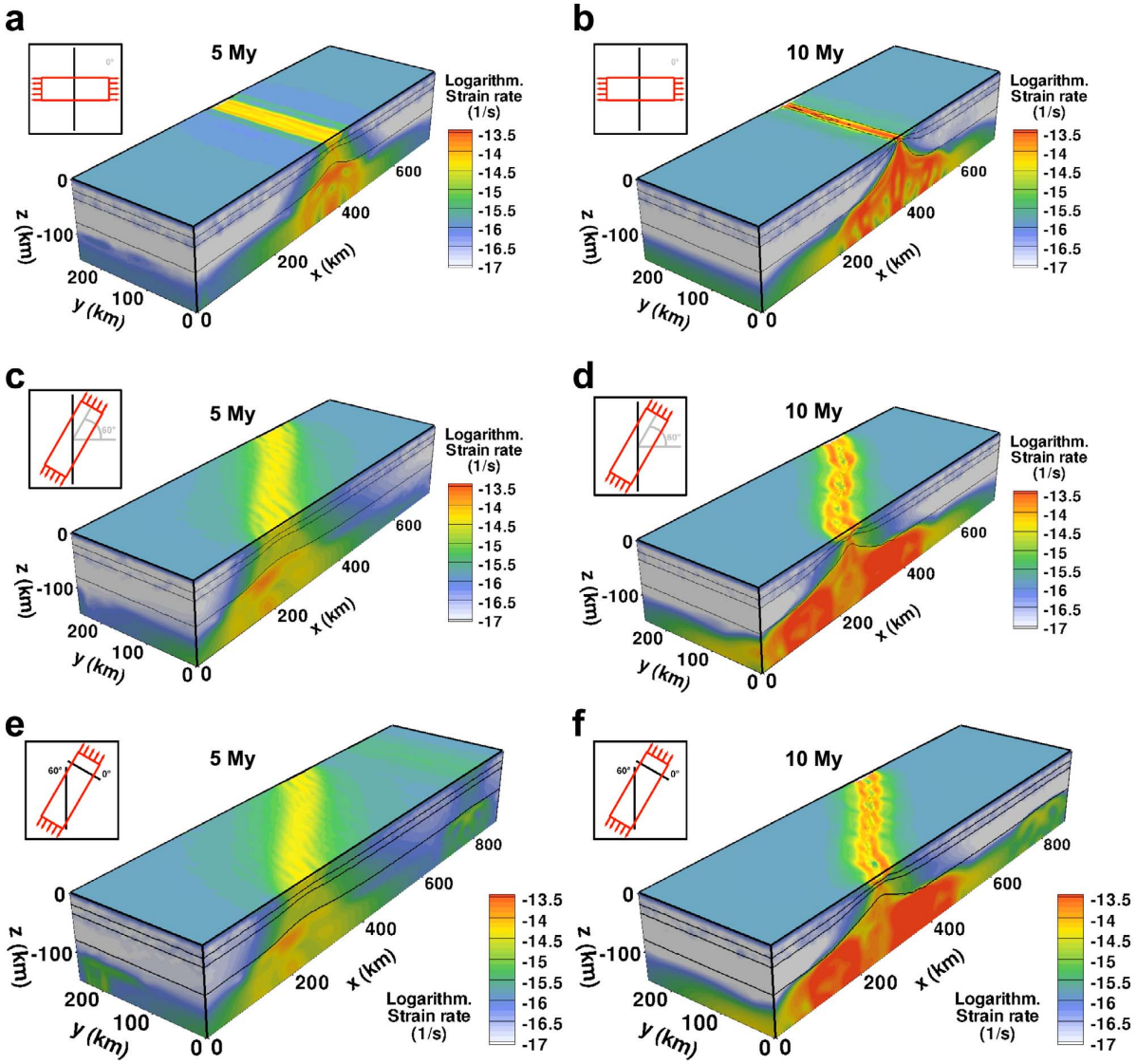

Figure 7. Oblique weak zones. Shown is the second invariant of strain rate at 5 My and 10 My. Black lines designate phase boundaries between upper and lower crust as well as strong and weak mantle. (a, b) Pure extension ($\alpha = 0°$). (c, d) High obliquity ($\alpha = 60°$). (e, f) Simultaneous deformation of extension-perpendicular ($\alpha = 0°$) and highly oblique weak zones ($\alpha = 60°$). Corresponding animations can be found in the supplementary material.

the prescribed initial lithospheric structure (Figure 8). Again, we consider distinct rift angles that vary between 0° (pure extension) and 90° (strike-slip deformation), while all other parameters are identical to those of section 3.1. Note that in Figure 5 the maximum force (13 TN/m) for a constant velocity of 10 mm/yr has been higher than the values in this experiment. The model that is most influenced by the force limit is that of pure extension (red curves in Figures 8a, 8c, and 8e). This follows from our previous result that pure extension requires the largest force to deform at constant strain. Its velocity remains at low levels below 5 mm/yr during the first 3 My. Only then lithospheric necking weakens the rift zone sufficiently so that velocities increase quickly up to 50 mm/yr within 1 My. Once the limiting velocity of 50 mm/yr is reached and hence break-up occurred, the force decreases below 2 TN/m. The oblique models result in similar behavior except that the limiting velocity is reached more quickly. The strike-slip end-member (blue line) even commences with 50 mm/yr, as is does not require 11 TN/m to reach the velocity limit. Nevertheless, all deformation is concentrated on the strike-slip zone so that no rifting and no break-up takes place. For the intermediate settings ($10^{\circ} \leq \alpha \leq 80^{\circ}$) rift-perpendicular extension does occur and deformation evolves faster than for the rift-perpendicular extension. The largest rift-perpendicular extension during the first 5 My can be observed for rift

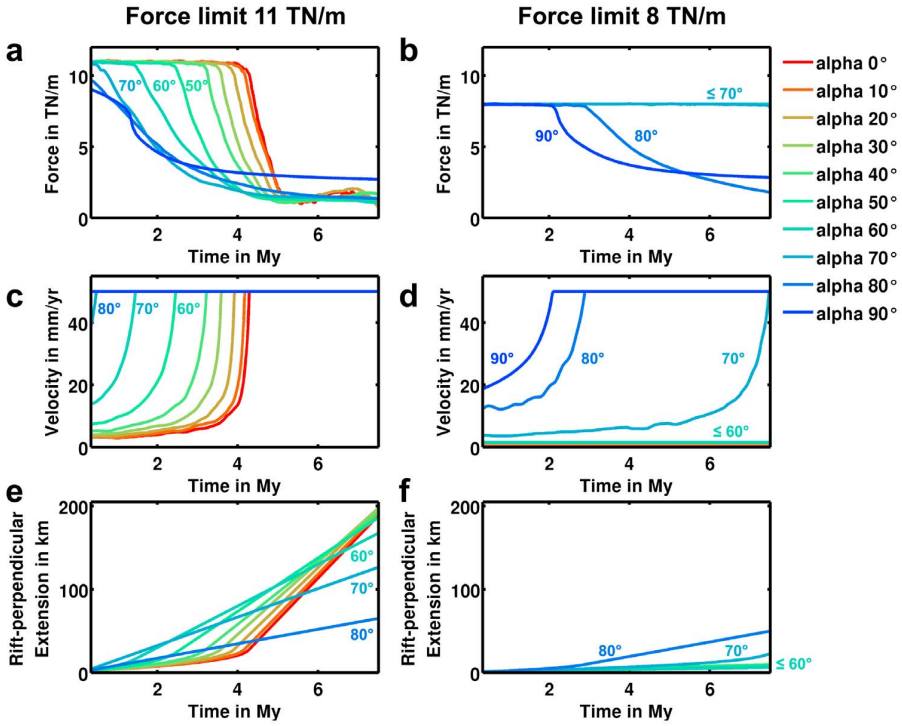

Figure 8. Dynamic boundary conditions: Boundary velocities are adjusted so that a maximum force of (a, c, e) 13 TN/m and (b, d, f) 8 TN/m is not exceeded. If forces fall below that threshold, velocities are fixed to 50 mm/yr (see text for further explanations).

angles of 60° and70° (Figure 8e); while $\alpha = 0°$ yields 20 km rift-perpendicular extension at 5 My, $\alpha = 60°$ results in 100 km. If force is lower, say 8 TN/m, only highly oblique rifts are developing (Figures 8b, 8d, and 8f) while settings with $\alpha \leq 60°$ do not exceed velocities of 1.5 mm/yr. In this case the largest extension (30 km) after 5 My is achieved for rifting with an obliquity of 80°. At forces below the lithospheric strength for the pure strike-slip (7 TN/m, see Figure 5) no rifting takes place for the considered lithospheric structure.

[60] This result implies that the optimal rift angle which maximizes rift-perpendicular extension decreases with time. We suggest that in the beginning of an oblique break-up process almost pure strike-slip faults tend to develop, like it is happening now at the Dead Sea Transform plate boundary. Later, less oblique faults may emerge and first break-up will likely take place at high-obliquity faults with α between 50° and 80°. Note that this hypothesis is best applicable if magmatic processes can be neglected, i.e. for non-volcanic rifts or during non-magmatic rift stages. If considerable amounts of melt are produced, dikes will intrude perpendicular to the principal direction of extension. This process decreases the required tectonic force for rift-perpendicular extension [*Buck*, 2007] and may strongly affect the dynamic evolution of the system. In nature, rifts are not free to evolve and this development interferes with the overall plate configuration. We therefore suggest to test whether this development can be observed in future kinematic reconstructions of break-up processes.

[61] Estimations of the continental lithospheric strength based on yield strength profiles show that the strength of continental lithosphere considerably exceeds the available tectonic forces [*Buck*, 2007]. The formulation of that problem is disputed since the apparent paradox resolves, when very low friction coefficients are used in the entire lithosphere [*Huismans and Beaumont*, 2003] or when additional mechanisms leading either to the weakening of the lithosphere (e.g., via Peierls creep [*Kameyama et al.*, 1999]), or to an increase in the effective extensional force are taken into account. Here we show that the tectonic force that is required to induce rifting depends on the angle of obliquity. Hence, a rift with zero obliquity may not be activated for a given tectonic force while an oblique rift generates sufficient extensional strain to result in continental break-up. If available tectonic forces are lower than pure strike-slip lithospheric strength no rifting takes place. In that case, continental break-up can only occur if the lithosphere experiences additional weakening either due to significant input of melts via diking [*Buck*, 2004] or interaction with a thermo-chemical plume [*Sobolev et al.*, 2011].

5. Conclusions

[62] Oblique extension facilitates the rift process. The major reason is that oblique motion requires less force in order to reach the plastic limit. Under idealized elasto-plastic conditions we analytically computed the necessary force to induce plastic behavior. It is approximately two times less for the strike-slip case if compared to pure extension. This result

is not in contradiction with classical fault mechanics since the observation that strike-slip motion requires more differential stress than pure extension can be reproduced by our calculations. The analytical computations agree very well with the numerical results derived from an elasto-visco-plastic model of a layered Earth segment. An important aspect of these findings becomes apparent if two rifts of identical properties compete in a non-magmatic setting whereby one rift is perpendicular and one oblique to the direction of extension: Our experiments show that the oblique rift zone will accommodate successively more extensional strain while deformation in the second rift stagnates. In force-limited settings, our modeling demonstrates that with realistic tectonic forces of less than 10 TN/m and a typical lithospheric thickness of about 100 km as encountered in mobile belts, oblique rifting is mechanically preferred. We suggest that rifts are most effective in accumulating rift-perpendicular extension if they start at high angles of obliquity and rotate to lower angles during rift maturation.

[63] **Acknowledgments.** This research is a product of SAMPLE (South Atlantic Margin Processes and Links with onshore Evolution), Priority Program 1375, funded by the German Research Foundation (DFG). We would like to thank Susanne Buiter and an anonymous reviewer for their detailed and productive comments that lead to significant improvements of the manuscript.

References

Agostini, A., G. Corti, A. Zeoli, and G. Mulugeta (2009), Evolution, pattern, and partitioning of deformation during oblique continental rifting: Inferences from lithospheric-scale centrifuge models, *Geochem. Geophys. Geosyst.*, *10*, Q11015, doi:10.1029/2009GC002676.

Allken, V., R. S. Huismans, and C. Thieulot (2011), Three-dimensional numerical modeling of upper crustal extensional systems, *J. Geophys. Res.*, *116*, B10409, doi:10.1029/2011JB008319.

Artemieva, I. M., (2006), Global $1^\circ \times 1^\circ$ thermal model TC1 for the continental lithosphere: Implications for lithosphere secular evolution, *Tectonophysics*, *416*, 245–277.

Artyushkov, E. V. (1973), Stresses in the lithosphere caused by crustal thickness inhomogeneities, *J. Geophys. Res.*, *78*, 7675–7708, doi:10.1029/JB078i032p07675.

Autin, J., N. Bellahsen, L. Husson, M. Beslier, S. Leroy, and E. d'Acremont (2010), Analog models of oblique rifting in a cold lithosphere, *Tectonics*, *29*, TC6016, doi:10.1029/2010TC002671.

Bellahsen, N., C. Faccenna, F. Funiciello, J. Daniel, and L. Jolivet (2003), Why did Arabia separate from Africa? Insights from 3-D laboratory experiments, *Earth Planet. Sci. Lett.*, *216*, 365–381.

Bialas, R. W., W. R. Buck, and R. Qin, (2010), How much magma is required to rift a continent?, *Earth Planet. Sci. Lett.*, *292*, 68–78.

Braun, J., and C. Beaumont, (1989), A physical explanation of the relation between flank uplifts and the breakup unconformity at rifted continental margins, *Geology*, *17*, 760–764.

Buck, W. R. (1991), Modes of continental lithospheric extension, *J. Geophys. Res.*, *96*, 20,161–20,178, doi:10.1029/91JB01485.

Buck, W. R. (2004), Consequences of asthenospheric variability on continental rifting, in *Rheology and Deformation of the Lithosphere at Continental Margins*, edited by G. D. Karner et al., pp. 1–30, Columbia Univ. Press, New York.

Buck, W. R. (2007), Dynamic processes in extensional and compressional settings - the dynamics of continental breakup and extension, in *Treatise on Geophysics*, vol, 6, *Crust and Lithosphere Dynamics*, edited by A. B. Watts, pp. 335–376, Elsevier, New York.

Chemenda, A., J. Déverchère, and E. Calais (2002), Three-dimensional laboratory modelling of rifting: application to the Baikal Rift, Russia, *Tectonophysics*, *356*, 253–273.

Clifton, A. E., R. W. Schlische, M. O. Withjack, and R. V. Ackermann (2000), Influence of rift obliquity on fault-population systematics: results of experimental clay models, *J. Struct. Geol.*, *22*, 1491–1509.

Corti, G. (2008), Control of rift obliquity on the evolution and segmentation of the main Ethiopian rift, *Nat. Geosci. 1*, 258–262.

Corti, G., M. Bonini, S. Conticelli, F. Innocenti, P. Manetti, and D. Sokoutis (2003), Analogue modelling of continental extension: A review focused on the relations between the patterns of deformation and the presence of magma, *Earth Sci. Rev.*, *63*, 169–247.

de Wit, M. J. (2003), Madagascar: Heads it's a continent, tails it's an island, *Annu. Rev. Earth Planet. Sci.*, *31*, 213–248.

Edwards, R. A., R. B. Whitmarsh, and R. A. Scrutton (1997), The crustal structure across the transform continental margin off Ghana, eastern equatorial Atlantic, *J. Geophys. Res.*, *102*, 747–772, doi:10.1029/96JB02098.

Engen, Ø., J. I. Faleide, and T. K. Dyreng (2008), Opening of the Fram Strait gateway: A review of plate tectonic constraints, *Tectonophysics*, *450*, 51–69.

Gaina, C., R. D. Müller, B. Brown, T. Ishihara, and S. Ivanov, (2007), Breakup and early seafloor spreading between India and Antarctica, *Geophys. J. Int.*, *170*, 151–169.

Gleason, G. C., and J. Tullis, J. (1995), A flow law for dislocation creep of quartz aggregates determined with the molten-salt cell, *Tectonophysics*, *247*, 1–23.

Hempton, M. R. (1987), Constraints on Arabian plate motion and extensional history of the Red Sea, *Tectonics 6*, 687–705.

Hirth, G., and D. Kohlstedt (2003), Rheology of the upper mantle and the mantle wedge: A view from the experimentalists, in *Inside the Subduction Factory*, *Geophys. Monogr. Ser.*, vol. 138, edited by J. Eiler, pp. 83–105, AGU, Washington, D. C., doi:10.1029/138GM06.

Huismans, R. S., and C. Beaumont (2003), Symmetric and asymmetric lithospheric extension: Relative effects of frictional-plastic and viscous strain softening, *J. Geophys. Res.*, *108*(B10), 2496, doi:10.1029/2002JB002026.

Huismans, R., and C. Beaumont (2011), Depth-dependent extension, two-stage breakup and cratonic underplating at rifted margins, *Nature*, *473*, 74–78.

Kameyama, M., D. A. Yuen, and S. I. Karato (1999), Thermal-mechanical effects of low-temperature plasticity (the peierls mechanism) on the deformation of a viscoelastic shear zone, *Earth Planet. Sci. Lett. 168*, 159–172.

Kusznir, N. J., and R. G. Park (1987), The extensional strength of the continental lithosphere: its dependence on geothermal gradient, and crustal composition and thickness, *Geol. Soc. Spec. Publ.*, *28*, 35–52.

Lizarralde, D., et al. (2007), Variation in styles of rifting in the Gulf of California, *Nature*, *448*, 466–469.

Macdonald, D., et al. (2003), Mesozoic break-up of SW Gondwana: Implications for regional hydrocarbon potential of the southern South Atlantic, *Mar. Pet. Geol.*, *20*, 287–308.

McKenzie, D. (1978), Some remarks on the development of sedimentary basins, *Earth Planet. Sci. Lett.*, *40*, 25–32.

Moulin, M., D. Aslanian, and P. Unternehr (2010), A new starting point for the South and Equatorial Atlantic Ocean, *Earth Sci. Rev.*, *98*, 1–37.

Müller, R. D., M. Sdrolias, C. Gaina, and W. R. Roest (2008), Age, spreading rates, and spreading asymmetry of the world's ocean crust, *Geochem. Geophys. Geosyst.*, *9*, Q04006, doi:10.1029/2007GC001743.

Nürnberg, D., and R. D. Müller (1991), The tectonic evolution of the South-Atlantic from late jurassic to present, *Tectonophysics*, *191*, 27–53.

Parsiegla, N., J. Stankiewicz, K. Gohl, T. Ryberg, and G. Uenzelmann-Neben (2009), Southern African continental margin: Dynamic processes of a transform margin, *Geochem. Geophys. Geosyst. 10*, Q03007, doi:10.1029/2008GC002196.

Popov, A. A., and S. V. Sobolev (2008), SLIM3D: A tool for three-dimensional thermo mechanical modeling of lithospheric deformation with elasto-visco-plastic rheology, *Phys. Earth Planet. Interiors 171*, 55–75.

Provost, A., and H. Houston (2003), Stress orientations in northern and central California: Evidence for the evolution of frictional strength along the San Andreas plate boundary system, *J. Geophys. Res. 108*(B3), 2175, doi:10.1029/2001JB001123.

Regenauer-Lieb, K., G. Rosenbaum, and R. F. Weinberg (2008), Strain localisation and weakening of the lithosphere during extension, *Tectonophysics*, *458*, 96–104.

Royden, L., and C. Keen (1980), Rifting process and thermal evolution of the continental margin of eastern Canada determined from subsidence curves, *Earth Planet. Sci. Lett.*, *51*, 343–361.

Schenk, O., and K. Gärtner (2004), Solving unsymmetric sparse systems of linear equations with PARDISO, *Future Generation Comput. Syst.*, *20*, 475–487.

Sibson, R. H. (1974), Frictional constraints on thrust, wrench and normal faults, *Nature*, *249*, 542–544.

Simo, J. C., and T. J. R. Hughes (2000), *Computational Inelasticity*, 2nd ed., Springer, New York.

Sobolev, A. V., S. V. Sobolev, D. V. Kuzmin, K. N. Malitch, and A. G. Petrunin (2009), Siberian meimechites: Origin and relation to flood basalts and kimberlites, *Russ. Geol. Geophys.*, *50*, 999–1033.

Sobolev, S. V., A. Petrunin, Z. Garfunkel, A. Y. Babeyko, and DESERT Group (2005), Thermomechanical model of the Dead Sea transform, *Earth Planet. Sci. Lett.*, *238*, 78–95.

Sobolev, S. V., A. V. Sobolev, D. V. Kuzmin, N. A. Krivolutskaya, A. G. Petrunin, N. T. Arndt, V. A. Radko, and Y. R. Vasiliev (2011), Linking mantle plumes, large igneous provinces and environmental catastrophes, *Nature*, *477*, 312–316.

Sokoutis, D., G. Corti, M. Bonini, J. P. Brun, S. Cloetingh, T. Mauduit, and P. Manetti (2007), Modelling the extension of heterogeneous hot lithosphere, *Tectonophysics*, *444*, 63–79.

Storey, M., J. J. Mahoney, A. D. Saunders, R. A. Duncan, S. P. Kelley, and M. F. Coffin (1995), Timing of hot spot-related volcanism and the break-up of Madagascar and India, *Science*, *267*, 852–855.

Suckro, S. K., K. Gohl, T. Funck, I. Heyde, A. Ehrhardt, B. Schreckenberger, J. Gerlings, V. Damm, and W. Jokat (2012), The crustal structure of southern Baffin Bay: Implications from a seismic refraction experiment, *Geophys. J. Int.*, *190*, 37–58, doi:10.1111/j.1365-246X.2012.05477.x.

Tommasi, A., and A. Vauchez (2001), Continental rifting parallel to ancient collisional belts: An effect of the mechanical anisotropy of the lithospheric mantle, *Earth Planet. Sci. Lett.*, *185*, 199–210.

Torsvik, T. H., S. Rousse, C. Labails, and M. A. Smethurst (2009), A new scheme for the opening of the South Atlantic Ocean and the dissection of an Aptian salt basin, *Geophys. J. Int.*, *177*, 1315–1333.

Tron, V., and J. Brun (1991), Experiments on oblique rifting in brittle-ductile systems, *Tectonophysics*, *188*, 71–84.

Turcotte, D. L., and G. Schubert (2002), *Geodynamics*, 2nd ed., Cambridge Univ. Press, New York.

van Wijk, J. W. (2005), Role of weak zone orientation in continental lithosphere extension, *Geophys. Res. Lett. 32*, L02303, doi:10.1029/2004GL022192.

Weber, M., et al. (2009), Anatomy of the Dead Sea transform from lithospheric to microscopic scale, *Rev. Geophys.*, *47*, RG2002, doi:10.1029/2008RG000264.

Whittaker, J. M., R. D. Müller, G. Leitchenkov, H. Stagg, M. Sdrolias, C. Gaina, and A. Goncharov (2007), Major Australian-Antarctic plate reorganization at Hawaiian-Emperor bend time, *Science*, *318*, 83–86.

Wilks, K. R., and N. L. Carter (1990), Rheology of some continental lower crustal rocks, *Tectonophysics*, *182*, 57–77.

Withjack, M. O., and W. R. Jamison (1986), Deformation produced by oblique rifting, *Tectonophysics*, *126*, 99–124.

Ziegler, P. A., and S. Cloetingh (2004), Dynamic processes controlling evolution of rifted basins, *Earth Sci. Rev. 64*, 1–50.

Zoback, M. D., et al. (1987), New evidence on the state of stress of the San Andreas fault system, *Science*, *238*, 1105–1111.

Oblique rifting of the Equatorial Atlantic: Why there is no Saharan Atlantic Ocean

Christian Heine[1] and Sascha Brune[1,2]
[1]EarthByte Group, School of Geosciences, University of Sydney, Sydney, NSW 2006, Australia
[2]Helmholtz Centre Potsdam, GFZ German Research Centre for Geosciences, Section 2.5, Geodynamic Modelling, Telegrafenberg, D-14473 Potsdam, Germany

ABSTRACT

Rifting between large continental plates results in either continental breakup and the formation of conjugate passive margins, or rift abandonment and a set of aborted rift basins. The nonlinear interaction between key parameters such as plate boundary configuration, lithospheric architecture, and extension geometry determines the dynamics of rift evolution and ultimately selects between successful or failed rifts. In an attempt to evaluate and quantify the contribution of the rift geometry, we analyze the Early Cretaceous extension between Africa and South America that was preceded by ~20–30 m.y. of extensive intracontinental rifting prior to the final separation between the two plates. While the South Atlantic and Equatorial Atlantic conjugate passive margins continued into seafloor-spreading mode, forming the South Atlantic Ocean basin, Cretaceous African intraplate rifts eventually failed soon after South America broke away from Africa. We investigate the spatiotemporal dynamics of rifting in these domains through a joint plate kinematic and three-dimensional forward numerical modeling approach, addressing (1) the dynamic competition of Atlantic and African extensional systems, (2) two-stage kinematics of the South Atlantic Rift System, and (3) the acceleration of the South America plate prior to final breakup. Oblique rifts are mechanically favored because they require both less strain and less force in order to reach the plastic yield limit. This implies that rift obliquity can act as selector between successful ocean basin formation and failed rifts, explaining the success of the highly oblique Equatorial Atlantic rift and ultimately inhibiting the formation of a Saharan Atlantic Ocean. We suggest that thinning of the last continental connection between Africa and South America produced a severe strength-velocity feedback responsible for the observed increase in South America plate velocity.

INTRODUCTION

Lithospheric extension related to the final dispersal of western Gondwana started with the formation of large intracontinental rift systems within and between the Africa and South America plates in the Early Cretaceous (Burke and Dewey, 1974; Unternehr et al., 1988). Four extensional domains developed between the main rigid continental lithospheric blocks during that time (Fig. 1A; Heine et al., 2013): (1) the Central African Rift System (CARS), extending from Sudan to the eastern part of the Benoue Trough (Fairhead, 1986), (2) the West African Rift System (WARS), extending from the eastern part of the Benoue Trough northward toward southern Libya (Burke and Dewey, 1974; Genik, 1992), (3) the South Atlantic Rift System (SARS), comprising the present-day conjugate South Atlantic marginal basins with the Benoue Trough–northeast Brazil at its northernmost extent (Nürnberg and Müller, 1991), and (4) the Equatorial Atlantic Rift System (EqRS), covering the conjugate West African and South American margins from the Guinea Plateau–Demarara Rise in the west to the Benoue Trough–northeasternmost Brazil in the east (Basile et al., 2005). While extension in the SARS and EqRS ultimately led to the formation of the South Atlantic and Equatorial Atlantic (Nürnberg and Müller, 1991; Torsvik et al., 2009; Moulin et al., 2010; Heine et al., 2013), the CARS and WARS never went beyond rift mode and eventually failed, being preserved as subsurface graben structures (Burke and Dewey, 1974; Fairhead, 1986; Genik, 1992).

Here we investigate the spatiotemporal evolution of continental extension leading to the abandonment of these large intracontinental rift systems and the breakup between Africa and South America. We analyze the geodynamics of rifting by combining plate kinematic and forward numerical models.

PLATE KINEMATIC MODEL

Our study builds upon a new plate kinematic model for the evolution of the West Gondwana rift systems (SARS, CARS, WARS, and EqRS) that quantitatively integrates crustal deformation from Cretaceous African and South American intraplate deforming zones as well as from the conjugate passive margins of the equatorial and South Atlantic (Heine et al., 2013). Stage poles of relative motions between the African plates, describing the lithospheric extension in the WARS and CARS, have been generated from published extension estimates (e.g., Genik, 1992; McHargue et al., 1992) and fitting of restored sediment basin widths (Heine et al., 2013; see the GSA Data Repository[1] for paleotectonic maps in 1 m.y. time steps).

Relative motions between the main rigid plates are initiated at 140 Ma and progress at slow extensional velocities, compounding to ~4 mm a^{-1} between South America and southern Africa until 126 Ma (southern Africa fixed reference frame, full spreading rates at 37.5°W, 5°S). Modeled plate motions between South America and northwest Africa result in ~10–15 km displacement during the initial phase. Nondeforming South American and northwest African plates surrounding this region (Heine et al., 2013) imply that an incipient, diffuse plate boundary along the future Equatorial Atlantic region may have existed during the Early Cretaceous, contemporaneous with rifting in the CARS and WARS. Marine magnetic anomalies in the southernmost South Atlantic document breakup and subsequent seafloor spreading in the southern rift segment (Nürnberg and Müller, 1991; Moulin et al., 2010), while the northern part still undergoes continental extension (Torsvik et al., 2009; Moulin et al., 2010; Heine et al., 2013). Relative plate velocities based on seafloor spreading patterns indicate an ~10-fold increase of spreading and/or extensional velocities from 4 mm a^{-1} to >39 mm a^{-1} toward the early Aptian (120.6 Ma; Heine et al., 2013). From then onward, breakup occurs successively in isolated segments of the northern SARS and EqRS, with complete breakup achieved by 104 Ma.

NUMERICAL MODEL SETUP

We investigate the dynamics of rift competition and the reason for the observed multiphase velocity behavior using the three-dimensional (3-D) thermomechanical code SLIM3D (Popov and Sobolev, 2008) with boundary conditions as specified in Figures 1C and 1D. The program solves the thermomechanically coupled conservation equations of momentum, energy, and mass. It includes a free surface and rheological

[1]GSA Data Repository item 2014073, methodological information on numerical model setup, paleo-tectonic reconstruction maps for the Equatorial Atlantic region for the time between 140 and 100 Ma in 1 m.y. time steps, and numerical model animations (Apple Quicktime®), is available online at www.geosociety.org/pubs/ft2014.htm, or on request from editing@geosociety.org or Documents Secretary, GSA, P.O. Box 9140, Boulder, CO 80301, USA.

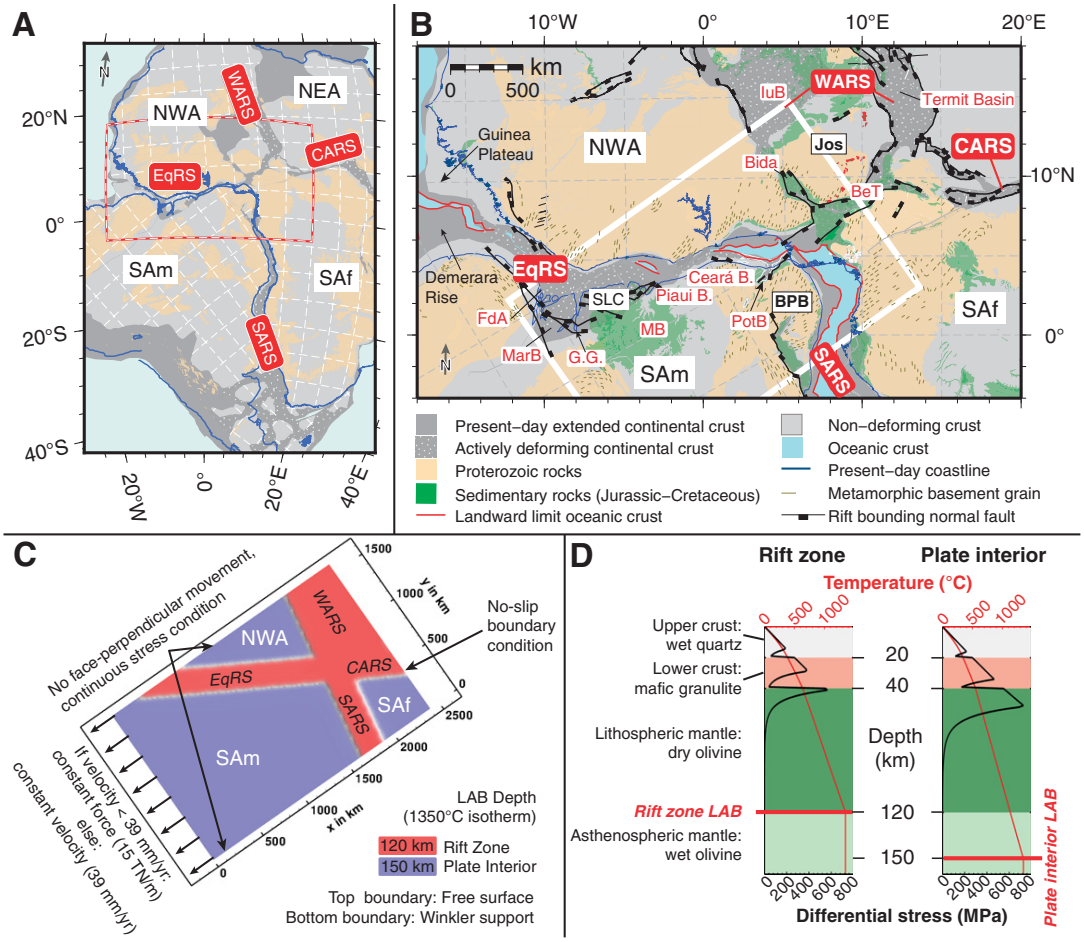

Figure 1. Overview map and numerical model setup. Southern Africa (SAf) is held fixed in present-day position in all reconstructions. A: Lambert azimuthal equal area view of pre-rift configuration at 140 Ma, showing major rigid plates and deforming crustal regions (Heine et al., 2013). Present-day South America and Africa plates are separated into four major rigid plates in region of interest during Late Jurassic–Early Cretaceous: NEA—northeast Africa, NWA—northwest Africa, SAf—southern Africa, SAm—South America. Rift systems (white font, red background): CARS—Central African rift, EqRS—Equatorial Atlantic rift, SARS—South Atlantic rift, WARS—West African rift. Red and white polygon indicates map frame (in B), white dashed lines are present-day 5° graticule. B: 117 Ma reconstruction (Heine et al., 2013). Northernmost segment of SARS is already in seafloor-spreading mode; in EqRS, breakup is incipient. Numerically modeled region is indicated by white rectangle. Minor rigid plates: BPB—Borborema province block (northeast Brazil), Jos—Jos subplate (northern Nigeria), SLC—São Luis craton. Basins (B): BarB—Barreirinhas Basin, BeT—Benoue Trough, FdA—Foz do Amazon Basin, G.G.—Gurupi graben, IuB—Iullemmeden Basin, MarB—Marajó Basin, MB—Maranhão Basin, PotB—Potiguar Basin. C: Initial geometric setup of three-dimensional numerical model involves prospective rift zones as thermal heterogeneities. Model size is 2400 × 1600 km horizontal and 200 km vertical. LAB—lithosphere-asthenosphere boundary. D: Lithospheric segment is vertically divided into four distinct petrological layers, upper crust, lower crust, lithospheric mantle, and asthenospheric mantle. Rheological parameters (see the Data Repository [see footnote 1]) of crust are chosen to represent narrow rift setting as supported by crustal architecture along conjugate equatorial margins (Azevedo, 1991). Rheology of lithospheric and asthenospheric mantle is based on laboratory creep measurements for dry and wet olivine, respectively.

flow laws that are strictly based on experimental rheological data for major rock types (for parameters and model details, see the Data Repository). We adopt rift geometries of the Equatorial Atlantic region (Fig. 1) and thereby extend previous fundamental simulations of oblique rifting (Brune et al., 2012; Brune and Autin, 2013). The model domain is oriented such that two edges are parallel to the extensional direction, composing the rift zones of EqRS, WARS, CARS, and SARS (Figs. 1A and 1B). Because Gondwana rifting reactivated predominantly Pan-African–aged mobile belts (Janssen et al., 1995; Ziegler and Cloetingh, 2004), we introduce prospective rift zones by elevating the depth of the thermal lithosphere-asthenosphere boundary (1350 °C) to 120 km, in contrast to 150 km of the surrounding Proterozoic lithosphere (Fig. 1C; Artemieva, 2006). Each prospective rift is represented by the same thermal heterogeneity (Fig. 1D). North of the Benoue Trough, Early Cretaceous intraplate magmatism of the Jos Plateau (Wilson and Guiraud, 1992) as well as faulting and subsidence in the Bida and Iullemmeden Basins (Fig. 1B; Petters, 1981; Ojo, 1990; Genik, 1992) confirm distributed extension west of the WARS and perturbance of lithospheric temperature gradients. We include these areas in our definition of the WARS extensional domain and therefore simplify the complex junction of WARS and CARS (Figs. 1A and 1B) by homogeneously weak lithosphere (Fig. 1C). During the rift process, we keep the extensional force constant (15, 16, or 17 TN m^{-1}), allowing for self-consistent evolution of extensional velocities. This approach is feasible because the model domain composes a large region, the strength of which is a major component in the overall force balance of the involved plates. Upon transition from rifting to seafloor spreading in nature, lithospheric strength at the plate boundary becomes negligible, such that extensional velocities evolve independent of the local stress balance, and become affected primarily by global-scale plate tectonic forcing (e.g., slab pull, mantle drag). We account for that transition by applying the force boundary condition only until velocities equate local seafloor spreading rates derived from the plate kinematic model (~39 mm a^{-1}), and use this criterion to link numerical model time with the plate kinematic model to evaluate the spatiotemporal rift evolution.

EVOLUTION OF THE EQUATORIAL ATLANTIC

In our preferred numerical model (15 TN m^{-1}) strain initially accumulates simultaneously along all three rift domains (SARS, EqRS, southwest WARS; Fig. 2, 10 m.y. model time). Modeled extensional velocities for these

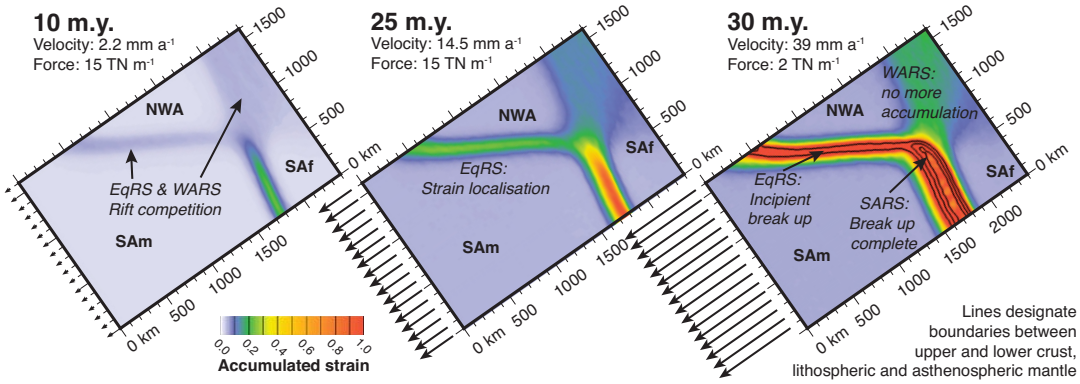

Figure 2. Accumulated strain over 30 m.y. after 10, 25, and 30 m.y. of model run time. Strain magnitude is colored, arrow length at bottom left boundary corresponds to velocity. For model animation in 1 m.y. time steps, see the Data Repository [see footnote 1]; abbreviations as in Figure 1.

domains (2–4 mm a^{-1} full rates) are in accordance with slow rifting compared to the plate kinematic model (Fig. 3). Tholeiitic dike swarms intrude the Ceará, Piaui, and Maranhão Basins (Ceará-Mirim dikes, Sardinha Formation) between 145 and 130 Ma (Bellieni et al., 1992). Crustal uplift, extension, and volcanism are reported from the Gurupí Graben and the Marajo, Foz do Amazon, and Potiguar Basins along the EqRS in pre-Aptian time (Azevedo, 1991; de Matos, 1992; Basile et al., 2005; Soares Júnior et al., 2011), indicating early extensional and transtensional deformation in the central EqRS at low strain rates. After 25 m.y. of model time, strain increasingly starts to localize along the proto–Equatorial Atlantic (Fig. 2; cf. 122 Ma reconstruction), with the rift tip of the SARS turning sharply west, converging into the weakness zone of the proto–Gulf of Guinea while subtle extension continues to affect the WARS. The numerical model suggests that increased strain accumulation in the EqRS and the simultaneous strain rate decrease in the WARS are due to their respective orientation toward plate divergence (EqRS, 60°; WARS, 30°), because all other parameters are the same. Analytical, numerical (Brune et al., 2012), and analogue models (Chemenda et al., 2002) corroborate these results, showing that highly oblique rifts are mechanically favored in both the elastic and viscous deformation regimes. The underlying reason is that oblique deformation requires less strain and as much as two times less force in order to reach the brittle yield stress (Brune et al., 2012). Once yield is reached, hot asthenospheric upwelling and friction softening promote extensive lithospheric weakening. While rift velocities remain low and both EqRS and WARS deform simultaneously until the ~25 m.y. model time (Fig. 2), the highly oblique EqRS accumulates more strain, causing lithospheric necking and strength loss. Subsequently, rifting accelerates in order to satisfy constant force boundary conditions. This nonlinear feedback between lithospheric strength and extensional velocity results in a strong velocity increase between the African and South American plates (Fig. 3) once strain localizes in the EqRS. Note that the duration of the plate velocity increase in the numerical model compares extremely well with independently derived kinematic plate reconstructions (Fig. 3; Nürnberg and Müller, 1991; Torsvik et al., 2009; Heine et al., 2013). From late Barremian time onward (ca. 123–112 Ma), rifting affects most proximal margin segments along the EqRS (Azevedo, 1991; Basile et al., 2005; Soares Júnior et al., 2011). Full lithospheric breakup along the EqRS is achieved in our numerical model after 34 m.y. due to further strain localization, whereas postrift thermal subsidence along the conjugate divergent Equatorial Atlantic marginal basins commences in late Aptian–early Albian time (ca. 114–106 Ma; Fig. 2; Azevedo, 1991; de Matos, 1992).

In order to constrain the effect of the boundary force, we recompute the evolution of numerical models with different forces of 16 and 17 TN m^{-1} but otherwise identical parameters; in both models, the strength-velocity feedback initiates earlier breakup along the EqRS at 23 and 18 m.y. model time, respectively (Fig. 3). However, the duration of the velocity increase remains the same, indicating that it is solely

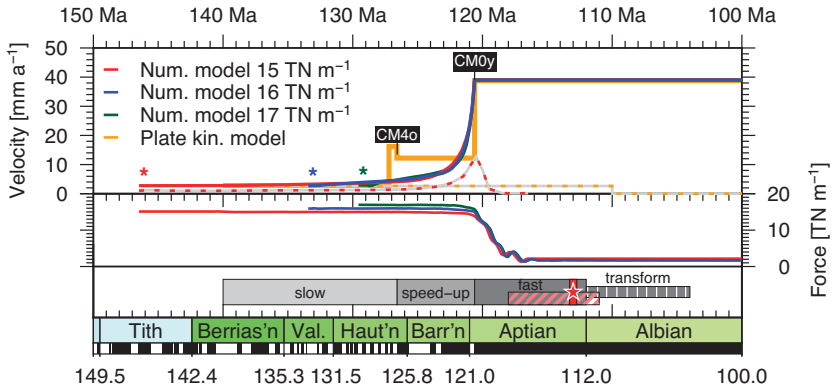

Figure 3. Velocities (top), forces (middle), and continental deformation along Equatorial Atlantic Rift System (EqRS, bottom) for selected forward numerical (Num.) models and plate kinematic (kin.) model (only velocities). Full extensional velocity calculated from plate kinematic model at 37.5°W, 5°S (on present-day South America plate, SAm) relative to fixed southern Africa (SAf). Magnetic anomalies: CM4o—anomaly CM4, old end (126.57 Ma), CM0y—anomaly CM0, young end (120.6 Ma). Stage pole for SAm-SAf rotations is based on cumulative extension in West African Rift System (WARS) and Central African Rift System (CARS) between fit reconstruction (140 Ma) and CM4o position (126.57 Ma), and allows for transtensional motion between SAm and northwest Africa (NWA). Rotations for CM4o–CM0y stage are derived from magnetic anomaly patterns in southern South Atlantic (Heine et al., 2013). Asterisks in upper plot indicate rift initiation time for numerical models. Dashed velocity lines on gray background indicate relative motions between northwest and northeast Africa as proxies for extensional velocities in WARS. Bottom: slow, speed-up, and fast indicate relative extensional velocities between rift onset and breakup along EqRS. Red line and star denote predicted breakup from numerical model. Oblique stripe pattern indicates duration of diachronous breakup along EqRS based on plate model. White vertical line pattern and transform denote transform stage after breakup that occurred along passive margin segments. Time scale shows geological ages; white and black scale below denotes magnetic polarity chrons (black—normal polarity, white—reversed polarity); absolute ages are based on hybrid time scale (Heine et al., 2013). Tith.—Tithonian; Berrias'n—Berriasian; Val.—Valanginian; Haut'n—Hauterivian; Barrem'n—Barremian.

affected by internal rift dynamics. Note that the required force to maintain rifting is relatively high in our models; however, it would decrease drastically if melt generation and dike emplacement were accounted for (Bialas et al., 2010).

WHY THERE IS NO SAHARAN ATLANTIC OCEAN

In conclusion, this joint plate kinematic and 3-D numerical modeling study elucidates the dynamics of rift competition during the final separation of South America and Africa in the Early Cretaceous. We are able to demonstrate that after ~20–25 m.y. of coexistence, strain localization along the EqRS caused the abandonment of the African intraplate rift systems (WARS-CARS) and hence inhibited the formation of a Saharan Atlantic Ocean during the Cretaceous. The success of the EqRS was strongly supported by its higher obliquity (60°), while orthogonal or less oblique extensional domains within the African plate became inactive. After 20 m.y. of slow rifting, a dramatic increase of the relative extensional velocity between the African and South American plates occurred over a short (~6 m.y.) period, followed by fast extension until final separation of the continental lithospheres. Our models suggest that the long period of rift competition was terminated by a severe strength-velocity feedback once the continental bridge between South America and northwest Africa had been weakened sufficiently.

Because rift evolution depends heavily on extensional velocity, we propose that the two-stage extension history of the South Atlantic and Equatorial Atlantic Rift System had a large impact on the evolution of the conjugate West African–Brazil margins in the northern and central South Atlantic segments. The acceleration of the South American plate also correlates with a change to a predominantly compressional regime along the South American Pacific margin, with existing backarc basins being successively closed (Maloney et al., 2013).

Our modeled multivelocity history of the South America plate during continental extension indicates a distinct control on the architectural evolution of the conjugate South Atlantic margin segments with an initial slow rifting episode in pre-Aptian time and subsequently increasing extensional velocities. This is supported by subsidence patterns of marginal basins in Angola and Gabon (Karner and Driscoll, 1999). Our results also call for a reevaluation of the timing of deformation along the frontier conjugate Equatorial Atlantic margins.

ACKNOWLEDGMENTS

Heine is funded by Australian Research Council Linkage Project LP0989312 with Shell and TOTAL. Brune is funded by German Research Foundation Priority Program 1375, SAMPLE (South Atlantic Margin Processes and Links with Onshore Evolution), and the European Research Council, Marie Curie International Outgoing Fellowship Project 326115, GLORY (Global Tectonics with Realistic Lithospheric Rheology). We are grateful for constructive reviews by C. Basile, S. Cloetingh, and M. Moulin. B. Steinberger and J. Whittaker commented on an earlier version.

REFERENCES CITED

Artemieva, I.M., 2006, Global 1° × 1° thermal model TC1 for the continental lithosphere: Implications for lithosphere secular evolution: Tectonophysics, v. 416, p. 245–277, doi:10.1016/j.tecto.2005.11.022.

Azevedo, R.P.D., 1991, Tectonic evolution of Brazilian equatorial continental margin basins [Ph.D. thesis]: London, Royal School of Mines, Imperial College, 455 p.

Basile, C., Mascle, J., and Guiraud, R., 2005, Phanerozoic geological evolution of the Equatorial Atlantic domain: Journal of African Earth Sciences, v. 43, p. 275–282, doi:10.1016/j.jafrearsci.2005.07.011.

Bellieni, G., and 11 others, 1992, Evidence of magmatic activity related to Middle Jurassic and Lower Cretaceous rifting from northeastern Brazil (Ceará-Mirim): K/Ar age, paleomagnetism, petrology and Sr-Nd isotope characteristics: Chemical Geology, v. 97, p. 9–32, doi:10.1016/0009-2541(92)90133-P.

Bialas, R.W., Buck, W.R., and Qin, R., 2010, How much magma is required to rift a continent?: Earth and Planetary Science Letters, v. 292, p. 68–78, doi:10.1016/j.epsl.2010.01.021.

Brune, S., and Autin, J., 2013, The rift to break-up evolution of the Gulf of Aden: Insights from 3D numerical lithospheric-scale modelling: Tectonophysics, v. 607, p. 65–79, doi:10.1016/j.tecto.2013.06.029.

Brune, S., Popov, A.A., and Sobolev, S.V., 2012, Modeling suggests that oblique extension facilitates rifting and continental break-up: Journal of Geophysical Research, v. 117, B08402, doi:10.1029/2011JB008860.

Burke, K., and Dewey, J.F., 1974, Two plates in Africa during the Cretaceous?: Nature, v. 249, p. 313–316, doi:10.1038/249313a0.

Chemenda, A., Déverchère, J., and Calais, E., 2002, Three-dimensional laboratory modelling of rifting: Application to the Baikal Rift, Russia: Tectonophysics, v. 356, p. 253–273, doi:10.1016/S0040-1951(02)00389-X.

de Matos, R.M.D., 1992, The Northeast Brazilian Rift System: Tectonics, v. 11, p. 766–791, doi:10.1029/91TC03092.

Fairhead, J.D., 1986, Geophysical controls on sedimentation within the African rift systems, *in* Frostick, L., et al., eds., Sedimentation in the African rifts: Geological Society of London Special Publication 25, p. 19–27, doi:10.1144/GSL.SP.1986.025.01.03.

Genik, G.J., 1992, Regional framework, structural and petroleum aspects of rift basins in Niger, Chad and the Central African Republic (C.A.R.): Tectonophysics, v. 213, p. 169–185, doi:10.1016/0040-1951(92)90257-7.

Heine, C., Zoethout, J., and Müller, R.D., 2013, Kinematics of the South Atlantic rift: Solid Earth, v. 4, p. 215–253, doi:10.5194/se-4-215-2013.

Janssen, M.E., Stephenson, R.A., and Cloetingh, S., 1995, Temporal and spatial correlations between changes in plate motions and the evolution of rifted basins in Africa: Geological Society of America Bulletin, v. 107, p. 1317–1332, doi:10.1130/0016-7606(1995)107<1317:TASCBC>2.3.CO;2.

Karner, G.D., and Driscoll, N.W., 1999, Tectonic and stratigraphic development of the west African and eastern Brazilian margins: Insights from quantitative basin modelling, *in* Cameron, N.R., et al., eds., The oil and gas habitats of the South Atlantic: Geological Society of London Special Publication 153, p. 11–40, doi:10.1144/GSL.SP.1999.153.01.02.

Maloney, K., Clarke, G.L., Klepeis, K.A., and Quevedo, L., 2013, The Late Jurassic to present evolution of the Andean margin: Drivers and the geological record: Tectonics, v. 32, p. 1–17, doi:10.1002/tect.20067.

McHargue, T.R., Heidrick, T.L., and Livingston, J.E., 1992, Tectonostratigraphic development of the Interior Sudan rifts, Central Africa: Tectonophysics, v. 213, p. 187–202, doi:10.1016/0040-1951(92)90258-8.

Moulin, M., Aslanian, D., and Unternehr, P., 2010, A new starting point for the South and Equatorial Atlantic Ocean: Earth-Science Reviews, v. 98, p. 1–37, doi:10.1016/j.earscirev.2009.08.001.

Nürnberg, D., and Müller, R.D., 1991, The tectonic evolution of the South Atlantic from Late Jurassic to present: Tectonophysics, v. 191, p. 27–53, doi:10.1016/0040-1951(91)90231-G.

Ojo, S.B., 1990, Origin of a major aeromagnetic anomaly in the Middle Niger Basin, Nigeria: Tectonophysics, v. 185, p. 153–162, doi:10.1016/0040-1951(90)90410-A.

Petters, S.W., 1981, Stratigraphy of Chad and Iullemmeden basins (West Africa): Eclogae Geologicae Helvetiae, v. 74, p. 139–159, doi:10.5169/seals-165095.

Popov, A.A., and Sobolev, S.V., 2008, SLIM3D: A tool for three-dimensional thermomechanical modeling of lithospheric deformation with elasto-visco-plastic rheology: Physics of the Earth and Planetary Interiors, v. 171, p. 55–75, doi:10.1016/j.pepi.2008.03.007.

Soares Júnior, A.V., Hasui, Y., Costa, J.B.S., and Machado, F.B., 2011, Evolução do Rifteamento e Paleogeografia da Margem Atlântica Equatorial do Brasil: Triássico ao Holoceno: Geociências, v. 30, p. 669–692.

Torsvik, T.H., Rousse, S., Labails, C., and Smethurst, M.A., 2009, A new scheme for the opening of the South Atlantic Ocean and the dissection of an Aptian salt basin: Geophysical Journal International, v. 177, p. 1315–1333, doi:10.1111/j.1365-246X.2009.04137.x.

Unternehr, P., Curie, D., Olivet, J.L., Goslin, J., and Beuzart, P., 1988, South Atlantic fits and intraplate boundaries in Africa and South America: Tectonophysics, v. 155, p. 169–179, doi:10.1016/0040-1951(88)90264-8.

Wilson, M., and Guiraud, R., 1992, Magmatism and rifting in western and Central Africa, from Late Jurassic to recent times: Tectonophysics, v. 213, p. 203–225, doi:10.1016/0040-1951(92)90259-9.

Ziegler, P.A., and Cloetingh, S., 2004, Dynamic processes controlling evolution of rifted basins: Earth-Science Reviews, v. 64, p. 1–50, doi:10.1016/S0012-8252(03)00041-2.

Manuscript received 3 September 2013
Revised manuscript received 24 November 2013
Manuscript accepted 3 December 2013

Printed in USA

AGU PUBLICATIONS

Geochemistry, Geophysics, Geosystems

RESEARCH ARTICLE
10.1002/2014GC005446

Key Points:
- 3-D numerical rift models are conducted covering the entire obliquity spectrum
- A constant extension direction can generate multiphase fault orientations
- A characteristic evolution of fault patterns from rift to breakup is identified

Supporting Information:
- Readme
- Supplementary Figures S1–S5
- Alpha A1–A7

Correspondence to:
S. Brune,
brune@gfz-potsdam.de

Citation:
Brune, S. (2014), Evolution of stress and fault patterns in oblique rift systems: 3-D numerical lithospheric-scale experiments from rift to breakup, *Geochem. Geophys. Geosyst.*, *15*, 3392–3415, doi:10.1002/2014GC005446.

Received 5 JUN 2014
Accepted 17 JUL 2014
Accepted article online 22 JUL 2014
Published online 21 AUG 2014

Evolution of stress and fault patterns in oblique rift systems: 3-D numerical lithospheric-scale experiments from rift to breakup

Sascha Brune[1,2]

[1]Helmholtz Centre Potsdam, GFZ German Research Centre for Geosciences, Geodynamic Modelling Section, Potsdam, Germany, [2]School of Geosciences, University of Sydney, EarthByte Group, Sydney, Australia

Abstract Rifting involves complex normal faulting that is controlled by extension direction, reactivation of prerift structures, sedimentation, and dyke dynamics. The relative impact of these factors on the observed fault pattern, however, is difficult to deduce from field-based studies alone. This study provides insight in crustal stress patterns and fault orientations by employing a laterally homogeneous, 3-D rift setup with constant extension velocity. The presented numerical forward experiments cover the whole spectrum of oblique extension. They are conducted using an elastoviscoplastic finite element model and involve crustal and mantle layers accounting for self-consistent necking of the lithosphere. Despite recent advances, 3-D numerical experiments still require relatively coarse resolution so that individual faults are poorly resolved. This issue is addressed by applying a post processing method that identifies the stress regime and preferred fault azimuth at each surface element. The simple model setup results in a surprising variety of fault orientations that are solely caused by the three-dimensionality of oblique rift systems. Depending on rift obliquity, these orientations can be grouped in terms of rift-parallel, extension-orthogonal, and intermediate normal fault directions as well as strike-slip faults. While results compare well with analog rift models of low to moderate obliquity, new insight is gained in advanced rift stages and highly oblique settings. Individual fault populations are activated in a characteristic multiphase evolution driven by lateral density variations of the evolving rift system. In natural rift systems, this pattern might be modified by additional heterogeneities, surface processes, and dyke dynamics.

1. Introduction

Oblique extension takes place when the relative velocity of two diverging plates is oblique to the rift trend (Figure 1). It occurs currently in both continental and oceanic settings such as the Ethiopian Rift System [*Corti*, 2008], the Malawi Rift [*Chorowicz and Sorlien*, 1992], the Aegean Rift [*Agostini et al*., 2010], the Reykjanes and Mohns ridge [*Dauteuil and Brun*, 1993], and the South West Indian Ridge [*Dick et al*., 2003; *Montési et al*., 2011]. During Pangaea fragmentation, oblique rifting often lead to continental breakup as for the separation of Africa and South America [*Nürnberg and Müller*, 1991; *Torsvik et al*., 2009; *Moulin et al*., 2010; *Heine and Brune*, 2014], Madagascar and Africa [*de Wit*, 2003], Madagascar and India [*Storey et al*., 1995], Sri Lanka and South India from Antarctica [*Gaina et al*., 2007], and Antarctica and Australia [*Whittaker et al*., 2007; *Williams et al*., 2011]. Oblique rifting took place during the formation of the Gulf of Aden [*Bellahsen et al*., 2003; *Brune and Autin*, 2013], the Gulf of California [*Lizarralde et al*., 2007; *Bennett and Oskin*, 2014] as well as in the North Atlantic upon formation of the Davis Strait [*Suckro et al*., 2012; *Hosseinpour et al*., 2013], and the Fram Strait [*Engen et al*., 2008].

Oblique rift systems exhibit a complex spatiotemporal fault evolution that may be due to activation of inherited crustal heterogeneities or anisotropies [*Smith and Mosley*, 1993; *Ring*, 1994], magmatic intrusions [*Buck*, 2006; *Rooney et al*., 2014], rotations of the extension direction [*Strecker et al*., 1990; *Ring*, 1994; *Bonini et al*., 1997], and interaction of tectonics with sedimentation [*Bialas and Buck*, 2009; *Dorsey*, 2010].

In order to elucidate the structures and evolution of oblique extensional systems analog modeling has been successful on both crustal and lithospheric scale: (i) Models on crustal scale simulate rifting via a brittle crust that is underlain by a basal zone of extension including an oblique velocity discontinuity [*Withjack and Jamison*, 1986; *Tron and Brun*, 1991; *McClay and White*, 1995; *Clifton et al*., 2000; *Mart and*

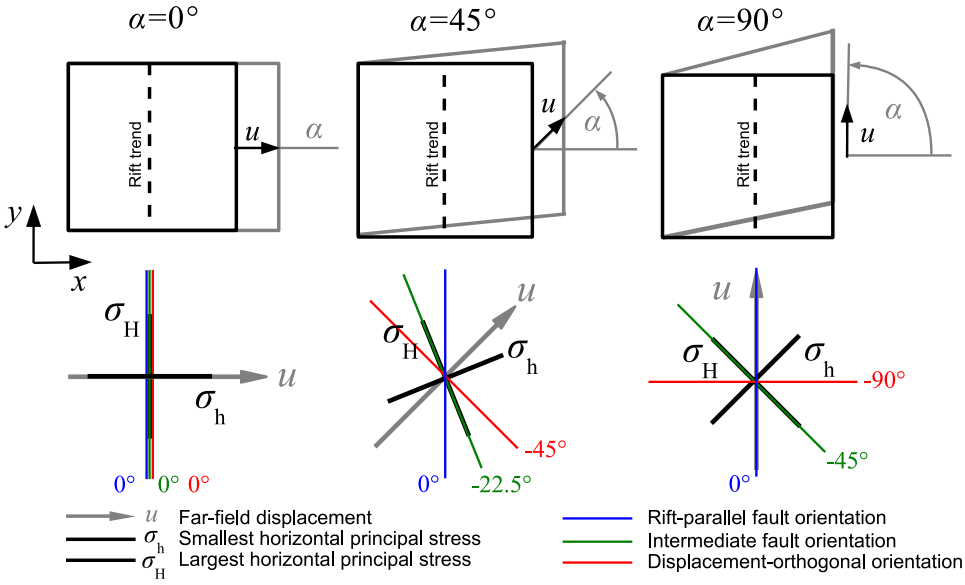

Figure 1. Geometry of oblique rifting. The angle of obliquity α is the angle between the far field extension and the rift normal; it is 0° for pure extension and 90° for large-scale simple shear motion. With increasing obliquity, the stress field and the associated fault orientations rotate to the indicated azimuth. The "intermediate" fault orientation is defined to lie in the middle between rift-parallel and extension-orthogonal direction.

Dauteuil, 2000; *Corti et al*., 2001, 2003]. With this approach, crustal strain patterns are investigated independently from mantle deformation. Hence, lithospheric necking and associated isostatic balancing are not accounted for which limits the model applicability to the initial rift stage. (ii) Recently, lithospheric-scale laboratory experiments have been conducted that incorporated thinning of the lithosphere and its influence on crustal fault patterns [*Sokoutis et al*., 2007; *Corti*, 2008; *Agostini et al*., 2009; *Autin et al*., 2010; *Corti*, 2012].

A main feature of all analog experiments with moderate obliquity (α<~60°, where α is the angle of obliquity measured between rift normal and direction of extension) is that the principal strain directions are generally not parallel to the direction of relative movement between the extending plates. *Withjack and Jamison* [1986] showed that for low amounts of bulk extension, the fault orientation within the rift trends halfway between the extensional-orthogonal direction and the rift trend (Figure 1). They also addressed the occurrence of strike-slip faults by showing that for crustal-scale models with low to moderate obliquity, the vertical principal stress σ_v is identified with σ_1 and the largest horizontal stress σ_H with σ_2. With higher obliquity, however, the difference between σ_v and σ_H decreases until σ_H becomes the largest principal stress. In this case, both σ_1 and σ_3 are horizontal and strike-slip deformation takes place. Using infinitesimal strain theory, *Withjack and Jamison* [1986] calculated that a critical angle of obliquity $\alpha_{crit} = 71°$ has to be exceeded in order for strike-slip faulting to occur. For larger amounts of bulk extension, rift-parallel and extension-orthogonal fault populations have been observed in lithospheric-scale models [*Agostini et al*., 2009; *Autin et al*., 2010].

Reproducing realistic, scalable rheologies, adequate boundary conditions and especially the introduction of temperature-dependent viscosity pose severe problems in laboratory experiments. Many numerical models, however, include these features and were used to study rifting in a 2-D setting [e.g., *Zuber and Parmentier*, 1986; *Braun and Beaumont*, 1989; *Bassi*, 1991; *Buck*, 1991; *Burov and Cloetingh*, 1997; *Lavier et al*., 2000; *Behn et al*., 2002; *Van Wijk and Cloetingh*, 2002; *Huismans and Beaumont*, 2003; *Pérez-Gussinyé et al*., 2006; *Lavier and Manatschal*, 2006; *Regenauer-Lieb et al*., 2006; *Buiter et al*., 2008; *Petersen et al*., 2010; *Huismans and Beaumont*, 2011; *Rey et al*., 2011; *Choi and Buck*, 2012; *Liao and Gerya*, 2014; *Brune et al*., 2014]. However, computational models of oblique rifting necessitate 3-D calculations which severely limits the model resolutions and constitutes a fundamental constraint to present-day numerical

models. Addressing only crustal deformation of a 3-D rift system strongly limits the computational effort which allows for comparatively higher resolution [*Katzman et al*., 1995; *Allken et al*., 2011, 2012]; however, it is valid only during the initial rift stage, where the influence of a deforming mantle lithosphere can be neglected. This disadvantage is overcome by 3-D numerical experiments that involve both crust and mantle layers [*Dunbar and Sawyer*, 1996; *van Wijk and Blackman*, 2005; *van Wijk*, 2005; *Gac and Geoffroy*, 2009; *Gerya*, 2010; *Le Pourhiet et al*., 2012; *Brune et al*., 2013; *Gerya*, 2013; *Heine and Brune*, 2014; *Le Pourhiet et al*., 2014].

In this paper, I investigate the structures of oblique rift systems by means of a lithospheric-scale numerical model that includes elastoviscoplastic rheology with laboratory-based flow laws for temperature and pressure-dependent viscosity. The presented models address the whole extensional process from initial fault coalescence to breakup. This analysis involves the conventional approach to compute and interpret shear zone patterns in terms of strain-rate and plastic strain. Additionally, a recently developed stress interpretation technique is used [*Brune and Autin*, 2013] that allows the evaluation of fault patterns on a sub-shear zone level.

2. Model Description

2.1. Numerical Model Setup

The numerical 3-D rift setup involves laterally homogeneous material layers without inherited structures, constant extension velocity, and direction. The thermomechanically coupled conservation equations of momentum, energy, and mass are solved using the implicit, finite element code SLIM3D (Semi-Lagrangian Implicit Model for 3-D). A detailed description of the numerical techniques is given in *Popov and Sobolev* [2008].

The presented models comprise a segment of the Earth that measures 249 km times 249 km horizontally and 120 km vertically (Figure 2). It is divided in 275,560 cubic elements with a length of 3 km. At the left and right model side, a velocity of 5 mm/yr is prescribed, resulting in a full extension velocity of 10 mm/yr. Hence, an extension of e.g., 200 km is reached after 20 My model time. The angle of obliquity α is defined as the angle between the boundary velocity vector and the boundary normal. A different obliquity is applied during each model run in order to scan from orthogonal extension (α=0°) over oblique rifting to strike-slip motion (α=90°). Note that the width of the model domain stays the same during extension, so that there is outflow of material across the left and right model boundaries. The code features a free surface at the top boundary, while at the bottom boundary isostatic equilibrium is realized by means of the Winkler foundation, where inflow of material is accounted for during remeshing. An important feature of the model is the periodic boundary condition that connects the front and back sides so that an effectively infinitely long rift zone is realized. In order to localize deformation to the model center, a small elongate temperature heterogeneity is applied in the middle of the prospective rift (Figure 2a). This approach effectively mimics a small amount of lithospheric thinning and importantly, it does not prescribe any fault structures at the surface.

The model comprises four distinct rheological layers, namely a 20 km thick upper crust featuring wet quartzite properties [*Gleason and Tullis*, 1995], a lower crust of 15 km thickness with granulite rheology [*Wilks and Carter*, 1990], a 45 km thick layer of lithospheric mantle with dry olivine rheology [*Hirth and Kohlstedt*, 2003], and an asthenospheric layer that is represented by the flow law of wet (i.e., 500 ppm H/Si) olivine below 90 km depth [*Hirth and Kohlstedt*, 2003]. A list of all thermomechanical parameters can be found in Table 1.

Thermomechanical weakening affects the model evolution by three mechanisms: (i) Friction softening: Crustal fault strength is successively reduced by continued deformation within a fault zone [*Zoback et al*., 1987; *Provost and Houston*, 2003]. This process is introduced using a strain-dependent effective friction coefficient that decreases linearly from 0.6 to 0.06 for plastic strains between 0 and 1, while it remains constant at 0.06 for plastic strains larger than 1. This corresponds to a decrease of the effective friction angle from 31° to 3.5°. (ii) Shear heating: An increased rate of deformation leads to heat production which lowers the effective viscosity. A smaller viscosity attracts deformation and thus increases the strain rate. (iii) Dislocation creep involves a power law dependency between strain rate and stress that allows localization in terms of viscosity reduction.

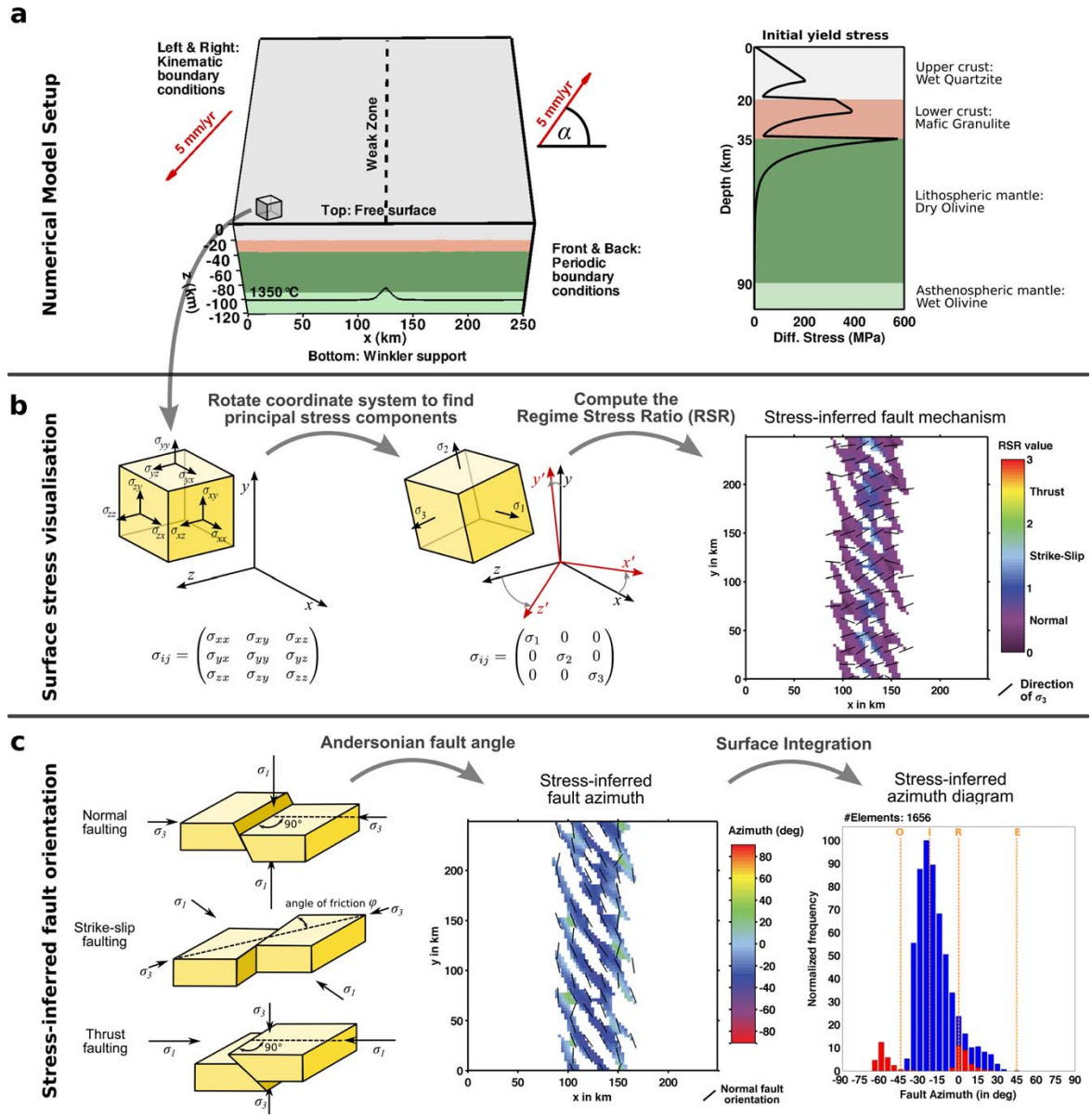

Figure 2. Model setup. (a) Extensional velocities are prescribed at the boundaries in *x* direction. Periodic boundary conditions in *y* direction realize an in principle infinitely long rift zone. A thermally weak zone initializes rifting by effectively introducing a small amount of lithospheric necking. (b) The stress tensor is used to calculate the regime stress ratio (RSR) at each surface element. (c) The optimal fault orientation with respect to the stress field is computed for each surface element and condensed in an azimuth diagram.

2.2. Stress Interpretation Method

In most thermomechanical codes (including SLIM3D), brittle deformation localizes in the form of shear bands with a typical width of few elements. This limits the capabilities of currently relatively coarse 3-D models to reproduce the fault patterns that are visible both in nature and in analog models. However, a great advantage of numerical models is to offer direct access to the stress tensor at any element of the model. Here we exploit this advantage by means of a simple post processing technique that analyzes the stress tensor at the model surface in order to infer stress regime and the optimal orientation of small-scale faults [*Brune and Autin*, 2013]. This method extracts information from the model which is not accessible to

Table 1. Model Parameters

Parameter	Upper Crust	Lower Crust	Strong Mantle	Weak Mantle
Density, ρ (kg m^{-3})	2700	2850	3280	3300
Thermal expansivity, α_T (10^{-5} K^{-1})	2.7	2.7	3.0	3.0
Bulk modulus, K (GPa)	55	63	122	122
Shear modulus, G (GPa)	36	40	74	74
Heat capacity, C_p (J kg^{-1} K^{-1})	1200	1200	1200	1200
Heat conductivity, λ (W K^{-1} m^{-1})	2.5	2.5	3.3	3.3
Radiogenic heat production, A (μW m^{-3})	1.5	0.2	0.0	0.0
Initial friction coefficient, μ (-)	0.6	0.6	0.6	0.6
Cohesion, c (MPa)	5.0	5.0	5.0	5.0
Preexponential constant for diffusion creep, log(B_{Diff}) (Pa^{-1} s^{-1})	-	-	−8.65	−8.65
Activation energy for diffusion creep, E_{Diff} (kJ/mol)	-	-	375	335
Activation volume for diffusion creep, V_{Diff} (cm^{-3}/mol)	-	-	6	4
Preexponential constant for dislocation creep, log(B_{Disloc}) (Pa^{-n}s^{-1})	−28.00	−21.05	−15.56	−15.05
Power law exponent for dislocation creep, n	4.0	4.2	3.5	3.5
Activation energy for dislocation creep, E_{Disloc} (kJ/mol)	223	445	530	480
Activation volume for dislocation creep, V_{Disloc} (cm^{-3}/mol)	0	0	13	10

Dislocation creep parameters for upper crust: wet quartzite [*Gleason and Tullis*, 1995], lower crust: Pikwitonian granulite [*Wilks and Carter*, 1990], lithospheric mantle: dry olivine [*Hirth and Kohlstedt*, 2003], asthenospheric mantle: wet olivine, i.e., 500 ppm H/Si [*Hirth and Kohlstedt*, 2003].

The friction coefficient μ decreases linearly by 90% of the initial value until plastic strain reaches 1, and remains constant for larger strains.

standard visualizations of strain or strain rate and thereby allows a more detailed interpretation of the numerical experiments. It applies the following recipe:

First, the principal stress components, i.e., the eigenvalues σ_1, σ_2, and σ_3 of the stress tensor and the corresponding eigenvectors, are computed at each surface element. The surface stress regime is evaluated in terms of the scalar Regime Stress Ratio (RSR) that indicates extension, strike-slip motion, and compression on a continuous scale [*Simpson*, 1997; *Delvaux et al*., 1997; *Buchmann and Connolly*, 2007; *Hergert and Heidbach*, 2011]. An equivalent alternative method that uses the nondimensional Argand Ratio has been successfully used in analyzing stress states of thin sheet models [*England and McKenzie*, 1982; *Houseman and England*, 1986; *Rey and Houseman*, 2006]. In order to compute the RSR value, the vertical, smallest horizontal, and largest horizontal stress components are used (σ_v, σ_h, and σ_H, respectively) to define the index n

$$n=\left\{\begin{array}{l} 0 \text{ if } \sigma_h<\sigma_H<\sigma_v \text{ (normal faulting)} \\ 1 \text{ if } \sigma_h<\sigma_v<\sigma_H \text{ (strike}-\text{slip faulting)} \\ 2 \text{ if } \sigma_v<\sigma_h<\sigma_H \text{ (thrust faulting)} \end{array}\right\}$$

and the ratio R between smallest and largest differential stress [*Bott*, 1959],

$$R=\left(\frac{\sigma_2-\sigma_3}{\sigma_1-\sigma_3}\right)$$

which allows to compute the RSR value via

$$\mathrm{RSR}=(n+0.5)+(-1)^n(R-0.5)$$

The RSR value maps all possible stress regimes to the interval between 0 and 3. The meaning of the RSR value is illustrated using two examples (Figure 3). The data are drawn from the non-oblique and the highly oblique scenarios of section 3 ($\alpha=0^\circ$ and $\alpha=60^\circ$, respectively). σ_v, σ_h, and σ_H are measured in the surface element at $x=125$ km and $y=125$ km. For $\alpha=0^\circ$, the identification of the principal stress components is obviously $\sigma_1=\sigma_v$, $\sigma_2=\sigma_H$, and $\sigma_3=\sigma_h$ indicating an extensional character of the stress tensor. Even though σ_v and σ_h vary significantly, the ratio R does not change much so that the RSR value remains in the normal faulting domain. The situation changes for $\alpha=60^\circ$, where σ_1 and σ_2 exchange their identification with σ_v and σ_H which leads from an initially transtensional regime through a strike-slip incursion at 10–14 My to pure extension at 20 My.

Once the stress regime at each element is known, an optimally oriented fault direction can be inferred. Assuming isotropic and homogeneous materials, the standard rules of Andersonian faulting are applied [*Anderson*, 1948] so that extensional (RSR$\leq$1) and compressive (RSR$>$2) stress regimes generate σ_3-orthogonal and σ_1-orthogonal fault azimuths, respectively. Strike-slip faults occur for 1$<$RSR$\leq$2 at $\pm\varphi_{eff}$ from σ_1

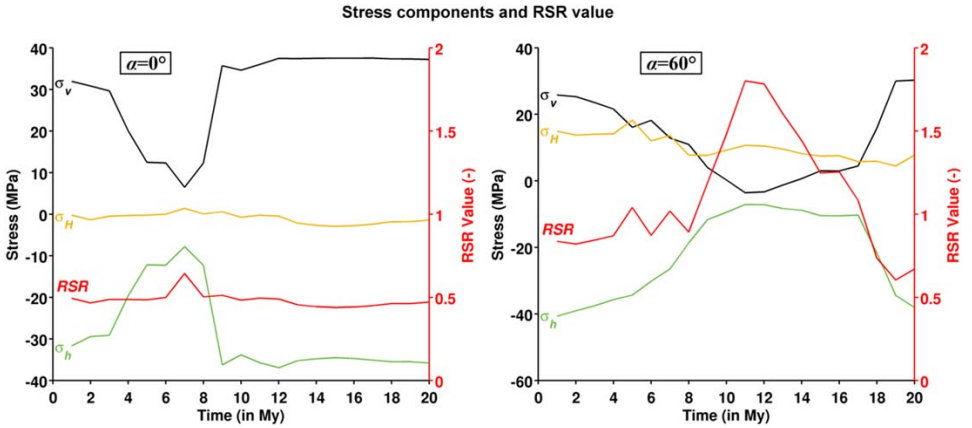

Figure 3. Illustration of the RSR value. The stress regime can be visualized using the RSR value that continuously varies between extension (RSR≤1), strike-slip motion (1<RSR≤2), and compression (RSR>2). Time series of deviatoric stress components are taken at the central coordinates (*x*, *y*) = (125 km, 125 km) of experiments shown in Figures 4 and 8.

(with the effective friction angle $\varphi_{\text{eff}} = 31°$). Note that the stress tensor information alone does not suffice to discriminate between the two strike-slip conjugates (dextral or sinistral) that differ by an azimuth of $2\varphi_{\text{eff}}$. While accounting for both conjugate fault populations, their number is hereafter scaled with a factor of 0.5 so that the overall number of strike-slip elements is not affected.

Azimuth diagrams (Figures 4e–10e) depict the significance of individual fault directions by binning the number of elements within a given azimuth interval. Thus, they can be directly compared to fault length histograms of analog models. Azimuth diagrams are normalized such that the dominant fault orientation is always depicted with a frequency of 100.

By computing optimal fault orientations as a function of local stress state, it is assumed that faults develop in homogeneous, isotropic material. This means that stress-inferred fault orientations only account for the infinitesimal strain field. In reality, the finite strain field involves long-lived faults that might rotate until they deform via oblique slip so that they are not optimally oriented anymore. Obviously, these faults can not be reproduced by this approach. However, a recent study of oblique-spreading oceanic ridges (Southwest Indian, Sheba, Carlsberg, Reykjanes, and Mohns Ridge) compared earthquake focal mechanisms which are markers of infinitesimal strain with normal fault orientations representing the finite strain field [*Fournier and Petit*, 2007]. It was shown that both observations correspond to the same direction of σ_h which implies that normal faults at ridge axes only accommodate a small amount of strain while they are in the zone of active deformation. Further evidence for dominating dip-slip motion of rift faults has been assembled in the Baikal Rift [*Petit et al*., 1996], the Western branch of the East African Rift [*Morley*, 2010], and the Main Ethiopian Rift [*Corti et al*., 2013]. These studies support the hereafter applied assumption of optimally oriented, Andersonian dip-slip faults for oceanic and continental rift systems.

The stress interpretation method allows the computation of fault mechanism and azimuth for any stress tensor, even though the considered element experiences no strain at all. Hence, it is necessary to exclude the quasi-nondeforming region outside the rift zone from the analysis. I restrict my analysis to the zone of tectonic activity, where the strain rate exceeds $10^{-15}\,s^{-1}$ (see black contour in Figures 4a–10a). This number is somewhat arbitrary, but the overall results are not affected if the threshold value is changed within the range of reasonable values (see supporting information Figures S4 and S5). Since the extent of the active region (i.e., with strain rate larger than $10^{-15}\,s^{-1}$) varies through time, the overall number of elements that contribute to the analysis changes for each time step and is indicated in the azimuth diagrams (Figures 4e–10e) in the upper left corner (#Elements).

3. Modeling Results

In this section, the general behavior of the numerical models is briefly discussed before individual models are interpreted. The next section relates the first rift stages of the presented models to previously conducted analog models.

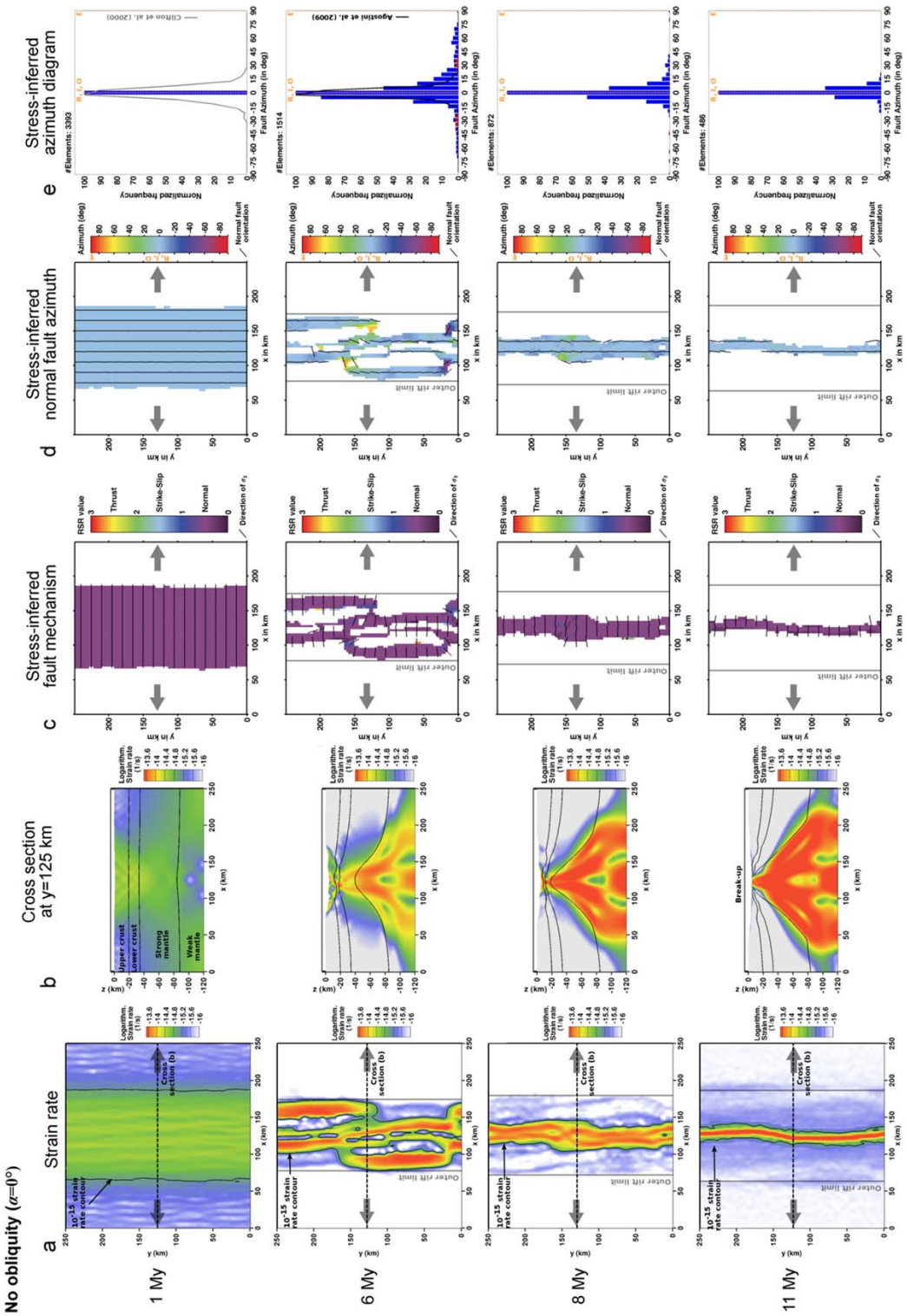

Figure 4. No obliquity (α=0°). (a) Two rift segments with a small offset emerge and unite. (b) The cross section depicts successive lithospheric necking and basinward fault localization. (c) Normal faulting is inferred from the state of stress throughout the experiment. Note that only the active deformation region inside the 10^{-15} s^{-1} strain rate isoline of Figure 4a is used for stress-based evaluation of fault characteristics. (d, e) The normal fault azimuth is 0° except at the rift offset. Abbreviated directions indicate the rift-parallel azimuth (R), intermediate fault orientation (I), extension-orthogonal direction (O), and the direction of extension (E). The number of contributing elements (with a strain rate of 10^{-15} s^{-1} or more) are marked in the upper left corner of each diagram in Figure 4e. The azimuth diagram shows the number of elements that fall within a 5° azimuth interval, while each diagram is normalized to 100%. For comparison, azimuth diagrams of *Clifton et al.* [2000] and *Agostini et al.* [2009] are plotted at 1 and 6 My, respectively. "Outer rift limit" in Figures 4a, 4c, and 4d indicates the moving location of outmost boundary faults as a reference. For a detailed model evolution in 1 My time steps, see supporting information animation A1.

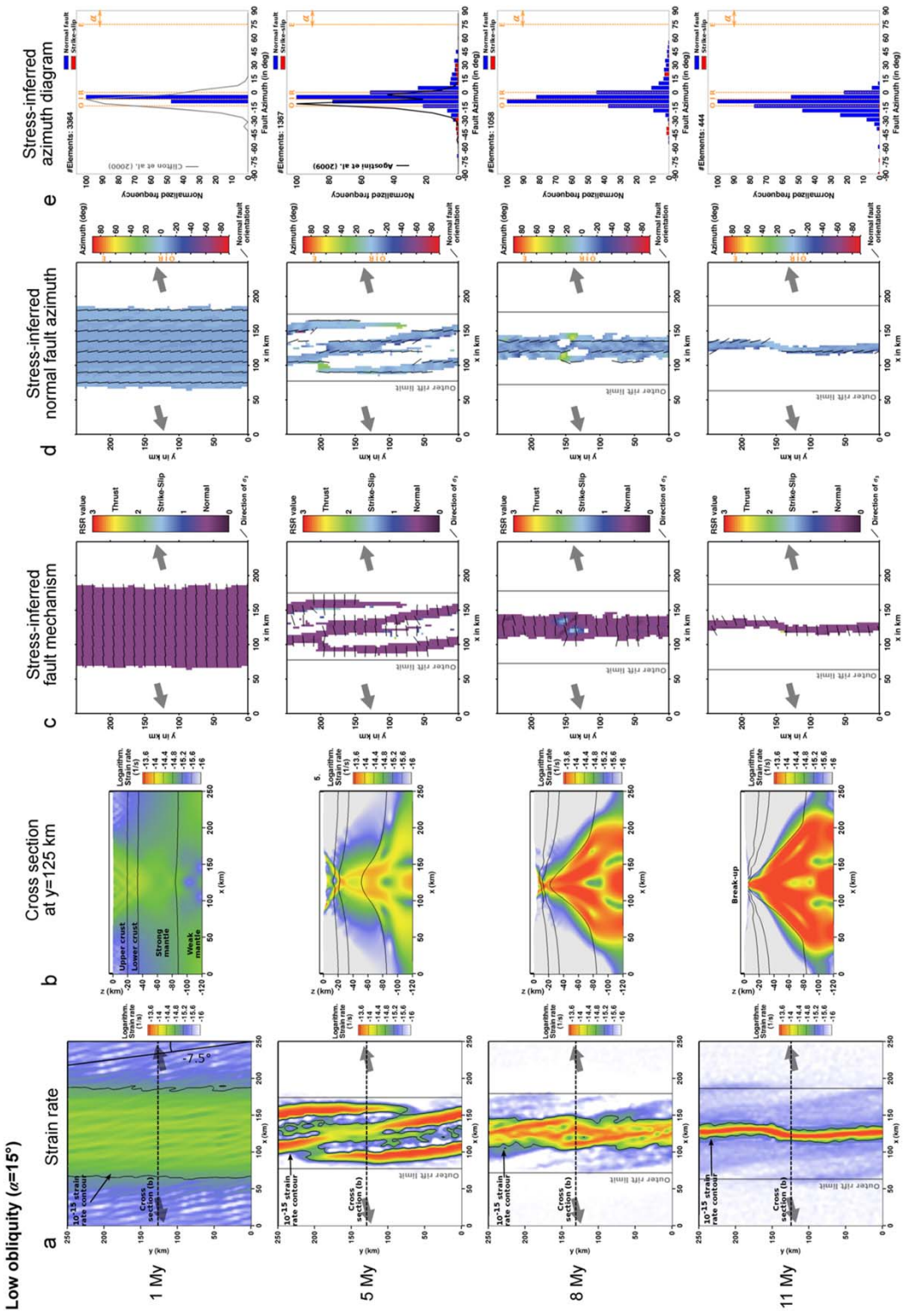

Figure 5. Low obliquity ($\alpha = 15°$). (a) Initial shear zones at 1 My are parallel to the expected shear zone azimuth with intermediate direction. Two en-échelon rift segments form (5 My) and unite (8 My). (b) Cross section showing the degree of lithospheric necking. (c, d, e) Normal faulting dominates the whole model with intermediate azimuth except for the region of the rift offset where azimuths rotate to higher values. Abbreviations are explained in the caption of Figure 4. For a detailed model evolution in 1 My time steps, see supporting information animation A2.

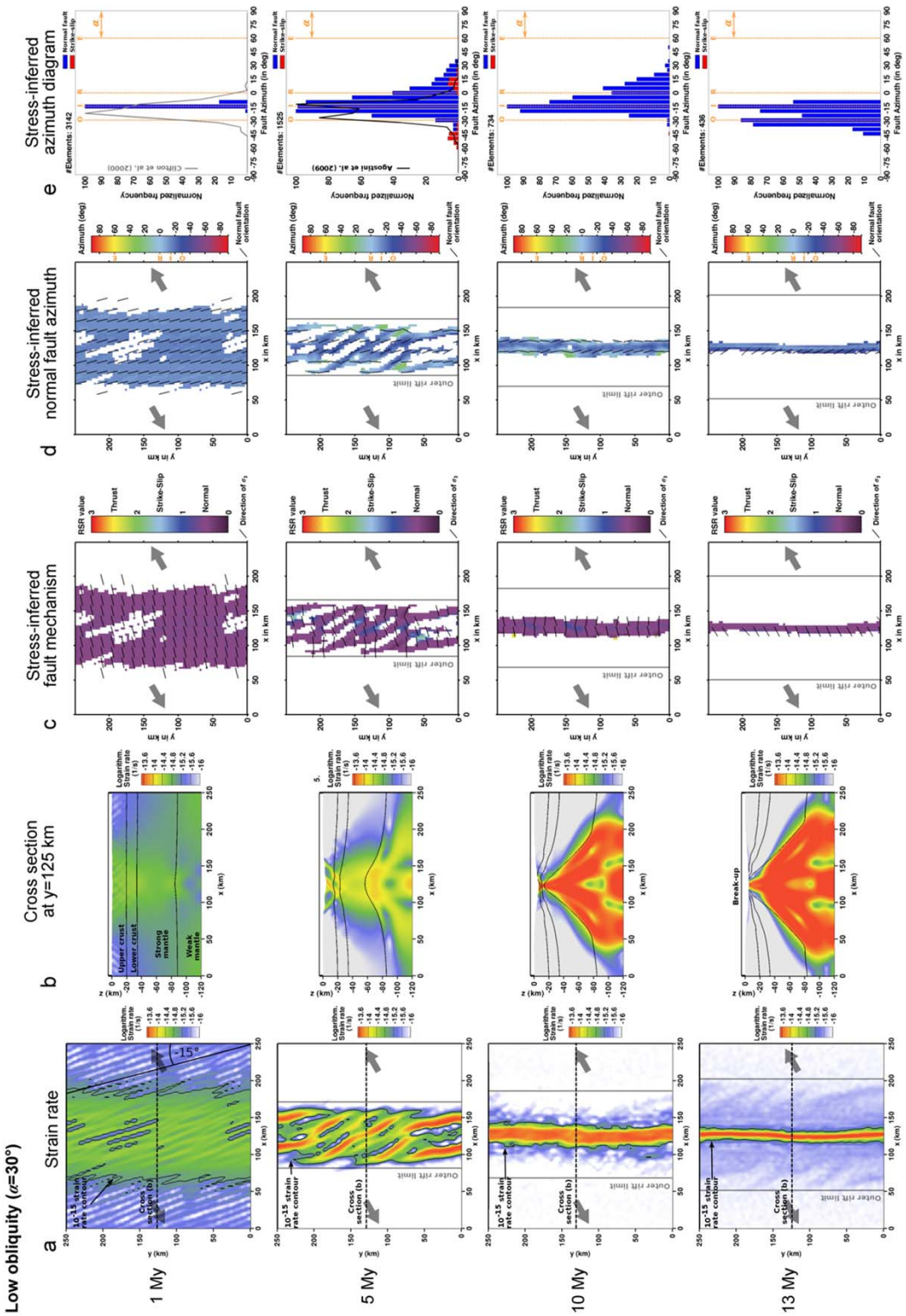

Figure 6. Low obliquity (α=30°). (a) Initial shear zones show an intermediate direction of −15°. (b) Cross section showing the degree of lithospheric necking. (c) The stress-inferred fault mechanism is normal except for a short period of strike-slip faulting in the rift center (5 My). (d, e) Stress-inferred normal fault azimuth deviates from intermediate orientation only between individual shear zones where they rotate toward a higher angle. Extension-orthogonal and intermediate fault directions dominate after breakup. Abbreviations are explained in the caption of Figure 4. For a detailed model evolution in 1 My time steps, see supporting information animation A3.

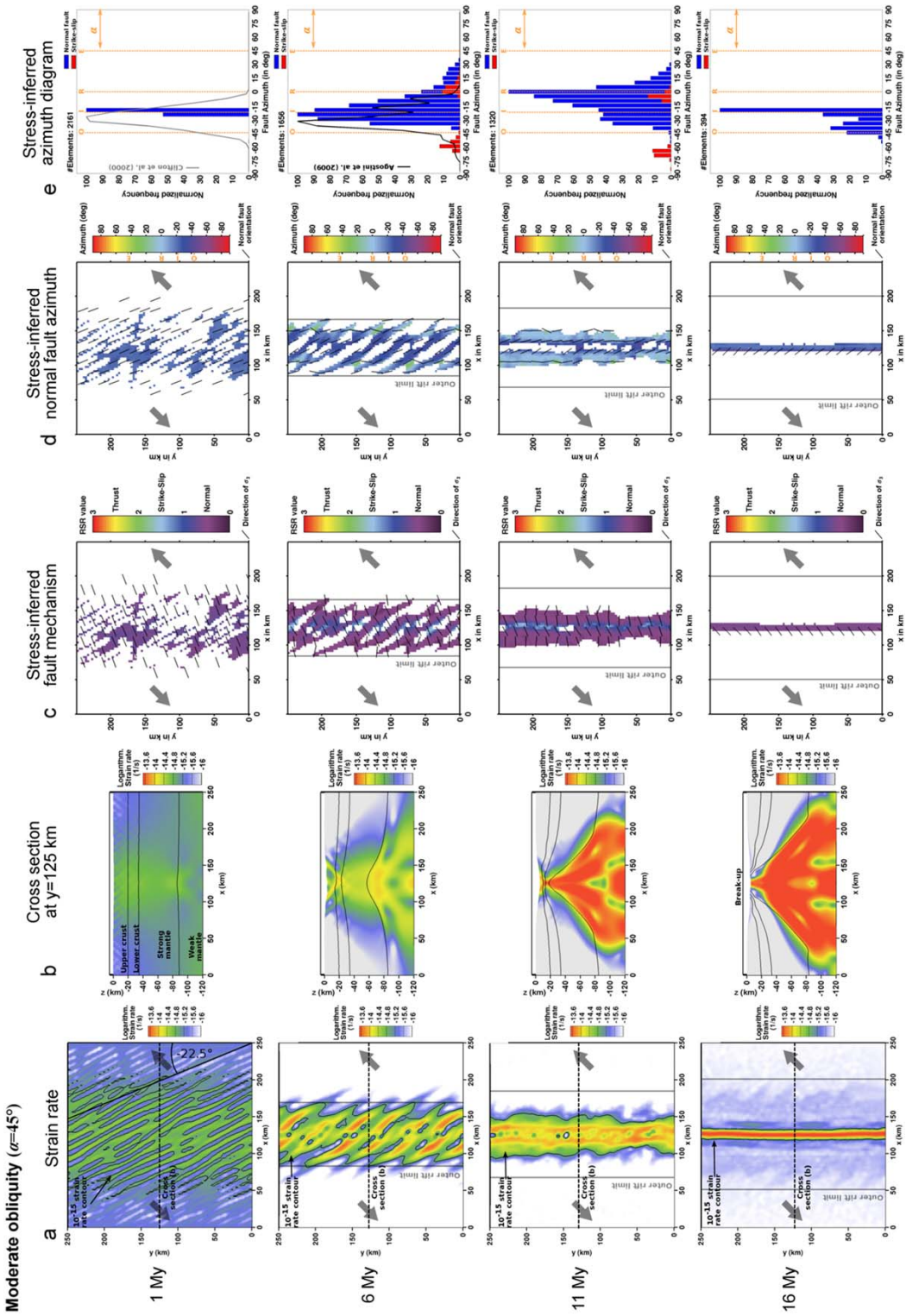

Figure 7. Moderate obliquity ($\alpha = 45°$). (a) Initial shear zones feature intermediate directions before they form a sigmoidal en-échelon pattern. (b) Cross section showing the degree of lithospheric necking. (c, d, e) A strike-slip region exists at 6 and 11 My in the otherwise normal-fault dominated rift. Simultaneously, normal fault azimuths successively shift from intermediate to rift-parallel direction. This shift also coincides with pronounced lithospheric necking in Figure 7b. During and after breakup, intermediate and extension-orthogonal orientations occur. Abbreviations are explained in the caption of Figure 4. For a detailed model evolution in 1 My time steps, see supporting information animation A4.

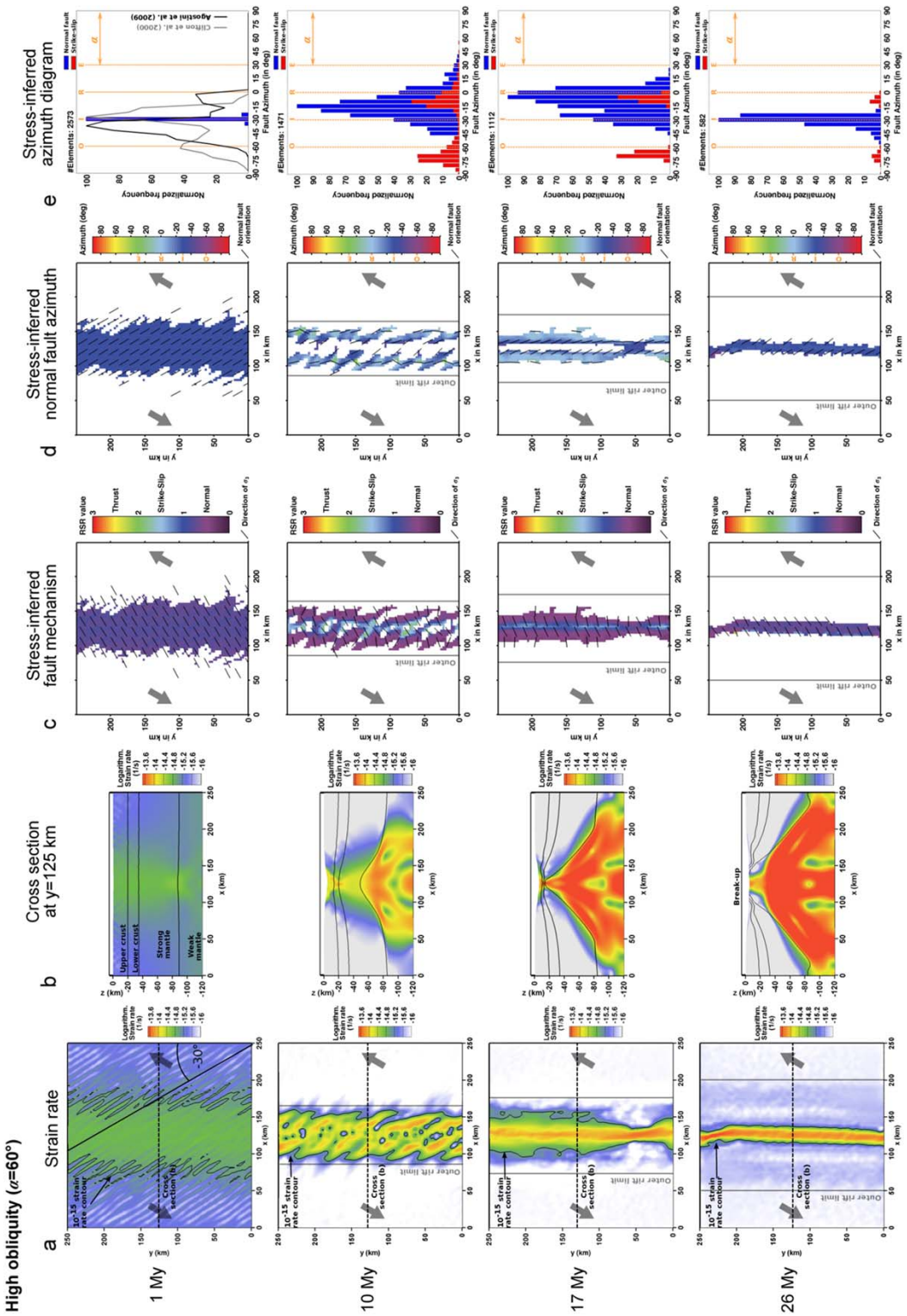

Figure 8. High obliquity (α=60°). (a) At 1 My, shear zones are parallel to the expected intermediate shear zone azimuth of −30°. (b) Cross section showing the degree of lithospheric necking (c) An initially transtensional stress regime gives way to a strike-slip zone in the rift center (10 and 17 My) and a normal fault domain adjacent to the rift center (strain partitioning). (d, e) Normal fault azimuths rotate from intermediate to rift-parallel while lithospheric necking takes place as seen in Figure 8b. Rift-parallel faulting ends abruptly during basinward localization, followed by intermediate fault directions. Abbreviations are explained in the caption of Figure 4. For a detailed model evolution in 2 My time steps, see supporting information animation A5.

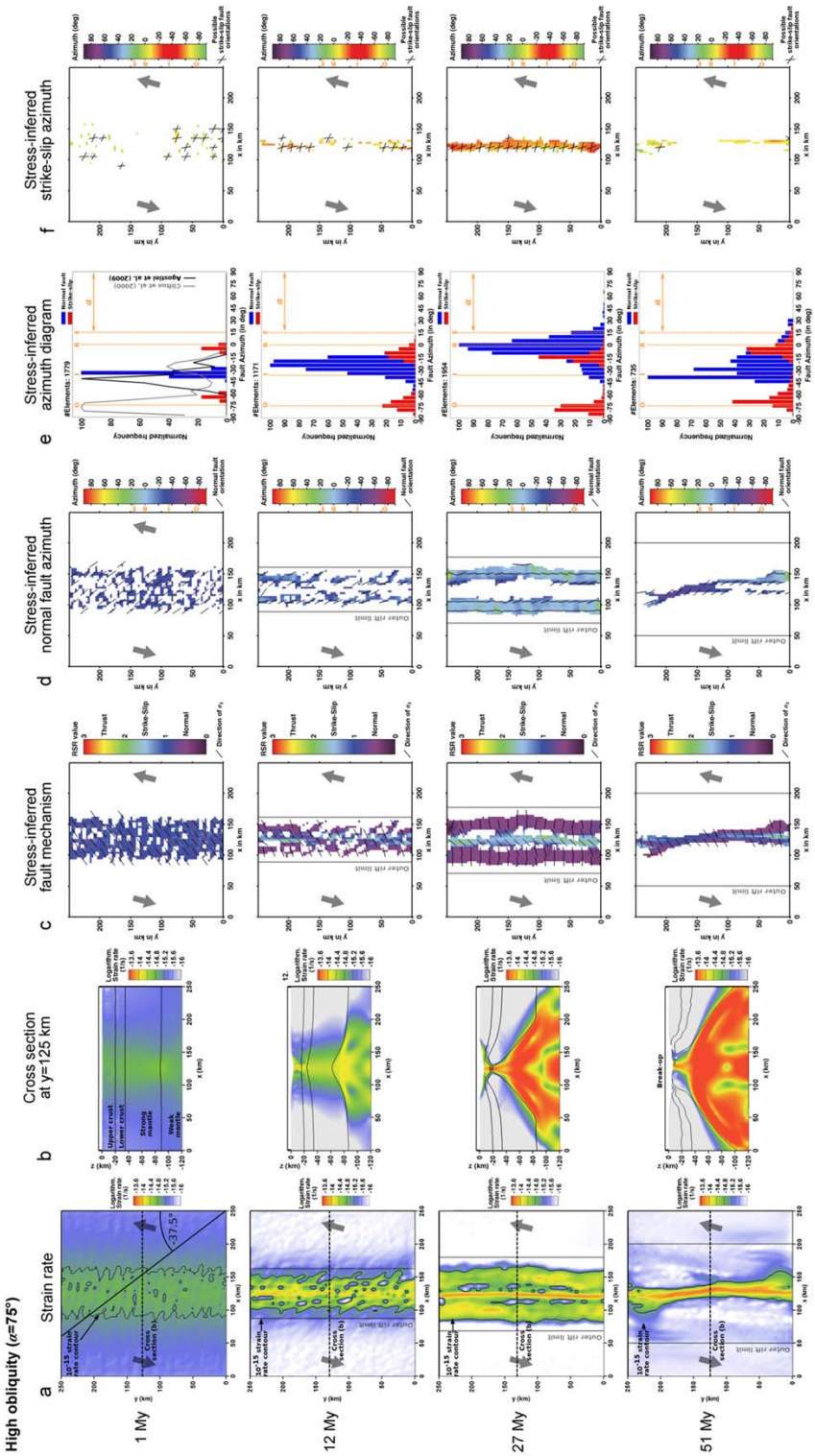

Figure 9. High obliquity ($\alpha = 75°$). (a) Diffuse shear zones are visible in the strain rate images. (b) Cross section showing the degree of lithospheric necking. (c, d, e) Strong strain partitioning occurs between rift center (strike-slip faults) and rift boundary (rift-parallel normal faults). Normal fault directions change from intermediate (1 My) to rift parallel (27 My) and back to intermediate (51 My). In contrast to previous figures, a Figure 9f exists that shows strike-slip azimuths. These are plotted as doublets which accounts for the impossibility to distinguish between sinistral and dextral faults based on stress-tensor information alone. Abbreviations are explained in the caption of Figure 4. For a detailed model evolution in 3 My time steps, see supporting information animation A6.

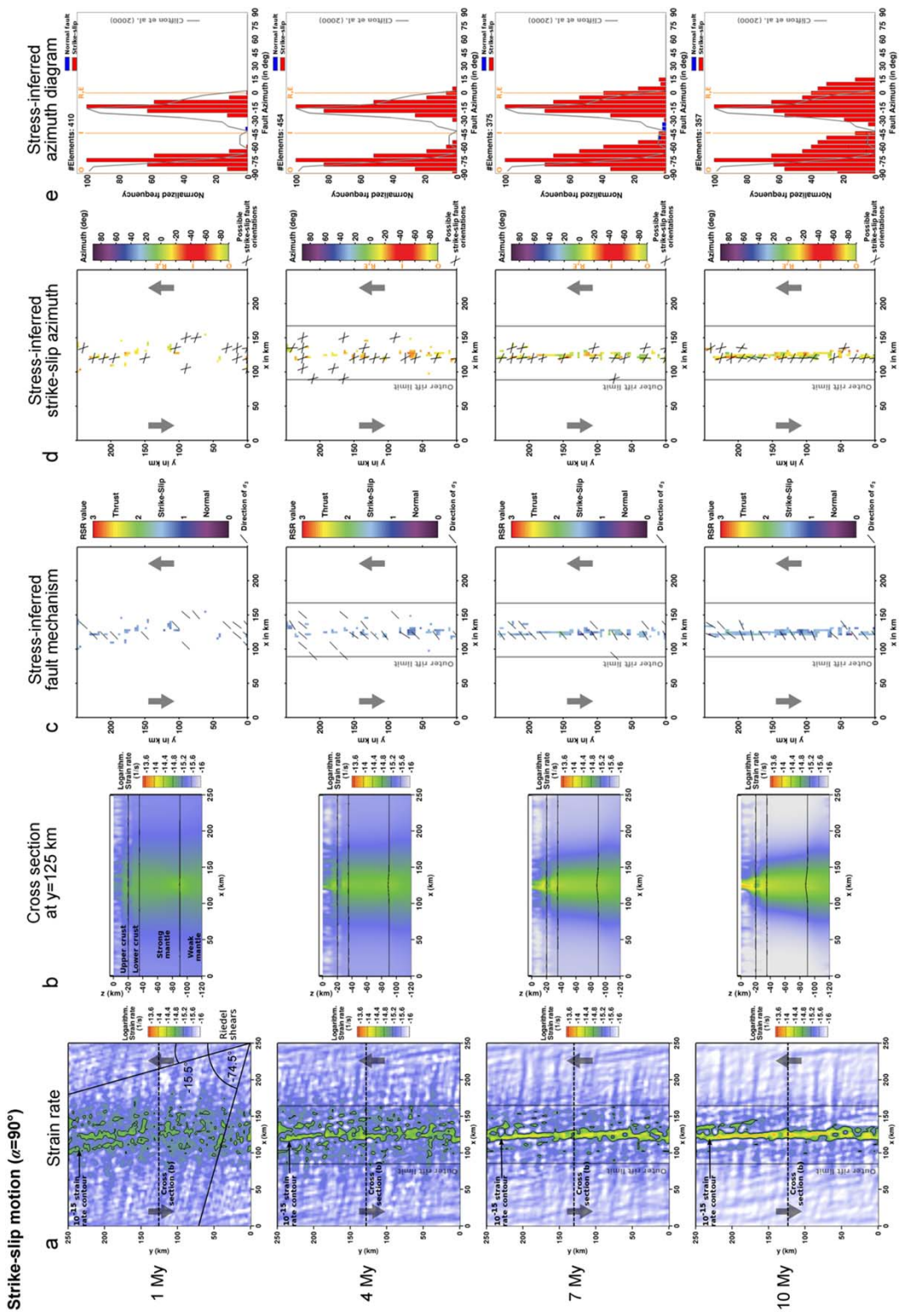

Figure 10. Strike-slip deformation (α=90°). (a) Two fault families are visible corresponding to synthetic and antithetic Riedel shears. (b) Cross sections show localization into a central strike-slip fault and its ductile continuation into lower crust and mantle. (c, d, e) Stress-inferred fault orientations show Riedel shear orientations throughout the experiment. In contrast to previous figures, plot (d) shows strike-slip fault azimuths, since normal faults do not exist. Abbreviations are explained in the caption of Figure 4. For a detailed model evolution in 1 My time steps, see supporting information animation A7.

3.1. General Behavior

During the first million years of extension, small-scale shear zones emerge spontaneously over the entire model width. They compete due to frictional softening until they coalesce into few dominant shear zones in the center of the model atop the lithospheric necking zone. These shear zones form a distinct en-échelon pattern in all models with oblique rift direction, whereby their overall number increases with obliquity. Note that the model resolution of 3 km does not allow to reproduce faults in a strict sense; however, finite-width shear zones with a typical width of several elements can be observed.

With continuing deformation, the central portion of the en-échelon shear zones appears to rotate counterclockwise with a vertical axis so that the shear zones develop a sigmoidal shape. The rotation is caused by the longevity of the shear zones [*Brune and Autin*, 2013]: Oblique rifting transforms long-lived shear zones via stretching which appears as a rotation. Due to basinward localization, shear zones at the rift margin become inactive at an early stage and hence accommodate less rotation than shear zones in the rift center which continue rotating until they are almost parallel to extension.

The normal faults that emerge from the initial phase of coalescence rotate to smaller dip with continued extension. When they reach a dip angle of approximately 30°, they become inactive and new, basinward located faults commence to accommodate brittle strain. In all model runs except the strike-slip end member, successive localization toward the rift center generates a graben-in-graben structure. The transition during an individual localization event can be very rapid (i.e., faster than 1 My), especially for a mature rift close to breakup.

Since the applied modeling approach does not account for the formation of oceanic crust, continental breakup is reached when the crust is broken and asthenospheric material reaches the surface. The required time to reach breakup grows with increased rift obliquity since the overall extension rate is kept constant for all setups so that the rift-perpendicular extension velocity is smaller for larger obliquity. For the case of α=90°, it is zero and no breakup takes place at all.

3.2. Orthogonal Rifting (α=0)

Initial deformation is distributed over the whole model (Figure 4a). Within 6 My, however, successive coalescence of small-scale shear zones leads to the emergence of distinct rift segments with a small offset in-between. There are two offset locations (at $y = 120-170$ km and $y = 0-30$ km). Each rift segment is bounded by a set of conjugate normal faults that cut through the whole crust and lead to Moho uplift (Figure 4b). With continued deformation, new basinward dipping normal faults localize close to the rift center until crustal breakup takes place at 11 My.

The stress regime (Figure 4c) is purely extensional during the whole experiment. This can also be seen for individual stress components and the nearly constant RSR value at the center of the model (Figure 3). The azimuth distribution shows more complexity than expected for an essentially 2-D setup (Figure 4d). This is caused by the formation of the aforementioned two rift segments. Within each segment, normal faults strike in *y* direction with 0° azimuth but at the offsets, the principal stress direction of σ_3 rotates smoothly so that the inferred normal fault azimuth reaches 70° and −70°, respectively.

The azimuth diagrams (Figure 4e) mirror the structural evolution of the system. The initial structures at 1 My with homogeneous 0° azimuth evolve into a widened distribution. At 6 My, the rift offsets contribute a small number of elements with azimuths of ±70°. When the rift segments merge into a single rift zone at 8 My, the azimuth distribution narrows again to 0° until breakup at 11 My.

3.3. Low Obliquity (α=15°, 30°)

At 1 My, the strain rate patterns of Figures 5a and 6a show small-scale shear zones that strike at an angle of −7.5° and −15°, respectively, that is exactly the intermediate azimuth of the extension-orthogonal direction and the rift orientation. Throughout this paper, I refer to this specific direction as "intermediate" fault orientation. At 5–6 My, along-strike segmentation of the rift is depicted in the strain rate plots that are characterized by en-échelon shear zone patterns. Successive localization toward the rift center ends the en-échelon deformation and leads to crustal breakup along a straight ridge.

The stress-inferred fault mechanism (Figures 5c and 6c) is of normal type at the beginning, followed by some minor strike-slip deformation in the rift center before finally returning to pure extension. Fault

azimuths develop in four phases (Figures 5d and 6d): (i) The coalescence phase involves intermediate directions. (ii) During en-échelon deformation, individual segments are connected by fault populations with diverse orientation of 0–70°. In contrast to the orthogonal setup with α=0°, the fault azimuth distribution is skewed toward higher values, which compensates the obliquity of the individual en-échelon shear zones. Some strike-slip faulting occurs with conjugate fault azimuths of 5° and −55° in the α = 30° scenario (Figure 6e). (iii) Lithospheric necking unites the rift segments prior to breakup and homogenizes normal fault azimuths to mainly intermediate directions. (iv) Breakup entails both extension-orthogonal and intermediate normal fault orientations.

3.4. Moderate Obliquity (α=45°)

In many structural aspects, the model with 45° obliquity shows a mixture between the low and the high-obliquity experiments. The coalescence phase starts with intermediately oriented fault azimuths (Figures 7a, 7d, and 7e) that develop into an en-échelon system at 6 My. Similar to the low-obliquity models, the en-échelon segments are connected at the rift boundaries with smoothly varying fault orientations that exceed the rift-parallel azimuth of 0°. In contrast to the low-obliquity models, however, rift-parallel faults adjacent to the rift center are much more pronounced (Figures 7d and 7e at 11 My). They emerge at the end of the en-échelon deformation when strong lithospheric necking occurs below the central part of the rift. Simultaneously, a thin, strike-slip dominated area emerges in the rift center and vanishes again upon crustal breakup. The latest stages of rifting show intermediate fault orientations while additional extension-orthogonal fault azimuths appear during breakup.

3.5. High Obliquity (α=60°, 75°)

The high-obliquity models are governed both by normal faulting and strike-slip deformation. Initial small-scale shear zones feature normal fault characteristics and strike with intermediate direction across the rift (Figures 8a and 9a). For α=60°, the initial RSR value indicates an extensional/transtensional stress regime (Figure 8c). For the rift center, a detailed evolution of the stress regime is depicted in Figure 3 illustrating the transition from extensional to strike-slip and back to extensional in terms of individual stress components. The α=75° model features a transtensional/strike-slip stress regime from the beginning of rifting (Figure 9c). Individual en-échelon segments exist for the 60° scenario at 10 My, while for 75° they are hardly distinguishable at 12 My.

With continuing deformation, a pronounced strike-slip zone emerges in the rift center of both models. For α=75°, the stress-inferred orientation of strike-slip faults is displayed in Figures 9e and 9f. The coexistence of strike-slip and normal faults indicates strain partitioning between the strike-slip dominated rift center and the surrounding normal fault system. Nevertheless, the period of rift-parallel faulting at the rift flanks coincides also with strong lithospheric necking and hence strong lateral density gradients, whereas both strain partitioning and lateral density gradients enhance rift-parallel faulting.

The two high-obliquity models differ during the breakup stage. For α=60°, lithospheric necking focuses the region of deformation prior to breakup until the central strike-slip region is replaced by intermediately oriented normal faults. For 75° obliquity, however, strike-slip faults persist before and after breakup.

3.6. Strike-Slip Deformation (α=90°)

As expected, the model with α=90° is entirely dominated by strike-slip faults. Synthetic and antithetic Riedel shears are visible in Figure 10a, oriented at $-\varphi_{eff}/2 = -15.5°$ and $-90° + \varphi_{eff}/2 = -74.5°$, respectively. (The effective friction angle φ_{eff} is 31° according to an effective friction coefficient μ of 0.6.). A single large shear zone with strike-slip characteristics (Figure 10c) localizes in the center of the model that continues into lower crustal portions and upper mantle as a single ductile shear zone (Figure 10b). An evaluation of the stress-inferred strike-slip azimuth yields again Riedel shear orientations. Note that the two strike-slip families in Figure 10e are due to the impossibility to discriminate between the two conjugate strike-slip fault orientations based on stress information only. This is also the reason for the symmetry in the color scale with respect to the direction of σ_1 (−45°) in Figure 10d.

3.7. Model Robustness and Limitations

Several alternative model runs have been conducted in order to test the influence of key parameters such as lower crustal rheology, extension velocity, model resolution, and the strain rate threshold of the stress-interpretation method. The resulting evolution of fault orientations is depicted for all angles of obliquity in supporting information Figures S1–S5. Even though some of these models differ in terms of timing, the characteristic evolution of fault patterns remains identical to the standard scenario displayed in Figure 11.

Due to the simplicity of the shown models, there are several limitations that should be considered when comparing the presented results to natural rift environments. Most importantly, inherited structures affect stress and localization pattern such that faults might align along preexisting faults and not with optimal orientation. Moreover, neither melting and magma migration nor subsequent dyke formation are taken into account and surface processes like erosion and sedimentation are omitted.

The limits of computational power impose severe constraints on the overall number of numerical elements. In this study, I use $83 \times 83 \times 40$ elements resulting in a model-wide resolution of 3 km. Only when more efficient solvers and adaptive mesh refinement techniques become available, will numerical lithospheric-scale models be able to directly resolve small-scale fault systems in three dimensions.

Three-dimensional variations in density and viscosity generate a stress field that can be vertically heterogeneous. By inferring a fault azimuth from the surface stress tensor, the model assumes that the generation of new faults is controlled by the shallow stress regime. This means that information about the model's stress structure at depth is discarded here, leaving room for future improvements of the stress visualization technique.

Mid-oceanic ridges with fast and intermediate spreading velocities are dominated by a characteristic zig-zag pattern of extension-orthogonal ridges and extension-parallel transforms. These fault orientations are not expressed in the strain rate pattern of the numerical model that produces a single straight ridge oblique to extensional direction. The reason is that the 10 mm/yr full extension velocity of the numerical model is typical for ultraslow spreading ridges that extend with a rate less than 12 mm/yr [*Dick et al*., 2003]. Slow and ultraslow spreading ridges often feature oblique extension with intermediate fault populations [*Tuckwell et al*., 1996; *Fournier and Petit*, 2007], which agrees very well with the stress-inferred fault patterns in the final phase after breakup.

4. Comparison to Analog Experiments

In this section, numerical results are compared to two sets of analog experiments, namely *Clifton et al*. [2000], and *Agostini et al*. [2009]. To my knowledge, these models constitute the latest crustal-scale and lithospheric-scale sets of experiments, respectively, that cover a large spectrum of obliquity (i.e., $0^\circ \leq \alpha \leq 90^\circ$ in *Clifton et al*. [2000], and $0^\circ \leq \alpha \leq 75^\circ$ in *Agostini et al*. [2009]). There are significant differences between the setup of *Clifton et al*. [2000] and the numerical model in terms of rheology, model dimensions, and total extension while only two major differences exist with the analog model of *Agostini et al*. [2009]; the implementation of the weak zone, and the boundary conditions, whereas dimensions and rheology are very similar. Nevertheless, it is especially the difference between the individual setups that allows relevant conclusions: Fault patterns that are robustly reproduced by both the analog experiments and the numerical model can be expected to represent fundamental features that should be visible in nature as well.

The experiments of *Clifton et al*. [2000] involve a single layer of clay which is considered as the laboratory analog of a crustal layer that is deformed without any interaction with the underlying mantle. According to their scaling, 1 cm in the model corresponds to roughly 0.1–1 km in nature. Hence their quadratic model setup with a length of 60 cm scales to 6–60 km in reality, while the thickness of the clay layer scales to 0.25–2.5 km. Fault orientations are measured at a scaled displacement of 0.6–6 km. The prospective rift zone is prescribed by a latex sheet at the bottom of the box whose width scales to 0.6–6 km. The definition of α in the original publication is opposite to the one applied here ($\alpha = 90^\circ - \alpha_{\mathrm{Clifton}}$). Since the clay-model allows only crust-scale deformation, the maximum total strain is only 10%, which corresponds to 2.5 My of extension in the numerical model. The final fault distribution of *Clifton et al*. [2000] is depicted at 1 My in Figures 4e–10e as a gray line.

The laboratory experiments of *Agostini et al*. [2009] are conducted using a complex layered setup that involves brittle rheology in the upper crust, a ductile lower crust, as well as lithospheric and asthenospheric mantle layers following *Corti* [2008]. The lithosphere-asthenosphere boundary lies at 42 km depth (2.8 cm in model dimension). The brittle upper crust is represented by K-feldspar powder while the depth-dependent viscosity of lower crust and mantle is realized by several layers composed of plasticine-silicone mixtures. Lateral model dimensions scale to 240 km times 180–270 km, while maximum extension is 42 km. A prescribed rift zone of 45 km width is introduced via a weak lower crustal domain. A major difference between *Agostini et al*. [2009]

and the numerical model exists in terms of the boundary condition. The analog model involves free-slip boundary conditions at the nonextending model sides imposing zero shear stress along these boundaries. The numerical setup features a periodic boundary condition that is best illustrated by an infinite concatenation of the model domain along the rift trend. Moreover, their imposed weak zone lies oblique to the model boundaries, so that it partially coincides with the extensional boundary for $\alpha > 45^\circ$. Note that the fault distribution of *Agostini et al.* [2009] has been measured after 23% total strain which corresponds to 58 km (i.e., 5.8 My) in the numerical experiments. Their resulting fault distribution is shown in Figures 4e–10e as a black line. The coordinate system of *Agostini et al.* [2009] differs from this study, so that for comparability, the fault distribution had to be adopted to the numerical model configuration.

The following subsections compare numerical and analog experiments in terms of individual fault populations in more detail. However, comparison is limited to the first stages of rifting, since final stages and breakup are not covered by analog models.

4.1. Faults with Intermediate Direction

Faults with intermediate direction (i.e., orientations between displacement-orthogonal and rift-parallel orientation) constitute the fundamental mode of faulting and are present in all experiments on oblique extension. They result from the orientation of the principal stress axes with respect to the rift zone [*Withjack and Jamison*, 1986] in accordance with Andersonian faulting. The faults cross the whole rift zone in *Clifton et al.* [2000] and in the first time steps of the numerical model. During lithospheric necking, the rift structure of the numerical model is dominated by major, basinward dipping boundary faults that organize in en-échelon shear zones, reproducing the structures observed by *Agostini et al.* [2009]. Strong agreement exists in terms of the small-scale surface structures of the rift boundary that consists of intermediately oriented faults. In both *Agostini et al.* [2009] and in the numerical model, basinward localization generates internal faults and graben-in-graben structures [*Corti et al.*, 2010].

However, intermediate faults are restricted in *Agostini et al.* [2009] to the rift margins while they develop in the numerical model throughout the rift valley. The reason possibly lies in different implementations of the weak zone: The analog models feature a sharp, rheological transition from normal to weak lower crust focusing reorientation of local extension to the boundaries of the weak zone. The numerical models, however, involve a gradual, thermal transition between the weak zone and normal crust without a focusing effect. Another possible explanation is that the numerical model's weak zone is stronger than in the analog models which leads to more crust-mantle coupling and a narrower rift [*Buck*, 1991] that cannot accommodate the central horst seen in the analog models.

4.2. Displacement-Orthogonal Faulting

This fault population occurs in the analog experiments of both *Clifton et al.* [2000] and *Agostini et al.* [2009] albeit in a different manner. It is found for high obliquity ($\alpha \geq 60^\circ$) in the experiments of *Clifton et al.* [2000], while in the setup of *Agostini et al.* [2009] it takes place only at moderate to low obliquity ($\alpha \leq 45^\circ$) and is manifested as internal faults. In the numerical model, displacement-orthogonal faults emerge at moderate to low obliquity ($\alpha \leq 45^\circ$). However, they are less important than in the analog models and emerge only at a very late rift stage reminiscent of the typical zig-zag mid-ocean ridge pattern of transform and extension-perpendicular deformation.

Displacement-orthogonal faults are generated when the local stress field is not affected by oblique structures. A homogeneous, isotropic material that is stretched in any direction will always show displacement-orthogonal faulting. An alternative reason for the occurrence of displacement-orthogonal faulting is a free-slip boundary condition which does not support any shear stress so that faults tend to be perpendicular to that side of the model.

One reason for sparsity of displacement-orthogonal faults in the numerical model is the periodic boundary condition that is less prone to displacement-orthogonal faulting than the free-slip boundary condition of the analog models. Another reason could be the low numerical resolution (if compared to analog models) that hampers the evolution of individual rift segments and segmented mid-ocean ridges [*Gerya*, 2013]. Additionally, the analog model's strong viscosity contrast between weak zone and normal crust induces a sharp local stress reorientation and thereby possibly generates a rift interior that is dominated by extension-orthogonal stresses.

4.3. Rift Parallel Faulting

Rift parallel faulting is present in the numerical model and the analog model of *Agostini et al*. [2009], but not in the crustal-scale experiments of *Clifton et al*. [2000], which suggests that lithospheric necking is controlling the occurrence of this fault family. Even though rift-parallel faulting takes place in the numerical model and in *Agostini et al*. [2009], they are generated by a different mechanism: In the analog experiments, these fault orientations occur for $\alpha \geq 30^\circ$ as strike-slip or oblique-slip faults at the area of minimum lithospheric thinning. They are secondary structures that connect two distinct extension-perpendicular segments in the center of the rift. In the numerical model, however, they occur much later, toward the end of the en-échelon phase (Figure 11) as a result of lithospheric necking.

Lithospheric necking may generate rift-parallel faulting by two means: (i) The density contrast of hot upwelling material below the rift center and the cold continental mantle lithosphere beneath the rift flanks generates a rift-perpendicular stress-component [*Sonder*, 1990; *Bellahsen et al*., 2006, 2013]. (ii) An additional factor enhancing rift-parallel faulting is strain partitioning. Strike-slip faults emerge at the weakest point of the rift, i.e., above the necking maximum. These strike-slip faults partially account for the rift-parallel component of the far-field extension velocity while normal faulting at the rift flanks accommodates the rift-orthogonal component [*Brune and Autin*, 2013].

4.4. Strike-Slip Faulting

Strike-slip faults play a major role for intermediate and high obliquity in the analog models and the numerical experiments. For $\alpha = 45^\circ - 75^\circ$, both the model of *Agostini et al*. [2009] and the numerical experiments exhibit a strong strike-slip zone with fault orientations subparallel to the rift trend. This strike-slip-dominated area locates in the rift center where lithospheric thinning resulted in maximum weakening. In the numerical model, rift-centered strike-slip faults occur simultaneously with rift-parallel fault orientations adjacent to the rift center indicating strain partitioning.

The numerical model of simple shear ($\alpha = 90^\circ$) features strike-slip faults with two populations whose respective orientations are both subparallel to the rift trend and the direction of extension. These direction are associated with Riedel shear orientations that exhibit characteristic azimuths of $-\varphi_{\text{eff}}/2 = -15.5^\circ$ and $\varphi_{\text{eff}}/2 - 90^\circ = -74.5^\circ$. These angles are visible both in the strain rate pattern (Figure 10a) as well as in the stress-inferred fault azimuth (Figure 10d and 10e). The experiment with $\alpha = 90^\circ$ compares very well to the corresponding model of *Clifton et al*. [2000]. However, the analog model displays only the sinistral fault family, while the dextral population seems to be shifted to the extension-normal orientation.

5. Discussion and Comparison to Selected Natural Examples

The presented numerical models show how the surface stress field in an oblique rift system varies significantly during different phases of rifting, even though the extension rate and direction remain constant. The underlying reason for this behavior is the interaction of far-field stresses with rift-intrinsic buoyancy and strength. This result agrees with previous field-based studies that infer local stress rotations in the Baikal Rift [*Petit et al*., 1996], the western branch of the East African Rift System [*Morley*, 2010], and the Main Ethiopian Rift [*Corti et al*., 2013]. The inference of rift-intrinsic, time-dependent variations of fault orientation complicates the approach to deduce palaeostress field and associated plate motion changes based on fault orientations of rift systems.

Strain partitioning has been recognized as an important process during transtension and transpression [*Teyssier et al*., 1995]. The numerical model indicates that strain partitioning between strike-slip in the rift center and adjacent rift-parallel normal faulting occurs for high rift obliquity. The reason for this behavior is that strike-slip deformation is more pronounced for high obliquities, as expected from infinitesimal strain theory [*Withjack and Jamison*, 1986]. While strike-slip faults account for a certain portion of the along-strike velocity component, the rift-perpendicular component generates normal faults that feature rift-parallel azimuths. The model shows strain-partitioning at the end of the en-échelon deformation. It might therefore explain the rift-parallel faults observed in the Gulf of Aden [*Bellahsen et al*., 2006]. Note that strain-partitioning occurs in a different manner than in previous analog models [*Agostini et al*., 2009], where boundary faults at the rift margin deform via oblique slip whereas the rift center shows pure extension.

Moreover, strain-partitioning occurs in their models for low obliquity ($\alpha<45°$) and not for highly oblique extension.

Strike-slip localization due to strain partitioning affects the rift process also in terms of mechanical energy. Since strike-slip motion requires less force (at constant velocity) than oblique extension [*Brune et al*., 2012], a strike-slip zone in the rift center will significantly facilitate the rift process.

Comparison to a previous numerical model of oblique extension [*van Wijk*, 2005] yields basic agreement but also significant differences. Similar to analog models [*Agostini et al*., 2009; *Autin et al*., 2010], this study prescribes a weak linear zone that is oblique to the model boundaries and uses the free-slip condition at lateral boundaries. Maximum model extension is ~120 km achieving crustal thinning factors of 1.2 so that break-up does not occur. Similar to the results presented here, *van Wijk* [2005] reports shear zones that cut across the inherited weak zone; however, these shear zones exhibit only extension-orthogonal strike whereas no intermediate directions are visible. A reason for the dominant extension-orthogonal orientation could be the free-slip boundary condition that prohibits shear stress at the model sides. This contrasts the periodic boundary condition of the models presented here that imposes less influence on shear zone orientation.

Oblique extensional systems worldwide differ in many aspects and clearly one single model cannot explain all rifts at the same time. However, the distinct fault populations occurring in the presented numerical model and their sequence of activity can elucidate observations from different rift systems.

The model with $\alpha=45°$ compares very well to the evolution of the Gulf of Aden featuring an obliquity of about 40° [see *Brune and Autin*, 2013 for a detailed discussion]. The succession of fault populations of the Gulf of Aden displays a three-phase chronology consistent of (i) initially intermediate and extension-orthogonal faulting, (ii) followed by rift-parallel azimuths, and (iii) a final phase of intermediate faults that have been found at the ocean-continent boundary and extension-orthogonal faults adjacent to the ridge [*Bellahsen et al*., 2013]. This fault evolution corresponds very well to the phases of the numerical model presented here. Large displacement-orthogonal basins that exist on-shore [*Leroy et al*., 2012] do not match the numerical model. These basins, however, correspond to areas of Mesozoic extension that have been reactivated during Gulf of Aden rift activity [*Ellis et al*., 1996; *Leroy et al*., 2012; *Autin et al*., 2013].

The curved Main Ethiopian Rift is characterized by ~30° obliquity in the central sector and ~45° in the northern sector [*Corti*, 2009]. Fault analysis shows a two phase evolution. At first, boundary faults developed with intermediate orientation along an area of significant strength contrast between the inherited weak zone and the surrounding strong lithosphere. The second phase is marked by strain migration to the rift center where en-échelon faulting takes place with extension-orthogonal azimuths [*Corti*, 2008]. The numerical model reproduces the major boundary faults and their small-scale structure that is dominated by intermediate fault directions. Basinward strain localization like in the Main Ethiopian rift takes place in the numerical model and is caused by lithospheric necking explaining the observed two-phase evolution. En-échelon faults develop in the numerical model and in the central parts of the Main Ethiopian Rift; however, instead of rift-parallel fault populations, the latter shows extension-orthogonal fault directions. This difference might originate from the geometry of the weak zone and its actual strength, both of which are submitted to the paramount influence of the Afar plume [*Ebinger and Sleep*, 1998].

The Gulf of California region constitutes a rift system that features high obliquity of $\alpha=60°-70°$. The tectonic setting is very complex and derives from an active margin featuring strong lateral density variations and an inherited belt of weak crust from a volcanic arc [*Umhoefer*, 2011]. Additional complexity arises from a possible two-phase evolution involving an orthogonal and an oblique phase of extension [*Stock and Hodges*, 1989]. Hence, any attempt to understand the Gulf of California by means of a simple model must be taken with due caution. Nevertheless, several structural aspects of this rift system can be related to the presented model. Counterclockwise rotation of long-lived shear zones in the numerical model (sinistral oblique rifting) corresponds to clockwise rotation when translated to the Gulf of California extensional configuration (dextral oblique rifting). These clockwise vertical-axis block rotations of fault systems have been interpreted in the northeastern part of Baja California [*Seiler et al*., 2010; *Bennett and Oskin*, 2014]. Moreover, strong rift-parallel faulting like in the numerical model has been inferred during the proto-Gulf phase of rifting [*Stock and Hodges*, 1989]. Strain partitioning has been interpreted during the formation of the proto-Gulf [*Stock and Hodges*, 1989; *Oskin and Stock*, 2003] with dextral strike-slip west of the peninsula (i.e., outside the rift) and rift-parallel normal faulting within

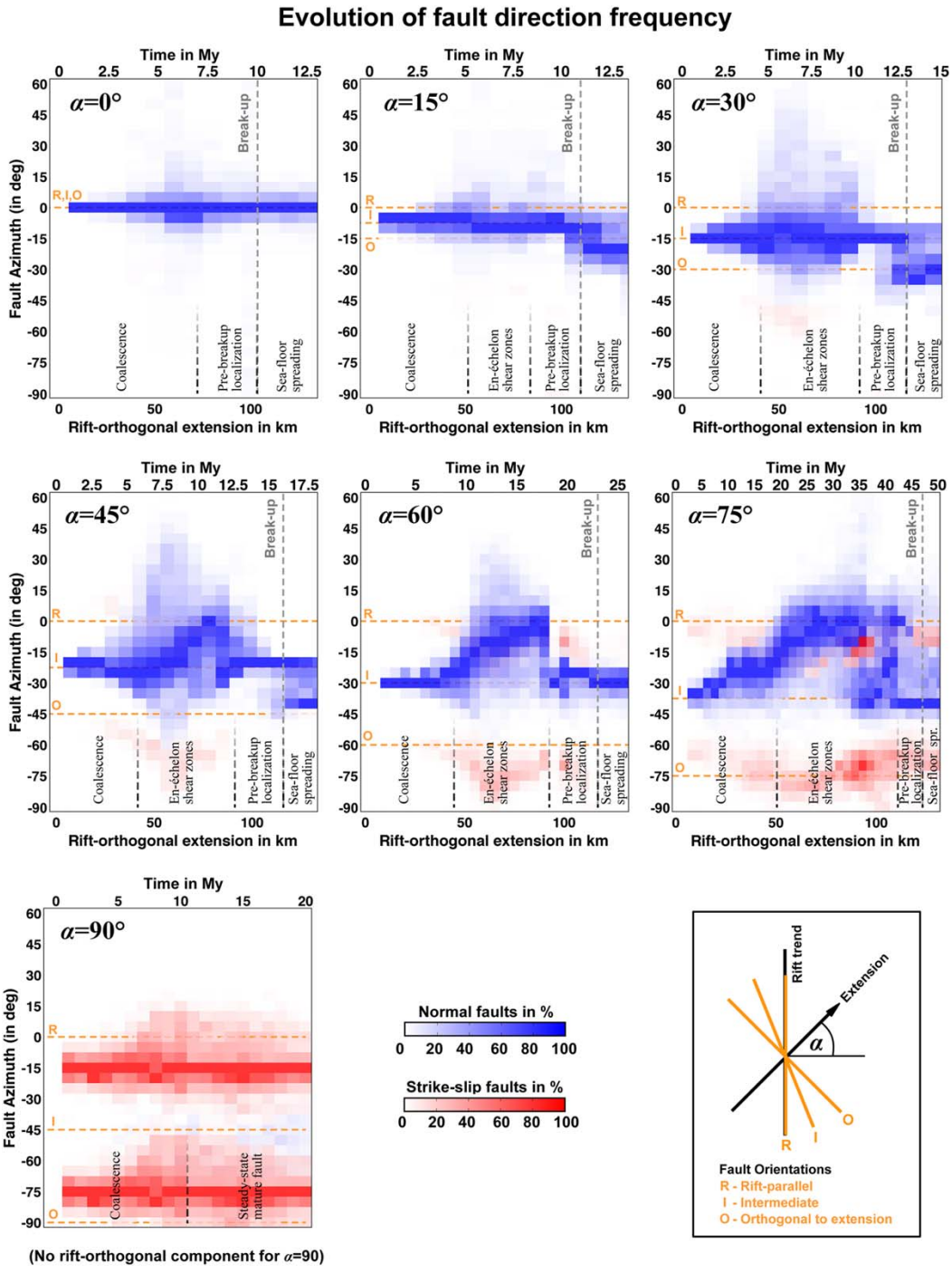

Figure 11. Summary plot. Azimuth diagrams shown in previous plots (Figures 4e–10e) are condensed into one plot for each angle of obliquity. This illustrates the evolution of normal faults (blue) and strike-slip faults (red) in distinct phases. The abscissa shows rift-orthogonal extension (bottom axis) and time (top axis). Breakup is indicated by a gray dashed line. Initially dominating intermediate fault directions (I) widen during fault coalescence and shift toward rift-parallel azimuths (R) during a phase of en-échelon deformation. Prebreakup localization towards the rift center ends the en-échelon phase within few million years and homogenizes fault orientations to intermediate directions. Post breakup sea floor spreading takes place with intermediate and extension-orthogonal faults (O) for $\alpha \leq 45°$ while only intermediate directions exist for $\alpha = 60°$ and $\alpha = 75°$. For obvious reasons, the model without obliquity ($\alpha = 0°$) and the strike-slip model ($\alpha = 90°$) do not feature an en-échelon phase. The strike-slip model ($\alpha = 90°$) exhibits a stage of fault maturity, but no break-up. The robustness of the presented models is illustrated in supporting information Figures S1–S5, where important model parameters are varied.

the rift, a result that is currently discussed [*Fletcher et al*., 2007; *Seiler et al*., 2010]. The presented high-obliquity numerical scenarios indicate a certain degree of strain partitioning. However, in the numerical models, the strike-slip zone occurs inside the rift center and not adjacent to the rift valley.

Even though the model was designed to understand continental rift systems, it can be very well applied to oblique oceanic extensional systems. These have been characterized by en-échelon graben patterns and intermediate fault orientations that are very similar to those of the presented models. Prominent examples are the Reykjanes and Mohns ridges [*Dauteuil and Brun*, 1993], the Viking graben [*Brun and Tron*, 1993], the Sogn graben [*Faerseth et al*., 1997], and the Southwest Indian Ridge [*Montési et al*., 2011].

6. Conclusions

The presented rift models generate complex time-dependent surface structures despite the fact that the setup is fairly simple. The only reason for this complexity is the intrinsic three-dimensionality of oblique rift systems. Other mechanisms such as surface processes, reactivation of inherited structures, melting, and dyke dynamics provide additional complexity for the tectonic evolution of individual rift systems.

The evolution of the inferred surface fault orientations is summarized for all angles of obliquity in Figure 11. Individual models can be described in four phases that mirror the structural evolution of the rift:

1. Initial fault coalescence with intermediate fault directions results from interaction of the far field stress with the obliquely oriented weak zone.

2. En-échelon deformation featuring a broad distribution of fault orientations occurs whereas rift-parallel faults gain successively more importance. Rift-parallel faults are favored both by necking-induced density variations and strain partitioning between strike-slip in the rift center and normal fault in its vicinity.

3. Prebreakup localization rapidly terminates the en-échelon phase yielding intermediate fault orientations.

4. Sea floor spreading involves intermediate and extension-orthogonal fault directions as a result of the waning influence of the inherited oblique weakness.

While fault directions are often used to infer palaeoplate movements, this study shows that local variations in crustal stress field and fault orientation may arise intrinsically during rift maturation and may not require plate motion changes. The evolution of crustal stress and fault directions follow a characteristic temporal pattern that is linked to the maturity of the rift system.

Acknowledgments

S. B. has been funded by SAMPLE (South Atlantic Margin Processes and Links with onshore Evolution), Priority Program 1375 of the German Research Foundation and by the European Research Council, through the Marie Curie International Outgoing Fellowship (Project 326115). I thank the reviewers, Giacomo Corti, Patrice Rey, and an anonymous reviewer for their detailed and constructive comments. This study benefited greatly from discussions with Oliver Heidbach, Julia Autin, Andrey Babeyko, and Jonathan Bull. Stephan Sobolev and Dietmar Müller are thanked for support. Furthermore, I thank Simon Williams for giving feedback on the manuscript.

References

Agostini, A., G. Corti, A. Zeoli, and G. Mulugeta (2009), Evolution, pattern, and partitioning of deformation during oblique continental rifting: Inferences from lithospheric-scale centrifuge models, *Geochem. Geophys. Geosyst.*, *10*, Q11015, doi:10.1029/2009GC002676.

Agostini, S., C. Doglioni, F. Innocenti, P. Manetti, and S. Tonarini (2010), On the geodynamics of the Aegean rift, *Tectonophysics*, *488*, 7–21, doi:10.1016/j.tecto.2009.07.025.

Allken, V., R. S. Huismans, and C. Thieulot (2011), Three-dimensional numerical modeling of upper crustal extensional systems, *J. Geophys. Res.*, *116*, B10409, doi:201110.1029/2011JB008319.

Allken, V., R. S. Huismans, and C. Thieulot (2012), Factors controlling the mode of rift interaction in brittle-ductile coupled systems: A 3D numerical study, *Geochem. Geophys. Geosyst.*, *13*, Q05010, doi:10.1029/2012GC004077.

Anderson, E. M. (1948), *The Dynamics of Faulting*, Oliver and Boyd, Edinburgh.

Autin, J., N. Bellahsen, L. Husson, M.-O. Beslier, S. Leroy, and E. d' Acremont (2010), Analog models of oblique rifting in a cold lithosphere, *Tectonics*, *29*, TC6016, doi:10.1029/2010TC002671.

Autin, J., N. Bellahsen, S. Leroy, L. Husson, M.-O. Beslier, and E. d' Acremont (2013), The role of structural inheritance in oblique rifting: Insights from analogue models and application to the Gulf of Aden, *Tectonophysics*, *607*, 51–64, doi:10.1016/j.tecto.2013.05.041.

Bassi, G. (1991), Factors controlling the style of continental rifting: Insights from numerical modelling, *Earth Planet. Sci. Lett.*, *105*, 430–452, doi:10.1016/0012–821X(91)90183-I.

Behn, M. D., J. Lin, and M. T. Zuber (2002), A continuum mechanics model for normal faulting using a strain-rate softening rheology: Implications for thermal and rheological controls on continental and oceanic rifting, *Earth Planet. Sci. Lett.*, *202*, 725–740, doi:10.1016/S0012-821X(02)00792-6.

Bellahsen, N., C. Faccenna, F. Funiciello, J. M. Daniel, and L. Jolivet (2003), Why did Arabia separate from Africa? Insights from 3-D laboratory experiments, *Earth Planet. Sci. Lett.*, *216*, 365–381, doi:10.1016/S0012-821X(03)00516-8.

Bellahsen, N., M. Fournier, E. d' Acremont, S. Leroy, and J. M. Daniel (2006), Fault reactivation and rift localization: Northeastern Gulf of Aden margin, *Tectonics*, *25*, TC1007, doi:10.1029/2004TC001626.

Bellahsen, N., L. Husson, J. Autin, S. Leroy, and E. d' Acremont (2013), The effect of thermal weakening and buoyancy forces on rift localization: Field evidences from the Gulf of Aden oblique rifting, *Tectonophysics*, *607*, 80–97, doi:10.1016/j.tecto.2013.05.042.

Bennett, S. E. K., and M. E. Oskin (2014), Oblique rifting ruptures continents: Example from the Gulf of California shear zone, *Geology*, *42*(3), 215–218, doi:10.1130/G34904.1.

Bialas, R.W., and W. R. Buck (2009), How sediment promotes narrow rifting: Application to the Gulf of California, *Tectonics*, *28*, TC4014, doi:10.1029/2008TC002394.

Bonini, M., T. Souriot, M. Boccaletti, J. P. Brun (1997), Successive orthogonal and oblique extension episodes in a rift zone: Laboratory experiments with application to the Ethiopian Rift, *Tectonics*, *16*, 347–362, doi:10.1029/96TC03935.

Bott, M. H. P. (1959), The mechanics of oblique slip faulting, *Geol. Mag.*, *96*, 109–117.

Braun, J., and C. Beaumont (1989), A physical explanation of the relation between flank uplifts and the breakup unconformity at rifted continental margins, *Geology*, *17*, 760–764, doi:10.1130/0091-7613(1989)017<0760:APEOTR>2.3.CO;2.

Brun, J.-P., and V. Tron (1993), Development of the North Viking Graben: Inferences from laboratory modelling, *Sediment. Geol.*, *86*, 31–51, doi:10.1016/0037-0738(93)90132-O.

Brune, S., and J. Autin (2013), The rift to break-up evolution of the Gulf of Aden: Insights from 3D numerical lithospheric-scale modelling, *Tectonophysics*, *607*, 65–79, doi:10.1016/j.tecto.2013.06.029.

Brune, S., A. A. Popov, and S. V. Sobolev (2012), Modeling suggests that oblique extension facilitates rifting and continental break-up, *J. Geophys. Res.*, *117*, B08402, doi:10.1029/2011JB008860.

Brune, S., A. A. Popov, and S. V. Sobolev (2013), Quantifying the thermo-mechanical impact of plume arrival on continental break-up, *Tectonophysics*, *604*, 51–59, doi:10.1016/j.tecto.2013.02.009.

Brune, S., C. Heine, M. Perez-Gussinye, and S. V. Sobolev (2014), Rift migration explains continental margin asymmetry and crustal hyperextension, *Nat. Commun. 5*, 4014, doi:10.1038/ncomms5014.

Buchmann, T. J., and P. T. Connolly (2007), Contemporary kinematics of the Upper Rhine Graben: A 3D finite element approach, *Global Planet. Change*, *58*, 287–309, doi:10.1016/j.gloplacha.2007.02.012.

Buck, W. R. (1991), Modes of continental lithospheric extension, *J. Geophys. Res.*, *96*, 20161–20178, doi:10.1029/91JB01485.

Buck, W. R. (2006), The role of magma in the development of the Afro-Arabian Rift System, *Geol. Soc. Spec. Publ.*, *259*, 43–54, doi:10.1144/GSL.SP.2006.259.01.05.

Buiter, S. J. H., R. S. Huismans, and C. Beaumont (2008), Dissipation analysis as a guide to mode selection during crustal extension and implications for the styles of sedimentary basins, *J. Geophys. Res.*, *113*, B06406, doi:10.1029/2007JB005272.

Burov, E., and S. Cloetingh (1997), Erosion and rift dynamics: New thermomechanical aspects of post-rift evolution of extensional basins, *Earth Planet. Sci. Lett.*, *150*, 7–26, doi:10.1016/S0012-821X(97)00069-1.

Choi, E., and W. R. Buck (2012), Constraints on the strength of faults from the geometry of rider blocks in continental and oceanic core complexes, *J. Geophys. Res.*, *117*, B04410, doi:10.1029/2011JB008741.

Chorowicz, J., and C. Sorlien (1992), Oblique extensional tectonics in the Malawi Rift, Africa, *Geol. Soc. Am. Bull.*, *104*, 1015–1023, doi:10.1130/0016-7606(1992)104<1015:OETITM>2.3.CO;2.

Clifton, A. E., R. W. Schlische, M. O. Withjack, and R. V. Ackermann (2000), Influence of rift obliquity on fault-population systematics: Results of experimental clay models, *J. Struct. Geol.*, *22*, 1491–1509, doi:10.1016/S0191–8141(00)00043-2.

Corti, G. (2008), Control of rift obliquity on the evolution and segmentation of the main Ethiopian rift, *Nat. Geosci.*, *1*, 258–262, doi:10.1038/ngeo160.

Corti, G. (2009), Continental rift evolution: From rift initiation to incipient break-up in the Main Ethiopian Rift, East Africa, *Earth Sci. Rev.*, *96*, 1–53, doi:10.1016/j.earscirev.2009.06.005.

Corti, G. (2012), Evolution and characteristics of continental rifting: Analog modeling-inspired view and comparison with examples from the East African Rift System, *Tectonophysics*, *522–523*, 1–33, doi:10.1016/j.tecto.2011.06.010.

Corti, G., M. Bonini, F. Innocenti, P. Manetti, and G. Mulugeta (2001), Centrifuge models simulating magma emplacement during oblique rifting, *J. Geodyn.*, *31*, 557–576, doi:10.1016/S0264–3707(01)00032-1.

Corti, G., M. Bonini, S. Conticelli, F. Innocenti, P. Manetti, and D. Sokoutis (2003), Analogue modelling of continental extension: A review focused on the relations between the patterns of deformation and the presence of magma, *Earth Sci. Rev.*, *63*, 169–247, doi:10.1016/S0012-8252(03)00035-7.

Corti, G., G. Ranalli, G. Mulugeta, A. Agostini, F. Sani, and A. Zugu (2010), Control of the rheological structure of the lithosphere on the inward migration of tectonic activity during continental rifting, *Tectonophysics*, *490*, 165–172, doi:10.1016/j.tecto.2010.05.004.

Corti, G., M. Philippon, F. Sani, D. Keir, and T. Kidane (2013), Re-orientation of the extension direction and pure extensional faulting at oblique rift margins: Comparison between the Main Ethiopian Rift and laboratory experiments, *Terra Nova*, *25*, 396–404, doi:10.1111/ter.12049.

Dauteuil, O., and J. P. Brun (1993), Oblique rifting in a slow-spreading ridge, *Nature*, *361*, 145–148, doi:10.1038/361145a0.

De Wit, M. J. (2003), Madagascar: Heads it's a continent, tails it's an Island, *Annu. Rev. Earth Planet. Sci.*, *31*, 213–248, doi:10.1146/annurev.earth.31.100901.141337.

Delvaux, D., R. Moeys, G. Stapel, C. Petit, K. Levi, A. Miroshnichenko, V. Ruzhich, and V. San'kov (1997), Paleostress reconstructions and geodynamics of the Baikal region, Central Asia, Part 2. Cenozoic rifting, *Tectonophysics*, *282*, 1–38, doi:10.1016/S0040-1951(97)00210-2.

Dick, H. J. B., J. Lin, and H. Schouten (2003), An ultraslow-spreading class of ocean ridge, *Nature*, *426*, 405–412, doi:10.1038/nature02128.

Dorsey, R. J. (2010), Sedimentation and crustal recycling along an active oblique-rift margin: Salton Trough and northern Gulf of California, *Geology*, *38*, 443–446. doi:10.1130/G30698.1.

Dunbar, J. A., and D. S. Sawyer (1996), Three-dimensional dynamical model of continental rift propagation and margin plateau formation, *J. Geophys. Res.*, *101*, 27845–27,863, doi:10.1029/96JB01231.

Ebinger, C. J., and N. H. Sleep (1998), Cenozoic magmatism throughout east Africa resulting from impact of a single plume, *Nature*, *395*, 788–791, doi:10.1038/27417.

Ellis, A. C., H. M. Kerr, C. P. Cornwell, and D. O. Williams (1996), A tectono-stratigraphic framework for Yemen and its implications for hydrocarbon potential, *Pet. Geosci.*, *2*, 29–42, doi:10.1144/petgeo.2.1.29.

Engen, Ø., J. I. Faleide, and T. K. Dyreng (2008), Opening of the Fram Strait gateway: A review of plate tectonic constraints, *Tectonophysics*, *450*, 51–69, doi:10.1016/j.tecto.2008.01.002.

England, P., and D. McKenzie (1982), A thin viscous sheet model for continental deformation, *Geophys. J. R. Astron. Soc.*, *70*, 295–321, doi:10.1111/j.1365-246X.1982.tb04969.x.

Faerseth, R.B., B.-E. Knudsen, T. Liljedahl, P. S. Midbøe, and S. Søderstrøm (1997), Oblique rifting and sequential faulting in the Jurassic development of the northern North Sea, *J. Struct. Geol.*, *19*, 1285–1302, doi:10.1016/S0191-8141(97)00045-X.

Fletcher, J. M., M. Grove, D. Kimbrough, O. Lovera, and g. E. Gehrels (2007), Ridge-trench interactions and the Neogene tectonic evolution of the Magdalena shelf and southern Gulf of California: Insights from detrital zircon U-Pb ages from the Magdalena fan and adjacent areas, *Geol. Soc. Am. Bull.*, *119*, 1313–1336, doi:10.1130/B26067.1.

Fournier, M., and C. Petit (2007), Oblique rifting at oceanic ridges: Relationship between spreading and stretching directions from earthquake focal mechanisms, *J. Struct. Geol.*, *29*, 201–208, doi:10.1016/j.jsg.2006.07.017.
Gac, S., and L. Geoffroy (2009), 3D Thermo-mechanical modelling of a stretched continental lithosphere containing localized low-viscosity anomalies (the soft-point theory of plate break-up), *Tectonophysics*, *468*, 158–168, doi:10.1016/j.tecto.2008.05.011.
Gaina, C., R. D. Müller, B. Brown, T. Ishihara, and S. Ivanov (2007), Breakup and early seafloor spreading between India and Antarctica, *Geophys. J. Int.*, *170*, 151–169, doi:10.1111/j.1365-246X.2007.03450.x.
Gerya, T. (2010), Dynamical instability produces transform faults at mid-ocean ridges, *Science*, *329*, 1047–1050, doi:10.1126/science.1191349.
Gerya, T.V. (2013), Three-dimensional thermomechanical modeling of oceanic spreading initiation and evolution, *Phys. Earth Planet. Inter.* *214*, *35–52*, doi:10.1016/j.pepi.2012.10.007.
Gleason, G. C., and J. Tullis (1995), A flow law for dislocation creep of quartz aggregates determined with the molten-salt cell, *Tectonophysics*, *247*, 1–23.
Heine, C., and S. Brune (2014), Oblique rifting of the equatorial Atlantic: Why there is no Saharan Atlantic Ocean, *Geology 42(3)*, *211–214*, doi:10.1130/G35082.1.
Hergert, T., and O. Heidbach (2011), Geomechanical model of the Marmara Sea region—II. 3-D contemporary background stress field, *Geophys. J. Int.*, *185*, 1090–1102, doi:10.1111/j.1365-246X.2011.04992.x.
Hirth, G., and D. L. Kohlstedt (2003), Rheology of the upper mantle and the mantle wedge: A view from the experimentalists, in Inside the Subduction Factory, Geophys. Monogr. Ser. vol. 138, edited by J. M. Eiler, pp. 83–105, AGU, Washington, D. C., doi:10.1029/138GM06.
Hosseinpour, M., R. D. Müller, S. E. Williams, and J. M. Whittaker (2013), Full-fit reconstruction of the Labrador Sea and Baffin Bay, *Solid Earth*, *4*, 461–479, doi:10.5194/se-4-461-2013.
Houseman, G., and P. England (1986), Finite strain calculations of continental deformation: 1. Method and general results for convergent zones, *J. Geophys. Res.*, *91*, 3651–3663, doi:10.1029/JB091iB03p03651.
Huismans, R. S., and C. Beaumont (2003), Symmetric and asymmetric lithospheric extension: Relative effects of frictional-plastic and viscous strain softening, *J. Geophys. Res.*, *108*(B10), 2496, doi:10.1029/2002JB002026.
Huismans, R. S., and C. Beaumont (2011), Depth-dependent extension, two-stage breakup and cratonic underplating at rifted margins, *Nature*, *473*, 74–78, doi:10.1038/nature09988.
Katzman, R., U. S. ten Brink, and J. Lin (1995), Three-dimensional modeling of pull-apart basins: Implications for the tectonics of the Dead Sea Basin, *J. Geophys. Res.*, *100*, 6295–6312, doi:10.1029/94JB03101.
Lavier, L. L., and G. Manatschal (2006), A mechanism to thin the continental lithosphere at magma-poor margins, *Nature*, *440*, 324–328, doi:10.1038/nature04608.
Lavier, L. L., W. R. Buck, and A. N. B. Poliakov (2000), Factors controlling normal fault offset in an ideal brittle layer, *J. Geophys. Res.*, *105*, 23431–23,442, doi:10.1029/2000JB900108.
Le Pourhiet, L., B. Huet, D. A. May, L. Labrousse, and L. Jolivet (2012), Kinematic interpretation of the 3D shapes of metamorphic core complexes, *Geochem. Geophys. Geosyst.*, *13*, Q09002, doi:10.1029/2012GC004271.
Le Pourhiet, L., B. Huet, and N. Traore (2014), Links between long-term and short-term rheology of the lithosphere: Insights from strike-slip fault modelling, *Tectonophysics*, doi:10.1016/j.tecto.2014.06.034, in press.
Leroy, S., et al. (2012), From rifting to oceanic spreading in the Gulf of Aden: A synthesis, *Arab. J. Geosci.*, *5*, 859–901, doi:10.1007/s12517-011-0475-4.
Liao, J., and T. Gerya (2014), Influence of lithospheric mantle stratification on craton extension: Insight from two-dimensional thermo-mechanical modeling, *Tectonophysics*, in press, doi:10.1016/j.tecto.2014.01.020.
Lizarralde, D., et al. (2007), Variation in styles of rifting in the Gulf of California, *Nature*, *448*, 466–469, doi:10.1038/nature06035.
Mart, Y., and O. Dauteuil (2000), Analogue experiments of propagation of oblique rifts, *Tectonophysics*, *316*, 121–132, doi:10.1016/S0040-1951(99)00231-0.
McClay, K. R., and M. J. White (1995), Analogue modelling of orthogonal and oblique rifting, *Mar. Pet. Geol.*, *12*, 137–151, doi:10.1016/0264-8172(95)92835-K.
Montési, L. G. J., M. D. Behn, L. B. Hebert, J. Lin, and J. L. Barry (2011), Controls on melt migration and extraction at the ultraslow Southwest Indian Ridge 10°–16°E, *J. Geophys. Res.*, *116*, B10102, doi:10.1029/2011JB008259.
Morley, C. K. (2010), Stress re-orientation along zones of weak fabrics in rifts: An explanation for pure extension in "oblique" rift segments?, *Earth Planet. Sci. Lett.*, *297*, 667–673, doi:10.1016/j.epsl.2010.07.022.
Moulin, M., D. Aslanian, and P. Unternehr (2010), A new starting point for the South and Equatorial Atlantic Ocean, *Earth Sci. Rev.*, *98*, 1–37, doi:10.1016/j.earscirev.2009.08.001.
Nürnberg, D., and R. D. Müller (1991), The tectonic evolution of the South-Atlantic from Late Jurassic to present, *Tectonophysics*, *191*, 27–53, doi:10.1016/0040–1951(91)90231-G.
Oskin, M., and J. Stock (2003), Pacific–North America plate motion and opening of the Upper Delfín basin, northern Gulf of California, Mexico, *Geol. Soc. Am. Bull.*, *115*, 1173–1190, doi:10.1130/B25154.1.
Pérez-Gussinyé, M., J. P. Morgan, T. J. Reston, and C. R. Ranero (2006), The rift to drift transition at non-volcanic margins: Insights from numerical modelling, *Earth Planet. Sci. Lett.*, *244*, 458–473, doi:10.1016/j.epsl.2006.01.059.
Petersen, K. D., S. B. Nielsen, O. R. Clausen, R. Stephenson, and T. Gerya (2010), Small-scale mantle convection produces stratigraphic sequences in sedimentary basins, *Science*, *329*, 827–830, doi:10.1126/science.1190115.
Petit, C., J. Déverchère, F. Houdry, V. A. Sankov, V. I. Melnikova, and D. Delvaux (1996), Present-day stress field changes along the Baikal rift and tectonic implications, *Tectonics*, *15*, 1171–1191, doi:10.1029/96TC00624.
Popov, A. A., and S. V. Sobolev (2008), SLIM3D: A tool for three-dimensional thermo mechanical modeling of lithospheric deformation with elasto-visco-plastic rheology, *Phys. Earth Planet. Inter. 171*, 55–75, doi:10.1016/j.pepi.2008.03.007.
Provost, A.-S., and H. Houston (2003), Stress orientations in northern and central California: Evidence for the evolution of frictional strength along the San Andreas plate boundary system, *J. Geophys. Res.*, *108*(B3), 2175, doi:10.1029/2001JB001123.
Regenauer-Lieb, K., R. F. Weinberg, and G. Rosenbaum (2006), The effect of energy feedbacks on continental strength, *Nature*, *442*, 67–70, doi:10.1038/nature04868.
Rey, P. F., and G. Houseman (2006), Lithospheric scale gravitational flow: The impact of body forces on orogenic processes from Archaean to Phanerozoic, *Geol. Soc. Spec. Publ.*, *253*, 153–167, doi:10.1144/GSL.SP.2006.253.01.08.
Rey, P. F., C. Teyssier, S. C. Kruckenberg, and D. L. Whitney (2011), Viscous collision in channel explains double domes in metamorphic core complexes, *Geology*, *39*, 387–390, doi:10.1130/G31587.1.
Ring, U. (1994), The influence of preexisting structure on the evolution of the Cenozoic Malawi rift (East African rift system), *Tectonics*, *13*, 313–326, doi:10.1029/93TC03188.

Rooney, T. O., I. D. Bastow, D. Keir, F. Mazzarini, E. Movsesian, E. B. Grosfils, J. R. Zimbelman, M. S. Ramsey, D. Ayalew, and G. Yirgu (2014), The protracted development of focused magmatic intrusion during continental rifting, *Tectonics*, *33*, 875–897, doi:10.1002/2013TC003514.

Seiler, C., J. M. Fletcher, M. C. Quigley, A. J. W. Gleadow, and B. P. Kohn (2010), Neogene structural evolution of the Sierra San Felipe, Baja California: Evidence for proto-gulf transtension in the Gulf Extensional Province?, *Tectonophysics*, *488*, 87–109, doi:16/j.tecto.2009.09.026.

Simpson, R. W. (1997), Quantifying Anderson's fault types, *J. Geophys. Res.*, *102*, 17,909–17,919, doi:199710.1029/97JB01274.

Smith, M., and P. Mosley (1993), Crustal heterogeneity and basement influence on the development of the Kenya Rift, East Africa, *Tectonics*, *12*, 591–606, doi:10.1029/92TC01710.

Sokoutis, D., G. Corti, M. Bonini, J. P. Brun, S. Cloetingh, T. Mauduit, and P. Manetti (2007), Modelling the extension of heterogeneous hot lithosphere, *Tectonophysics*, *444*, 63–79, doi:10.1016/j.tecto.2007.08.012.

Sonder, L. J. (1990), Effects of density contrasts on the orientation of stresses in the lithosphere: Relation to principal stress directions in the Transverse Ranges, California, *Tectonics*, *9*, 761–771, doi:10.1029/TC009i004p00761.

Stock, J. M., and K. V. Hodges (1989), Pre-Pliocene Extension around the Gulf of California and the transfer of Baja California to the Pacific Plate, *Tectonics*, *8*, 99–115, doi:10.1029/TC008i001p00099.

Storey, M., J. J. Mahoney, A. D. Saunders, R. A. Duncan, S. P. Kelley, and M. F. Coffin (1995), Timing of Hot Spot—Related Volcanism and the Breakup of Madagascar and India, *Science*, *267*, 852–855, doi:10.1126/science.267.5199.852.

Strecker, M. R., P. M. Blisniuk, and G. H. Eisbacher (1990), Rotation of extension direction in the central Kenya Rift, *Geology*, *18*, 299–302, doi:10.1130/0091-7613(1990)018<0299:ROEDIT>2.3.CO;2.

Suckro, S. K., K. Gohl, T. Funck, I. Heyde, A. Ehrhardt, B. Schreckenberger, J. Gerlings, V. Damm, and W. Jokat (2012), The crustal structure of southern Baffin Bay: Implications from a seismic refraction experiment, *Geophys. J. Int.*, *190*(1), 37–58, doi:10.1111/j.1365-246X.2012.05477.x.

Teyssier, C., B. Tikoff, and M. Markley (1995), Oblique plate motion and continental tectonics, *Geology*, *23*, 447–450, doi:10.1130/0091–7613(1995)023<0447:OPMACT>2.3.CO;2.

Torsvik, T. H., S. Rousse, C. Labails, M. A. Smethurst (2009), A new scheme for the opening of the South Atlantic Ocean and the dissection of an Aptian salt basin, *Geophys. J. Int.*, *177*, 1315–1333, doi:10.1111/j.1365-246X.2010.04727.x.

Tron, V., and J.-P. Brun (1991), Experiments on oblique rifting in brittle-ductile systems, *Tectonophysics*, *188*, 71–84, doi:10.1016/0040–1951(91)90315-J.

Tuckwell, G. W., J. M. Bull, and D. J. Sanderson (1996), Models of fracture orientation at oblique spreading centres, *J. Geol. Soc.*, *153*, 185–189, doi:10.1144/gsjgs.153.2.0185.

Umhoefer, P. J. (2011), Why did the Southern Gulf of California rupture so rapidly?—Oblique divergence across hot, weak lithosphere along a tectonically active margin, *GSA Today*, *21*(11), 4–10, doi:10.1130/G133A.1.

Van Wijk, J. W. (2005), Role of weak zone orientation in continental lithosphere extension, *Geophys. Res. Lett.*, *32*, L02303, doi:10.1029/2004GL022192.

Van Wijk, J. W., and D. K. Blackman (2005), Dynamics of continental rift propagation: The end-member modes, *Earth Planet. Sci. Lett.*, *229*, 247–258, doi:10.1016/j.epsl.2004.10.039.

Van Wijk, J. W., and S. A. P. L. Cloetingh (2002), Basin migration caused by slow lithospheric extension, *Earth Planet. Sci. Lett.*, *198*, 275–288, doi:10.1016/S0012–821X(02)00560-5.

Whittaker, J. M., R. D. Müller, G. Leitchenkov, H. Stagg, M. Sdrolias, C. Gaina, and A. Goncharov (2007), Major Australian-Antarctic plate reorganization at Hawaiian-Emperor bend time, *Science 318*, *83–86*, doi:10.1126/science.1143769.

Wilks, K. R., and N. L. Carter (1990), Rheology of some continental lower crustal rocks, *Tectonophysics*, *182*, 57–77, doi:10.1016/0040–1951(90)90342-6.

Williams, S. E., J. M. Whittaker, and R. D. Müller (2011), Full-fit, palinspastic reconstruction of the conjugate Australian-Antarctic margins, *Tectonics*, *30*, TC6012, doi:201110.1029/2011TC002912.

Withjack, M. O., and W. R. Jamison (1986), Deformation produced by oblique rifting, *Tectonophysics*, *126*, 99–124, doi:10.1016/0040–1951(86)90222-2.

Zoback, M. D., et al. (1987), New evidence on the state of stress of the San Andreas fault system, *Science 238*, 1105–1111, doi:10.1126/science.238.4830.1105.

Zuber, M. T., and E. M. Parmentier (1986), Lithospheric necking: A dynamic model for rift morphology, *Earth Planet. Sci. Lett.*, *77*, 373–383, doi:10.1016/0012-821X(86)90147-0.

Chapter IV - Global Analyses

Article 9

Brune, S., Williams, S.E., Müller, R.D. (2018): Oblique rifting: the rule, not the exception. ***Solid Earth Discussions***, 1-26, doi: 10.5194/se-2018-63.

Article 10

Brune, S., Williams, S.E., Müller, R.D. (2017): Potential links between continental rifting, CO_2 degassing and climate change through time: ***Nature Geoscience***, 10, 941–946, doi: 10.1038/s41561-017-0003-6.

Solid Earth Discuss., https://doi.org/10.5194/se-2018-63
Manuscript under review for journal Solid Earth
Discussion started: 16 July 2018

Solid Earth Discussions
Open Access
EGU

Oblique rifting: the rule, not the exception.

Sascha Brune[1,2], Simon E. Williams[3], & R. Dietmar Müller[3,4]

[1] GFZ German Research Centre for Geosciences, 14473 Potsdam, Germany
[2] Institute of Earth and Environmental Science, University of Potsdam, 14476 Potsdam-Golm, Germany
[3] EarthByte Group, School of Geosciences, University of Sydney, NSW 2006, Australia
[4] Sydney Informatics Hub, University of Sydney, Sydney, NSW, Australia.

Correspondence to: Sascha Brune (brune@gfz-potsdam.de)

Abstract. Movements of tectonic plates often induce oblique deformation at divergent plate boundaries. This is in striking contrast with traditional conceptual models of rifting and rifted margin formation, which often assume 2D deformation where the rift velocity is oriented perpendicular to the plate boundary. Here we quantify the validity of this assumption by analysing the kinematics of major continent-scale rift systems in a global plate tectonic reconstruction from the onset of Pangea breakup until present-day. We evaluate rift obliquity by joint examination of relative extension velocity and local rift trend using the script-based plate reconstruction software pyGPlates. Our results show that the global mean rift obliquity amounts to 34° with a standard deviation of 24°, using the convention that the angle of obliquity is spanned by extension direction and rift trend normal. We find that more than ~70% of all rift segments exceeded an obliquity of 20° demonstrating that oblique rifting should be considered the rule, not the exception. In many cases, rift obliquity and extension velocity increase during rift evolution (e.g. Australia-Antarctica, Gulf of California, South Atlantic, India-Antarctica), which suggests an underlying geodynamic correlation via obliquity-dependent rift strength. Oblique rifting produces 3D stress and strain fields that cannot be accounted for in simplified 2D plane strain analysis. We therefore highlight the importance of 3D approaches in modelling, surveying, and interpretation of most rift segments on Earth where oblique rifting is the dominant mode of deformation.

1 Introduction

The relative motion of Earth's tectonic plates often causes oblique deformation at divergent plate boundaries. This is primarily due to the fact that irregularly shaped plate boundaries generally do not align with small-circles of relative plate movement and that changes in plate motion additionally lead to time-dependent plate boundary obliquity (Philippon and Corti, 2016; Díaz-Azpiroz et al., 2016). Traditionally, rift evolution and passive margin formation has been investigated using 2D conceptual and numerical models assuming an alignment of relative plate motion and plate boundary normal. These studies yielded major insights into first-order subsidence patterns (McKenzie, 1978; White, 1993), described key phases controlling the architecture of rifted margins (Lavier and Manatschal, 2006; Huismans and Beaumont, 2011; Brune et

Solid Earth Discuss., https://doi.org/10.5194/se-2018-63
Manuscript under review for journal Solid Earth
Discussion started: 16 July 2018

al., 2016) and provided insight into the fault evolution during rifting (Ranero and Pérez-Gussinyé, 2010; Brune et al., 2014. The applicability of these concepts and models is often rooted in the assumption that rifts can be understood via plane strain cross-sections orthogonal to the rift trend and that the direction of extension aligns with the orientation of these cross-sections. Many rifts and passive margins however involve segments where the extension direction is not perpendicular to the rift strike such that oblique, non-plane strain configurations occur (Sanderson and Marchini, 1984; Dewey et al., 1998).

Oblique rift segments differ from classical orthogonal examples in several major aspects:

1) In contrast to orthogonal rifts, the initial phase of oblique rifting is characterized by segmented en-échelon border faults that strike transversely to the rift trend. The orientation of these faults is controlled by the interplay of inherited heterogeneities with far-field stresses, whereas diverse modelling studies independently suggest a fault orientation that lies in the middle between the rift trend and the extension-orthogonal direction (Withjack and Jamison, 1986; Clifton et al., 2000; Agostini et al., 2009; Brune and Autin, 2013). These large en-échelon faults generate pronounced relay structures (Fossen and Rotevatn, 2016) which act as a major control on fluvial sediment transport (Gawthorpe and Leeder, 2000).
2) Seismic cross sections at rifted margins are often taken perpendicular to the rift trend, which in most cases is also perpendicular to the coastline. Considering that faults in oblique rifts do not strike parallel to the rift trend, seismic profiles will observe a projection of the fault surface that features a smaller dip angle than the actual 3D fault, an error that might cascade further into seismic restorations.
3) Besides these structural-observational implications, oblique rifting appears to be a major factor in governing the geodynamic evolution of extensional systems. This has been shown via several lines of evidence: (i) Oblique rifting has been inferred to enhance strain localisation by enabling the formation of pull-apart basins and large-offset strike-slip faults, for instance during the Gulf of California opening (Bennett and Oskin, 2014; van Wijk et al., 2017). (ii) Analytical and numerical modelling suggests that the force required to maintain a given rift velocity is anti-correlated with the rift's obliquity. The reason for this behaviour is that plastic yielding takes place at smaller tectonic force when the extension is oblique to the rift trend (Brune et al., 2012). (iii) At the same extension velocity, oblique rifts deform with a certain rift parallel shear rate, which is balanced by a lower rift-perpendicular extension velocity. This means that oblique segments of a particular rift accommodate lithospheric and crustal thinning at a lower rate than orthogonal segments of the same rift, a difference that effects the thermal configuration and therefore the structural and magmatic evolution of each segment (Montési and Behn, 2007).
4) Oblique rifting holds geodynamic implications on the global scale because of its relation to toroidal plate motion, i.e. vertical axis rotation components of plate movements and associated strike-slip deformation. Toroidal motion is enigmatic from the perspective of plate driving forces, because its purely horizontal motion cannot be directly caused by buoyancy forces in Earth's interior (Lithgow-Bertelloni et al., 1993; Bercovici, 2003). Oblique rifts

Solid Earth Discuss., https://doi.org/10.5194/se-2018-63
Manuscript under review for journal Solid Earth
Discussion started: 16 July 2018

feature strike-slip velocity components and therefore contribute to toroidal motion, while orthogonal rifts are an expression of purely buoyancy-driven (poloidal) flow.

The impact of rift obliquity on the structural architecture of continental extensional systems varies between natural cases. This is mainly due to rift variability in general, which arises from tectonic inheritance (Manatschal et al., 2015; Morley, 2016; Hodge et al., 2018; Phillips et al., 2018), or from along-strike changes in rheology, crustal configuration, temperature and rift velocity (e.g. Sippel et al., 2017; Molnar et al., 2017; Brune, et al., 2017b; Mondy et al., 2017).

Oblique rifting in presently active rifts can be easily deduced by combining the local rift trend and GNSS-based surface velocities (Díaz-Azpiroz et al., 2016). Prominent examples are the Main Ethiopian rift (Corti, 2008), the Levant rift system including the Dead Sea rift (Mart et al., 2005), the Gulf of California rift (Atwater and Stock, 1998; Fletcher et al., 2007) and the Upper Rhine Graben (Bertrand et al., 2005). Structure and kinematics of past rift systems has been studied by surveying obliquely rifted margins (Fournier et al., 2004; Lizarralde et al., 2007; Klimke and Franke, 2016) and transform continental margins (Basile, 2015; Mericer de Lépinay et al., 2016). However, quantifying rift obliquity of a specific rift system through time is more difficult since the syn-rift velocity evolution needs to be reconstructed from available geophysical and geological data sets. Therefore, a global statistical analysis of rift obliquity through geological time has been missing so far.

Here we strive to fill this gap by deducing the first-order obliquity history of Earth's major rifts from the onset of Pangea fragmentation to present-day. We first describe the applied methods and data sets, then we focus on major individual rift systems that lead to the formation of the Atlantic and Indian Ocean basins before we assess rift obliquity evolution and average obliquity on a global scale.

2 Methods and data

2.1. Rift kinematics

We quantify extension velocity using the global kinematic plate reconstruction of Müller et al. (2016). This plate model integrates the latest syn-rift reconstructions for the South Atlantic (Heine et al., 2013), North Atlantic (Barnett-Moore et al., 2016; Hosseinpour et al., 2013), Australia-Antarctica separation and India-Antarctica breakup (Williams et al., 2011; Whittaker et al., 2013; Gibbons et al., 2015), as well as Gulf of California opening (McQuarrie and Wernicke, 2005) among others (Figure 1).

Solid Earth Discuss., https://doi.org/10.5194/se-2018-63
Manuscript under review for journal Solid Earth
Discussion started: 16 July 2018

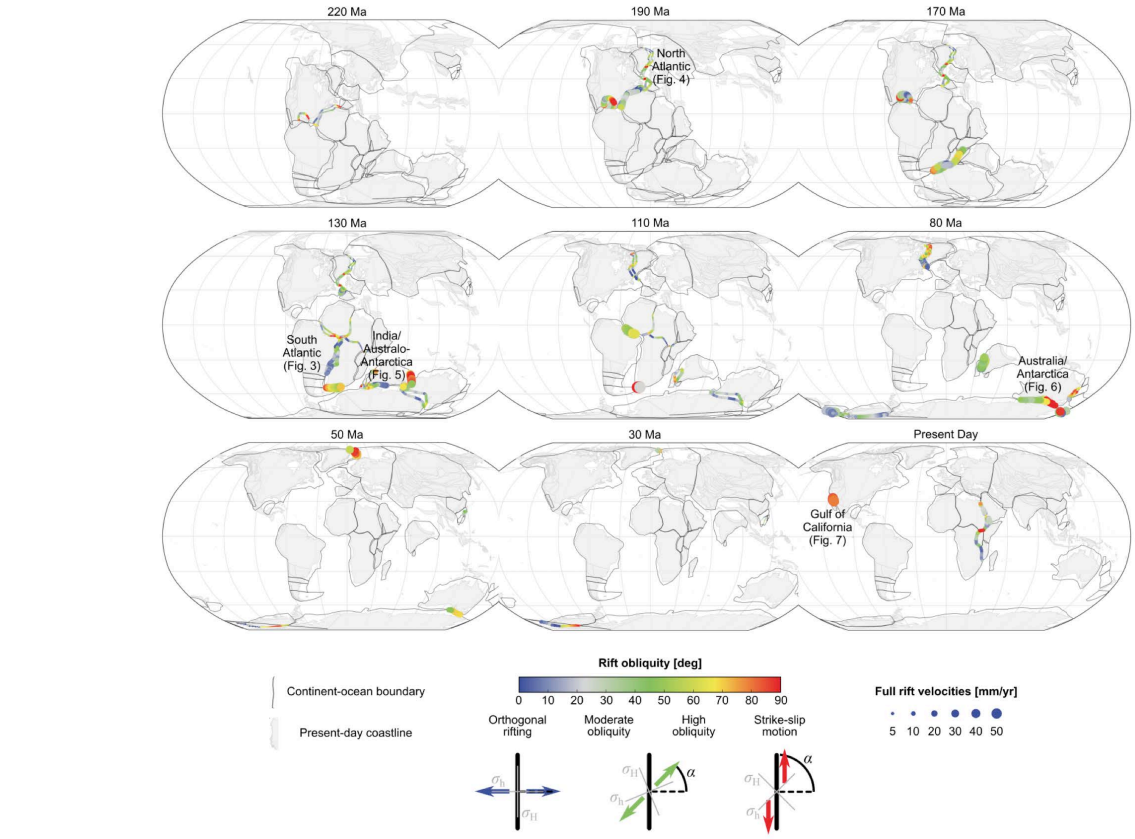

Figure 1. Global overview of rift obliquity and velocity. Rift obliquity is measured as angle α spanned by the relative plate velocity vector and the rift trend normal. The impact of rift obliquity on the rotation of largest and smallest horizontal stress components (σ_H and σ_h, respectively) is depicted at the bottom of the figure. Rotations from Müller et al. (2016). Continent-ocean boundaries from Brune et al. (2016).

Restoration of the relative position of continents prior to rifting in aforementioned regional studies is largely based on deriving the amount of syn-rift extension from present-day crustal thickness (e.g. Williams et al., 2011; Kneller et al., 2012). The kinematic evolution before breakup, i.e. prior to the occurrence of oceanic fracture zones and oceanic magnetic anomalies, has to be inferred via careful joint interpretation of several geological indicators. Rift initiation for instance can be constrained through the ages of syn-rift sediments and rift-related volcanism, which give a minimum age for the beginning of rifting. Later syn-rift kinematics can be inferred from seismic tectono-stratigraphy and dating of rocks that have

Solid Earth Discuss., https://doi.org/10.5194/se-2018-63
Manuscript under review for journal Solid Earth
Discussion started: 16 July 2018

been drilled or dredged within the continent–ocean transition, while additional information can be derived from kinematic indicators at neighbouring plate boundaries.

2.2. Rift trend

We define the rift trend as the general direction of a rift segment. Considering a typical rift width of ~100 km, the most suitable wavelength to analyse rift trend variations is several hundred kilometres. Here we associate rift trend variations with the present-day boundary between continental and oceanic crust, often referred to as continent-ocean boundaries (COBs). COBs better reflect the actual rift trend than for instance present-day coastlines, since the latter are primarily affected by eustatic sea-level variations and local vertical motions (Figure 2a).

Considering COBs as sharp boundaries does not reflect the crustal complexity in these areas, which mirrors the convoluted interplay of tectonic, magmatic, and sedimentary processes. We therefore define two COB end-member sets that reflect the earliest and latest possible breakup based on available seismic refraction data (Brune et al., 2016). These COBs have simplified geometries and are designed to capture the regional geometry of boundaries between continental and oceanic crust

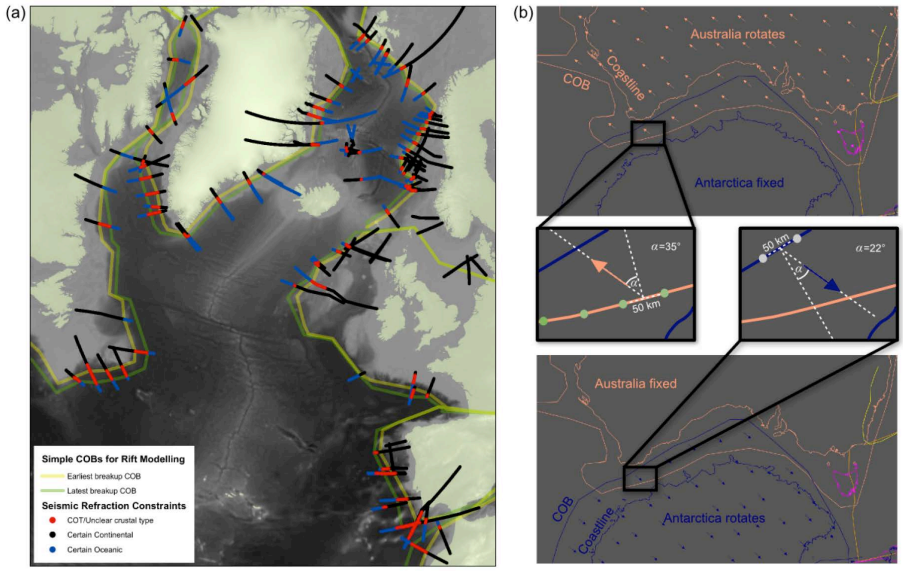

Figure 2. Methods illustration. (a) End-member sets of continent-ocean boundaries are based on seismic refraction data, here exemplified for the North Atlantic. The latest breakup COB constitutes our reference model while the earliest breakup COB is used for robustness tests. **(b)** Kinematic analysis approach exemplified for Australia-Antarctica rifting.

Solid Earth Discuss., https://doi.org/10.5194/se-2018-63
Manuscript under review for journal Solid Earth
Discussion started: 16 July 2018

without a detailed assimilation of local data reflecting fine-scale deviations from these regional trends. Figure 2a depicts both the early and the late breakup COB data sets exemplified for the North Atlantic illustrating that the overall direction of the rift trend is not affected by the precise location of the COB.

The employed reconstruction is using rigid plate polygons and does not directly capture plate boundary deformation. Thus, in a pre-rift reconstruction, present-day COBs from conjugate passive margins will show significant overlap (Figure 1), where the amount of overlap is a proxy for the subsequent extension before breakup. As the plates move apart the overlap decreases, and the moment within the reconstructions where there is no longer overlap in each segment defines the transition from rifting to seafloor spreading. Within this methodology, the two central implications of how we interpret COB geometries for our purposes is that they control the time of breakup along the margins, and that they define the orientation of each rift segment.

2.3 Rift obliquity

Using the COB orientation as a proxy for the rift trend, and accounting for the local direction of relative plate motions, we calculate rift obliquity for all points within an active rift at any time during post-Pangea extension. This workflow is illustrated in Figure 2b, where we first keep Antarctica fixed in order to evaluate the rift obliquity at an Australian COB location and secondly we fix Australia and estimate rift obliquity for a point at the Antarctic COB. Note that the conjugate values for local rift obliquity are very similar but not the same. We therefore average obliquity values from conjugate margins during our statistical analysis. This analysis is repeated in 1 million year intervals until the conjugate COBs do not overlap anymore and the tectonic formation of the rifted margin ends.

We apply our workflow in an automated way using the python library pyGPlates that allows script-based access to GPlates functionality. GPlates is a free plate reconstruction software (www.gplates.org) that allows reconstructing and analysing plate motions through geological time (Müller et al., 2018). In the following, we use a spacing of 50 km between individual sample points where we extract relative plate velocity and obliquity. That spacing is dense enough to capture the relevant changes in rift trend. We also tested smaller point distances, which did not affect our conclusions.

The limitations of this analysis workflow coincide with the limits of plate tectonic reconstructions in general. Many rifts and especially failed rifts are not included in plate tectonic reconstructions yet, which somewhat biases our study towards rifted margins. Future improvements in plate tectonic reconstructions and in defining COBs will enhance our results, however, by testing several end-member scenarios in section 4 we can already anticipate that our main conclusions will still hold even though the detailed values might change.

Solid Earth Discuss., https://doi.org/10.5194/se-2018-63
Manuscript under review for journal Solid Earth
Discussion started: 16 July 2018

In this study we follow the convention that defines the angle of obliquity as the angle between extension direction and local rift trend normal. This means that 0° represents orthogonal rifting while 90° stands for strike-slip motion. Note that this definition follows many previous studies (e.g. Fournier and Petit, 2007; Philippon et al., 2015; Brune, 2016; Zwaan and Schreurs, 2017; Ammann et al., 2017), but is opposite to the convention used in almost as many articles (e.g. Tron and Brun, 1991; Teyssier et al., 1995; Clifton and Schlische, 2001; Deng et al., 2018).

There is clearly a gradual transition from orthogonal rifting to oblique extension, especially since individual fault evolution is subject to natural variability. In this study, however, where we investigate the frequency of oblique rifting, it appears to be useful to draw a line between orthogonal and oblique extension. In simplified model settings, previous studies suggested that qualitative differences in the rifting style emerge when rift obliquity exceeds 15 to 20° (Clifton et al., 2000; Agostini et al., 2009; Brune, 2014; Zwaan et al., 2016). Keeping in mind that the specific value is somewhat arbitrary, we will use 20° as the critical obliquity separating orthogonal from oblique rifts.

3 Regional analysis of individual rift systems

In this section our plate tectonic analysis is employed focussing on individual post-Pangea rift systems (Fig. 1). In doing so, we relate the structural history of each rift with its obliquity and velocity evolution.

3.1. South Atlantic Rift

The orientation of the different South Atlantic Rift segments has been affected by reactivation of mobile belts, which formed during the pan-African orogeny in the Neoproterozoic and early Paleozoic (Kröner and Stern, 2004). This reactivation of inherited weaknesses is an ubiquitous process of the Wilson cycle that has also been evoked to explain the formation of the present-day East African Rift System (Daly et al., 1989; Hetzel and Strecker, 1994). It has been suggested that 65% of the South Atlantic Rift developed with near-parallel orientation to the pan-African fabric (de Wit et al., 2008) evidencing the strong control of tectonic inheritance on the South Atlantic rift obliquity.

We find that low obliquity predominates in the central and southern segment of the South Atlantic rift (Figure 3). High rift obliquities are encountered in the Equatorial Atlantic and in the southernmost shear zone that ultimately develops into the Falkland-Agulhas fracture zone. Our analysis shows that this system initially features a wide range of rift obliquities (Figure 3b) and trends to higher obliquity after 120 million years ago (Ma) when only the northern and southernmost segments are active. The frequency diagram of rift obliquity displays a bimodal distribution with the 0-25° range representing the southern South Atlantic while the 45-65° range is dominated by Equatorial South Atlantic rift geometry (Figure 3c). The overall mean obliquity at 38° lies in–between these two peaks while 68% of the rift formed at moderate to high rift obliquity larger than 20°.

Solid Earth Discuss., https://doi.org/10.5194/se-2018-63
Manuscript under review for journal Solid Earth
Discussion started: 16 July 2018

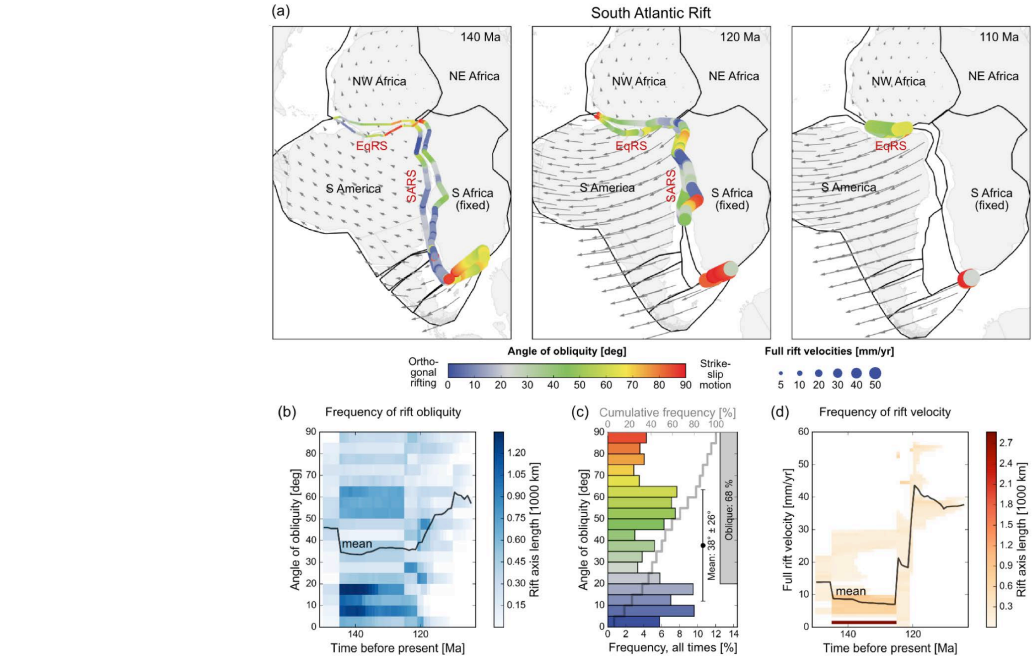

Figure 3. South Atlantic rift. Low rift obliquity prevails in the central and southern segment of the South Atlantic rift whereas high obliquities and strike-slip motion dominates the northern and southernmost segments. Rift velocity and obliquity increase jointly starting at 120 Ma. EqRS – Equatorial Atlantic Rift System; SARS – South Atlantic Rift System.

The rotational rifting of the South Atlantic with an initial Euler pole close to West Africa leads to higher rift velocities in the south than in the north. The mean rift velocity of the entire rift displays an initial, slow phase lasting more than 20 million years, followed by rift acceleration during a few million years and finally a fast phase of rifting prior to the transition to sea-floor spreading (Heine et al., 2013; Brune et al., 2016). This two-phase evolution can also be seen in alternative reconstructions (Nürnberg and Müller, 1991; Torsvik et al., 2009; Moulin et al., 2010; Granot and Dyment, 2015) although it is partitioned between individual South American blocks for some studies (Brune et al., 2016). Interestingly, the evolution of rift obliquity and velocity appears to be correlated. On one side this shows that oblique segments need more time to reach breakup since the effective rift-perpendicular velocity is smaller than in neighbouring purely orthogonal rift segments. To a certain degree, however, this might be due to the fact that oblique rifting requires less tectonic force, which leads to a higher rift velocity at constant extensional stress (Brune et al., 2012).

Solid Earth Discuss., https://doi.org/10.5194/se-2018-63
Manuscript under review for journal Solid Earth
Discussion started: 16 July 2018

3.2. North Atlantic Rift

The formation of the North Atlantic involved a protracted rift history involving several major plates (Eurasia, Greenland, Iberia, North America). Initial inherited weaknesses from the Caledonian orogeny have been reactivated in episodic continental extension that is recorded in Carboniferous to Permian basins (Doré, 1991; Lundin and Doré, 1997). The Mesozoic is marked by extensive crustal thinning that lead to formation and abandonment of major rift arms like the Rockall Trough, the Porcupine, Orphan, Møre, and Faroe-Shetland Basin (Skogseid et al., 2000; Faleide et al., 2008; Peron-Pinvidic et al., 2013). However, Mesozoic rifting also induced continental breakup in the Iberia-Newfoundland segment, the Bay of Biscay, and the North Atlantic rift south of Greenland (Féraud et al., 1996; Nirrengarten et al., 2018; Tugend et al., 2014). Opening of the Labrador Sea and rifting between Greenland and Europe competed for many tens of million years (Dickie et al., 2011; Hosseinpour et al., 2013; Barnett-Moore et al., 2016) before the present-day North East Atlantic mid-ocean ridge formed in Eocene times (Gernigon et al., 2015; Gaina et al., 2017) possibly due to the arrival of the Iceland hotspot (Coffin and Eldholm, 1992; Storey et al., 2007). Final separation between Greenland and Europe took place along the sheared margin of the Fram Strait in Miocene times ~17-15 Ma (Jakobsson et al., 2007; Knies and Gaina, 2008).

Multiple plate motion changes reflect the complex tectonic history of the North Atlantic during the last 200 million years. These changes translate to time-dependent rift obliquity in each of the major rift branches (Figure 4). Between 200 and 120 Ma, the rift branches east and south of Greenland deform at 35° to 60° rift obliquity which leads to a pronounced peak within this obliquity range in Figure 4b and 4c. This changes in the Early Cretaceous with the more northward movement of Greenland and generates almost orthogonal rifting between Greenland and Europe until breakup. Due to the northward propagation of sea-floor spreading, the Iberia-Newfoundland rift is excluded from the later plate motion changes and hence formed during low extension obliquity. The latest stage of continental rifting is marked by more than 30 million years of high-obliquity shear between northern Greenland and northwest Europe.

The absolute frequency of rift obliquity is marked by two peaks at 0° and 45° (Figure 4c). While this bears some similarity with the South Atlantic (Figure 3c), the underlying reason for these two distinct peaks is not linked to the different orientation of two rift branches (like in the South Atlantic), but is a result of Greenland's plate motion change at around 120 Ma (Figure 4a,b). Except for Iberia-Newfoundland and the Labrador Sea, which evolved at low obliquity, most rift branches experienced moderate or high rift obliquity during the entire rift history. More than 70% of the rifts involved an obliquity of more than 20° and the overall mean obliquity of the North Atlantic rift amounts to 34° (Figure 4c).

Solid Earth Discuss., https://doi.org/10.5194/se-2018-63
Manuscript under review for journal Solid Earth
Discussion started: 16 July 2018

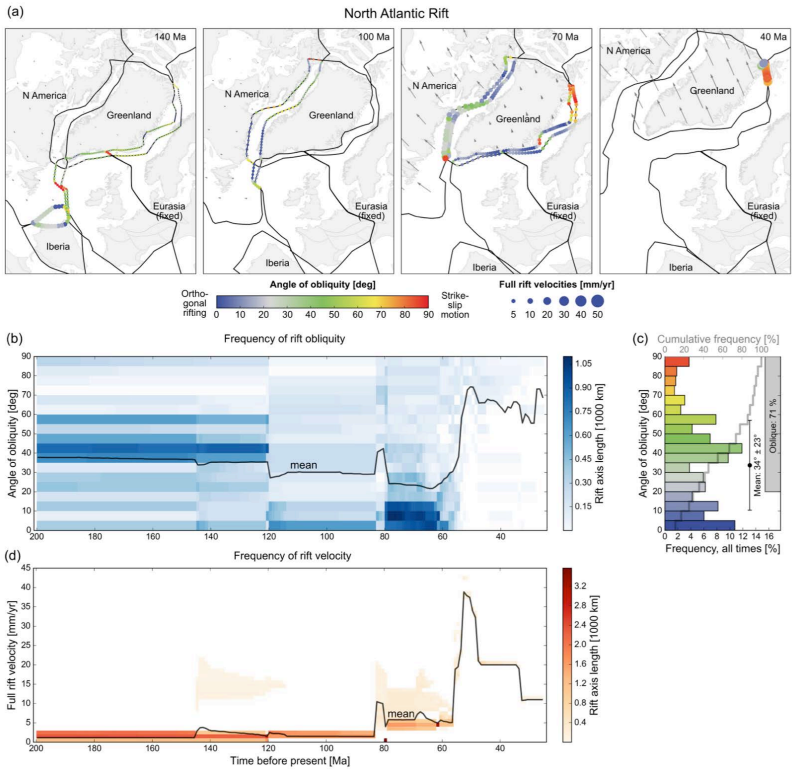

Figure 4. North Atlantic rift. Several changes in plate motion mirror the complex tectonic history of the North Atlantic during the last 200 million years. A distinct increase in syn-rift obliquity occurs at 50 Ma prior to final breakup between northern Greenland and northwest Europe.

3.3. Rifting between India and Australo-Antarctica

Mesozoic rifting within eastern Gondwana lead to continental fragmentation beginning with the separation of India (together with Sri Lanka and Madagascar) from Australia and Antarctic in the Early (Powell et al., 1988; Gibbons et al., 2013). The timing and kinematics of breakup and spreading between Australia and India is well constrained (Williams et al., 2013; Whittaker et al., 2016) and although the precise geometry of greater India is obscured by subsequent deformation during India-Eurasia collision, the divergence between India and Australia is thought to have involved a significant component of oblique motion along greater India's northern margin recorded by the Wallaby-Zenith Fracture Zone (Ali and Aitchison, 2014). Initial breakup between India and Antarctica is recorded in the Enderby Basin becoming progressively younger to the

Solid Earth Discuss., https://doi.org/10.5194/se-2018-63
Manuscript under review for journal Solid Earth
Discussion started: 16 July 2018

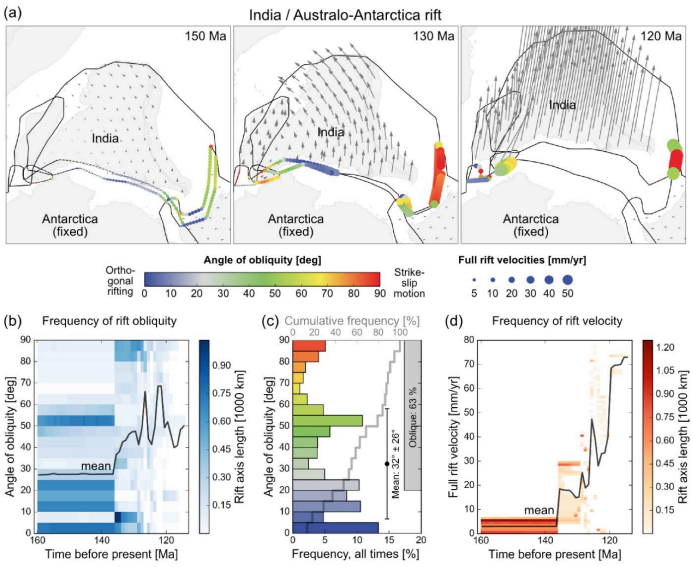

Figure 5. India / Australo-Antarctica rift. Rift obliquity is dominated by two major rift trends – the low obliquity India-Antarctica branch and the highly oblique India-Australia branch. For simplicity, we neglect low-velocity relative motion between Antarctica and Australia, which will be discussed in Figure 6.

west (Gibbons et al., 2013; Davis et al., 2016) and involved significant ridge jumps that isolated the Elan Bank microcontinent (Borissova et al., 2003).

Rotational rifting between East India and Australo-Antarctica with an Euler pole close to the southwestern tip of India induces almost orthogonal rifting between India and Antarctica, and predominantly oblique rifting between India and West Australia (Figure 5). After 135 Ma, continued high obliquity shear along the northern Indian margin and Australia finally culminates in the formation of the Wallaby–Zenith Fracture Zone, the northern boundary of the Perth abyssal plain. At the same time breakup propagates from east to west along the East Indian margin, so that the mean rift obliquity is more and more dominated by high-angle shearing.

The rift obliquity distribution in Figure 5c reflects the existence of two major rift trends – the low obliquity India-Antarctica branch of 0° to 25° and the highly oblique India-Australia branch with more than 45°. The mean obliquity of the entire rift system amounts to 32° while more than 63% of the rift evolved at obliquity angles higher than 20°. Prior und during large parts of the breakup, the velocity and obliquity of the rift system are positively correlated.

Solid Earth Discuss., https://doi.org/10.5194/se-2018-63
Manuscript under review for journal Solid Earth
Discussion started: 16 July 2018

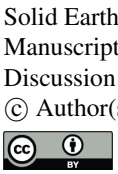

Solid Earth
Discussions
Open Access
EGU

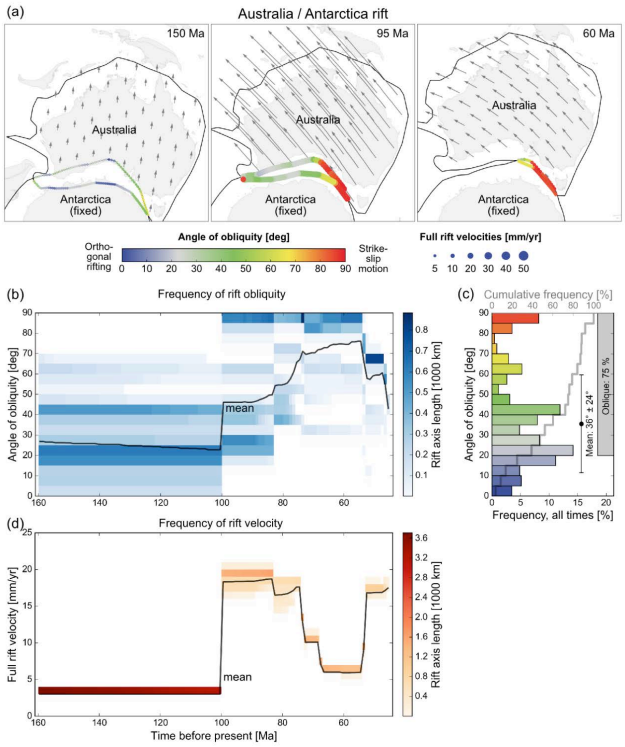

Figure 6. Australia / Antarctica rift. A distinct change in plate motion takes place at 100 Ma generating two discrete phases: (1) slow rifting at moderate obliquity, (2) fast rifting at high obliquity.

3.4. Australia / Antarctica

Phases of rifting between Australia and Antarctica are recorded beginning in the Late Jurassic (Powell et al., 1988; Ball et al., 2013) but continental breakup did not begin until the late Cretaceous and progressed diachronously from west to east. Within this rift system, the signatures of oblique extension have been previously recognised along Australia's southern margin (Willcox and Stagg, 1990; Norvick and Smith, 2001). Lithospheric breakup was complex and protracted (Gillard et al., 2015, 2016), leaving unresolved questions surrounding the nature of the crust in the continent-ocean transition and the oldest interpreted seafloor spreading magnetic lineations. Reconstructions of the rift kinematics must therefore incorporate other geological constraints from along the Australia-Antarctica plate boundary system (Whittaker et al., 2013). This

Solid Earth Discuss., https://doi.org/10.5194/se-2018-63
Manuscript under review for journal Solid Earth
Discussion started: 16 July 2018

reconstruction, in common with earlier studies (Powell et al., 1988; Royer and Sandwell, 1989), comprises an oblique component of divergence during the Late Cretaceous prior to a change in plate motion direction in the early Cenozoic.

The first-order history of rift obliquity can be understood by considering two distinct conditions. (i) Due to the concave shape of the southern Australian margin and their Antarctic conjugates, there are two major rift trends along the Australia-Antarctica rift (Figure 6). (ii) According to the plate tectonic reconstruction (Williams et al., 2011), there has been a significant change in relative plate motion at around 100 Ma from a northward to a northwestward directed plate velocity. The two existing rift trends explain the dichotomy in rift obliquity of 10°-20° and 35°-45° from the onset of rifting until 100 Ma (Figure 6b). The plate motion change at 100 Ma however, shifts the rift obliquity in both branches to higher angles of 20°-45° and 80°-90°, respectively.

The velocity history displays a prominent increase at 100 Ma that corresponds to the increased rift obliquity via a plate motion change. An increase in the rate of plate divergence in the Late Cretaceous is corroborated by structural restoration studies based on seismic profiles (Espurt et al., 2012) and the rate of divergence is similar to that interpreted from initial seafloor spreading anomalies (Tikku and Cande, 1999; Whittaker et al., 2013). Interestingly, after more than 20 million years of fast divergence, the relative plate velocity inferred from magnetic anomalies decreases again. If correct, this decrease cannot be related to Australia-Antarctica plate boundary dynamics, since at this time the rift system consists only of the last remaining continental bridge between Tasmania and Antarctica while the majority of the plate boundary already transitioned to sea floor spreading.

A further noteworthy aspect of Australia-Antarctic divergence is the failure of rifting between Tasmania and the southeast Australian mainland. Extension in the Bass and Gippsland basins occurred predominantly in the Early Cretaceous (e.g. Power et al., 2001). In the Late Cretaceous, rifting between Australia and Antarctica localised between western Tasmania and Cape Adare, where breakup eventually occurred. The higher obliquity of the successful plate boundary compared to the failed rift arm in Bass Strait may explain why this rift was favoured, similar to the successful opening of the Equatorial Atlantic in favour of a Saharan Ocean during South Atlantic formation (Heine and Brune, 2014).

3.5. Gulf of California

The Gulf of California constitutes the youngest rift system in our analysis, which is why its temporal evolution is known in much greater detail than the previous case examples. The first phase of the Gulf of California rift is closely linked to the Greater Basin and Range extensional zone. Tectono-stratigraphy and dated rift-related magmatic rocks show that the onset of continental extension must have occurred before the mid-Miocene (Ferrari et al., 2013; Duque-Trujillo et al., 2015). This first phase of slow rifting is marked by a wide rift style characteristic of the present-day Basin and Range region. An increase in both rift velocity and rift obliquity has been suggested as the underlying reason for basin-ward localisation and finally the

Solid Earth Discuss., https://doi.org/10.5194/se-2018-63
Manuscript under review for journal Solid Earth
Discussion started: 16 July 2018

Solid Earth Discussions
Open Access
EGU

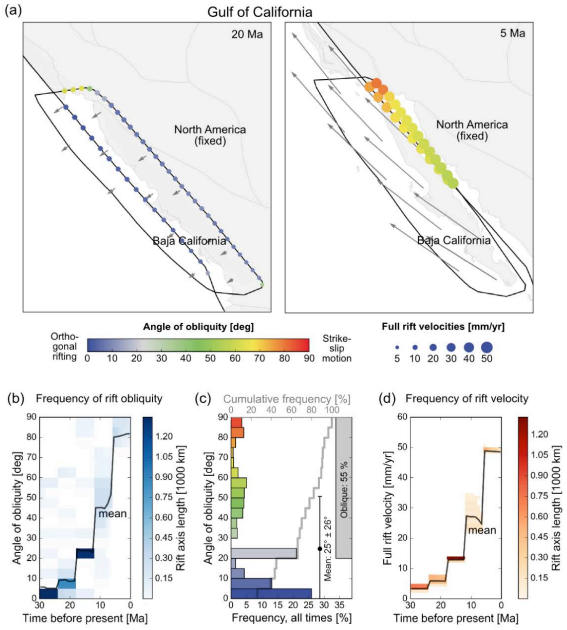

Figure 7. Gulf of California rift. The initial rift phase is characterised by slow, predominantly orthogonal rifting and associated with a wide rift. An increase in rift obliquity enhances localisation between 20 and 10 Ma inducing continental breakup. The obliquity and velocity of this rift increases almost proportionally.

transition to sea floor spreading in the southern Gulf of California (Bennett and Oskin, 2014; Darin et al., 2016; van Wijk et al., 2017). This change in plate motion at ~12 Ma has been explained by the final cessation of subduction in this region so that most of the relative plate motion between Pacific and North America had to be taken up by transform motion between Baja California and the North American mainland (Atwater and Stock, 1998; Oskin and Stock, 2003).

The transition from orthogonal to highly oblique rifting is captured by the tectonic reconstruction (McQuarrie and Wernicke, 2005) our plate model is built on (Figure 7a). According to that reconstruction, the transition occurs during a time frame of less than 10 million years between 20 and 10 Ma (Umhoefer, 2011). That transition is mirrored in our analysis by a gradual increase in rift obliquity from less than 10° prior to 18 Ma to 20-25° between 18 and 12 Ma up to 40-90° from 12 Ma until present-day (Figure 7b).

A striking feature of the Gulf of California rift is that throughout the existence of this plate boundary the velocity evolved almost proportional to the rift obliquity (Figure 7b,d) hinting at a causal relationship between these two variables. Two

Solid Earth Discuss., https://doi.org/10.5194/se-2018-63
Manuscript under review for journal Solid Earth
Discussion started: 16 July 2018

processes have been proposed to explain this proportionality: (i) Numerical and analytical modelling suggests that oblique extension requires less tectonic force than orthogonal rifting (Brune et al., 2012). The reason is that when extension is oblique to the rift trend, the plastic yield strength is reached at up to 50% less tectonic force. (ii) Localization within the lithosphere is enhanced by obliquity-related formation of pull-apart basins and associated energy-efficient strike-slip faults (Umhoefer, 2011; Bennett and Oskin, 2014; van Wijk et al., 2017). Both processes apply to the Gulf of California and may in fact be simply different expressions of the same underlying cause, namely that oblique rifting is mechanically preferred.

4 Global analysis

In this section we evaluate global rift obliquity since the onset of Pangea fragmentation in terms of temporal and spatial variability. Analysing all rift systems of our global plate tectonic model during the last 230 million years, we here test the robustness of our study by additionally considering the impact on passive margin area and by employing an alternative set of continent-ocean boundaries.

The extent of major rift systems varied through time (Figure 8a), with a pronounced peak between 160 and 110 million years ago when many rifts of the Atlantic and Indian Ocean where simultaneously active. Figure 8b illustrates that almost all angles of obliquity are represented at any given time. Interestingly, obliquities in the range between 70° and 85° seem to be underrepresented while almost pure strike-slip systems are an ubiquitous feature. This finding might be explained by the fact that the transition from normal faulting to strike-slip faulting in ideal materials occurs at around 70° (Withjack and Jamison, 1986). We therefore speculate that once major continental strike-slip faults form, the plate boundary adjusts to a velocity-parallel configuration entailing the formation of a transform margin (Ammann et al., 2017), which also explains the relatively high peak at 90° obliquity (Figure 8b,c).

In our reference model, we compute a mean global obliquity of 34° with a standard deviation of 24° since the inception of Pangea breakup. We also find that 69% of all rifts deform in oblique rift mode, i.e. with obliquities exceeding 20° (Figure 8c), illustrating that oblique rifting appears to be the rule on Earth rather than the exception.

So far, we analysed the frequency of obliquity with respect to rift length, where transform margins and rifted margins are given the same relative importance. Now we focus briefly on the surface area that is generated during passive margin formation, which is also a proxy for the size of sedimentary basins. We note that it is the rift-orthogonal velocity component, which leads to lithospheric stretching and generates passive margin area, while the rift parallel component merely induces an along-strike offset. Hence we compute how many square kilometres of passive margin are generated per million year by multiplying the rift length of each small rift segment with its segment-orthogonal velocity component. The resulting distribution reflects the relative importance of rift obliquity weighted by passive margin area, which essentially leads to a

Solid Earth Discuss., https://doi.org/10.5194/se-2018-63
Manuscript under review for journal Solid Earth
Discussion started: 16 July 2018

shift towards lower obliquity values. Nevertheless, we find an average obliquity of 29° and a total of 67% of passive margin area affected by obliquity angles larger than 20° (Figure 8e).

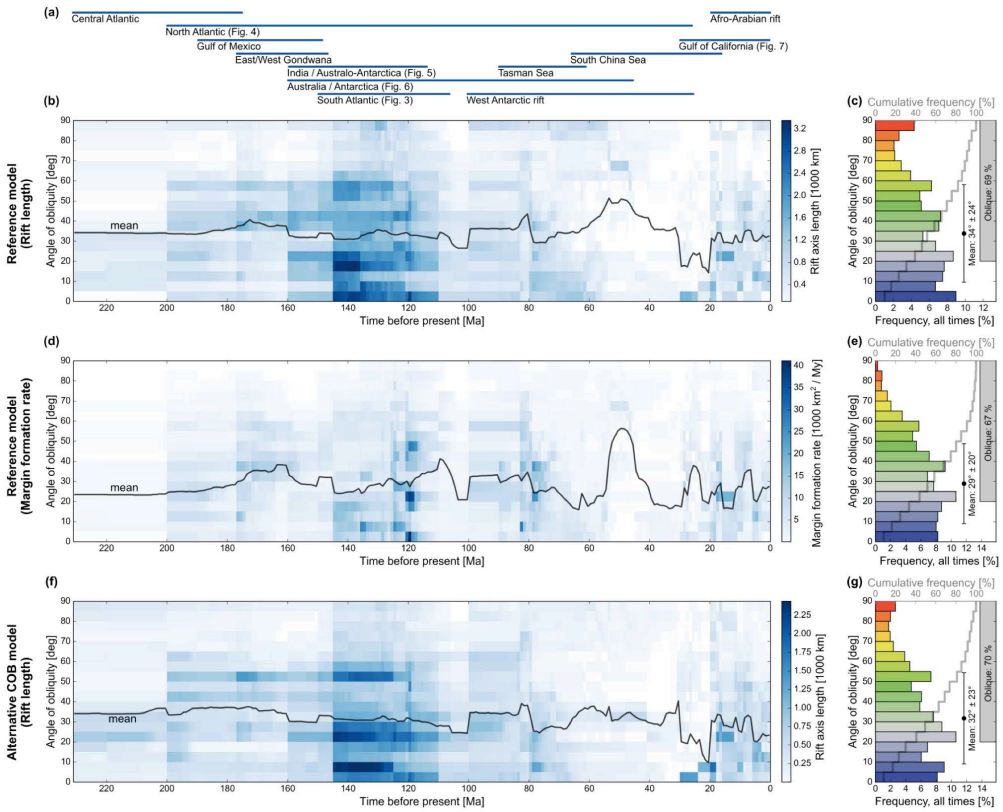

Figure 8. Global analysis of rift obliquity. (a) Variations of major rift system activity. Note that many rifts of the Atlantic and Indian Ocean where simultaneously active between 160 and 110 Ma**. (b,c)** Rift obliquity in terms of rift length for the reference model employing late-breakup COBs (see Sect. 2.2 and Fig. 2 for more details). **(d,e)** The reference model analysed in terms of margin formation rate (i.e. rift segment length multiplied with segment-orthogonal velocity component). **(f,g)** An alternative model employing early-breakup COBs. All three models result in global mean rift obliquities of ~30° and oblique rifting for more than ~70% illustrating the robustness of our results.

Solid Earth Discuss., https://doi.org/10.5194/se-2018-63
Manuscript under review for journal Solid Earth
Discussion started: 16 July 2018

We test the impact of an alternative set of continent-ocean boundaries (Figure 2), which represents the continent-ward end member and hence stands for an earlier breakup time (Section 2.2). While the total rift length is reduced with respect to the reference model, we find that the first-order pattern of obliquity evolution is not affected. Also, the mean rift obliquity of 32° and the rift length percentage affected by oblique deformation (70%) is almost identical to the late-breakup end-member.

Finally, we map the time-averaged obliquity at each rift element (Figure 9). The advantage of this approach is that one can easily identify each point's rift obliquity that dominated the tectonic evolution, however, one has to keep in mind that changes in rift obliquity are not visualised. Figure 9 shows that only a few rifts exhibit a pure rift-orthogonal extension velocity such as the Labrador Sea, the east Indian margin and some locations in the North and South Atlantic. Instead, many rifted margins feature moderate rift obliquity between 20° and 40° like the West Iberia margin, the Red Sea, as well as the central and southern segment of the South Atlantic. To a large extent, however, the dominant rift obliquity exceeds even 40°, for instance in the Gulf of Mexico, the Equatorial South Atlantic, the Gulf of Aden, the east African margins, the West Antarctic Rift, the Tasman Sea and also the sheared margins of the Fram Strait, Madagascar, and Western Australia.

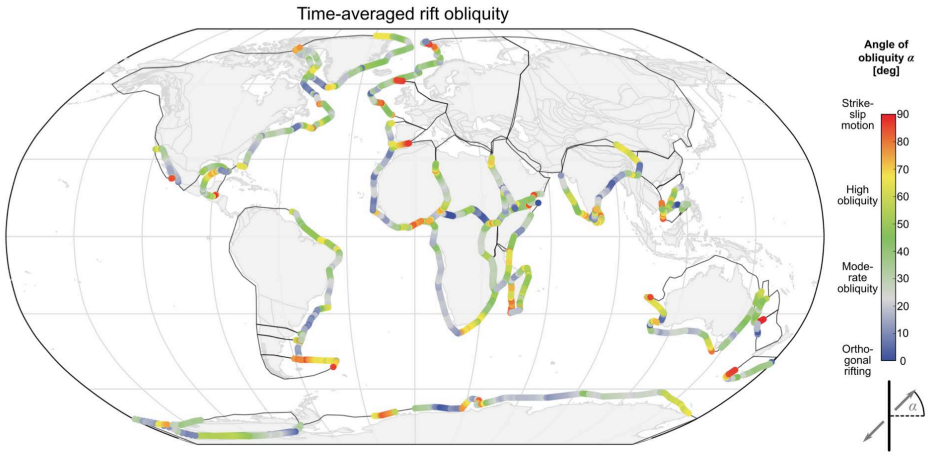

Figure 9. Global map of mean rift obliquity. For each rift point we display the time-averaged rift obliquity illustrating the prevalence of oblique rifting since Pangea fragmentation. Note that temporal changes of rift obliquity cannot be visualised in this plot.

Solid Earth Discuss., https://doi.org/10.5194/se-2018-63
Manuscript under review for journal Solid Earth
Discussion started: 16 July 2018

5 Discussion

Previous studies quantified the present-day plate boundary obliquity in general terms and on long wavelength by considering extensional, compressional, and transform plate boundary types. Woodcock (1986) noted that 59% of all present-day plate boundaries feature obliquities larger than 22 degrees. A more detailed recent study found even higher obliquity by showing that 65% of present-day plate boundaries exhibit >30° obliquity (Philippon and Corti, 2016). In the latter study, this result was further decomposed by plate boundary type illustrating that 73% of rifts and mid-ocean ridges extend at more than 30° obliquity. While these previous studies did not focus on rift obliquity, they nevertheless are consistent with our results by highlighting that oblique plate boundary deformation constitutes the rule and not the exception.

Jeanniot and Buiter (2018) quantified the margin width of transtensionally formed rifted margins and thereby estimated the rift obliquity of 26 major rift segments worldwide. They find a weak positive correlation between obliquity and width of a rift system; however, at highly oblique margins this relationship breaks down and these margins are not only significantly narrower than orthogonal margins, but they also exhibit large-offset transform faults. In contrast to our approach, Jeanniot and Buiter (2018) did not focus on the temporal evolution of rift obliquity. Nonetheless, for the time-averaged obliquity (Figure 9) we find a very good correspondence with their results illustrating the robustness of both approaches.

In general terms, oblique deformation takes place whenever a plate boundary exhibits irregular trends (Dewey et al., 1998) and is therefore an obvious ingredient of plate boundary tectonics. However, we speculate that the unexpectedly high percentage of oblique rifts and rifted margins could also reflect the existence of an underlying geodynamic process that influences plate velocities and thereby affects the resulting obliquity distribution. Previous analogue and numerical models suggest oblique rifting as a mechanically preferred type of continental extension (Chemenda et al., 2002; Brune et al., 2012). The reason for this behaviour has been deduced by means of analytical modelling suggesting that plastic yielding takes place at less tectonic force when the relative plate velocity is oblique to the rift trend (Brune et al., 2012) exerting additional control on rift strength that is otherwise governed by thermo-rheological properties, strain localisation and inherited weaknesses (Burov, 2015; Buck, 2015; Brune, 2018). As a consequence, during rift competition, oblique rifting should prevail over orthogonal rifting if all other rift parameters are similar. This appears to be the case for the West African and Equatorial Atlantic rift systems, which were active at the same time until localisation along the more oblique Equatorial Atlantic rift induced the failure of the West African rift (Heine and Brune, 2014). The same process could explain the kinematic evolution of the Australia-Antarctica and Gulf of California rifts. In both cases a change in the direction of plate divergence induced higher rift obliquity and simultaneously the rift velocity increased. We suggest that following the change in extension direction the higher localisation efficiency of oblique rifts sparked a significant loss in rift strength (Brune et al., 2016), which ultimately generated a speed-up of Baja California and Australia.

Oblique rifting is closely linked to toroidal plate motion, i.e. the spin of plates and associated strike-slip deformation. The concept of decomposing Earth's plate motions into toroidal (plate boundary parallel) and poloidal (plate boundary perpendicular) components is motivated by the insight that toroidal motion does not affect the buoyancy configuration of Earth's mantle. It is hence not directly driven by mantle convection and in a homogeneous plate-mantle system, energy consumption due to toroidal motion should therefore be minimized (O'Connell et al., 1991). Large lateral rheological contrasts within and between Earth's plates have been invoked to explain some part of the toroidal motion component (Becker, 2006; Rolf et al., 2017). However, an additional part of the toroidal plate motion might be due to rift obliquity: since oblique rifting reduces rift strength, it favours the development of oblique plate boundaries, which enhances large-scale plate rotation and associated toroidal surface velocity components. Lithgow-Bertelloni and Richards (1993) showed that the toroidal component of plate motions slowly declined since 120 Ma, despite large variations in the poloidal component of plate velocities. Notwithstanding significant uncertainty, the ratio of toroidal/poloidal velocities appears to be especially high between 120 and ~80 Ma. This period corresponds to a distinct decline in the lengths of rifts involved in Pangea breakup (Fig. 8, and also Brune et al., 2017c). Hence we speculate that the toroidal/poloidal ratio could be higher during continental breakup because of the rift characteristic to favour oblique motion, a process that has less impact on plate motions once the continents become dispersed.

6 Conclusions

The 2D assumption that the extension direction is perpendicular to the rift trend is not justified in most cases. We find that the majority of rift systems leading to continental breakup during the last 230 million years involved moderate to high rift obliquity. Approximately 70% of all rift segments involved a distinct obliquity higher than 20° while the global average in terms of rift obliquity is 34°. This high contribution of oblique deformation can be explained through the generally irregular shape of plate boundaries, possibly related to tectonic inheritance, and by the concept of obliquity-dependent plate boundary strength. Oblique deformation generates intrinsically 3D stress and strain fields that hamper simplified tectonic interpretation via 2D cross sections, models and seismic profiles. Our results indicate that oblique plate boundary deformation should be considered the rule and not the exception when investigating the dynamics of rifts and rifted margins.

References

Agostini, A., Corti, G., Zeoli, A., and Mulugeta, G., 2009, Evolution, pattern, and partitioning of deformation during oblique continental rifting: Inferences from lithospheric-scale centrifuge models: Geochemistry Geophysics Geosystems, v. 10, p. Q11015, doi: 10.1029/2009GC002676.

Ali, J.R., and Aitchison, J.C., 2014, Greater India's northern margin prior to its collision with Asia: Basin Research, v. 26, p. 73–84, doi: 10.1111/bre.12040.

Ammann, N., Liao, J., Gerya, T., and Ball, P., 2017, Oblique continental rifting and long transform fault formation based on 3D thermomechanical numerical modeling: Tectonophysics, doi: 10.1016/j.tecto.2017.08.015.

Atwater, T., and Stock, J., 1998, Pacific-North America Plate Tectonics of the Neogene Southwestern United States: An Update: International Geology Review, v. 40, p. 375–402, doi: 10.1080/00206819809465216.

Ball, P., Eagles, G., Ebinger, C., McClay, K., and Totterdell, J., 2013, The spatial and temporal evolution of strain during the separation of Australia and Antarctica: Geochemistry, Geophysics, Geosystems, v. 14, p. 2771–2799, doi: 10.1002/ggge.20160.

Barnett-Moore, N., Müller, D.R., Williams, S., Skogseid, J., and Seton, M., 2016, A reconstruction of the North Atlantic since the earliest Jurassic: Basin Research, p. 1–26, doi: 10.1111/bre.12214.

Basile, C., 2015, Transform continental margins - part 1: Concepts and models: Tectonophysics, v. 661, p. 1–10, doi: 10.1016/j.tecto.2015.08.034.

Bayrakci, G., Minshull, T.A., Sawyer, D.S., Reston, T.J., Klaeschen, D., Papenberg, C., Ranero, C., Bull, J.M., Davy, R.G., Shillington, D.J., Perez-Gussinye, M., and Morgan, J.K., 2016, Fault-controlled hydration of the upper mantle during continental rifting: Nature Geoscience, v. 9, p. 384–388, doi: 10.1038/ngeo2671.

Becker, T.W., 2006, On the effect of temperature and strain-rate dependent viscosity on global mantle flow, net rotation, and plate-driving forces: Geophysical Journal International, v. 167, p. 943–957.

Bennett, S.E.K., and Oskin, M.E., 2014, Oblique rifting ruptures continents: Example from the Gulf of California shear zone: Geology, v. 42, p. 215–218, doi: 10.1130/G34904.1.

Bercovici, D., 2003, The generation of plate tectonics from mantle convection: Earth and Planetary Science Letters, v. 205, p. 107–121, doi: 16/S0012-821X(02)01009-9.

Bertrand, G., Horstmann, M., Hermann, O., and Behrmann, J.H., 2005, Retrodeformation of the southern Upper Rhine Graben: new insights on continental oblique rifting: Quaternary Science Reviews, v. 24, p. 345–352, doi: 10.1016/j.quascirev.2004.07.011.

Borissova, I., Coffin, M.F., Charvis, P., and Operto, S., 2003, Structure and development of a microcontinent: Elan Bank in the southern Indian Ocean: Geochemistry, Geophysics, Geosystems, v. 4, doi: 10.1029/2003GC000535.

Brune, S., 2014, Evolution of stress and fault patterns in oblique rift systems: 3-D numerical lithospheric-scale experiments from rift to breakup: Geochemistry, Geophysics, Geosystems, v. 15, p. 3392–3415, doi: 10.1002/2014GC005446.

Brune, S., 2016, Rifts and rifted margins: A review of geodynamic processes and natural hazards (J. C. Duarte & W. P. Schellart, Eds.): Plate Boundaries and Natural Hazards, v. 219, p. 11–37, doi: 10.1002/9781119054146.ch2.

Brune, S., 2018, Forces within continental and oceanic rifts: Numerical modeling elucidates the impact of asthenospheric flow on surface stress: Geology, v. 46, p. 191–192, doi: 10.1130/focus022018.1.

Brune, S., and Autin, J., 2013, The rift to break-up evolution of the Gulf of Aden: Insights from 3D numerical lithospheric-scale modelling: Tectonophysics, v. 607, p. 65–79, doi: 10.1016/j.tecto.2013.06.029.

Brune, S., Popov, A.A., and Sobolev, S.V., 2012, Modeling suggests that oblique extension facilitates rifting and continental break-up: Journal of Geophysical Research, v. 117, p. B08402, doi: 10.1029/2011JB008860.

Brune, S., Heine, C., Perez-Gussinye, M., and Sobolev, S.V., 2014, Rift migration explains continental margin asymmetry and crustal hyper-extension: Nature Communications, v. 5, doi: 10.1038/ncomms5014.

Brune, S., Williams, S.E., Butterworth, N.P., and Müller, R.D., 2016, Abrupt plate accelerations shape rifted continental margins: Nature, v. 536, p. 201–204, doi: 10.1038/nature18319.

Brune, S., Heine, C., Clift, P.D., and Pérez-Gussinyé, M., 2017a, Rifted margin architecture and crustal rheology: Reviewing Iberia-Newfoundland, Central South Atlantic, and South China Sea: Marine and Petroleum Geology, v. 79, p. 257–281, doi: 10.1016/j.marpetgeo.2016.10.018.

Brune, S., Corti, G., and Ranalli, G., 2017b, Controls of inherited lithospheric heterogeneity on rift linkage: Numerical and analog models of interaction between the Kenyan and Ethiopian rifts across the Turkana depression: Tectonics, v. 36, p. 2017TC004739, doi: 10.1002/2017TC004739.

Brune, S., Williams, S.E., and Müller, R.D., 2017c, Potential links between continental rifting, CO2 degassing and climate change through time: Nature Geoscience, p. 1, doi: 10.1038/s41561-017-0003-6.

Buck, W.R., 2015, The Dynamics of Continental Breakup and Extension, *in* Treatise on Geophysics, 2nd Edition, Vol 6 - Crust and Lithosphere Dynamics, Oxford, Elsevier.

Burov, E.B., 2015, Plate Rheology and Mechanics, *in* Schubert, G. ed., Treatise on Geophysics (Second Edition), Oxford, Elsevier, p. 95–152, doi: 10.1016/B978-0-444-53802-4.00112-3.

Chemenda, A., Déverchère, J., and Calais, E., 2002, Three-dimensional laboratory modelling of rifting: application to the Baikal Rift, Russia: Tectonophysics, v. 356, p. 253–273, doi: 10.1016/S0040-1951(02)00389-X.

Clifton, A.E., and Schlische, R.W., 2001, Nucleation, growth, and linkage of faults in oblique rift zones: Results from experimental clay models and implications for maximum fault size: Geology, v. 29, p. 455–458, doi: 10.1130/0091-7613(2001)029<0455:NGALOF>2.0.CO;2.

Clifton, A.E., Schlische, R.W., Withjack, M.O., and Ackermann, R.V., 2000, Influence of rift obliquity on fault-population systematics: results of experimental clay models: Journal of Structural Geology, v. 22, p. 1491–1509, doi: 10.1016/S0191-8141(00)00043-2.

Coffin, M.F., and Eldholm, O., 1992, Volcanism and continental break-up: a global compilation of large igneous provinces: Geological Society, London, Special Publications, v. 68, p. 17–30, doi: 10.1144/GSL.SP.1992.068.01.02.

Corti, G., 2008, Control of rift obliquity on the evolution and segmentation of the main Ethiopian rift: Nature Geoscience, v. 1, p. 258–262, doi: 10.1038/ngeo160.

Daly, M.C., Chorowicz, J., and Fairhead, J.D., 1989, Rift basin evolution in Africa: the influence of reactivated steep basement shear zones: Geological Society, London, Special Publications, v. 44, p. 309–334, doi: 10.1144/GSL.SP.1989.044.01.17.

Darin, M.H., Bennett, S.E.K., Dorsey, R.J., Oskin, M.E., and Iriondo, A., 2016, Late Miocene extension in coastal Sonora, México: Implications for the evolution of dextral shear in the proto-Gulf of California oblique rift: Tectonophysics, v. 693, p. 378–408, doi: 10.1016/j.tecto.2016.04.038.

Davis, J.K., Lawver, L.A., Norton, I.O., and Gahagan, L.M., 2016, New Somali Basin magnetic anomalies and a plate model for the early Indian Ocean: Gondwana Research, v. 34, p. 16–28, doi: 10.1016/j.gr.2016.02.010.

Deng, C., Gawthorpe, R., Fossen, H., and Finch, E., 2018, How does the orientation of a pre-existing basement weakness influence fault development during renewed rifting? Insights from three-dimensional discrete element modeling: Tectonics, v. 0, doi: 10.1029/2017TC004776.

Dewey, J.F., Holdsworth, R.E., and Strachan, R.A., 1998, Transpression and transtension zones: Geological Society, London, Special Publications, v. 135, p. 1–14, doi: 10.1144/GSL.SP.1998.135.01.01.

Díaz-Azpiroz, M., Brune, S., Leever, K.A., Fernández, C., and Czeck, D.M., 2016, Tectonics of oblique plate boundary systems: Tectonophysics, v. 693, Part B, p. 165–170, doi: 10.1016/j.tecto.2016.07.028.

Dickie, K., Keen, C.E., Williams, G.L., and Dehler, S.A., 2011, Tectonostratigraphic evolution of the Labrador margin, Atlantic Canada: Marine and Petroleum Geology, v. 28, p. 1663–1675, doi: 10.1016/j.marpetgeo.2011.05.009.

Doré, A.G., 1991, The structural foundation and evolution of Mesozoic seaways between Europe and the Arctic: Palaeogeography, Palaeoclimatology, Palaeoecology, v. 87, p. 441–492, doi: 10.1016/0031-0182(91)90144-G.

Duque-Trujillo, J., Ferrari, L., Orozco-Esquivel, T., López-Martínez, M., Lonsdale, P., Bryan, S.E., Kluesner, J., Piñero-Lajas, D., and Solari, L., 2015, Timing of rifting in the southern Gulf of California and its conjugate margins: Insights from the plutonic record: Geological Society of America Bulletin, v. 127, p. 702–736, doi: 10.1130/B31008.1.

Espurt, N., Callot, J.-P., Roure, F., Totterdell, J.M., Struckmeyer, H.I.M., and Vially, R., 2012, Transition from symmetry to asymmetry during continental rifting: an example from the Bight Basin–Terre Adélie (Australian and Antarctic conjugate margins): Terra Nova, v. 24, p. 167–180, doi: 10.1111/j.1365-3121.2011.01055.x.

Faleide, J.I., Tsikalas, F., Breivik, A.J., Mjelde, R., Ritzmann, O., Engen, O., Wilson, J., and Eldholm, O., 2008, Structure and Evolution of the Continental Margin off Norway and the Barents Sea: Episodes, v. 31, p. 82–91.

Féraud, G., Beslier, M.-O., and Cornen, G., 1996, 40Ar/39Ar dating of gabbros from the ocean/continent transition of the western Iberia Margin: Preliminary results, *in* Proceedings of the Ocean Drilling Program. Scientific results, Ocean Drilling Program, v. 149, p. 489–495.

Ferrari, L., López-Martínez, M., Orozco-Esquivel, T., Bryan, S.E., Duque-Trujillo, J., Lonsdale, P., and Solari, L., 2013, Late Oligocene to Middle Miocene rifting and synextensional magmatism in the southwestern Sierra Madre Occidental, Mexico: The beginning of the Gulf of California rift: Geosphere, p. GES00925.1, doi: 10.1130/GES00925.1.

Fletcher, J.M., Grove, M., Kimbrough, D., Lovera, O., and Gehrels, G.E., 2007, Ridge-trench interactions and the Neogene tectonic evolution of the Magdalena shelf and southern Gulf of California: Insights from detrital zircon U-Pb ages from the Magdalena fan and adjacent areas: Geological Society of America Bulletin, v. 119, p. 1313–1336, doi: 10.1130/B26067.1.

Fossen, H., and Rotevatn, A., 2016, Fault linkage and relay structures in extensional settings—A review: Earth-Science Reviews, v. 154, p. 14–28, doi: 10.1016/j.earscirev.2015.11.014.

Fournier, M., Bellahsen, N., Fabbri, O., and Gunnell, Y., 2004, Oblique rifting and segmentation of the NE Gulf of Aden passive margin: Geochemistry, Geophysics, Geosystems, v. 5, p. Q11005, doi: 10.1029/2004GC000731.

Fournier, M., and Petit, C., 2007, Oblique rifting at oceanic ridges: Relationship between spreading and stretching directions from earthquake focal mechanisms: Journal of Structural Geology, v. 29, p. 201–208, doi: 10.1016/j.jsg.2006.07.017.

Gaina, C., Nasuti, A., Kimbell, G.S., and Blischke, A., 2017, Break-up and seafloor spreading domains in the NE Atlantic: Geological Society, London, Special Publications, v. 447, p. SP447.12, doi: 10.1144/SP447.12.

Gawthorpe, R.L., and Leeder, M.R., 2000, Tectono-sedimentary evolution of active extensional basins: Basin Research, v. 12, p. 195–218.

Gernigon, L., Blischke, A., Nasuti, A., and Sand, M., 2015, Conjugate volcanic rifted margins, seafloor spreading, and microcontinent: Insights from new high-resolution aeromagnetic surveys in the Norway Basin: Tectonics, v. 34, p. 2014TC003717, doi: 10.1002/2014TC003717.

Gibbons, A.D., Whittaker, J.M., and Müller, R.D., 2013, The breakup of East Gondwana: Assimilating constraints from Cretaceous ocean basins around India into a best-fit tectonic model: Journal of Geophysical Research: Solid Earth, v. 118, p. 808–822, doi: 10.1002/jgrb.50079.

Gibbons, A.D., Zahirovic, S., Müller, R.D., Whittaker, J.M., and Yatheesh, V., 2015, A tectonic model reconciling evidence for the collisions between India, Eurasia and intra-oceanic arcs of the central-eastern Tethys: Gondwana Research, v. 28, p. 451–492, doi: 10.1016/j.gr.2015.01.001.

Gillard, M., Autin, J., and Manatschal, G., 2016, Fault systems at hyper-extended rifted margins and embryonic oceanic crust: Structural style, evolution and relation to magma: Marine and Petroleum Geology, v. 76, p. 51–67, doi: 10.1016/j.marpetgeo.2016.05.013.

Gillard, M., Autin, J., Manatschal, G., Sauter, D., Munschy, M., and Schaming, M., 2015, Tectonomagmatic evolution of the final stages of rifting along the deep conjugate Australian-Antarctic magma-poor rifted margins: Constraints from seismic observations: Tectonics, v. 34, p. 2015TC003850, doi: 10.1002/2015TC003850.

Granot, R., and Dyment, J., 2015, The Cretaceous opening of the South Atlantic Ocean: Earth and Planetary Science Letters, v. 414, p. 156–163, doi: 10.1016/j.epsl.2015.01.015.

Heine, C., and Brune, S., 2014, Oblique rifting of the Equatorial Atlantic: Why there is no Saharan Atlantic Ocean: Geology, v. 42, p. 211–214, doi: 10.1130/G35082.1.

Heine, C., Zoethout, J., and Müller, R.D., 2013, Kinematics of the South Atlantic rift: Solid Earth, v. 4, p. 215–253, doi: 10.5194/se-4-215-2013.

Hetzel, R., and Strecker, M.R., 1994, Late Mozambique Belt structures in western Kenya and their influence on the evolution of the Cenozoic Kenya Rift: Journal of Structural Geology, v. 16, p. 189–201, doi: 10.1016/0191-8141(94)90104-X.

Hodge, M.S., Fagereng, Å., Biggs, J., and Mdala, H., 2018, Controls on early-rift geometry: new perspectives from the Bilila-Mtakataka fault, Malawi: Geophysical Research Letters, doi: 10.1029/2018GL077343.

Hosseinpour, M., Müller, R.D., Williams, S.E., and Whittaker, J.M., 2013, Full-fit reconstruction of the Labrador Sea and Baffin Bay: Solid Earth, v. 4, p. 461–479, doi: 10.5194/se-4-461-2013.

Huismans, R.S., and Beaumont, C., 2011, Depth-dependent extension, two-stage breakup and cratonic underplating at rifted margins: Nature, v. 473, p. 74–78, doi: 10.1038/nature09988.

Jakobsson, M., Backman, J., Rudels, B., Nycander, J., Frank, M., Mayer, L., Jokat, W., Sangiorgi, F., O'Regan, M., Brinkhuis, H., King, J., and Moran, K., 2007, The early Miocene onset of a ventilated circulation regime in the Arctic Ocean: Nature, v. 447, p. 986–990, doi: 10.1038/nature05924.

Jeanniot, L., and Buiter, S.J.H., 2018, A quantitative analysis of transtensional margin width: Earth and Planetary Science Letters, v. 491, p. 95–108, doi: 10.1016/j.epsl.2018.03.003.

Klimke, J., and Franke, D., 2016, Gondwana breakup: no evidence for a Davie Fracture Zone offshore northern Mozambique, Tanzania and Kenya: Terra Nova, v. 28, p. 233–244, doi: 10.1111/ter.12214.

Kneller, E.A., Johnson, C.A., Karner, G.D., Einhorn, J., and Queffelec, T.A., 2012, Inverse methods for modeling non-rigid plate kinematics: Application to mesozoic plate reconstructions of the Central Atlantic: Computers & Geosciences, v. 49, p. 217–230, doi: http://dx.doi.org/10.1016/j.cageo.2012.06.019.

Knies, J., and Gaina, C., 2008, Middle Miocene ice sheet expansion in the Arctic: Views from the Barents Sea: Geochemistry, Geophysics, Geosystems, v. 9, doi: 10.1029/2007GC001824.

Kröner, A., and Stern, R.J., 2004, Pan-African Orogeny, *in* Encyclopedia 0f Geology, Elsevier.

Lavier, L.L., and Manatschal, G., 2006, A mechanism to thin the continental lithosphere at magma-poor margins: Nature, v. 440, p. 324–328, doi: 10.1038/nature04608.

Lithgow-Bertelloni, C., Richards, M.A., Ricard, Y., O'Connell, R.J., and Engebretson, D.C., 1993, Toroidal-poloidal partitioning of plate motions since 120 MA: Geophysical Research Letters, v. 20, p. 375–378, doi: 10.1029/93GL00168.

Lizarralde, D., Axen, G.J., Brown, H.E., Fletcher, J.M., Gonzalez-Fernandez, A., Harding, A.J., Holbrook, W.S., Kent, G.M., Paramo, P., Sutherland, F., and Umhoefer, P.J., 2007, Variation in styles of rifting in the Gulf of California: Nature, v. 448, p. 466–469, doi: 10.1038/nature06035.

Lundin, E.R., and Doré, A.G., 1997, A tectonic model for the Norwegian passive margin with implications for the NE Atlantic: Early Cretaceous to break-up: Journal of the Geological Society, v. 154, p. 545–550, doi: 10.1144/gsjgs.154.3.0545.

Manatschal, G., Lavier, L., and Chenin, P., 2015, The role of inheritance in structuring hyperextended rift systems: Some considerations based on observations and numerical modeling: Gondwana Research, v. 27, p. 140–164, doi: 10.1016/j.gr.2014.08.006.

Mart, Y., Ryan, W.B.F., and Lunina, O.V., 2005, Review of the tectonics of the Levant Rift system: the structural significance of oblique continental breakup: Tectonophysics, v. 395, p. 209–232, doi: 10.1016/j.tecto.2004.09.007.

McKenzie, D., 1978, Some remarks on the development of sedimentary basins: Earth and Planetary Science Letters, v. 40, p. 25–32, doi: 10.1016/0012-821X(78)90071-7.

McQuarrie, N., and Wernicke, B.P., 2005, An animated tectonic reconstruction of southwestern North America since 36 Ma: Geosphere, v. 1, p. 147–172, doi: 10.1130/GES00016.1.

Mericer de Lépinay, M., Loncke, L., Basile, C., Roest, W.R., Patriat, M., Maillard, A., and De Clarens, P., 2016, Transform continental margins - Part 2: A worldwide review: Tectonophysics, doi: 10.1016/j.tecto.2016.05.038.

Molnar, N.E., Cruden, A.R., and Betts, P.G., 2017, Interactions between propagating rotational rifts and linear rheological heterogeneities: Insights from three-dimensional laboratory experiments: Tectonics, v. 36, p. 2016TC004447, doi: 10.1002/2016TC004447.

Mondy, L.S., Rey, P.F., Duclaux, G., and Moresi, L., 2017, The role of asthenospheric flow during rift propagation and breakup: Geology, v. 46, p. 103–106, doi: 10.1130/G39674.1.

Montési, L.G.J., and Behn, M.D., 2007, Mantle flow and melting underneath oblique and ultraslow mid-ocean ridges: Geophysical Research Letters, v. 34, p. L24307, doi: 10.1029/2007GL031067.

Morley, C.K., 2016, The impact of multiple extension events, stress rotation and inherited fabrics on normal fault geometries and evolution in the Cenozoic rift basins of Thailand: Geological Society, London, Special Publications, v. 439, p. SP439.3, doi: 10.1144/SP439.3.

Moulin, M., Aslanian, D., and Unternehr, P., 2010, A new starting point for the South and Equatorial Atlantic Ocean: Earth-Science Reviews, v. 98, p. 1–37, doi: 10.1016/j.earscirev.2009.08.001.

Müller, R.D., Cannon, J., Qin, X., Watson, R.J., Gurnis, M., Williams, S., Pfaffelmoser, T., Seton, M., Russell, S.H.J., and Zahirovic, S., 2018, GPlates – Building a Virtual Earth Through Deep Time: Geochemistry, Geophysics, Geosystems, v. (in press), doi: 10.1029/2018GC007584.

Müller, R.D., Seton, M., Zahirovic, S., Williams, S.E., Matthews, K.J., Wright, N.M., Shephard, G.E., Maloney, K.T., Barnett-Moore, N., Hosseinpour, M., Bower, D.J., and Cannon, J., 2016, Ocean Basin Evolution and Global-Scale Plate Reorganization Events Since Pangea Breakup: Annual Review of Earth and Planetary Sciences, v. 44, p. 107–138, doi: 10.1146/annurev-earth-060115-012211.

Naliboff, J.B., Buiter, S.J.H., Péron-Pinvidic, G., Osmundsen, P.T., and Tetreault, J., 2017, Complex fault interaction controls continental rifting: Nature Communications, v. 8, p. 1179, doi: 10.1038/s41467-017-00904-x.

Nirrengarten, M., Manatschal, G., Tugend, J., Kusznir, N., and Sauter, D., 2018, Kinematic Evolution of the Southern North Atlantic: Implications for the Formation of Hyperextended Rift Systems: Tectonics, p. 2017TC004495, doi: 10.1002/2017TC004495.

Norvick, M.S., and Smith, M.A., 2001, Mapping the plate tectonic reconstruction of southern and southeastern Australia and implications for petroleum systems: The APPEA Journal, v. 41, p. 15–35, doi: 10.1071/aj00001.

Nürnberg, D., and Müller, R.D., 1991, The Tectonic Evolution of the South-Atlantic from Late Jurassic to Present: Tectonophysics, v. 191, p. 27–53, doi: 10.1016/0040-1951(91)90231-G.

O'Connell, R.J., Gable, C.W., and Hager, B.H., 1991, Toroidal-Poloidal Partitioning of Lithospheric Plate Motions, *in* Glacial Isostasy, Sea-Level and Mantle Rheology, Springer, Dordrecht, NATO ASI Series, p. 535–551, doi: 10.1007/978-94-011-3374-6_25.

Oskin, M., and Stock, J., 2003, Marine incursion synchronous with plate-boundary localization in the Gulf of California: Geology, v. 31, p. 23–26, doi: 10.1130/0091-7613(2003)031<0023:MISWPB>2.0.CO;2.

Peron-Pinvidic, G., Manatschal, G., and Osmundsen, P.T., 2013, Structural comparison of archetypal Atlantic rifted margins: A review of observations and concepts: Marine and Petroleum Geology, doi: 10.1016/j.marpetgeo.2013.02.002.

Philippon, M., and Corti, G., 2016, Obliquity along plate boundaries: Tectonophysics, v. 693, Part B, p. 171–182, doi: 10.1016/j.tecto.2016.05.033.

Philippon, M., Willingshofer, E., Sokoutis, D., Corti, G., Sani, F., Bonini, M., and Cloetingh, S., 2015, Slip re-orientation in oblique rifts: Geology, v. 43, p. 147–150, doi: 10.1130/G36208.1.

Phillips, T.B., Jackson, C.A.-L., Bell, R.E., and Duffy, O.B., 2018, Oblique reactivation of lithosphere-scale lineaments controls rift physiography – the upper-crustal expression of the Sorgenfrei–Tornquist Zone, offshore southern Norway: Solid Earth, v. 9, p. 403–429, doi: https://doi.org/10.5194/se-9-403-2018.

Powell, C.M., Roots, S.R., and Veevers, J.J., 1988, Pre-breakup continental extension in East Gondwanaland and the early opening of the eastern Indian Ocean: Tectonophysics, v. 155, p. 261–283, doi: 10.1016/0040-1951(88)90269-7.

Power, M.R., Hill, K.C., Hoffman, N., Bernecker, T., and Norvick, M., 2001, The Structural and Tectonic Evolution of the Gippsland Basin: Results from 2D Section Balancing and 3D Structural Modelling:, http://archives.datapages.com/data/petroleum-exploration-society-of-australia/conferences/001/001001/pdfs/373.htm (accessed June 2018).

Ranero, C.R., and Pérez-Gussinyé, M., 2010, Sequential faulting explains the asymmetry and extension discrepancy of conjugate margins: Nature, v. 468, p. 294–299, doi: 10.1038/nature09520.

Rolf, T., Capitanio, F.A., and Tackley, P.J., 2017, Constraints on mantle viscosity structure from continental drift histories in spherical mantle convection models: Tectonophysics, doi: 10.1016/j.tecto.2017.04.031.

Royer, J.-Y., and Sandwell, D.T., 1989, Evolution of the eastern Indian Ocean since the Late Cretaceous: Constraints from Geosat altimetry: Journal of Geophysical Research: Solid Earth, v. 94, p. 13755–13782, doi: 10.1029/JB094iB10p13755.

Sanderson, D.J., and Marchini, W.R.D., 1984, Transpression: Journal of Structural Geology, v. 6, p. 449–458, doi: 10.1016/0191-8141(84)90058-0.

Sippel, J., Meeßen, C., Cacace, M., Mechie, J., Fishwick, S., Heine, C., Scheck-Wenderoth, M., and Strecker, M.R., 2017, The Kenya rift revisited: insights into lithospheric strength through data-driven 3-D gravity and thermal modelling: Solid Earth, v. 8, p. 45–81, doi: 10.5194/se-8-45-2017.

Skogseid, J., Planke, S., Faleide, J.I., Pedersen, T., Eldholm, O., and Neverdal, F., 2000, NE Atlantic continental rifting and volcanic margin formation: Geological Society, London, Special Publications, v. 167, p. 295–326, doi: 10.1144/GSL.SP.2000.167.01.12.

Storey, M., Duncan, R.A., and Tegner, C., 2007, Timing and duration of volcanism in the North Atlantic Igneous Province: Implications for geodynamics and links to the Iceland hotspot: Chemical Geology, v. 241, p. 264–281, doi: 10.1016/j.chemgeo.2007.01.016.

Teyssier, C., Tikoff, B., and Markley, M., 1995, Oblique plate motion and continental tectonics: Geology, v. 23, p. 447–450, doi: 10.1130/0091-7613(1995)023<0447:OPMACT>2.3.CO;2.

Tikku, A.A., and Cande, S.C., 1999, The oldest magnetic anomalies in the Australian-Antarctic Basin: Are they isochrons? Journal of Geophysical Research: Solid Earth, v. 104, p. 661–677, doi: 10.1029/1998JB900034.

Torsvik, T.H., Rousse, S., Labails, C., and Smethurst, M.A., 2009, A new scheme for the opening of the South Atlantic Ocean and the dissection of an Aptian salt basin: Geophysical Journal International, v. 177, p. 1315–1333.

Tron, V., and Brun, J.-P., 1991, Experiments on oblique rifting in brittle-ductile systems: Tectonophysics, v. 188, p. 71–84, doi: 10.1016/0040-1951(91)90315-J.

Tugend, J., Manatschal, G., Kusznir, N.J., Masini, E., Mohn, G., and Thinon, I., 2014, Formation and deformation of hyperextended rift systems: Insights from rift domain mapping in the Bay of Biscay-Pyrenees: Tectonics, v. 33, p. 2014TC003529, doi: 10.1002/2014TC003529.

Umhoefer, P.J., 2011, Why did the Southern Gulf of California rupture so rapidly?—Oblique divergence across hot, weak lithosphere along a tectonically active margin: GSA Today, v. 21, p. 4–10, doi: 10.1130/G133A.1.

White, N., 1993, Recovery of strain rate variation from inversion of subsidence data: Nature, v. 366, p. 449–452, doi: 10.1038/366449a0.

Whittaker, J.M., Williams, S.E., Halpin, J.A., Wild, T.J., Stilwell, J.D., Jourdan, F., and Daczko, N.R., 2016, Eastern Indian Ocean microcontinent formation driven by plate motion changes: Earth and Planetary Science Letters, v. 454, p. 203–212, doi: 10.1016/j.epsl.2016.09.019.

Whittaker, J.M., Williams, S.E., and Müller, R.D., 2013, Revised tectonic evolution of the Eastern Indian Ocean: Geochemistry, Geophysics, Geosystems, v. 14, p. 1891–1909, doi: 10.1002/ggge.20120.

van Wijk, J., Axen, G., and Abera, R., 2017, Initiation, evolution and extinction of pull-apart basins: Implications for opening of the Gulf of California: Tectonophysics, v. 719–720, p. 37–50, doi: 10.1016/j.tecto.2017.04.019.

Willcox, J.B., and Stagg, H.M.J., 1990, Australia's southern margin: a product of oblique extension: Tectonophysics, v. 173, p. 269–281, doi: 10.1016/0040-1951(90)90223-U.

Williams, S.E., Whittaker, J.M., Granot, R., and Müller, D.R., 2013, Early India-Australia spreading history revealed by newly detected Mesozoic magnetic anomalies in the Perth Abyssal Plain: Journal of Geophysical Research: Solid Earth, v. 118, p. 3275–3284, doi: 10.1002/jgrb.50239.

Williams, S.E., Whittaker, J.M., and Müller, R.D., 2011, Full-fit, palinspastic reconstruction of the conjugate Australian-Antarctic margins: Tectonics, v. 30, p. TC6012, doi: 201110.1029/2011TC002912.

de Wit, M.J., Stankiewicz, J., and Reeves, C., 2008, Restoring Pan-African-Brasiliano connections: more Gondwana control, less Trans-Atlantic corruption: Geological Society, London, Special Publications, v. 294, p. 399–412.

Withjack, M.O., and Jamison, W.R., 1986, Deformation produced by oblique rifting: Tectonophysics, v. 126, p. 99–124, doi: 10.1016/0040-1951(86)90222-2.

Woodcock, N.H., 1986, The Role of Strike-Slip Fault Systems at Plate Boundaries: Philosophical Transactions of the Royal Society of London. Series A, Mathematical and Physical Sciences, v. 317, p. 13–29.

Zwaan, F., and Schreurs, G., 2017, How oblique extension and structural inheritance influence rift segment interaction: Insights from 4D analog models: Interpretation, p. SD119–SD138, doi: 10.1190/INT-2016-0063.1.

Zwaan, F., Schreurs, G., Naliboff, J., and Buiter, S.J.H., 2016, Insights into the effects of oblique extension on continental rift interaction from 3D analogue and numerical models: Tectonophysics, v. 693, Part B, p. 239–260, doi: 10.1016/j.tecto.2016.02.036.

nature geoscience

ARTICLES

https://doi.org/10.1038/s41561-017-0003-6

Potential links between continental rifting, CO_2 degassing and climate change through time

Sascha Brune[1,2*], Simon E. Williams[3] and R. Dietmar Müller[3,4]

The concentration of CO_2 in the atmosphere is a key influence on Earth's climate. Today, significant quantities of CO_2 are emitted at continental rifts, suggesting that the spatial and temporal extent of rift systems may have influenced deep carbon fluxes and thus climate change throughout geological time. Here we test this hypothesis by conducting a worldwide census of continental rift lengths over the last 200 million years. We estimate tectonic CO_2 release rates through time and show that along the extensive Mesozoic and Cenozoic rift systems, rift-related CO_2 degassing rates reached more than 300% of present-day values. Using a numerical carbon cycle model, we find that two prominent periods of enhanced rifting 160 to 100 million years ago and after 55 million years ago coincided with greenhouse climate episodes, during which atmospheric CO_2 concentrations were more than three times higher than today. We therefore propose that continental fragmentation and long-term climate change could plausibly be linked via massive CO_2 degassing in rift systems.

There are two carbon cycles on Earth: the short-term, surficial cycle that connects atmospheric CO_2 to the biosphere, soils and oceans; and the long-term or deep carbon cycle, which links the carbon content of the crust and mantle to Earth's surface[1,2]. The mass of carbon stored within the crust and mantle exceeds that of the surface reservoirs by several orders of magnitude[1,3]. Thus, solid Earth degassing rates exert a major control on long-term atmospheric CO_2 variations and, via the greenhouse effect, on palaeo-temperatures. Despite being a key quantity in long-term carbon cycle modelling, CO_2 degassing remains one of the least-constrained parameters[4].

According to current knowledge, deep carbon is released to the surface by four major sources[1,5]: volcanism at mid-oceanic ridges, subduction zones and hotspots, and metamorphism of carbonate rocks in regions of plate convergence. At the same time, silicate weathering and marine carbonate formation bind CO_2 into the lithosphere that may be subducted back into the mantle[6]. Despite general agreement that the length of plate boundaries exerts a first-order control on fluxes of the deep carbon cycle[5,7,8], reconstructing plate boundary length through deep time remains challenging. Moreover, plate boundaries can simultaneously act as CO_2 sources and sinks: mid-ocean ridges release large amounts of CO_2 via extensive volcanism[9], but hydrothermal activity in young ocean floor causes CO_2 to be sequestered in carbonates[10–12]. This process may even outweigh the CO_2 release at oceanic spreading centres so that mid-ocean ridges could in fact constitute net CO_2 sinks[2].

Much of our understanding of the global carbon budget is derived from analysing present-day Earth. However, our planet is currently in a state of continental dispersal that is not representative for other stages of the supercontinent cycle, such as the fragmentation of Pangaea and Gondwana, which occurred during the Jurassic and Early Cretaceous periods. Although it is clear that the extent of rift systems was much larger during supercontinental breakup than today, a quantitative analysis of continental rift length and its impact on atmospheric CO_2 since Mesozoic times is lacking.

Here we investigate the hypothesis that rift-related CO_2 degassing affects the deep carbon cycle. We deduce the worldwide length of continental rift systems using plate tectonic reconstructions and the geological rift record. We illustrate that rift length history correlates with the long-term palaeo-atmospheric CO_2 evolution, suggesting that rift-related CO_2 degassing may plausibly constitute a missing key component of the deep carbon cycle.

CO_2 degassing in present-day continental rifts

CO_2 and other volatiles released in continental rifts are derived primarily from the mantle[13–15], where they significantly reduce the peridotite solidus and thus enable deep decompression melting[16], while mantle lithosphere that was metasomatically enriched in CO_2 is thought to be an additional source of deep carbon[17–19]. CO_2 behaves as an incompatible element[1] and is readily transported to shallow crustal levels during melt migration. Although a certain fraction is released to the atmosphere during volcanic eruptions, recent studies indicate that much higher CO_2 release occurs due to circulation of hydrothermal fluids and degassing along normal faults without eruptive volcanism[20–22]. This insight stems from significant recent advances in measuring surface CO_2 flux and discriminating between hydrothermal and biogenic contributions[15].

Fault formation and fluid migration in rifts are intrinsically linked, since fluid flow enhances local pore pressure and reduces the frictional yield limit while faults, in turn, provide pathways for migrating fluids. This connection is supported by deep earthquake swarms detected in continental rifts worldwide[23]. A close geological link between faulting and CO_2 degassing has been documented in continental transform faults[24,25], and is evidenced by a growing body of CO_2 flux measurements in many different types of rift systems: the wide Basin and Range Rift[21], the narrow Rio Grande Rift[26], the collision-related Eger Rift[14], the East African Rift System's magma-rich eastern branch[22] and its magma-poor western branch[27,28]. In many cases, carbon and helium isotope analyses of collected gas samples reveal a mantle fingerprint. All of these studies corroborate that rift faults constitute the shallow component of a CO_2

[1]GFZ German Research Centre for Geosciences, Potsdam, Germany. [2]Institute of Earth and Environmental Science, University of Potsdam, Potsdam-Golm, Germany. [3]EarthByte Group, School of Geosciences, University of Sydney, Sydney, NSW 2006, Australia, [4]Sydney Informatics Hub, University of Sydney, Sydney, NSW, Australia. *e-mail: brune@gfz-potsdam.de

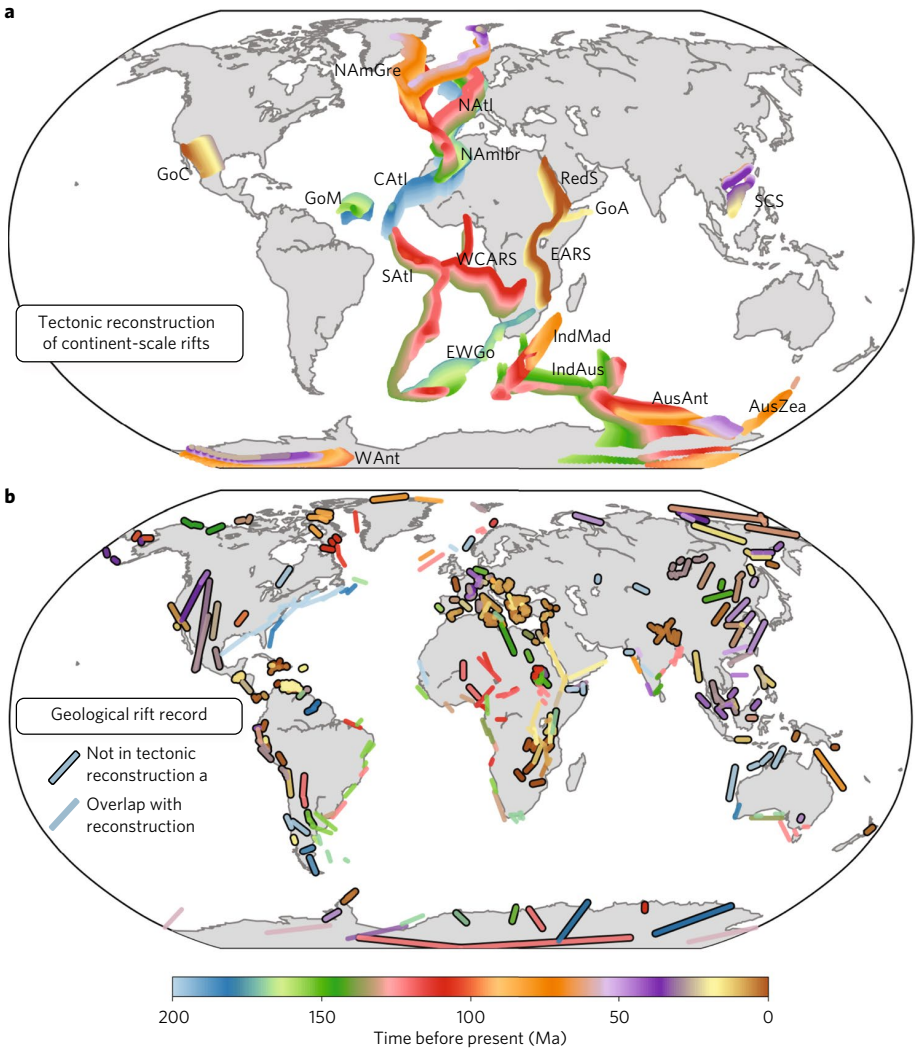

Fig. 1 | Timing and location of continental rifting. a,**b**, Data are derived from analysing tectonic reconstructions[31] using a recent workflow[32], reconstructed in a mantle reference frame (**a**) and the rift compilation of Şengör and Natal'in[33] (**b**). Colour indicates mean time of rift activity. Rift segments in **b** that are not accounted for by the plate reconstruction in **a** are designated via black outlines. AusAnt, Australia/Antarctica; AusZea, Australia/New Zealand; CAtl, central Atlantic; EARS, East African Rift System; EWGo, East and West Gondwana; GoA, Gulf of Aden; GoC, Gulf of California; GoM, Gulf of Mexico; IndAus, India/Australia and Antarctica; IndMad, India/Madagascar; NAmGre, North America/Greenland; NAmIbr, North America/Iberia; NAtl, northeast Atlantic; RedS, Red Sea; SAtl, South Atlantic; SCS, South China Sea; WAnt, West Antarctic Rift; WCARS, West and Central Africa.

pathway that connects the vast carbon reservoir in Earth's mantle to the atmosphere.

To explore the connection between CO_2 degassing and the global extent of rifts through geological time, we require a representative CO_2 flux density φ that relates CO_2 mass flux to the area of a rift basin. Regional flux densities have been derived in several currently active rift segments: the Magadi–Natron Basin[13] in the East African Rift ($\varphi = 440\,t\,km^{-2}\,yr^{-1}$ over 9,200 km^2); the Taupo Volcanic Zone[29], a back-arc rift in New Zealand ($\varphi = 59\,t\,km^{-2}\,yr^{-1}$ over 7,500 km^2); the Eger Rift[14] in central Europe ($\varphi = 11\,t\,km^{-2}\,yr^{-1}$ over 1,500 km^2); and the peri-Tyrrhenian region of central Italy[30] ($\varphi = 211\,t\,km^{-2}\,yr^{-1}$ over 18,000 km^2). The mean of these values equals $180\,t\,km^{-2}\,yr^{-1}$, or $230\,t\,km^{-2}\,yr^{-1}$ if weighted by basin area. Even though these studies exhibit a considerable spread of values, they consistently show that present-day continental rifts release large amounts of CO_2. In the following, we use a rounded mean flux density $\varphi_{ref} = 200\,t\,km^{-2}\,yr^{-1}$ as a reference value along with a conservative estimate $\varphi_{cons} = 50\,t\,km^{-2}\,yr^{-1}$.

Worldwide rift census since 200 million years ago

To compute rift length through time, we build on a global plate kinematic reconstruction[31] that incorporates the latest regional models of continent-scale rift systems (see Supplementary Movie). This reconstruction is analysed using a recently established pyGPlates workflow[32], which allows script-based access to the plate reconstruction software GPlates (Fig. 1). Since a number of rifts from the geological record are not explicitly represented in the global plate model yet, we also analyse a global rift compilation[33] (see Methods for details).

Fragmentation of the supercontinent Pangaea commenced with the separation of Laurasia and Gondwana along the Central Atlantic Rift in a 3,900-km-long rift zone. The most extensive rift phase, however, occurred in the Cretaceous with the simultaneous activity of several major rift systems: the South Atlantic (9,600 km) and North Atlantic Rift (5,600 km), the failed rifts of West and Central Africa (6,100 km), and the split of India and Australia from Antarctica (8,400 km). These and other contemporaneous rifts

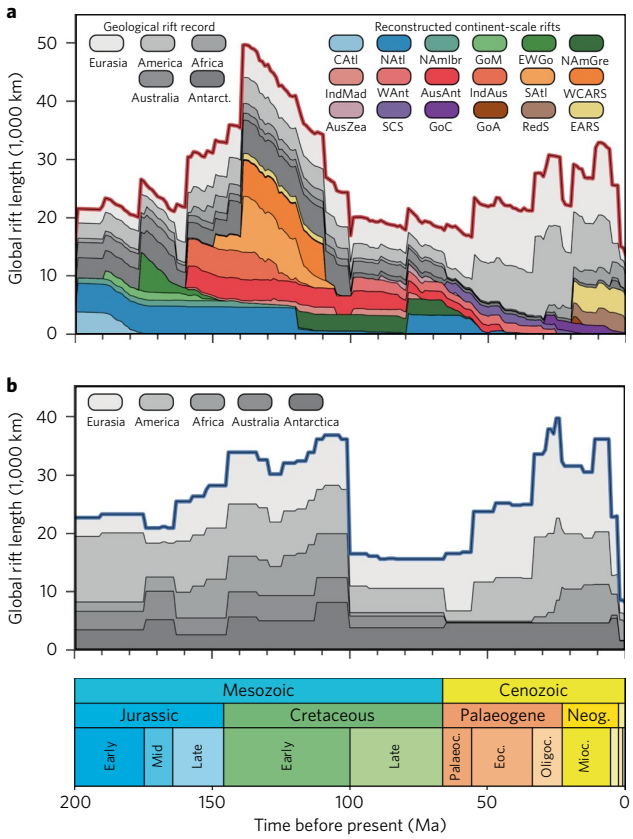

Fig. 2 | Cumulative rift length through time. a, Rift length history combining continent-scale rifts (Fig. 1a) with additional rifts from the geological record (Fig. 1b) in 1-Myr intervals. **b**, An alternative rift length evolution based on the geological record alone (Fig. 1b). In both cases, a Mesozoic rift period at 160–100 Ma accompanies the climax of Pangaea fragmentation. A Cenozoic rift period initiates at 55 Ma, which is dominated by rifts in west America, East Africa and Eurasia. For definition of abbreviations, see the caption of Fig. 1.

generated a major Mesozoic rift period (Fig. 2a) with more than ~50,000 km length that accomplished Pangaea's fragmentation. During the Late Cretaceous, in the aftermath of this massive rift episode, global continental rift length dropped by 60% to 20,000 km. Renewed major rift activity started in the Eocene epoch, involving rifting in the Basin and Range province of western North America as well as in Southeast Asia spanning from the Gulf of Thailand and South China Sea to the East China Sea. In Oligocene and Neogene times, the Baikal and Rio Grande Rift initiated followed by the East African Rift, and the Gulf of California. Altogether these rifts formed a second, Cenozoic rift period with more than 30,000 km length. In an alternative approach, we investigate the geological rift record without incorporating plate tectonic reconstructions (Fig. 2b). We find that details in the shape of global rift length history differ between both plots, owing to the uncertainty in timing of rift systems. However, the two distinct rift periods are robustly represented in both analyses and we suggest that they are first-order features of Earth's plate tectonic history.

Continental rifting and palaeo-atmospheric CO_2

We focus on the long-term rift trend by binning the rift length time series of Fig. 2a,b in 10 Myr intervals (curves L1 and L2 of Fig. 3a, respectively). To estimate rift-related CO_2 release rates, we make two assumptions: we use a rift width of $W = 50$ km, which is a minimum estimate representative of currently active narrow rifts such as Baikal and the East African Rift segments; the CO_2 flux density φ of past rifts is equivalent to regional-scale values of present-day rifts. This approach allows direct scaling of rift length to CO_2 flux using the factor $W\varphi$. We find that the Mesozoic and Cenozoic rift periods generate elevated CO_2 release rates with amplitudes exceeding ~300 Mt yr^{-1} and ~80 Mt yr^{-1} for reference and conservative flux density estimations φ_{ref} and φ_{cons}, respectively. These fluxes are comparable or even significantly higher than most recent estimates[34,35] of present-day CO_2 degassing at ridges and ocean islands (29–154 Mt yr^{-1}) and subduction zones (66–158 Mt yr^{-1}).

The palaeo–atmospheric CO_2 content is controlled by the combined effect of the deep and shallow carbon cycles. A widely used carbon cycle model is GEOCARBSULF[4,7,36], which calculates palaeo–atmospheric CO_2 concentrations by accounting for multiple interdependent effects such as climate, chemical weathering and vegetation cover as estimated from the geologic record. The release of Earth's deep carbon is represented in GEOCARBSULF by a single tectonic CO_2 source term, which traditionally accounts solely for degassing related to oceanic crust production at oceanic spreading centres[4]. In doing so, any contribution of other plate boundary types to CO_2 degassing is neglected, which might be responsible for model underprediction of proxy data during Mesozoic and Cenozoic CO_2 highs (for example, model R14[4] in Fig. 3b). In a first approximation, we employ global rift length histories L1 and L2 as GEOCARBSULF's tectonic source term, while keeping all other parameters identical to the reference values of R14[4], resulting in the computed CO_2 concentration histories C1 and C2, respectively. Note that GEOCARBSULF normalizes all models relative to the mean Quaternary atmospheric CO_2 concentration of ~250 ppmv[37]. This implies that the computed CO_2 curves depend only on changes in CO_2 degassing relative to present-day, not on absolute fluxes. Hence, employing different values for the mean CO_2 rift flux density φ does not change the computed palaeo-CO_2 curve.

We compare computed CO_2 histories C1 and C2 with the reference curve R14 and independent palaeo-CO_2 proxy indicators[38] in Fig. 3b. We find that during the Mesozoic and Cenozoic rift periods, C1 and C2 exceed the reference model by a factor of up to five and thereby broadly coincide with the proxy data range of both the Mesozoic CO_2 high and the Eocene greenhouse episode. Even though the latter CO_2 high is clearly mirrored in oceanic temperature proxies such as $\delta^{18}O$ (ref. [39]), its cause has so far remained elusive[4]. The Oligocene drawdown in CO_2 and onset of late Cenozoic icehouse climate, however, does not correspond to decreasing rift activity, and therefore CO_2 sinks emerging from increased weatherability associated with Himalayan orogeny[40], weathering of basaltic provinces in the equatorial humid belt[8,41,42], changes in ocean circulation[43] or a combination of these processes more than counteracted CO_2 degassing from rifting. Figure 3b also depicts results of two previous studies that suggest alternative causes for the Mesozoic CO_2 high by accounting for longer Mesozoic subduction zones[7] (vdM14) or less efficient chemical weathering of gymnosperms, which dominated forests between Late Devonian and Early Cretaceous times[4] (R14′). However, none of these models is able to explain the onset of the Cenozoic CO_2 high.

Other solid Earth sources are known to release deep CO_2 into the atmosphere[1,2], such as hotspot volcanism during the formation of large igneous provinces[44]. However, due to their limited activity period of ~1–5 Myr, these mega-eruptions can induce only comparatively short pulses of atmospheric CO_2 excursions. These CO_2 pulses, however, are buffered by rapid weathering feedbacks acting on time scales of ~1 Myr and cannot affect long-term climate change[45]. This is corroborated by the lacking temporal correlation with the long-term palaeo–atmospheric CO_2 evolution presented in Fig. 4a.

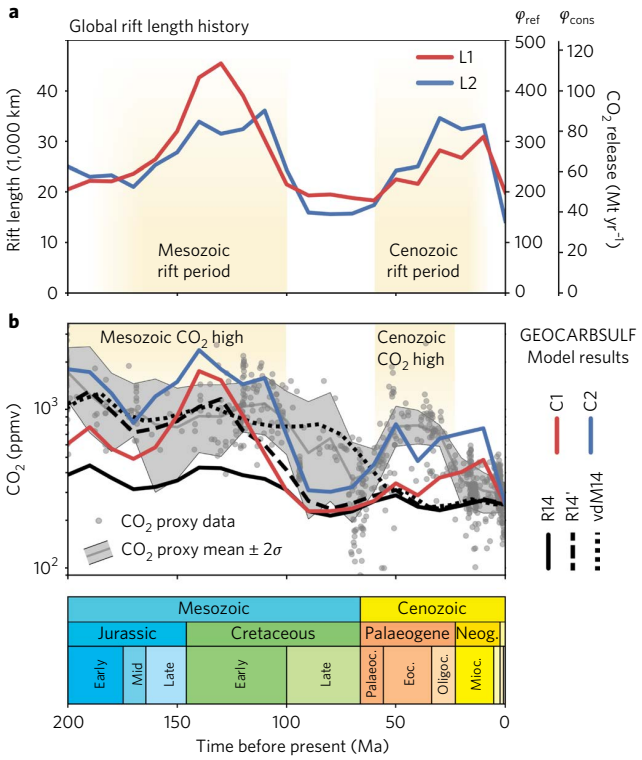

Fig. 3 | Rift controls on palaeo-atmospheric CO_2 levels. a, Long-term trends of rift length history and estimated CO_2 release. Rift length histories L1 and L2 are derived from binning global rift length of Fig. 2a,b in 10 Myr intervals, respectively. Associated CO_2 flux (right axis) is computed using the reference CO_2 flux density $\varphi_{ref} = 200\,t\,km^{-2}\,yr^{-1}$ and a conservative estimate $\varphi_{cons} = 50\,t\,km^{-2}\,yr^{-1}$. Note that 3.67 tonnes of CO_2 contain 1 tonne of pure carbon. **b**, GEOCARBSULF modelling results and palaeo-atmospheric CO_2 from proxy data[38]. CO_2 degassing histories C1 and C2 are based on rift length histories L1 and L2. The two CO_2 highs in Mesozoic and Cenozoic times correlate with distinct contemporaneous rift periods. The GEOCARBSULF reference model[4] R14, an alternative set-up[4] R14′ and the subduction-zone-based model[7] vdM14 are shown for comparison. All data except vdM14 are binned in 10 Myr intervals.

Non-rift plate boundaries constitute further degassing sources, but their relative contributions to deep carbon release are difficult to constrain[1]. We compile data on the extent of mid-ocean ridges and subduction zones by analysing a global plate reconstruction[31] of the last 200 Myr (M16, Fig. 4a). Note that the short worldwide extent of mid-ocean ridges before 130 Myr ago involves high uncertainties since no more than 10% of ocean floor prior to this time is preserved today. A curve for continental arc length (C17) is added from a recent study[46]. We model the palaeo–atmospheric CO_2 concentration due to these plate boundaries assuming that each type provides the only contribution to tectonic degassing (Fig. 4b). We find only minor CO_2 changes related to mid-ocean ridge and subduction zone length evolution. The continental arc curve exhibits a long-wavelength decrease throughout the last 200 Myr ranging at the lower limit of the Mesozoic CO_2 proxy data, but does not provide an explanation for the Cenozoic CO_2 high. Although not a statistically significant improvement compared with existing models, the first-order correlation between proxy data and rift length provides a qualitative improvement, especially for the Cenozoic CO_2 high. This suggests that CO_2 degassing in rifts may exert a strong control on deep carbon release rates.

Finally, we investigate the effect of simultaneous degassing at all plate boundary types. For simplicity, we first assume that the global present-day CO_2 flux at rifts, ridges, subduction zones and continental arcs is equal. This approach is equivalent to employing the conservative estimate of CO_2 rift flux density φ_{cons}, which leads to a present-day rift-related CO_2 flux of ~40 Mt yr^{-1} (Fig. 3a) that lies within the possible flux range of the other plate boundaries[1,34,35]. The resulting CO_2 curves C1″ and C2″, which are derived from rift length histories L1 and L2, respectively, largely underestimate the palaeo-CO_2 proxy data (Fig. 4c). However, when employing the four times larger reference flux density φ_{ref}, while keeping the other plate boundaries identical to the previous case, the corresponding curves C1′ and especially C2′ successfully reproduce large parts of the CO_2 proxy data history. Keeping in mind the simplicity of our assumptions, we conclude that rift-related degassing may have played an important role in controlling the long-term CO_2 evolution of Earth's atmosphere.

Beyond rift length

The time-dependency of CO_2 degassing during the long-term evolution of rift systems remains elusive. One might expect that CO_2 release intensifies through time, proportional to the amount of decompression melting that increases during rift maturation[47]. However, diffuse CO_2 degassing and associated earthquake swarms are not restricted to mature, magma-rich rifts, but also occur in initial rift stages and magma-poor systems[23], supporting the view that the subcontinental mantle lithosphere acts as a major degassing source[14,48] of potentially recycled carbon[17,35]. During the final transition from rifting to seafloor spreading, the effective CO_2 release rate can be even expected to decrease, because the melt source within carbon-rich subcontinental lithospheric mantle[17,19,48] diminishes during continental thinning and rupturing, and submergence beneath sea level allows hydrothermal circulation to sequester CO_2 in carbonates near the spreading axis[10–12].

One major challenge of our analysis is that the timing of rift activity within a large portion of our database, particularly for failed rifts, is inferred only in terms of stratigraphic ages. This restricts the temporal resolution of our approach and results in sharp rift length jumps at stratigraphic boundaries such as around 100 million years ago (Ma; Fig. 2b). Changes in active rift length were probably more gradual in nature, as shown by our more well-constrained results for ocean-forming rifts. Another important limit to our knowledge on past rifting arises from the preservation bias, such that rift activity in the most recent past tends to be better recognizable in the geological record. Further, we employ the same factor to scale from rift length to CO_2 degassing rates for all continental rifts, without distinguishing between different rift types[33] (such as volcanic versus non-volcanic, wide versus narrow) or rift stages[32] (slow versus fast). We suggest that future studies isolate differences in degassing between these rift types and stages, which combined with tighter age constraints on the global rift compilation, will allow a better-constrained projection of rift-related degassing rates throughout the geological past.

Recent work has identified correlations between palaeo–atmospheric CO_2 concentration and the fluctuations in continental arc magmatism that accompany supercontinent cycles[5,46,49]. These studies infer that the rifting and breakup of supercontinents (specifically Pangaea and Rodinia) leads to enhanced length of subduction zones[7] and therefore increased global CO_2 degassing at continental arcs. Our analysis, accounting for CO_2 release within continental rifts, provides a more direct link between supercontinent fragmentation and palaeo-atmospheric CO_2 that nevertheless fully agrees with the correlation of ref. [49].

Tectonic CO_2 degassing rates are only one component of Earth's long-term climate system, which is further affected by time-dependent contributions[50] from weathering of flood basalt provinces[41,42] and orogenic plateaus[51], continental runoff[52], cascading events of the ocean–atmosphere climate system[43] and associated

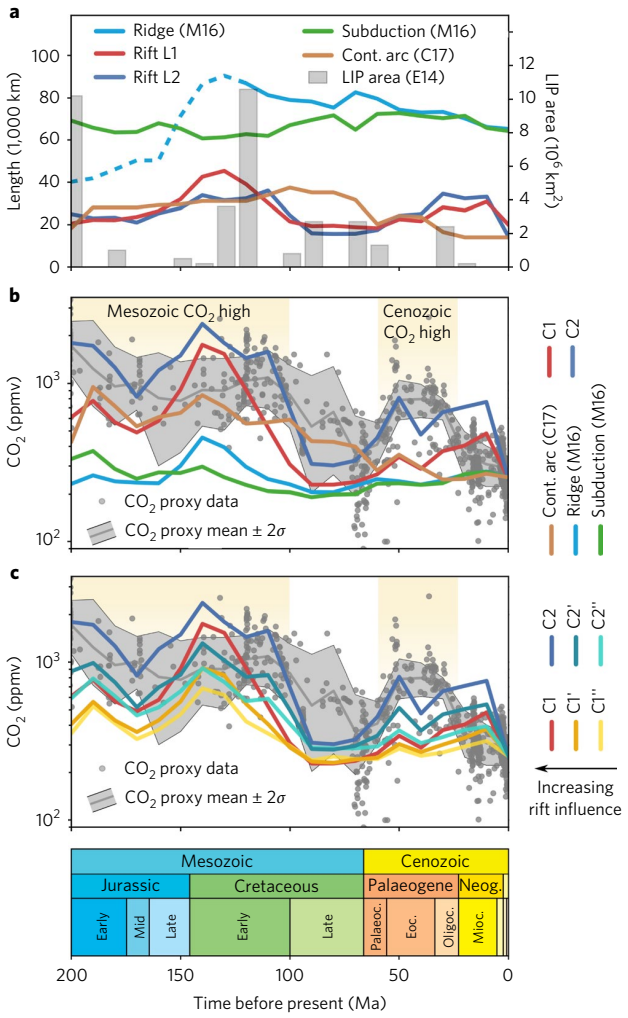

Fig. 4 | Effect of rifts, ridges, subduction zones and continental arcs. **a**, Lengths of rifts L1 and L2 compared with lengths of other plate boundaries thought to affect atmospheric CO_2 concentration (left axis). Area and timing of the emplacement of large igneous provinces (LIPs, right axis). Sources: C17[46], M16[31] and E14[44]. **b**, GEOCARBSULF results assuming that each plate boundary history in **a** is the only CO_2 degassing source. C1 and C2 employ rift length histories L1 and L2, respectively. **c**, Combination of ridge, subduction and continental arc length with rift length histories L1 and L2. C1″ and C2″ assume equal weights for each contributing plate boundary type, representing a conservative estimate of the rift CO_2 flux density φ_{cons}. C1′ and C2′ use fourfold stronger rift fluxes equivalent to the reference flux density φ_{ref} and provide a first-order fit to CO_2 proxy data.

palaeo–geographic control[53]. Hence, the changes in degassing rates provided in our study have to be considered as a base line estimate for the contribution of tectonic processes driving Earth's climate.

Rift-related melting and degassing along faults transfers not only carbon but also other volatiles such as water, sulfur and nitrogen from the mantle into the atmosphere[21,54]. Our analysis of plate boundary lengths therefore opens the possibility to quantify the effect of volatile degassing on other aspects of Earth system dynamics, establishing new quantitative links between plate tectonics, geochemical cycles and palaeo–climate through deep time.

Received: 13 March 2017; Accepted: 4 October 2017;
Published online: 13 November 2017

References

1. Dasgupta, R. & Hirschmann, M. M. The deep carbon cycle and melting in Earth's interior. *Earth Planet. Sci. Lett.* **298**, 1–13 (2010).
2. Kerrick, D. M. Present and past nonanthropogenic CO_2 degassing from the solid Earth. *Rev. Geophys.* **39**, 565–585 (2001).
3. Sleep, N. H. & Zahnle, K. Carbon dioxide cycling and implications for climate on ancient Earth. *J. Geophys. Res. Planets* **106**, 1373–1399 (2001).
4. Royer, D. L., Donnadieu, Y., Park, J., Kowalczyk, J. & Goddéris, Y. Error analysis of CO_2 and O_2 estimates from the long-term geochemical model GEOCARBSULF. *Am. J. Sci.* **314**, 1259–1283 (2014).
5. Lee, C.-T. A. et al. Continental arc–island arc fluctuations, growth of crustal carbonates, and long-term climate change. *Geosphere* **9**, 21–36 (2013).
6. Hoareau, G. et al. Did high Neo-Tethys subduction rates contribute to early Cenozoic warming? *Clim. Past* **11**, 1751–1767 (2015).
7. van der Meer, D. G. et al. Plate tectonic controls on atmospheric CO_2 levels since the Triassic. *Proc. Natl Acad. Sci. USA* **111**, 4380–4385 (2014).
8. Jagoutz, O., Macdonald, F. A. & Royden, L. Low-latitude arc–continent collision as a driver for global cooling. *Proc. Natl Acad. Sci. USA* **113**, 4935–4940 (2016).
9. Li, M. et al. Quantifying melt production and degassing rate at mid-ocean ridges from global mantle convection models with plate motion history. *Geochem. Geophys. Geosyst.* **17**, 2884–2904 (2016).
10. Alt, J. C. & Teagle, D. A. H. The uptake of carbon during alteration of ocean crust. *Geochim. Cosmochim. Acta* **63**, 1527–1535 (1999).
11. Gillis, K. M. & Coogan, L. A. Secular variation in carbon uptake into the ocean crust. *Earth Planet. Sci. Lett.* **302**, 385–392 (2011).
12. Müller, R. D., Dutkiewicz, A., Seton, M. & Gaina, C. Seawater chemistry driven by supercontinent assembly, breakup, and dispersal. *Geology* **41**, 907–910 (2013).
13. Lee, H. et al. Massive and prolonged deep carbon emissions associated with continental rifting. *Nat. Geosci.* **9**, 145–149 (2016).
14. Weinlich, F. H. et al. An active subcontinental mantle volatile system in the western Eger rift, Central Europe: gas flux, isotopic (He, C, and N) and compositional fingerprints. *Geochim. Cosmochim. Acta* **63**, 3653–3671 (1999).
15. Chiodini, G. et al. Carbon isotopic composition of soil CO_2 efflux, a powerful method to discriminate different sources feeding soil CO_2 degassing in volcanic-hydrothermal areas. *Earth Planet. Sci. Lett.* **274**, 372–379 (2008).
16. Dasgupta, R. & Hirschmann, M. M. Melting in the Earth's deep upper mantle caused by carbon dioxide. *Nature* **440**, 659–662 (2006).
17. Sleep, N. H. Stagnant lid convection and carbonate metasomatism of the deep continental lithosphere. *Geochem. Geophys. Geosyst.* **10**, Q11010 (2009).
18. Rooney, T. O., Nelson, W. R., Dosso, L., Furman, T. & Hanan, B. The role of continental lithosphere metasomes in the production of HIMU-like magmatism on the northeast African and Arabian plates. *Geology* **42**, 419–422 (2014).
19. Foley, S. F. & Fischer, T. P. The essential role of continental rifts and lithosphere in the deep carbon cycle. *Nat. Geosci.* https://doi.org/s41561-017-0002-7 (2017).
20. Hutchison, W., Mather, T. A., Pyle, D. M., Biggs, J. & Yirgu, G. Structural controls on fluid pathways in an active rift system: a case study of the Aluto volcanic complex. *Geosphere* **11**, 542–562 (2015).
21. Jolie, E., Klinkmueller, M., Moeck, I. & Bruhn, D. Linking gas fluxes at Earth's surface with fracture zones in an active geothermal field. *Geology* **44**, 187–190 (2016).
22. Muirhead, J. D. et al. Evolution of upper crustal faulting assisted by magmatic volatile release during early-stage continental rift development in the East African Rift. *Geosphere* **12**, 1670–1700 (2016).
23. Ibs-von Seht, M., Plenefisch, T. & Klinge, K. Earthquake swarms in continental rifts — a comparison of selected cases in America, Africa and Europe. *Tectonophysics* **452**, 66–77 (2008).
24. Kennedy, B. M. et al. Mantle fluids in the San Andreas Fault System, California. *Science* **278**, 1278–1281 (1997).
25. Ring, U. et al. Recent mantle degassing recorded by carbonic spring deposits along sinistral strike-slip faults, south-central Australia. *Earth Planet. Sci. Lett.* **454**, 304–318 (2016).
26. Smith, J. *CO_2 Flux Along Faults of the Central Rio Grande Rift, New Mexico.* MSc thesis, Univ. New Mexico (2016).
27. Lindenfeld, M., Rümpker, G., Link, K., Koehn, D. & Batte, A. Fluid-triggered earthquake swarms in the Rwenzori region, East African Rift—evidence for rift initiation. *Tectonophysics* **566–567**, 95–104 (2012).
28. Barry, P. H. et al. Helium and carbon isotope systematics of cold 'mazuku' CO_2 vents and hydrothermal gases and fluids from Rungwe Volcanic Province, southern Tanzania. *Chem. Geol.* **339**, 141–156 (2013).
29. Seward, T. M. & Kerrick, D. M. Hydrothermal CO_2 emission from the Taupo Volcanic Zone, New Zealand. *Earth Planet. Sci. Lett.* **139**, 105–113 (1996).
30. Frondini, F. et al. Carbon dioxide degassing from Tuscany and Northern Latium (Italy). *Glob. Planet. Change* **61**, 89–102 (2008).
31. Müller, R. D. et al. Ocean basin evolution and global-scale plate reorganization events since Pangea breakup. *Annu. Rev. Earth Planet. Sci.* **44**, 107–138 (2016).

32. Brune, S., Williams, S. E., Butterworth, N. P. & Müller, R. D. Abrupt plate accelerations shape rifted continental margins. *Nature* **536**, 201–204 (2016).
33. Şengör, A. M. C. & Natal'in, B. A. Rifts of the world. *Geol. Soc. Am. Spec. Pap.* **352**, 389–482 (2001).
34. Kagoshima, T. et al. Sulphur geodynamic cycle. *Sci. Rep.* **5**, 8330 (2015).
35. Kelemen, P. B. & Manning, C. E. Reevaluating carbon fluxes in subduction zones, what goes down, mostly comes up. *Proc. Natl Acad. Sci. USA* **112**, E3997–E4006 (2015).
36. Berner, R. A. The rise of plants and their effect on weathering and atmospheric CO_2. *Science* **276**, 544–546 (1997).
37. Zeebe, R. E. & Caldeira, K. Close mass balance of long-term carbon fluxes from ice-core CO_2 and ocean chemistry records. *Nat. Geosci.* **1**, 312–315 (2008).
38. Foster, G. L., Royer, D. L. & Lunt, D. J. Future climate forcing potentially without precedent in the last 420 million years. *Nat. Commun.* **8**, 14845 (2017).
39. Friedrich, O., Norris, R. D. & Erbacher, J. Evolution of middle to Late Cretaceous oceans—a 55 m.y. record of Earth's temperature and carbon cycle. *Geology* **40**, 107–110 (2012).
40. Zachos, J. C. & Kump, L. R. Carbon cycle feedbacks and the initiation of Antarctic glaciation in the earliest Oligocene. *Glob. Planet. Change* **47**, 51–66 (2005).
41. Kent, D. V. & Muttoni, G. Modulation of Late Cretaceous and Cenozoic climate by variable drawdown of atmospheric pCO_2 from weathering of basaltic provinces on continents drifting through the equatorial humid belt. *Clim. Past* **9**, 525–546 (2013).
42. Lefebvre, V., Donnadieu, Y., Goddéris, Y., Fluteau, F. & Hubert-Théou, L. Was the Antarctic glaciation delayed by a high degassing rate during the early Cenozoic? *Earth Planet. Sci. Lett.* **371**, 203–211 (2013).
43. Elsworth, G., Galbraith, E., Halverson, G. & Yang, S. Enhanced weathering and CO_2 drawdown caused by latest Eocene strengthening of the Atlantic meridional overturning circulation. *Nat. Geosci.* **10**, 213–216 (2017).
44. Ernst, R. E. *Large Igneous Provinces*. (Cambridge University Press, Cambridge, 2014).
45. Dessert, C. et al. Erosion of Deccan Traps determined by river geochemistry: impact on the global climate and the $^{87}Sr/^{86}Sr$ ratio of seawater. *Earth Planet. Sci. Lett.* **188**, 459–474 (2001).
46. Cao, W., Lee, C.-T. A. & Lackey, J. S. Episodic nature of continental arc activity since 750 Ma: a global compilation. *Earth Planet. Sci. Lett.* **461**, 85–95 (2017).
47. Ebinger, C. & Scholz, C. A. in *Tectonics of Sedimentary Basins* (eds Busby, C. & Azor, A.) 183–208 (John Wiley & Sons, Chichester, 2011).
48. Lee, H. et al. Incipient rifting accompanied by the release of subcontinental lithospheric mantle volatiles in the Magadi and Natron basin, East Africa. *J. Volcanol. Geotherm. Res.* https://doi.org/10.1016/j.jvolgeores.2017.03.017 (in the press, 2017).
49. McKenzie, N. R. et al. Continental arc volcanism as the principal driver of icehouse–greenhouse variability. *Science* **352**, 444–447 (2016).
50. Mills, B., Daines, S. J. & Lenton, T. M. Changing tectonic controls on the long-term carbon cycle from Mesozoic to present. *Geochem. Geophys. Geosyst.* **15**, 4866–4884 (2014).
51. Raymo, M. E. & Ruddiman, W. F. Tectonic forcing of late Cenozoic climate. *Nature* **359**, 117–122 (1992).
52. Donnadieu, Y., Goddéris, Y., Ramstein, G., Nédélec, A. & Meert, J. A. 'Snowball Earth' climate triggered by continental break-up through changes in runoff. *Nature* **428**, 303–306 (2004).
53. Goddéris, Y., Donnadieu, Y., Le Hir, G., Lefebvre, V. & Nardin, E. The role of palaeogeography in the Phanerozoic history of atmospheric CO_2 and climate. *Earth-Sci. Rev.* **128**, 122–138 (2014).
54. Fischer, T. P. Fluxes of volatiles (H_2O, CO_2, N_2, Cl, F) from arc volcanoes. *Geochem. J.* **42**, 21–38 (2008).

Acknowledgements

We thank D. Royer for publicly sharing the R script of GEOCARBSULF and R. Ernst for kindly providing the data on large igneous provinces. This research has been funded by the German Academic Exchange Service (DAAD), Project 57319603. S.B. was supported through the Helmholtz Young Investigators Group CRYSTALS (VH-NG-1132). S.E.W. and R.D.M were supported by Australian Research Council grant IH130200012.

Author contributions

S.B. and S.E.W. developed the analytical workflow. S.B. conducted the numerical models. S.B., S.E.W. and R.D.M. discussed and integrated the results. The manuscript was written by S.B. with contributions from all authors.

Competing interests

The authors declare no competing financial interests.

Additional information

Supplementary information is available for this paper at https://doi.org/10.1038/s41561-017-0003-6.

Reprints and permissions information is available at www.nature.com/reprints.

Correspondence and requests for materials should be addressed to S.B.

Methods

Tectonic reconstruction of continent-scale rifts. Our plate kinematic rift database has been described in a previous publication focusing on rift velocity evolution during continental breakup[32]. The database derives from analysing a kinematic model of global plate tectonics[31], which in turn incorporates many regional tectonic reconstructions. This global plate model is constructed such that it incorporates the full length of extended margins formed during Pangaea fragmentation in a self-consistent framework, including the incorporation of major intracontinental rift systems that are required to reconcile the pre-rift configuration of west Gondwana. Evidence for detailed plate kinematics at continental rifted margins and failed rifts is often hidden beneath several kilometres of sediments and water, and recent efforts to build full-fit plate tectonic reconstructions incorporating a wealth of new geophysical, geological and geochronological data provide powerful constraints on the full rift history from inception to breakup and seafloor spreading[55–59].

To infer the rift length history, we first define present-day oceanward borders of rigid, continental polygons through the location of continent–ocean boundaries (COBs). The continental polygons are then reconstructed back to their pre-rift position using a global plate reconstruction model[31]. Lithospheric stretching during continental rupture generates new surface area, which is why reconstructed polygons overlap in areas that have been rifting since the start time of the model. Stepping forward in time, we discern continental breakup at a specific location when there is no overlap of plate polygon segments anymore. This allows us to calculate the length of a rift system at any given time by simply integrating the length of divergent plate boundaries with overlapping polygons. Note that this workflow does not require any assumptions about initial crustal or lithospheric thickness and that it is independent of the existence of previous rift phases.

The COB definitions are subject to a number of uncertainties (see ref. [32] for a more detailed discussion); here, we use polygons based on a more oceanward interpretation amongst plausible COB locations, with the implication that alternative COB locations would lead to earlier breakup in the associated rift and so reduce the presented rift lengths. We have updated our COB data set[32] to include some of the more poorly constrained rifts that were omitted before, so that we are now able to provide a complete global description of continental rifting within the kinematic reconstructions. Updates to the polygon geometries include some margins of the Indian Ocean where little information is available to constrain the extent of continental crust robustly. First, we incorporated the complex region of the West Somali and Mozambique basins that formed through oblique rifting between East Africa and Madagascar. According to seismic reflection profiles[60], the extent of continental basement offshore East Africa may be more than 200 km oceanward than previously supposed[61]. Second, for the Gulf of Aden, we modified the COBs where seismic data are not available according to recent interpretations[62,63]. Third, south of Madagascar, we follow previous studies[64,65] in assuming that parts of the Madagascar Rise south of Madagascar, and the Gunnerus Ridge are continental in origin. Even though this is not conclusively demonstrated by geological or geophysical data, it avoids unlikely gaps that would otherwise appear in the reconstructed configuration of the Gondwana continental mass prior to the onset of rifting.

Geological rift record. Many intracontinental rifts do not lead to continental breakup and formation of an ocean basin and are therefore often not explicitly incorporated in global kinematic reconstructions. However, their extent and time of activity can be deduced in geological field studies and has been compiled in a global database comprising 568 individual rifts[33]. Here, we quantify the contribution of these rifts to global rift length and associated CO_2 degassing estimates in 1 Myr intervals since 200 Ma. Note that the tabulated values in the compilation of Şengör and Natal'in[33] include a number of characteristics for each rift that must be addressed to make them suitable for a quantitative analysis, and a number of caveats apply to their interpretation, as described in the next three paragraphs.

For both rift length and width, in some cases the maximum value is quoted, in some cases an average, and in some cases a range. Where a range is given, we use the largest value; hence, the total rift length at any given time in our plots is the maximum rift length permissible by the values in the table.

The ages for which each rift is active are defined through stratigraphic time ranges, typically through names of periods, epochs or ages for which a formal definition exists. In some cases, the minimum or maximum age is quoted with a question mark, for example, 'early? Miocene'; in which case we ignored the question mark and use the name directly. Instead of featuring explicit start and end times, most rift ages are given by one stratigraphic time range. In this case, we assumed that the rift was active from the beginning of this time range until its end. Note that the table contains many rifts that have been active relatively recently (for example, Miocene, Neogene) and where the time range does not extend to present day. In some cases, time ranges are defined using names with no standard definition (for example 'earliest Jurassic'), in which case we used early in place of earliest. In general, where ages are to some extent ambiguous, we erred on the side of preserving a larger age range, such that the rift length in our plots may include rifts that were not in fact active. We thus regard the deduced rift length as a maximum estimate. In Fig. 1b where we have plotted rift locations, the colour assigned to the rift symbol is taken as the mid-point within the age range determined by the method outlined above.

In the geographic plot of the geological rift record (Fig. 1b), the rift location is determined from the centre of the bounding box given in the source table, and the orientation of the rift is taken as the average angle from the range of orientations quoted. For example, if the rift orientation is given as 'N,NW', we use a symbol with azimuth of 337.5, centred on the middle of the bounding box, and with a length matching the rift length determined as described previously. We corrected a few minor inconsistencies in the locations and orientations of basins given by Şengör and Natal'in[33]. Specifically, we updated the longitude of the Hornsund and Møre basins and changed the orientation of the Orange and Walvis basins. This does not affect the rift length summation but does influence the locations at which these rifts are plotted in Fig. 1b.

The corresponding table can be found as a csv file in the Supplementary Information together with an overview map of all rifts. In Fig. 2b, we plot the rift length history that is solely derived from our analysis of the Şengör and Natal'in rift database[33]. As their compilation is based only on field geological evidence, it lacks some rifts that can be inferred from plate tectonic considerations. For example, the northwestern passive margin of Africa is known to be the conjugate of the western US continental margin, yet it is not represented in Şengör and Natal'in[33], presumably because no studies existed at the time of compilation. The same problem occurs for the Antarctic, East Australian, East African and South East Greenland margins. We account for this problem by combining the geological rift database[33] with our reconstruction-based rift length analysis (Fig. 2a). In order to not include some rifts twice, we ignore the entries from the rift database[33] that overlap with rifts from the plate reconstruction. Those rifts that remain in this analysis are marked with black outlines in Fig. 1b.

Carbon cycle modelling. Carbon cycle models evaluate the long-term transfer of carbon between Earth's surface (atmosphere, biosphere, soils and oceans) and the rock reservoirs. Here we employ GEOCARBSULFvolc[4,66,67], which for convenience we refer to as GEOCARBSULF. The R code of this model is available at http://droyer.web.wesleyan.edu/links.htm. This model is based on reconstructions of key sinks and sources through geological time that are each based on estimates from the geologic record[68] with additional constraints from an isotopic mass balance[69]. Focusing on time scales on the order of ~10 Myr, it is assumed that the surficial reservoirs are in steady state. GEOCARBSULF accounts for carbon sinks via burial of organic carbon, chemical weathering of Ca–Mg silicate minerals and formation of carbonate rocks. Carbon sources are weathering of sedimentary organic carbon and release of carbon through metamorphism, diagenesis and volcanism.

In this study, we employ the tectonic degassing parameter f_{SR} to introduce rift-related CO_2 degassing to the model. This parameter was previously used to account for mid-ocean ridge volcanism assuming proportionality to the seafloor spreading rate. Apart from changing f_{SR}, we adopt all other input parameters such as ACT = 0.09, NV = 0.0075, LIFE = 0.25, GYM = 0.875 and FERT = 0.4 from the reference model[4]. We tested the influence of NV on our results, a coefficient that relates physical erosion to the mean $^{87}Sr/^{86}Sr$ of non-volcanic silicate rocks. NV is poorly constrained and variations between 0 and 0.015 are possible[66]. We explored this parameter range and find that the largest effect occurs for Mesozoic peak amplitudes, but these amplitudes never exceed 25% with respect to our reference rift models C1 and C2 and do not affect our conclusions. For a detailed error analysis of GEOCARBSULF, including a variation of all input parameters, see ref. [4].

Plate boundary length. We compute the total lengths of different plate boundary types using pyGPlates and the gpml files provided as part of the continuously closing plate polygons[31]. At each time snapshot, the geometries of resolved topological plate boundaries can be extracted and subdivided on the basis of their assigned type (for example 'subduction zone' or 'mid-ocean ridge'). GPlates has the ability to resolve individual plate boundary segments shared between different plates, from which the total lengths of different types can be summed (as described at https://www.gplates.org/docs/pygplates/sample-code/pygplates_find_total_ridge_and_subduction_zone_lengths.html). Plate boundary segments are prone to subtle topological errors that result in the same segment being counted twice. Hence, we validated our estimates using an alternative summation in which we iterate through each plate polygon at every time step and sum the total length of different plate boundary types, such that all plate boundaries are deliberately counted twice (each plate boundary should be shared by two plates, whether or not the topological segments are exactly correct). Dividing this value by two yields robust estimates of total plate boundary length from a topological plate polygon set. During the computation of mid-ocean ridge length from the plate model, we need to distinguish between ridge and transform segments using the stage pole describing the relative plate kinematics for each time snapshot. We thereby assume that transform segments are parallel to the local spreading direction, with a threshold of 20 degrees from parallel[70]. Sample code illustrating this operation in more detail can be found at https://www.gplates.org/docs/pygplates/sample-code/pygplates_split_isochron_into_ridges_and_transforms.html). For better comparability to the long-term CO_2 trends, we present all plate boundary lengths in Fig. 4a binned to 10 Myr intervals. In doing so, we capture the long-term trend and for a discussion of subduction length on a shorter time scale refer to a recent study[71], where a previous global plate model[72] has been analysed.

Data availability. The data supporting the findings of this study are available within the article and Supplementary Information.

Code availability. The code used for the carbon cycle modelling is GEOCARBSULFvolc[4,66,67], and is available at http://droyer.web.wesleyan.edu/links.htm. The software used to reconstruct plate boundary lengths is pyGPlates and can be downloaded from https://www.gplates.org/download.html.

References

55. Williams, S. E., Whittaker, J. M. & Müller, R. D. Full-fit, palinspastic reconstruction of the conjugate Australian-Antarctic margins. *Tectonics* **30**, TC6012 (2011).
56. Kneller, E. A., Johnson, C. A., Karner, G. D., Einhorn, J. & Queffelec, T. A. Inverse methods for modeling non-rigid plate kinematics: Application to mesozoic plate reconstructions of the Central Atlantic. *Comput. Geosci.* **49**, 217–230 (2012).
57. Heine, C., Zoethout, J. & Müller, R. D. Kinematics of the South Atlantic rift. *Solid Earth* **4**, 215–253 (2013).
58. Hosseinpour, M., Müller, R. D., Williams, S. E. & Whittaker, J. M. Full-fit reconstruction of the Labrador Sea and Baffin Bay. *Solid Earth* **4**, 461–479 (2013).
59. Barnett-Moore, N., Müller, D. R., Williams, S., Skogseid, J. & Seton, M. A reconstruction of the North Atlantic since the earliest Jurassic. *Basin Res.* https://doi.org/10.1111/bre.12214 (in the press, 2016).
60. Klimke, J. & Franke, D. Gondwana breakup: no evidence for a Davie Fracture Zone offshore northern Mozambique, Tanzania and Kenya. *Terra Nova* **28**, 233–244 (2016).
61. Müller, R. D., Sdrolias, M., Gaina, C. & Roest, W. R. Age, spreading rates, and spreading asymmetry of the world's ocean crust. *Geochem. Geophys. Geosyst.* **9**, 18–36 (2008).
62. Autin, J. et al. Continental break-up history of a deep magma-poor margin based on seismic reflection data (northeastern Gulf of Aden margin, offshore Oman). *Geophys. J. Int* **180**, 501–519 (2010).
63. Fournier, M. et al. Arabia-Somalia plate kinematics, evolution of the Aden-Owen-Carlsberg triple junction, and opening of the Gulf of Aden. *J. Geophys. Res.* **115**, B04102 (2010).
64. Eagles, G. & König, M. A model of plate kinematics in Gondwana breakup. *Geophys. J. Int* **173**, 703–717 (2008).
65. Reeves, C. The position of Madagascar within Gondwana and its movements during Gondwana dispersal. *J. Afr. Earth Sci.* **94**, 45–57 (2014).
66. Berner, R. A. Inclusion of the weathering of volcanic rocks in the GEOCARBSULF model. *Am. J. Sci* **306**, 295–302 (2006).
67. Berner, R. A. Addendum to 'Inclusion of the Weathering of Volcanic Rocks in the GEOCARBSULF Model' (R. A. Berner, 2006, V. 306, p. 295–302). *Am. J. Sci.* **308**, 100–103 (2008).
68. Berner, R. A. *The Phanerozoic Carbon Cycle: CO_2 and O_2.* (Oxford University Press, Oxford, 2004).
69. Berner, R. A. GEOCARBSULF: A combined model for Phanerozoic atmospheric O_2 and CO_2. *Geochim. Cosmochim. Acta* **70**, 5653–5664 (2006).
70. Bird, P., Kagan, Y. Y. & Jackson, D. D. in *Plate Boundary Zones* (eds Stein, S. & Freymueller, J. T.) 203–218 (American Geophysical Union, Washington, D. C., 2002).
71. Zahirovic, S., Müller, R. D., Seton, M. & Flament, N. Tectonic speed limits from plate kinematic reconstructions. *Earth Planet. Sci. Lett.* **418**, 40–52 (2015).
72. Seton, M. et al. Global continental and ocean basin reconstructions since 200 Ma. *Earth-Sci. Rev.* **113**, 212–270 (2012).